Damage sensitivity of Groningen masonry structures – Experimental and computational studies

Stream 1

Korswagen Eguren, Paul; Longo, Michele; Meulman, Edwin; van Hoogdalem, C.A.

Publication date
2017

Document Version
Final published version

Citation (APA)
Korswagen Eguren, P., Longo, M., Meulman, E., & van Hoogdalem, C. A. (2017). *Damage sensitivity of Groningen masonry structures – Experimental and computational studies: Stream 1*. Delft University of Technology.

Project number C31B69
File reference C31B69WP0-12
Date 30th of December 2017
Corresponding author p.a.korswageneguren@tudelft.nl

Damage sensitivity of Groningen masonry structures – Experimental and computational studies

STREAM 1 - REPORT

Authors:
Paul Korswagen, Michele Longo, Edwin Meulman, Carlijn van Hoogdalem

Cite as: Korswagen, P., Longo, M., Meulman, E., Van Hoogdalem, C. (2017). Damage sensitivity of Groningen masonry structures – Experimental and computational studies. Report number C31B69WP0-12, Final report, version 1.2, 30th of December of 2017.

This research work was funded by Nederlandse Aardolie Maatschappij B.V., who is gratefully acknowledged. Any opinion, finding, and conclusion or recommendation expressed in this report are those of the authors and do not necessarily reflect the view of the funding body.

TU Delft

I. Summary

1800 words (5 minutes)

To observe the influence of frequent, light earthquakes on minor, aesthetic damage (DS1) to masonry structures in Groningen, the project "Damage sensitivity of Groningen masonry structures – Experimental and Computational studies" - first phase, has been conducted by TU Delft on behalf of NAM. The goal is to investigate the phenomena of crack initiation and propagation in masonry for light earthquakes with an in-depth look into crack patterns, crack widths, and the effect of repetitive and combined loadings.
In this first phase, the case of a sample masonry wall has been leading. The single-wythe wall was built with clay bricks and cement mortar replicating masonry of the period before 1950 in the Netherlands (Figure I.1).

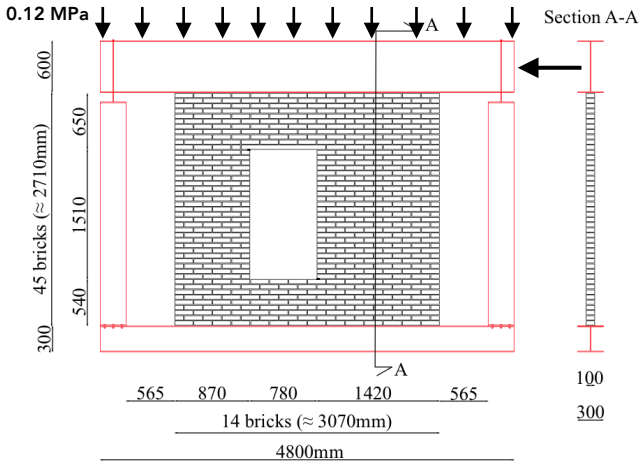

Figure I.1. (1.1) Dimensions of the in-plane solid clay wall with asymmetric window opening.

Since the focus is on mostly minor, visible damage, cracking has been selected as a measure of damage for masonry walls. A new damage level parameter (Ψ) has been proposed such that the narrowest visible cracks with a width of 0.1mm result in a value of around one (Ψ=1), slightly larger cracks of close to 1mm correspond to two (Ψ=2) and cracks of approximately 4mm give a value of three (Ψ=3). This range has been defined as DS1.
The evaluation of this parameter however, includes the number of cracks, the crack width, and the crack length with a mathematical expression that objectively quantifies damage. This allows for the direct damage evaluation of computational results using finite elements, and of laboratory experiments using Digital Image Correlation (Figure I.2).

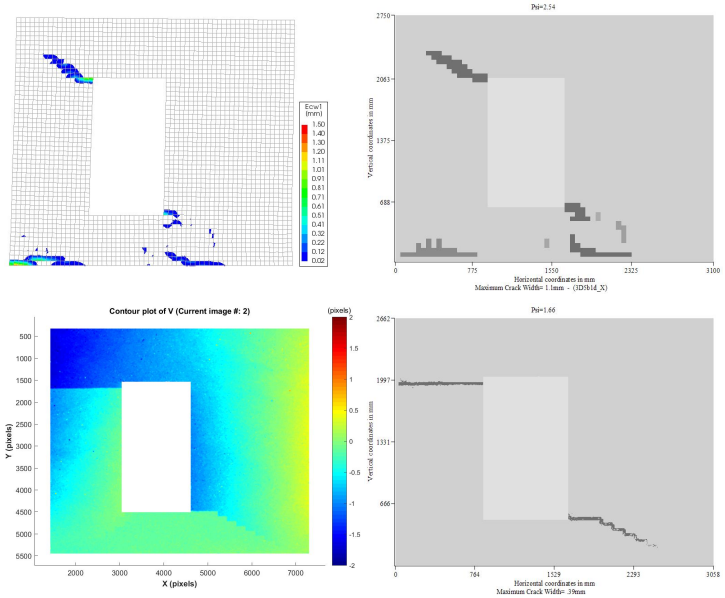

Figure I.2. (2.13) Examples of analyses with the damage assessment program for numerical output (top) and DIC output (bottom). The former corresponds to shrinkage damage followed by earthquake damage and results in a value of Ψ=2.5, while the latter computes to Ψ=1.7 due to a lateral top displacement of the wall of 2mm (Wall TUD-COMP-40, Test 79, Record 1075).

Smeared, continuum, anisotropic computational models were run to formulate predictions prior to laboratory testing and with a view to design the tests and incremental, repetitive loading schemes. The predictions indicated a maximum lateral shear of 20kN and a maximum crack width of 0.6mm for a quasi-static application of a top lateral displacement of 0.7mm (Figure I.3).

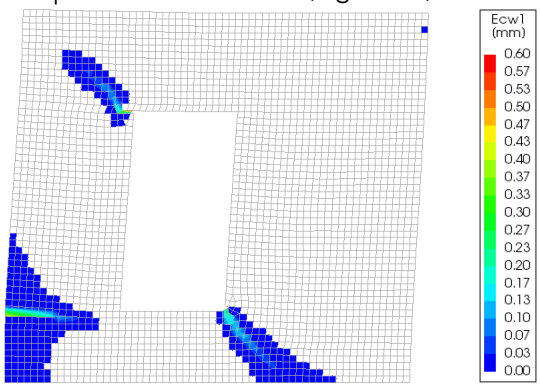

Figure I.3. (3.8) Final damage pattern of the in-plane wall in terms of principal crack width with the prediction computational model.

Then, three specimens of the wall were assayed in the laboratory with a repetitive one direction static loading condition. The crack patterns observed were similar to the predictions (Figure I.4). Five increasing sets of equal top lateral displacement were applied with 3, 10 or 20 repetitions per set. Cracks developed progressively up to a width of almost 0.7mm for a top lateral displacement of 2.2mm (drift of 0.83‰) in the case of one representative specimen (Figure I.5, left). The maximum shear force was 22kN. The repetitions in each set revealed a minor, yet visible force reduction, mainly in the first repetitions of a set, and the largest reduction was found in the set with the lateral displacement closest to the peak load capacity of the wall. In some cases, this reduction corresponded to up to 3.5% (Figure I.5, right) and was also accompanied by an increase in notch opening displacements of up to 6%.

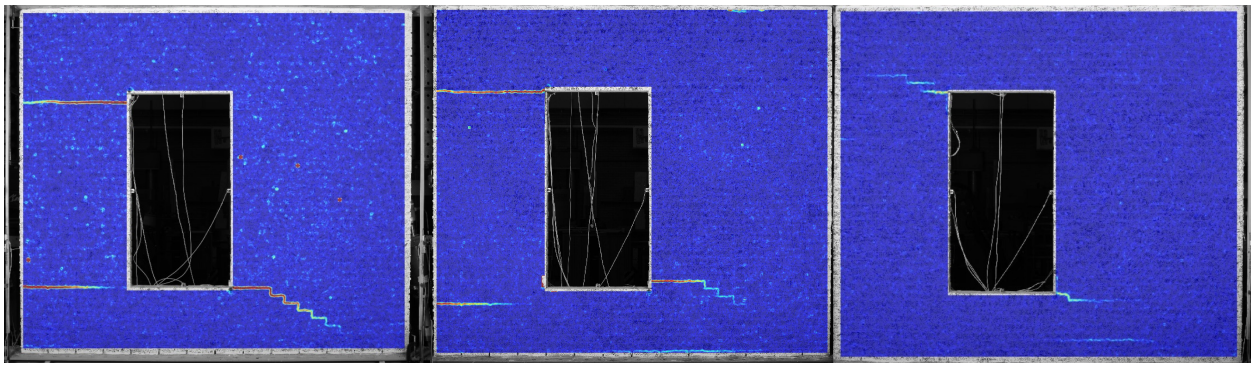

Figure I.4. (4.54) Strain plots of repetition R5 of TUD_COMP-40, TUD_COMP-41 and TUD_COMP-42.

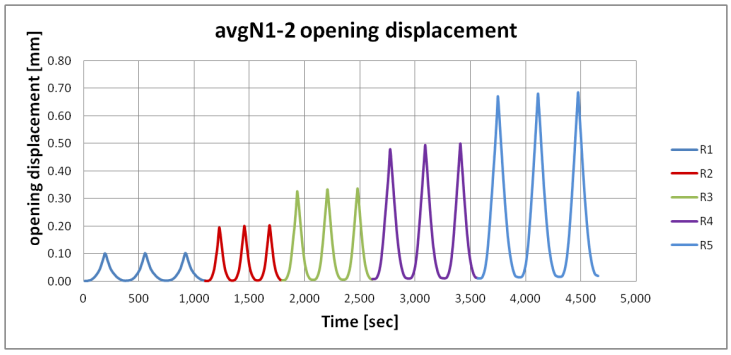

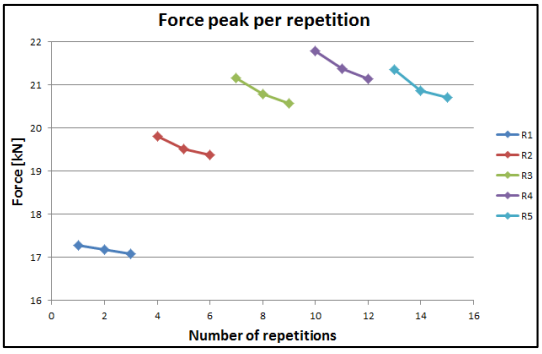

Figure I.5. (4.8) Left: Average crack opening displacement at bottom-right and top-left corner of window. (4.12) Right: Force peak per repetition.

Complementary to the wall, laboratory experiments included tests of window banks (Figure I.6). These had the goal of closely monitoring the propagation of vertical cracks in bending, and were performed monotonically and repetitively. Here, the reduction in force was up to 22% as average of seven specimens. It was also observed that the force reduction after approximately 10 repetitions of the same mid-span displacement, significantly decreased and appears to become stable (Figure I.6, right).

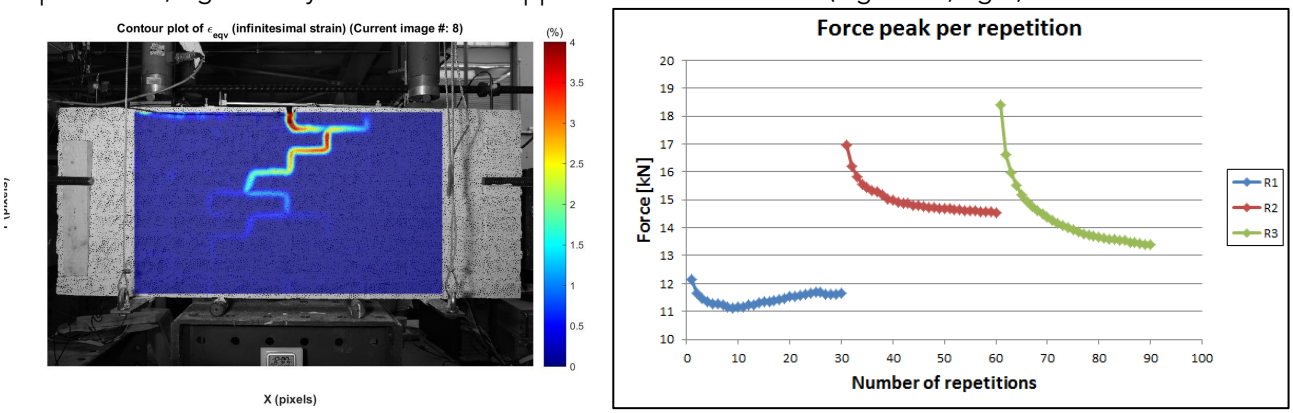

Figure I.6. (4.73) Left: DIC strain plot of sample TUD_MAT-50J.
(4.86) Right: Force vs number of repetitions of sample TUD_MAT-50M.

The prediction computational models were then improved based on the experimental results to include the observed degradation and better reflect the stiffness and crack width. A smeared, continuum Engineering Masonry Model, recently developed by TU Delft and DIANA FEA was chosen. Further calibrating the material parameters and including the bottom steel beam in the models allowed for results consistent with the experiments (Figure I.7 and Figure I.8). While the hysteresis of the experiments is well represented, the observed degradation has not yet been included in the material model.

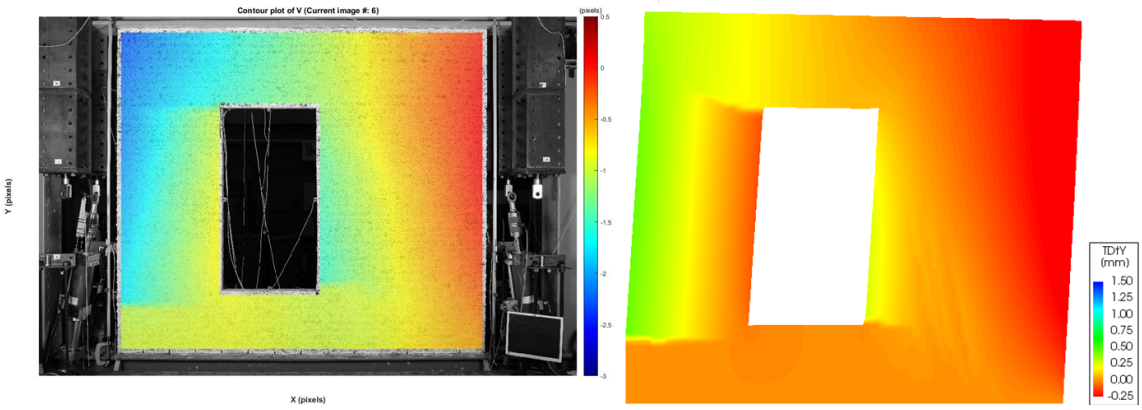

Figure I.7. (5.9) TUD_COMP-41: R4a. Horizontal displacement comparison between (left) DIC related to experimental record number 16764 and (right) FEM post-test. Model deformed shape magnified by 100.

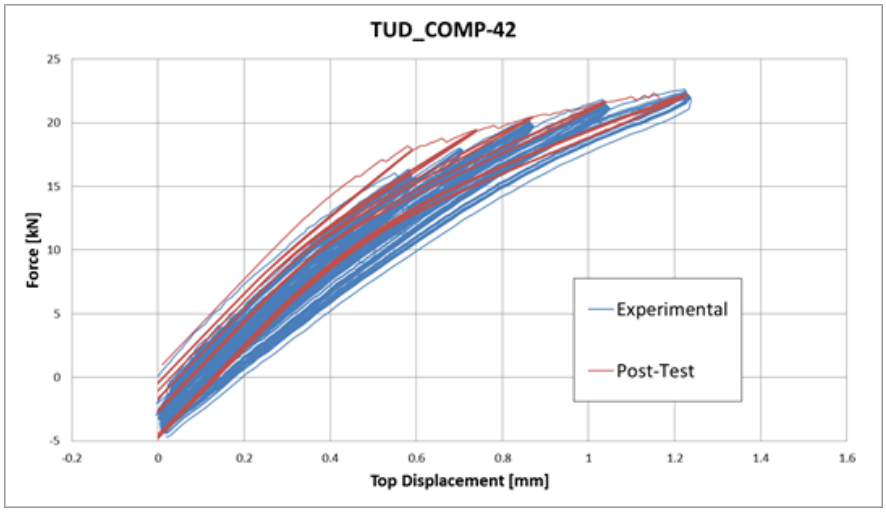

Figure I.8. (5.15) TUD_COMP-42: experimental and FEM post-test force-displacement curve.

The improved models were then extrapolated to multiple scenarios which are difficult to perform in the laboratory. These are: a) earthquake excitation at the base (Huizinge of 2012); b) earthquake followed by another earthquake; c) sagging settlement damage followed by the earthquake; and, d) hygro-thermal shrinkage damage followed by the earthquake. The goal was to observe the cracking behaviour and assess the influence of the pre-damage on the final cracking patters and its intensity, after an earthquake (Figure I. 9).

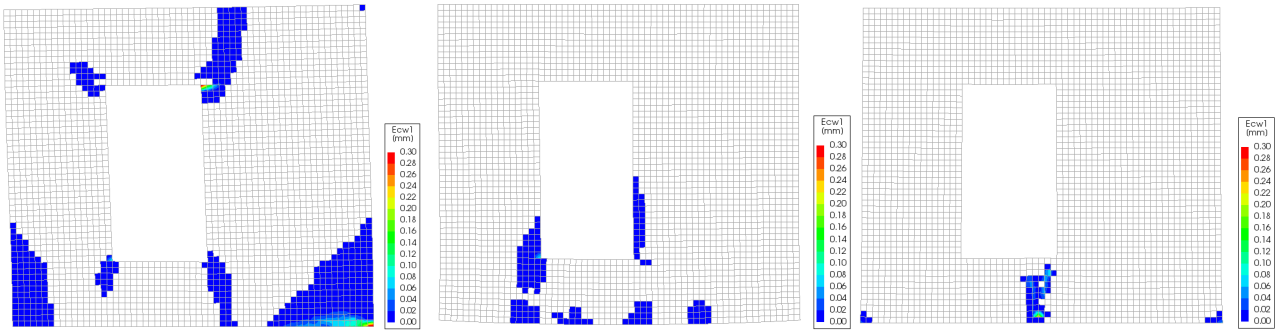

Figure I.9. (6.12) Crack width plots related to the moment of maximum pre-damage for: (a) pre-earthquake (0.17g), (b) 5mm settlement, (c) 0.4‰ shrinkage. Deformed shape magnified by 100.

It was observed that earthquake pre-damage consisted of cracks in all four corners of the window, settlement pre-damage consisted of multiple cracks underneath the window and in the two bottom corners of the window, and shrinkage pre-damage involved a single vertical crack in the window bank.
Cracks from the settlement pre-damage case appear to grow the most, followed by cracks from the earthquake pre-damage scenario, and finally the shrinkage case (Figure I.10).

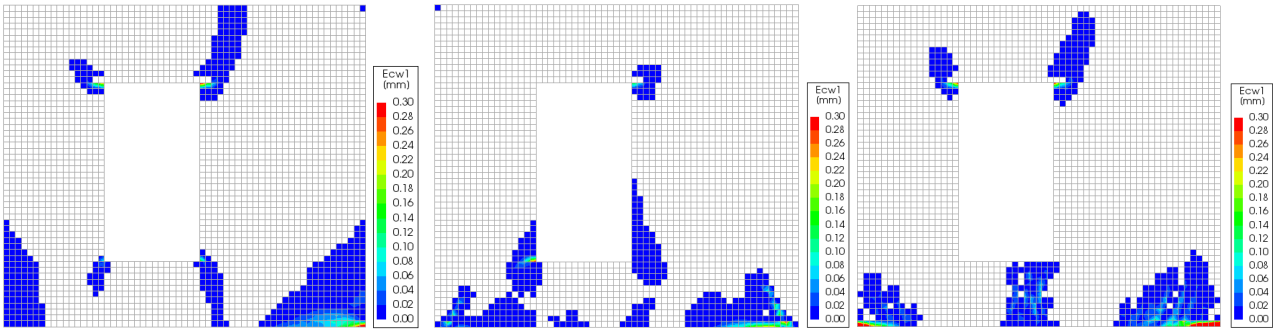

Figure I.10. (part of 6.13) Cumulative crack width plots for standard material at the end of 0.10g motion for different initial conditions: (a) pre-earthquake (0.17g), (b) 5mm settlement, (c) 0.4‰ restrained shrinkage. Undeformed mesh.

Non-linear, time-domain analyses were run on models for different intensities of pre-damage, followed by varying earthquake intensities. Moreover, a standard, weak, and strong version of the material was used; as anticipated, the cases with weaker material experienced more damage than the ones with the stronger material.

The results from the scenario analyses were subsequently used to establish a relationship between the quality of the material, the level of pre-damage, the intensity of the earthquake, and the final value of damage as evaluated with the damage level parameter (Ψ). Based on this regressed relation obtained from the more than 100 extrapolated models, a MonteCarlo simulation was run to compute the probabilities of damage against values of peak ground velocity (PGV) for this single masonry wall (Figure I.11 and Figure I. 12).
Curves developed for DS1 by other authors appear to fit well in the range of $1<\Psi<3$ (Figure I.13).

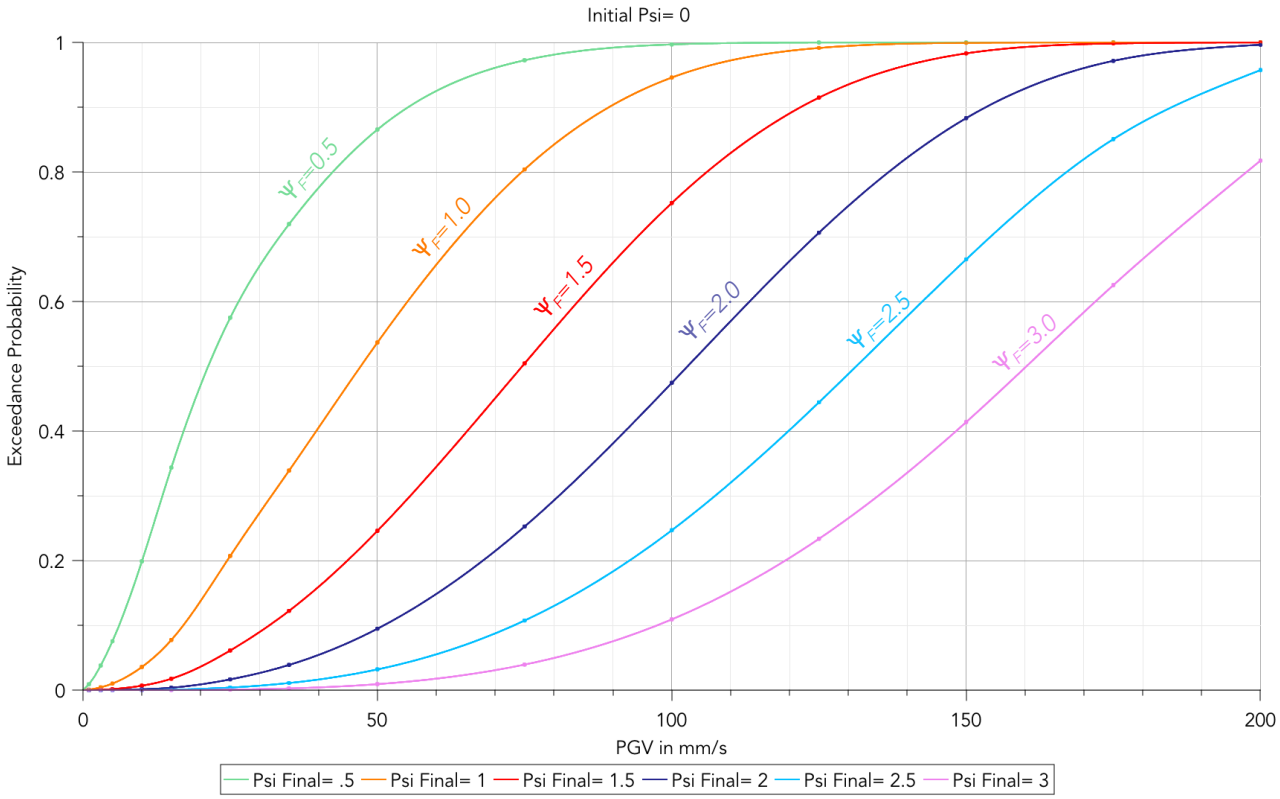

Figure I.11. (7.20) Indicative resistivity curves for computational wall results for zero initial damage, Ψ_0=0 against PGV.

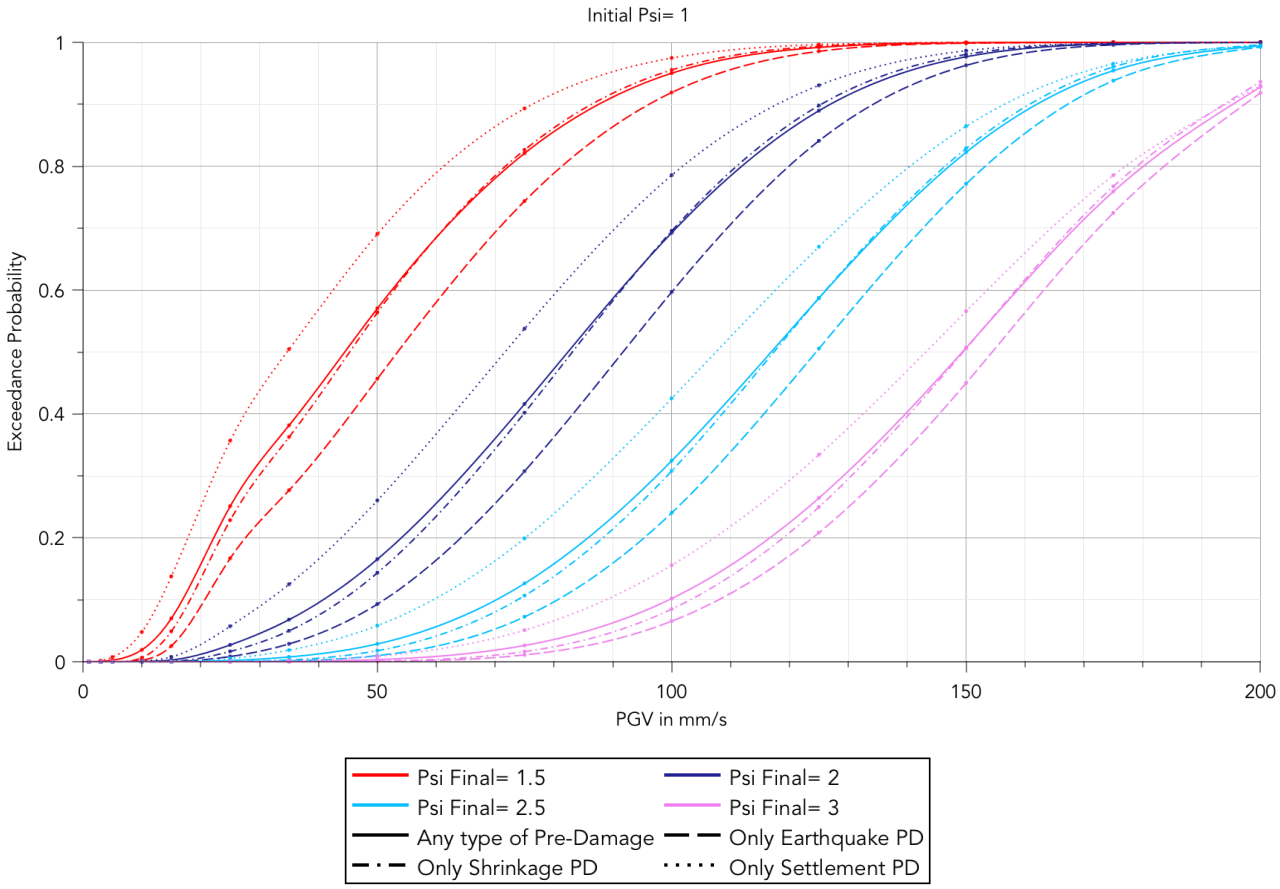

Figure I.12. (7.22) Indicative resistivity curves for computational wall results for some initial pre-damage Ψ_0=1.0 against PGV. Showing also the difference between pre-damage types.

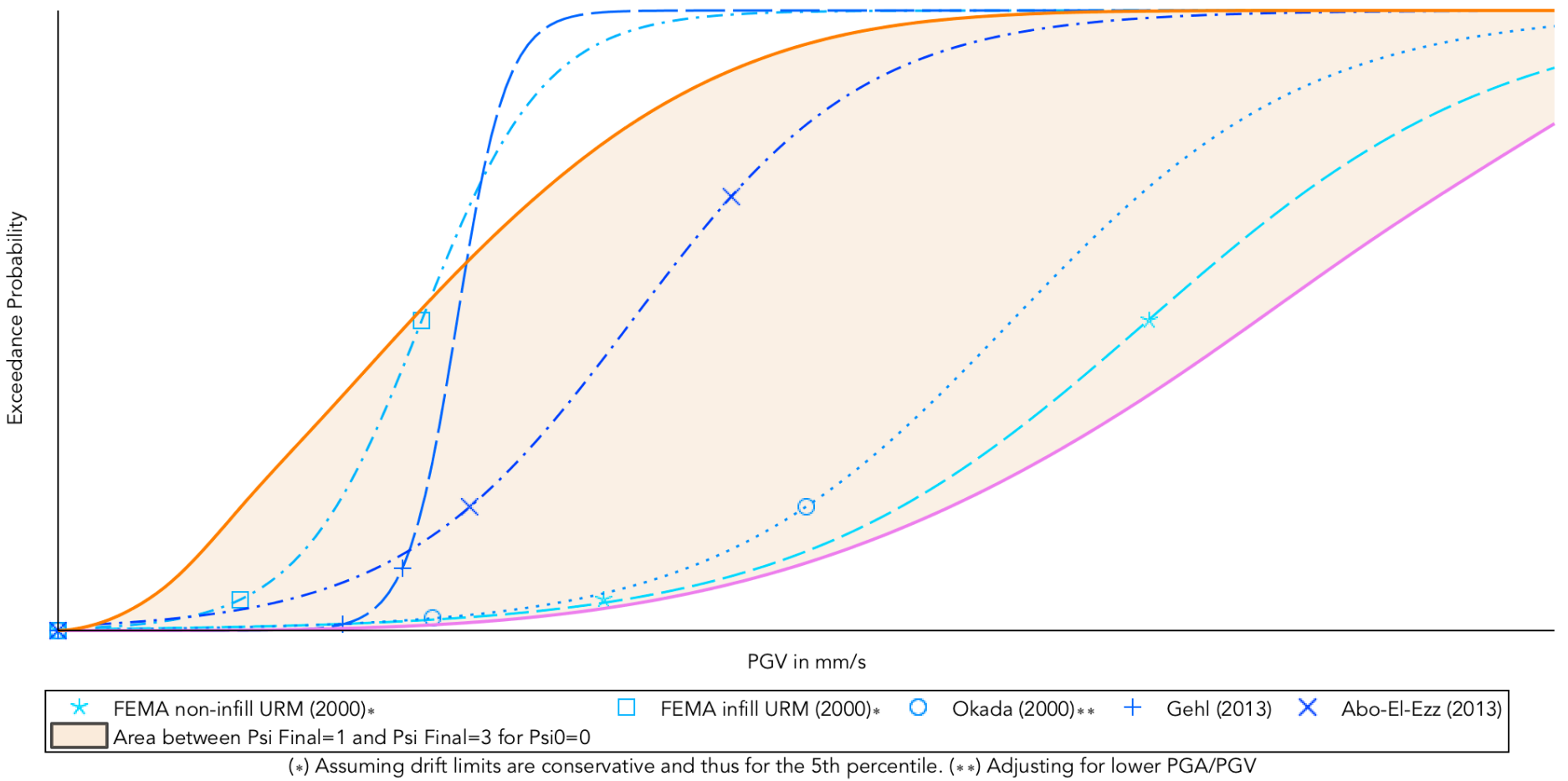

Figure I.13. (7.25) Comparison with curves and points for DS1 from various authors. According to the definition for the damage level of this study, depending on the structure, DS1 starts between Ψ=1 and Ψ=3: the shaded area. Indicative Resistivity curves for computational results for Ψ_0=0 against PGV for these two values are shown.
Note that the comparison curves are log-normal S-curve fits to a few available points and that their behaviour away from the marked points may differ.

From these indicative curves, it can be observed that while the probability for entering DS1 is high (Ψ>1), that is, cracks of 0.1mm are likely, the probability of exceeding DS1 (Ψ>3) is low.
However, it should be realised that this holds for the specific case of this particular in-plane wall with a window and three leading cracks.

Table I.1. Interest values read from the indicative resistivity curves.

Intensity	p($\Psi \geq 1$)		p($\Psi \geq 3$)	
	Ψ_0=0	Ψ_0=0.5	Ψ_0=0	Ψ_0=0.5
5 mm/s	1.5%	<1%	≈0%	≈0%
20 mm/s	15%	30%	<1%	<1%
48 mm/s	50%	75%	5%	<5%

Ψ_0 is the initial damage value and Ψ is the final damage level.

Additionally, low pre-damage seems to reduce the probability for further damage for low levels of vibrations, which is in line with experimental results where the propagation of cracks occurs mostly in the first few repetitions of a certain displacement and appears to become stable when many more repetitions are applied.

The Light Damage Framework (LDF) proposed combines a quantitative damage definition with experimentally validated non-linear models. As such, it serves as an improvement of the linear, onset-of-cracking based framework of Waarts (1997) for walls. It offers a true quantification of the observable damage into discrete levels, the possibility for inclusion of prior damage, and earthquake time-history analyses.
Conceptually, the LDF opens up a perspective to assess damage and its aggravation for light earthquakes. However, as like the framework of Waarts, the LDF is currently filled by results from the analysis of only one wall detached from its interaction with an entire structure, and with constrained material characteristics. Additionally, it is based on a limited number of quasi-statically tested laboratory specimens.

Accordingly, in a future phase of the project, these limitations could be overcome by extending tests to different geometries, pre-damaged samples, different materials, and out-of-plane effects; and complement the quasi-static tests with dynamic tests on a shaking table to gain more knowledge about the crack initiation and propagation in masonry.
The experimental tests could and will also be used to improve the constitutive models like the Engineering Masonry model and micro brick-to-brick interface models, specifically, to include the observed degradation. The additional experimental tests and numerical models of different geometries and damage scenarios would then serve as an enriched and extended input for the extension and improvement of the damage framework and resistivity curves for the light damage.
Moreover, since the already-tested walls are only lightly damaged and have been stored, they can be reused for future testing: additional repetitions could be applied as was done for the window bank test, and eventually, the walls could be tested to the near-collapse state.

II. Table of Contents

I. Summary I

II. Table of Contents 8

1. Introduction 2

1.1. Scope and Outline of Research 2

1.2. Limitations of This Study 3

1.3. Study Case 4

2. Damage in Masonry and its Assessment 6

2.1. Introduction 6

2.2. About the Fundamentals of Cracking in Masonry 7

2.3. Damage in Masonry 11

2.3.1. Damage due to Cracking 12

2.3.2. Damage due to Failure Mechanisms Other Than Cracking 13

2.3.3. The concepts of Initiation and Cumulation of Damage 14

2.4. Quantitative Measure of Damage via Cracks 15

2.4.1. Sub-scale of Damage Levels Within Damage States 15

2.4.2. Proposal for the Evaluation into One Parameter (Ψ) 16

2.4.3. Limitations of the One Parameter Approach 19

2.5. Notes on the Perception and Transitoriness of Damage 20

2.5.1. The Perception of Damage 20

2.5.2. Transitory Damage 22

2.6. Application of the Damage Parameter to Experimental and Computational Results 23

2.6.1. Digital Image Correlation and Experimental Results for Damage Analysis 23

2.6.2. Output of Computational Results for Damage Analysis 24

2.6.3. Direct Assessment of the Damage Parameter 25

2.7. Conclusions of Chapter Two 27

3. Preliminary Computational Models to Define Tests 30

3.1. Introduction 30

3.2. Specimen Description 31

3.3. Finite Element Model Description 32

3.4. Results from the Blind Prediction 36

3.5. Conclusions of Chapter Three 40

4. Experimental Tests 42

4.1. In-plane Wall Tests 43

4.1.1. Sample Descriptions 43

4.1.2. TUD_COMP-40 45

4.1.3. TUD_COMP-41 56

4.1.4. TUD_COMP-42 67

4.1.5. Comparison TUD_COMP-40, TUD_COMP-41 and TUD_COMP-42 78
4.2. Window Bank Test 84
4.2.1. Sample Description 84
4.2.2. Monotonic Tests 87
4.2.3. Repetitive 95
4.3. Discussion and Limitations of the Experimental Tests 103
4.4. Conclusions of Experimental Tests 105
5. Validation and Calibration of Computational Models 108
5.1. Introduction 108
5.2. Refined In-Plane Wall Post-Test Analysis (Post-Diction) 108
5.2.1. Prediction model versus Experimental Results 108
5.2.2. Update to the Prediction FEM 112
5.2.3. Results of the Post-test Model 116
5.2.4. Mesh Objectivity 124
5.3. Conclusions of Chapter Five 128
6. Computational Models for Resistivity Curves 130
6.1. Introduction 130
6.2. Model Description 131
6.2.1. Geometry 131
6.2.2. Input Ground Motions 132
6.2.3. Static Versus Dynamic Condition 135
6.2.4. The Effect of the Vertical Component of the Motion 136
6.3. Pre-damage Scenarios 138
6.4. Model Results 141
6.5. Conclusions of Chapter Six 148
7. Probabilistic Framework Towards Resistivity Curves 150
7.1. Introduction 150
7.2. Background: Reproduced Framework of Waarts (1997) 151
7.2.1. Description of the Framework of Waarts 151
7.2.2. Limitations of the Framework of Waarts 153
7.2.3. Reproduction of the Framework of Waarts 154
7.2.4. Comparison and Discussion 155
7.3. General Overview of the Light Damage Framework 157
7.3.1. Overview and Description of the Framework and its Elements 157
7.3.2. Actions: Frequent Earthquakes and Secondary Actions 160
7.4. Indicative Resistivity Curves from Computational Models 167
7.4.1. Expanded Computational Models and Their Results 168
7.4.2. Regression of the Results from EC Models 170

7.4.3. Figures of Indicative Resistivity Curves from Computational Models 173
7.4.4. Discussion of the Computational Resistivity Curves 178
7.5. Resistivity Curves from Experimental Tests 179
7.5.1. Results and Regression from the Experimental Tests 180
7.5.2. Parameters and Single Degree of Freedom Model for Experimental RCs 183
7.5.3. Figures of Experimental Resistivity Curves 186
7.5.4. Discussion of the Experimental Resistivity Curves 188
7.6. Discussion of Computational and Experimental Curves 192
7.6.1. Comparison between Computational and Experimental Curves 192
7.6.2. Limitations of the Resistivity Curves of this Report 194
7.7. Conclusions of Chapter Seven 196
8. Conclusions and Recommendations **198**
8.1. Conclusions 198
8.2. Recommendations 200
References **201**
9. Appendix **ii**
9.1. List of Figures and Tables iii
9.2. Companion Tests xii
9.3. Nomenclature xiii
9.3.1. Symbols xiii
9.3.2. Abbreviations xvi
9.4. Abaqus Modelling xviii
9.4.1. Discussion: Modelling with Abaqus/Explicit xviii
9.4.2. Constitutive Models xxii
9.4.3. Calibration & Examples xxv
9.4.4. Prediction Models xxxi
9.4.5. Post-diction Models - Window Bank xxxiii
9.4.6. Conclusions of Explicit Modelling with Abaqus xxxvi
9.5. Experimental Pre-compression Test Results xxxvii
9.6. Program to Analyse Damage xxxviii

Chapter 1

Introduction

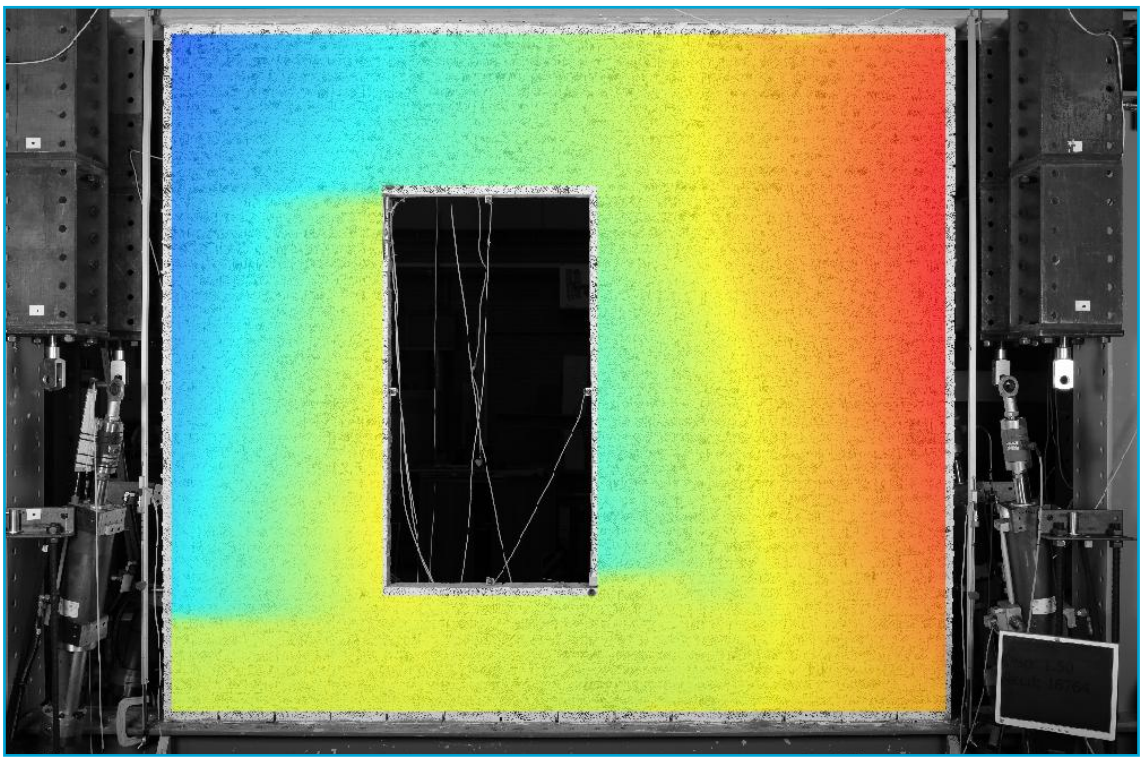

TU Delft

1. Introduction

1.1. Scope and Outline of Research

International research for tectonic earthquakes and recent national research for the case of gas-induced Groningen earthquakes have focused on near-collapse limit states or ultimate limit states of unreinforced masonry structures. However, the lower damage states corresponding to serviceability limit states for frequent, light earthquakes, potentially in combination with existing damage, appear to be relevant and influential in the assessment of building damage and societal impact, but have not yet been studied intensively.

Consequently, the TU Delft project of "Damage Sensitivity of Groningen Masonry Structures-Computational and Experimental Studies" was started in December of 2016 in order to investigate the behaviour of unreinforced masonry structures in the lower damage states.

Structures are subjected to a myriad of natural and anthropogenic phenomena that result in damage of all levels. Common phenomena such as daily or seasonal temperature changes subject structures to stresses that result in minor, mostly unobservable damage which has been tackled by proper design of the structures. Conversely, less frequent phenomena such as heavy storms may result in observable and directly attributable damage to these structures. Minor earthquakes may also damage structures in a way that is hardly observable at first but may become more visible after repeated loading. This is a complex physical interaction that instils the question:

How do frequent, light earthquakes contribute to the initiation and cumulation of (light) damage to masonry structures of the Groningen area?

To answer this question it is first necessary to define damage. Light damage commonly attributed to earthquakes takes the expression of cracking: fissures in masonry walls that run mostly along the joints and which may affect the durability, aesthetics, structural safety, and perhaps most prominently, the perception of damage and safety of the structure. Chapter 2 explores the types of damage in unreinforced masonry structures and proposes a method for categorising it quickly, objectively, and quantitatively. The concepts of initiation of cracking and damage, as well as its propagation or cumulation are also treated here.

Chapter 3 introduces numerical (computational) models to replicate masonry and attempt to predict the damage and its patterns as the effect of various actions. Various models for crack initiation and crack propagation are proposed and applied to specific walls and window banks. Based on these predictive analyses, a set of experimental laboratory tests have been designed.
Chapter 4 details the nature of these laboratory tests. The tests serve as validation and calibration for the models. The experimental campaign explores questions about the behaviour of masonry, such as: the conditions for the initiation of cracking, its propagation, its aggravation under repetitive and cyclic actions, and the cumulation of damage. The experimental results are pursued in detail, including crack patterns, crack width, and results from Digital Image Correlation techniques.

Based on the findings of laboratory experiments, Chapter 5 calibrates the computational models, and Chapter 6 extrapolates them to situations that were not possible in the laboratory. Here, the damage resulting from the combination of actions such as settlements and earthquakes is investigated.

Then, Chapter 7 briefly analyses the framework of Waarts (1997) and introduces a Light Damage Framework as an improvement. It proceeds to summarise the effects that have been observed to contribute to damage in connection with earthquakes and processes the results from Chapters 4 and 6 in order to fabricate fragility-like curves. These indicative curves incorporate the uncertainties of the partaking parameters in

order to output damage probabilities for various levels given an intensity of ground vibration due to earthquakes.

This study is a first exploration into light damage in masonry; as such, its scope is limited: to help understand the fundamentals of light damage, the analyses have been focused on one, simple, but still representative case of a wall with an opening. Moreover, out-of-plane effects have not been considered. A future research phase will incorporate these additional complexities starting off from the results of this first study.
These limitations and the featured case of a wall with an opening are introduced in the next sections.

1.2. Limitations of This Study

This report deals with the first phase of a detailed study into light damage to masonry caused by frequent, light earthquakes. To be able to successfully draw conclusions from the phenomena observed, the report focuses on the case of damage due to in-plane stresses for masonry representative of old, baked-clay, unreinforced masonry, extrapolated from the result of one representative 2D wall geometry (see next subchapter).

As such, it does **not** observe:

- Entire structures,
- Out-of-plane and 3D stress effects, such as T, U or box (□) configurations that carry 3D stress situations,
- Varying geometry configurations, such as opening dimensions, or wall slenderness,
- Loading rate for slow processes such as settlement,
- Potential strengthening measures.

Nevertheless, the results aim to be the most representative of the situation in the field; and, in the future, the aforementioned topics may need to be addressed as well.

It is emphasised that the results of this report, in particular the resistivity curves presented in Chapter 7, are based on models calibrated (Chapter 5) with a limited number of experimental tests on a particular geometry of masonry walls constructed from a single type of material (Chapter 4), and extrapolated to additional scenarios (Chapter 6), including a single, albeit representative, earthquake signal. These curves are also based on a new damage definition (Chapter 2).
Therefore, care needs to be exercised when extrapolating observations from this report to cases differing from the ones treated here.

Additionally, while the effect of load repetition is part of this study, fatigue is not addressed in its traditional definition. Fatigue is a weakening of the material by means of thousands or millions of load cycles occurring before the material has reached its (tensile) strength. In masonry, micro-cracks appear early and the elasticity of the material is lost, even though a pseudo-elastic behaviour can be observed in a macro sense. These cracks may grow (and become visible) when subjected to tens or hundreds of load repetitions, mimicking the behaviour of fatigue. The material degradation following from this non-elastic loading of relatively few cycles is observed in this study (see Section 4.2).

1.3. Study Case

To exemplify damage in masonry and its progress, a wall with one window has been taken as the leading case for this study. The material of the wall has been selected to be representative of the buildings in Groningen. The reader is referred to Meulman et al. (2017) for a full description of the selected masonry material, the study case and the aim of the experimental tests. Below, the aim of the experimental tests is captured within three bullet points. In the test protocol (Meulman et al., 2017) and in the introduction of Chapter 4, the aim of the experimental tests is described in more detail.

- When does cracking start? That is, under which strain, strength, stress configuration or structural displacement does this occur?
- When do cracks propagate and/or widen, and which types of cracks propagate under what conditions?
- Do repetitive actions foster the propagation of cracks?

The dimensions of the wall (see Figure 1.1) have been selected to coincide with previously tested walls in order to be able to realise laboratory experiments in a constrained time frame by using the available equipment. The wall was chosen to be single-wythe, as opposed to the double-wythe type more representative of old masonry, with the purpose of making the surveillance of cracking easier and minimising 3D stress effects.

Further, the dimensions of the window and its position were selected to produce an asymmetric situation that evidenced the differences between various loading types, as well as to concentrate the initiation of damage around the corners of the window such that its measurement was more easily accomplished. Additionally, from some damage cases analysed, it was observed that damage usually starts around windows. Moreover, it would seem that walls with little overburden are also more likely to be damaged. Hence, these conditions have been selected.
After applying the overburden, the wall is subjected to shear by controlling the horizontal displacement at the top, which produces a typical crack initiation and propagation process.

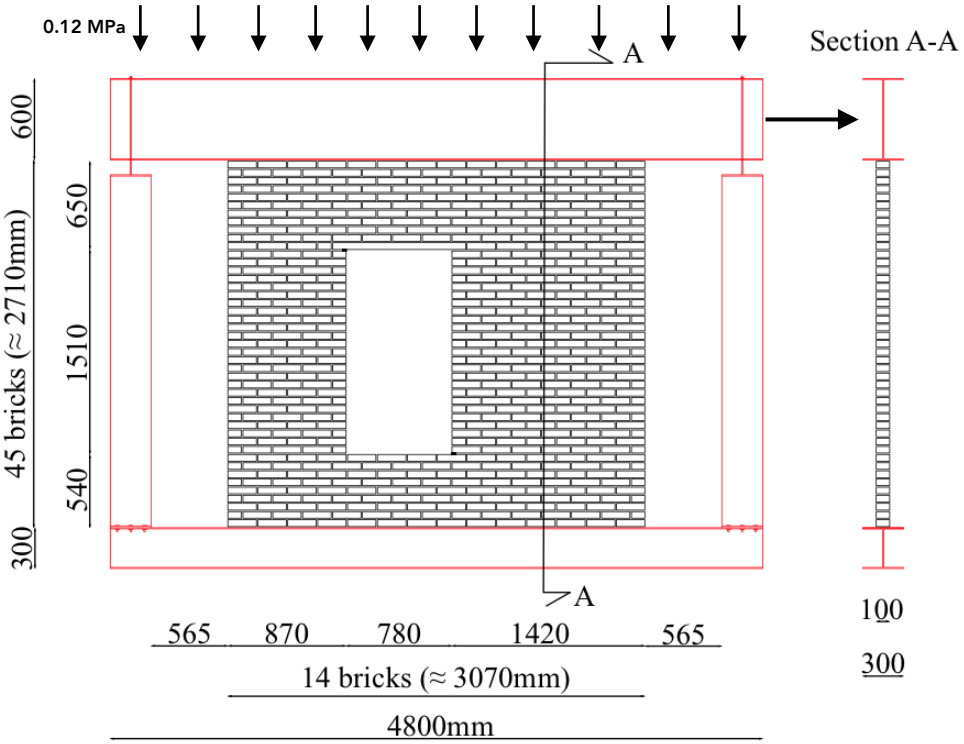

Figure 1.1 Dimensions of the in-plane, solid-clay wall with asymmetric window opening.

Chapter 2

Damage in Masonry and its Assessment

TU Delft

2. Damage in Masonry and its Assessment

2.1. Introduction

In general, any state deviating from the original state or the intended state of a structure can be categorised as damage. The deviating state can be a direct result of a particular action on a structure or its components. Loss of strength due to cracks in walls, crushing of bricks or loss of elements, as well as loss of section due to chemical action or freezing, or high distortions due to creep behaviour or overloading, are all examples of damage in masonry.

When observing minor levels of damage, strategies developed for near-collapse or ultimate limit states like surveying if there is a severe loss of strength or excessive distortion of the structure do not help to identify the small increase in damage. Additionally, these expressions of damage may not be readily detectable or are difficult to assess by an inexperienced observer or inspector.
Cracking, on the other hand, the occurrence of cracks and fissures on or through walls and other elements, is easily observable and directly relatable to some degree of damage. Moreover, earthquakes are commonly observed to cause cracking.
Consequently, in this study, the evaluation of damage for lower degrees of damage will be limited to the expression of cracks resulting from stresses on the structure. No cracks corresponds to no damage, a few small cracks to very light damage, and bigger cracks to more intense damage.

Nonetheless, even if a clear expression of damage is set (cracking, for instance) the quantitative evaluation of the damage remains unclear. It is thus necessary to categorise the diverse expressions and intensities of cracking into damage categories and be able to quickly and objectively quantify and compare the intensity of damage between different cases or for different actions.

In other words, it is paramount to formulate a strict definition of damage. Many studies, news bulletins and other reports mention damage without a clear indication of what damage actually is and what intensity of damage is meant; the interpretation of damage is thus subjective: for some, “damage” is regarded as intense while for others, negligible.

First, however, this chapter covers the fundamentals of cracking in a review that attempts to set the stage for how damage is assessed in this research project. The behaviour of masonry when fracturing and the current knowledge regarding this phenomenon is detailed and the areas where understanding is limited are highlighted.
Next, damage as a result of cracking is presented, followed by a proposal for objectively measuring this damage. Then, the subjectivity of measuring damage is argued with a scheme to assess the difference between perceived, actual, and transitory damage.
Finally, the proposal for a measure of damage via a single parameter is complemented with a description of the implementation of a direct and objective method for computing this damage parameter in this study. The procedure runs fully parallel for experiments and future simulations.

Key questions that follow are thus:
- What is cracking in masonry?
- What is damage, and in particular, how does it manifest itself in masonry?
- How can damage be measured?
- How is damage measured and quantified in this study and what parameters are relevant for this?

2.2. About the Fundamentals of Cracking in Masonry

Cracks occur when the maximum tensile stress of the material is exceeded. For ductile materials, a large amount of deformation and distortion can occur before a crack develops, generating a space between two new (external) surfaces in the material. It can be noted that since, the stress-strain relationship up to the peak strength is almost elastic, meaning that the maximum stress criterion complies with a maximum strain criterion.

For (quasi-) brittle materials, such as unreinforced masonry, the maximum tensile strain is near the maximum elastic strain, meaning that shortly after reaching the maximum tensile strength, a crack will form suddenly, without warning prior to it. (Almeida et al., 2012). Additionally, because of this extremely low ductility pre-peak, cracks can also appear in shear of compressive zones, where the conjugated stress direction is in tension. In comparison to ductile materials, brittle ones exhibit no hardening in tension, that is, a stress higher than the maximum elastic stress is not possible and the material exhibits a post-peak "softening" in the stress-strain relation (Hillerborg, 1985). This means that cracks are unstable: If a crack initiates, the load applied to (the fracture surface of) the material needs to be reduced otherwise the crack will rapidly "snap" through the entire section (Rots et al., 1997). Figure 2.1 illustrates this fundamental difference between ductile and brittle materials. It is worth noting that perfectly brittle materials have a theoretical softening region of zero, while quasi-brittle materials have a "longer" softening curve; since the point of transition between perfectly and quasi-brittle materials is subjective, the materials are here denoted as simply brittle. Masonry and concrete are also known as elastic-softening materials, implying that the strains localise into a crack, while the material at either side of the crack unloads elastically (e.g. Rots, 1985). Micro-cracks coalesce into a visible macro-crack.

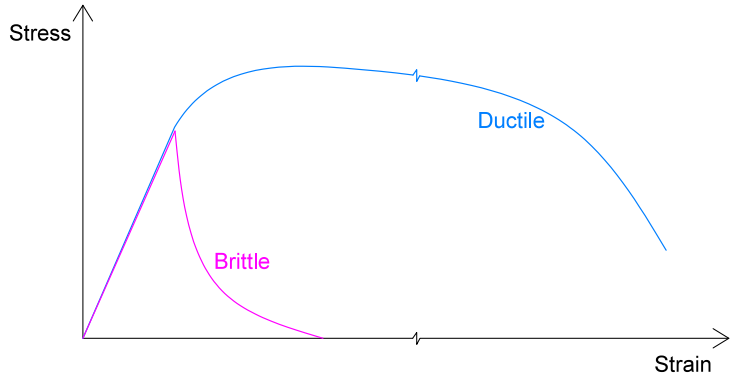

Figure 2.1. Tension stress-strain diagram illustrating the behaviour difference between ductile (plastic, hardening) and brittle (with softening, i.e. quasi-brittle) materials.

Unreinforced masonry is a heterogenous, composite material consisting of bricks and mortar. Cracks in masonry can develop through the bricks, the mortar, or at the interface between mortar and brick (see Figure 2.2); all three possibilities behave in a brittle manner. This means that masonry is extremely susceptible to cracking.

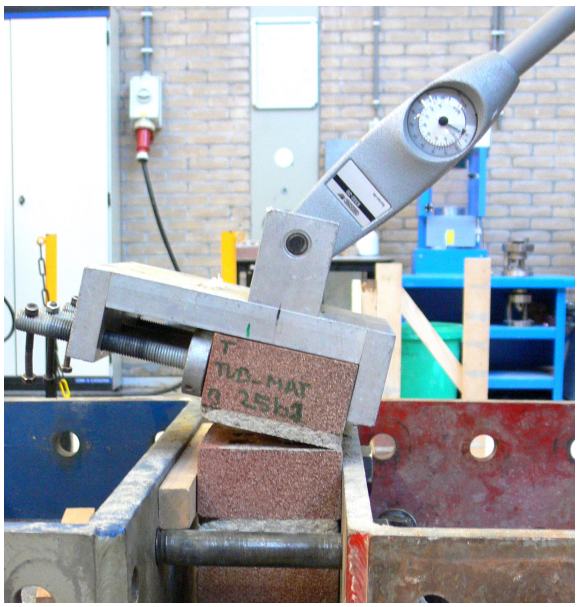

Figure 2.2. Photography of a bond-wrench test showing a clean debonding occurring at the interface between brick and mortar.

Settlements, for instance, cause cracking in masonry and the stresses are relieved once the newly developed crack has allowed the structure to accommodate to the settlement. Similarly, contraction and expansion due to environmental temperature changes, may also lead to cracks which relieve the stresses caused by these actions. Other loads of a dynamic nature, such as vibrations or earthquakes, also produce transient tensile stresses which trigger cracking in masonry. Unless these loads are extreme, cracking is focused around areas where stresses are higher and the dynamic loads cease before the cracks extend.

Sufficient literature is available on the (tensile) strength of masonry and the brittle nature of cracking, but the propagation of brittle cracking under repetitive loading appears to require additional research. Vandoren et al. (2012) also explored the initiation and propagation patterns with a computational model, but did not observe the case of repetitive loading and damage.
The propagation and growth of cracks due to repetitive loading (some dozens of applications) must not be confused with the phenomenon of fatigue, common to ductile materials and where the loss of strength is related to an internal weakening of the material due to thousands or millions of stress variations (e.g. traffic or wave loading).
In a masonry element, such as a wall, the loss of local stiffness due to an initiated crack, may be sufficient to accommodate the amplitude of the repetitive load without further cracking; or, the load progresses the crack until the failure of the entire fracture surface. Figure 2.3 demonstrates this dichotomy.
Consequently, the fundamental aspect of this research project will focus on expanding the knowledge about the propagation of cracks in masonry.

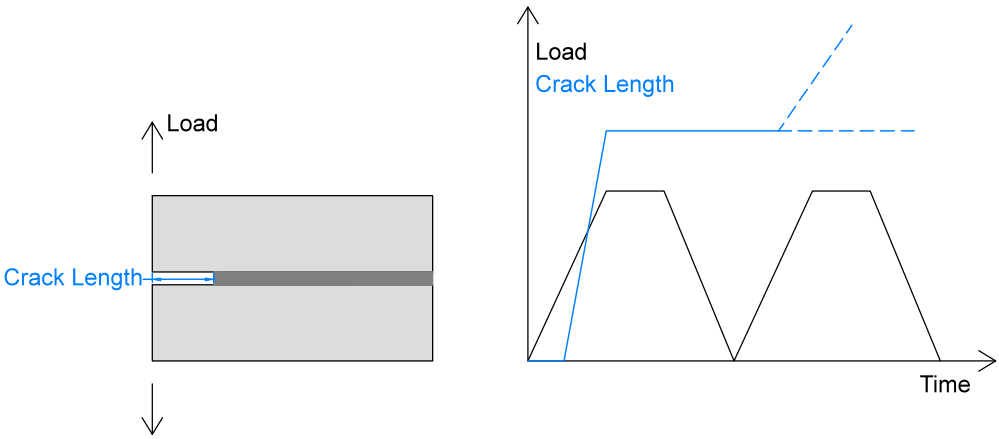

Figure 2.3. Behaviour possibilities for illustrative crack propagation when subjected to a load repetition of equal intensity.

Fracture Mechanics of Masonry

This section is a brief summary of what is known about the mechanics of fracture in masonry. For an extensive elaboration on the topic, the reader is referred to the quoted literature.

As has been mentioned, masonry is a composite material, consisting of bricks and mortar joints, which is vulnerable to brittle failure in tension (Curtin et al., 2008). In the Netherlands, masonry is commonly composed of baked clay bricks or calcium silicate bricks with cement mortar joints (e.g. de Vent et al., 2011); other configurations are possible, but are not as common. The behaviour of clay or calcium silicate bricks is nonetheless, quite similar, with the main differences relating to the size of the bricks as calcium silicate ones are sometimes much larger (blocks with thin layer joints). This can generate different crack patterns, but the mechanics of the cracks appear to be alike (Esposito et al., 2016.a).
Cracking in masonry occurs due to fracture of mortar and/or bricks or debonding of mortar and bricks. While the parameters governing these three cases are not equal, all seem to be accurately described by a brittle fracture with softening theory (CUR, 1990; Almeida et al., 2012), such as developed for concrete brittle fracture by Hillerborg et al. (1976 and 1985). The application of this theory has been executed successfully by many authors including: Červenka et al. (1998) including a mixed-mode behaviour (that is, observing the modification of shear on the fracture), or by Schneemayer et al. (2014) who observed the influence of groves on the fracture's characteristics.
The main properties of the fracture are described by a maximum tensile strength followed by a rapidly decreasing softening to zero stress when the crack is fully developed. Softening in masonry can be represented linearly, bi-linearly or exponentially (Lorenço et al., 1995; Vandoren et al., 2012; among others). The softening area can be represented with a fracture energy as a material parameter (Hillerborg et al., 1976). The fracture energy for masonry is very low, around 10N/m (Rots et al., 1997); more specific tests point out that this corresponds almost entirely to the fracture energy of the mortar alone (Almeida et al., 2012). The fracture energy of the brick is much higher, but only due to the brick's higher tensile capacity, the brittle nature of the fracture is similar. When masonry specimens are large enough (all the real cases), for light earthquakes mostly mode I (pure tension) fractures seem to be relevant. Crack directions then follow the principal tensile stress direction. The compressive stress levels and shear stress levels remain rather low compared to their strength levels, implying that mode-I tension is the dominant mechanism.
Cracks in masonry usually follow the mortar joints unless the failure mechanism forces cracks to run through bricks, as is the case when shear effects are predominant (Rots et al., 1997).

The compressive behaviour of masonry is more complex (Vermeltfoort, 2005). Here, failure occurs via the crushing of mortar, or of bricks, or spalling of mortar, or of bricks, or by instabilities. Since masonry is heterogeneous, it is particularly prone to buckling instabilities. Local instabilities also contribute to spalling. Here, compressive stresses result in high perpendicular tension stresses that cause fracture of the bricks (Ewing et al., 2004). Masonry in compression has a small hardening region before gradually softening (Lourenço, 1996). This can be modelled as following a bi-parabolic curve.
Nonetheless, the compressive behaviour of masonry is not of much relevance when observing light damage due to cracking for low-rise masonry dwellings, and as such, won't be treated further.

It is important to note that the physical properties of masonry can be divided as those of the anisotropic, heterogeneous composite, or of the individual elements that compose it (bricks, mortar and bond). In the latter case, the parameters of the head (vertical) joints or of the bed (horizontal) joints, as well as the bond between bricks and mortar in these cases, may all be different.
This makes reproducing, testing, and modelling masonry quite difficult and vulnerable to uncertainties.

Questions About the Propagation of Cracks in Masonry

Olivito et al. (2001), Grünberg et al. (2005), Reyes et al. (2008), Wang et al. (2012), and Vandoren et al. (2012) in particular, have all looked at the initiation and propagation of cracks in masonry.

All of these studies agree that: the tensile capacity of masonry is low, that the bond between bricks and mortar is the most likely place for failure, and that cracks can propagate rapidly due to the brittle nature of the bond.

From these and other studies, the path of the crack (or crack pattern), can be inferred based on the stress conditions. As such, the initiation and propagation of tensile cracks is a fairly certain phenomenon when the load and boundary configurations and material properties are known.

However, none of these studies addresses the propagation of cracks under cyclic or repetitive loading. Here, the behaviour of a crack or of a crack pattern on a wall is still unknown. Engineering judgement predicts that for repetitive increasing loading, cracks should grow, but for repetitive constant loading this is difficult to infer.

From this follow the next questions:

- When do cracks initiate in masonry?
- Do repetitive and/or cyclic loads trigger crack propagation?
  - What parameters/size-effects affect this?

2.3. Damage in Masonry

Damage can be measured as economic loss by estimating the monetary investment that is required to bring the structure back to its original or intended state, or as a measure of a parameter of structural integrity such as floor distortion, inter-story drift, amount of corrosion, crack width, etc.
For example, damage to masonry structures subjected to lateral loads can be measured based on the predicted or measured lateral deformation of the structure. The more the structure is deformed, the more damage is expected. Damage can then be categorised onto a scale consisting of various states (DS) or grades as presented in Table 2.1.

Table 2.1. Common qualitative descriptions of Damage States.

Damage		Description
DS0	**None**	No damage
DS1	**Light**	Non-structural damage only
DS2	**Minor**	Significant non-structural damage, minor structural damage
DS3	**Moderate**	Significant structural and non-structural damage
DS4	**Severe**	Irreparable structural damage, will require demolition
DS5	**Collapse**	Complete structural collapse

Considering the uncertainties, the damage to a structure can be probabilistically assigned onto the scale. For example, the Hazus Guideline by FEMA (2012) sets inter-story drift as the parameter that limits the damage state.
Nevertheless, the scale tries to express damage as how it is perceived. In this sense, the perception of damage is sometimes more important than the actual physical damage to the structure. In fact, the perception of damage, being subjective, does not necessarily correlate to the actual damage of a structure.
Additionally, there is an important difference between damage that compromises the performance and durability of the structure and damage which has no repercussions on the structure. While the former would certainly be considered as damage, the latter might be disregarded as part of the normal usage of the structure, even though the structure might display signs of damage. Particularly, damaged non-structural elements contribute to the perception of damage but are not relevant to the criteria of damage to the safety of structure.

Also, unreinforced masonry structures have never been designed with respect to the service-ability state and cracking, but only for the ULS. This contrasts with reinforced concrete structures, where cracks are controlled in the design to prevent that wide cracks allow moisture to reach and corrode the reinforcement.

2.3.1. Damage Due to Cracking

In masonry structures, the most evident expression of (the initiation of) damage are cracks and fissures on the walls and other structural elements. For the example of a lateral deformation of the structure, the width and the number of cracks on the walls will be greater for a larger deformation as shown in Figure 2.4.

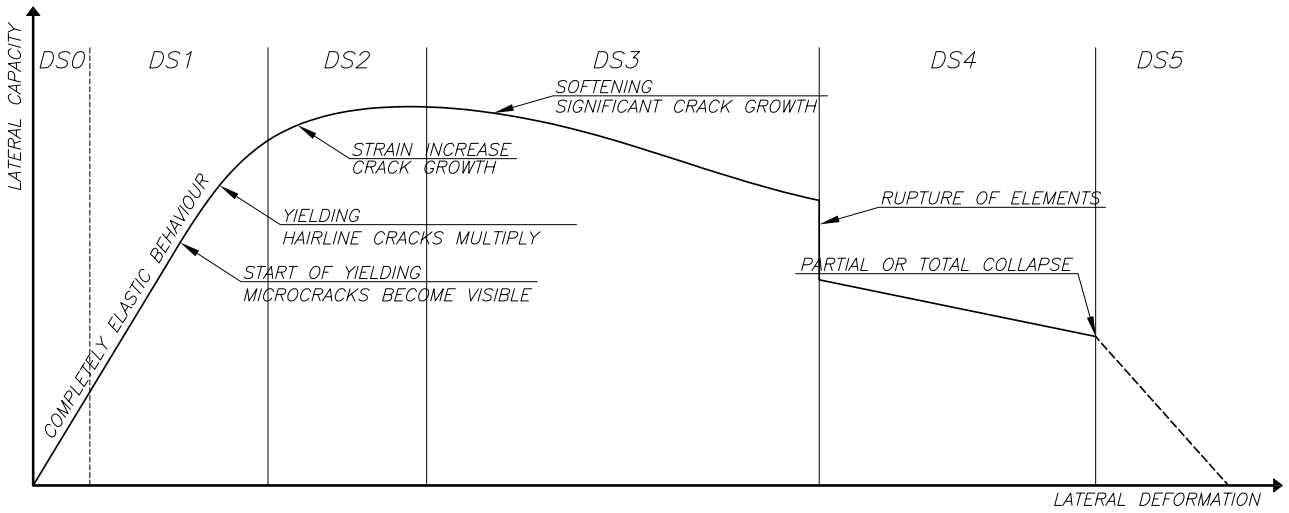

Figure 2.4. Typical lateral capacity curve related to crack characteristics.

However, when multiple actions participate in damaging the structure, a single parameter for measuring and serving for the categorisation of damage cannot be selected; additionally, the definition of the limits of the lower damage states is fuzzier, so relating these to an expression of damage is imprecise. Therefore, these cases warrant the use of the actual expression of damage as a (direct) damage parameter, that is: the crack width.

Contrary to the loss of stiffness, for instance, cracking can be both a measure and an expression of damage. For minor damage, its function as an expression of damage is particularly convenient, while, for severe damage it may not directly correlate to damage; in this case, an (indirect) measure of damage, such as inter-story drift, may prove more accurate.

Nonetheless, the use of the crack width as damage parameter allows for a higher resolution in the lower damage states and this is precisely favourable for this study as it allows a better and quantifiable look into the slow progression of minor damage.

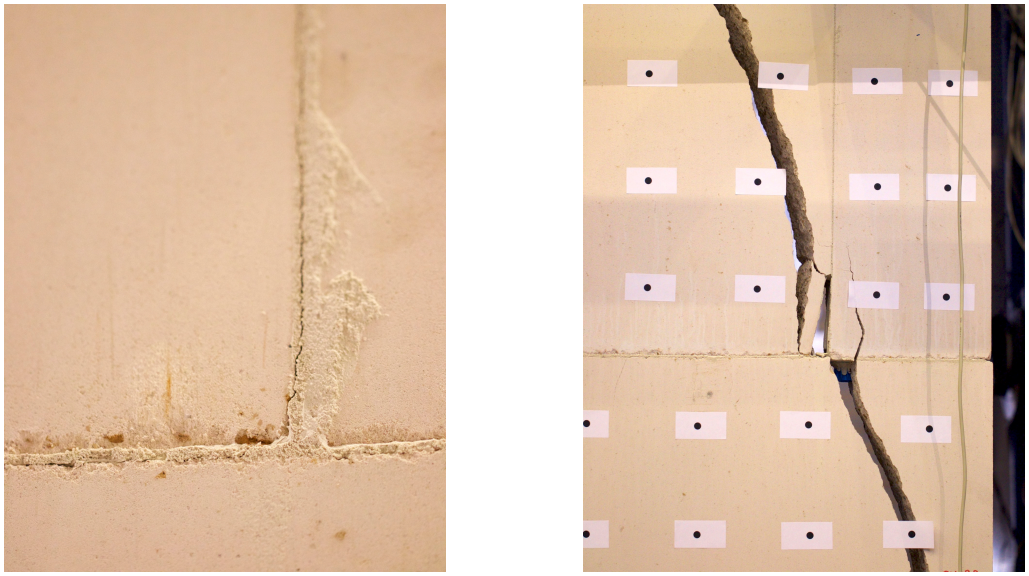

Figure 2.5. Left, Small crack, around 1mm running through the mortar between bricks, DS1, part of this study. Right, major crack running through bricks, around 25mm, DS3-DS4, not part of this study..

2.3.2. Damage Due to Failure Mechanisms Other Than Cracking

It is important to mention that damage in masonry is not limited to -nor only reflected by- cracking. Loss of section due to spalling, blistering or scaling is also common. Additionally, loss of strength due to weakening of the bond between elements or weakening of the elements themselves is another mechanism that shows damage in masonry.

Table 2.2 presents an overview (yet far from complete) of some of the relevant processes and the main expressions of damage associated with them.

Table 2.2. Expressions of damage commonly associated with various processes with mostly mechanically-based processes at the top and chemically-based processes at the bottom.

Actions / Processes	Expressions of Damage			
	Cracking	Section Loss		Internal Weakening
		Spalling/Scaling	Blistering	
Overloading	•			
Vibrations	•	•		
Earthquakes	•	•		
Wind loading	•	•		
Settlements	•			•
Thermal-hygro variations	•			•
Freeze-thaw cycles	•	•		•
Erosion by wind or water		•		
Biological (insects or animals)		•	•	•
Salt crystalisation		•	•	•
Formation of expansive compounds (including pollutants)	•	•	•	•
Dissolution and leaching		•		•
Ageing		•		•

Since earthquake actions are always related to cracking (though in some cases of severe earthquake damage, also produce spalling), only the appearance of cracks will be observed and incorporated into the damage assessment of this study.

2.3.3. The Concepts of Initiation and Cumulation of Damage

This report addresses the topic of the initiation of damage and its aggravation; hence, these concepts need to be clarified.

The initiation of damage refers to the determination of the point where damage can be considered to have started. This means that damage needs to be detectable in at least one of its expressions (see Table 2.2). Depending on the method and measure of damage considered, the threshold for the initiation of damage may then differ. Accordingly, for when cracking is used as a measure of damage, the initiation of cracking, when in relation to damage, also adopts a minimum threshold. Undetectable cracks are neglected and only when they surpass the set threshold can cracking be considered to have started.
Conversely, the initiation of (micro-)cracking, in the context of fracture mechanics, refers to the cracking strain directly after the maximum tensile stress has been reached. When observing damage, the mechanics of fracture are relevant. However, the behaviour of masonry in a micro-context, regarding fracture mechanics, has already been researched (see Section 2.2). It is the relationship to damage that requires attention.
Moreover, in a macro-context, the micro-fracture behaviour of masonry cannot be measured; here, cracks need to develop beyond the softening region of the material before they can be detected.
Hence, in this study, the initiation of cracking is related to damage. The initiation of micro-cracking is considered but not measured (see Section 4.3).

The cumulation of damage is connected to the propagation of cracks. Once cracks have started to develop, they may propagate throughout the masonry. This means that cracks become longer or branch out. Additional actions on masonry will foster cracks to propagate and widen. This represents an aggravation of the damage. If damage is not repaired, its aggravation will accumulate. When the results of multiple actions on masonry are observed, it is possible that damage has cumulated; the contribution of each action towards the final degree of damage can also be assessed.

2.4. Quantitative Measure of Damage via Cracks

Possibly, the most accurate parameter to measure cracking in unreinforced masonry is the width of the crack. It follows that, the wider the crack, the more damage has occurred. Additionally, the wider the crack, the more difficult and costly it is to repair the damage. For small crack widths, painting the wall might be sufficient, while wider cracks will require filling and much wider cracks, replacement of the units.
Consequently, it is logical to form a damage scale based on cracking, with distinctions varying according to the cost or ease of repair required.
This subchapter deals with such a damage scale and proposes a clear parameter to represent damage onto this scale.

2.4.1. Sub-Scale of Damage Levels Within Damage States

Giardina (2013.a) summaries a damage scale in which the crack width is related to an ease of repair based on the type of intervention required (see Table 2.3). On this scale, the traditional damage states can be subdivided into additional grades. This allows for a better estimation of the degradation (that is, the slowly increasing damage) of the structure. This study will mention "damage states" as rough indications of the degree of damage spread over the traditional scales from none to collapse, and "damage levels" as the finer subdivisions of these damage states, corresponding to the ease of repair.

Table 2.3. Damage scale with damage levels based on ease or repair. From Giardina (2013.a).

Category of damage	Damage		Description of typical damage and ease of repair	Approx. crack width (mm)
Aesthetic damage (DS1)	Negligible	DL1	Hairline cracks of less than about 0.1mm width.	up to 0.1mm
	Very slight	DL2	Fine cracks which can easily be treated during normal decoration. Perhaps isolated slight fracturing in building. Cracks in external brickwork visible on close inspection.	up to 1mm
	Slight	DL3	Cracks easily filled. Redecoration probably required. Several slight fractures showing inside of building. Cracks are visible externally and some repainting may be required externally to ensure water tightness. Doors and windows may stick slightly.	up to 5mm
Functional damage, affecting serviceability (DS2-DS3)	Moderate	DL4	The cracks require some opening up and can be patched by a mason. Recurrent cracks can be masked by suitable linings. Repainting of external brickwork and possibly a small amount of brickwork to be replaced. Doors and windows sticking. Service pipes may fracture. Weather-tightness often impaired.	5 to 15mm or a number of cracks > 3 mm
	Severe	DL5	Extensive repair work involving breaking out and replacing sections of walls, especially over doors and windows. Windows and door frames distorted, floors sloping noticeably. Walls leaning or bulging noticeably, some loss of bearing in beams. Service pipes disrupted.	15 to 25mm but depends on number of cracks
Structural damage, affecting stability (DS3-DS4)	Very severe	DL6	This requires a major repair involving partial or complete rebuilding. Beams lose bearing, walls lean badly and require shoring. Windows broken with distortion. Danger of instability.	> 25mm but depends on number of cracks

2.4.2. Proposal for the Evaluation Into One Parameter (Ψ)

Nonetheless, the scale presented in Table 2.3 remains subjective because the number of cracks or combination of multiple crack widths is not (and cannot be) listed such that all the cases are covered.
It is thus necessary to be able to summarise any crack pattern (a picture of damage) into one parameter which corresponds to the degree of damage and is proportionally related to the cost of repairing such damage.

Additionally, one consolidating parameter, which can be measured and observed in laboratory tests as well as computational models, will serve for a good estimation and comparison of damage. Therefore, this study proposes the use of a damage parameter Ψ_D as defined further ahead.

Table 2.4. Categorisation of DL by the result of a damage parameter.

Damage State	DS0	DS1			DS2
Damage Level	DL0	DL1	DL2	DL3	DL4
Parameter of Damage	$\Psi_D < 1$	$1 < \Psi_D < 1.4$	$1.5 < \Psi_D < 2.4$	$2.5 < \Psi_D < 3.4$	$\Psi_D > 3.5$
Aproximate Crack Width	Imperceptible cracks	up to 0.1mm	up to 1mm	up to 5mm	5 to 15mm

The parameter is proposed to be computed as follows:

$$\Psi_D = 2 \cdot n_c^{0.15} \cdot \dot{c}_w^{0.3} \tag{2.1}$$

Where:
n_c is the number of cracks in the structure
$\dot{c}_w$ is the width-weighted and length-averaged crack width (in mm) calculated with:

$$\dot{c}_w = \frac{\sum_{i=1}^{n_c} c_{w,i}^2 \cdot c_{L,i}}{\sum_{i=1}^{n_c} c_{w,i} \cdot c_{L,i}}$$

Where:
c_w is the maximum crack width along each crack in mm
c_L is the crack length in mm
For $n_c=1$, $\dot{c}_w = c_w$
In this expression, the crack width of each crack is measured at their widest point.

Figure 2.6 and Figure 2.7 give an impression of actual crack widths in relation to the damage parameter, and an example of its application can be observed in Figure 2.8.

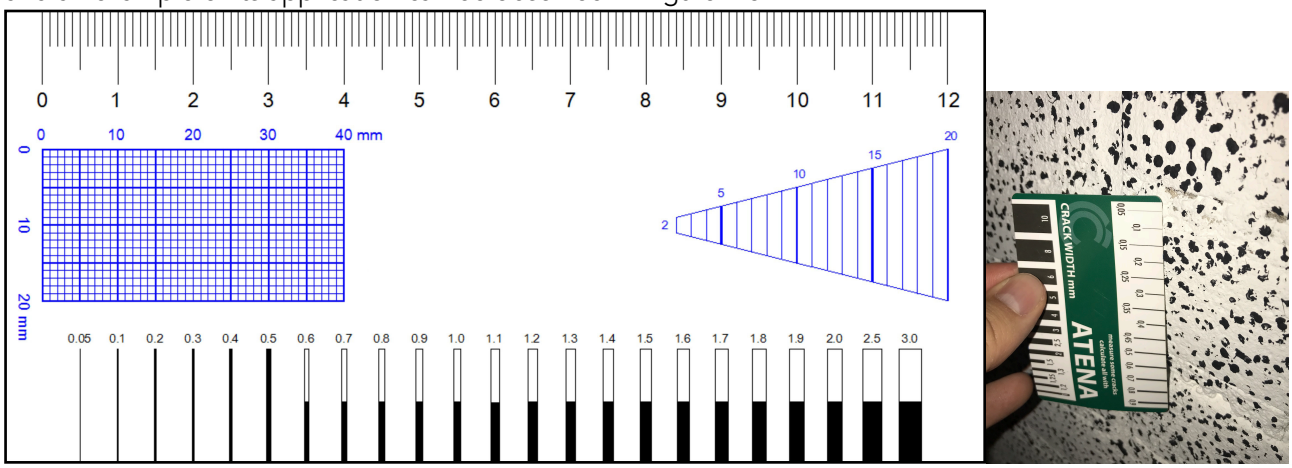

Figure 2.6. Ruler to measure observed crack width. Scale on A4 paper is 1:1. Right: usage of such a ruler in the field; the ruler is positioned next to a crack so that the inspector can note its width by comparing the crack to the thickness of the lines on the ruler.

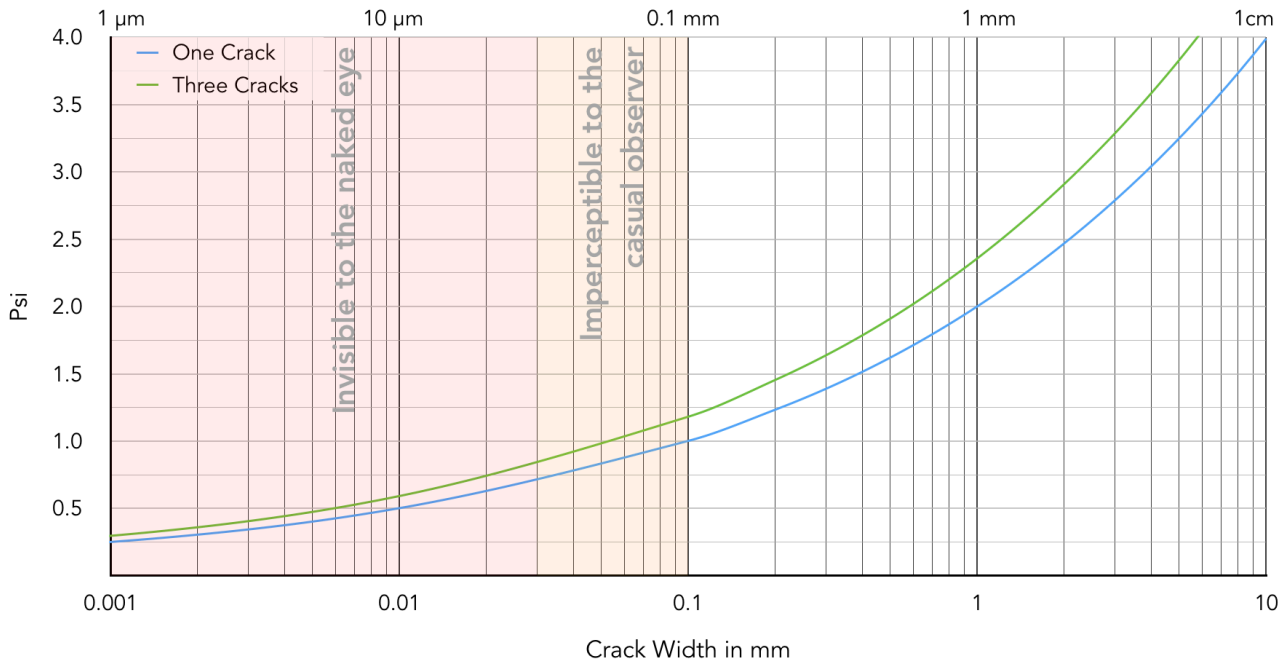

Figure 2.7. Graph showing the relationship of Psi (Ψ_D) for a given crack width. Cracks below 0.1mm require special attention to be detected.

The scale is also adjusted to provide insight into the importance of a certain damage value. Based on observations and experience, cracks with a width below 0.1mm are very difficult to detect, even for the trained inspector. Therefore, the value of Ψ=1, relating to crack widths around 0.1mm, has been set as the limit above which damage can be perceived.

As additional background information, it is known that in the best of lighting and contrast conditions, the normal human eye can distinguish lines down to 30µm in width (see for instance, Österberg, 1935). The highest display resolutions on available mobile devices today have pixel sizes of 45µm, while high-resolution computer monitors have pixel sizes of approximately 0.2mm and conventional LCD monitors of 0.5mm. It follows that on a rough surface such as a wall, in particular when it has not been plastered, cracks narrower than 0.1mm are already almost impossible to detect. This means that damage values below 1.0 are negligible. Based on practical experience during testing, the limit of 0.1mm was confirmed as a sensible lower boundary to detect damage.

The coefficients and exponents in Equation 2.1 have been selected in combination with Table 2.4 such that the output values match the descriptions in Table 2.3. The resulting curves (as presented in Figure 2.7) become the definition of the parameter.

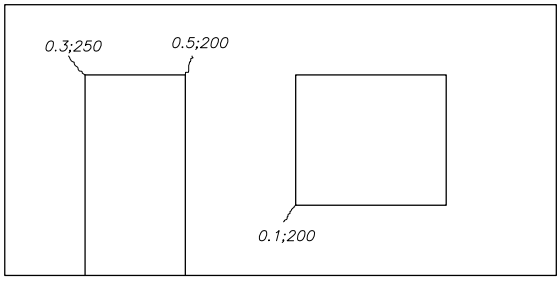

Ψ=1.8

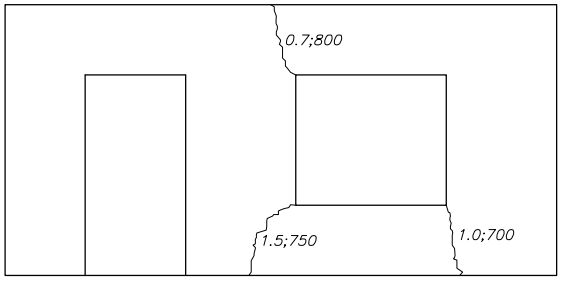

Ψ=2.5

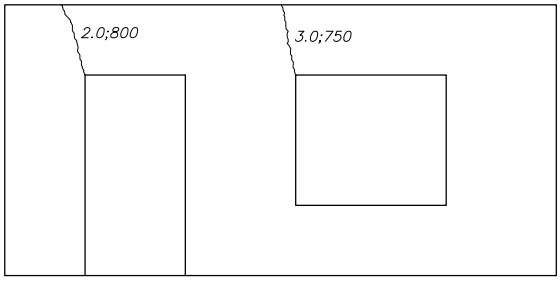

Ψ=3.0

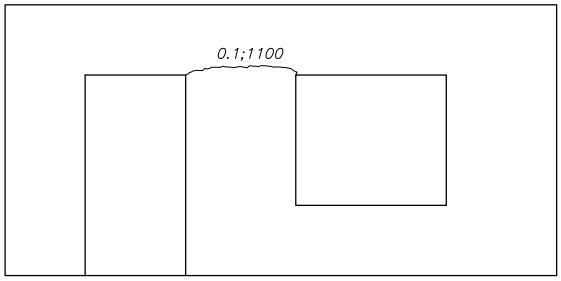

Ψ=1.0

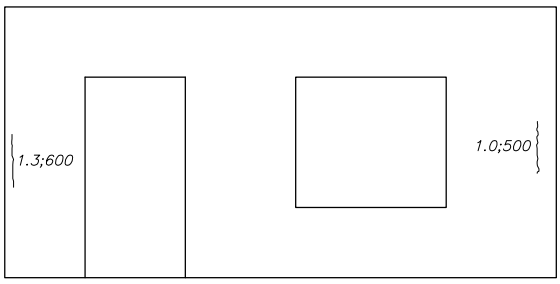

Ψ=2.3

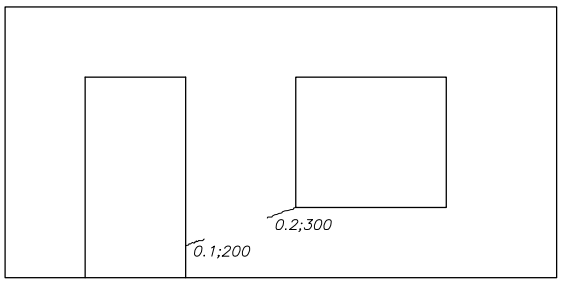

Ψ=1.3

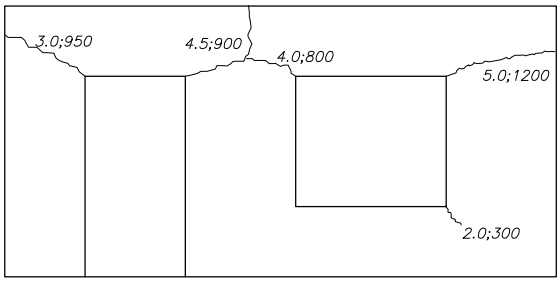

Ψ=3.9

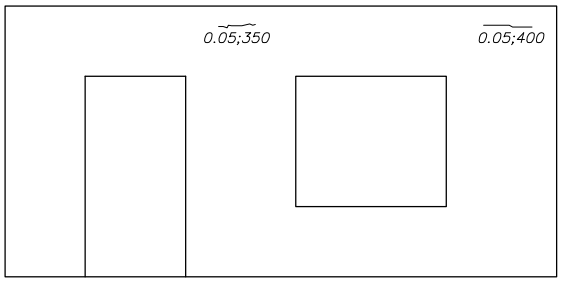

Ψ=0.9

Figure 2.8. Examples of a wall with various crack patterns (c_w;c_L) and its corresponding computed crack parameter.

2.4.3. Limitations of the One Parameter Approach

First, the expression for the proposal has been made as simple as possible while including the most relevant parameters that define damage from cracking. It is tuned to produce reliable results based on realistic cases; but some particular situations may produce incorrect results:
In most real cases, wider cracks are also the longest, and the expression has been formulated under this assumption, but this may not always be the case. In the rare situations where the widest cracks are significantly shorter than other, significantly narrower cracks; the expression will underestimate damage. Care should be exercised if the damage pattern has narrow cracks that are more than three times as long as the widest cracks. In this case, the length of the cracks can be dropped from the expression.
Similarly, an increase in length of a narrower crack (without any change in width or length of any of the other cracks) will decrease, instead of increasing, the computed damage. This is physically not correct, but is a result of the way the expression has been formulated. However, and again, in the way the expression has been defined, this change should never represent a change of more than 0.1 damage units.
In fact, it is worth noting, that the expression should only be evaluated up to one decimal point. This is the maximum resolution of the parameter.
Because of the limitations (such as the one mentioned), the expression does not offer more precision than one decimal point (e.g. 1.7). Additional precision is not possible with an expression such as this. To obtain a comparatively more accurate evaluation of damage, it would be necessary to introduce additional parameters such as the area and thickness of the wall, the crack width evolution along the crack (indicating whether the crack is tapered or not), and the location of the cracks. This becomes a case-by-case basis, defeating the simplicity and comparability of using one parameter that reflects crack width damage.

Second, while a single parameter is easy to use and employ for comparison between cases, it only provides an indication of the intensity of damage, but, unlike a full damage picture, it does not hint at the cause of the damage.
Some actions or combination of actions may leave particular crack patterns behind which may then be of use to identify the actions; such a pattern recognition procedure (e.g. de Vent et al., 2011) is not possible when using a single parameter for describing damage.

Finally, because of the limited precision of the parameter, very slight differences in damage will not be reflected within the resolution of the parameter. An increase in crack length, for instance, will in most cases, not lead to an increase of the damage parameter. This is correct for the formulation based on Table 2.4, but may not be accurate enough in some cases.

Nevertheless, the resolution given by this parameter is greater than that of the common damage states; in this context, the limited resolution has been selected purposely and serves two motives: first, to reflect that minute changes in damage cannot be perceived in real cases; and second, that attempting to produce a higher resolution is only possible with numerical tools, and given the uncertainties inherent to masonry, the partaking actions, and damage, becomes unrealistic.

Furthermore, it is worth noting that the proposed damage scale is focused on a, primarily, aesthetic expression of damage that does not necessarily correlate to safety. In Table 2.3 damage levels are loosely related to damage states, commonly associated with structural safety; here, damage levels above five seem to correspond to definitions of damage states above three, however, while it has been observed that bigger cracks usually appear in the higher damage states, smaller cracks can also be evidence of lack of structural safety. This is not expressed in this scale.
Consequently, since this scale has been developed for the evaluation of mostly aesthetic damage, it should not be used for analysis of individual risk and safety.

2.5. Notes on the Perception and Transitoriness of Damage

2.5.1. The Perception of Damage

Two identical houses subjected to similar actions will be similarly damaged; however, if one house has walls covered in a plaster that is old and stiff while the other has walls covered in flexible wallpaper, the former will display any crack prominently, while the latter will hide cracks. The first house will be perceived to be more damaged than the second one. This is the perceived damage state which may differ from the actual damage state.

This study focuses on real damage and observes the physical processes that lead to it, but it is still important to acknowledge that damage can be subjective and that certain combinations of architectural building parameters will lead to more *reported damage*. Understanding how damage is likely to be perceived also gives insight into overall damage conditions in the region.

The following is an empirical proposal of how and which parameters relating to the aesthetic and architectural disposition of the structure, as well as the situation in which damage was observed, may affect the way in which damage is perceived.

$$\Psi_{PD}=\Psi_{D}^{\frac{k}{3}} \tag{2.2}$$

Where:

Ψ_D is the damage level parameter (see Section 2.4.2),

k is the average of the influence parameters for each category as shown in Table 2.5 next.

It is possible to include as many categories as deemed relevant into the evaluation of the perception of damage. Additionally, the relation can be inverted to try to estimate the actual damage of a structure from a study case report.

In the former case, an estimation of how damage will be perceived can be inferred from a numerical model, while in the latter, a more accurate estimation of damage can be registered from an uncertain field report.

Table 2.5.a. Influence value scale.

Value	Description
1	Reduces the perception of damage significantly.
2	Reduces the perception of damage.
3	Does not influence the perception of damage. $\Psi_{PD}=\Psi_{D}$
4	Increases the perception of damage.
5	Increases the perception of damage significantly.

Table 2.5.b. Influence values for various non-structural aspects influential in damage perception. Empiric exemplary values.

Category	Subcategories	Influence Value	Description
Age	very old	2	Older than 1970
	older	3	Between 1970 and 2000
	new	4	Newer than 2000
Material	baked clay	3	
	calcium silicate	4	
Wall type	slim	4	Less than 120mm
	thick	3	Greater than 120mm
	double	2	More than one layer of bricks
Cavity	without cavity	3	One single leaf
	cavity and aesthetic	4	Two leaves, where only one is structural
	cavity and structural	3	Two leaves, both structural
Brick Type	regular bricks	3	units with a height smaller than 150mm
	large blocks	4	units with a height larger than 150mm
	hollow units	3	units that are not solid
Mortar	slim	4	the joints are around 3mm according to EC
	free verticals	2	the vertical joints between the bricks are not filled
	normal	3	all joint are filled and greater than 3mm
Finish	exposed	2	the bricks and joints can be seen
	plaster + paint	3	the wall is covered with plaster and painted
	mortar + paint	4	the wall is covered with mortar and painted
	elastomeric paint	2	the wall is (covered and) painted with flexible paint
	Wall paper	1	the wall is plastered and covered with paper
Any Additional Category	Location of cracks, experience of the observer, light conditions during observation, etc.		

2.5.2. Transitory Damage

So as "perceived damage", transitory damage will differ from the actual damage level of a structure. As its name suggests, transitory damage reflects the state of a structure at a certain point in time and may not be the same as the damage state at the moment of observation.
For example, during an earthquake, a structure may deform such that cracks of 1mm appear on the walls at the moment of maximum deformation; but, by the end of the earthquake, the cracks may have partially closed. If a picture had been taken at the moment of maximum deformation, the damage level would likely appear higher than the residual damage state.

In this study, damage will be analogous to transitory damage. This is a conservative approach yet especially suited for light damage due to the following reasons:

Firstly, unlike larger cracks exceeding DS1 which may close significantly compared to their maximum transitory state, narrower cracks corresponding to DS1 are not able to close once open because of the roughness of the newly developed crack interface. Moreover, cracks through bricks or in finished walls are irreversible: once a crack appears it will remain visible. Thus, when observing light damage, transitory and residual damage are more alike.

Secondly, since unreinforced masonry is designed without taking into account its tensile strength, it is usually not subjected to forces that would keep the cracks open once they have formed. However, when additional tensile stresses in more directions are present, such as those generated by hygro-thermal expansion or settlement actions, small cracks are more likely to remain open after they have formed. Additionally, unlike laboratory experiments where a restitutory force may exert the work required to close the cracks, in real cases, such a force may not be present; in fact, in real cases, forces might be present that keep the cracks open.

Thirdly, in contrast to field cases, observing transitory damage in laboratory experiments is possible and easier than the sometimes hardly-noticeable residual damage of lightly damaged cases subjected to only one action. Here, transitory damage will be higher than residual damage, and it is not possible to determine what the actual residual damage would have been, had the laboratory case been a real case in the field with complex interactions with other structural or non-structural elements and finishings.
Furthermore, the maximum (transitory) and residual damage can also be obtained easily from computational models, which provides an additional point of comparison.

Fourthly, when analysing the effect of a combination of actions or of repeated actions, the true damaged state of the structure is that revealed by the maximum transitory state. The transitory state will be a more accurate representation of the loss of strength experienced by the structure and hence its response to subsequent excitations. The analysis of the behaviour of the structure to subsequent damage causes or events should be performed with the maximum damage and not the (perhaps inapparent) residual damage. Thus, when multiple damaging causes are considered, the residual damage would not be adequately suited.

Fifthly, when considering the structural design of a structure and whether it adheres to regulations, drift limits are specified towards the maximum displacement of the structure and not the residual displacement. It is thus common practice to look at the maximum transitory state of a structure when assessing its final damage state.

Therefore, transitory damage is used consistently in this report when referring to damage, and while it is expected that for light damage, the transitory damage will be close to the final damage, it must be noted that the final damage is bound to be slightly lower than the transitory damage measure employed.

2.6. Application of the Damage Parameter to Experimental and Computational Results

The key strength of the single damage parameter is that it can be directly evaluated for results of laboratory tests or computational models. The latter already outputs crack-width information for each integration point in a cell, while the former can be evaluated in search of cracks.
The implementation of this assessment is described next.

2.6.1. Digital Image Correlation and Experimental Results for Damage Analysis

Digital Image Correlation (DIC) analyses the relative displacements between clusters of patterns in different photographs. The patterns are obtained by analysing areas of contrast and shape in the pictures; therefore, the samples are painted with a random array of dots or patterns which are sized to be picked up clearly by a camera, see Figure 2.9.

Figure 2.9. Patterns being applied to the wall.

The DIC divides the photographs into cells which can take the size of a few pixels, and the displacement of each cell in comparison to a base photograph is output. Depending on the size of the patterns and the real size of the pixels of the photograph, a certain accuracy can be expected. During the laboratory experiments, the full wall of 3.07x2.70m fit inside the frame of a 51MP camera such that the pixel size was approximately 0.52mm. In combination with the camera available and the selected shooting settings, the DIC code employed allowed for reasonable results at resolutions of down to 0.05 pixels, effectively setting a lower boundary of approximately 25µm for the detection of displacements. While this value is higher than the precision of LVDTs and other sensors attached to the wall, the monitoring of displacements occurs in the entirety of the wall, in any direction, and in relation to any point on the wall; this versatility is the reason for utilising a DIC method. Figure 2.10 shows the displacement results of a DIC analysis.

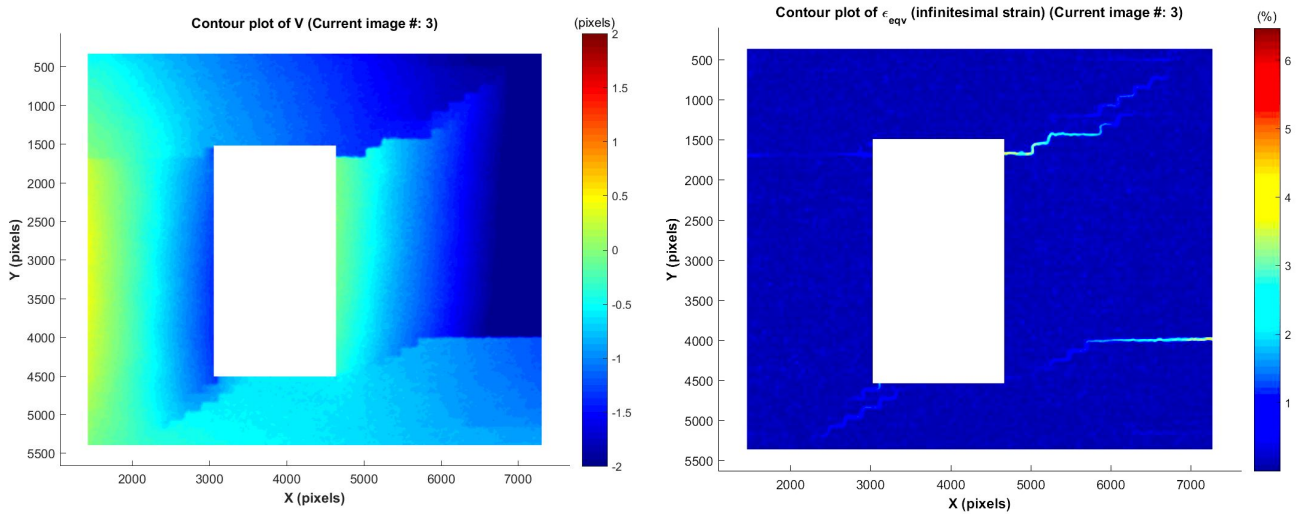

Figure 2.10. Examples of filled contour plots of vertical displacements (left) and computed infinitesimal strain (right) obtained from a DIC analysis of wall TUD-COMP-40 towards the end of the test (Test 65, Record point 2742). The maximum crack width is 0.6mm.

In sum, the primary output of the DIC analysis is matrices of displacements which can reveal cracks as discontinuities. From here, strains can be computed revealing the location and patterns of small cracks.

2.6.2. Output of Computational Results for Damage Analysis

Computational Models can output a variety of results depending on the program and material model employed. To analyse damage, both the displacement fields and the crack width information are useful. Figure 2.11 exemplifies this output.

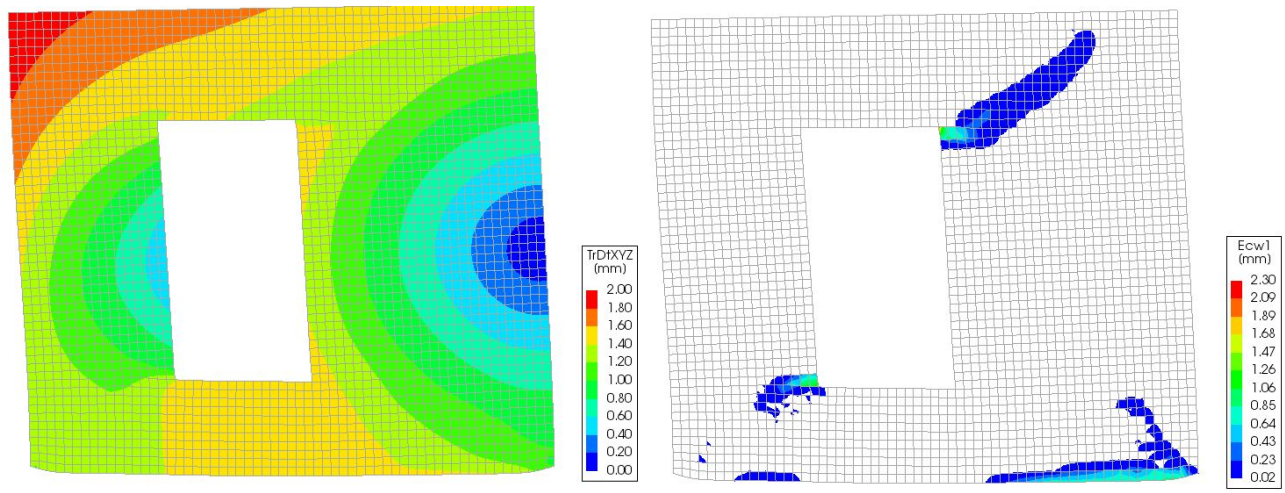

Figure 2.11. Global displacement and crack-width output of a DIANA numerical model for the case of a wall damaged by a combination of sagging settlement and earthquake excitation. Deformed shape magnified by 50.

2.6.3. Direct Assessment of the Damage Parameter

Since the primary output of the DIC analysis and computational models can be matrices of displacements as has been shown, a program was written to analyse these automatically and determine the damage value. The flowchart in Figure 2.12 gives an overview of the sequence of analysis which is elaborated upon next.

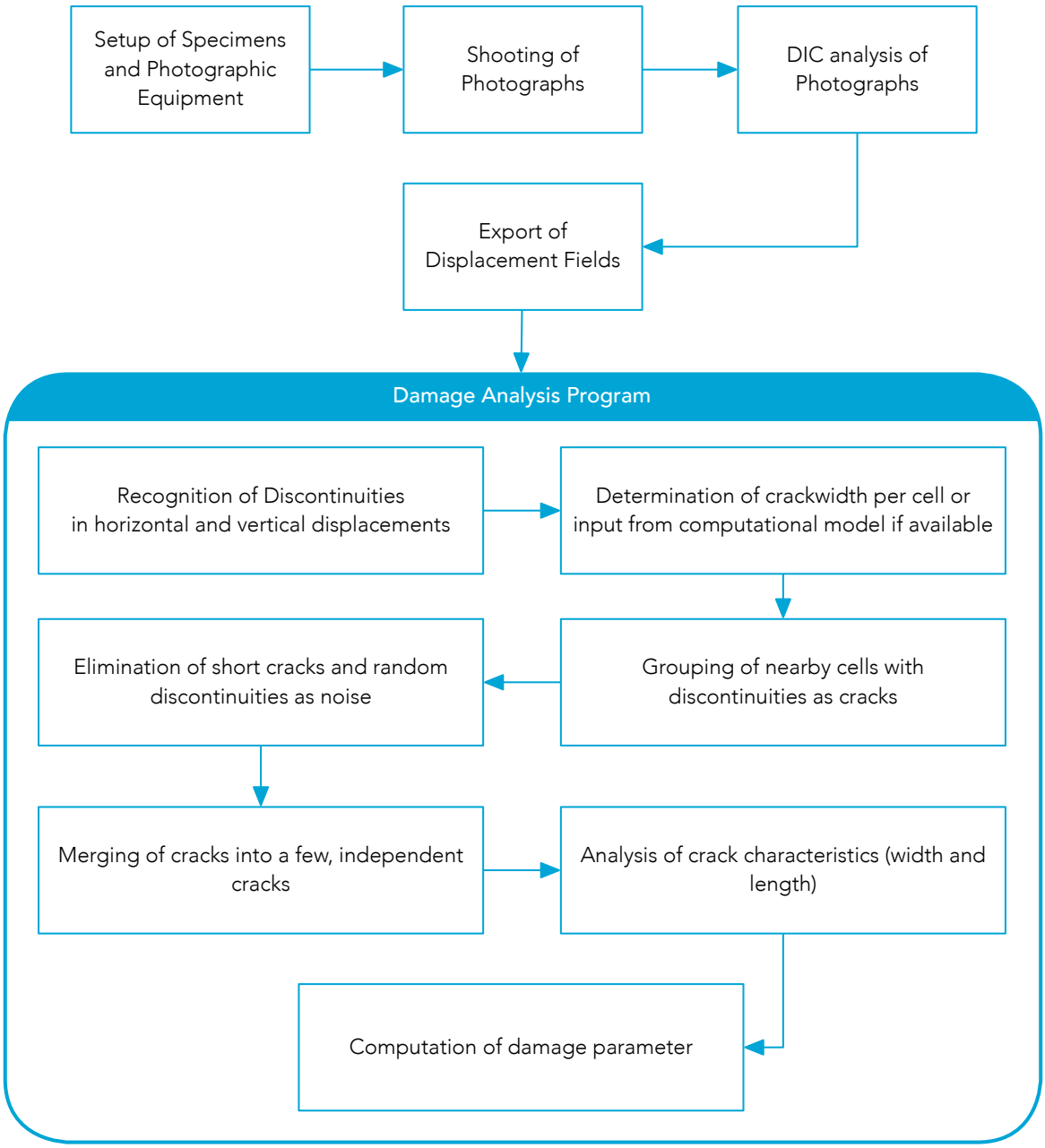

Figure 2.12. Flowchart for the process of computing the damage parameter from DIC or computational results.

The first step in the program is searching for discontinuities in the horizontal or vertical displacement fields; this evidences potential cracks. The crack width for each cell is computed from the discontinuity with nearby cells or imported directly from the results of a computational model if this is available.

Next, nearby cells that present crack-width information are grouped together and categorised as a crack. From their orientation and collective crack-width information, some noise cases are disregarded. Then, cracks that are close to each other are merged into a few cracks and their characteristics (such as width and length) are evaluated. Cracks that are shorter that a certain length are also disregarded as noise.

Finally, from the number of cracks, their width, and their length, the damage parameter can be computed.

The result of this evaluation is exported into a list for later integration with other analyses, but (optionally) also plotted for visual assessment of the results of the program. Figure 2.13 compares both analyses of DIC and computational output.

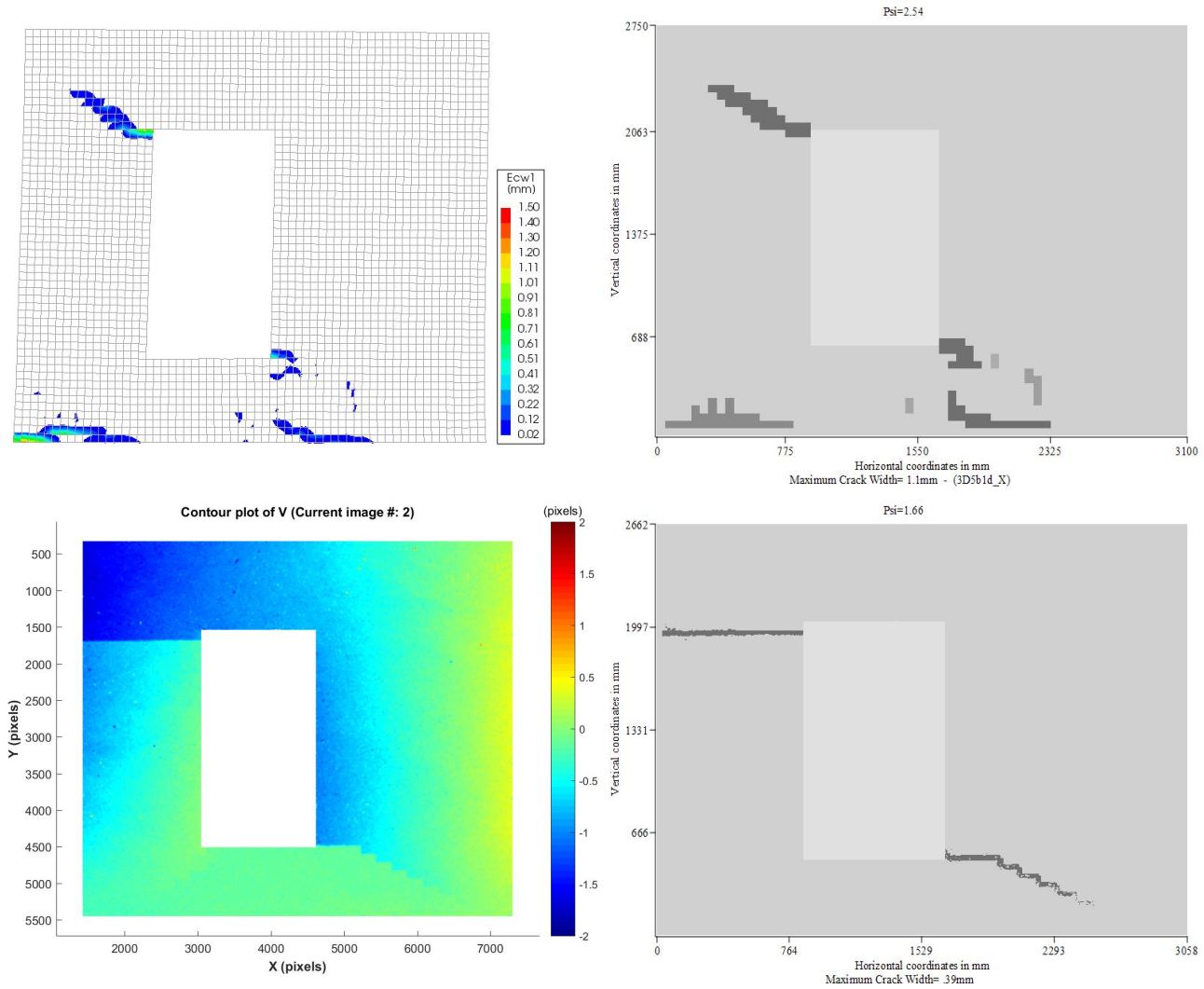

Figure 2.13. Examples of analyses with the damage assessment program for numerical output (top) and DIC output (bottom). The former corresponds to shrinkage damage followed by earthquake damage and results in a value of Ψ=2.5, while the latter computes to Ψ=1.7 due to a lateral top displacement of the wall of 2mm (Wall TUD-COMP-40, Test 79, Record 1075).

2.7. Conclusions of Chapter Two

The assessment of damage relies in the application of two parameters: the damage level and the damage picture. Together, a more general damage state can be computed. Additionally, the inclusion of parameters regarding the location of the cracks, the finish of the walls and the number of the cracks may allow for an estimation of the perceived damage state. This overview is illustrated in Figure 2.14.

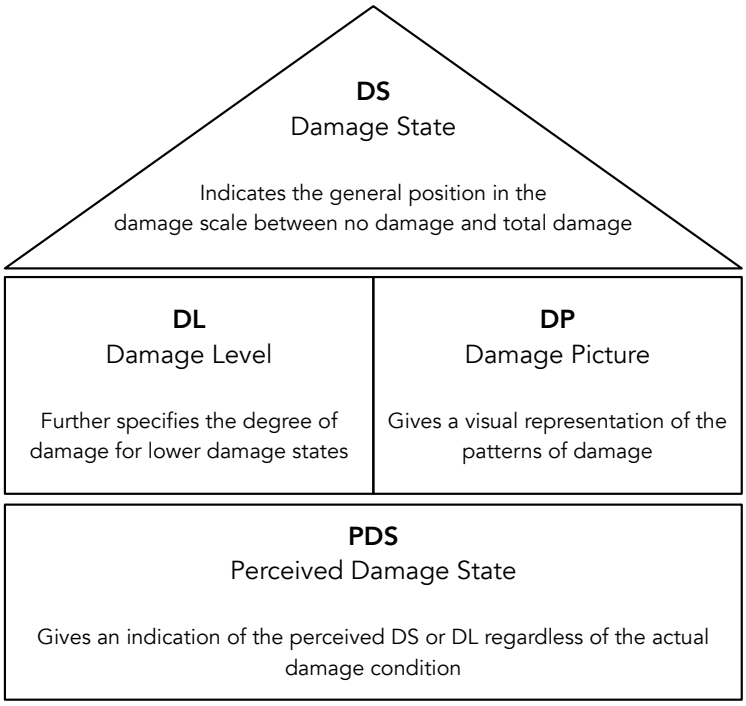

Figure 2.14. The main parameters categorising damage.

In the context of "Damage Sensitivity of Groningen Masonry Structures" it is important to have a clear measurement and understanding of damage. This study is based on the evaluation of minor damage as the initiation and propagation of cracks through unreinforced masonry walls. For a successful representation of the intensity of damage, it is necessary to qualify and quantify cracking patterns into discrete categories tailored to the assessment of this type of damage. Moreover, it is vital that the measurement of damage be objectively compared between laboratory specimens, computational models, and field study cases.

To accomplish this, on the basis of the fundamentals of fracture and cracking, a refined damage scale has been proposed for observing minor damage within the common damage grade definitions of aesthetic damage (DS1) and minor functional damage (DS2). The damage scale is subdivided into damage levels (DL) corresponding to the ease of repair (and associated cost) of cracks and of crack patterns on walls.

Further, the categorisation onto the scale is achieved by the use of a mathematical expression that evaluates any cracking pattern consisting of any number of cracks, with their respective crack width and crack length, into a single damage parameter (Ψ_D). This parameter offers a continuous measure of the relative cost to repair damage, but is also discretised on the defined damage levels.

$$\Psi_D = 2 \cdot n_c^{0.15} \cdot \dot{c}_w^{0.3} \tag{2.1}$$

Where:

n_c is the number of cracks in the structure

$\dot{c}_w$ is the width-weighted and length-averaged crack width (in mm) calculated with:

$$\dot{c}_w = \frac{\sum_{i=1}^{n_c} c_{w,i}^2 \cdot c_{L,i}}{\sum_{i=1}^{n_c} c_{w,i} \cdot c_{L,i}}$$

Where:

c_w is the maximum crack width along each crack in mm

c_L is the crack length in mm

For $n_c=1$, $\dot{c}_w = c_w$

In this expression, the crack width of each crack is measured at their widest point.

Damage State	DS0	DS1			DS2
Damage Level	DL0	DL1	DL2	DL3	DL4
Parameter of Damage	$\Psi_D < 1$	$1 < \Psi_D < 1.4$	$1.5 < \Psi_D < 2.4$	$2.5 < \Psi_D < 3.4$	$\Psi_D > 3.5$
Aproximate Crack Width	Imperceptible cracks	up to around 0.1mm	around 1mm	around 5mm	5 to 15mm

Finally, the evaluation of this parameter on laboratory experiments and computational model has been conducted automatically by a computer program and is thus done objectively.

Chapter 3

Preliminary Computational Models to Define Tests

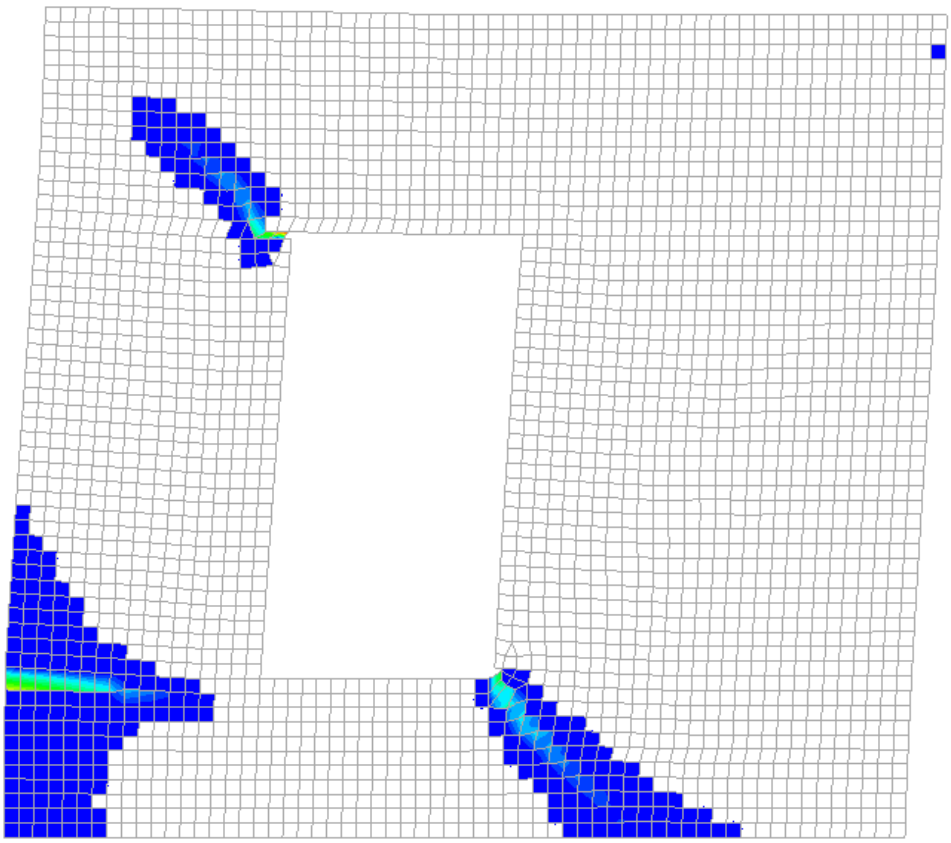

TU Delft

3. Preliminary Computational Models to Define Tests

3.1. Introduction

In the 'Damage sensitivity of Groningen Structures' project, modelling studies have been performed to estimate the response of unreinforced masonry structures (URM) subjected to in-plane actions.

First, predictions of laboratory experiments have been studied. Windowed walls with pre-existing cracks (notches) have now been tested in the Stevin Lab of the TU Delft. Incremental horizontal static loading was applied at the top of the specimens in order to investigate the effects of repetitions and how they influence crack propagation. A smeared continuum model approach was used to predict the behaviour of these walls. The aim of the wall model is to investigate where the cracks start (for which top horizontal displacement, in which location) and their propagation (increment in crack width, crack length). The evolution of the cracks has been examined against different horizontal displacement amplitudes. Repetitive actions have been taken into account as well.

The models presented in this chapter are preliminary and were mainly used to gain insight into the behaviour of the wall and to design the experimental tests. They are important to realise how traditional models can be improved. Revised, improved models are then presented in Chapter 5.

Questions answered are:

- What are appropriate, preliminary computational models for predicting the behaviour of experimental walls?
- Where are cracks expected for the case study and what are their characteristics?

3.2. Specimen Description

The specimen tested in the TU Delft's Stevin Lab is an in-plane wall with a window opening and pre-existing cracks (notches). The sample is a solid clay wall and it has a length of 3.07m and a height of 2.71m. The wall is single-wythe, with a thickness of 0.10m. The wall is tested in a cantilever configuration. The specimen contains an asymmetric opening representing a window of 0.78m in width and 1.51m in height.
Two horizontal notches are added to the bottom right window corner and to the top left window corner respectively. Both of them have a length of half a brick (25mm) and a height equal to the mortar joint (10mm).

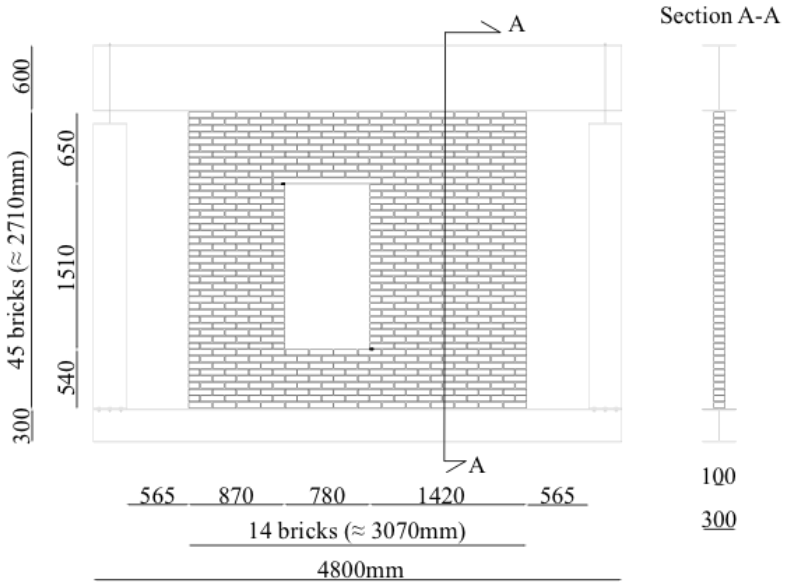

Figure 3.1. Dimensions of the in-plane solid clay wall with asymmetric window opening. (Meulman et al., 2017).

The inclusion of a window aims to concentrate the stress at the corners which may foster cracks to start and grow inward from these points.
A reinforced concrete beamlet, 0.98m long and 0.05m high, is used as lintel on top of the opening.
A low vertical stress is applied on top of the load (about 0.10MPa) to allow cracking at an early stage without the need of a high horizontal displacement. Moreover, this kind of load is typical of non-bearing walls observed in the field.
The specimen is subjected to repetitive quasi-static horizontal loading (i.e. one direction displacement).

For additional information, see Meulman et al. (2017).

3.3. Finite Element Model Description

The in-plane wall has been modelled with the software DIANA FEA 10.1. Although a brick to brick micro model is able to better understand the crack pattern and the local behaviour of the masonry due to the different properties between two different elements (i.e. joints and units), it is not adequate to study big structural elements as walls and/or buildings, because of its increased demand of computational resources (see appendix, Section 9.4).
A smeared continuum approach seems the best way to investigate an entire wall in-plane. Clearly, by using this approach the computational time and memory are dramatically reduced. The macro-modelling is the best choice to maximise efficiency and accuracy of a model.

Three different materials have been used for modelling the test: masonry, concrete for the lintel above the opening, and steel for the rigid top beam over the wall. The finite element model does not include a bottom beam. The nodes at the base of the wall are fixed. The horizontal displacement is applied at the top-left corner of the wall and it is provided along the entire the top edge by using tyings (the software's notation for ties). Generally, these connections are used to equalise degrees of freedom, in this case, equal horizontal displacement (Manie, 2016). The imposed deformation describes a repetitive pull, i.e. a displacement to the right direction (Figure 3.2). A top vertical load of 0.10MPa is applied as line load at the top wall edge. This DIANA finite element model is shown in Figure 3.2.

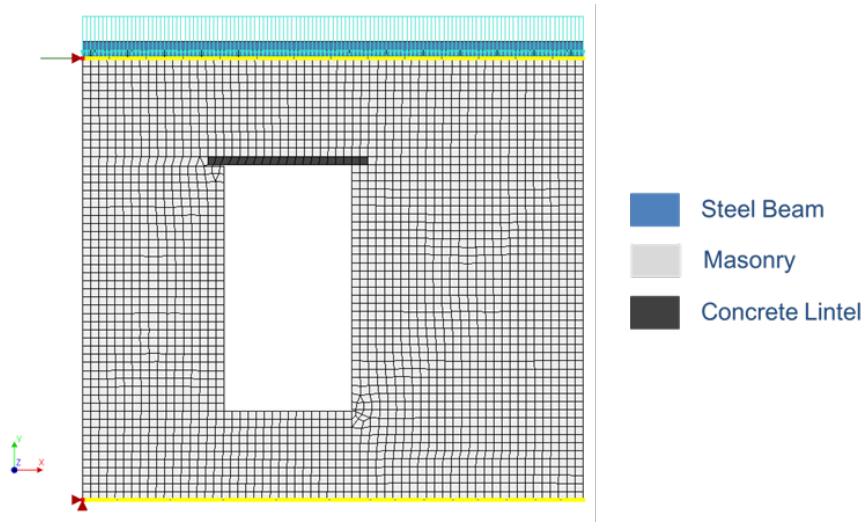

Figure 3.2. Diana FEM model of the in-plane wall.

The two notches in the bottom right and top left window corners are also included in the model (Figure 3.3).

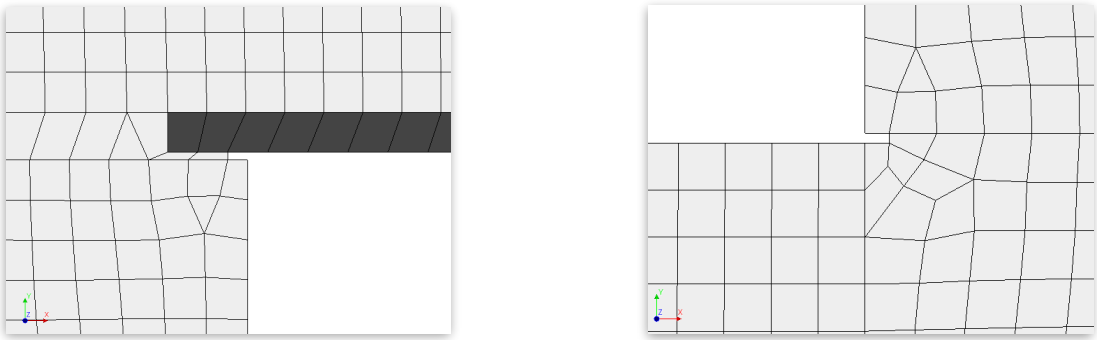

Figure 3.3. Notches in the opening corners: (a) top left window corner and (b) bottom right window corner.

For the entire model, eight-node, quadrilateral, iso-parametric plane stress elements (CQ16M) with an integration scheme of 3x3 have been used.
Both concrete and steel have been considered as elastic materials. For the masonry material the adopted constitutive model is the Total Strain Rotating Crack Model with a linear, energy-based softening curve in tension (Figure 3.4.a), and compression behaviour defined by a parabolic nonlinear curve (Figure 3.4.b).

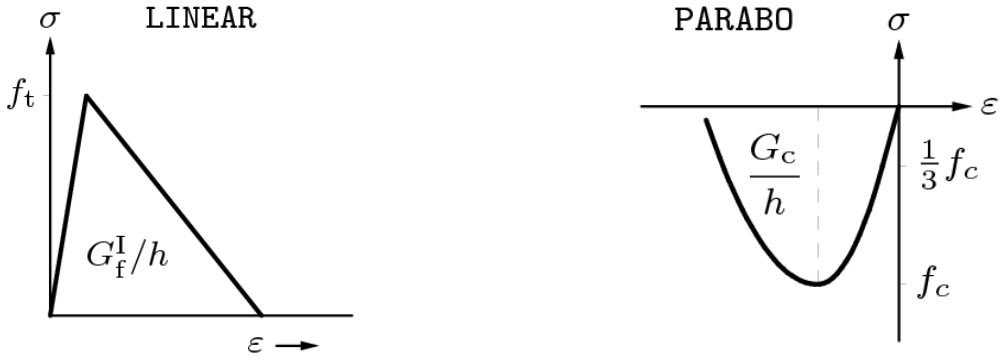

(a) (b)

Figure 3.4 Total Strain Crack Model, defined softening for (a) tensile behaviour and (b) compressive behaviour. (Manie, 2016).

For the rotating crack model, the only status parameters are the maximum tensile and compressive principal strains that are ever reached in the integration point. This is an efficient model for situations where crack strains are relatively small (Manie, 2016).

The clay masonry material properties are summarised in Table 3.1.

Table 3.1. Clay masonry material properties for the in-plane FEM wall.

Clay Masonry Properties	
Density	1680Kg/m^3
Young's Modulus	4030MPa
Poisson's Ratio	0.10
Tensile Strength	0.12MPa
Tensile Fracture Energy G_f^I	10N/m
Compressive Strength	14MPa
Compressive Fracture Energy G_c	20000N/m

These values have been assumed based on a previous prediction of an in-plane clay wall studied by Messali et al. (2017). The parameters used were derived from the experimental campaign on materials, as detailed by Jafari et al. (2016).

For the concrete, an isotropic linear-elastic material has been used; its properties are shown in Table 3.2.

Table 3.2. Concrete material properties for the lintel above the window.

Concrete Properties	
Density	2400Kg/m3
Young's Modulus	31000MPa
Poisson's Ratio	0.20

Also for the steel beam above the wall, an isotropic linear elastic material has been adopted. A high stiffness value has been assigned to the beam in order to simulate the rigid behaviour of the laboratory frame. The steel material of the frame beam has been considered density-less because its weight has been already included in the vertical load. A summary of the beam properties is shown in Table 3.3.

Table 3.3 Steel material properties for the beam above the wall.

Steel Properties	
Density	$1 \cdot 10^{-15} kg/m^3$
Young's Modulus	2100000MPa
Poisson's Ratio	0.30

In order to reproduce and predict the laboratory test, the experimental loading protocol has been used for the FEM model as well.
The pre-compression is kept constant during the entire test. Then, the wall is subjected to a horizontal displacement at the top. First, a monotonic controlled displacement is applied until a visible crack of 0.1mm in width is identified in one of the two notches at the window corners. After that, in the following steps, the displacement measured in the first step is re-run ten times. This repetitive loading (starting from zero displacement to the amplitude and then back to zero) is repeated for 10 more times with a higher rate in terms of mm/s (10 times higher). The amplitude is then increased by a factor of 1.25, 1.50, 1.75 and 2.00 times of the start displacement (Meulman et al., 2017).
The full loading protocol is summarised in Table 3.4.

Table 3.4. Loading protocol for in-plane test. (Meulman et al., 2017).

Step	Horizontal Top Displacement [mm]	Rate [mm/s]
1	Monotonic until 1st crack (0.10mm)	0.005
2…10	u(1)	0.005
11…20	u(1)	0.050
21…30	1.25 · u(1)	0.005
31…40	1.25 · u(1)	0.050
41…50	1.50 · u(1)	0.005
51…60	1.50 · u(1)	0.050
61…70	1.75 · u(1)	0.005
71…80	1.75 · u(1)	0.050
81…90	2.00 · u(1)	0.005
91…100	2.00 · u(1)	0.050

An illustration of the first 20 steps for the repetition loading is pictured in Figure 3.5.

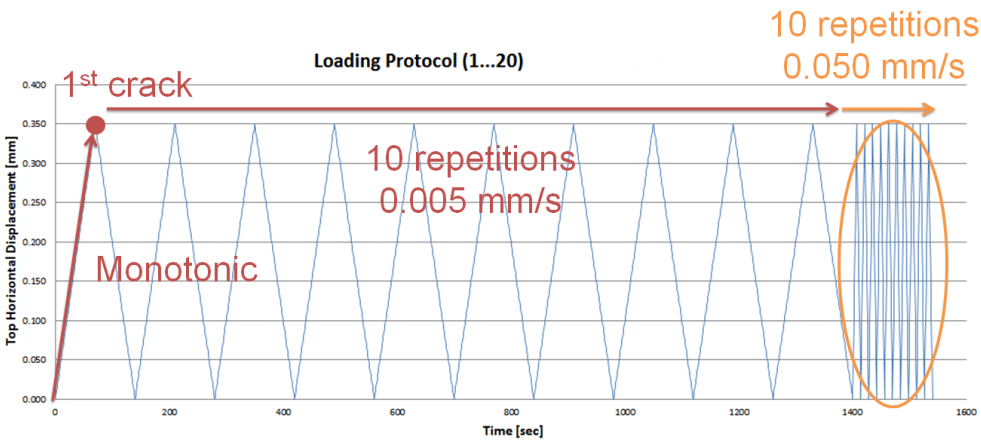

Figure 3.5 Loading protocol for the first 20 steps for the in-plane wall.

Finally, a picture of the full loading protocol for the in-plane wall is shown in Figure 3.6.

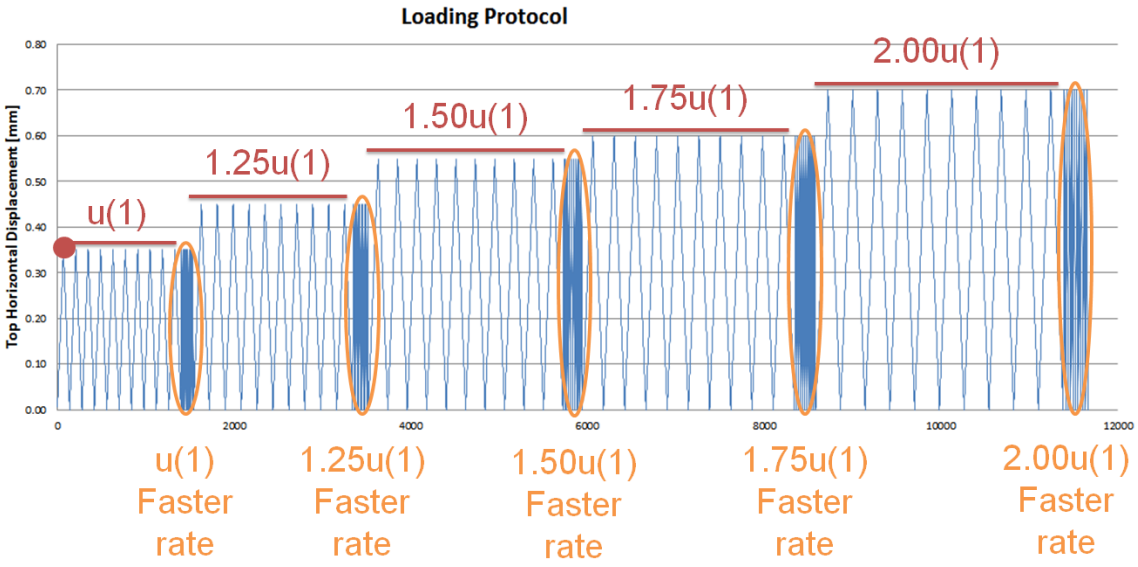

Figure 3.6. Full loading protocol for the in-plane wall.

The above mentioned protocol has been used and applied to the top left node of the FEM model wall. Both gravity loads and overburden of 0.10MPa (as line load) have been considered in the model.

3.4. Results From the Blind Prediction

The results obtained from the DIANA model are in terms of crack evolution and force-displacement curves.

The first crack, 0.10mm in width, appears in one integration point when the top horizontal displacement in the wall reaches 0.35mm. This value is kept as reference for the amplitude of the following steps. The displacement amplitudes chosen for the loading protocol are summarised in Table 3.5.

Table 3.5. Loading protocol for the FEM in-plane wall.

Step	Top Horizontal Displacement [mm]
1	0.35
2…20	0.35
21…40	0.45
41…60	0.55
61…80	0.60
81…100	0.70

The first crack is located at the top left window corner notch (Figure 3.7.a). In the following step with higher amplitude, the crack at the top corner extends over the lintel length for about 15cm; a small crack appears in the bottom right opening corner as well (Figure 3.7.b). The two cracks increase in length and in width during step 41. At step 61, when a displacement of 1.75 times the first monotonic amplitude is applied, a bed joint on the left edge of the wall (approximately one row below the window height) starts opening due to the rocking mechanism of the left pier (Figure 3.7.c). The repetitive load allows this crack to grows in terms of length, from 15cm to 31cm, and width, from 0.12mm to 0.28mm. In the last repetition stage, the three cracks grow until reaching a maximum crack width of 0.57mm in the top left window corner (Figure 3.7.d).

The final crack pattern of the wall, including the micro-cracks (crack width less than 0.10mm) is depicted in Figure 3.8.

Figure 3.9 shows the failure mechanism of the in-plane DIANA model. In the final stage the wall segments into three different parts due to the two diagonal cracks in the notches plus the lateral crack. The spandrel (number 2 in Figure 3.9) is divided by the horizontal crack of the left edge and the diagonal crack in the bottom corner of the opening. The rocking mechanism of the left pier (number 1 in Figure 3.9) is very clear. The mechanism is generated by the lateral and the top left cracks.

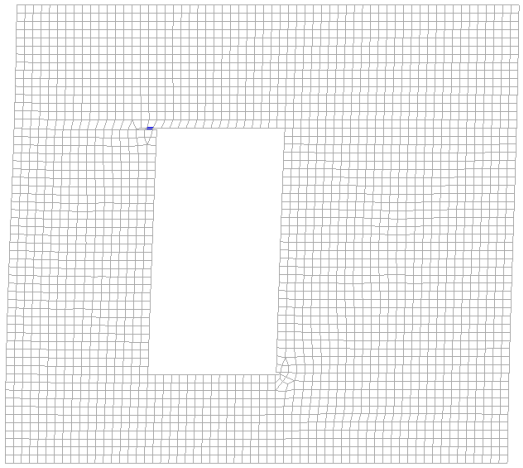

Step 1 – Top Horizontal Displacement: 0.35mm
Max crack width: 0.13mm
(a)

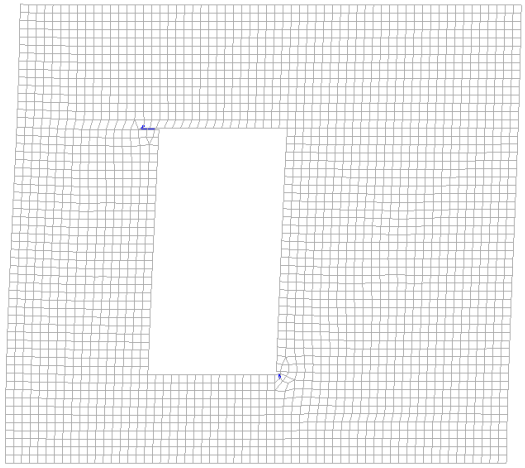

Step 21 – Top Horizontal Displacement: 0.45mm
Max crack width: 0.27mm
(b)

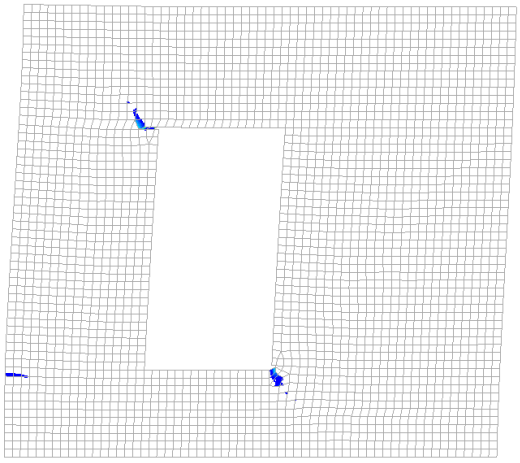

Step 61 – Top Horizontal Displacement: 0.60mm
Max crack width: 0.52mm
(c)

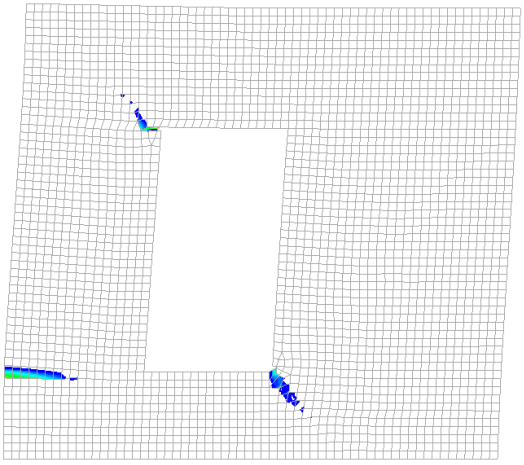

Step 81 – Top Horizontal Displacement: 0.70mm
Max crack width: 0.57mm
(d)

Figure 3.7. Evolution of the crack pattern in terms of principal crack width at different stage: (a) after applying the monotonic loading, (b) at the first peak of 1.25 times the first displacement, (c) at the first peak of 1.75 times the first displacement and (d) at the first peak of 2 times the first displacement.

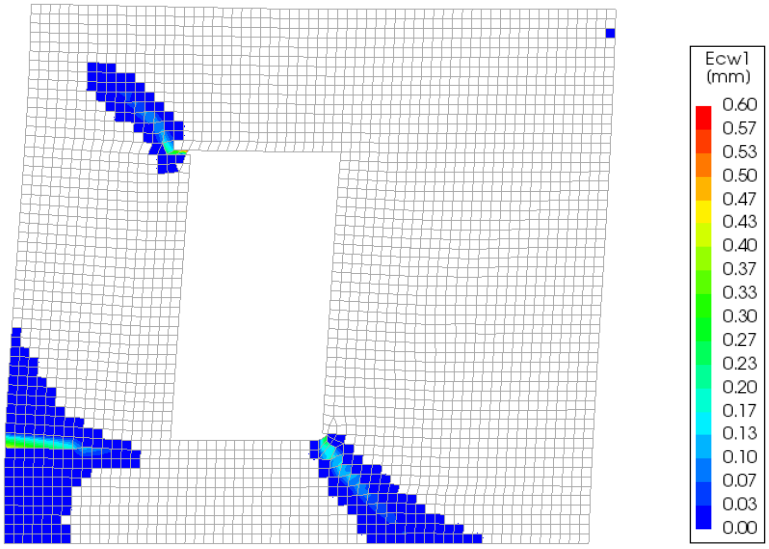

Figure 3.8. Final damage pattern of the in-plane wall in terms of principal crack width.

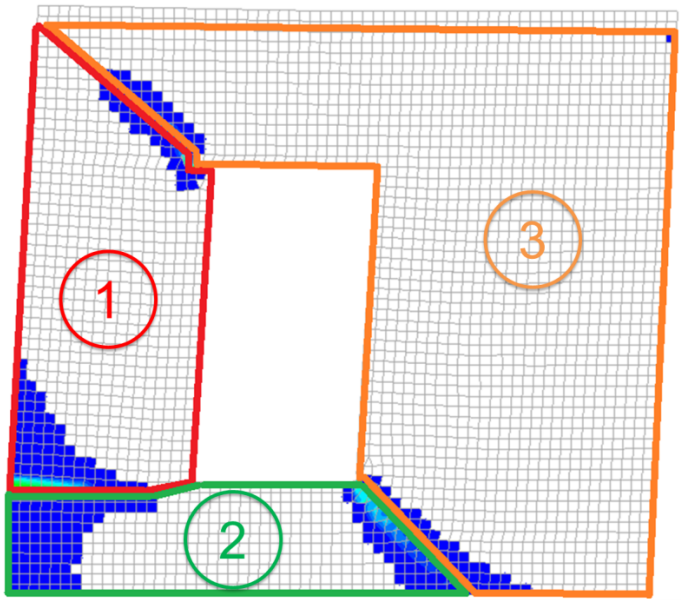

Figure 3.9. Failure mechanism of the FEM in-plane wall.

A plot with the evolution of the three crack widths, measured in the point of maximum crack width are shown in Figure 3.10.

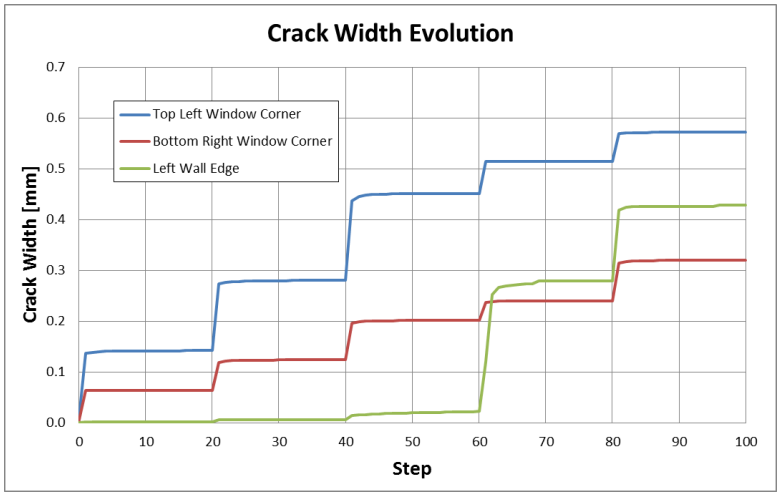

Figure 3.10. Crack width evolution for the three cracks during the entire loading process.

The evolution of the crack widths are summarised in Table 3.6.

Table 3.6. Crack width evolution during the loading protocol.

Step	Crack Width, Top Left Window Corner [mm]	Crack Width, Bottom Right Window Corner [mm]	Crack Width, Left Wall Edge [mm]
1	0.137	0.063	0.002
10	0.142	0.063	0.002
20	0.142	0.063	0.002
21	0.273	0.119	0.005
30	0.280	0.124	0.006
40	0.280	0.124	0.006

Step	Crack Width, Top Left Window Corner [mm]	Crack Width, Bottom Right Window Corner [mm]	Crack Width, Left Wall Edge [mm]
41	0.437	0.196	0.014
50	0.451	0.201	0.019
60	0.451	0.201	0.022
61	0.515	0.237	0.120
70	0.515	0.240	0.279
80	0.515	0.240	0.280
81	0.569	0.315	0.418
90	0.572	0.320	0.426
100	0.573	0.320	0.429

Both cracks located in the window corners grow more during the increase in the top horizontal displacement amplitude. Small increments in width are detected during the repetitions. The width of the crack on the lateral side rises more than two times between the step 61 and 70 instead.

The base shear versus top horizontal displacement plot divided for different amplitudes is shown in Figure 3.11. The initial stiffness of the model is 45.4kN/mm. The peak load of the model is obtained during step 61 (top horizontal displacement of 0.60mm) and is equal to 20.3kN.

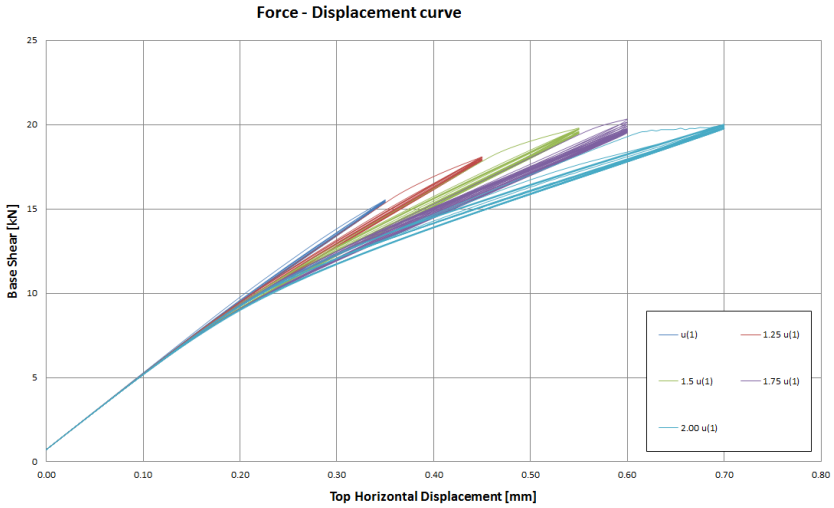

Figure 3.11. Force-displacement curve for the FEM model.

During the unloading phase, the open cracks fully close again and no large hysteresis is generated from the model.

3.5. Conclusions of Chapter Three

The FEM model for the in-plane wall predicts rocking behaviour of the left pier. A maximum load of 20.3kN is obtained for a lateral top horizontal displacement of 0.60mm.
The first visible crack (i.e. crack width of 0.10mm) is detected in the top left window corner notch for a top horizontal displacement of 0.35mm. During the following higher amplitude stage (0.45mm of top displacement) a new crack starts growing diagonally from the bottom right window corner. The last major crack appears during step 61 (0.60mm top wall displacement); it develops horizontally from the left lateral edge due to the rocking mechanism of the small pier.

The application of a continuum approach leads to reduced computational time. Moreover, the macro-modelling helps to simplify and speed up the calibration and validation process of the model. In this way, a post-refined study and a calibration of the model was possible immediately after the test campaign. The post-test model has been studied and is discussed in Chapter 5.

Chapter 4

Experimental Tests

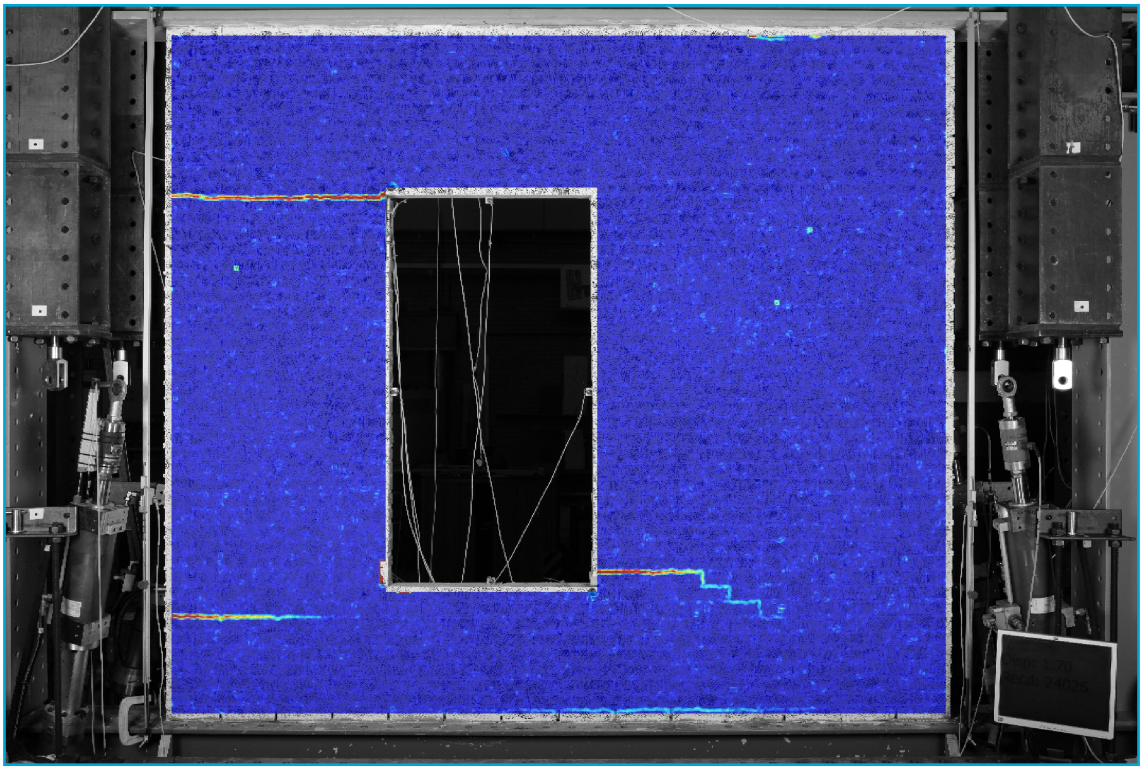

TU Delft

4. Experimental Tests

The goal of the laboratory experiments presented in this chapter, is to investigate the mechanism of crack initiation and propagation in masonry related to the minor damage in structures found in the Groningen region. Models (see Chapter 3) are used to design the tests and the test results are used to validate and calibrate the models (Chapter 5).

- When does cracking start? That is, under which strain, strength, stress configuration and structural displacement does this occur?
- When do cracks propagate and/or widen, and which types of cracks propagate under what conditions?
- Do repetitive actions foster the propagation of cracks?

In this light, two particular types of tests were chosen to investigate crack initiation and propagation as part of this study, namely: the window bank and the in-plane (IP) wall with a window opening. These tests were selected considering and balancing criteria of representativeness and feasibility, and the narrow timeframe of the study. An elaboration upon these aspects is given below:

Firstly, the tests needed to be executed and analysed within the strict deadline set for the first deliverable of this study. This means that, preferably, re-use is made of existing test setups, minimising the calibration of new equipment and testing frame configurations. Additionally, materials were to correspond to those already tested.
Secondly, the tests should resemble typical and frequently observed cracking patterns in Groningen[1]. Here, two typical cracking patterns were targeted: cracking that is usually observed below or above windows where cracks follow vertical paths and compressive stresses are minimal, and cracking occurring throughout the rest of walls, where paths are commonly diagonal and stress configurations vary.

Consequently, two tests have been selected with minor modifications of: the four point bending test and the in-plane (IP) wall test, both recently assayed as part of another study for NAM.
In both cases, to increase redundancy and reduce complexity, especially when observing cracks, only single-wythe specimens were selected.

This chapter describes the results of these experimental tests. For the IP wall test the focus is on the repetitive pull loading type applied on undamaged, single-wythe, clay-brick masonry walls with a window opening which are named TUD_COMP-40, TUD_COMP-41 and TUD_COMP-42 (Section 4.1).
Then, in Section 4.2 the window bank test results are covered.
Details about both experimental tests, including: loading schemes, test set-ups, instrumentation, etc. can be found in the document of the test protocol (Meulman et al., 2017).

1. Update after publication of this report. Reference:
P. Van Staalduinen, K. Terwel, J.G. Rots (2018). Onderzoek naar de oorzaken van bouwkundige schade in Groningen Methodologie en case studies ter duiding van de oorzaken. Delft University of Technology. Report number CM-2018-01, 11 July 2018 - Downloadable from www.NationaalCoordinatorGroningen.nl

4.1. In-Plane Wall Tests

4.1.1. Sample Descriptions

Five single-wythe clay brick masonry walls with a window opening have been constructed in the TU Delft's Stevin lab II, all with the same type of material and identical geometry (Figure 4.2). Two notches with a dimension of 10x50mm are located in the bottom right and in the top left window corner. The specimens have a thickness of 100mm. An overburden of 0.12MPa is applied during the tests. Different loading schemes have been chosen (see Table 4.1). More details about the samples and tests are provided in the test protocol (Meulman et al., 2017). For the tests, pulling is associated with the positive direction, while pushing is associated with the negative direction (see Figure 4.1).

Table 4.1. Samples and loading protocol.

Sample	Loading Protocol	Date of Test
TUD_COMP-40	Repetitive pull, repetitive push, cyclic, dynamic*	22 June 2017
		23 June 2017
TUD_COMP-41	Repetitive pull	30 June 2017
TUD_COMP-42	Repetitive pull	7 July 2017
TUD_COMP-43	Dynamic*	25 July 2017
TUD_COMP-44	Repetitive pull**	7 August 2017

* Dynamic means in this case displacing the top beam in both directions at 1Hz or more
** Pre-damaged in push direction

Some additional comments are listed:

- TUD_COMP-40: multiple types of loading protocol have been tested.
- TUD_COMP-41: a repetitive pull protocol is applied.
- TUD_COMP-42: have the same repetitive pull protocol.
- TUD_COMP-43: dynamic loading protocol
- TUD_COMP-44: same protocol as COMP-41 and COMP-42 but the wall was pre-damaged in the push direction.

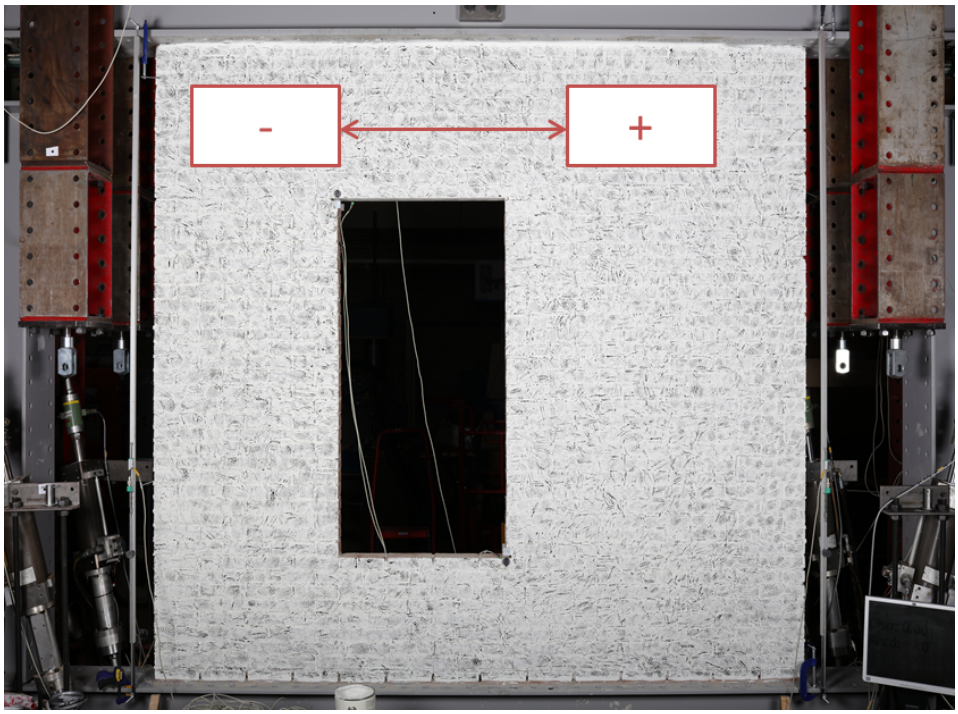

Figure 4.1. Set-up and wall sample at the initial stage of the test.

Figure 4.2. IP wall test sample.

In this report, the result of TUD_COMP-43 is not included. During this dynamic test two key measurement systems/sensors where not able to capture the desired data reliably. The vibration of the test was transmitted through the floor to the free standing column which was set as a reference to measure the displacement of the top beam. Especially in the later stage of the test, the measured top beam displacement became unreliable. In addition, the DIC measurement could not capture the crack initiation and propagation throughout the test, because the test was too fast. The dynamic loading takes place in about 2 seconds. With the current setup of the DIC system it was virtually impossible to capture the wall at its maximum displacement, because the point in time of this maximum displacement was unknown due to its potential phase shift. Pictures were taken before and directly after a dynamic load was applied. Since the cracks had mostly closed again after the dynamic load had been applied, the DIC results could not provide the desired results. To use the same DIC measurement technique for dynamic testing, a high speed camera could be used. In this way, many frames are taken during the vibration load and therefore also capture the wall at peak displacement. Frames of interesting moments during the vibration load can be selected for DIC analysis.
The sensor that measures the top beam displacement should be isolated from the lab floor for future dynamic testing, since the test set-up transfers vibrations through the floor to the free standing column of the sensor. Another option is to use a damping system between the test set-up and the lab floor.

Further, the test of TUD_COMP-44 deviates from the planned test as described in the test protocol (Meulman et al., 2017). During the first script-controlled loading the test set-up became unstable when it switched from the push direction to the pull direction. This resulted in an uncontrolled displacement of about 6mm of the top beam in the push direction. A large diagonal crack was formed in the wall due to this displacement. The planned test protocol could not be applied anymore, and it was thus changed to the same repetitive pull protocol as applied to TUD_COMP-41 and TUD_COMP-42. During the test, it had been assumed that the wall had only been damaged in the push direction; however, from DIC analyses it appeared that cracks had also formed in other parts of the wall which affected the pull direction. During the repetitive pull test no new cracks were able to develop and it was merely opening and closing of already formed cracks. Consequently, the test of TUD_COMP-44 is not included in this report. Nonetheless, the lack of energy dissipation in the graphs corresponding to component 44, in contrast to the graphs of the previous walls that do show energy dissipation, serves as a validation that new cracks are being formed during the increased cycles of these previous walls.
Both TUD_COMP-43 and TUD_COMP-44 will be used for future testing, and the captured data during these two test may possibly be used for later research. Data of these two tests have yet to be be fully analysed.

4.1.2. TUD_COMP-40

The TUD_COMP-40 test could be considered as a trial test on which multiple loading types have been applied. The first loading type applied during the test is repetitive pull and is used as a basis for the loading scheme of TUD_COMP-41 and TUD_COMP-42. As mentioned before, only the repetitive pull type of loading is taken into account in the report and therefore also only that part of the TUD_COMP-40 is elaborated in this section.

Repetitive Pull Test Results

Table 4.2 shows an overview of the repetition displacement steps (sets) that are applied to the TUD_COMP-40. In the first repetition the top beam displacement u(1) is determined by pulling the top beam until one of the notches reaches an opening of 0.1mm. The loading scheme is described in more detail in the test protocol (Meulman et al., 2017).

Table 4.2. Repetitive pull loading protocol of TUD_COMP-40 (Meulman et al., 2017).

Repetition displacement step	Top beam displacement u
1 x R1	+CMOD (crack 0.1mm)
2 x R1	u(1)
3 x R2	1.25 u(1)
3 x R3	1.50 u(1)
3 x R4	1.75 u(1)
3 x R5	2.00 u(1)

In the first repetition, the first crack was detected from the sensor located at the notch in the bottom right window corner (Figure 4.3).

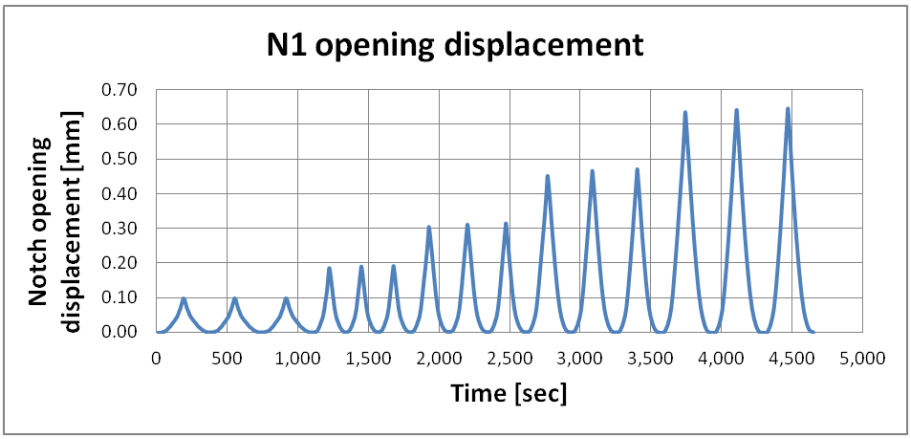

Figure 4.3. Notches sensors at the window corners.

Table 4.3 shows the displacement of the jack, top beam, and the calculated wall displacement for every repetition displacement step. The jack is displacement-controlled in the test. The ratio between jack displacement and top beam displacement is about 2.1 for the first repetitions but will decrease when larger displacements are applied. This is due to the fact that the "play" that is in the system is constant and becomes a smaller percentage of the displacement that is applied. The 2.1 ratio of the first repetitions is determined with test results of IP wall test from the NAM2016 project (Esposito et al., 2016.b). The equation used to calculate the wall displacement can be found in the test protocol (Meulman et al., 2017)

Table 4.3. Jack and average wall top displacement. (measured value, ** calculated with use of multiple sensors).*

Repetition displacement step	Jack displacement [mm]*	Top beam horizontal displacement [mm]*	Wall displacement [mm]**
R1	1.80	0.85	0.70
R2	2.25	1.18	1.00
R3	2.70	1.55	1.38
R4	3.15	1.95	1.80
R5	3.60	2.39	2.23

Figure 4.4 and Figure 4.5 show the displacement of the top beam and wall against time for every repetition displacement step.

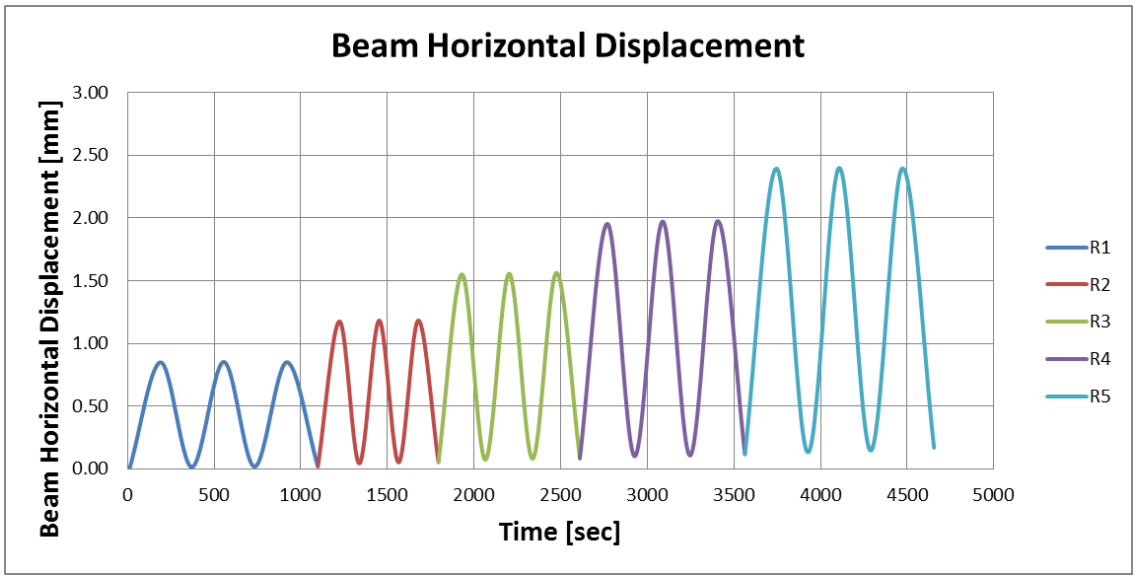

Figure 4.4. Beam horizontal displacement.

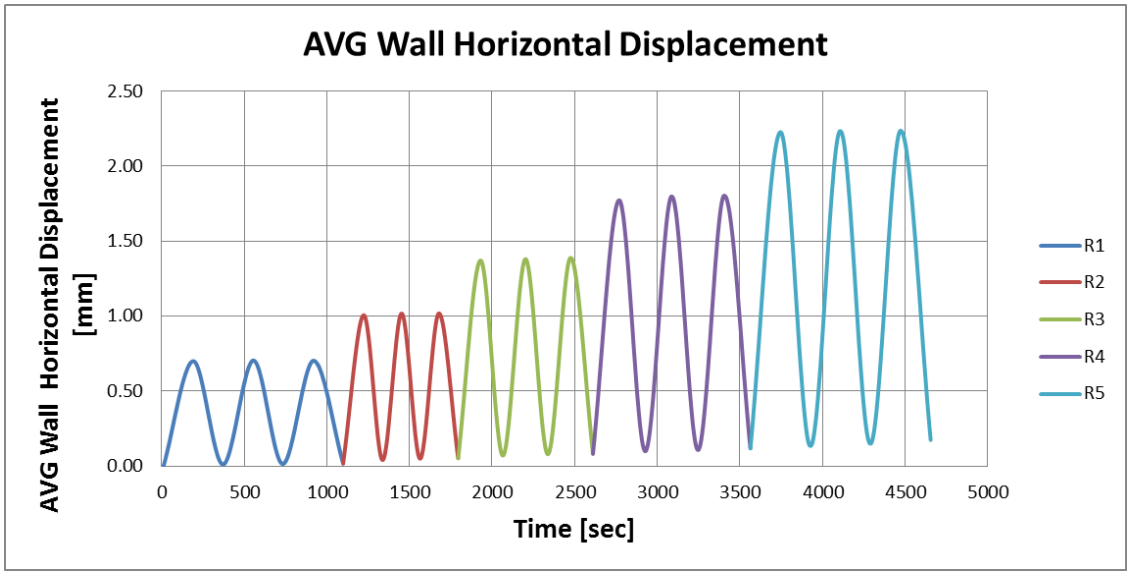

Figure 4.5. Average wall top horizontal displacement.

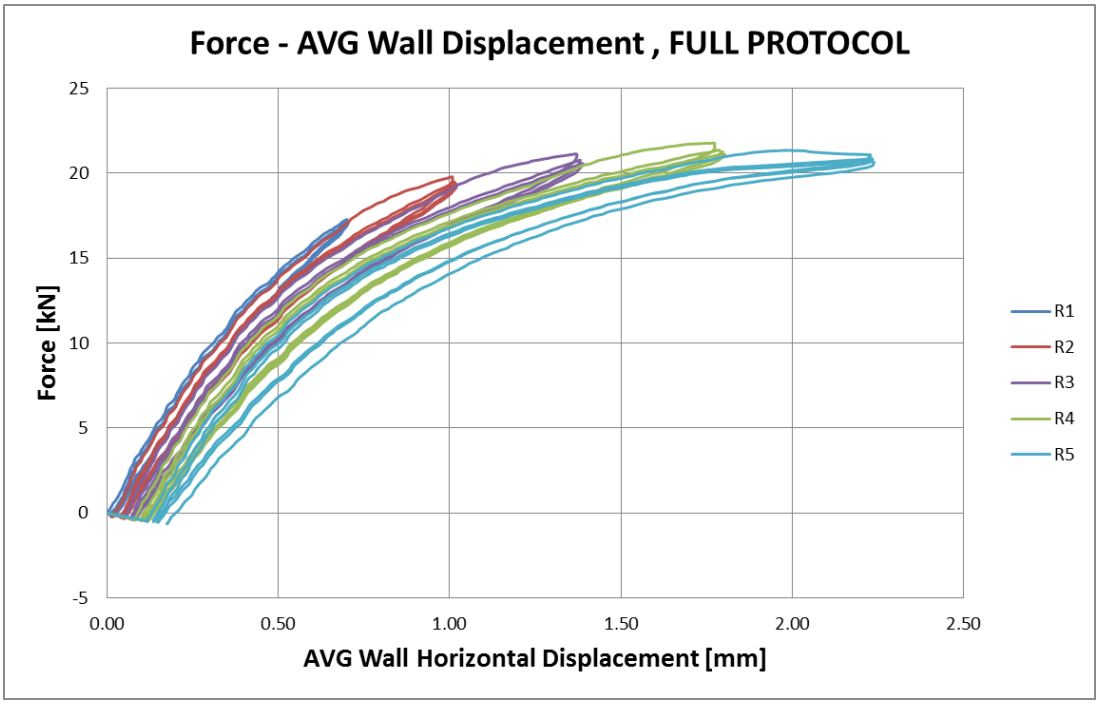

Figure 4.6. Hysteresis graph for the repetitive pull test.

Figure 4.6 shows the force-wall displacement hysteresis graph of TUD_COMP-40. The peak load reached in the test is 21.8kN. It was obtained during R4. The initial stiffness is 35.1kN/mm. The initial stiffness is determined in the first loading of the wall when the displacement of the top beam for the first repetition, R1, is determined. The stiffness from the AVG wall displacement curve is taken between 0mm and 0.3mm. Figure 4.7 shows the separated repetition displacement steps with the related average stiffness of that particular repetition displacement step.

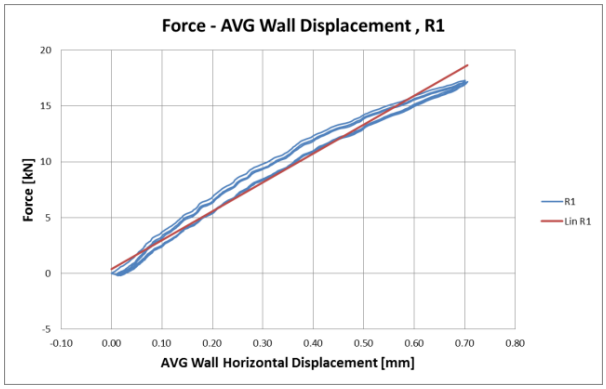

Repetition 1: K=25.92kN/mm

(a)

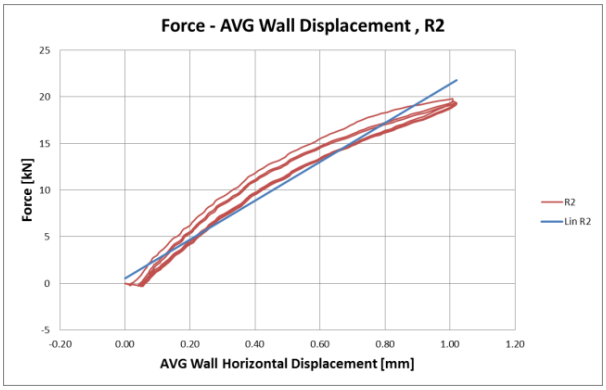

Repetition 2: K=20.85kN/mm

(b)

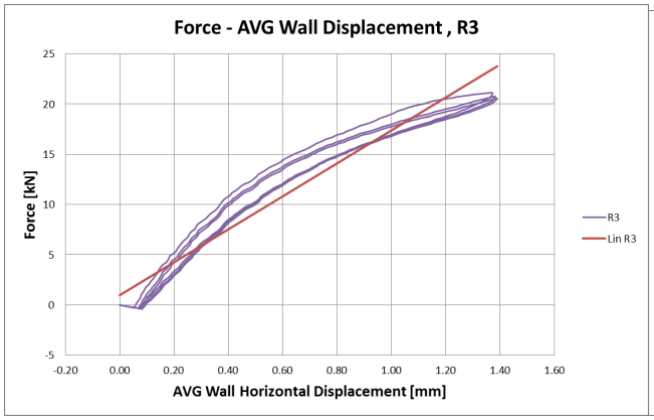

Repetition 3: K=16.42kN/mm
(c)

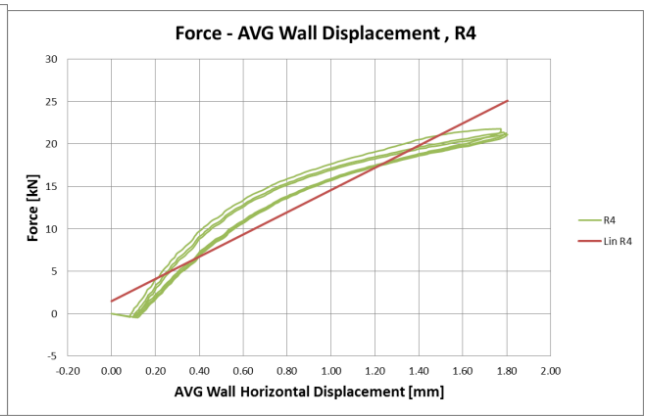

Repetition 4: K=13.11kN/mm
(d)

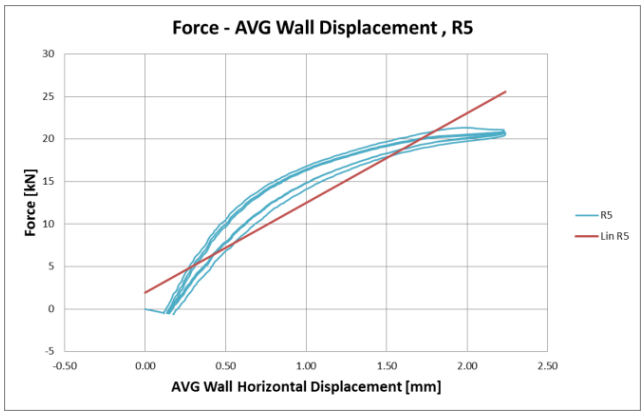

Repetition 5: K=10.57kN/mm
(e)

Figure 4.7. Hysteresis plots for each repetition displacement step.

The horizontal wall displacement can be expressed in terms of drift. The drift of each separate repetition displacement step is shown in Table 4.4. Wall drift is defined as the horizontal displacement of the top of the wall divided by the height of the wall expressed in percentage.

Table 4.4. Wall drift during the repetitive pull test of TUD_COMP-40.

Repetition displacement step	Wall drift
R1	0.026%
R2	0.038%
R3	0.051%
R4	0.067%
R5	0.083%

Figure 4.8 and Figure 4.9 show the average notch opening displacement of notch 1 and notch 2 which are located on the bottom right corner of the window (front and back side). The graphs show the progression of the notch opening during the test plotted against time and coloured according to the displacement step. In Figure 4.9 it can be seen that in R1 and R2 there is almost no increase in notch opening visible during the repetitions within that step. However in R3, R4 and R5 there is an increase visible between the first and last repetition in a repetition displacement step.

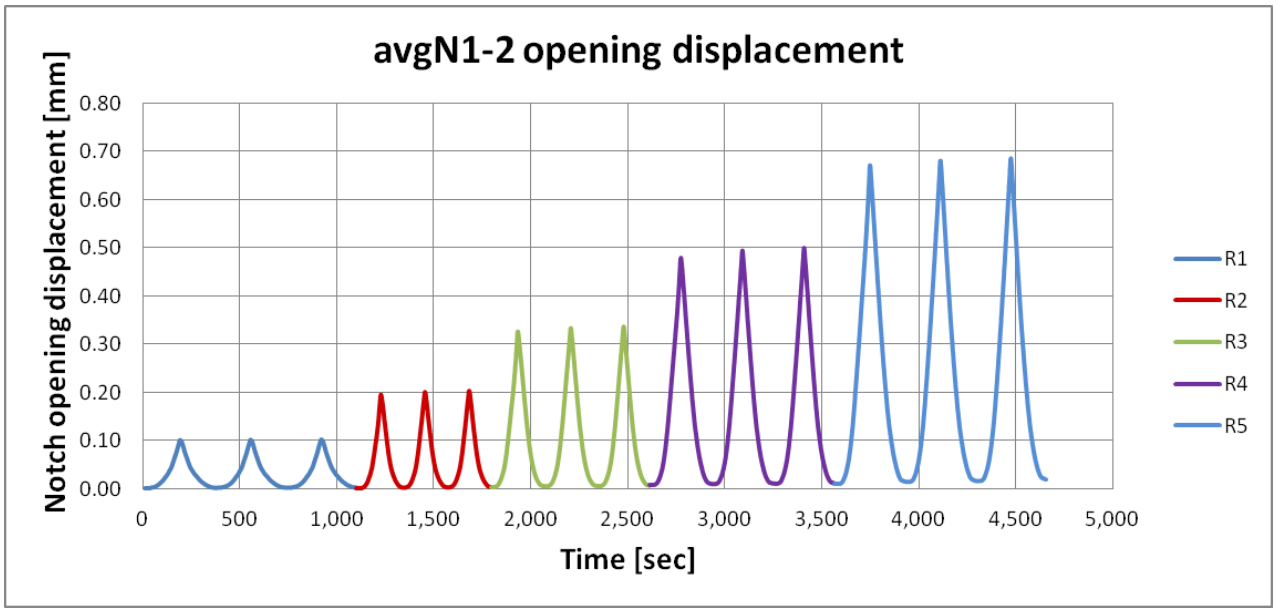

Figure 4.8. Average opening displacement of notch 1 and 2.

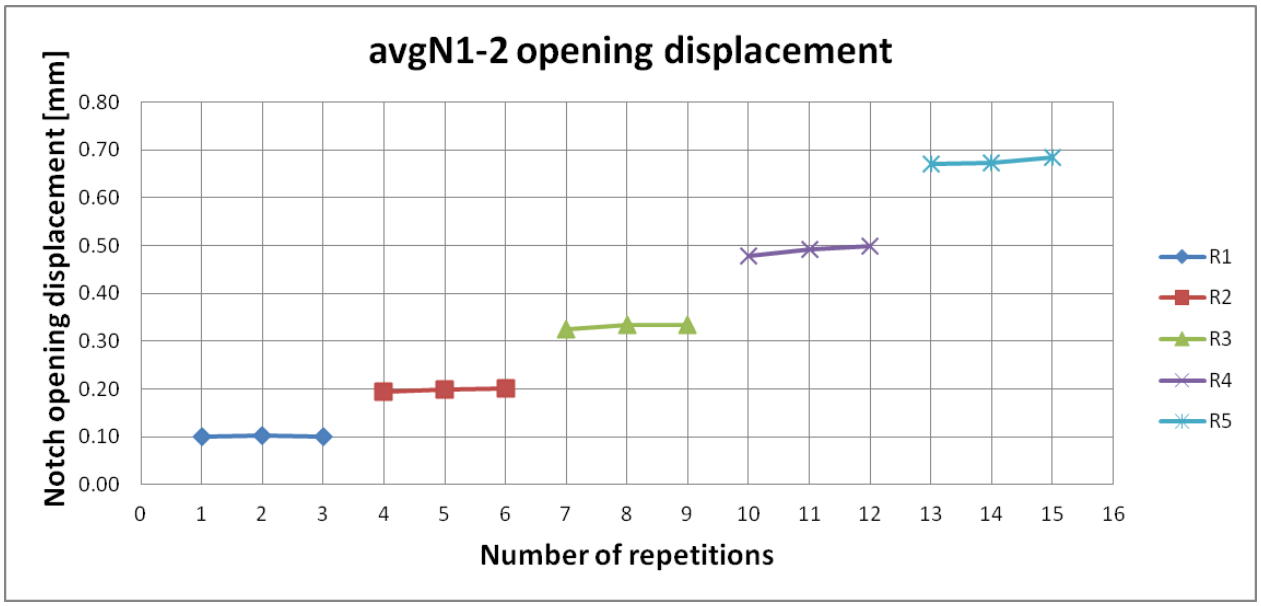

Figure 4.9. Average opening displacement of notch 1 and 2 per number of repetitions.

Since the absolute displacement difference between the first and last repetition within a step is small, it can be expressed in a percentage of the notch opening based on the first repetition of the repetition displacement step or referred to as a set (of repetitions). Table 4.5 contains the notch opening displacement increase within a repetition displacement step.

Table 4.5. Notch opening increase within repetition displacement step of N1.

	R1	R2	R3	R4	R5
N1 first peak opening displacement (mm)	0.099	0.187	0.305	0.452	0.636
Difference first-last peak (mm)	0.00013	0.00551	0.00992	0.01910	0.01049
Percentage	0.13%	2.95%	3.26%	4.23%	1.65%

The percentage of increase in notch opening within a repetition displacement step from Table 4.5 are plotted in Figure 4.10.

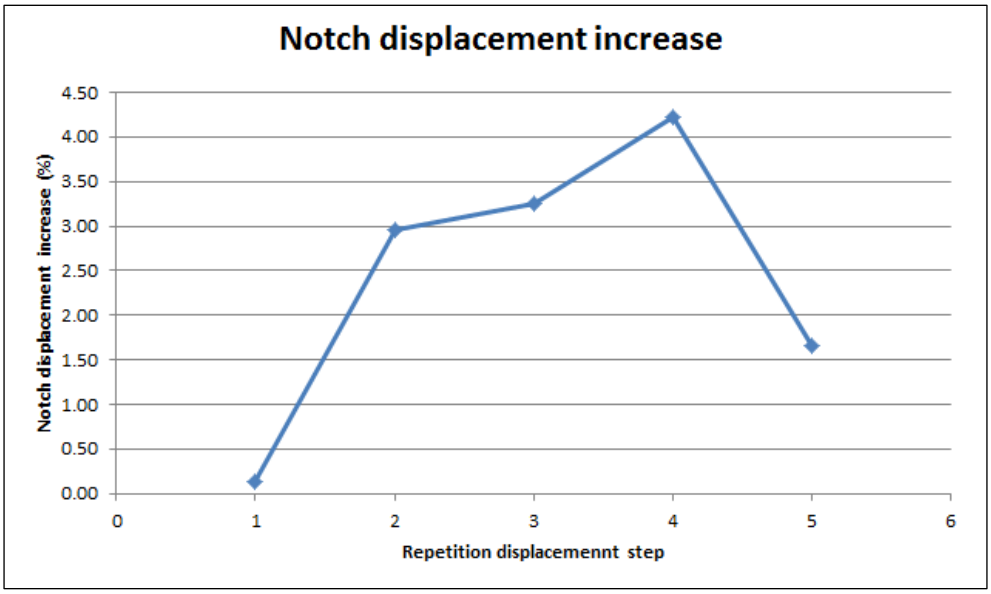

Figure 4.10. Notch displacement increase between first and last repetition within a repetition displacement step.

Besides the increase in notch opening observed within a repetition displacement step, a reduction of force is observed. The same principle as described for determining the notch opening displacement increase expressed in percentage is used for the reduction in force. Figure 4.11 shows the plot of the force reduction within a repetition displacement step expressed in percentage of the force of the first repetition of a certain repetition displacement step.

The reduction of force within a set is visible in Figure 4.12 where the the peak force of every repetition is shown. In both Figure 4.11 and Figure 4.12 it can be seen that the force reduction within a repetition displacement step becomes larger when the displacement of the wall increases.

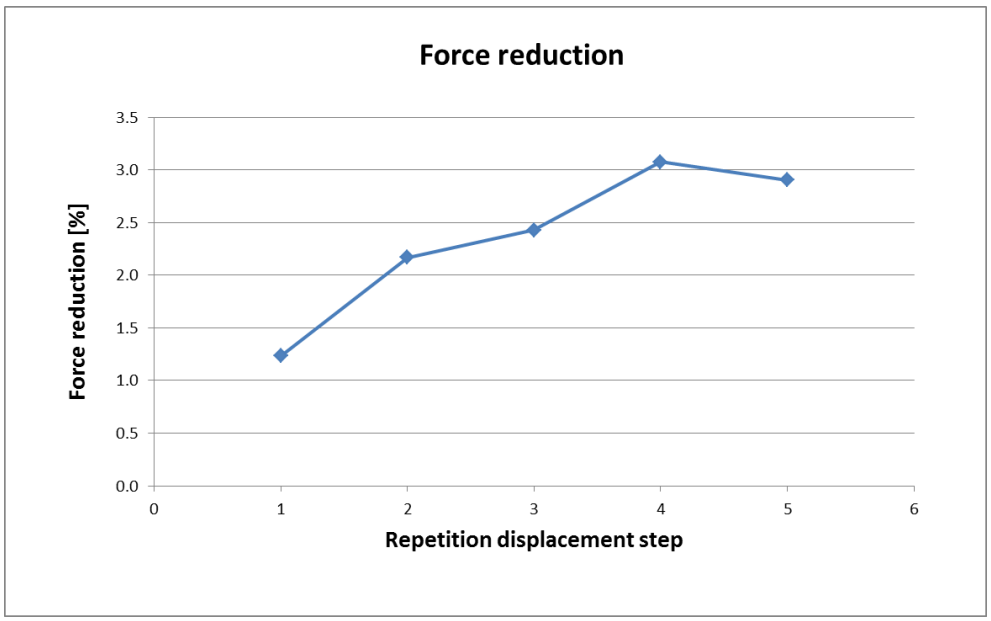

Figure 4.11. Reduction in measured horizontal force within a repetition displacement step expressed in percentage.

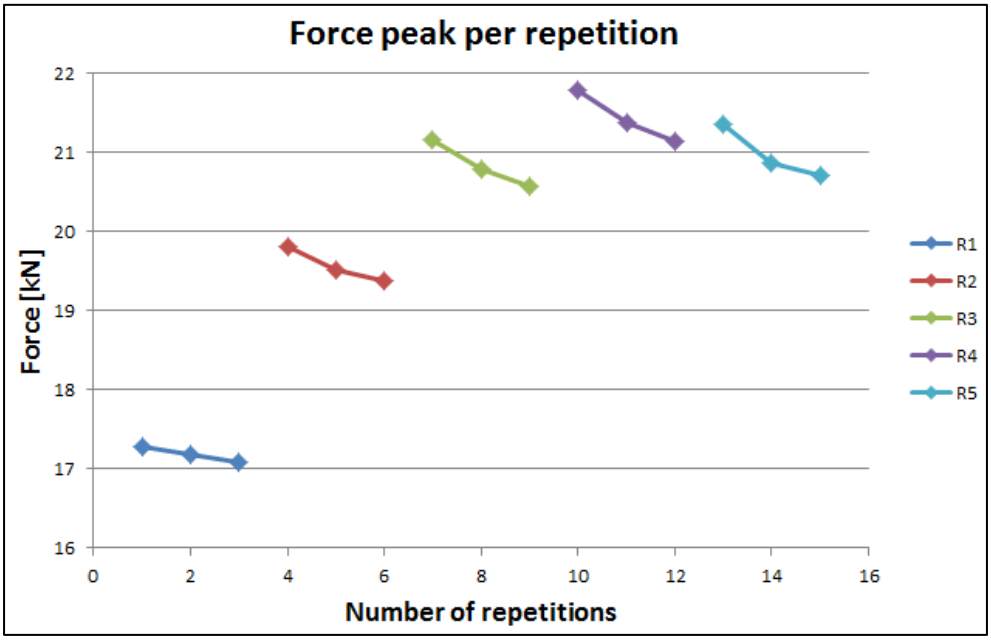

Figure 4.12. Force peak per repetition.

DIC is the main measurement system for crack surveillance of the masonry samples and is described in more detail in Section 2.6 and in the test protocol (Meulman et al., 2017). With DIC it is possible to produce horizontal displacement, vertical displacement, and strain plots. Crack initiation and propagation throughout the test can be analysed. Secondly, the plots become a reference for numerical model validation and calibration. Every pixel of the photograph has a size of approximately 0.5mm. The strain plot is produced by using the pixels as a grid to generate bi-cubic finite elements; similarly as in a finite element model, a shape function is used to determine strain in the elements. If the strain becomes too high, the material will crack. In this case the cracked material leaves a void, so considering strain over the crack opening is not entirely correct. The DIC strain plot function, however, serves to indicate clearly where the cracks are but, again, should not be considered real strain. These plots will be further denoted as "crack plots". To obtain values of crack width from the DIC method, the relative displacement of points at both sides of the crack edges need to be observed (see Section 2.6).

DIC plots of the cracks in the wall from every repetition displacement step (R1 to R5) are shown in Figure 4.13 to Figure 4.17. The crack plots show where the cracks initiate and propagate through the masonry.

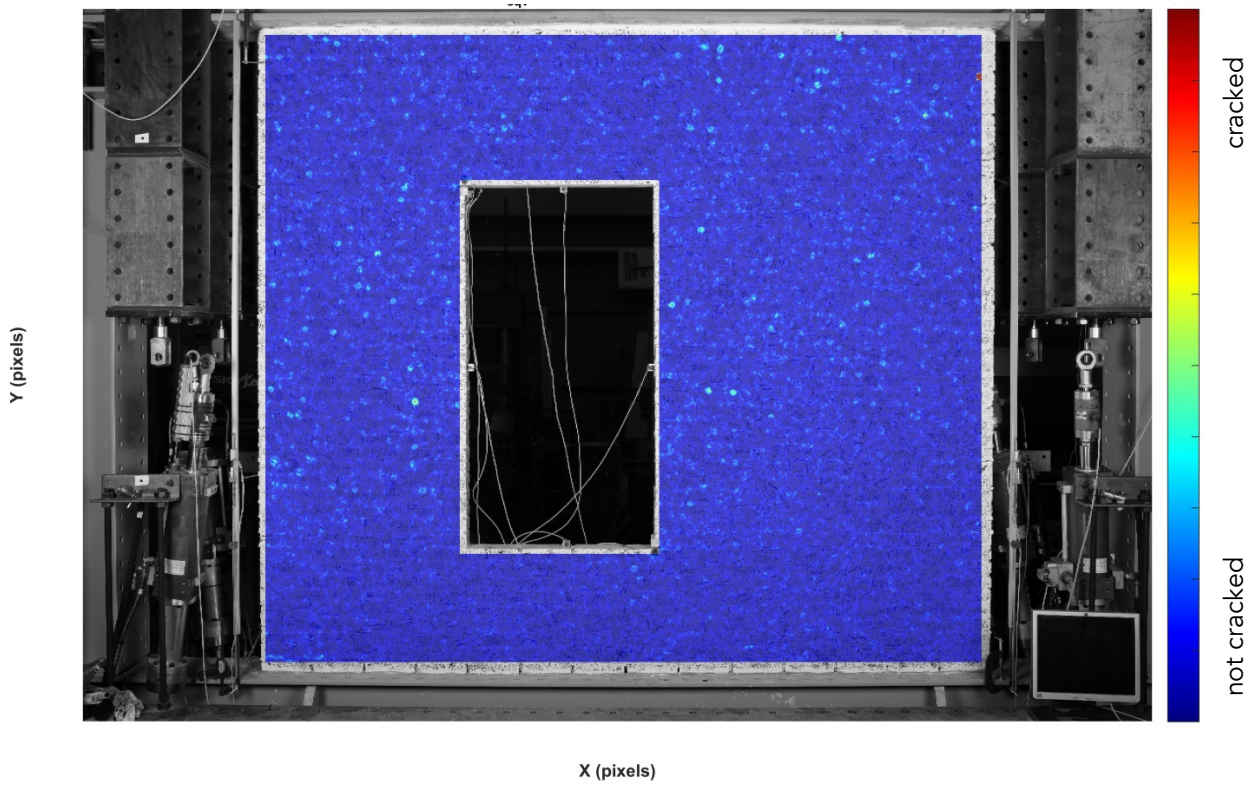

Figure 4.13. A crack plot of R1 of the repetition displacement steps.

In the R1 phase (Figure 4.13) the notch is 0.1mm opened, which indicates the initiation of the crack. This opening is measured by the sensors but difficult to detect in the figure due to noise in the DIC picture.

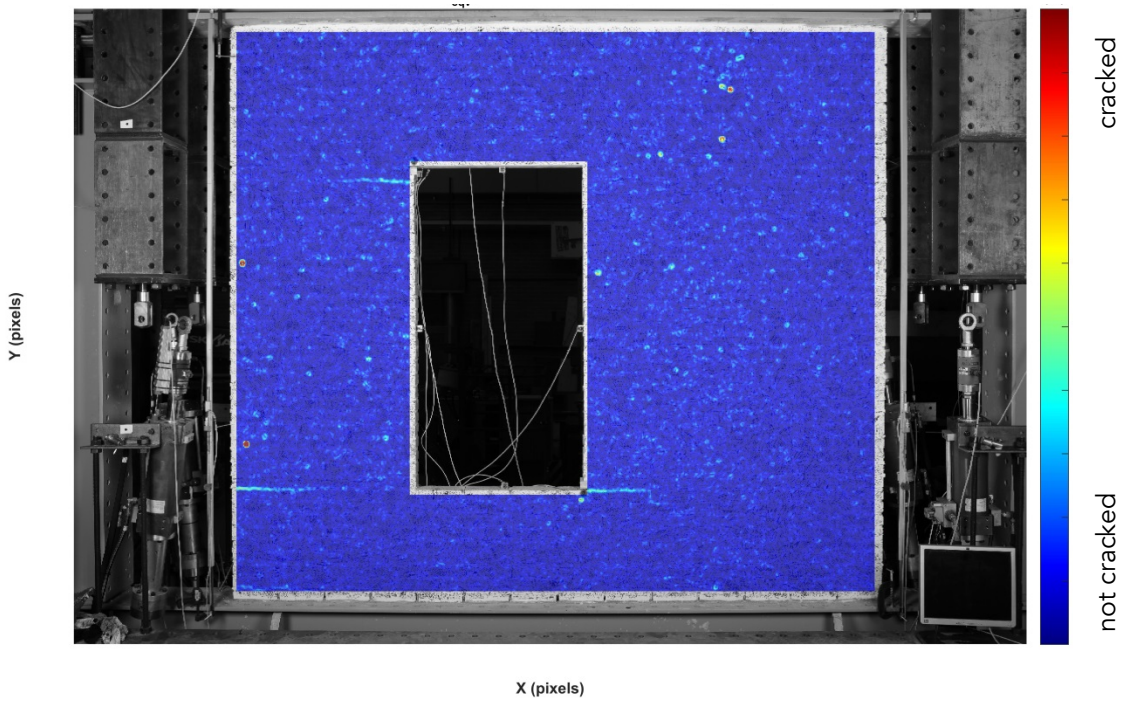

Figure 4.14. A crack plot of R2 of the repetition displacement steps.

In the R2 phase the notch opening is about 0.2mm and the crack initiation location and crack propagation through the masonry is now more clearly visible in the DIC crack plot. The cracks are located at the bottom right corner and top left corner of the window. Due to the rotating effect of the left pier, another crack is initiated from the left edge of the wall.

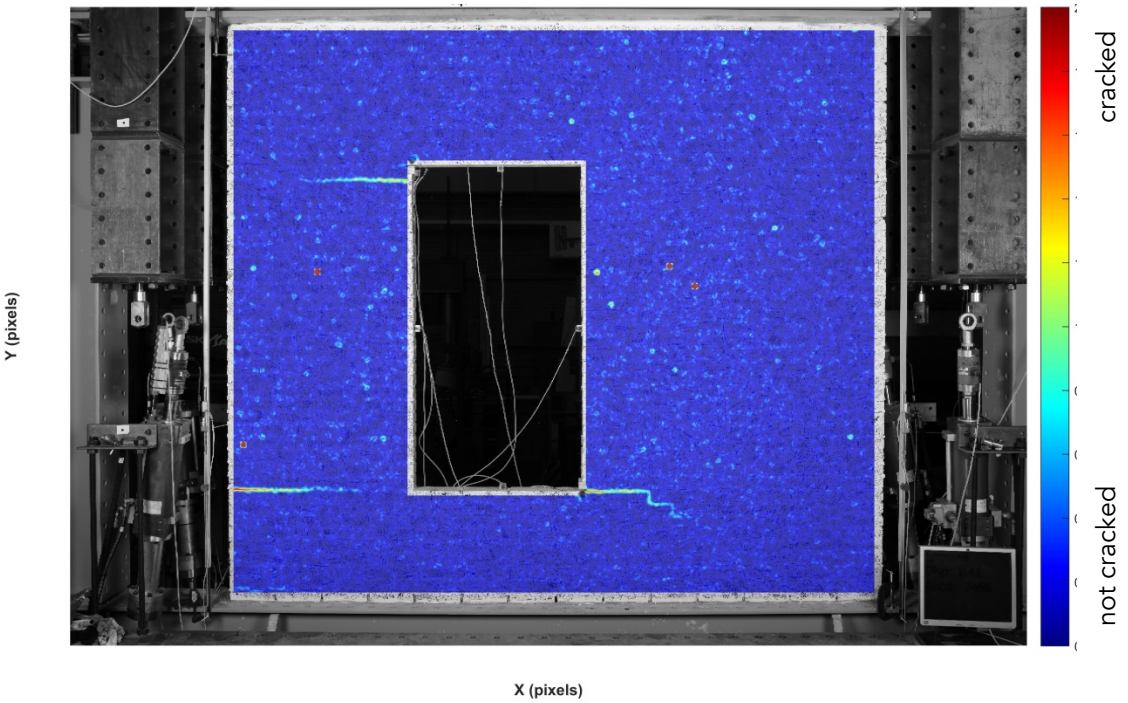

Figure 4.15. A crack plot of R3 of the repetition displacement steps.

In the R3 phase, the crack from the bottom right window corner transfers from horizontal direction in a stepwise direction. The crack length of all three cracks have increased along with the width, which is visible by the change in colour.

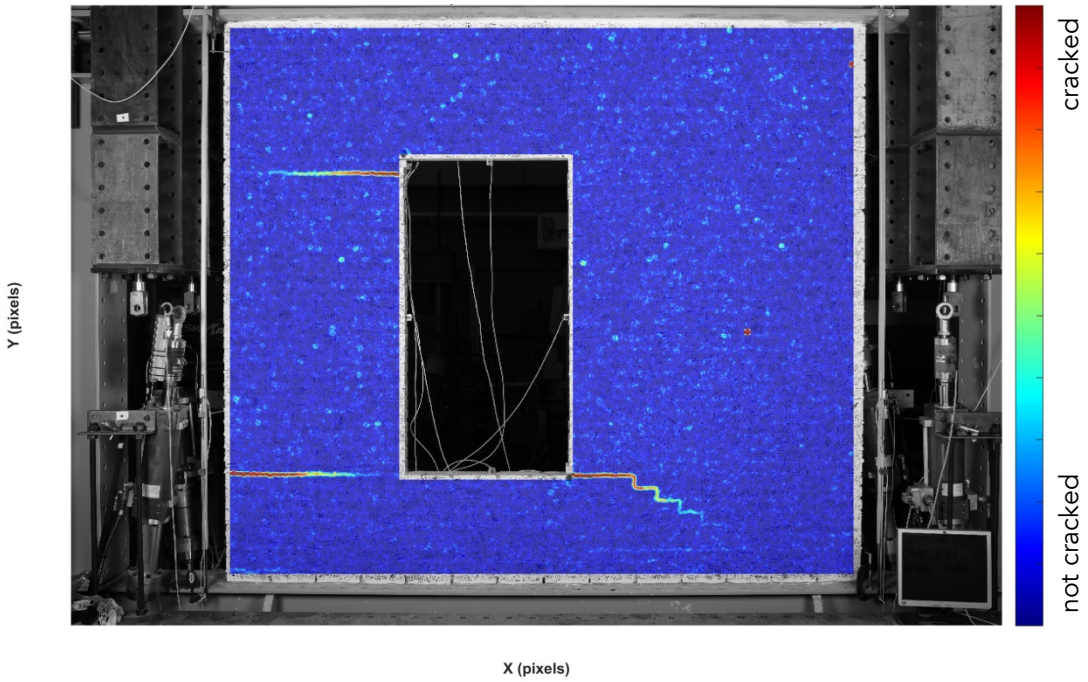

Figure 4.16. A crack plot of R4 of the repetition displacement steps.

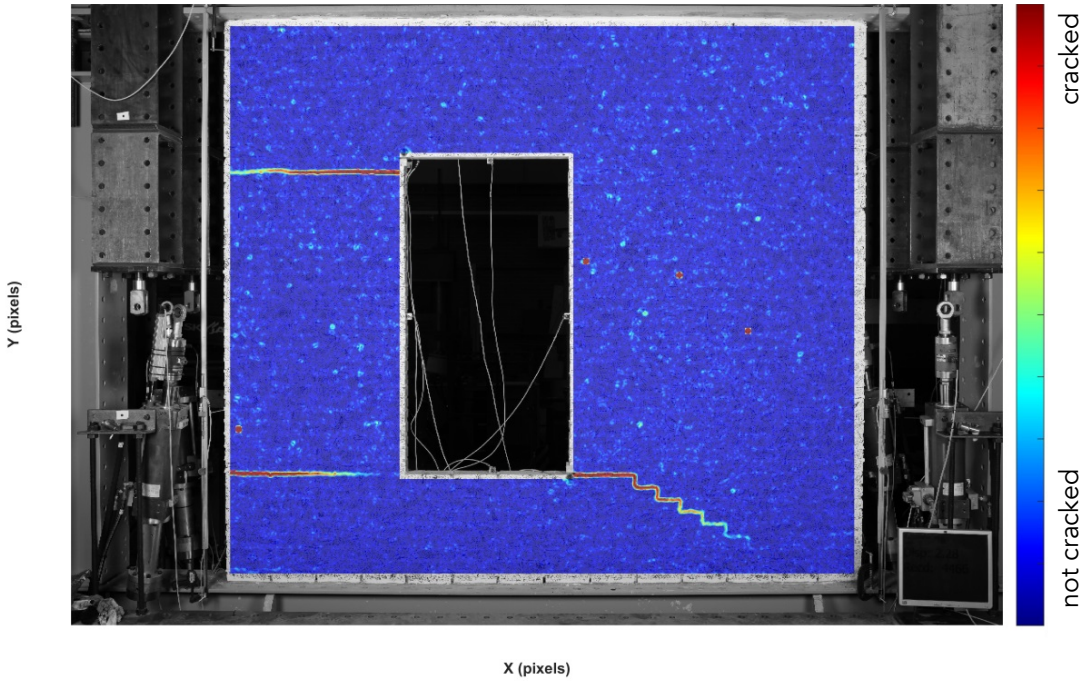

Figure 4.17. A crack plot of R5 of the repetition displacement steps.

In the last phase, R5, of the test, the two cracks on the left side have fully extent from the window edge to the wall edge. The crack in the bottom right has propagated further as a diagonal crack, which in masonry takes a stair-like pattern. In Figure 4.18 a close up is shown of the crack in the bottom right corner of the window when the displacement of the beam is at it maximum for R5.

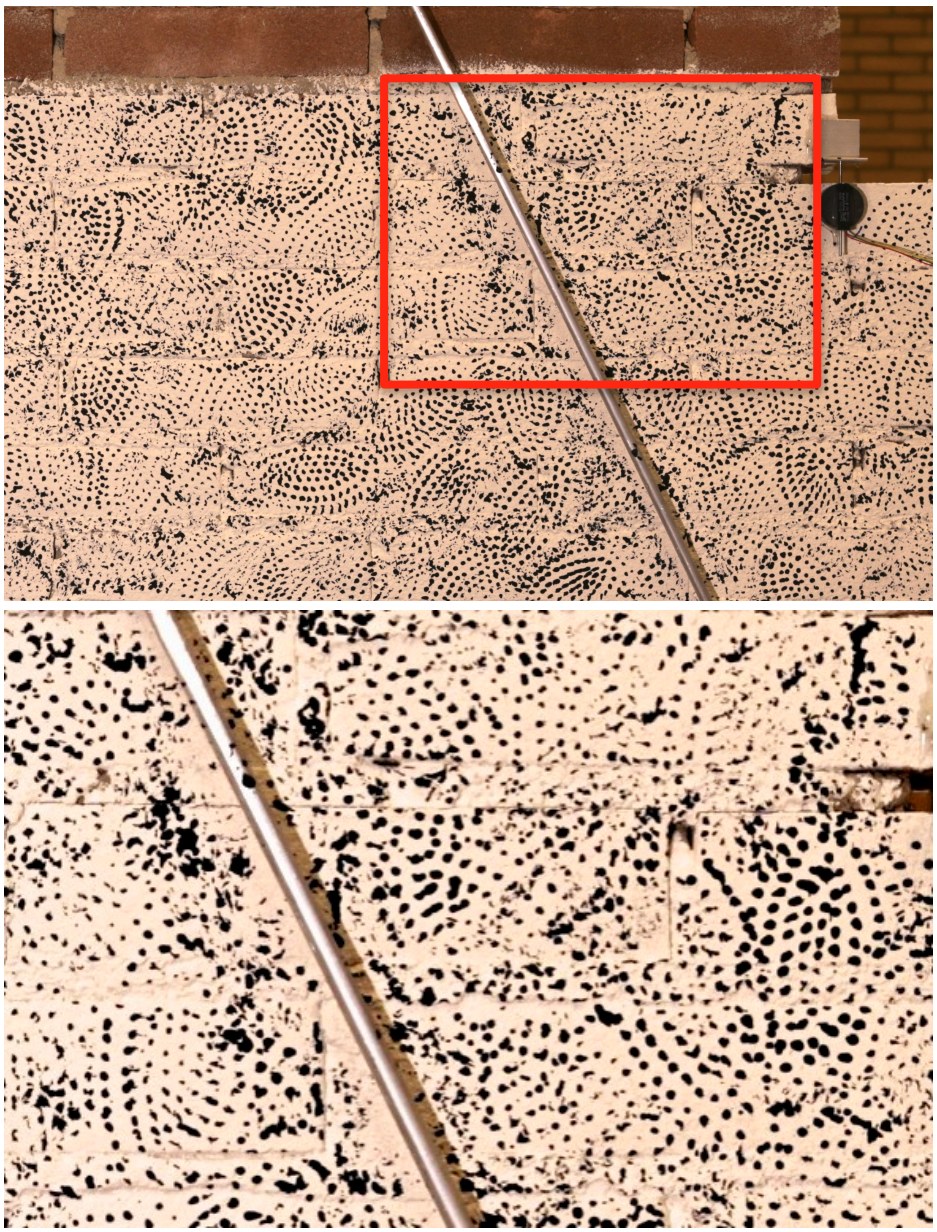

Figure 4.18. Top: back side of the wall at bottom right corner of window (when in front view). Bottom: zoomed in section on crack, location marked by red rectangle.

4.1.3. TUD_COMP-41

The protocol for the repetitive pull test is shown in Table 4.6 which is described in more detail in the test protocol (Meulman et al., 2017). For TUD_COMP-41, ten repetitions per displacement step are applied to investigate the effect of multiple repetitions on the propagation of cracks in masonry. Additionally, two types of loading rate are applied to be able to test the effect of the loading rate on the crack propagation in masonry.

Table 4.6. Repetitive pull loading protocol of TUD_COMP-41. (Meulman et al., 2017).

Repetition displacement step	Top beam displacement u	Repetitions
R1a	+CMOD (crack 0.1 mm)	1, slow rate
R1a	u(1)	9, slow rate
R1b	u(1)	10, **fast** rate
R2a	1.25 u(1)	10, slow rate
R2b	1.25 u(1)	10, **fast** rate
R3a	1.50 u(1)	10, slow rate
R3b	1.50 u(1)	10, **fast** rate
R4a	1.75 u(1)	10, slow rate
R4b	1.75 u(1)	10, **fast** rate
R5a	2.00 u(1)	10, slow rate
R5b	2.00 u(1)	10, **fast** rate

The first crack opening to 0.1mm was detected at the sensor located in the top left window corner (sensor N3), see Figure 4.19.

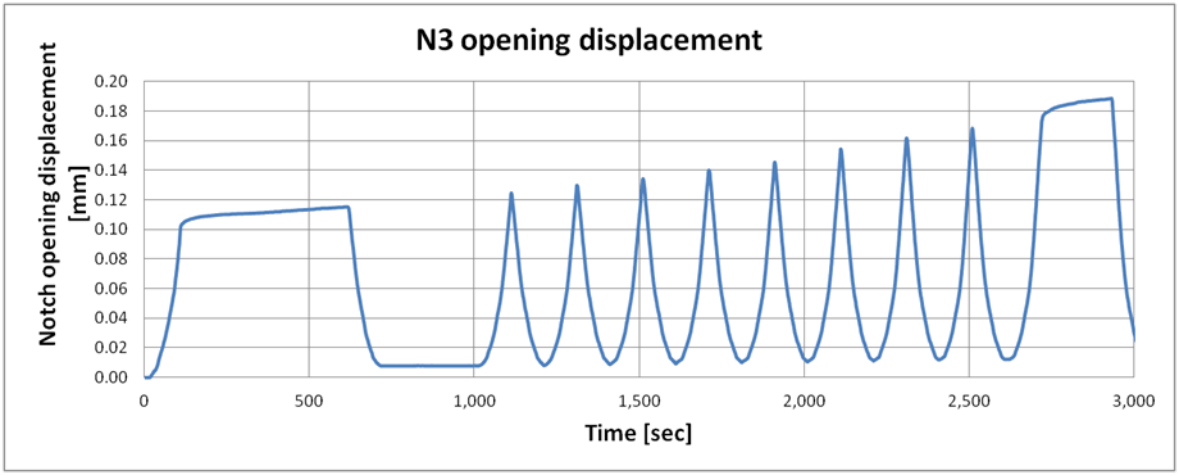

Figure 4.19. N3 opening displacement in R1a to determine top beam displacement for R1.

In Figure 4.19 it is visible that there is a clear increase of notch opening displacement at every repetition. However this trend was also noticed during this phase of the test in the top beam displacement (see Figure 4.20). This should not be the case because the top beam displacement should have a constant peak displacement at a certain repetition displacement step. The displacement is controlled by the jack which showed a constant peak displacement during the test (Figure 4.21). This effect was not noticed during the test of the TUD_COMP-40 test. It was concluded that the jack displacement sensor was not measuring correctly. Since it is the top beam displacement that requires to be controlled it was decided to switch the

controlling system from the jack displacement sensor to the top beam horizontal displacement sensor. This way of controlling the system increases the risk of an unstable control system but makes it possible to directly control the displacement of the top beam.

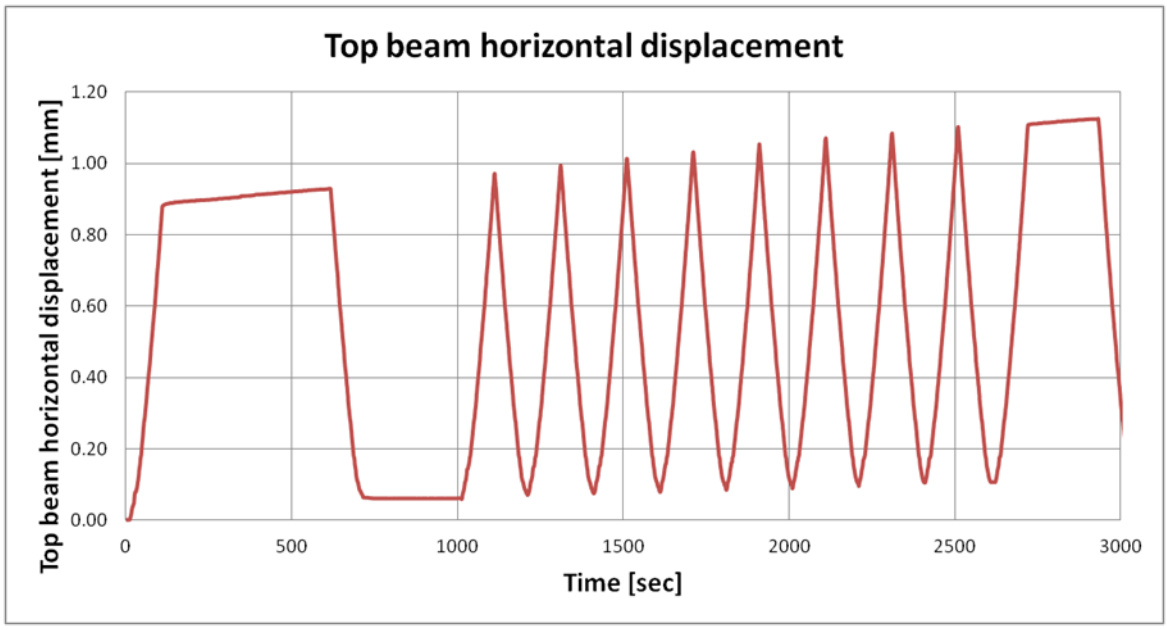

Figure 4.20. Top beam horizontal displacement of R1a.

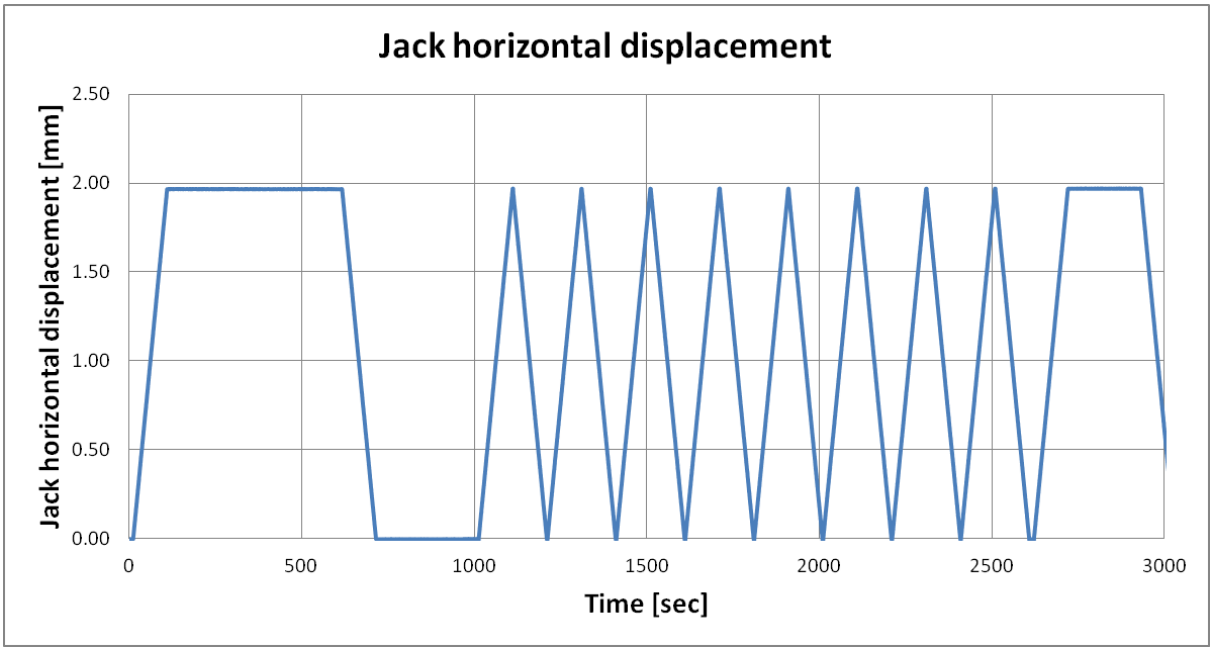

Figure 4.21. Jack horizontal displacement of R1a.

Because of the issue with the top beam displacement the R1a phase is excluded from the test results. Only the top beam displacement at the first time the notch opens 0.1mm is used from the R1a phase since in this repetition the test set-up is stopped manually when the notch reached 0.1mm of opening. In this way, the result is not affected by the issue described. Table 4.7 shows the peak displacement of the top beam and the average wall top displacement.

Table 4.7. Beam and AVG wall top displacement. (measured value, ** calculated with use of multiple sensors).*

Repetition displacement step	Top beam horizontal displacement [mm]*	Wall displacement [mm]**
R1	0.87	0.69
R2	1.09	0.89
R3	1.31	1.09
R4	1.53	1.30
R5	1.74	1.52

Figure 4.22 and Figure 4.23 show, respectively, the repetitions for the top beam horizontal displacement, and the average wall displacement.

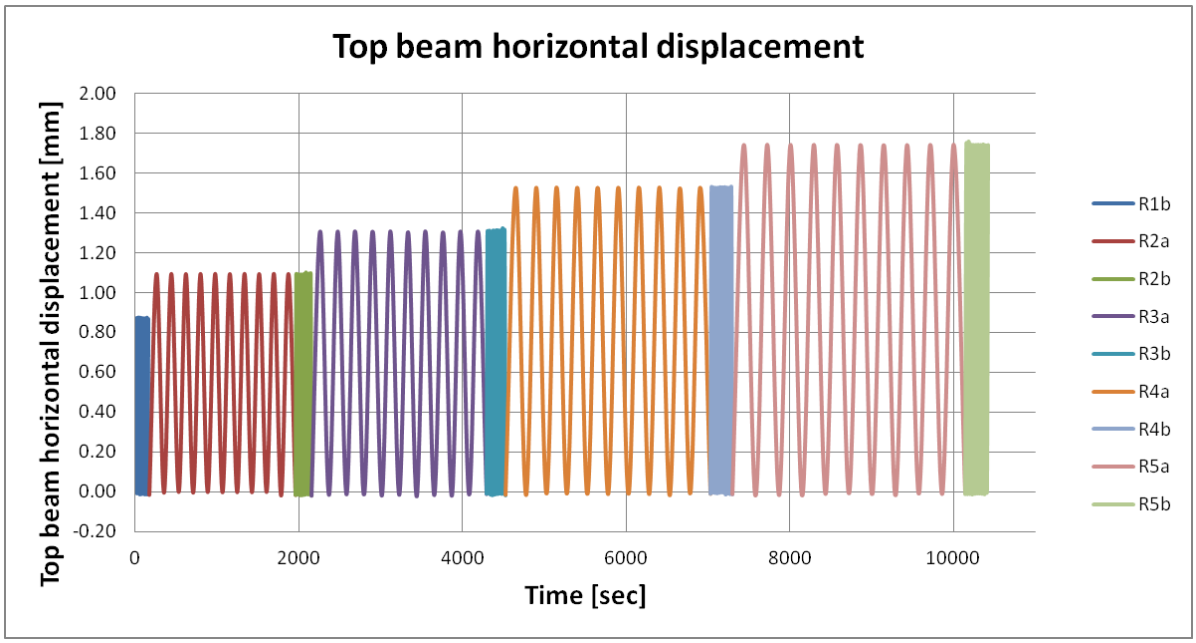

Figure 4.22. Top beam horizontal displacement.

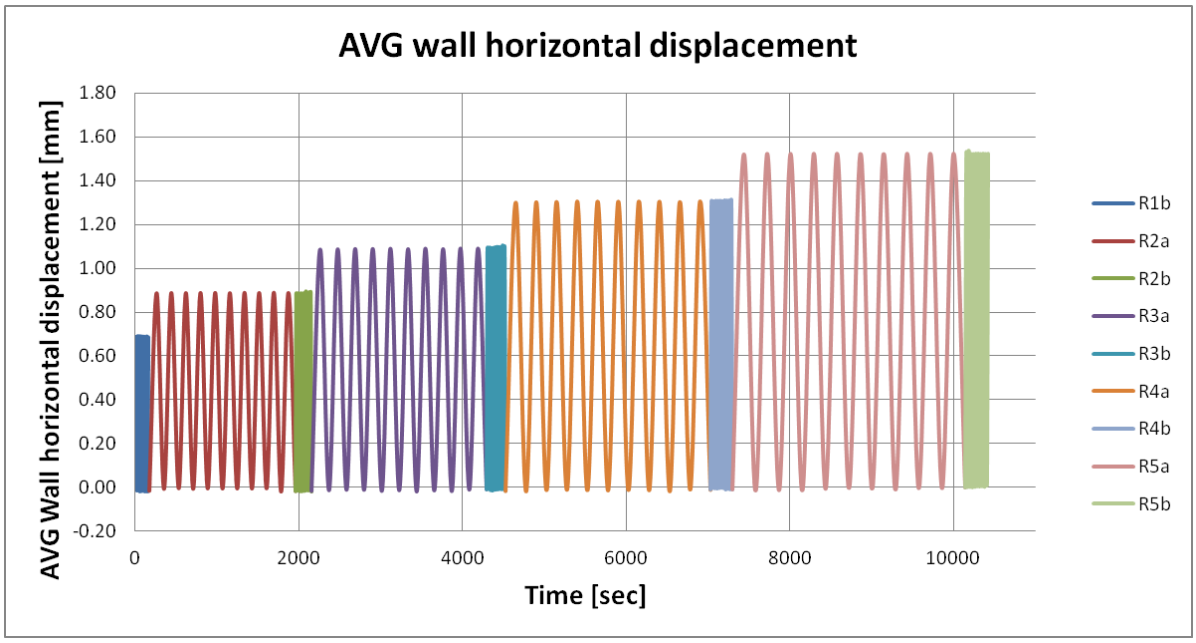

Figure 4.23. Wall horizontal displacement.

The force-displacement hysteresis graph of TUD_COMP-41 is shown in Figure 4.24. The peak load reached in the test is: 22.05kN. It was obtained during R4. The initial stiffness is 38.1kN/mm. In Figure 4.25 all repetition displacement steps are plotted separately with the corresponding stiffness.

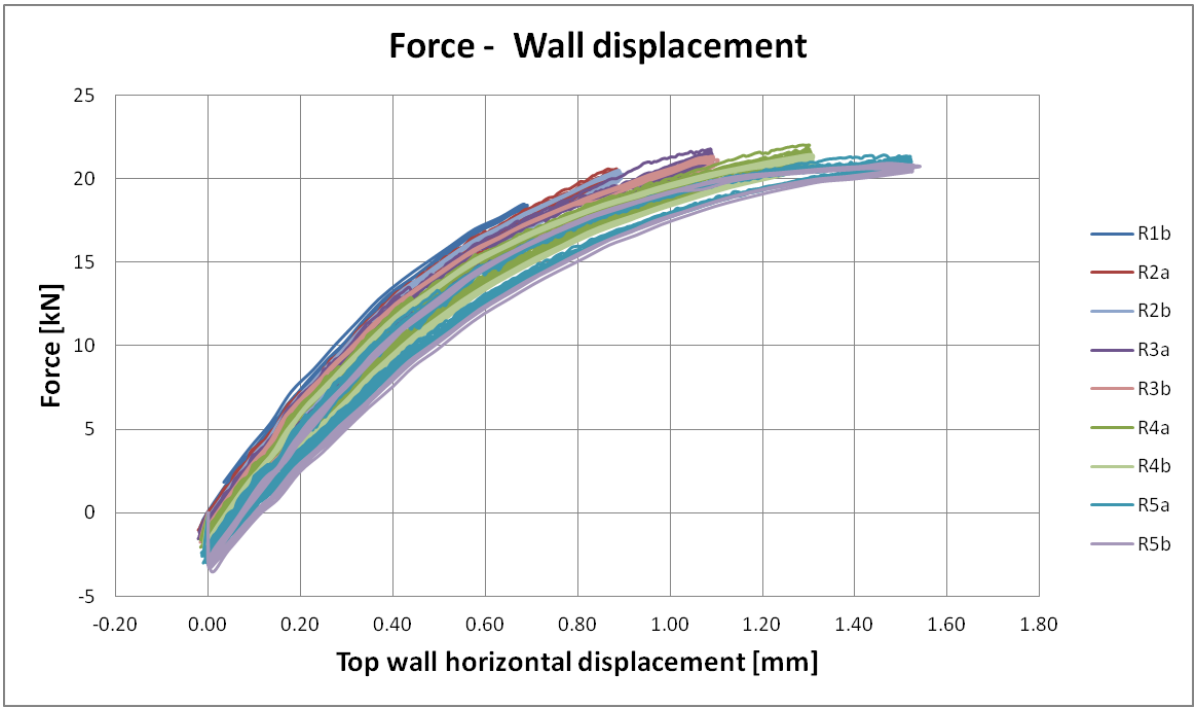

Figure 4.24. Hysteresis graph for the repetitive pull test TUD-COMP-41.

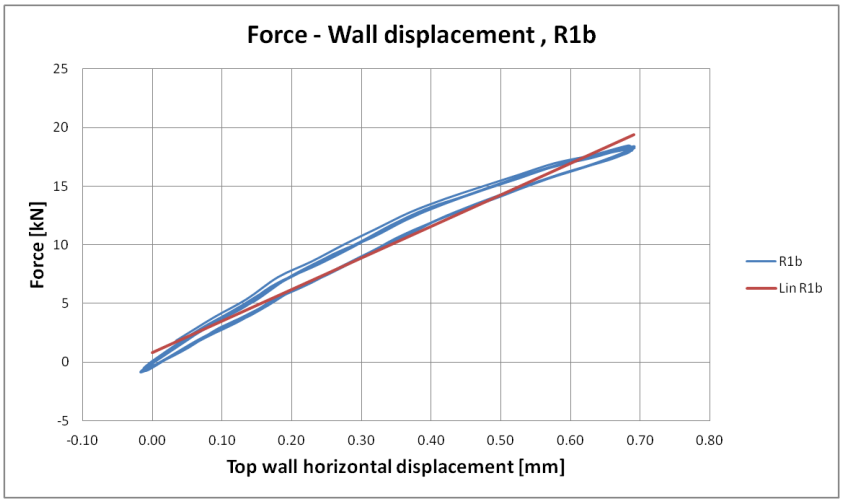

Repetition 1b: K=26.88kN/mm

(a)

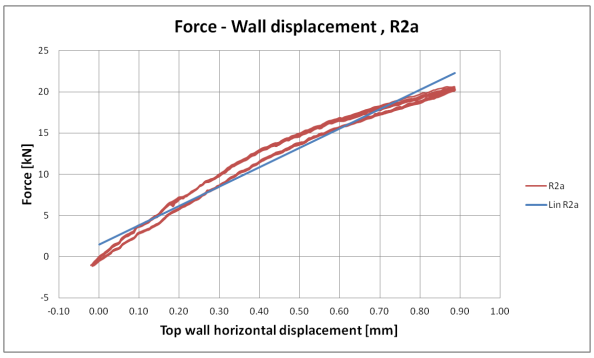

Repetition 2a: K=23.44kN/mm

(b)

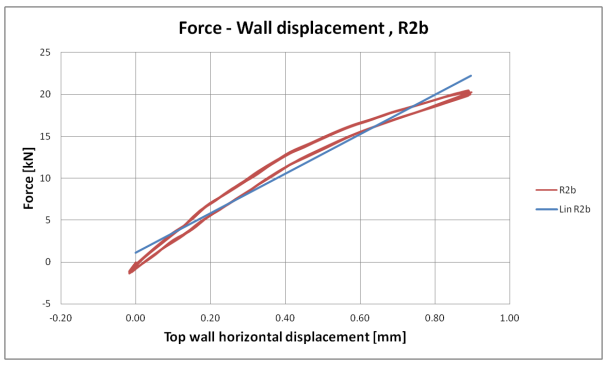

Repetition 2b: K=23.60kN/mm

(c)

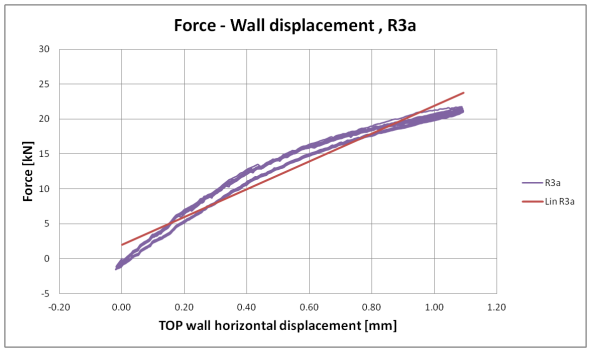

Repetition 3a: K=19.88kN/mm

(d)

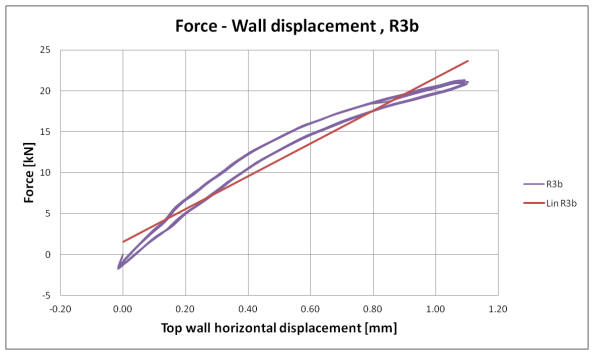

Repetition 3b: K=20.07kN/mm

(e)

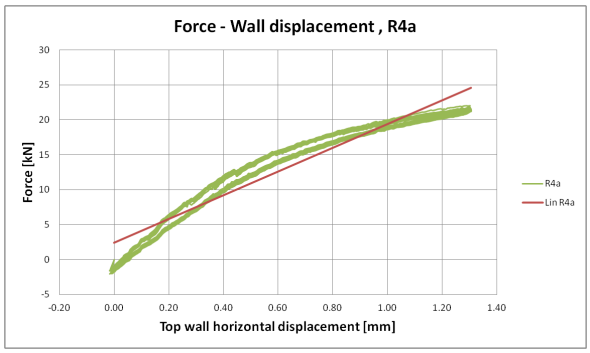

Repetition 4a: K=16.99kN/mm

(f)

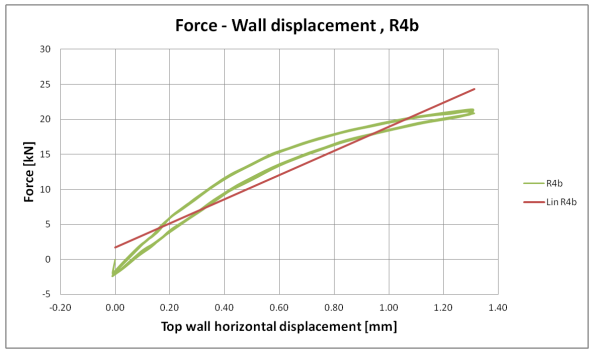

Repetition 4b: K=17.20kN/mm

(g)

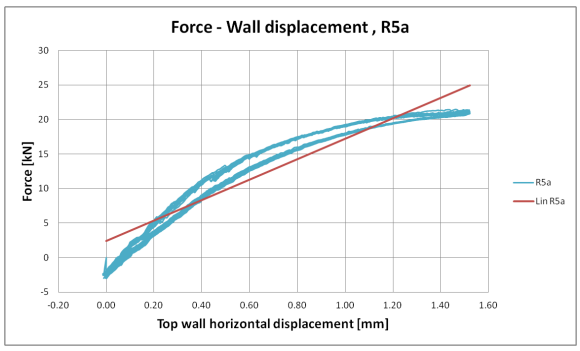

Repetition 5a: K=14.81kN/mm

(h)

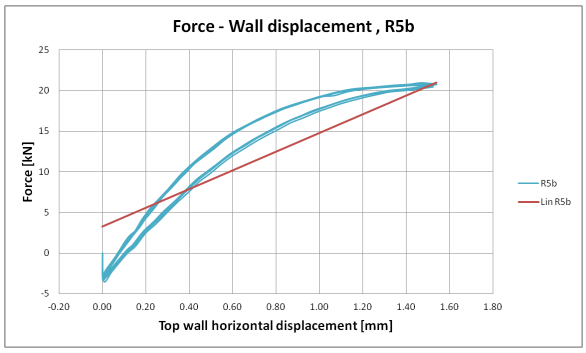

Repetition 5b: K=11.52kN/mm

(i)

Figure 4.25. Hysteresis plots for each repetition displacement step.

The horizontal drift of the wall for each repetition displacement step is shown in Table 4.8.

Table 4.8. Wall drift during the repetitive pull test TUD_COMP-41.

Repetition displacement step	Drift AVG wall drift
R1	0.025%
R2	0.032%
R3	0.04%
R4	0.048%
R5	0.056%

In Figure 4.26 and Figure 4.27 the notch opening displacement is plotted against time and number of repetitions respectively. It is visible in Figure 4.27 that the absolute value of the notch opening displacement increases during the repetitions within a certain loading step.

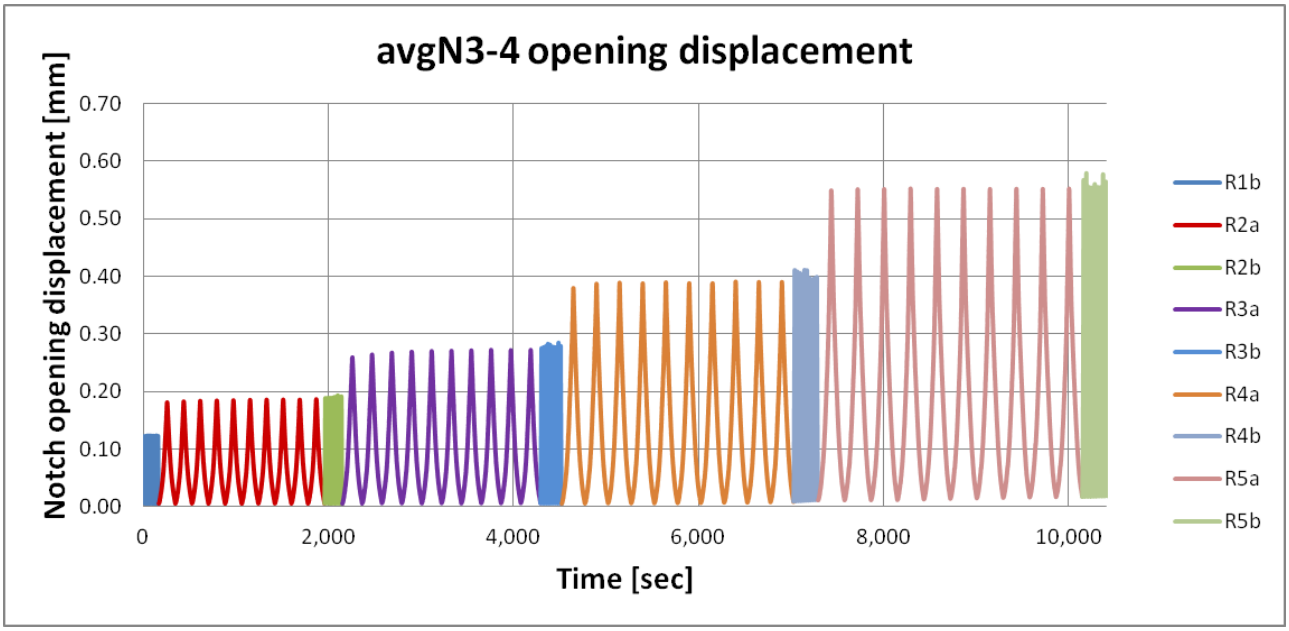

Figure 4.26. Average opening displacement of Notch 3 and 4.

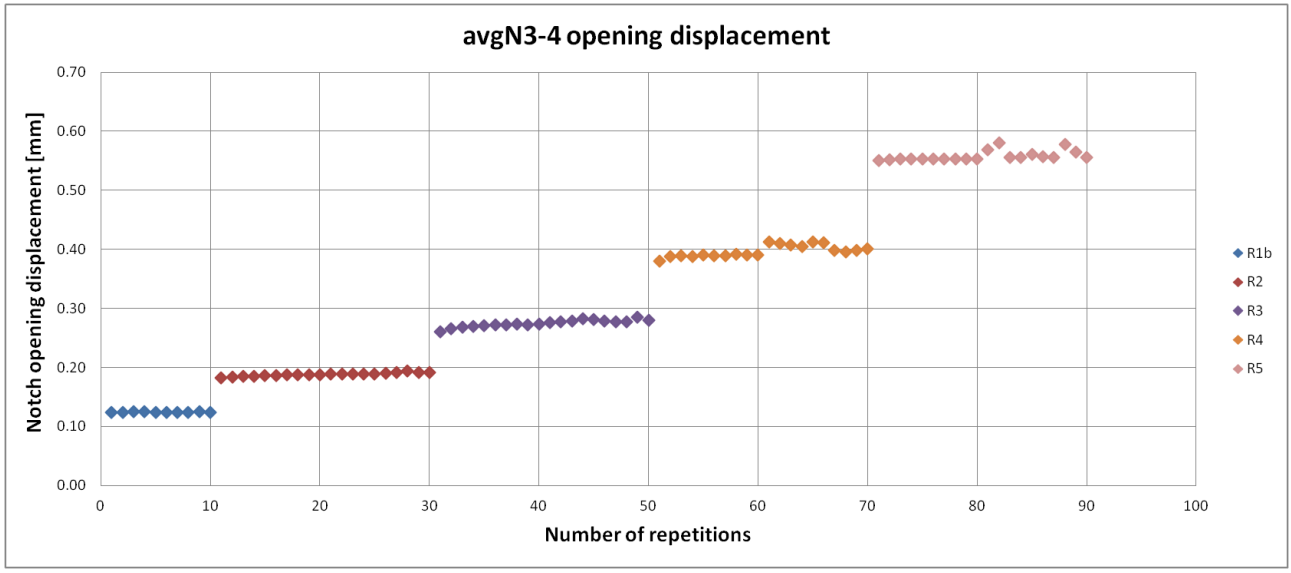

Figure 4.27. Average opening displacement of Notch 3 and 4 per number of repetitions.

Table 4.9 translates the relation between the number of repetitions and the notch opening displacement to a percentage increase relative to the notch opening displacement of the first repetition of each displacement step. This provides insight in wether the amount of notch opening increment differs during the displacement steps. These percentages are subsequently plotted against the displacement steps, shown in Figure 4.28, to visualise these differences. It can be seen that the increase in notch opening displacement is larger in the first 10 slow repetition displacement steps compared to the 10 fast repetition displacement steps.

Table 4.9. Notch opening increase within each displacement step with respect to the N3 displacement.

	R1b	R2a	R2b	R3a	R3b	R4a	R4b	R5a	R5b
N3 first peak opening displacement (mm)	0.139	0.205	0.211	0.293	0.313	0.441	0.473	0.610	0.627
Difference first-last peak (mm)	0.0011	0.0063	0.0031	0.0194	0.0059	0.0113	-0.0136	0.0047	-0.0114
Percentage	0.78%	3.06%	1.47%	6.62%	1.88%	2.57%	-2.88%	0.77%	-1.82%

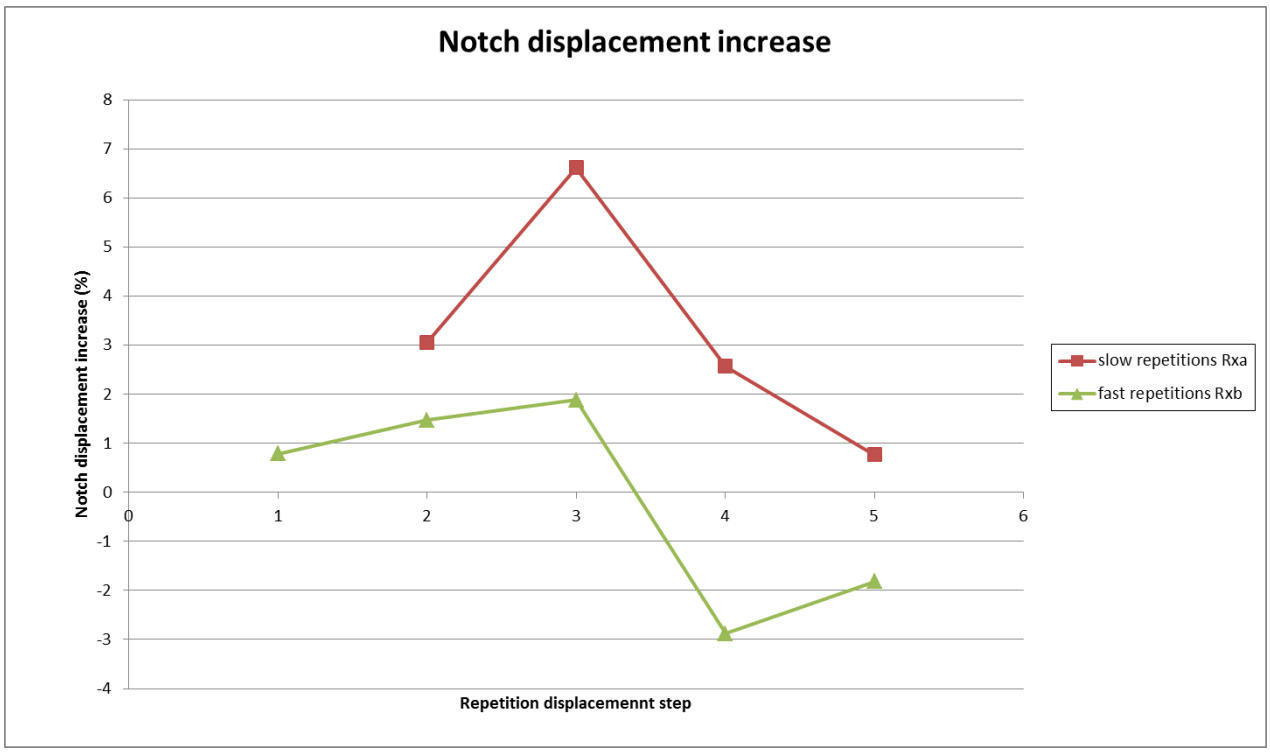

Figure 4.28. Notch displacement increase between first and last repetition within a repetition displacement step.

Similar to TUD_COMP-40, also the force reduction can be taken into account to investigate material degradation within a certain set. Figure 4.29 shows the force reduction related to the displacement steps and in Figure 4.30 the peak force of every repetition is plotted.

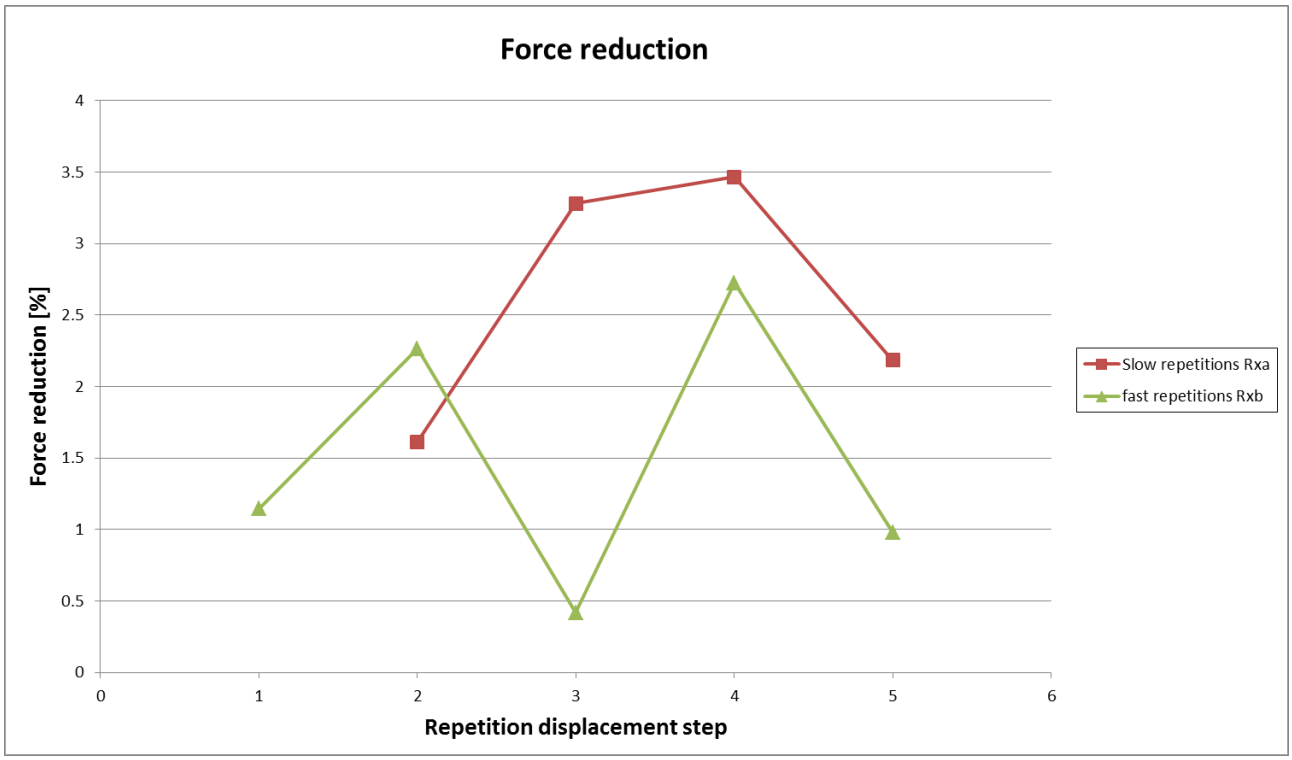

Figure 4.29. Reduction in measured horizontal force within a repetition displacement step expressed in percentage.

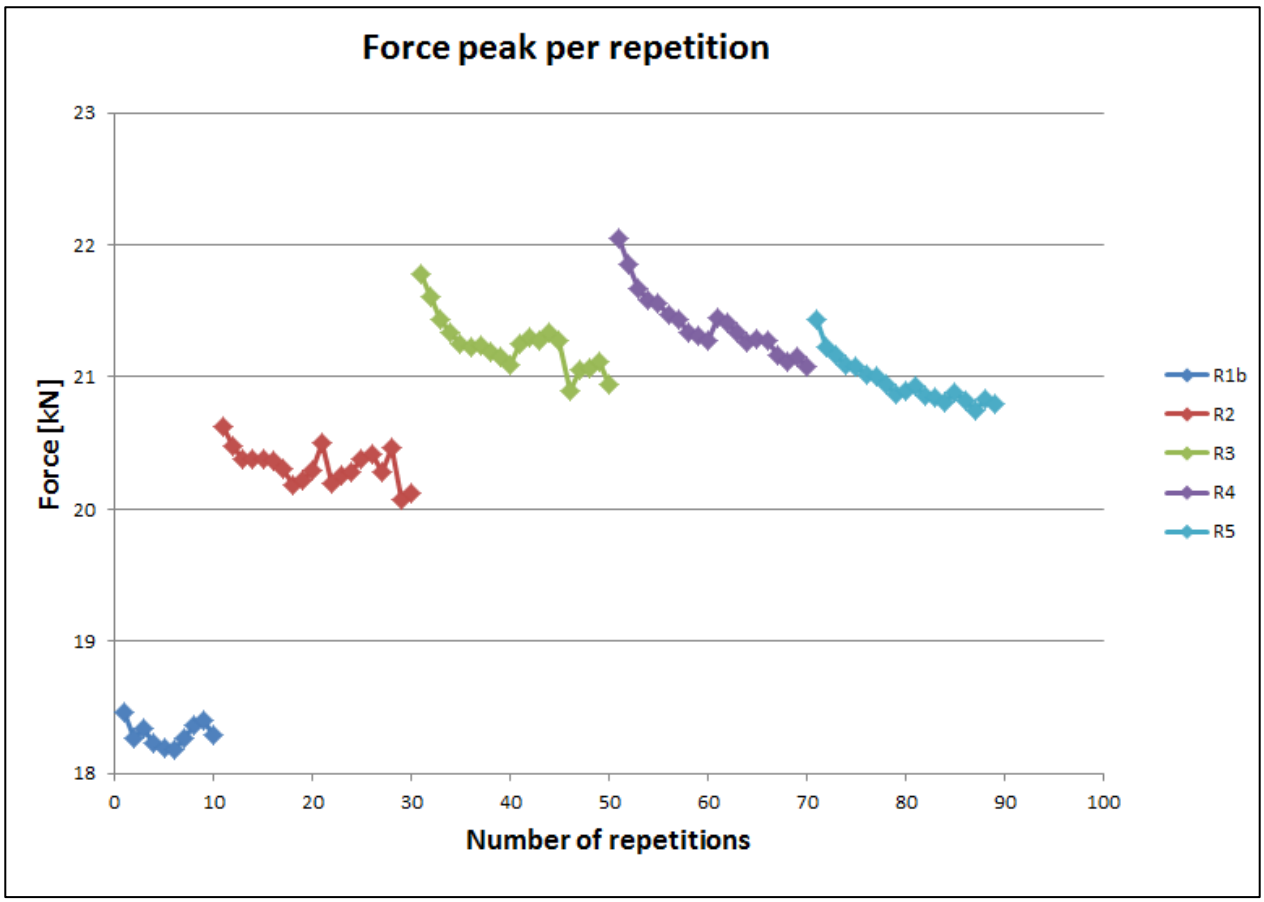

Figure 4.30. Force peak per repetition.

Figure 4.31 to Figure 4.35 present the DIC crack plots of the TUD_COMP-41 R1 to R5 repetition displacement steps.

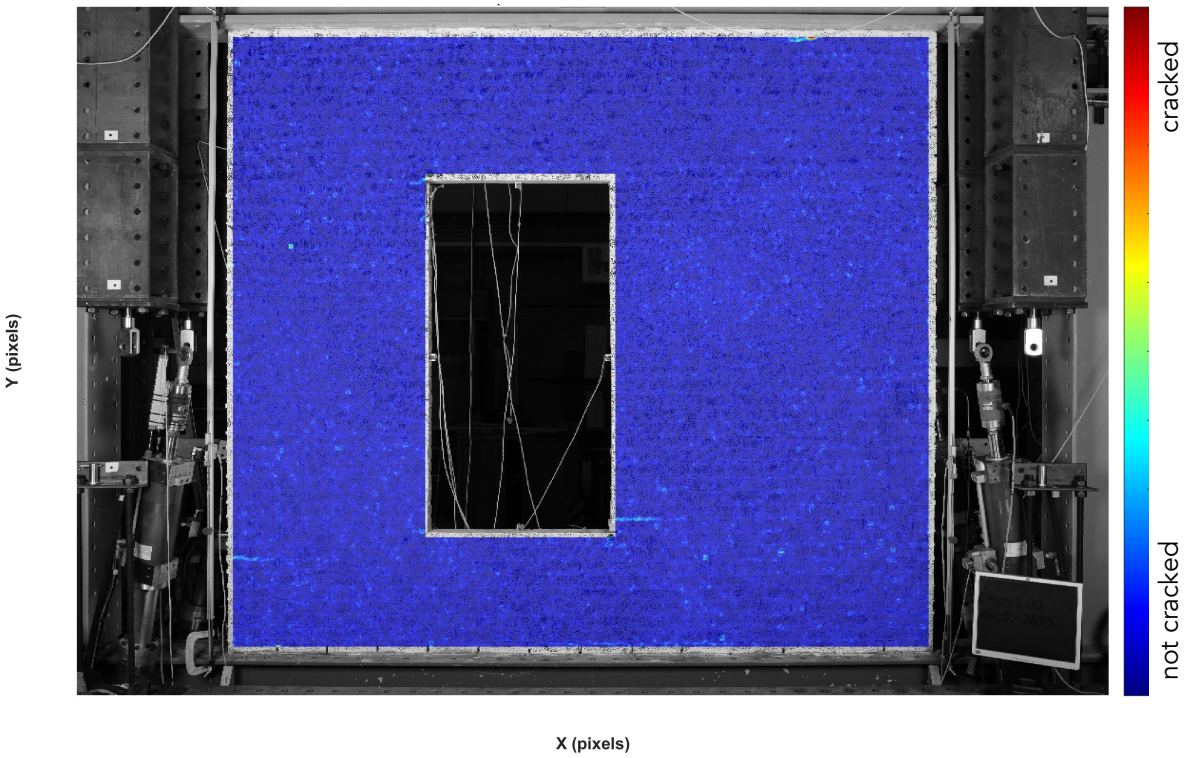

Figure 4.31. A crack plot of R1 of the repetition displacement steps.

In R1 the cracks have already initiated since in this phase the notch is opened to at least 0.1mm in the first repetition. The cracks start in the bottom right and top left window corner and also on the left edge of the wall.

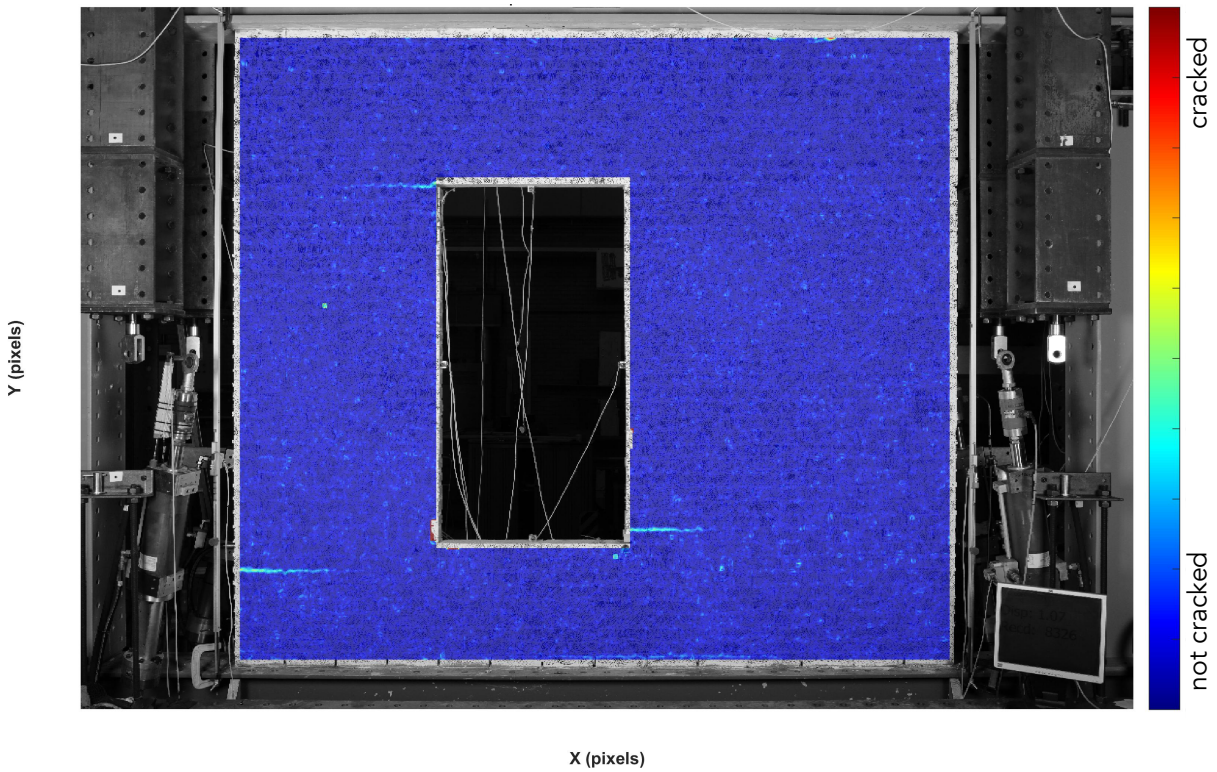

Figure 4.32. A crack plot of R2 of the repetition displacement steps.

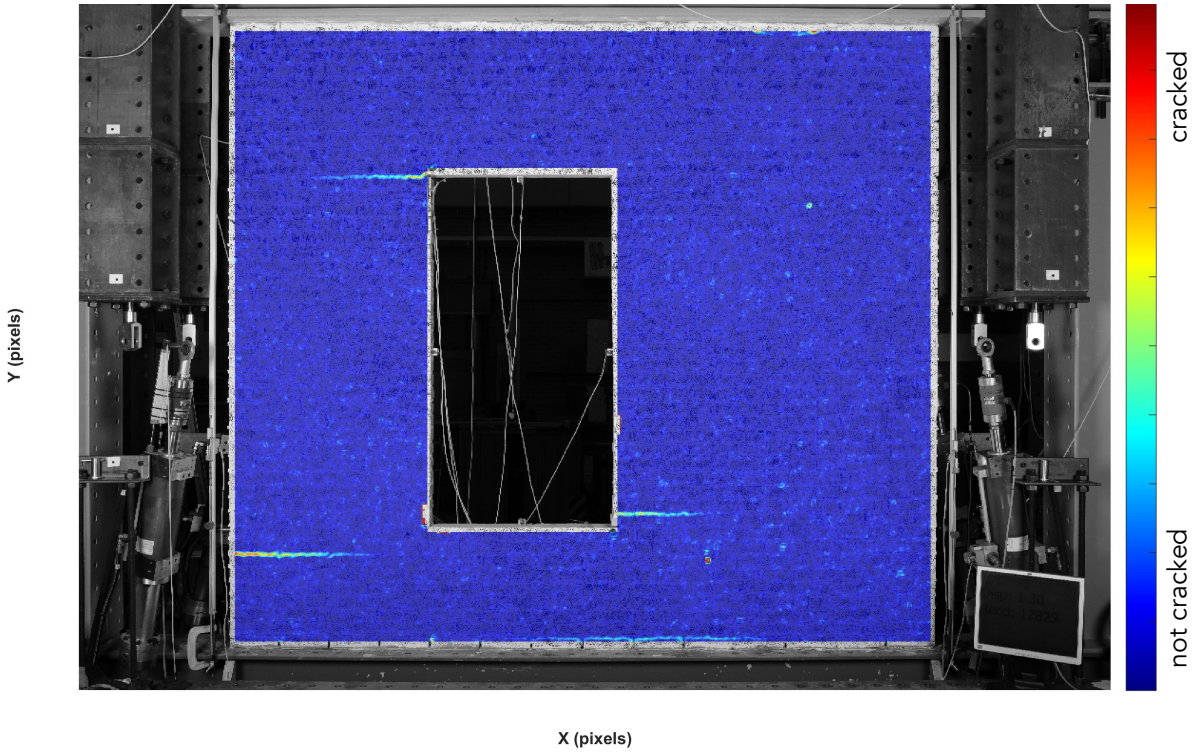

Figure 4.33. A crack plot of R3 of the repetition displacement steps.

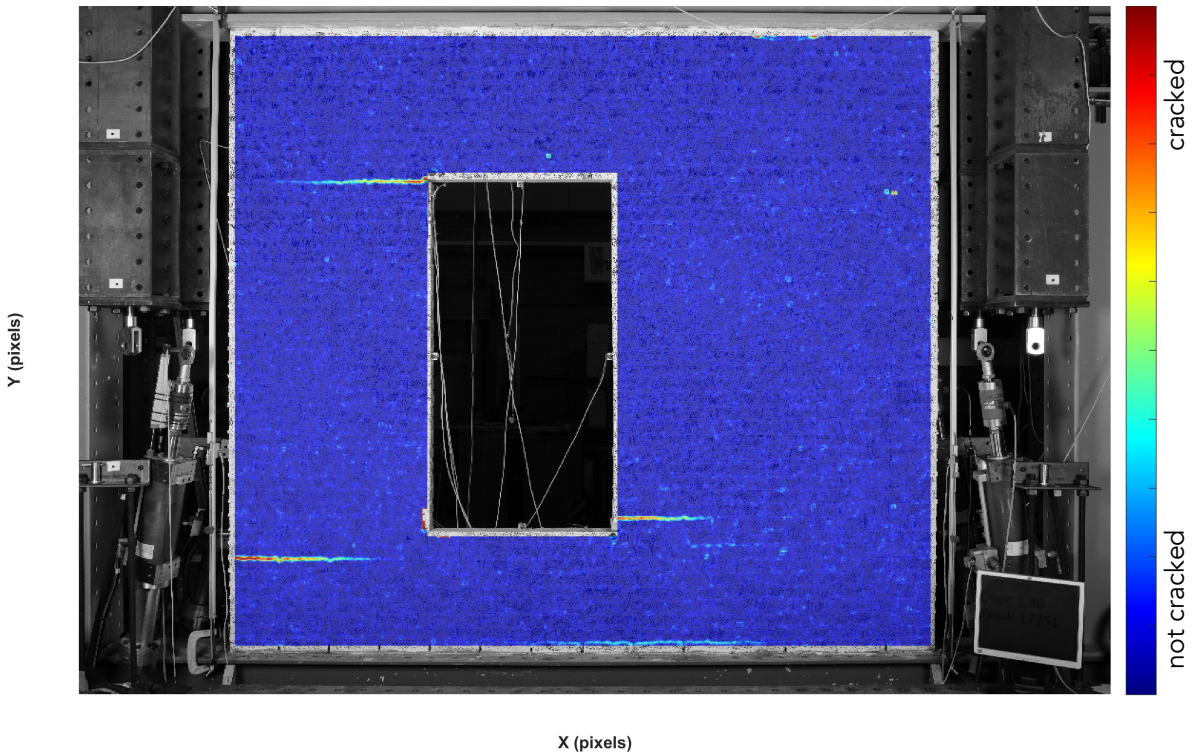

Figure 4.34. A crack plot of R4 of the repetition displacement steps.

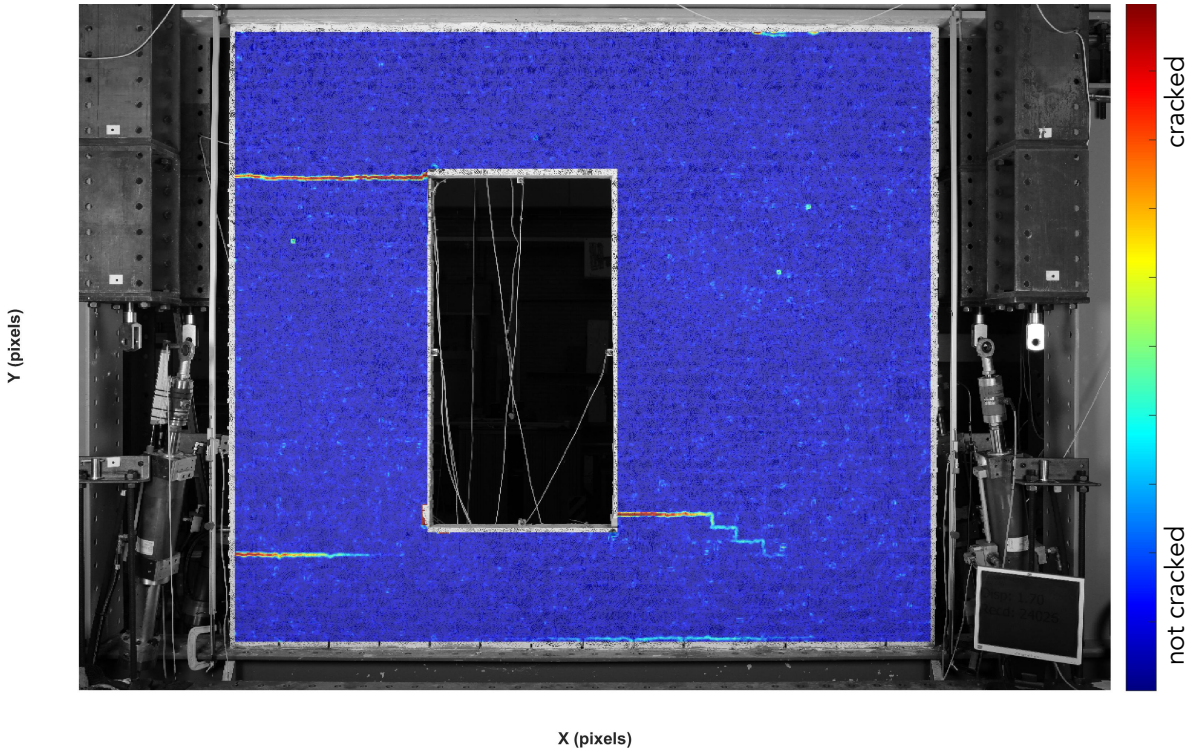

Figure 4.35. A crack plot of R5 of the repetition displacement steps.

In the repetition displacement steps R2 to R5 it is visible that the three cracks extent in length and that the crack widths increase (colour change of the crack). The crack that initiated in the bottom right corner of the window eventually follows a stair-like crack pattern.

4.1.4. TUD_COMP-42

The protocol for the repetitive pull test of sample TUD_COM-42 is shown in Table 4.10 and is identical to the TUD_COMP-41 protocol. TUD_COMP-42 can be seen as a repetition of the TUD_COMP-41 test.

Table 4.10. Repetitive pull loading protocol of TUD_COMP-42. (Meulman et al., 2017).

Repetition displacement step	Top beam horizontal displacement u	Repetitions
R1a	+CMOD (crack 0.1mm)	1, slow rate
R1a	u(1)	9, slow rate
R1b	u(1)	10, **fast** rate
R2a	1.25 u(1)	10, slow rate
R2b	1.25 u(1)	10, **fast** rate
R3a	1.50 u(1)	10, slow rate
R3b	1.50 u(1)	10, **fast** rate
R4a	1.75 u(1)	10, slow rate
R4b	1.75 u(1)	10, **fast** rate
R5a	2.00 u(1)	10, slow rate
R5b	2.00 u(1)	10, **fast** rate

The first crack opening to 0.1mm was detected at the sensor located in the bottom right window corner (sensor N1), see Figure 4.36.

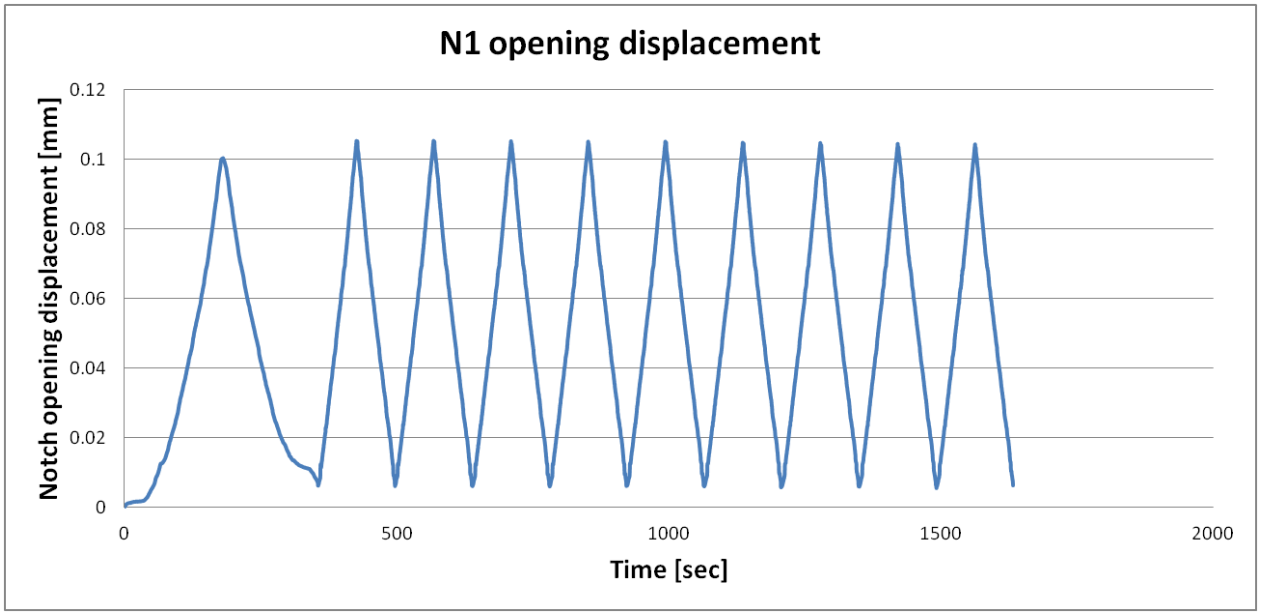

Figure 4.36. N1 opening displacement in R1a to determine top beam displacement for R1.

Table 4.11. Top beam and wall displacement. (measured value, ** calculated with use of multiple sensors).*

Repetition displacement step	Top beam horizontal displacement [mm]*	Wall displacement [mm]**
R1	0.87	0.58
R2	1.09	0.74
R3	1.31	0.86
R4	1.53	1.04
R5	1.74	1.23

During the test, at R2b, a small instability of the system occurred; the test had to be stopped. The reason was an out-of-plane instability of the top beam. There was too much space between the vertical columns and the top beam. The vertical columns should constrain the out-of-plane displacement of the top beam. The top beam started to vibrate in out-of-plane direction which influences the sensor that measures the horizontal top beam displacement. This sensor is also the input parameter for the control system of the jack. The control system then tries to control the displacement caused by the vibration but by doing so ends up actually amplifying the vibration. The space between the vertical columns and the top beam was filled to constrain the out-of-plane movement of the top beam before the test was continued. The system had to be restarted and no damage was caused to the wall or the test; however, a small irregularity remains visible in the R2b repetition displacement step (Figure 4.37 and 4.38).

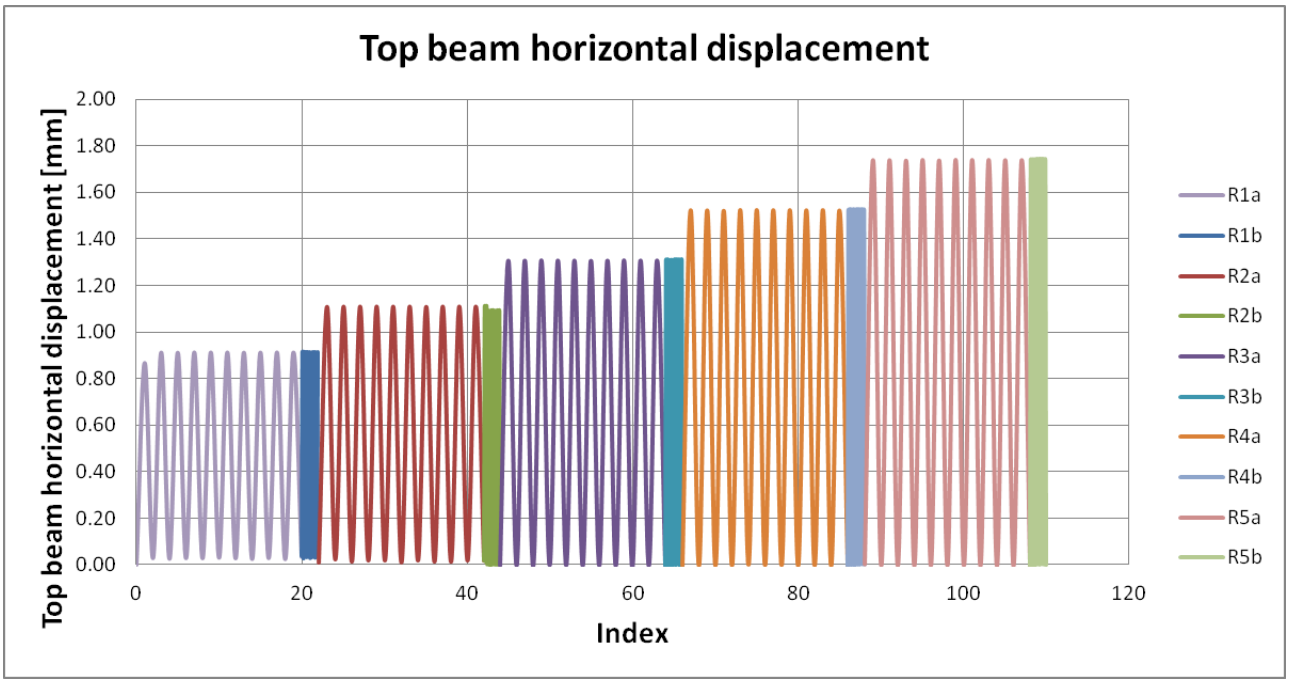

Figure 4.37. Top beam horizontal displacement.

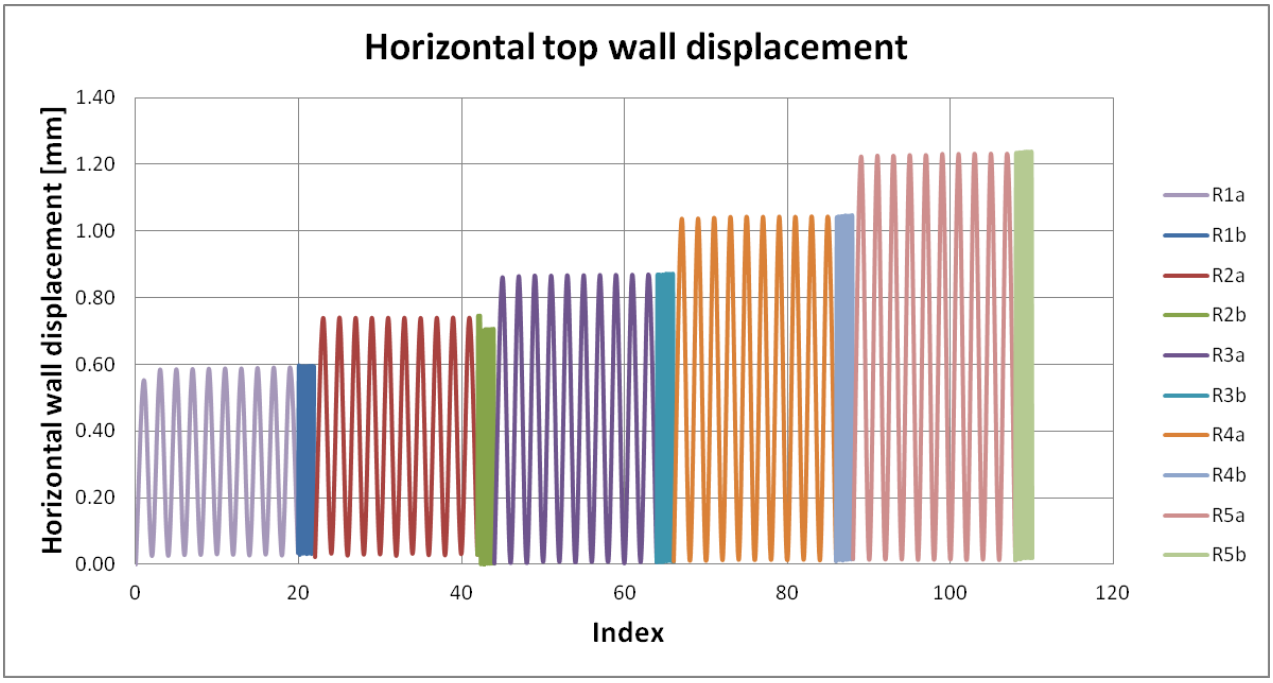

Figure 4.38. Horizontal wall displacement.

Figure 4.39 shows the force-displacement graph of TUD_COMP-42. The peak load reached in the test is: 22.63kN. It was obtained during R5. The initial stiffness is 36.32kN/mm.

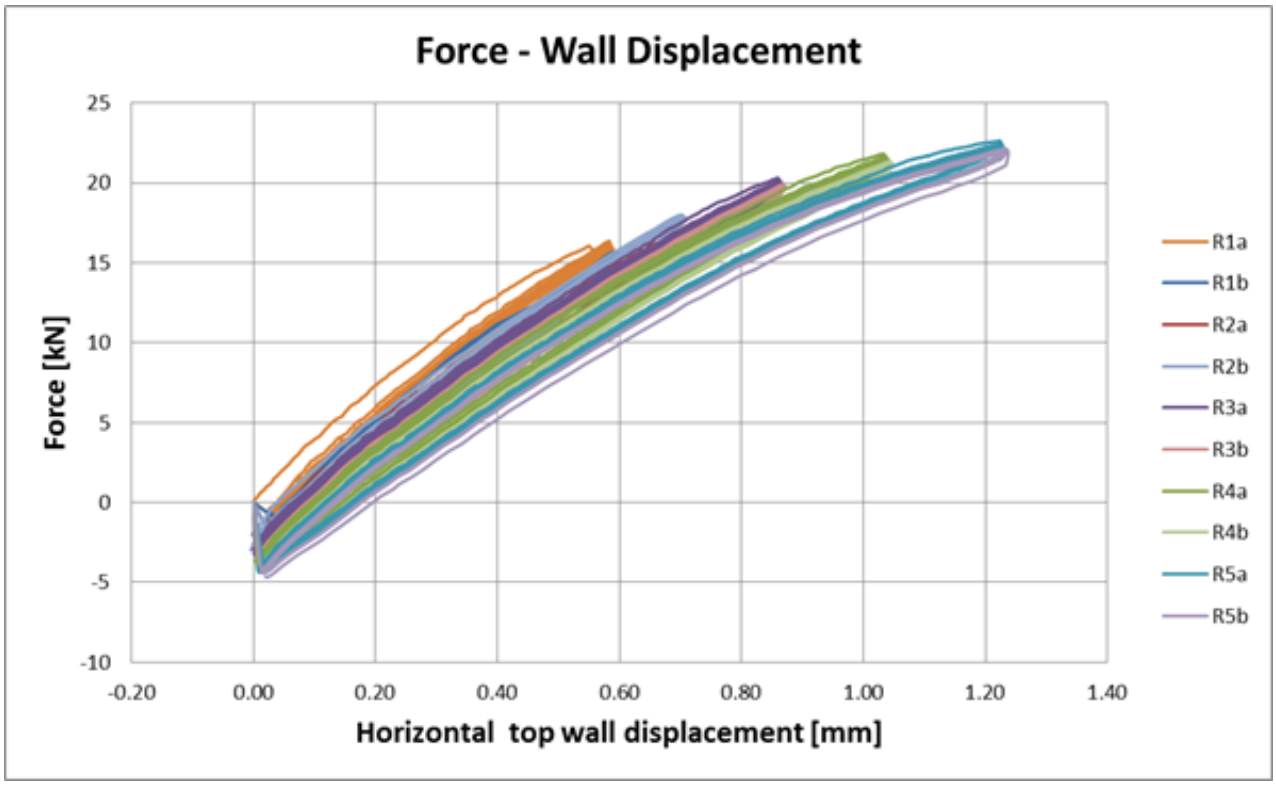

Figure 4.39. Hysteresis graph for the repetitive pull test TUD-COMP-42.

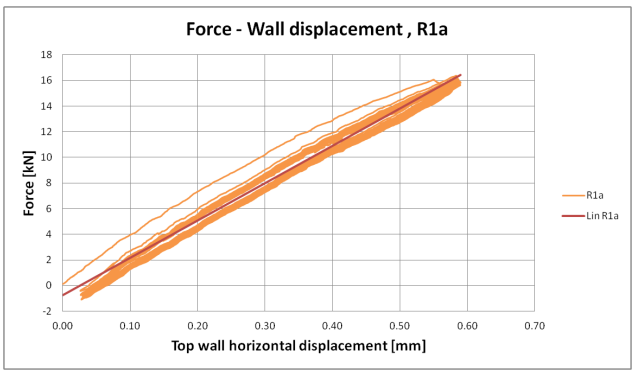

Repetition 1a: K=29.14kN/mm
(a)

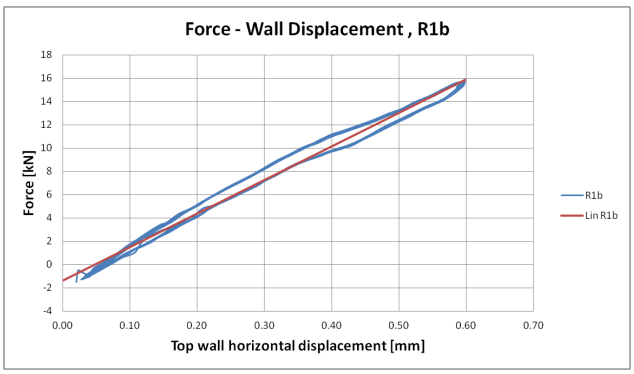

Repetition 1b: K=28.82kN/mm
(b)

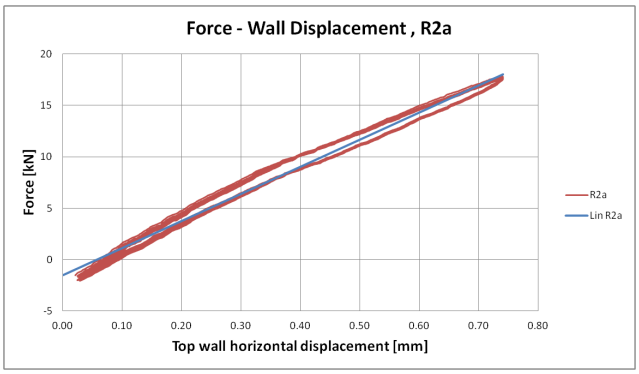

Repetition 2a: K=26.33kN/mm
(c)

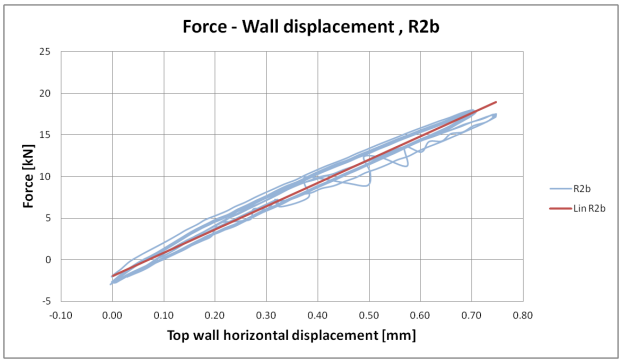

Repetition 2b: K=27.90kN/mm
(d)

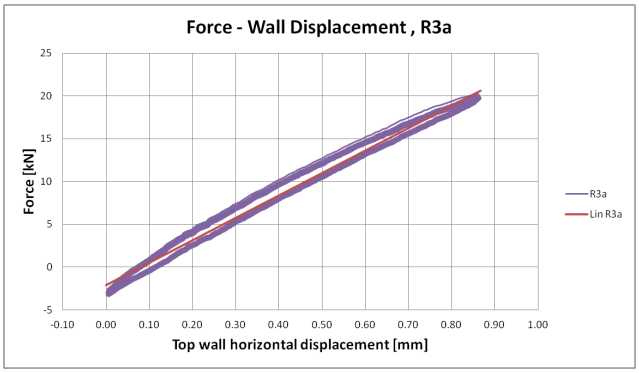

Repetition 3a: K=26.15kN/mm
(e)

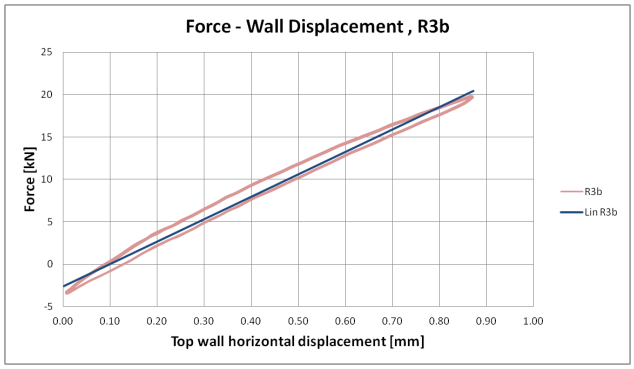

Repetition 3b: K=26.46kN/mm
(f)

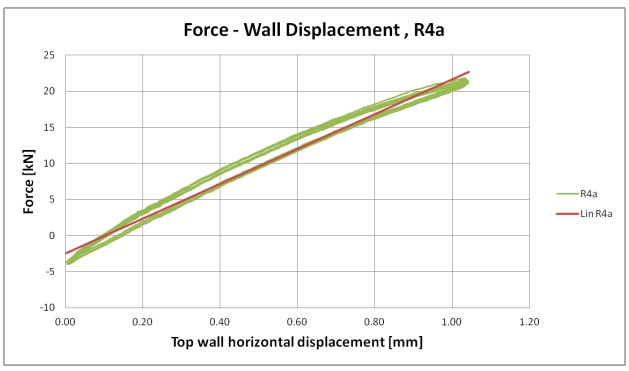

Repetition 4a: K= 24.16kN/mm
(g)

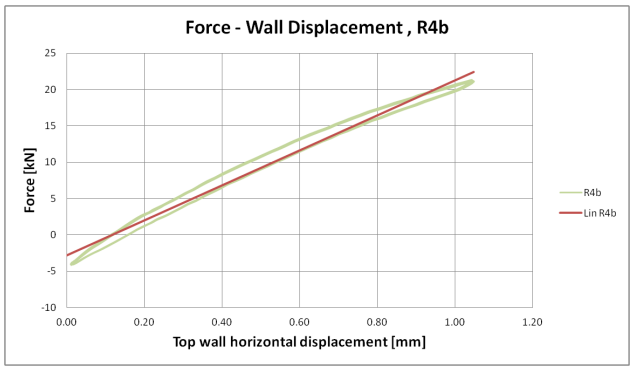

Repetition 4b: K=24.10kN/mm
(h)

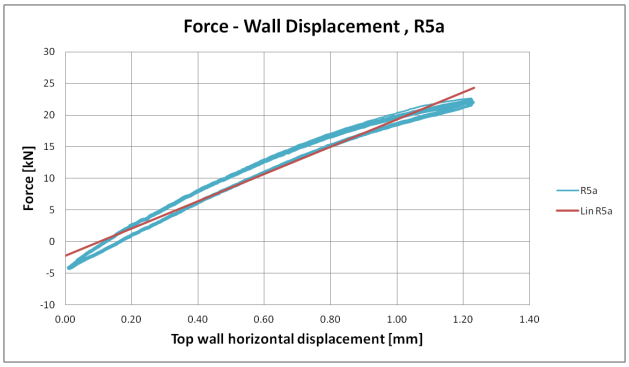

Repetition 5a: K=21.59kN/mm

(i)

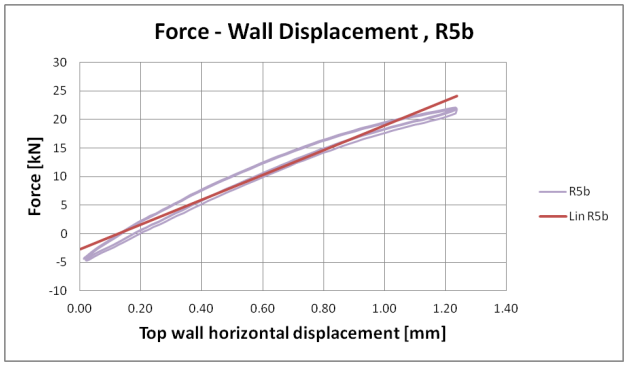

Repetition 5b: K=21.64kN/mm

(j)

Figure 4.40. Hysteresis plots for each repetition displacement step.

The instability in the system during R2b is also visible in the force-displacement graph of R2b in Figure 4.40 (d). The horizontal drift of the wall for each repetition displacement step is shown in Table 4.12.

Table 4.12. Wall drift during the repetitive pull test TUD_COMP-42.

Repetition displacement step	Drift AVG wall drift
R1	0.022%
R2	0.027%
R3	0.032%
R4	0.039%
R5	0.046%

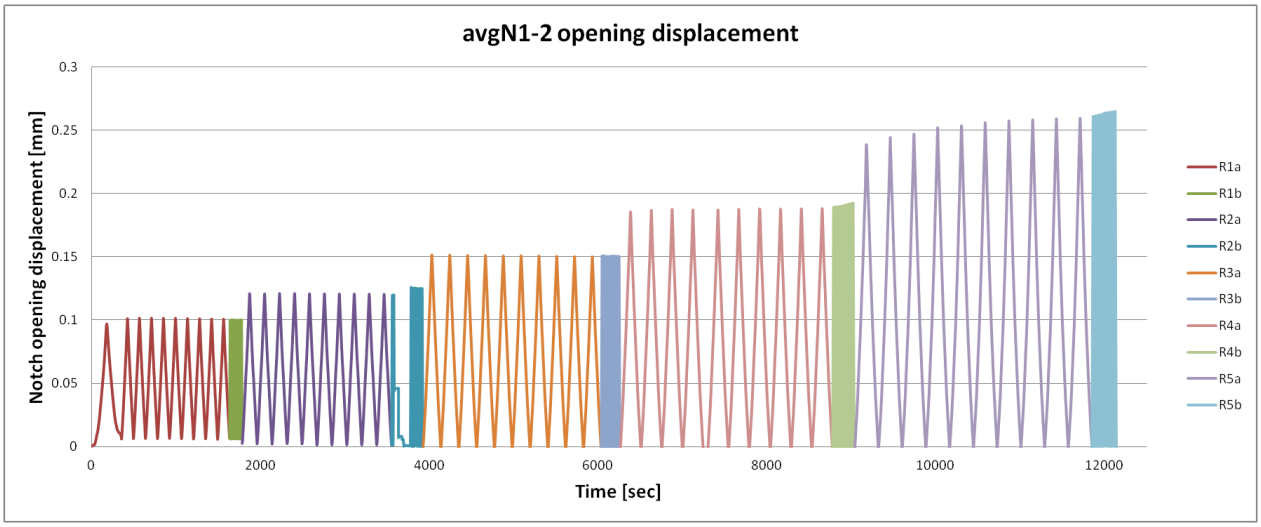

Figure 4.41. Average opening displacement of notch 1 and 2.

During the out-of-plane instability fix, the top beam had to be pushed by hand slightly to the back side to be able to fill the space between the vertical column and top beam. This push is visible in the notch sensors in Figure 4.41 and Figure 4.42 as a small increase in opening of the notch displacement after the test is continued.

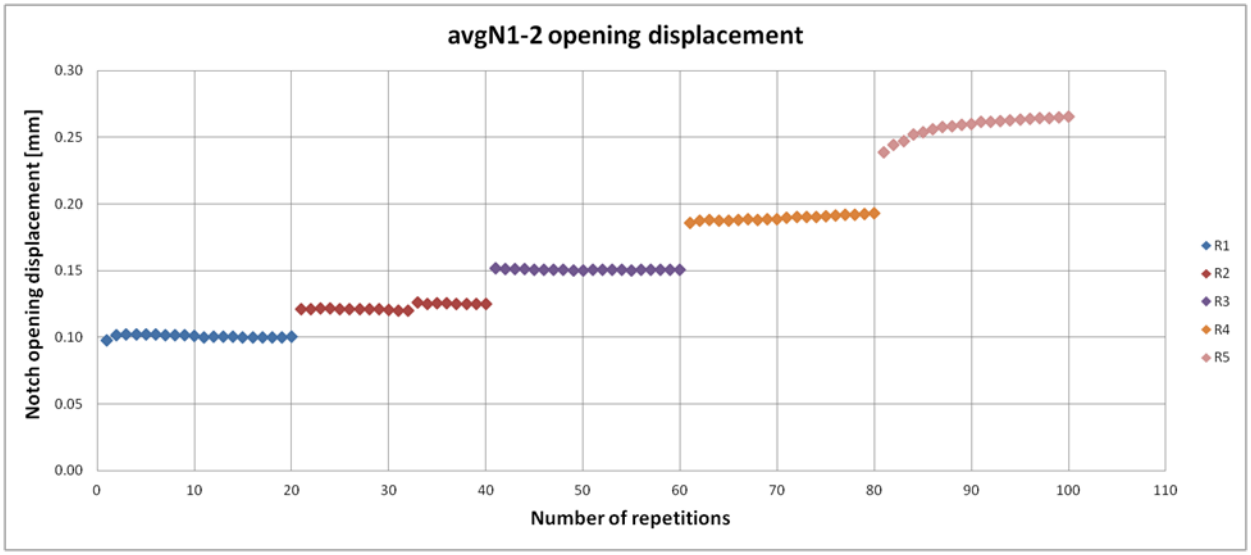

Figure 4.42. Average opening displacement of notch 1 and 2 per number of repetitions.

Table 4.13 contains the difference found between the first and last repetition in a repetition displacement step. For R2b the difference is taken from the third to the last repetition in that step because of the out-of-plane instability as described before. The Third repetition is the first repetition after the continuation of the test after the instability fix.

Table 4.13. Crack increase within repetition displacement step of N1.

	R1a	R1b	R2a	R2b*	R3a	R3b	R4a	R4b	R5a	R5b
N1 first peak opening displacement (mm)	0.101	0.104	0.125	0.124	0.165	0.165	0.202	0.208	0.259	0.284
Difference first-last peak (mm)	0.004	-0.000	-0.001	-0.001	-0.001	-0.000	0.005	0.004	0.023	0.004
Percentage	3.63%	-0.05%	-1.14%	-0.78%	-0.39%	-0.18%	2.3%	2.02%	8.86%	1.42%

* measured between third and last repetition in the set

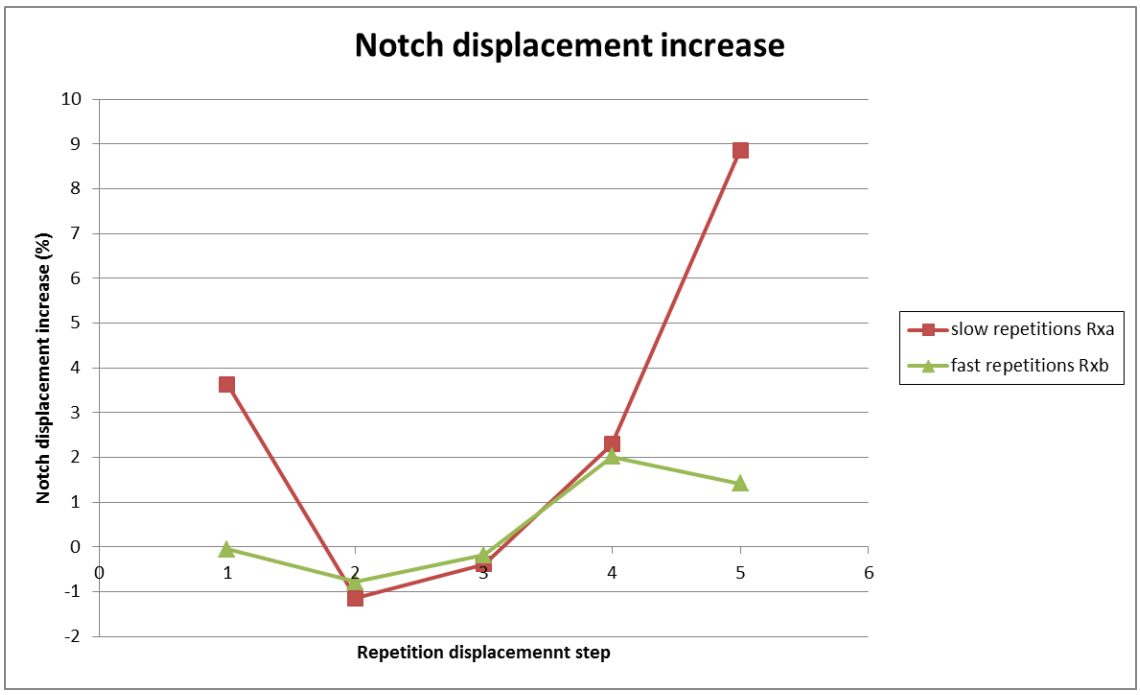

Figure 4.43. Notch displacement increase between first and last repetition within a repetition displacement step.

Figure 4.43 show the notch displacement expressed in percentage for TUD_COMP-42. For R2 to R4 the notch opening for the 10 slow repetitions of these steps is almost equal to the 10 fast repetitions and goes to negative which means the crack is slight closed.
In Figure 4.44 the reduction in the load is plotted for each repetition displacement step.

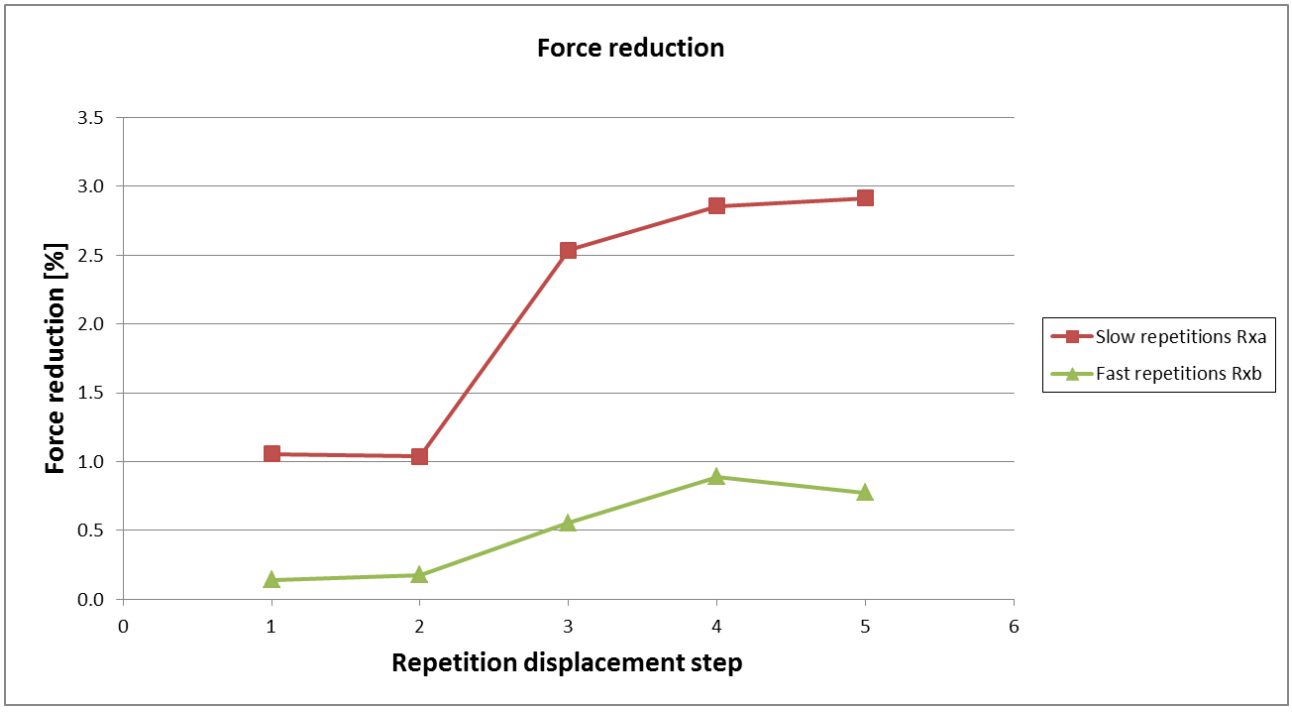

Figure 4.44. Reduction in measured horizontal force within a repetition displacement step expressed in percentage.

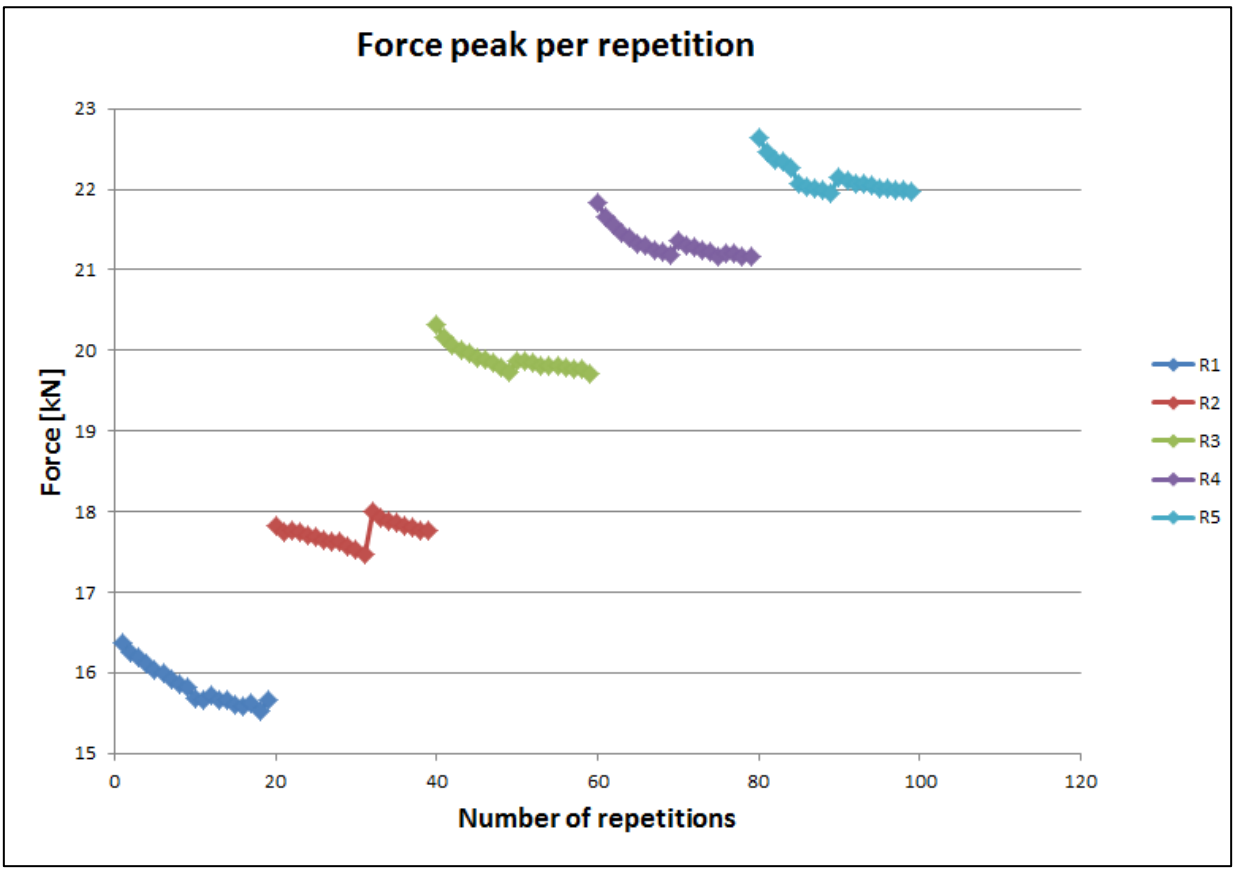

Figure 4.45. Force peak per repetition.

In Figure 4.45 the peak force is plotted for each repetition.
Figure 4.46 and Figure 4.48 to Figure 4.51 show the DIC crack plot for the repetition displacement steps from R1 to R5.

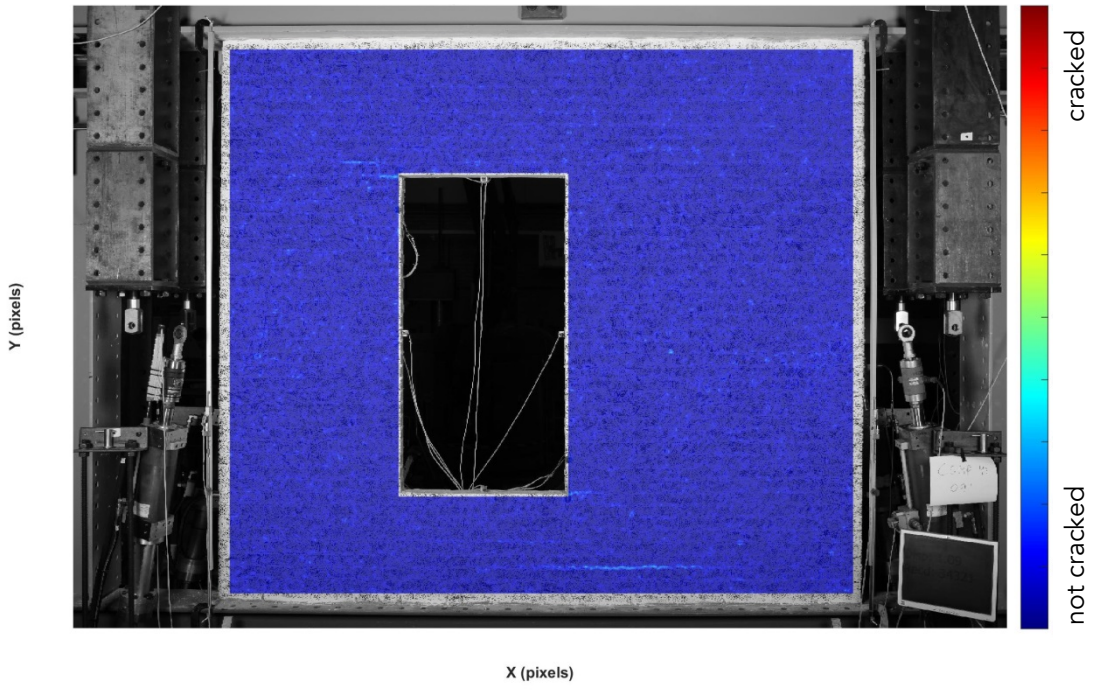

Figure 4.46. A crack plot of R1 of the repetition displacement steps.

In the R1 phase the initiation of a crack is visible in the top left and bottom right corner of the window. But there is also a long horizontal crack visible in the bottom part of the wall. This crack is already visible in the early stage of loading of the wall. It is very unlikely that this crack was initiated during the test which means

that it was already there before the test started. The most likely cause for the crack could be that it was formed during transport of the wall from the location in the lab where the wall is constructed to the test set-up. The steel frame around the wall is lifted from the bottom steel beam. It is likely that the bottom beam bended during lifting causing for a horizontal crack in the bottom middle section of the wall (Figure 4.45).

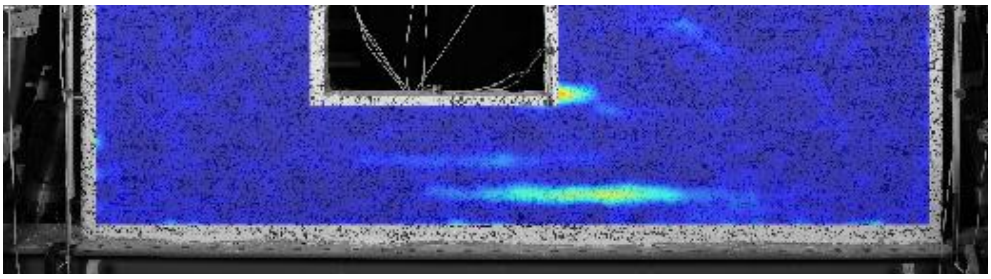

Figure 4.47. Horizontal crack in the bottom middle part of the wall.

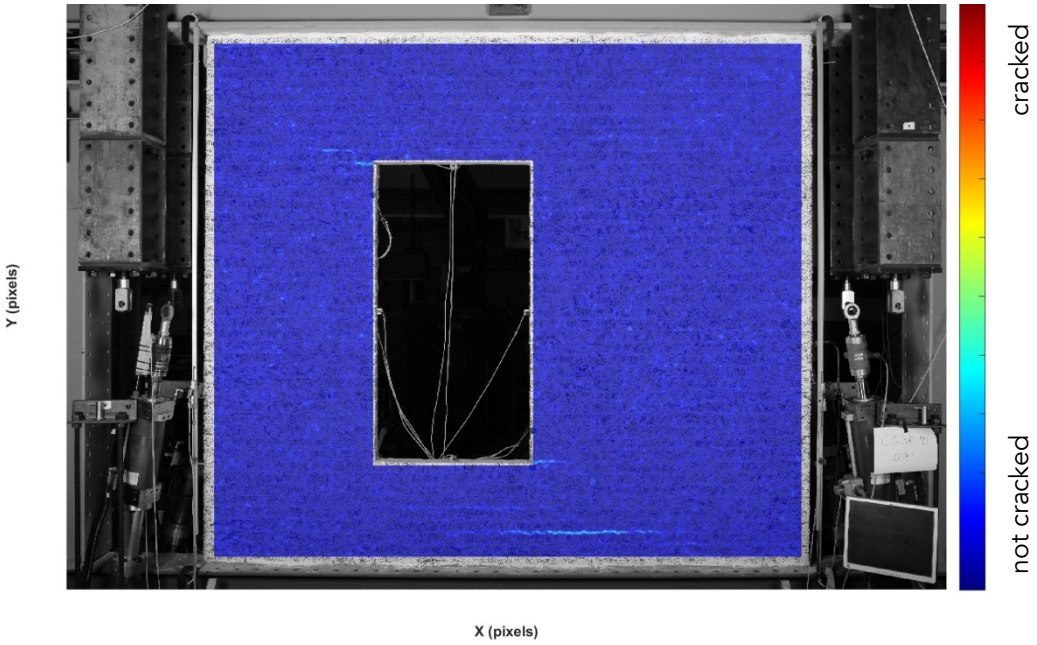

Figure 4.48. A crack plot of R2 of the repetition displacement steps.

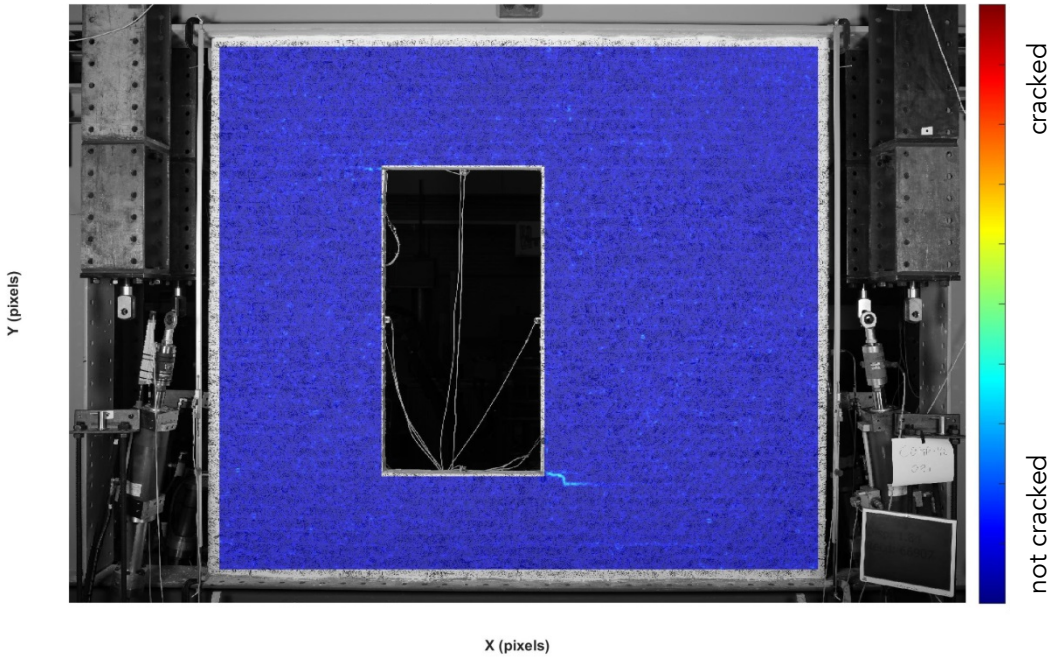

Figure 4.49. A crack plot of R3 of the repetition displacement steps.

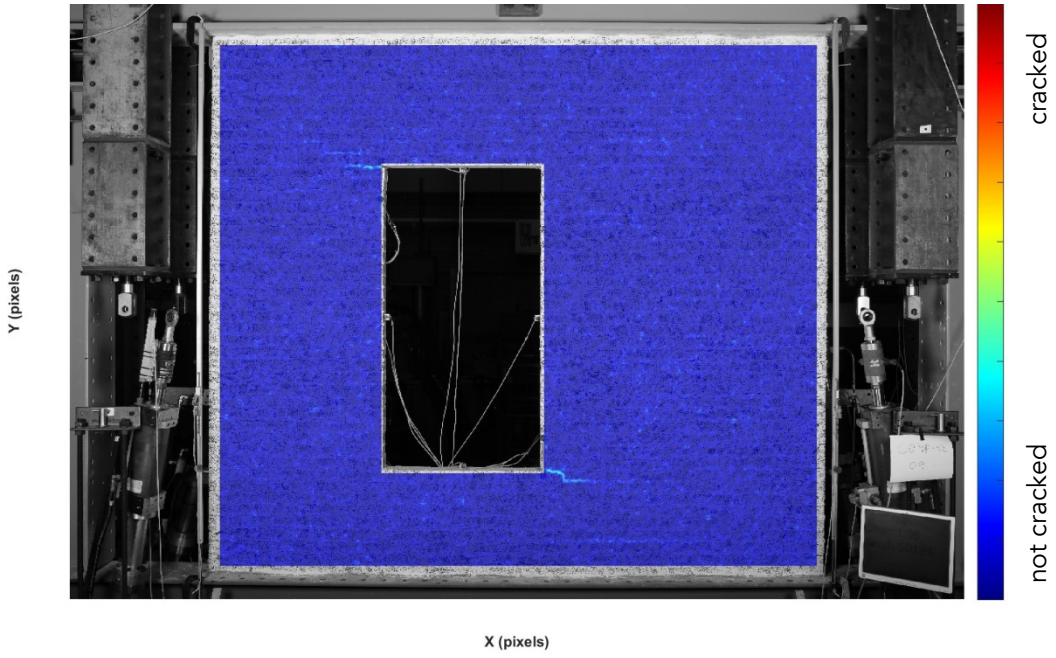

Figure 4.50. A crack plot of R4 of the repetition displacement steps.

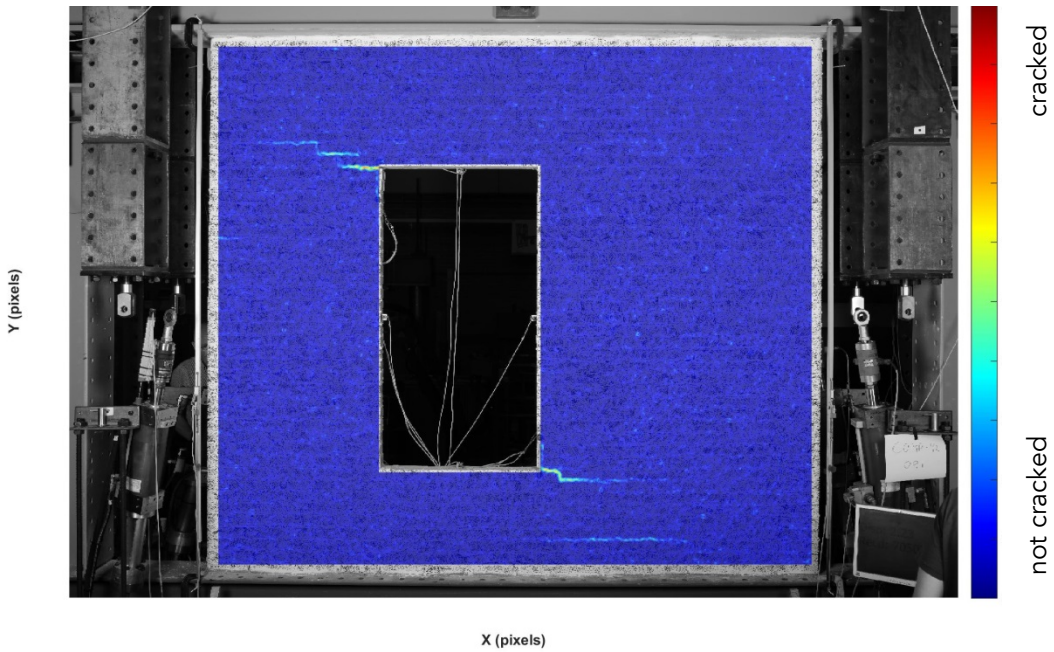

Figure 4.51. A crack plot of R5 of the repetition displacement steps.

Cracks progress by extending in length and width during the repetition displacement steps. The cracks initiated in the top left and bottom right corner of the window propagated in diagonal direction.

4.1.5. Comparison TUD_COMP-40, TUD_COMP-41 and TUD_COMP-42

In the previous sections the results of the three repetitive pull IP wall test results have been presented. In this section, interesting points are compared between the three samples focussing on the crack initiation and propagation (material degradation) due to multiple repetitions in the pull direction throughout the tests.

All three samples have the same geometry and are tested with similar loading. Table 4.14 shows the top beam displacement at which a notch reached an opening of 0.1mm (R1), initial stiffness and the peak load that was measured during the test. For all three samples the values are very similar indicating that the samples itself are well comparable.

Table 4.14. Top beam displacement at 0.1mm notch opening displacement (R1).

	TUD_COMP-40	TUD_COMP-41	TUD_COMP-42
Top beam displacement at R1 [mm]	0.85	0.87	0.87
Initial stiffness [kN/mm]	35.08	38.43	36.91
peak load [kN]	21.78	22.05	22.79

The notch displacement was plotted in previous Sections (4.1.2 - 4.1.4) for each sample in which it was visible that the largest relative notch opening increase takes place in the first repetitions of a repetition displacement step. The increase was relatively less in the fast repetitions (Rxb) that followed the slow repetitions (Rxa) in every set. In Figure 4.52 the notch displacement increase between the first and the last repetition in a slow repetition displacement step (Rxa) is expressed in percentage for all three samples. It can be seen that TUD_COMP-40 and TUD_COMP-41 show a similar trend, increasing notch displacement close to the maximum load measured (R4) and decreasing again in the step after the maximum load is reached.

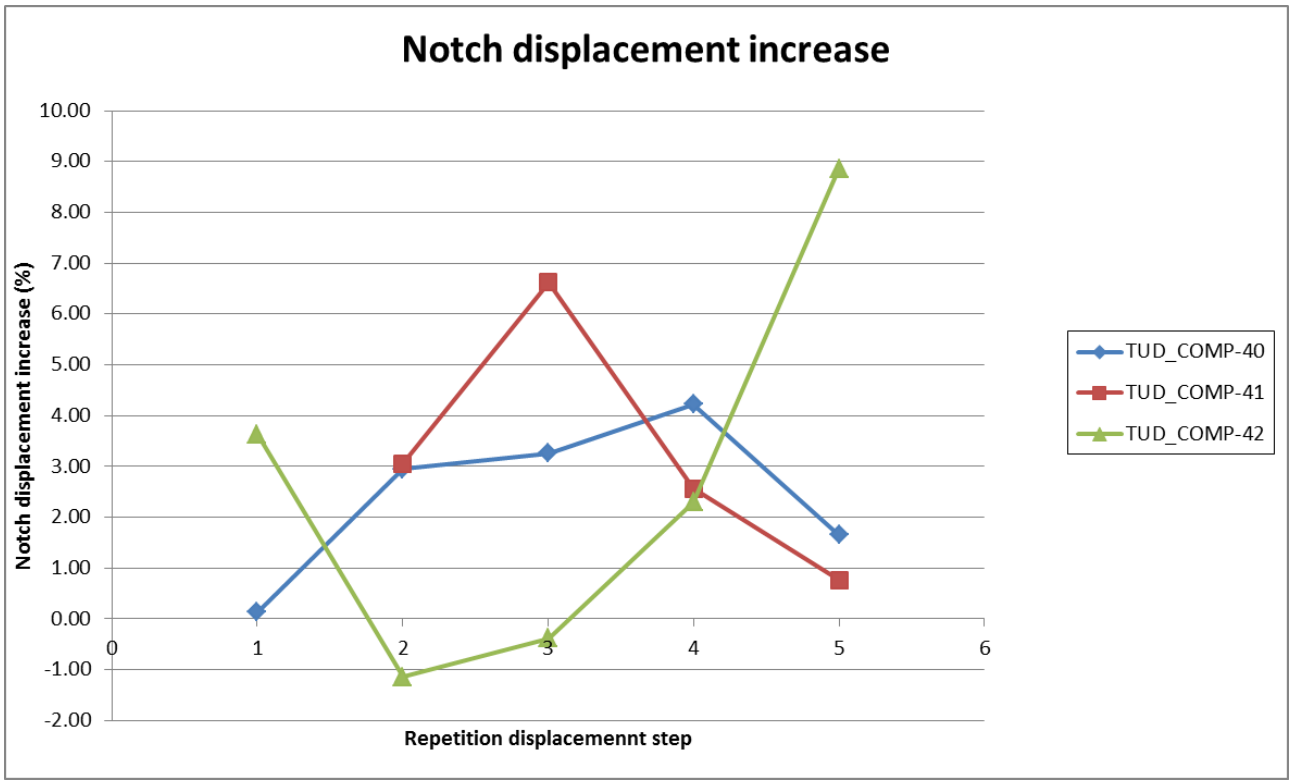

Figure 4.52. Comparison of the notch displacement increase per repetition displacement step of the slow repetitions (Rxa).

However, TUD_COMP-42 shows a different trend which may have been a result from the damage in the bottom middle part of the wall that was discovered during the DIC analysis which was likely the effect of bending of the bottom beam during transportation of the wall with the crane. Although the values presented in Table 4.14 are very similar, the force-displacement graph of TUD_COMP-41 and TUD_COMP-42 show some differences as can be seen in Figure 4.53. In TUD_COMP-40 and TUD_COMP-41 the force was not increasing after R4 but in TUD_COMP-42 it does.

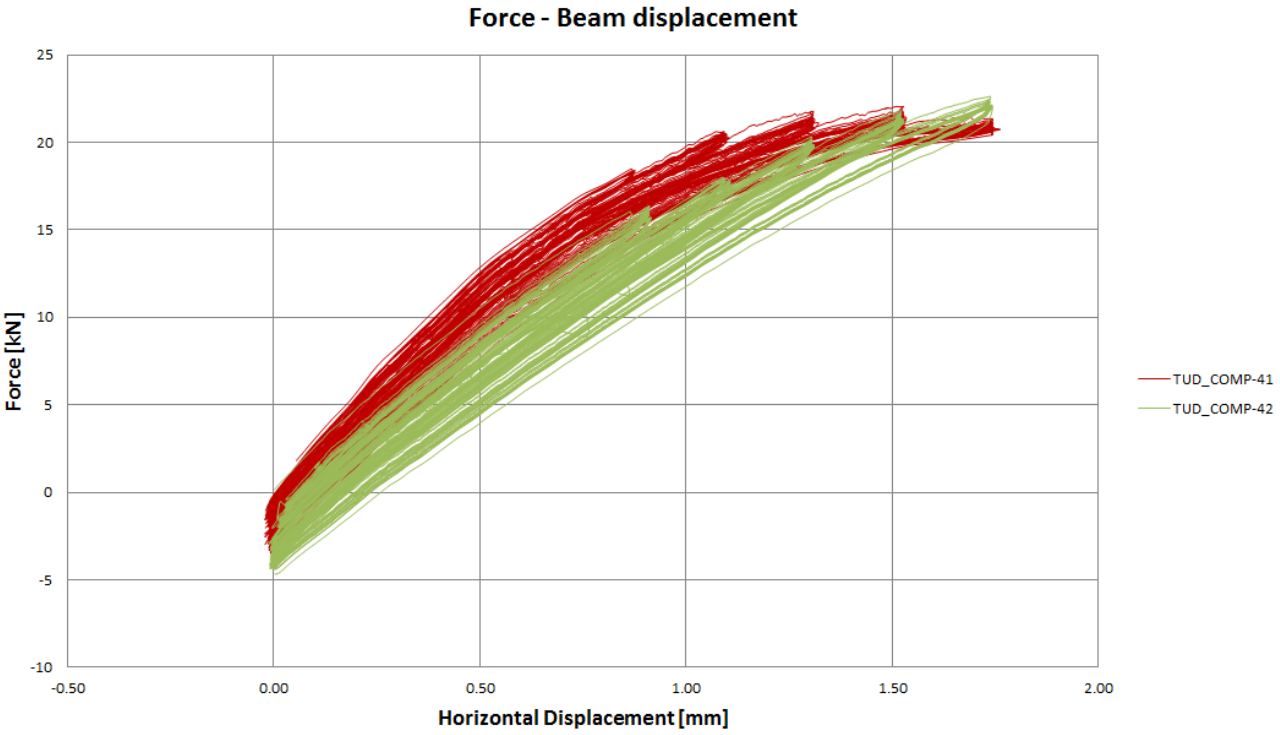

Figure 4.53. Comparison Force reduction per repetition displacement step.

If the crack patterns are compared for the three samples it can be seen that the crack pattern for TUD_COMP-42 is also different compared to TUD_COMP-40 and TUD_COMP-41 (Figure 4.54). In the top left window corner a diagonal crack is formed instead of a horizontal one like in TUD_COMP-40 and TUD_COMP-41. This could be an indication that the stress state in the sample is different likely caused by the horizontal crack in the bottom middle part. This horizontal crack could provide a more flexible behaviour of the wall. Resulting in less high stress concentration around the cracks which causes less crack growth. As discussed in previous sections the force reduction observed during a test is an indication of progression of damage. Less crack growth will result in less force reduction which could be a reason that the maximum load seems not to be reached yet in R5 like in TUD_COMP-40 and TUD_COMP-41.

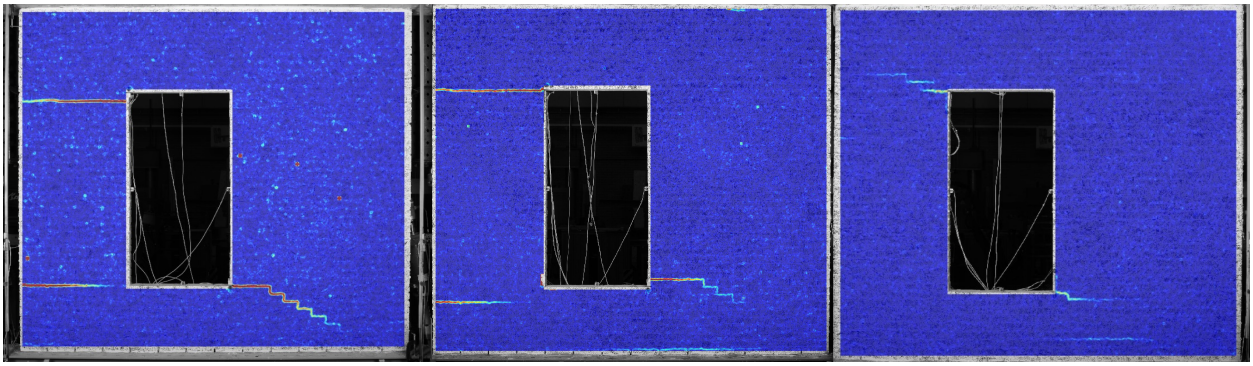

Figure 4.54. Crack plots of repetition R5 of TUD_COMP-40, TUD_COMP-41 and TUD_COMP-42.

With DIC analysis the first picture of the presumed undamaged sample is used as a reference to make the cracks visible in the DIC. If the horizontal crack was already there before the first picture for the DIC was

taken it means that the horizontal crack is more extensive in width and length than is visible in the DIC crack plots. As a side note, the pattern for the DIC was improved (less noise and more contrast) after component 40 and this can also be observed in Figure 4.54.

The force reduction observed between the first and last repetition in a set can be considered as material degradation within that set. Comparing the force reduction for the three tested samples, a more comparable trend can be observed in which the relative force reduction increases in the first repetition displacement steps (R1-R3) and levels off or decreases in the later repetition displacement steps (R4-R5) (Figure 4.55).

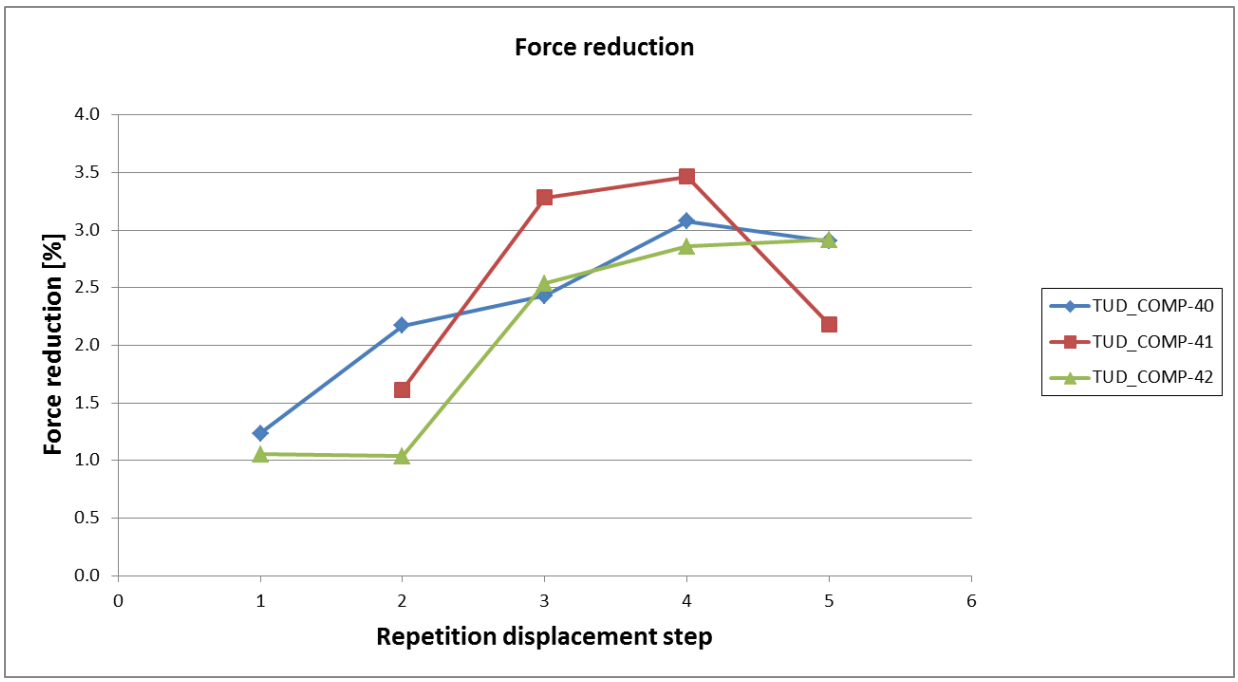

Figure 4.55. Comparison Force reduction per repetition displacement step.

It can be seen within a set that the force reduction plotted against the number or repetitions show a similar trend for a certain repetition displacement step but also compared to the other samples. In Figure 4.56 the comparison is made between TUD_COMP-41 and TUD_COMP-42 since both have 10 repetitions per repetition displacement step. As could be seen in the force-displacement graph in Figure 4.53 the force for every set was different; however, in Figure 4.56 the force has been rescaled to the first repetition of the set so that it matches for both samples. In this way the curves can be plotted on top of each other to make the trend in the force reduction more clear.

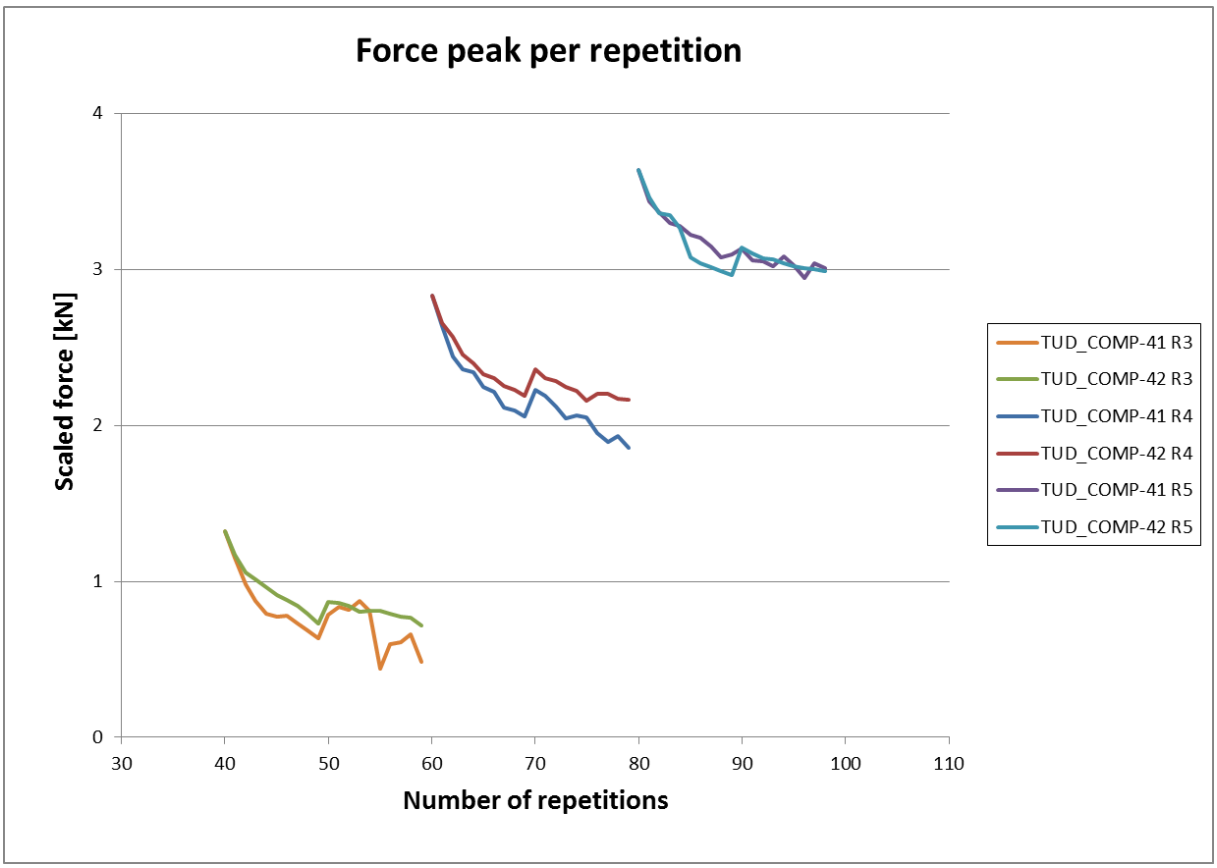

Figure 4.56. Comparison force peak per repetition of TUD_COMP-41 and TUD_COM-42 for R3-R5.

The force reduction of TUD_COMP-40 is shown in Figure 4.57. Although TUD_COMP-40 has only three repetitions per set, a similar trend can be observed in which the largest reduction takes place in the first part of the repetition displacement step and than appears to even out throughout the repetition displacement step.

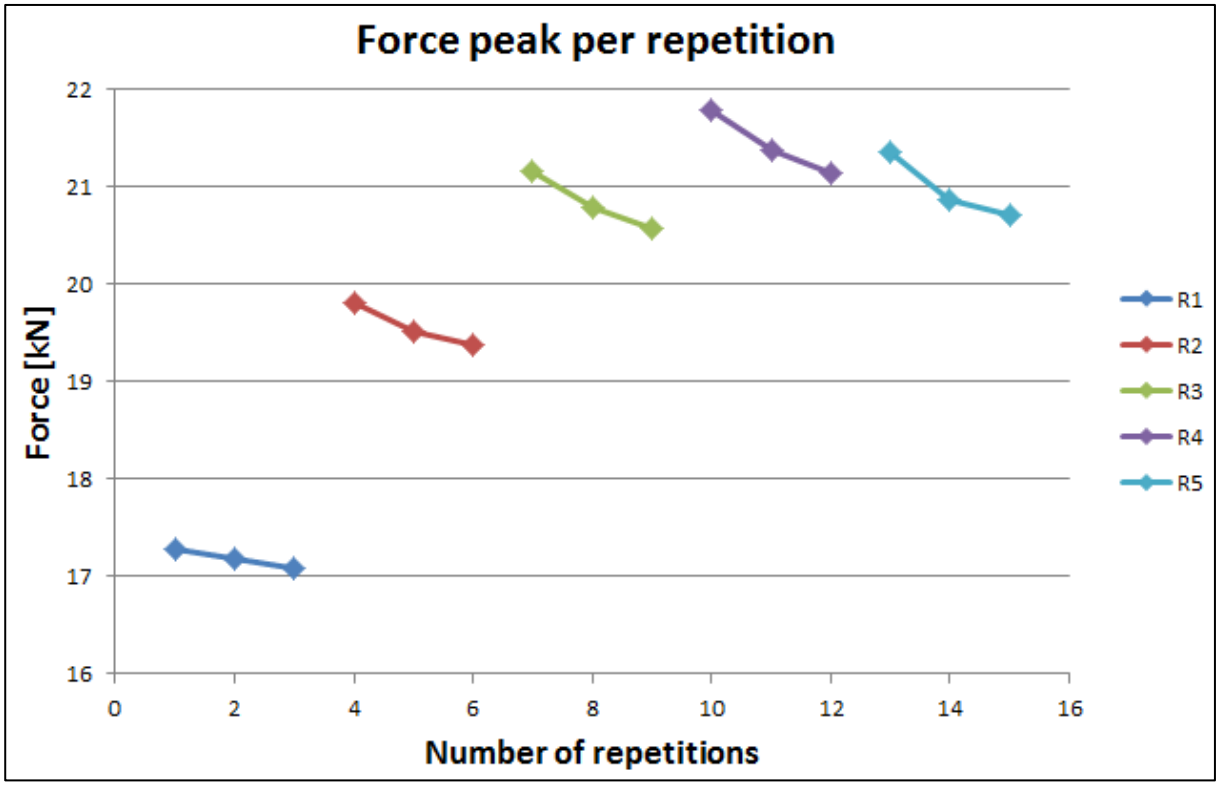

Figure 4.57. Force peak per repetition of TUD_COMP-40.

With software developed in-house (Section 2.6) the crack length can be estimated from the DIC analysis (Figure 4.58). For this report, the DIC analyses and the software to measure cracks have been newly implemented and not yet validated sufficiently; therefore, the results presented in Figure 4.59 should be considered preliminary.

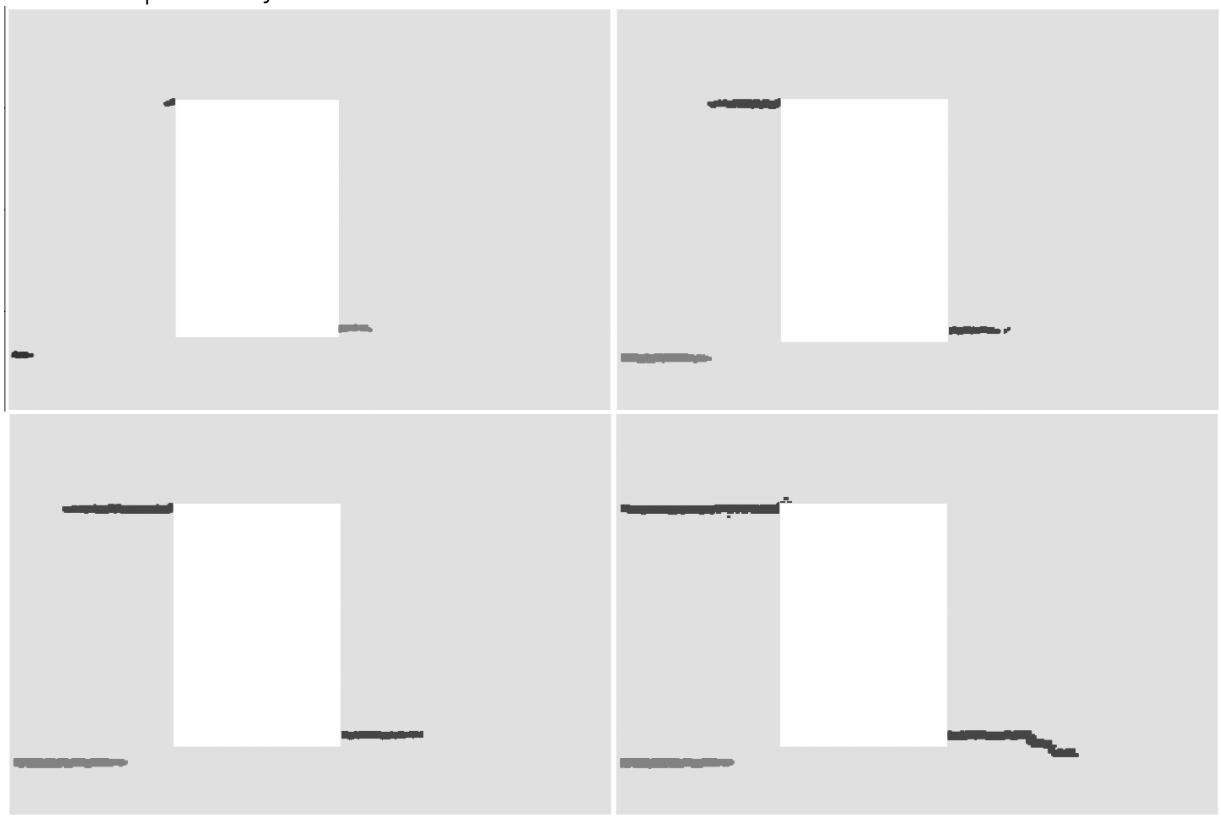

Figure 4.58. Example of COMP-41 of which the sequence of cracks is identified by the program for repetitions R1 to R4.

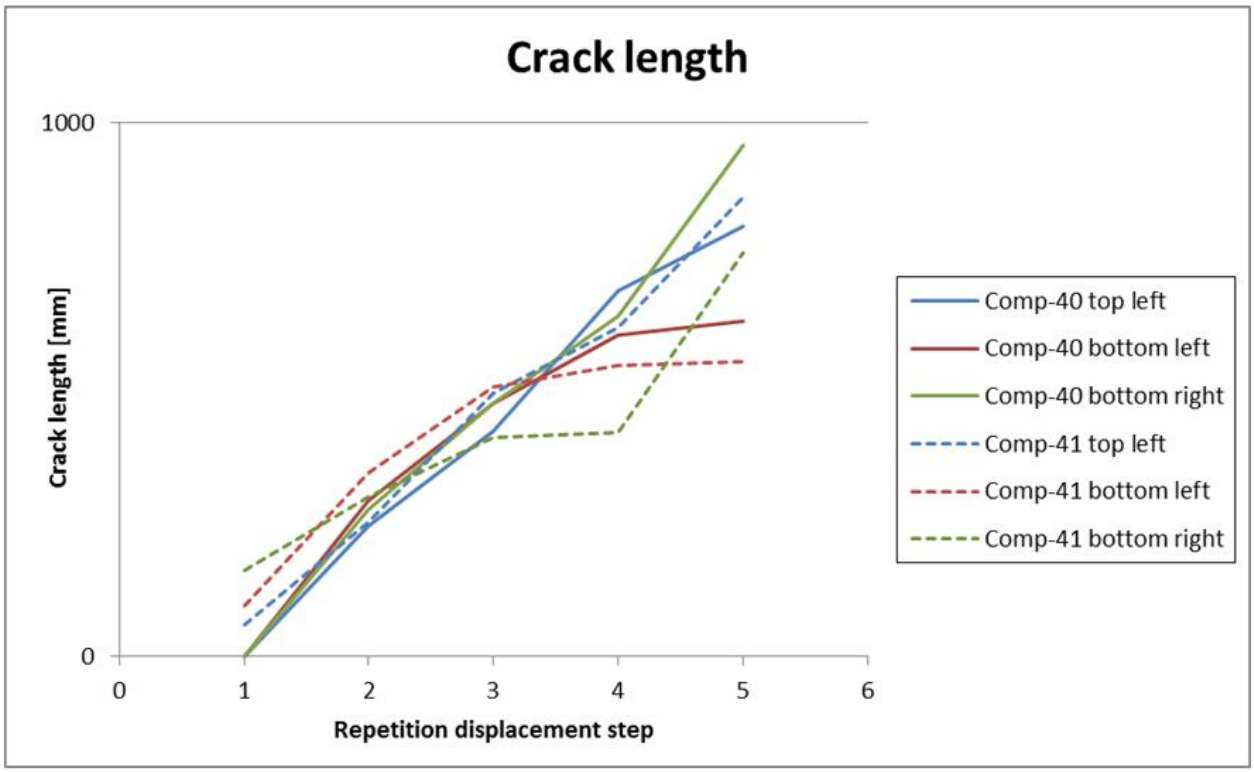

Figure 4.59a. Crack length comparison of COMP-40 and COMP-41 (preliminary results).

As can be seen in Figures 4.59 a comparison is made between COMP-40 and COMP-41. These two samples have similar crack patterns as can be seen in Figure 4.54. In Figures 4.59 the three cracks are referred to as: 'top left' which is the crack starting from the top left window corner, 'bottom left' which starts from the left wall edge around the height of the bottom of the window opening, and 'bottom right' which starts from the bottom right window corner. In Figure 4.58 it is visible that COMP-40 for repetition displacement step 1 (R1) no cracks where detected by the software. In Figure 4.54 it can be seen that the DIC of COMP-40 contains more noise compared to the others. When considering small cracks the software cannot yet distinguish the noise from the small cracks. In the future, noise will be reduced by tuning the patterns on the wall and the program will be improved to better detect it.
The comparison of the different cracks for COMP-40 and COMP-41 in Figures 4.59 shows a similar trend. The cracks on the left side are limited by the width of the pier on the left side of the window opening. It is visible that when those cracks approach their limit, the rate of increase of the crack in the bottom right steepens.
This trend is better visible in Figure 4.59b in which the difference between, for instance R3 and R4, is divided by the crack length of R3 and expressed as a percentage. The bottom right crack length growth decreases to R4 and then deflects upwards for R5, meaning that crack growth increases again. If the left pier is fully cracked (both top and bottom) and the wall section at the bottom right crack is not, then this part of the wall acts stiffer and will, therefore, lead to an increase of stress around the bottom right crack fostering its growth.

Improving the DIC method and crack measuring software will be key to be able to increase the confidence in the measurements of crack width and crack length from the experimental tests using DIC. In theory, the DIC is able to replace all displacement sensors during a test since it is able to measure displacements at every point in the masonry sample. Redundant systems, however, are even better at reliably measuring samples.

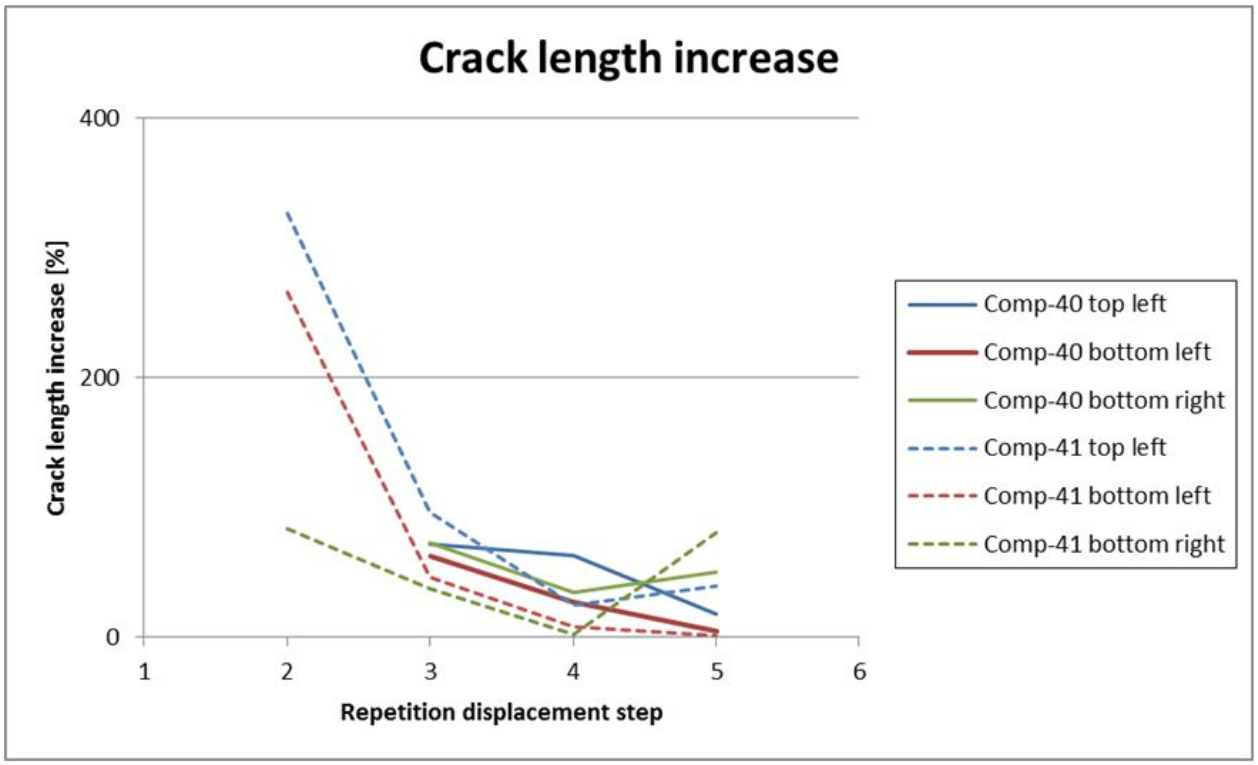

Figure 4.59b. Crack length increase comparison of COMP-40 and COMP-41 (preliminary results).

4.2. Window Bank Test

The window bank tests target cracking patterns that are typical and frequently observed in Groningen below or above windows, where cracks follow vertical paths and compressive stresses are minimal[1]. The window bank test could be considered as a modified four-point bending test.

This test complements the larger walls because only one crack is present allowing for a direct relation between the crack characteristics and the resistance and displacements of the specimen. Moreover, these cracks zig-zag vertically around the bricks (see Figure 4.73 for instance), differing significantly in behaviour in comparison to the in-plane wall's cracks which propagate mostly horizontally.
This allows, firstly, for the calibration of additional parameters in the computational models, specifically when vertical cracks, present when shrinkage or settlement actions are observed, need to be replicated. This calibration is not fully part of this report, because it needs to be included in the optimisation of the material model (see Chapter 5 and Section 8.2); however, insight with a micro-model is provided in Section 9.6.5 of the appendix.
Secondly, since the influence of the single crack is more evident in the displacement and force results of the test, stronger observations can be made regarding the behaviour of the crack.
Thirdly, since the smaller experiment is cheaper, easier, and faster to perform, a higher number of samples and additional variations can be tested. This increases the reliability of the results.

4.2.1. Sample Description

The dimensions of the window bank samples are derived from the in-plane wall, as explained in the test protocol (Meulman et al., 2017, Section 5.1). The window bank sample is the section below the window opening of the in-plane sample, tested separately to investigate the aforementioned vertical cracking patterns observed in Groningen area.
The modified four point bending test will cause tension stresses at the top of the sample. To prevent sudden failure of the sample, the bottom is supported by counterweights; this also allows for repetitive testing of the same sample.
Figure 4.60 shows the front of the sample painted with the random patterns necessary for DIC. The sample is supported by two rollers visible above the red block. Additional support is provided by counterweights (not visible) that are hanging from cables which lift the bottom of the sample. Figure 4.62 shows the schematisation of the sample. Aligned to the point of application of the counterweight's forces (48 kg) are the hydraulic jacks at the top of the specimen. In the middle of the jacks a head joint is left open representing a notch. A sensor is placed across this notch, while at the top of the sample, another sensor runs along all three head joints. Figure 4.61 shows the sample from the back, without counterweights and with the jacks lifted. Additional sensors are placed on this side of the sample.

Two types of window bank tests are performed: monotonic and repetitive tests. The monotonic tests include variations in the loading rate and the repetitive tests include variations in the amount of repetitions (see also Table 4.15 and Table 4.17).

The tests are terminated when either of the following occurs:
1. The displacement controlled load reaches the limit value of 2kN, after which the displacement controlled system could become unstable;
2. The sensor on the top of the wall, which gives the input for the displacement controlled loading, reaches its limit displacement of 90% of its maximum displacement, which is about 2mm.

[1] Update after publication of this report. Reference:
P. Van Staalduinen, K. Terwel, J.G. Rots (2018). Onderzoek naar de oorzaken van bouwkundige schade in Groningen Methodologie en case studies ter duiding van de oorzaken. Delft University of Technology. Report number CM-2018-01, 11 July 2018 - Downloadable from www.NationaalCoordinatorGroningen.nl

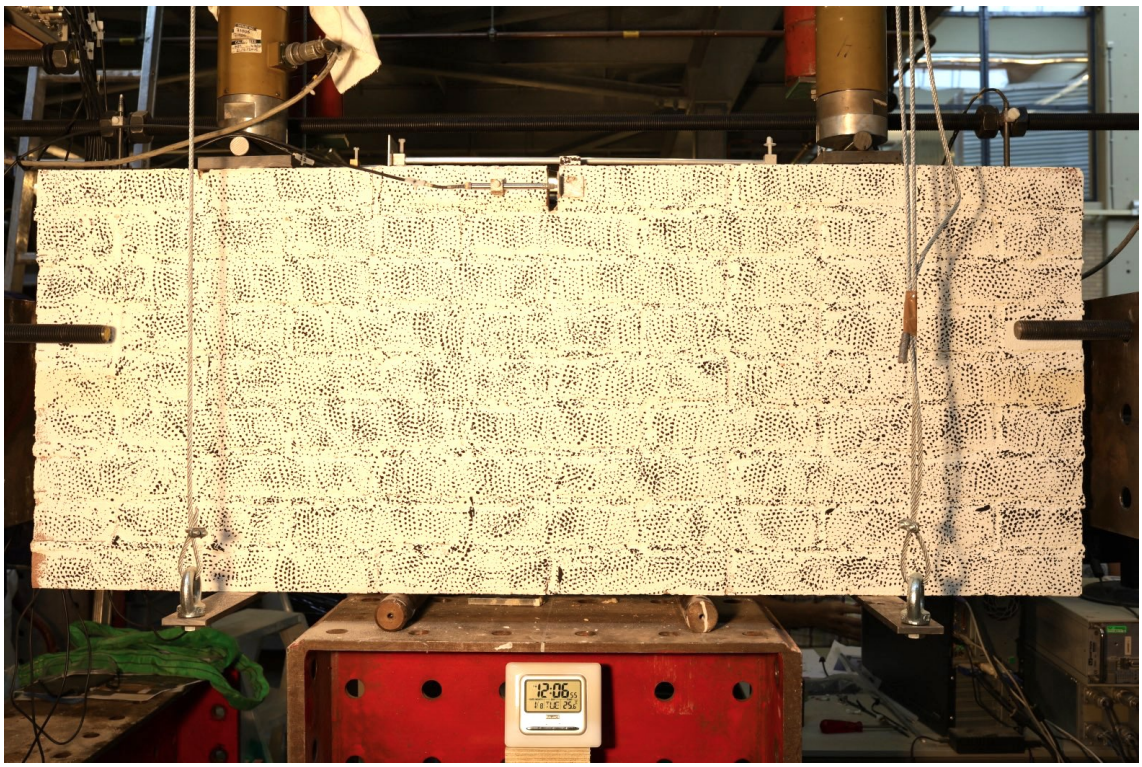

Figure 4.60. Window bank test sample (front side).

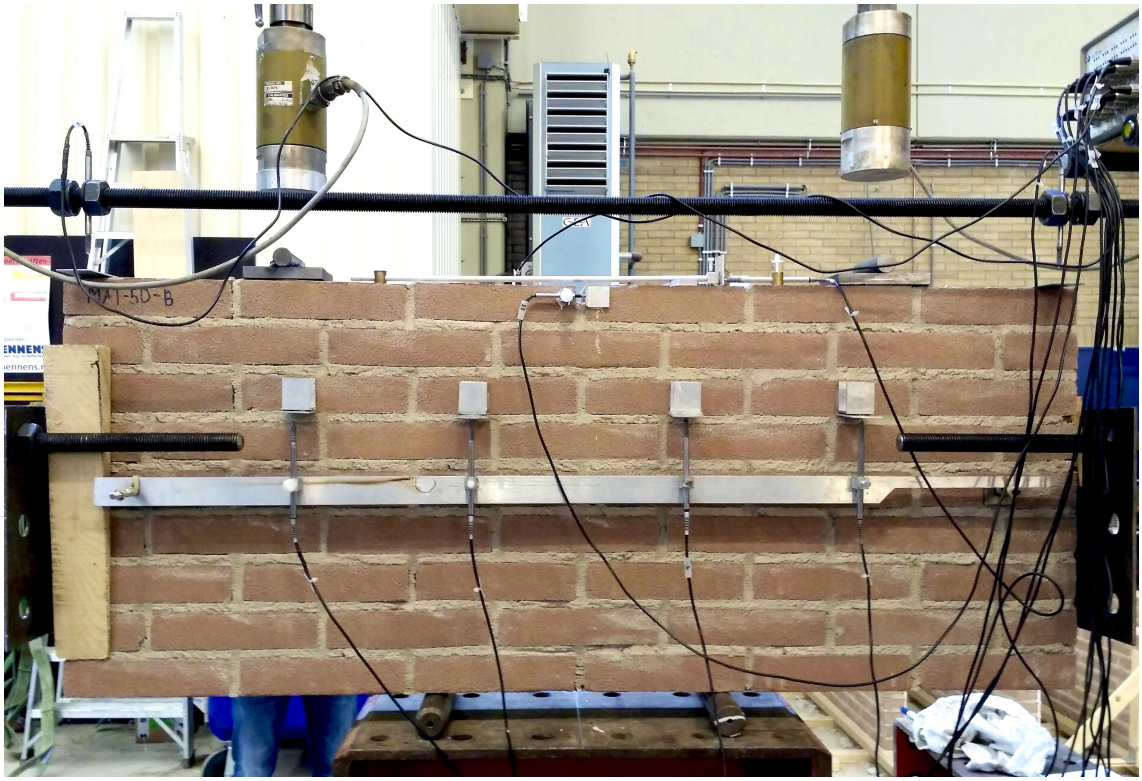

Figure 4.61. Window bank test sample (back side).

The configuration results in the following maximum bending moment in the sample (see also Figure 4.62):

$$M_{\max} = (F - CW) \cdot d_3 \tag{4.1}$$

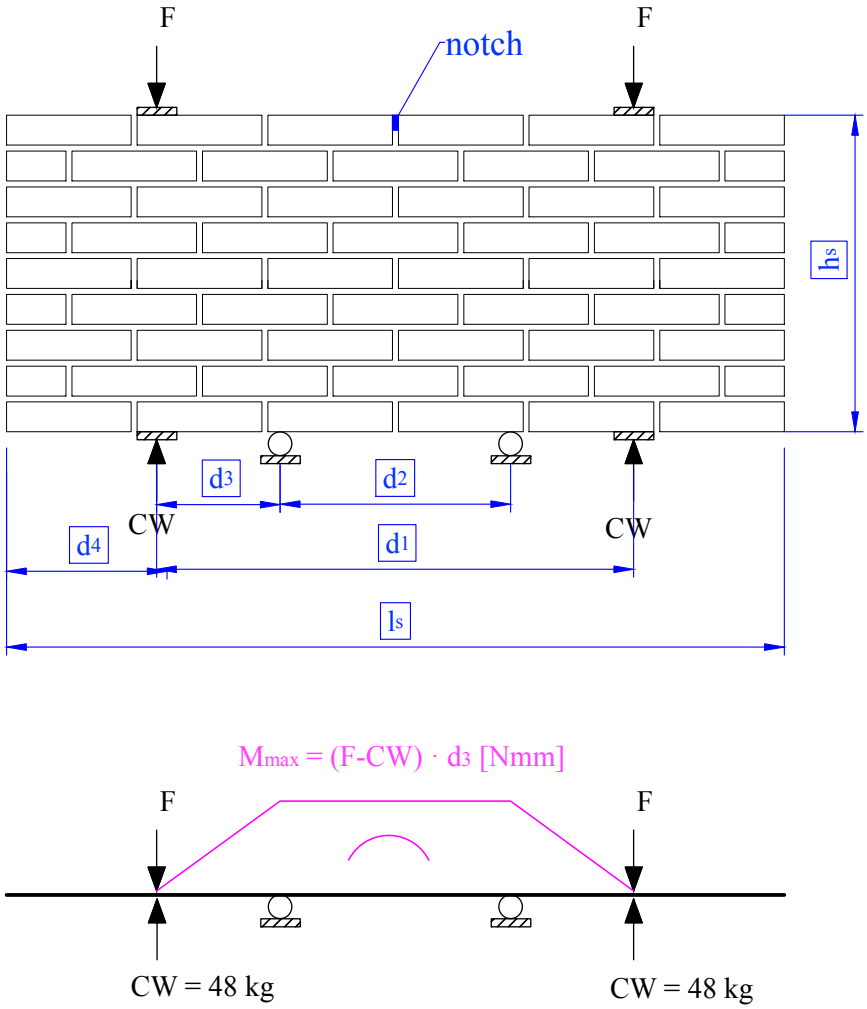

Figure 4.62. Bending moment diagram of the window bank samples.

From the measured displacements and forces, the following characteristics of the samples are calculated:

$$I = \frac{1}{12} t_s h_s^3 \tag{4.2}$$

$$W = \frac{1}{6} t_s h_s^2 \tag{4.3}$$

$$\sigma = \frac{M}{W} \tag{4.4}$$

$$f = \sigma_{\max} \tag{4.5}$$

$$\varkappa_{max} = \frac{u_{h,top}}{\frac{d_2}{e_{top}}} \tag{4.6}$$

$$E = \frac{M}{\varkappa I} \tag{4.7}$$

With **e** as the radial distance equal to half the sample height.

4.2.2. Monotonic Tests

Table 4.15. Overview of the monotonically tested window bank samples.

WINDOW BANK IP 4PT BENDING TEST		l_s	h_s	t_s	d_1	d_2	d_3	d_4	Rate	F_{max}	f	E
		mm	mm	mm	mm	mm	mm	mm	mm/s	kN	MPa	MPa
1	TUD_MAT-50D	1303	530	100	775	370	200	257	0.0005	20.2	0.41	5956
2	TUD_MAT-50E	1310	530	100	780	380	200	262	0.0005	17.6	0.36	4120
3	TUD_MAT-50F	1309	528	100	776	369	203	275	0.005	25.0	0.52	2548
4	TUD_MAT-50G	1300	530	100	750	380	174	282	0.0005	19.0	0.33	3364
5	TUD_MAT-50H	1300	531	100	783	375	210	256	0.005	30.0	0.65	4616
6	TUD_MAT-50I	1310	530	100	759	375	192	275	0.0005	17.0	0.29	2412
7	TUD_MAT-50J	1304	530	100	797	375	210	255	0.005	17.0	0.35	3918

average	0.42	5038
st. dev.	0.12	918
c.o.v.	0.28	0.18

Loading Rate Variation 1

Figures 4.63 to 4.66 show force-displacement, moment-curvature, and stress-strain relations, respectively, of the samples loaded by a slow monotonic loading scheme.

Figure 4.63 shows a drop in force right after the elastic phase for all four samples. The tests are displacement controlled with a constant rate, so the drop in the F-u (Force-Displacement) diagram means that a lower force is needed in order to obtain the same amount of displacement, suggesting crack development.
The graphs also show a long plateau after reaching the peak capacity, but softening is not clearly present.

Figure 4.64 shows the force-displacement relation measured at the notch of the samples. It can be seen that for three of the four samples the cracks did not develop at the notch, the displacement at this location remains minimal. Sometimes a diagonal crack formed starting from the left or right head joint next to the notch as can been seen in Figure 4.68 (sample TUD_MAT-50G).

Figure 4.67 shows the DIC result at the final testing stage of sample TUD_MAT-50E, the sample where the cracks did initiate at the notch. It can be seen that the cracks develop in a vertical or diagonal manner from the top but also go to the centre of the bottom part of the sample. This could explain the plateau in the graphs; due to the interlocking effect of the bond pattern in the bottom part where the crack follows a vertical direction through the joints.

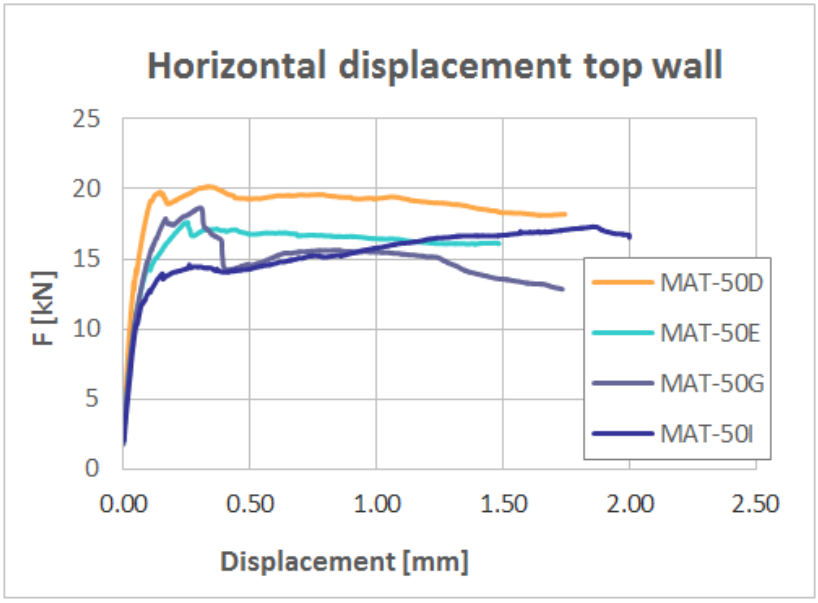

Figure 4.63. Force-displacement graph of the monotonic samples with loading rate of 0.0005mm/s (slow).

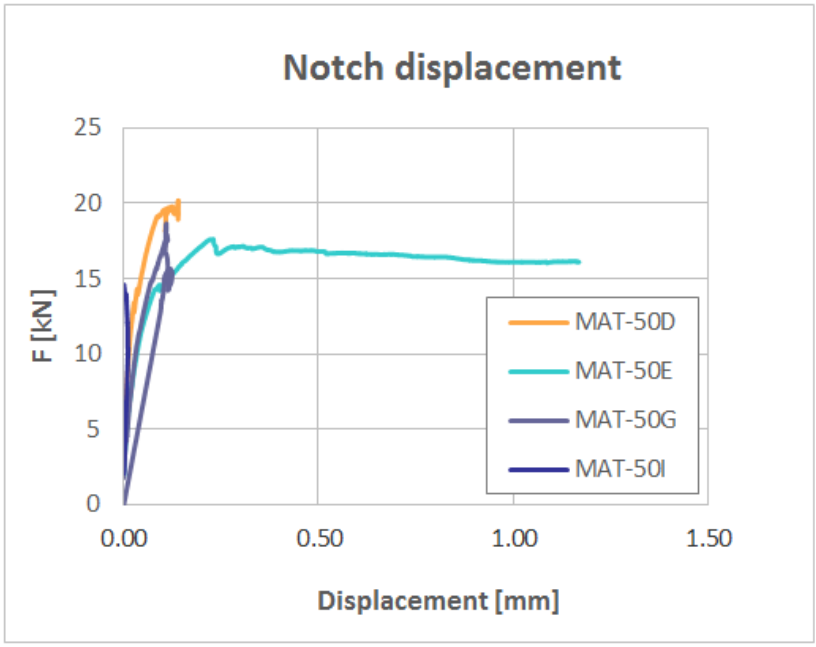

Figure 4.64. Notch opening displacement graph of the monotonic samples with loading rate of 0.0005mm/s (slow).

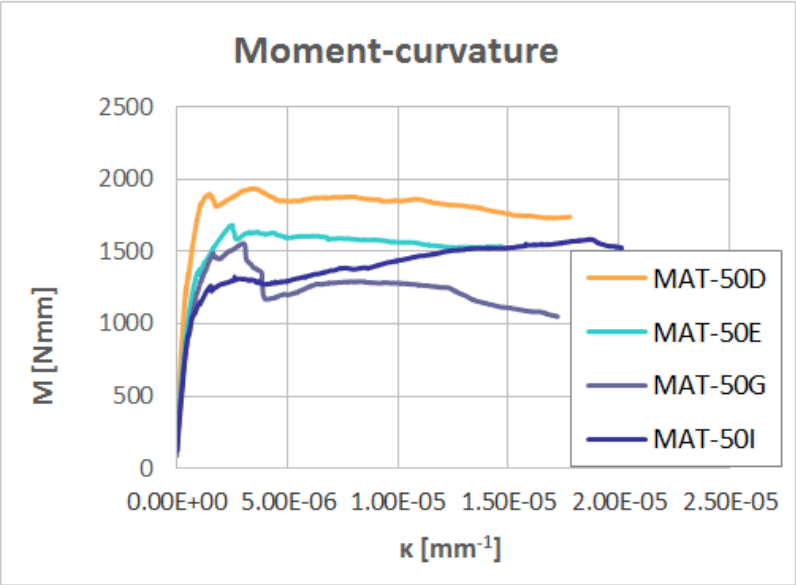

Figure 4.65. Moment curvature graph of the monotonic samples with loading rate of 0.0005mm/s (slow).

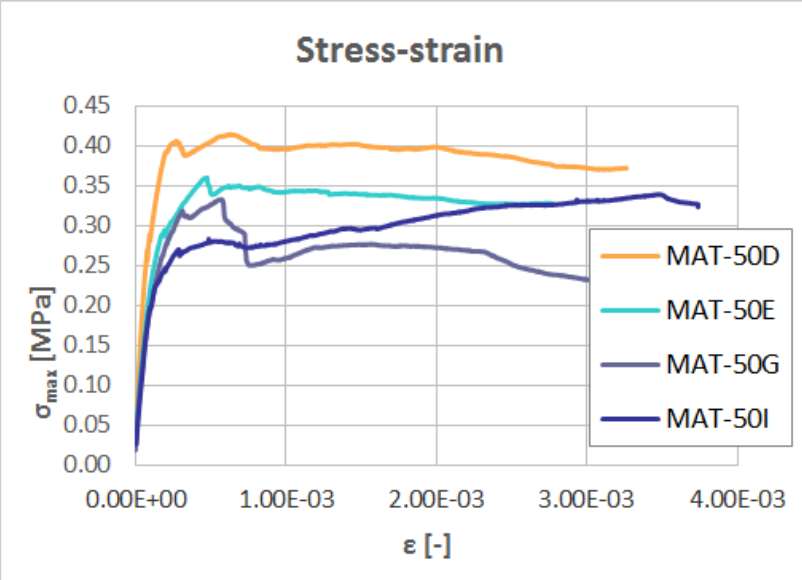

Figure 4.66. Stress-strain graph of the monotonic samples with loading rate of 0.0005mm/s (slow).

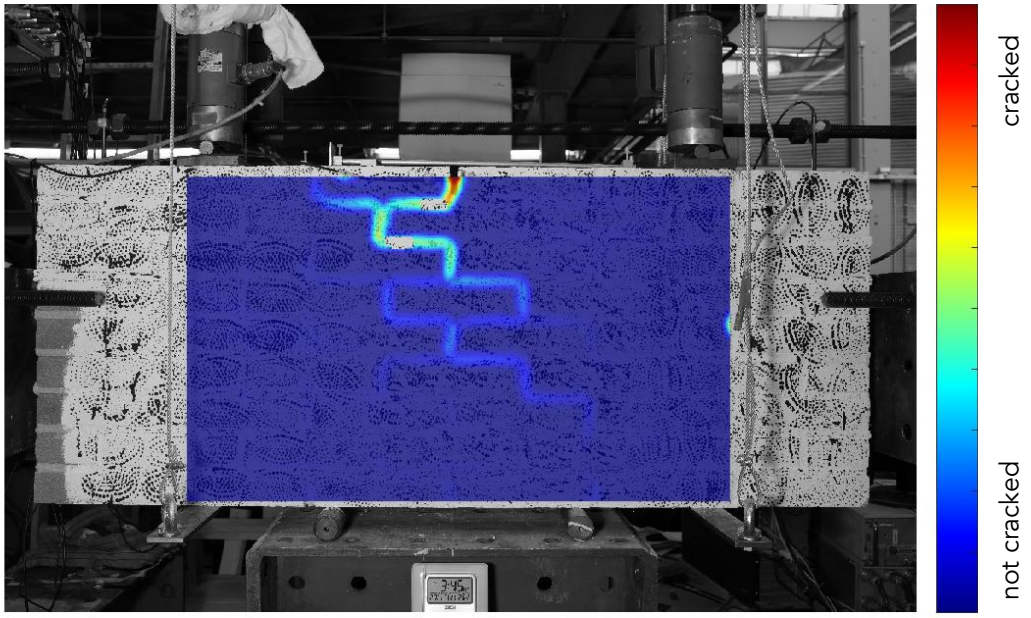

Figure 4.67. DIC crack plot of sample TUD_MAT-50E.

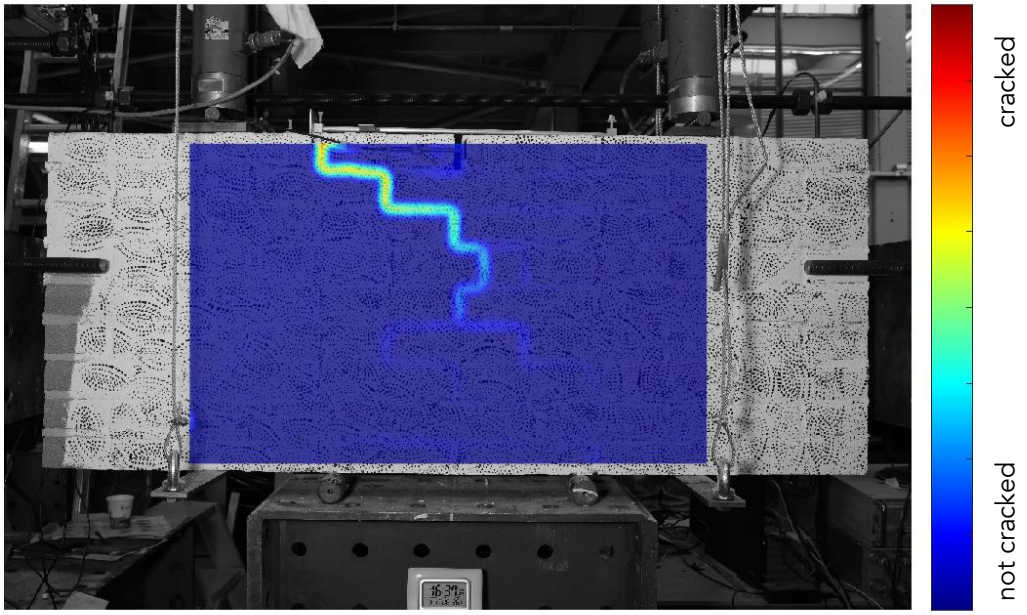

Figure 4.68. DIC crack plot of sample TUD_MAT-50G.

Loading Rate Variation 2

Figures 4.69 to 4.72 show force-displacement, moment-curvature, and stress-strain relations respectively, of the samples loaded by a fast monotonic loading scheme.

The figures show a long plateau after reaching the peak capacity for the TUD_MAT-50F and TUD_MAT-50J samples, while the TUD_MAT-50H sample undergoes a softening phase. All three tests were terminated when the limit displacement was reached.

Figure 4.69 shows the force-displacement relation measured at the notch of the samples. It can be seen that for the TUD_MAT-50F sample the cracks did not develop at the notch, the displacement at this location remains minimal.

Figure 4.72 shows the DIC result at the final testing stage of sample TUD_MAT-50J. The cracks develop in a diagonal manner.

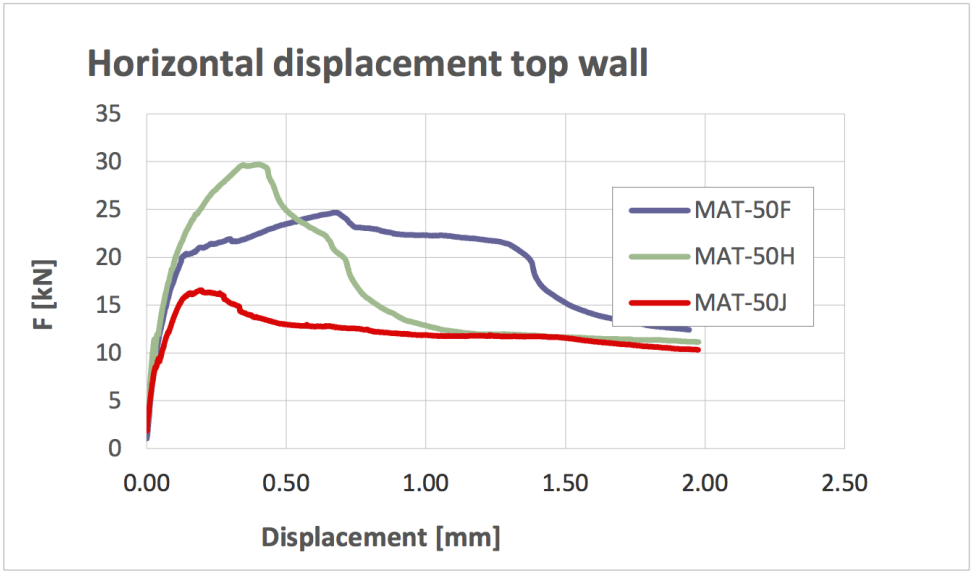

Figure 4.69. Force-displacement graph of the monotonic samples with loading rate of 0.005mm/s (fast).

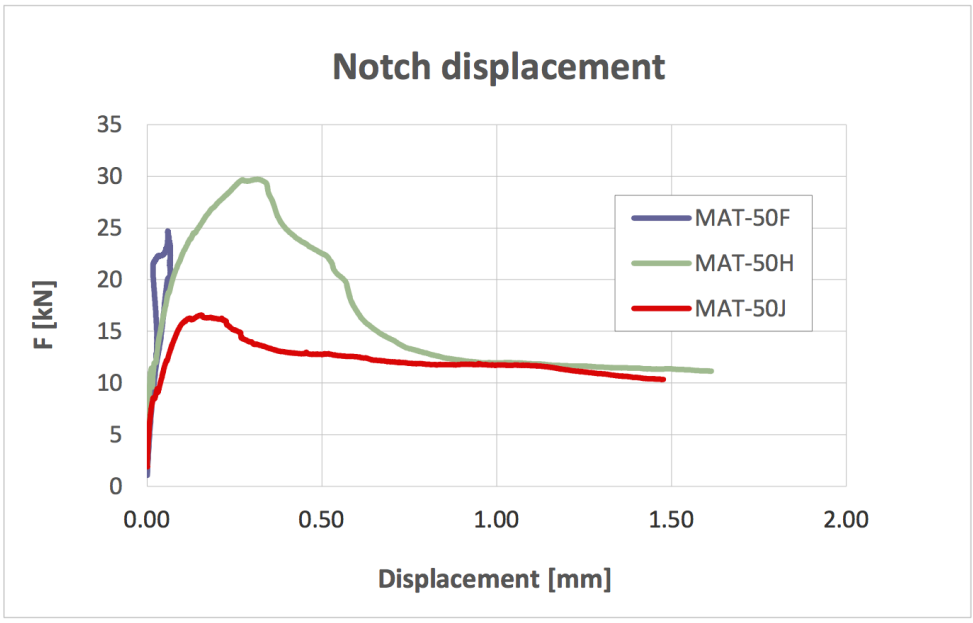

Figure 4.70. Notch opening displacement graph of the monotonic samples with loading rate of 0.005mm/s (fast).

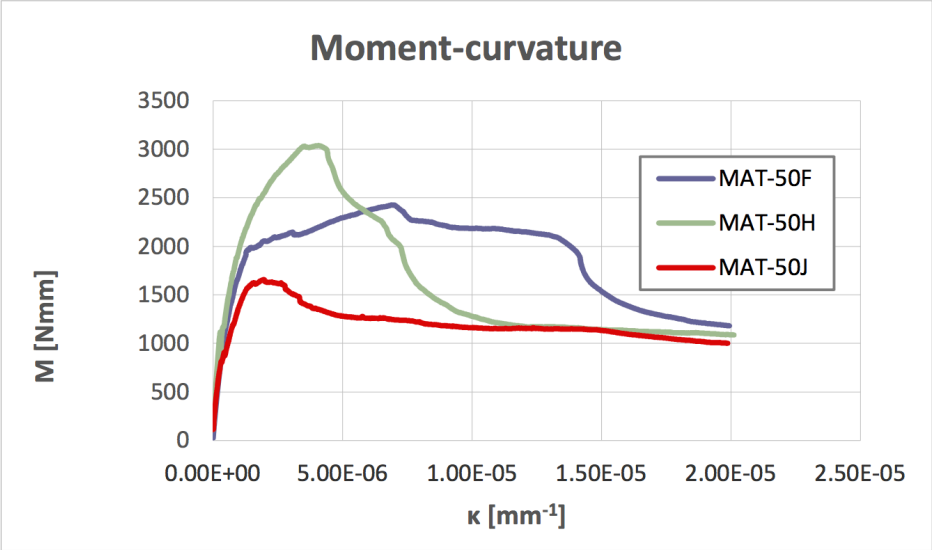

Figure 4.71. Moment-curvature graph of the monotonic samples with loading rate of 0.005mm/s (fast).

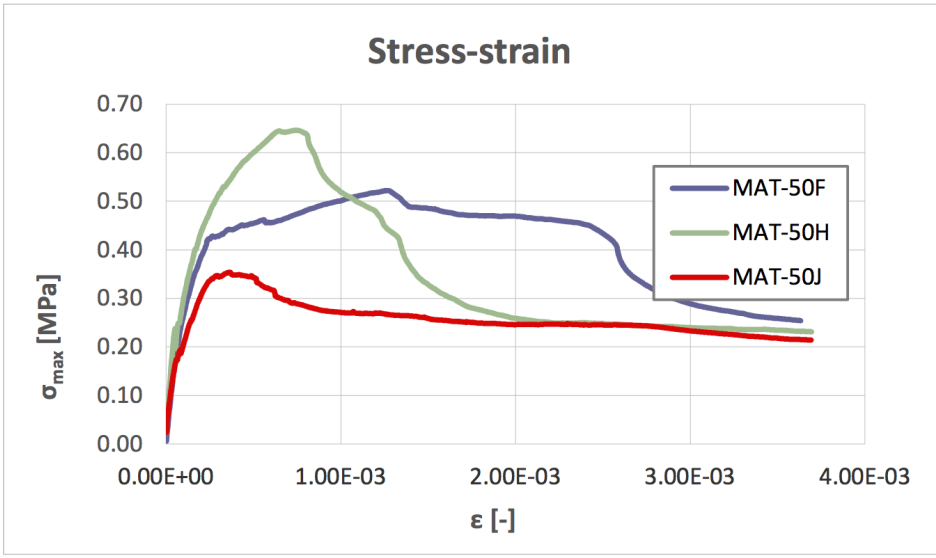

Figure 4.72. Stress-strain graph of the monotonic samples with loading rate of 0.005mm/s (fast).

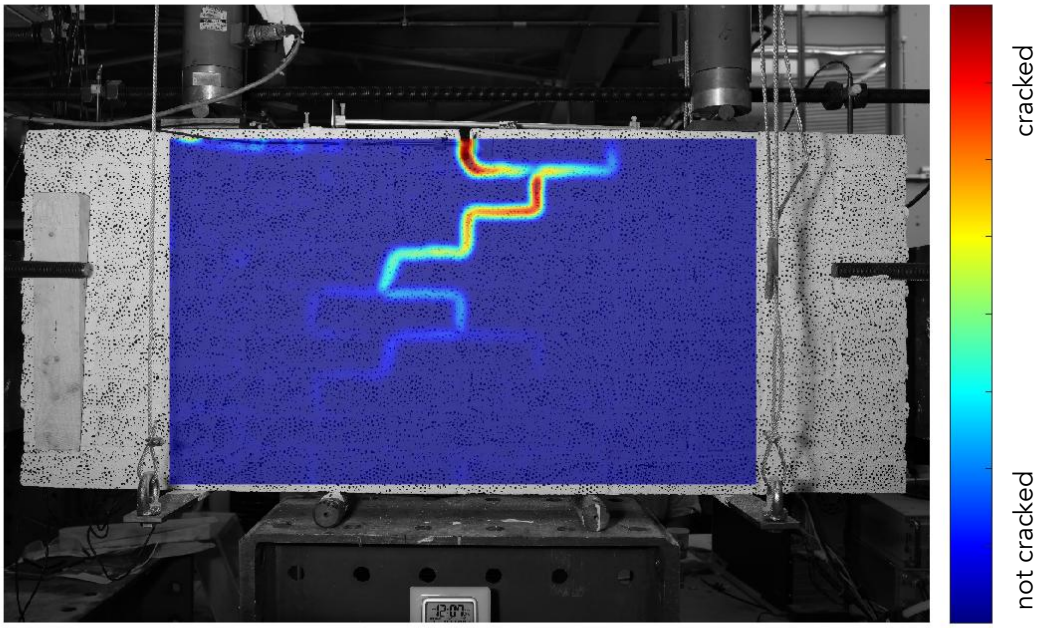

Figure 4.73. DIC crack plot of sample TUD_MAT-50J.

Comparison

Figures 4.74 to 4.77 show the previously presented graphs, with the slow and fast loading rate combined for comparison. It can be seen that the fast loading rate results in a wider range (higher variability) in the capacity of the samples, whereas the samples with a slow loading rate show comparable test results. Table 4.16 gives an overview of the average characteristic values of the two monotonic sample types, which, like the graphs, shows a lower standard deviation in the maximum load and stress measured for the slow loading rate samples compared to the fast loading rate samples. This could be explained by the amount of stress redistribution allowed by the loading rate; faster loading could lead to less stress redistribution and therefore more abrupt crack development. Where the slow loading rate samples show a lower standard deviation in the maximum force and stress, Table 4.16 shows a higher standard deviation in the stiffness of these samples (see also Figure 4.77). The stiffness of the fast loading rate samples are more comparable. Again, this could be explained by the amount of stress redistribution related to the loading rate. At a slower rate, the cracks could possibly develop more smoothly, resulting in deviating stiffness in the samples at an early stage, where at a higher loading rate these cracks develop at a later stage in the F-u diagram in a more abrupt manner.

Table 4.16. Comparing average values of the samples tested slow and fast loading rate.

Rate		**F_{max}**	**f**	**E**
mm/s		kN	MPa	MPa
0.0005 (slow)	**average**	20.95	0.37	3907
	st. dev.	4.37	0.03	1368
	c.o.v.	0.21	0.08	0.35
0.005 (fast)	**average**	23.66	0.51	3694
	st. dev.	5.41	0.12	859
	c.o.v.	0.23	0.24	0.23

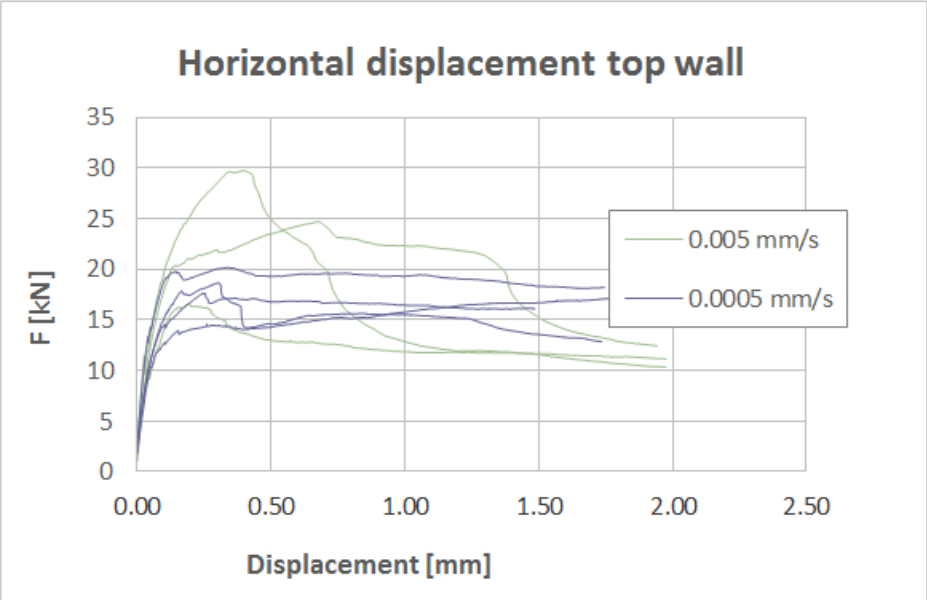

Figure 4.74. Force-displacement graph of all monotonic samples.

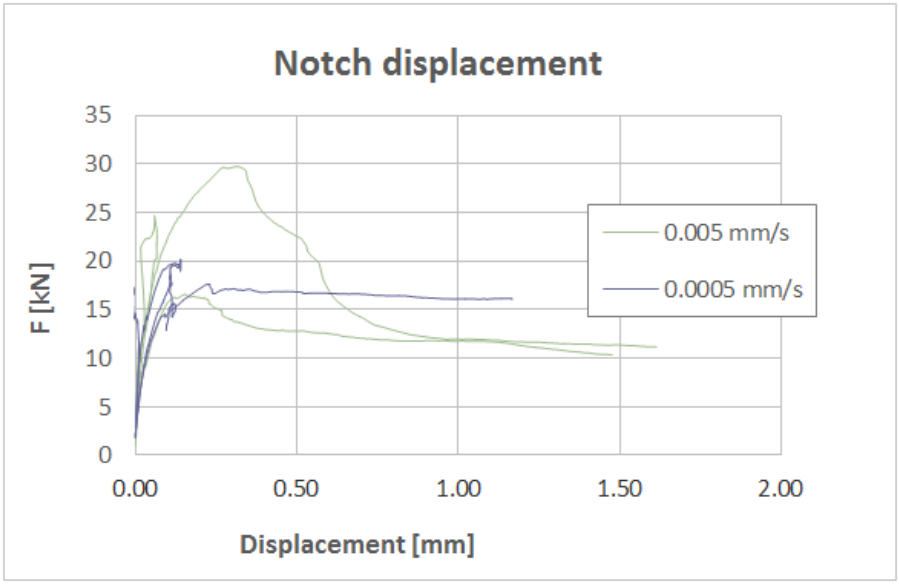

Figure 4.75. Notch opening displacement graph of all monotonic samples.

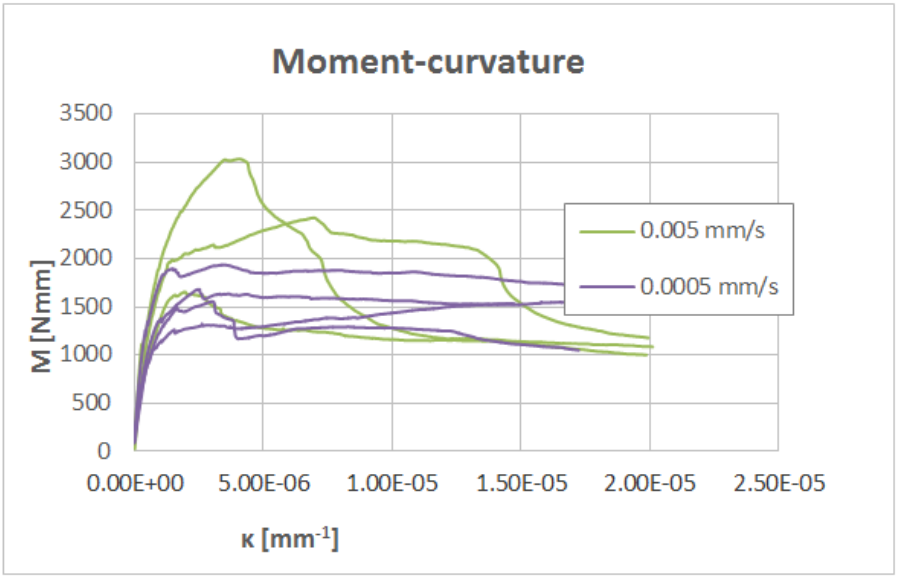

Figure 4.76. Moment-curvature graph of all monotonic samples.

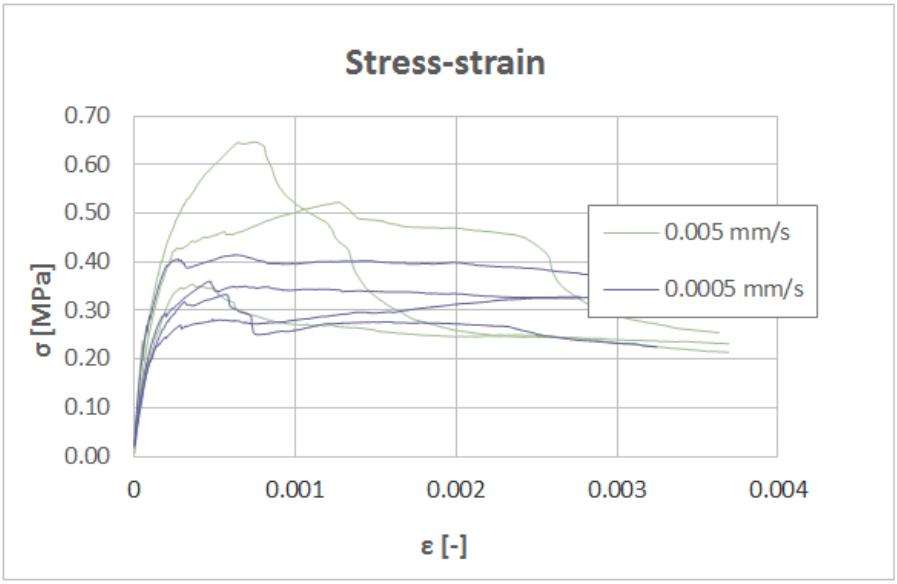

Figure 4.77. Stress-strain graph of all monotonic samples.

4.2.3. Repetitive

Table 4.17. Overview of the repetitive tested window bank samples.

WINDOW BANK IP 4PT BENDING TEST		l_s	h_s	t_s	d_1	d_2	d_3	d_4	Rate	Rep.	F_{max}	f	E
		mm	mm	mm	mm	mm	mm	mm	mm/s	-	kN	MPa	MPa
1	TUD_MAT-50U	1302	528	100	775	372	203	273	0.00275	10	25	0.53	6831
2	TUD_MAT-50N	1320	530	100	788	373	212	264	0.00275	10	18	0.35	2276
3	TUD_MAT-50O	1310	530	100	770	372	180	294	0.00275	10	15	0.28	3208
4	TUD_MAT-50R	1320	530	100	788	373	212	264	0.00275	30	21	0.31	2006
5	TUD_MAT-50S	1298	526	100	774	374	184	277	0.00275	30	20	0.38	4081
6	TUD_MAT-50M	1298	533	100	760	368	173	290	0.00275	30	18	0.32	2679
7	TUD_MAT-50P	1306	530	100	785	370	202	259	0.00275	100	24	0.37	4257

average	0.34	3243
st. dev.	0.09	1489
c.o.v.	0.27	0.46

Repetition Variation 1

Figures 4.78 to 4.82 show backbone curves of the force-displacement relations of the samples with 10 repetitions, 30 repetitions, and a combined graph, respectively. The backbone curve is obtained by selecting peak values from the repetitive testing data, followed by the data from the monotonic loading phase. Figure 4.81 shows the complete data set of sample TUD_MAT-50U.

In Figure 4.78 it can be seen that the initial stiffness of sample TUD_MAT-50N is considerably lower than that of samples TUD_MAT-50O and TUD_MAT-50U.

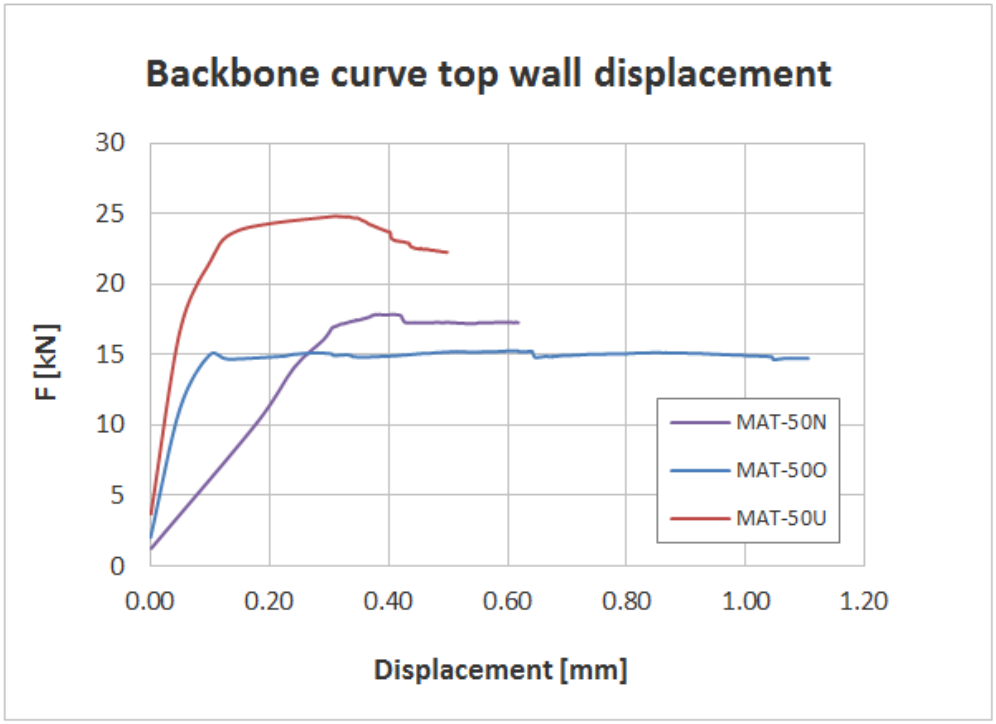

Figure 4.78. Backbone curve repetitive samples with 10 repetitions per repetition displacement step.

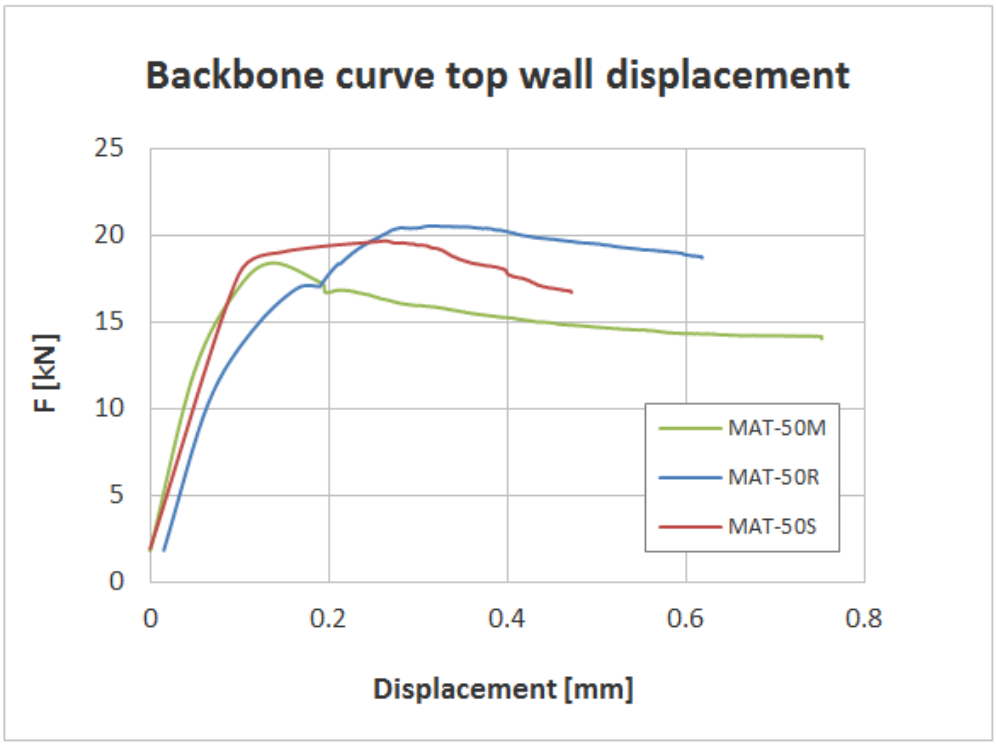

Figure 4.79. Backbone curve repetitive samples with 30 repetitions per repetition displacement step.

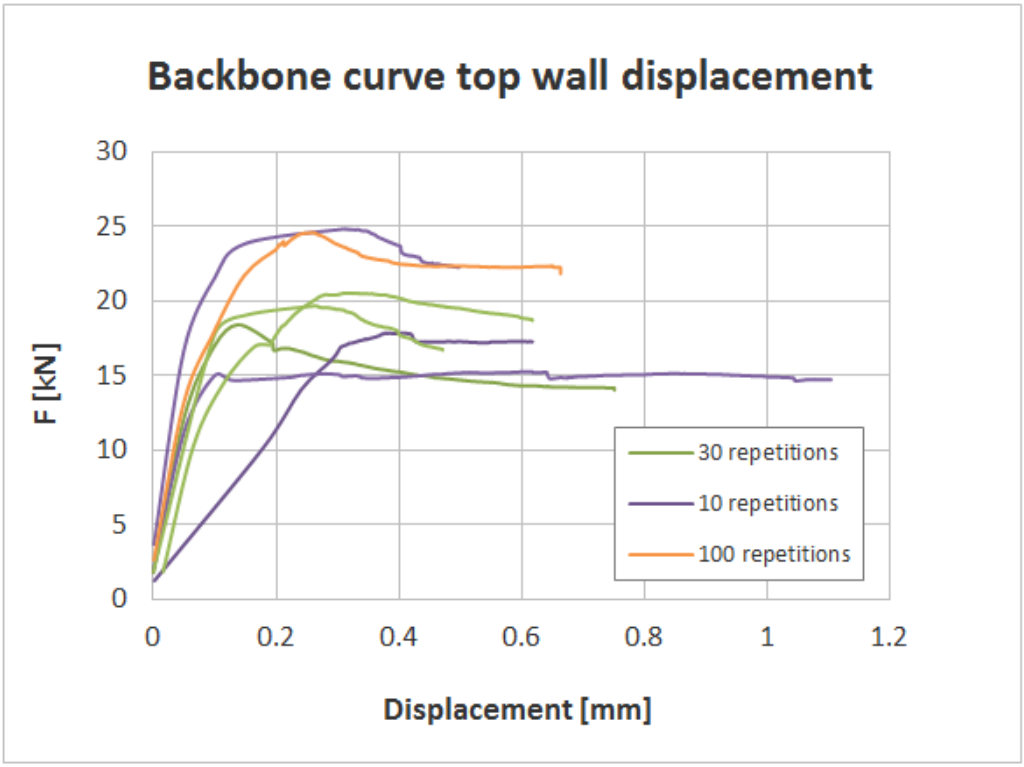

Figure 4.80. Backbone curve all repetitive samples.

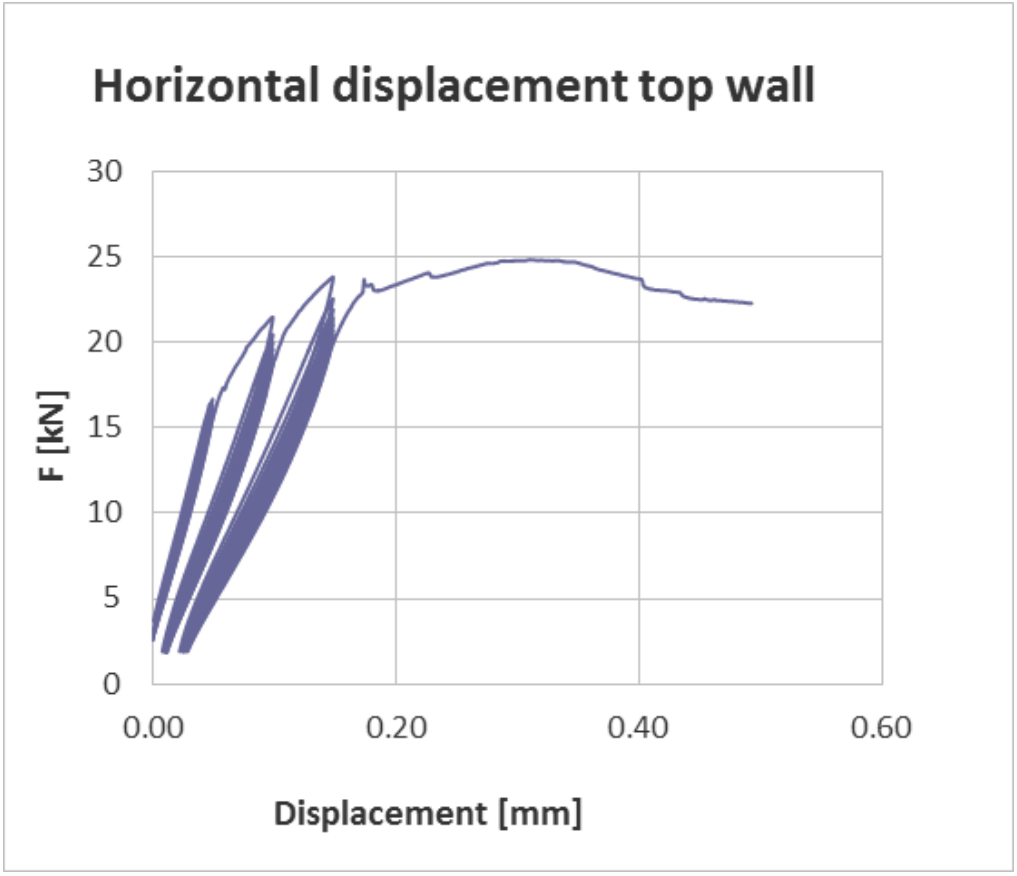

Figure 4.81. Force displacement graph of TUD_MAT-50U.

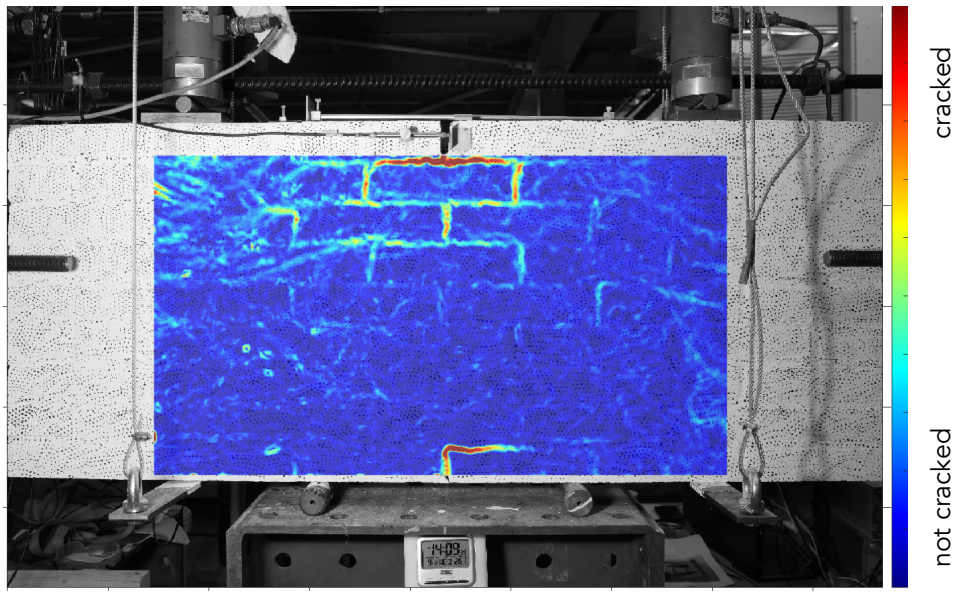

Figure 4.82. DIC crack plot of sample TUD_MAT-50U.

Figure 4.83 shows the force at each repetition divided in the three repetition displacement steps applied during the test. The repetition displacement step contains 10 repetitions. The test result shows a similar trend as was found in the IP wall tests (Section 4.1). In the lower repetition displacement steps the reduction force is less if the first repetition is compared with the last repetition within the repetition displacement step. Later in the test this force reduction within the repetition displacement step increases. If only one of the later repetition displacement step is considered it is visible that the force reduction is larger in the first repetitions and then levels off.

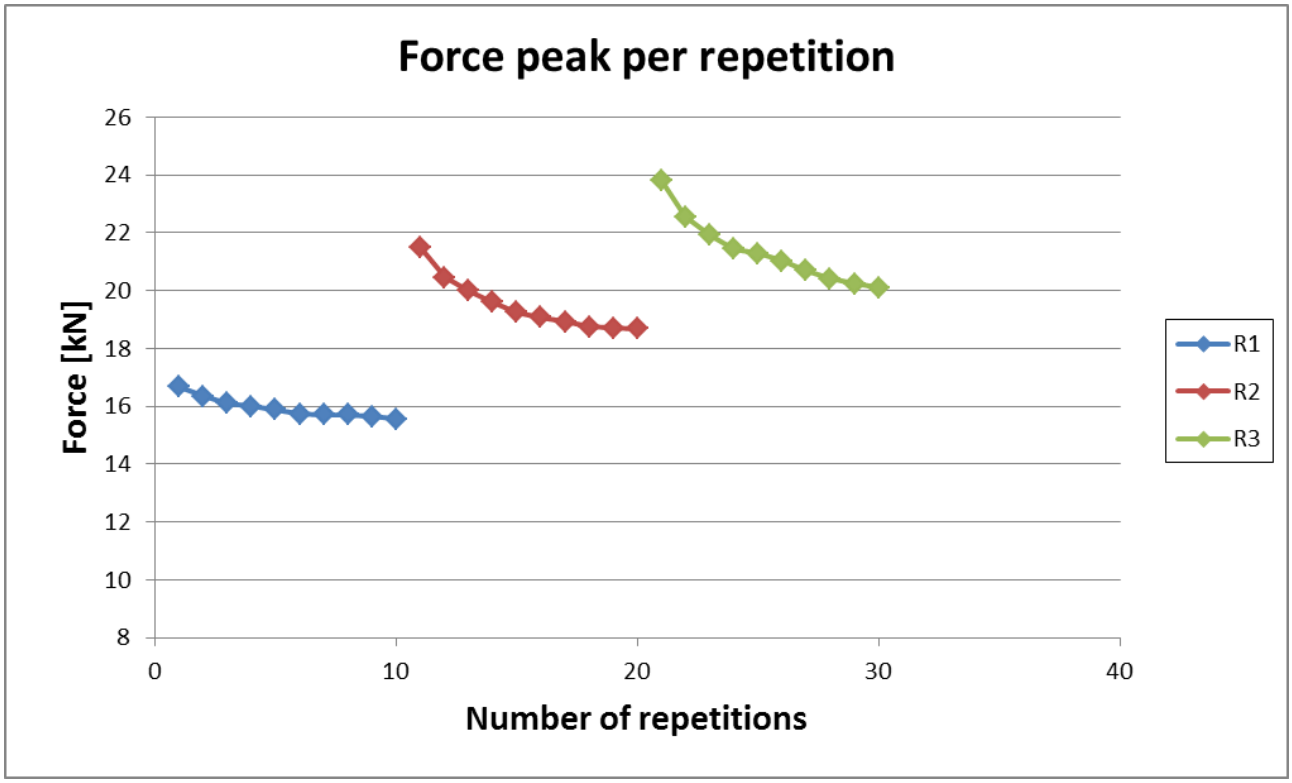

Figure 4.83. Force vs number of repetitions of sample TUD_MAT-50U.

Repetition Variation 2

The second loading variation applied on the window bank test contains 30 repetitions per repetition displacement step (set) as is described in more detail in de test protocol (Meulman et al., 2017). Figure 4.84 is a force-displacement graph of one of the window bank samples (TUD_MAT-50M) that was tested with repetitive loading variation 2.

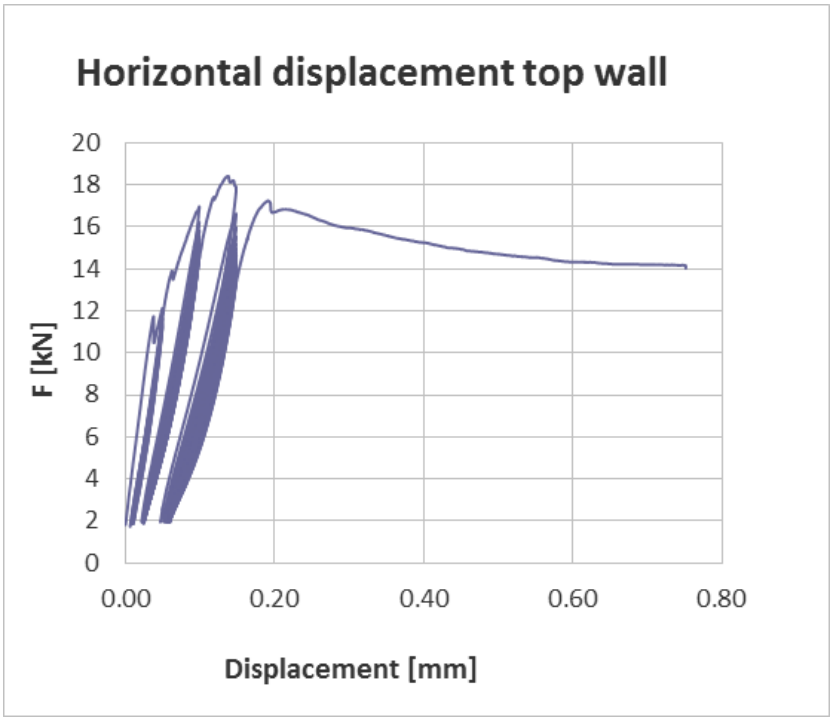

Figure 4.84. Force-displacement graph of TUD_MAT-50M.

Figure 4.85 shows the DIC crack plot of one of the last stages of the TUD_MAT-50M test. The crack initiated in the notch of the sample and propagated through the middle, around the bricks, down.

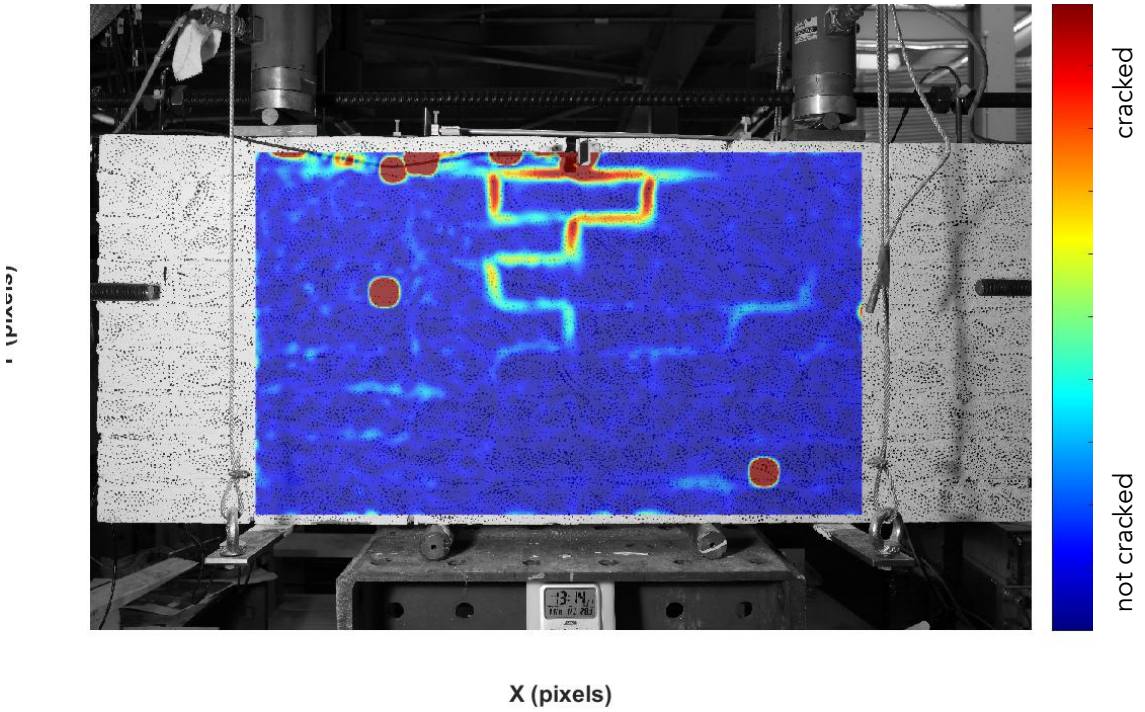

Figure 4.85. DIC crack plot of sample TUD_MAT-50M.

Figure 4.86 shows the force versus the number of repetitions of sample TUD_MAT-50M. The same trend is observed with the 30 repetitions variations as in the 10 repetitions variation. In the later repetitions

displacement steps the first repetitions show a larger force reduction which then almost levels out. Although the force reduction becomes less smaller, it seems that it does not stabilise completely.

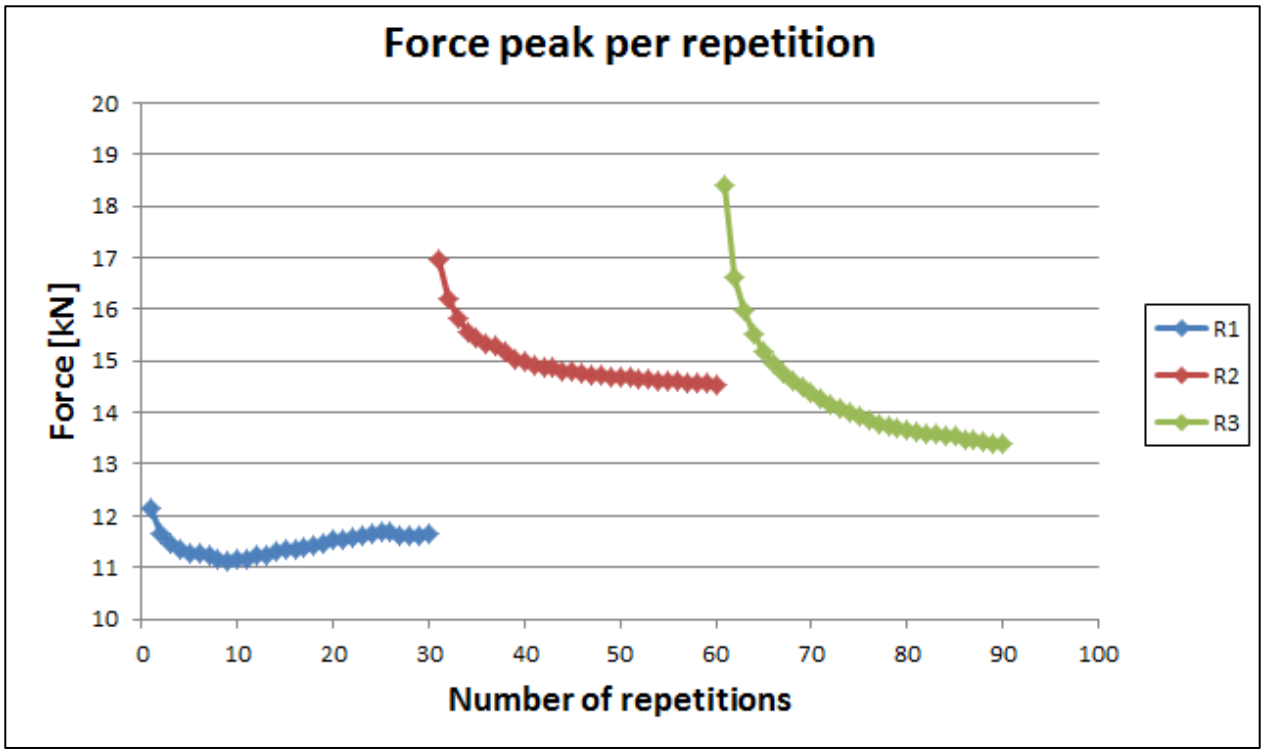

Figure 4.86. Force versus number of repetitions of sample TUD_MAT-50M.

To check the effect of the progressing force reduction and to investigate whether it would stabilise within a repetitions displacement step, an extra sample (TUD_MAT-50P) was tested with 100 repetitions per set. Figure 4.87 shows the force-displacement graph of sample TUD_MAT-50P.

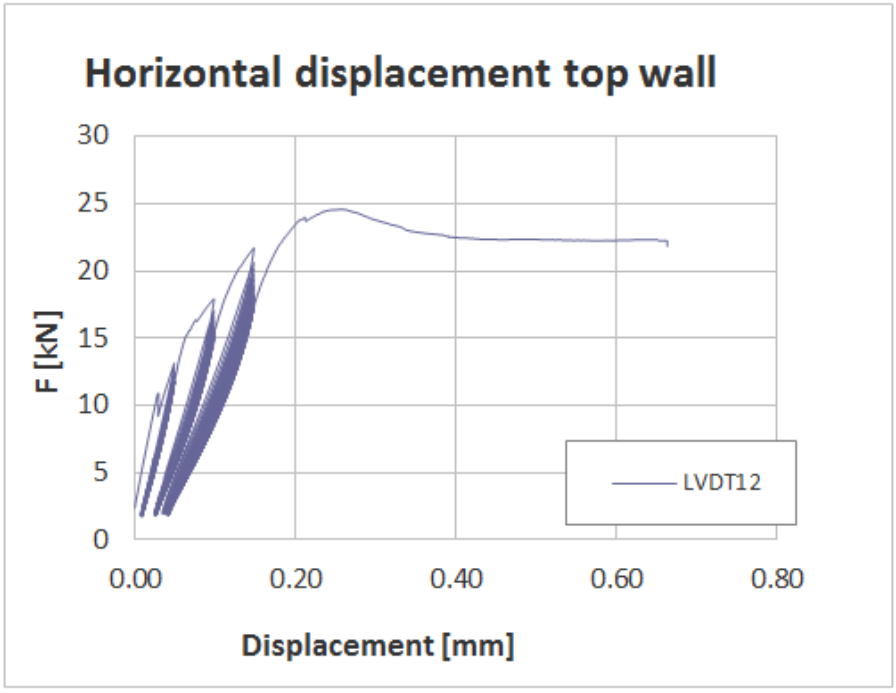

Figure 4.87. Force-displacement graph of TUD_MAT-50P.

Figure 4.88 shows the DIC crack plot of one of the last stages of the test of sample TUD_MAT-50P.

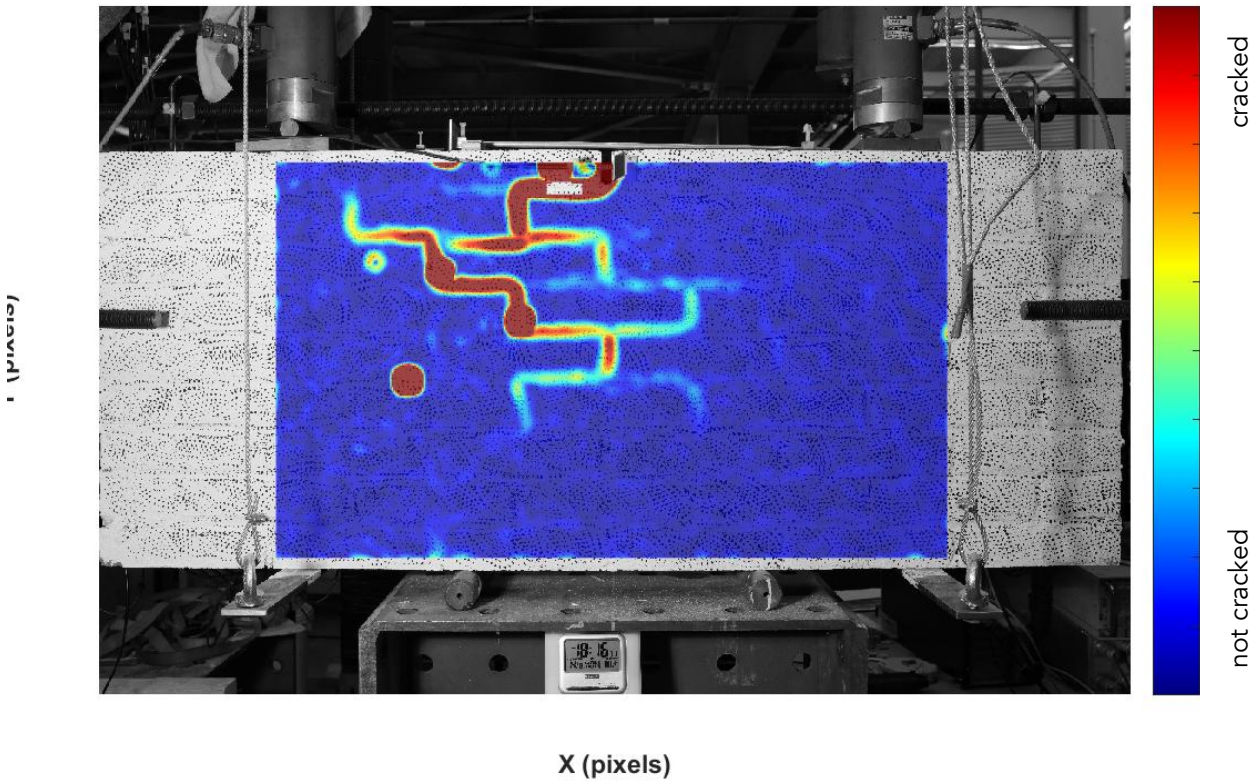

Figure 4.88. DIC crack plot of sample TUD_MAT-50P.

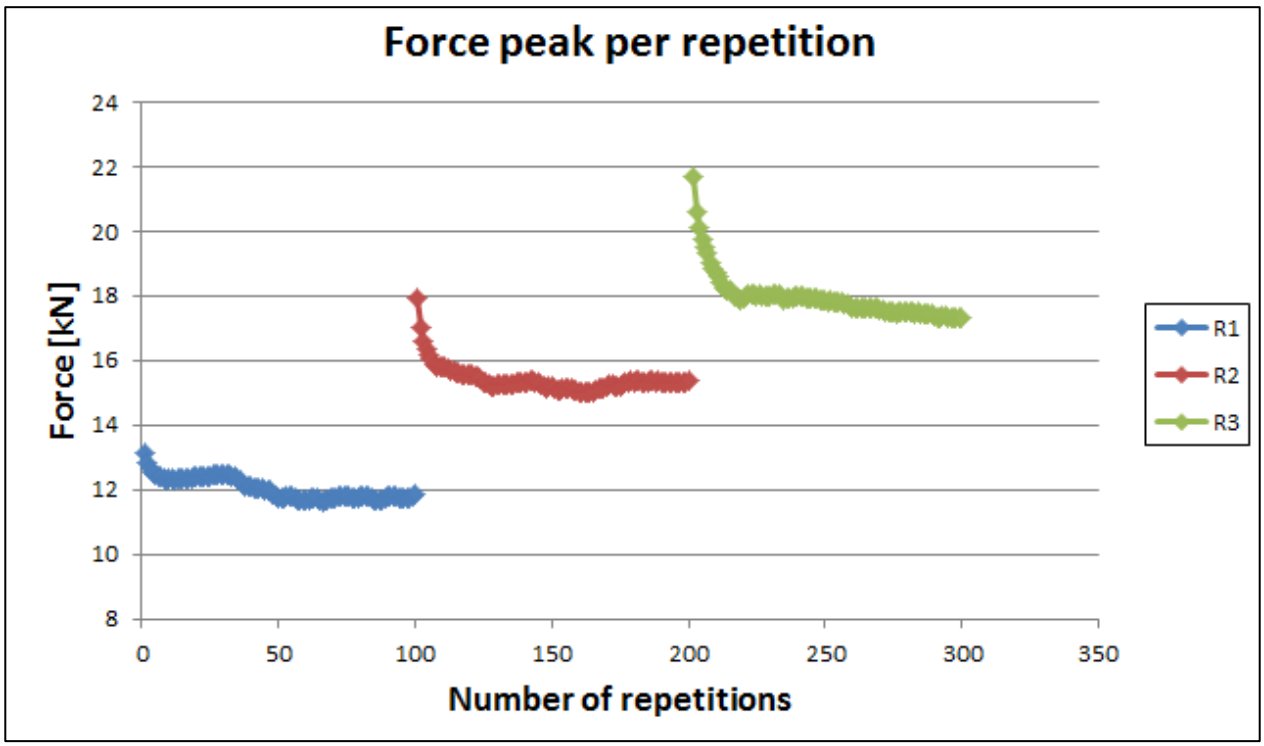

Figure 4.89. Force vs number of repetitions of sample TUD_MAT-50P.

In Figure 4.89 the force against the number of repetitions is plotted for TUD_MAT-50P. Compared to TUD_MAT-50M (Figure 4.86) the first 30 repetitions are very similar with a large reduction in the beginning of a repetition displacement step and then levelling off. It is visible that R1 and R2 eventually go to a stable situation but that for R3 the progression of the force reduction keeps progressing after 100 repetitions, albeit at a slower pace.

Comparison

For comparison of the number of repetition per repetition displacement step the sample principle can applied as was done with the IP wall test (paragraph 4.1) by determining the difference in force between the first and last repetition of a repetition displacement step and expressing this in a percentage of the force at the first repetition of the that particular repetition displacement step. Table 4.18 contains an overview of tested samples with the force reduction per repetition displacement step.

Table 4.18. Force reduction per repetition displacement step expressed in percentage of the force measured in the first repetition in that particular step.

Sample	Number of repetitions	R1 [%]	R2 [%]	R3 [%]	Average
N	10	12.1%	17.0%	17.8%	15.6%
O	10	7.8%	16.7%	22.9%	15.8%
U	10	6.6%	13.0%	15.6%	11.7%
M	30	4.0%	14.2%	27.2%	15.1%
R	30	16.4%	15.0%	17.8%	16.4%
S	30	13.8%	19.0%	28.9%	20.6%
P	100	10.1%	14.2%	20.3%	14.9%
Average		10.1%	15.6%	21.5%	

In Figure 4.90 the values of Table 4.18 are plotted together with the average of the three repetition displacement steps. It can be seen, as in Table 4.18, that in average, the force reduction increases when the repetition displacement step increases. The percentages in Table 4.18 do not show a significant difference between the samples with different number of repetitions. Which means that the degradation mainly takes place in the first 10 repetitions. In other words, the repetitions after the 10th repetition show a lower progress of degradation. However, in particular for the first repetitions of a set, the intensity of the force reduction is very similar.

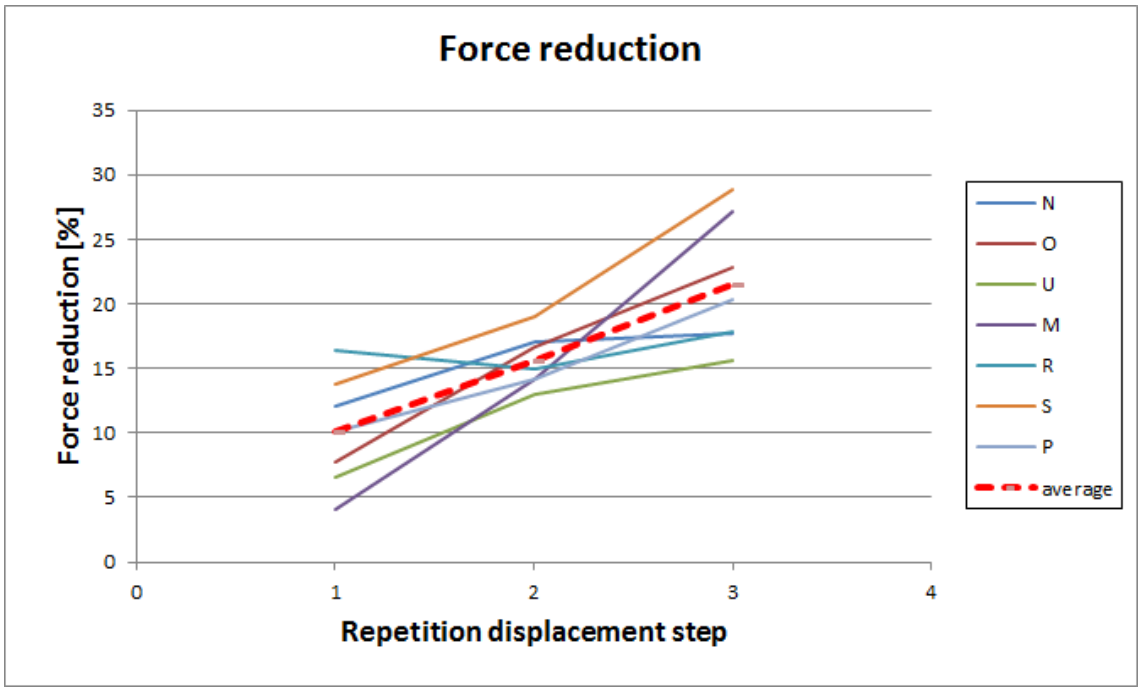

Figure 4.90. Force reduction per repetition displacement step plot of Table 4.18.

4.3. Discussion and Limitations of the Experimental Tests

This study focusses on light damage in masonry. Experimental tests and FEM models are used to get a better understanding of the mechanism involved in damage progression in masonry. In experimental tests measurements are mainly done with use of displacement sensors which are able to measure small displacements accurately. The disadvantage is that measurements are local to where the sensors are placed: at locations where cracks are expected like in the notches at the window corners. In previous sections it is shown that crack widening for each repetition displacement step (set) occurs. However, within such a set no significant increase in crack widening at the initiation point is observed; but, a trend is visible when the force reduction within each set is considered. Force reduction is an indication of progressing damage within a set.

A first hypothesis is that the measured reduction is an aberration of the laboratory equipment. However, multiple samples and two types of tests (wall and window bank) confirm the same observations, validating the measures and loads applied at the tests.

A second hypothesis is that this reduction in force is related to the increase in crack length when considering multiple repetitions within a set. If the length of a crack increases, it means that there is less material to withstand a stress, and that there is a smaller arm to produce a bending moment.
To measure small increases in crack length accurately, a different measuring system is required. DIC is capable of capturing and analysing displacements at every point of the sample in a 2D view. This is advantageous compared to local displacement sensors since, in masonry, predicting which joints the crack will run through is difficult and would thus require a high number of local sensors. Moreover, a parameter that should be defined to determine the crack length is the minimum width of the tip of the crack. In this project a cut-off crack width of 0.1mm is used to define a crack.
Crack plots are presented throughout Chapter 4 that show cracks for each set and an increase in crack length is visible in each increasing set. In-house-developed software is able to identify the cracks from the DIC results and measure crack width and crack length. Nevertheless, this program is still in development and at the moment of writing is subjected to certain limitations. Moreover, the patterns and analysis with the DIC software can still be improved and better calibrated for the type of test. If there is an increase in crack length within a set, then this increase is likely to be too small to be confidently picked up by the program. Perhaps a similar trend as with the force reduction would be observed.

If significant crack length increases within a set is not the reason for the progression of damage then a third hypothesis would be a stress redistribution within the masonry sample. A newly opened crack is no longer capable of withstanding tensile stresses but the sample cannot accommodate a new deformation while the load is active. When the load is removed, the sample goes back to an “undeformed state” and, when the load is reapplied, the sample deforms in a new way, likely propagating the previous crack.

Further, most of this re-distribution would take place at a micro level in which a concentration of strain can occur around heterogeneities in the material (grains, precipitates or voids) resulting in micro cracking. This mechanism is also present when considering the phenomenon of fatigue in a material. The difference is that with fatigue a lot more cycles are required at a load that is below the tensile strength of the material. However, a redistribution of stress is not likely to explain a reduction of the force. Only if it is related (or the cause) for lengthening of the cracks, which then can be connected to a reduction in force.

The micro-cracking could be accompanied by micro-sliding of the micro-protuberances at the cracking surface. Each repetition would dislodge more and more protuberances at the surfaces. See Figure 4.91.

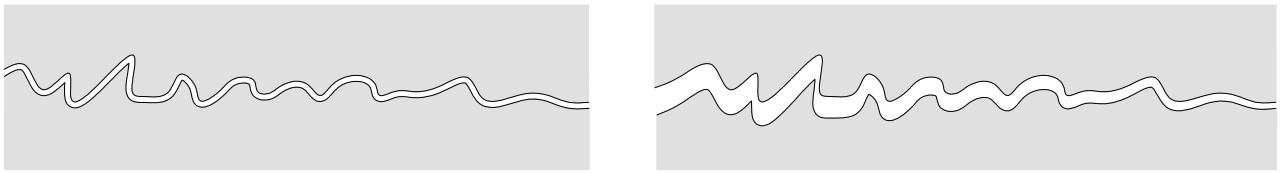

Figure 4.91. Protuberances at the micro-level dislodge or break between repetitions making the crack interface weaker every time.

During every repetition in the test, cracks are being opened and closed. When a crack is formed the state of the crack surfaces are changed meaning that when the crack is closed again it likely does not go back to the original situation. The crack surfaces will provide resistance when a crack is closed but will also change due to the stresses introduced at the crack surface. This could be considered damage progression of the crack surface at the micro level which results in lower resistance if the cracks are opened and closed again in the following repetitions.

Similarly, a fourth hypothesis is that the crack interfaces are sliding between repetitions and sets. Since cracks are in many cases not fully opened, for instance, from one side of the pier to the other; and the fact that they are not open can be seen on some crack plots which means that sliding cannot occur. Nevertheless, a small amount of sliding is possible due to elastic deformation and elastic slip. This sliding would damage the crack interface at a micro-level as recently mentioned.

Finally, in-plane wall tests were forced back to zero-displacement which grounded concerns that this produced crushing damage at the crack interfaces. However, window bank tests were never subjected to a force lower than 2kN (approximately 10% of the capacity) meaning that the stress situation at cracks was never inverted.

In sum, the reduction in force within a set could be explained by micro-damage of the crack surfaces or lengthening of the cracks, the latter due also to micro-damage of the surfaces or stress-redistribution within the sample.

It must also be noted that in these tests, the displacement was controlled and reapplied, and its effect on the force was monitored. Similar tests could be performed in the opposite configuration, where the force is repeated and its effect on the displacement is monitored. Extrapolating from the observed force reduction, it is likely that these tests would need to be constrained also by displacement in case the force repetitions trigger sudden displacements in the sample.
These types of hybrid force-controlled tests would likely show significant crack widening when reapplying the same force and are interesting to pursue in the future.

Additionally, at the TU Delft, this is the first project in which DIC is applied on masonry. Optimising and improving the software to analyse DIC results and measure crack length and width will make DIC a proper tool to measure and quantify light damage in masonry. This could be done in future projects with the DIC data that is already captured during the experimental tests of this project. Other physical improvements for the DIC method applied to masonry can be done for experimental tests in future projects.

In this light, it is important to realise that the results of these experiments are applicable only to masonry with bricks and mortar joints of sizes similar to those that have been tested. The strength properties of the bricks, the mortar, and their bond must also be comparable to the masonry assayed. The boundary conditions and stress configuration also play a role.
Consequently, since currently only one type of masonry has been tested, the conclusions drawn from these tests should not be extrapolated to cases differing significantly to those treated in this chapter.

4.4. Conclusions of Experimental Tests

Three In-Plane walls with the same geometry and window opening were tested; the materials and loading type were also similar. The focus of the tests was on the lower damage states to investigate crack initiation and propagation. Due to the brittleness of masonry it is likely that cracks form at a very early stage although the crack width is too small to be detected by the naked eye. The minimum visible crack width that can be observed with the naked eye has been set at around 0.1mm. This value has been selected to mark crack initiation. Sensors as well as Digital Image Correlation (DIC) were used to measure displacements and detect cracks. Notches are added to two window corners to localise the initiation of cracks. The top beam is displaced horizontally up to five different values. First the displacement of the top beam was moved to a displacement such that a crack opening of 0.1mm was measured in one of the notches in the window corners. For the subsequent four displacement steps the top beam displacement was increased with respectively 25%, 50%, 75% and 100% of the top beam displacement measured in the first step.

Crack opening can be considered as a measure of damage in masonry (Chapter 2). First, the trend of crack opening in the repetition displacement steps (sets) was studied. In samples TUD_COMP-40 and TUD_COMP-41 the trend for crack opening is similar. Within the first 3 sets the crack opening measured between the first and last repetition in that particular set increases, where in the latter sets the increase is much smaller (see Figure 4.52). The increase of the crack opening in a repetition displacement step can be expressed as a percentage of the crack opening of the first repetition in that particular set. For TUD_COMP-40 and TUD_COMP-41 the maximum increase in crack opening ranges from 3.0% to 6.6%.
TUD_COMP-42 shows a different trend compared to the other two samples in which the notch opening decreases in the first two sets and increases in the following sets (see Figure 4.52). The deviating trend could be caused by pre-test damage induced during transportation with the crane, in the middle bottom part of the sample (described in more detail in Section 4.1.4).

The deviation between TUD_COMP-42 and the other two samples is also observed in the DIC analyses considering the crack pattern (Figure 4.54). The cracks initiate for both TUD_COMP-40 and TUD_COMP-41 at the bottom right window corner, top left window corner, and left edge of the wall. All cracks were observed to mainly propagate through the bed joints. However, the bottom right window corner crack later follows a diagonally stepped path. In TUD_COMP-42 the cracks also initiate at the bottom right and top left corners but no crack forms on the left edge of the wall. The two cracks that did form mainly propagated in the diagonal direction. In addition, the maximum measured crack opening in the notches was significantly smaller compared to the other two tests (42: 0.27mm, versus 41: 0.58mm and 40: 0.68mm). The pre-test damage may have altered the loading paths that are followed during the test.

Crack propagation through masonry during repetitive, but equal loading can also be considered as material degradation. Another way to measure the potentially ongoing crack propagation or material degradation is to look at the change in resistance of the sample throughout the test. Since the displacement of the top beam is controlled, a reduction in force would indicate a reduction in resistance and therefore also progressing degradation. Similar trends are observed for all three samples when the force reduction is calculated for each set. The same principle is applied as with the crack opening measurement. The difference in force between the first and last repetition of a set is taken and expressed as a percentage of the force measured at the first repetition of that particular set. The total force reduction within a set increases when the displacement increases. The maximum force reduction for all three sample ranges from 2.9% to 3.5%. The observed trend of force reduction within a set is similar for the three samples. The largest reduction takes place in the first couple of repetitions and then levels out, yet does not completely stabilise within 10 repetitions, which means degradation continues to proceed, albeit less intensively.

The trend in force reduction is also observed in the repetitive window bank test. Samples with 10, 30 and 100 repetitions per set are tested and the same type of force reduction in the first 10 repetitions within a

certain repetition displacement step is visible (Figure 4.83, Figure 4.86 and Figure 4.89). The reduction in force between the first and last repetition of a set is larger for repetitions at higher displacements. Similar to the IP wall tests, the force reduction does not completely stabilise except for the two lower repetition displacement steps of the sample with 100 repetitions suggesting that the stabilisation is dependent to the proximity to the load capacity of the sample.

Based on the resistance reduction behaviour of both the IP wall and window bank tests, it can be concluded that the material degradation mainly takes place in the first repetitions of a certain applied displacement. It appears that after 10 repetitions the reduction of resistance and likely crack progression proceeds much slower than in the first few repetitions. It may stabilise also for higher displacements, but would require to perform more than 10 repetitions for the higher repetitions displacement steps.
The effect of the decreasing resistance due to repetitions is largest when the displacement of the sample is close to the displacement at maximum load capacity (about 3% for the IP test and 21% for the window bank test).
For lower load levels in the initial ascending part of the load-displacement curve the reduction of resistance within a repetition displacement step is significantly lower (about 1% for the IP test and 10% for the window bank test).
The 10-fold increase in loading rate for the fast repetitions in TUD_COMP-41 and TUD-COMP-42 did not affect the reduction in resistance significantly. In R3-R5 it can be seen that there is a very small increase in resistance in the first fast repetition of that set but quickly returns to the trend-line of the first 10 slow repetitions of that particular set (Figure 4.56). Both loading rates are performed in static repetitive pull loading conditions. The effect of static cyclic rather than repetitive loading, much higher loading rates, or dynamic loading, could result in a different behaviour for crack propagation in masonry.

Finally, likely hypotheses for the observed progression of damage are lengthening of the cracks due to micro-damage of the crack surfaces or redistribution of stresses with the samples.

Chapter 5

Validation and Calibration of Computational Models

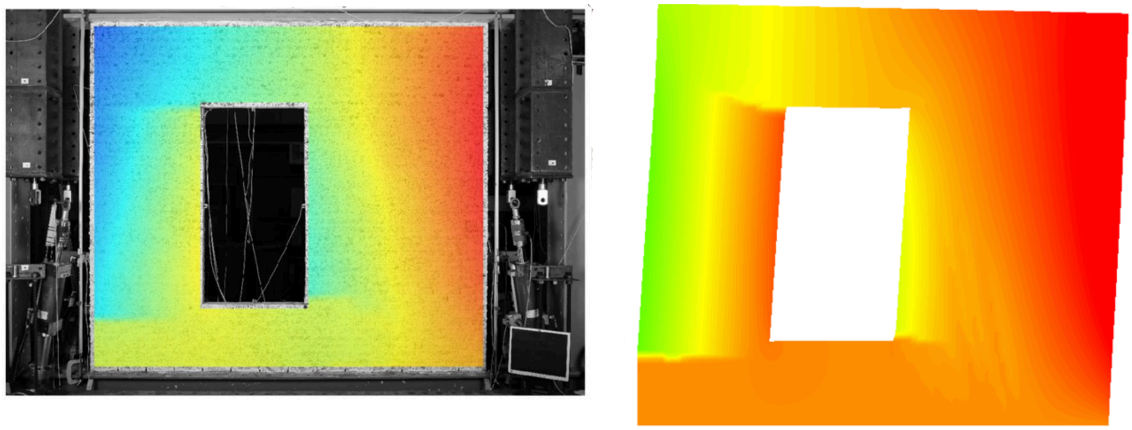

TU Delft

5. Validation and Calibration of Computational Models

5.1. Introduction

This chapter builds up on the results from the laboratory experiments and describes and discusses the modelling approach used to produce models that are capable of reproducing the cracking behaviour of masonry specimens and which later will be used to assess the cumulation of damage from various actions.

After the experimental tests on the in-plane walls, a calibration and validation of the DIANA FEM model has been performed. Starting from the prediction model (Chapter 3), a refined model of the in-plane wall has been analysed. The wall has been calibrated based on the repetitive pull tests of the TUD_COMP-41 and TUD_COMP-42. Compared to the predictions, the loading scheme has been updated in order to match the experimental loading protocol. The Total-Strain Crack model used for the prediction has been replaced with the new Engineering Masonry model (Schreppers et al., 2016; Rots et al., 2016). Elastic and inelastic parameters of the model have been adapted and calibrated to the experiment to have reasonable agreement with initial stiffness, force-displacement curves, and crack patterns.

5.2. Refined in-Plane Wall Post-Test Analysis (Post-Diction)

5.2.1. Prediction Model Versus Experimental Results

A prediction of the repetitive pull test was modelled with the software DIANA before the start of the experimental campaign. Plane stress elements were used for the in-plane wall model using a smeared continuum approach. The Total-Strain Rotating Crack model was used as material model. More information about this prediction model can be found in Chapter 3. For both the prediction and the final laboratory test, the target was to find a point to such an extent that a crack width of 0.1mm width would occur. Then, this displacement amplitude was subsequently applied nine more times in a repetitive way (i.e. from zero displacement to the desired amplitude and then back to zero again). After that, the initial amplitude is increased by 25% for each set. For each additional amplitude, ten pulling repetitions are applied. More details about the loading protocol are described by Meulman et al. (2017).
A comparison of the walls top horizontal displacement between the prediction model and the two experimental resulting tests, TUD_COMP-41 and TUD_COMP-42, is shown in Table 5.1.

Table 5.1. Comparison between the loading protocol of FEM prediction model and experimental tests of the in-plane walls TUD_COMP-41/42.

Step	PREDICTION MODEL Top Horizontal Displacement [mm]	EXPERIMENTAL TUD_COMP-41 Top Horizontal Displacement [mm]	EXPERIMENTAL TUD_COMP-42 Top Horizontal Displacement [mm]
Monotonic	0.35	0.69	0.59
R1a - R1b	0.35	0.69	0.59
R2a - R2b	0.45	0.89	0.74
R3a - R3b	0.55	1.09	0.87
R4a - R4b	0.60	1.30	1.04
R5a - R5b	0.70	1.52	1.23

The prediction FEM model shows a lower value of required horizontal displacement as necessary to induce the first 0.1mm crack with respect to the two experimental walls, 0.35mm versus 0.69mm and 0.59mm respectively. This value influences the amplitude of the remaining steps.

Force-displacement curves for the experiments and the prediction are depicted in Figure 5.1 and Figure 5.2.

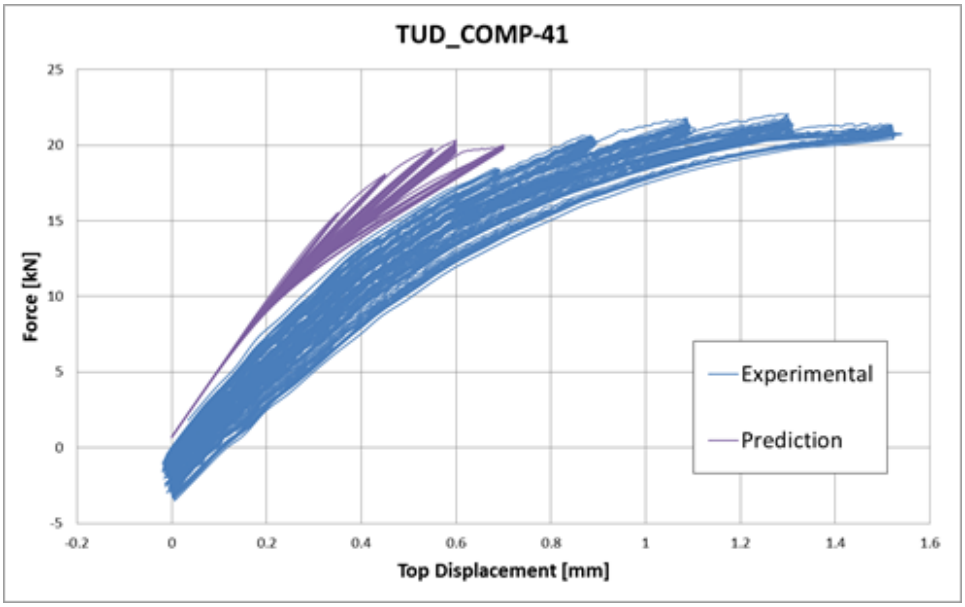

Figure 5.1. TUD_COMP-41: experimental and FEM prediction force-displacement curve.

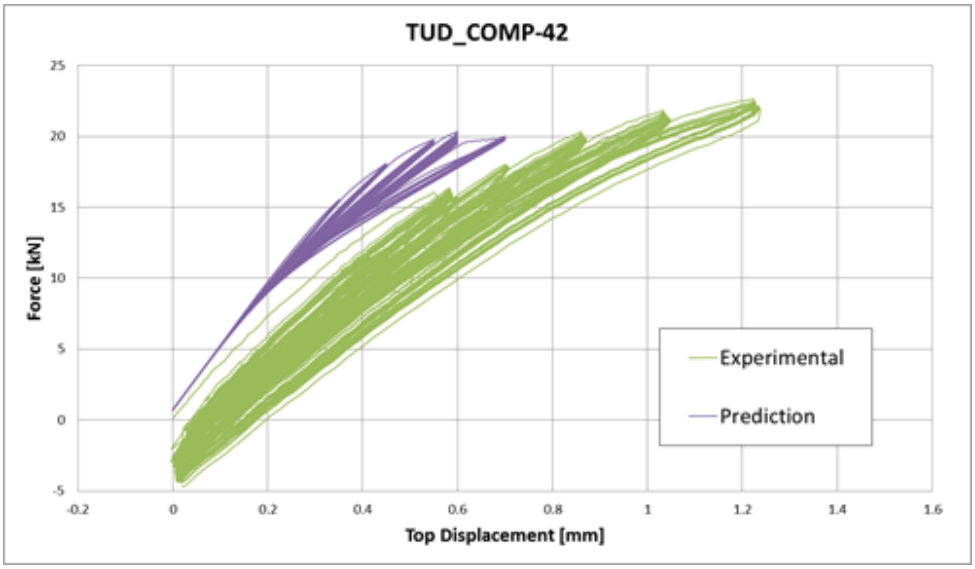

Figure 5.2. TUD_COMP-42: experimental and FEM prediction force-displacement curve.

A summary regarding load capacity and average stiffness for each step is shown in Table 5.2.

Table 5.2. Load capacity and stiffness for experimental and FEM in-plane walls .

Step	Load Capacity [kN]			Stiffness [kN/mm]		
	TUD_COMP_41	TUD_COMP_42	Prediction	TUD_COMP_41	TUD_COMP_42	Prediction
Initial	-	-	-	38.14	36.32	45.29
R1a	20.35	16.37	15.52	25.59	29.14	41.88
R1b	18.46	15.72	15.54	26.88	28.82	42.18
R2a	20.63	17.83	18.08	23.44	26.33	37.80
R2b	20.50	18.00	18.08	23.60	27.90	38.14
R3a	21.78	20.32	19.79	19.88	26.15	33.32
R3b	21.33	19.87	19.76	20.07	26.46	33.75
R4a	22.05	21.83	20.32	16.99	24.16	30.59
R4b	21.45	21.36	19.74	17.20	24.10	30.47
R5a	21.43	22.63	19.93	14.81	21.59	25.63
R5b	20.93	22.14	20.02	11.52	21.64	26.03

From the force-displacement results in Figure 5.1, Figure 5.2 and Table 5.2, a difference in the initial stiffness is identified between the prediction model and the experiments. The initial stiffness of the model is 18.7% higher than test TUD_COMP-41 and 24.70% higher than test TUD_COMP-42. This difference in the initial stiffness can be explained from the value of the Young's modulus. The value of the masonry Young's modulus was chosen from the previous testing campaign, where double-wythe clay brick masonry walls were tested in-plane (Messali et al., 2017; Jafari et al., 2016). Moreover the Total-Strain Crack model does not take into account the orthotropic behaviour of the masonry since the material is considered to be isotropic. These assumptions explain the overestimation of the lateral stiffness of the wall.

Regarding the load capacity, the prediction FEM model slightly underestimates the maximum value of the base shear force. In addition, the peak value is reached earlier in the model, with a capacity of 20.32kN around 0.60mm of top horizontal displacement against 22.05kN at 1.30mm for the lab test TUD_COMP-41 and 22.63kN at 1.23mm for the lab test TUD_COMP-42.
Furthermore, the two experiments show a more pronounced hysteresis than the model. Again, this can be explained by the use of the Total-Strain Crack model. This constitutive model was derived for isotropic material with secant-based unloading-reloading curves which may underestimate the energy dissipation under cyclic/repetitive loading schemes (Schreppers et al., 2016; Rots et al., 2016).

The equivalent strain plot of lab test TUD_COMP-41, derived from the DIC measurements, is shown in Figure 5.3. The plot shows an increment in strain in the crack locations. It reveals three major cracks: an the top left notch, at one brick row above the bottom right notch and at two brick rows below the window on the left lateral edge of the wall. At this stage, all three cracks were growing along the bed joints. The picture was taken when the top displacement of the wall was 0.69mm. A similar crack pattern was found for the lab test TUD_COMP-40. In TUD_COMP-42, comparable cracks were identified from the two notches, but the crack on the lateral left edge was not detected (a fact which maybe related to a possible stress redistribution due to transportation, see Chapter 4).
The experimental crack patterns at 0.69mm are compared to the prediction for a displacement of 0.70mm (Figure 5.4).

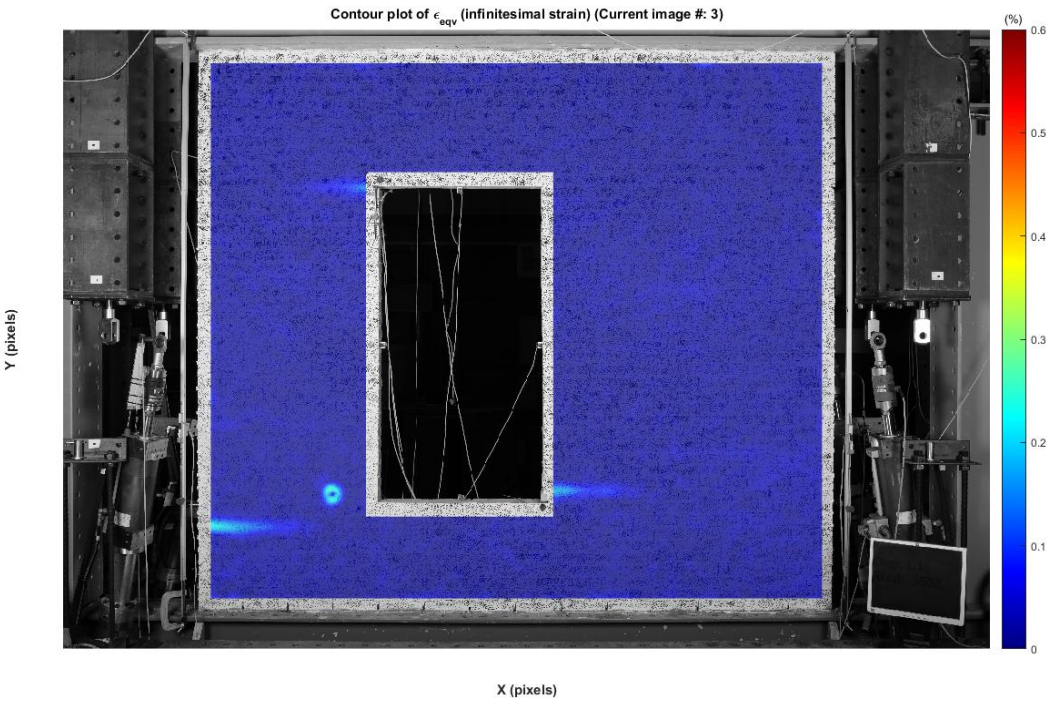

Figure 5.3. TUD_COMP-41 DIC Equivalent strain plot at top displacement about 0.69mm (during R1b).

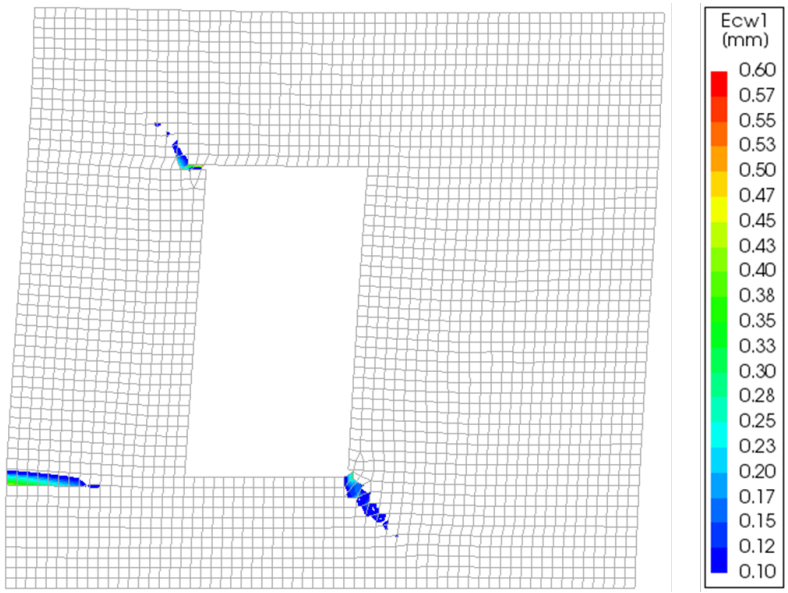

Figure 5.4. Crack width plot at wall top displacement of 0.70mm (R5b).

In the prediction FEM model the location of the cracks is in good agreement with the experiment. However, regarding the propagation, the cracks located in the window corners extend diagonally rather than horizontally. This is explainable from the nature of the Total-Strain Rotating Crack model in which the principal stress drives the crack propagation direction, but greatly differs from the experimentally observed propagation behaviour.

In conclusion, both constitutive models and material stiffness affect the overall behaviour of the model. The model underestimates the top displacement required to induce the 0.1mm crack, and the load capacity. Also, the energy dissipated during the repetitions is lower than the experiments, again mainly due to the Total-Strain Rotating Crack model, where a secant unloading-reloading branch is need. The failure mode related to the rocking mechanism of the left pier and the initiation of cracking in the window corners is in agreement with the experiment.

5.2.2. Update to the Prediction FEM

After the experimental test of in-plane walls subjected to repetitive horizontal loading (TUD_COMP-41, TUD_COMP-42) and after confronting the predictions with the tests, the nonlinear FEM model has been updated based on the behaviour of the wall during the test. In other words the model has been calibrated and validated.
The adjustments applied to the model are listed below:

- Modification of the constitutive model of the masonry by replacing the Total-Strain Rotating Crack model with the Engineering Masonry model;
- Addition of a stiff steel beam underneath the wall;
- Improvement of the modelling of stress concentrations at the window corners;
- Calibration of the masonry material parameters based on experimental stiffness and companion tests on small samples (Meulman et al., 2017);
- Update of the loading protocol to match the observed horizontal displacement at the top of the wall; and matching of the vertical overburden to coincide with the applied weight in the experiments.

As has been already explained in Section 5.2.1, the application of the Total-Strain Crack model underestimates the energy dissipation during the hysteresis. Moreover, the direction of the cracks in the window corners are drawn mainly diagonally. In order to improve upon these deficiencies, a different constitutive model has been used for the in-plane walls. A validated constitutive model for masonry walls is the Engineering Masonry Model (Schreppers et al., 2016; Rots et al., 2016). It is a smeared failure model which includes the orthotropy by using different elastic properties for different directions. Moreover, the wall can crack at the bed joint or at the head joint, of which the orientation is predefined by the user. It is then possible to reproduce diagonal stair-case cracks.
Additionally, the Engineering Masonry model defines a more realistic unloading behaviour by using secant, elastic and mixed hysteresis loop for different failure modes. A shear failure mechanism based on Coulomb friction is included in the model. The use of this model is especially recommended for non-linear, quasi-static and dynamic analyses (Schreppers et al., 2016; Rots et al., 2016).

Sensitivity tests also performed, show that the omission of the two notches at the window corners does not influence the response of the wall model. So, compared to the prediction, no notches have been considered in the model. In the end, only quadrilateral elements have been used producing a regular mesh, thus avoiding the use of triangular elements around the corners which might affect the accuracy of some of the integration points.
A stiff steel beam has been placed below the wall. It was assigned the same properties and dimensions as for the top beam, i.e. 200mm in height and 3050mm in length. This element is essential to mimic the laboratory test and later define different initial loads to the wall to generate the data required for the resistivity curves (Chapter 6).

The in-plane clay masonry wall has been modelled with the same dimensions of the prediction model. The wall is 3050mm large and 2700mm high with a thickness of 100mm; an opening of 800x1500mm is located 900mm far from the left edge and 550mm distant from the bottom beam. The concrete lintel above the window has been modelled with a dimension of 1000x50mm. A mesh size of 50x50mm has been adopted.
Three materials have been defined for the in-plane wall: masonry by using the above mentioned Engineering Masonry model, steel for the beams and concrete for the lintel.
Since the boundary condition considered at the top is cantilever, only the bottom beam base nodes are constrained. To simulate the experimental repetitive test, two different loads have been used: vertical load applied as a line load on the top wall edge, and horizontally prescribed deformation applied at the top-left corner of the wall. The same horizontal displacement for the top wall edge has been guaranteed by using tyings (software equivalent to ties).
The updated DIANA finite element model is shown in Figure 5.5:

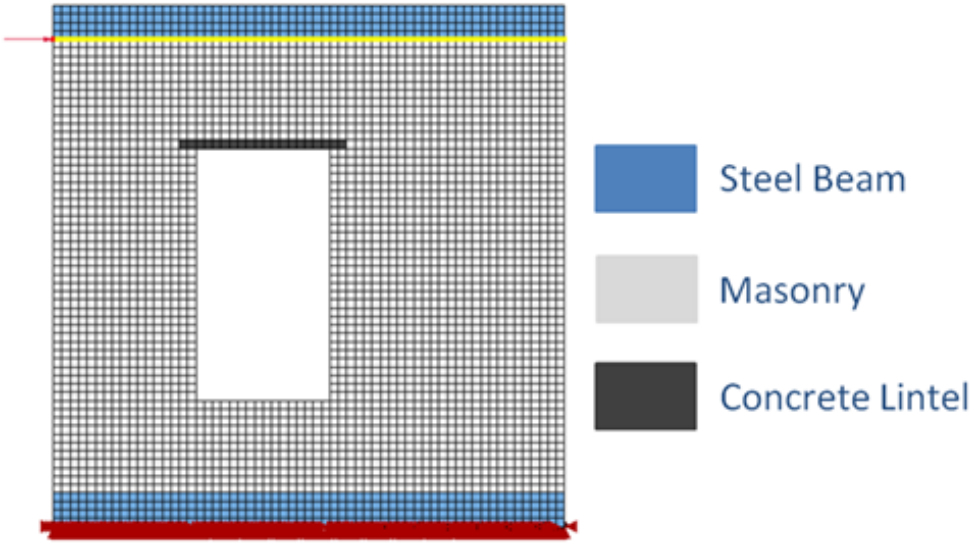

Figure 5.5. Diana FEM model of the refined post-test of the in-plane wall.

Eight-node quadrilateral isoparametric plane stress elements (CQ16M) have been used. Full (3x3) Gauss integration scheme has been selected in order to minimize the occurrence of spurious modes due to softening.

Steel and concrete material for beams and lintel respectively have been considered as linear elastic. The same properties as for the prediction have been used:

Table 5.3. Steel material properties for the beams above and below the wall.

Steel Properties	
Density	$1 \cdot 10^{-15}$Kg/m^3
Young's Modulus	2100000MPa
Poisson's Ratio	0.30

Table 5.4. Concrete material properties for the lintel above the window.

Concrete Properties	
Density	2400Kg/m^3
Young's Modulus	31000MPa
Poisson's Ratio	0.20

The properties of the prediction model were based on properties used in a similar model and taken from the previous experimental campaign on materials (Jafari et al., 2016). In the refined post-test model the material parameters have been updated with properties obtained in part, directly calibrated from the experiment curves, and from the new companion tests which were constructed at the same time of the specimens (Appendix 9.2). For additional information about the companion tests performed, see Meulman et al., 2017.
The Young's modulus of masonry in the direction perpendicular to bed joints has been evaluated directly from the pre-compression tests (described in the Appendix 9.5) on the experimental walls. The average value of the vertical elastic parameter from all the pre-compression tests has been used. The average value calculated is about 3400MPa.

This value has been applied in the model for the Young's modulus in the direction perpendicular to bed joints. Concerning the elastic modulus in the horizontal direction, a value between 1/2 and 2/3 of the vertical elastic parameter is recommended (Schreppers et al., 2016; Messali et al., 2017). Both the elastic parameter parallel to the bed joint direction and the shear modulus have been calibrated on the initial lateral stiffness of the experimental walls.
The tensile strength perpendicular to bed-joints and the fracture energy in tension have been reduced in respect to the prediction model. The value extrapolated for the former was taken from the results of the companion tests (Appendix 9.2); for the latter, no experimental data exist and it has been calibrated to match the experimental wall crack pattern.
Since the tests are investigating the lower damage state and no toe crushing was detected during the experimental test, compression strength and fracture energy in compression have been kept as in the prediction model.
The predefined angle for diagonal cracking is evaluated based on the masonry pattern of the wall with the formulation of Equation 5.1.

$$\tan\alpha=\frac{2\cdot h_b+h_m}{b_b} \tag{5.1}$$

Where:
h_b is the height of the brick,
h_m is the height of the mortar bed joint, and
b_b is the length of the brick.

The clay masonry material properties for the refined post-test FEM model are summarised in Table 5.5.

Table 5.5. Clay masonry material properties for the refined post-test of the in-plane wall.

Clay Masonry Properties			
Engineering Masonry model – Diagonal stair case cracks option active			
Density	ρ	1680Kg/m^3	2
Young's modulus perpendicular to bed-joints	E_y	3400MPa	1
Young's modulus parallel to bed-joints	E_x	2200MPa	2
Shear modulus	G_{xy}	1300MPa	2
Tensile strength perpendicular to bed-joints	f_t	0.10MPa	1
Tensile fracture energy	G_f^I	5N/m	2
Compressive Strength	f_c	14MPa	2
Compressive Fracture Energy	G_c	20000N/m	2
Friction angle	φ	0.6rad	2
Cohesion	c	0.15MPa	2
Predefined angle for diagonal cracking	α	0.5rad	3

[1] Tested Value
[2] Estimated Value
[3] Computed Value

The two lab tests, 41 and 42, have been simulated with the refined post-test model. The average top displacements of the experimental walls have been used as input for the imposed horizontal deformations. The loading protocols of the two models are shown in Table 5.6.

Table 5.6. Loading protocol for the FEM models based on the experimental tests of the in-plane walls TUD_COMP-41/42.

Step	MODEL_COMP-41 Top Horizontal Displacement [mm]	MODEL_COMP-42 Top Horizontal Displacement [mm]
Monotonic	0.69	0.59
R1a – R1b	0.69	0.59
R2a – R2b	0.89	0.74
R3a – R3b	1.09	0.87
R4a – R4b	1.30	1.04
R5a – R5b	1.52	1.23

In addition to the modification of the lateral top displacement of the wall, the vertical overburden has been changed as well. The final vertical stress applied on top of the wall has been increased from 0.10MPa of the prediction model to 0.12MPa for the refined post-test model. This value for the compression has been raised to match the experimental value.

5.2.3. Results of the Post-Test Model

Results of the two models, MODEL_COMP-41 and MODEL_COMP-42 are presented in this section. The results of the models are compared with experimental data and plots extrapolated from the Digital Image Correlation (DIC). The DIC measurement system is used during the experimental tests. The system correlates pictures made during the test with a reference picture representative of the initial undeformed state. Based on the correlation between these pictures, the DIC is able to evaluate and generate displacements and strains contour plots. Additional information about the DIC measurement system can be found in (Meulman et al., 2017). This type of contour plots can be easily compared with the model results.

TUD_COMP-41

The experimental, in-plane wall TUD_COMP-41 has been analysed with the software DIANA. The loading protocol related to the top horizontal displacement used in the model is specified in Table 5.6. It is based on the average experimental wall displacement evaluated from the data after the test considering top beam displacement and bottom beam rotation. After applying dead load and overburden to the model, a monotonic horizontal displacement of 0.69mm has been applied to the top part of the wall. After that, 20 runs of the same amplitude have been applied. The top wall displacement is then increased for a total of 5 repetitions (with 20 runs for each repetition) for a maximum horizontal displacement of 1.52mm.

A comparison between experimental and model force-displacement curves is shown in Figure 5.6. The capacity of the experimental wall is 22.05kN obtained during the repetition R4a. The model shows a maximum force of 22.81kN (+3.4% to the original) reached throughout the repetition R5a.

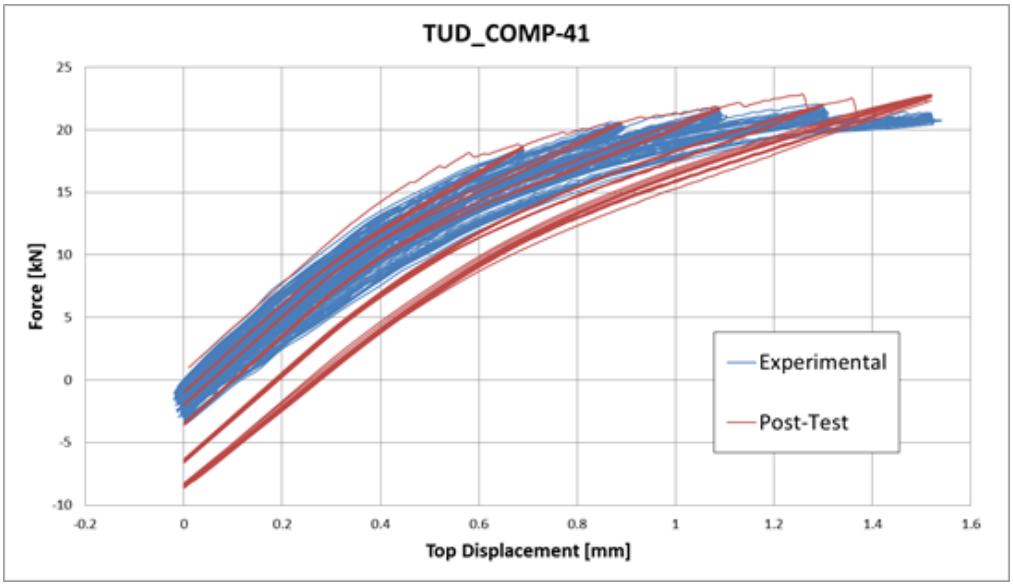

Figure 5.6. TUD_COMP-41: experimental and FEM post-test force-displacement curve.

In comparison with the experiment, the model shows agreement in terms of initial stiffness and maximum capacity reached during the different steps. Moreover, the new Engineering Masonry model is able to generate more dissipation in contrast to the prediction constitutive model (Section 5.2.1).
Model forces at the final repetitions (R5a-b) results in a slight overestimation, mainly due to the lower damage in the top left pier. In fact, this part of the experimental specimen fully cracks in the repetition R5a producing a slight loss in force, but this does not occur in the model.
The correlation in terms of load and stiffness is presented in Table 5.7. The force in the table is the maximum load detected during the repetitions. The stiffness is evaluated as the average slope of the ten runs of each repetition.

Table 5.7. TUD_COMP-41: load capacity and stiffness for experimental and FEM post-test.

Step	Load Capacity [kN]		Stiffness [kN/mm]	
	TUD_COMP_41	Post-Test	TUD_COMP_41	Post-Test
Initial	-	-	38.14	35.35
R1a	20.35	18.84	25.59	28.22
R1b	18.46	18.70	26.88	28.29
R2a	20.63	20.61	23.44	24.75
R2b	20.50	20.60	23.60	24.81
R3a	21.78	21.89	19.88	22.34
R3b	21.33	21.78	20.07	22.42
R4a	22.05	22.78	16.99	21.04
R4b	21.45	22.02	17.20	21.21
R5a	21.43	22.81	14.81	19.93
R5b	20.93	22.70	11.52	20.01

The stiffness of the model represents well the experimental in-plane TUD_COMP-41 wall for the repetition R1-R2. After that the overall model stiffness is slight overestimated as well as the energy dissipation.

TUD-COMP-41 Results

The results obtained from the model (mesh size 50x50mm) have been compared with the displacement and the strain plots generated by the DIC measuring system.
Figure 5.7 shows the comparison of horizontal displacement during the repetition R4a. The contour of the DIC and model has been set to the same scale in order to produce compatibility of the results. Since the DIC contour scale limits are expressed in pixels, the values on the scale need to be multiplied for 0.5mm which is the maximum pixel resolution obtainable with the camera used for the DIC measurement.
DIC and model comparison of horizontal damage in the repetition R5a is depicted in Figure 5.8.

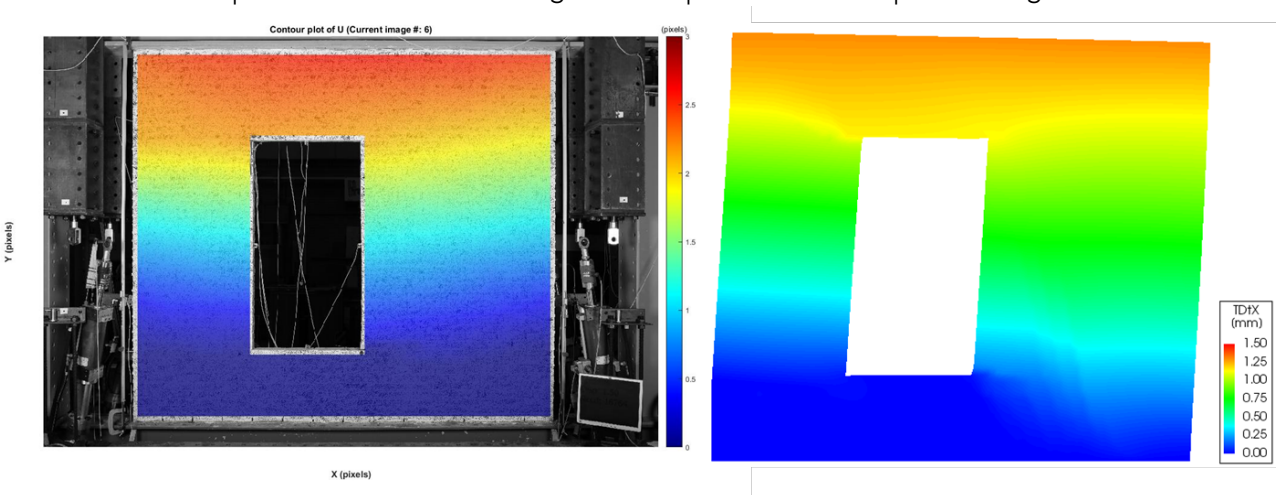

(a) (b)

Figure 5.7. TUD_COMP-41: R4a. Horizontal displacement comparison between (a) DIC related to experimental record number 16764 and (b) FEM post-test. Model deformed shape magnified by 100.

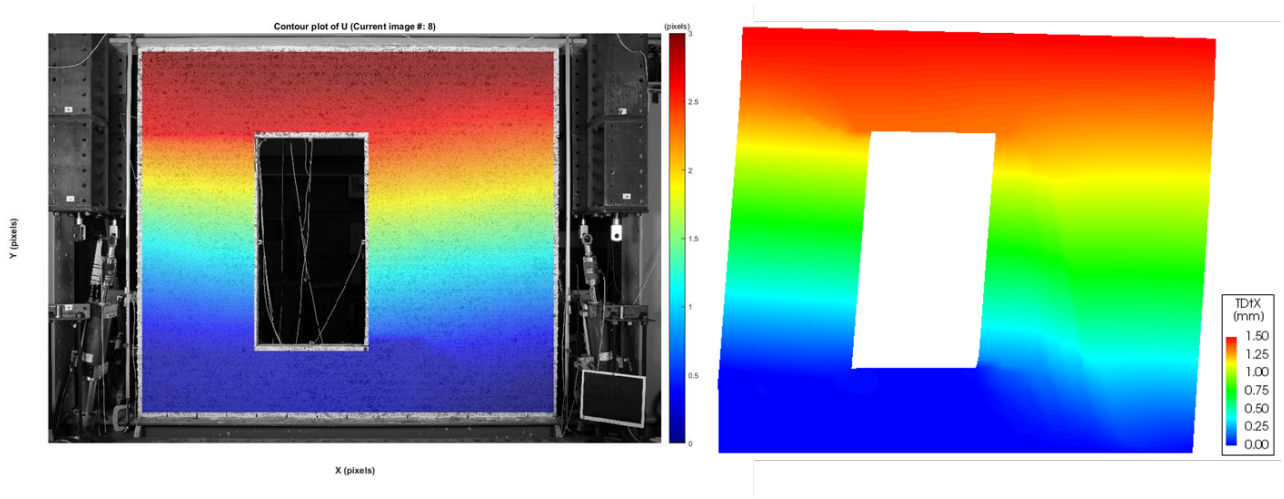

(a) (b)

Figure 5.8. TUD_COMP-41: R5a. Horizontal displacement comparison between (a) DIC related to experimental record number 22321 and (b) FEM post-test. Model deformed shape magnified by 100.

Both graphs represent well the distribution of the horizontal displacement of the wall. The displacement in the lower part of the right pier following the diagonal direction of the crack is well described by the model.

Vertical displacements at the same experimental record number are compared as well. The contour relation related to the repetition R4a is represented in Figure 5.9 whereas the repetition R5a is shown in Figure 5.10. For the DIC plots, negative values correspond to an upward movement of the specimen.

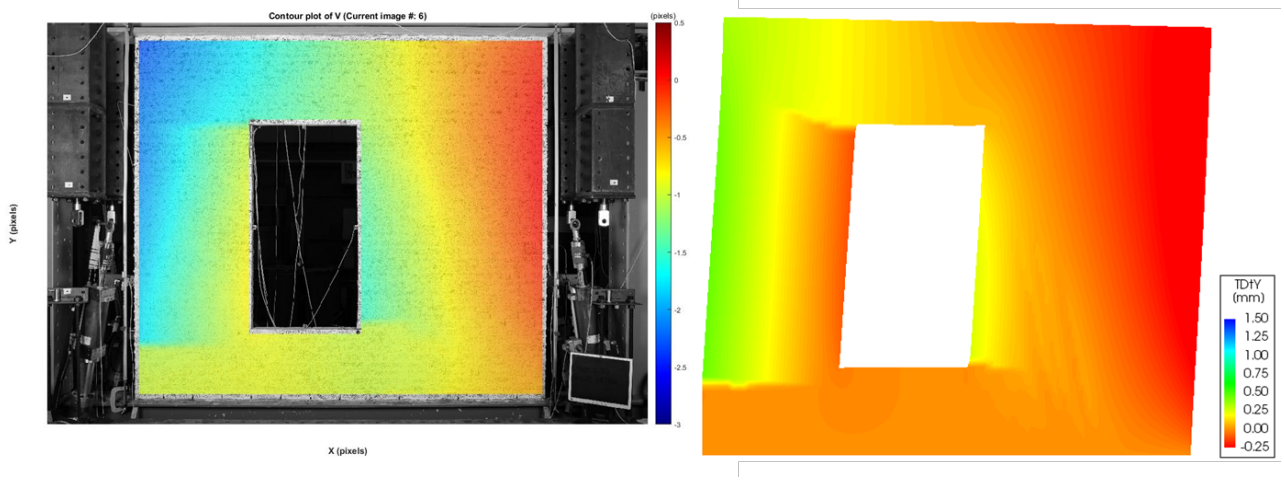

(a) (b)

Figure 5.9. TUD_COMP-41: R4a. Horizontal displacement comparison between (a) DIC related to experimental record number 16764 and (b) FEM post-test. Model deformed shape magnified by 100.

The model contour slightly underestimates the vertical displacement of the wall for both the repetitions. A reason for this difference can be found in the hypothesis of the infinite stiffness in the bottom beam of the model which gives null displacement at the base of the wall. Contrarily, the base of the experimental frame inevitably allows for slight movements.

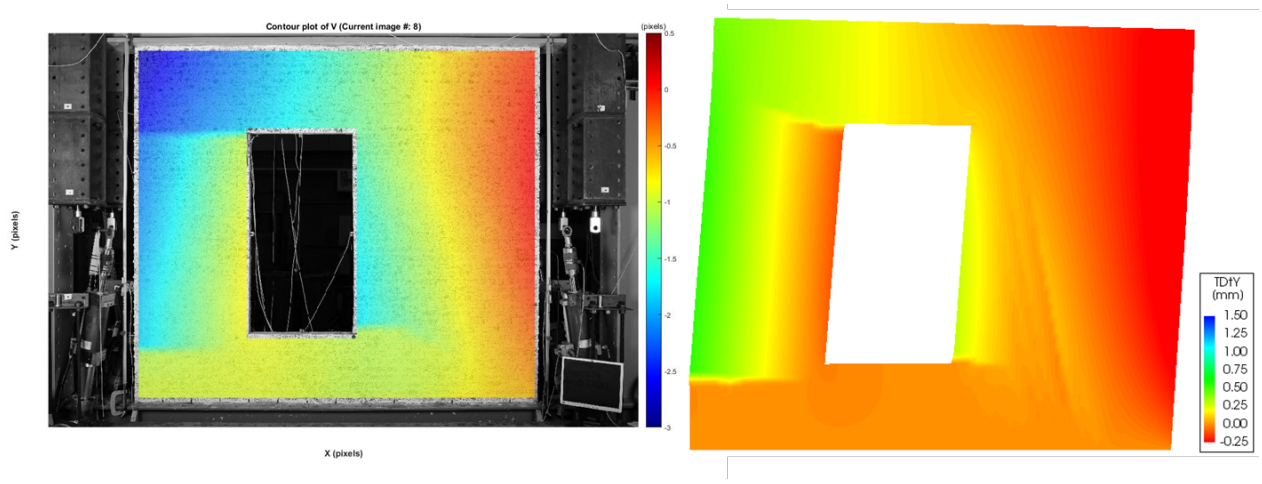

(a) (b)

Figure 5.10. TUD_COMP-41: R5a. Horizontal displacement comparison between (a) DIC related to experimental record number 22321 and (b) FEM post-test. Model deformed shape magnified by 100.

Nevertheless, the bed joints cracks appear clearly in the vertical displacement plots. Three cracks, one on the edge of the left pier and two located in the window corners are evident for both DIC and FEM model contour plots. During R5a the top left corner of the experimental wall is subjected to an upward movement due to the full horizontal crack in the top part of the small pier. From the top left window corner, the crack of the model develops for about the 65% of the pier length.

To better compare the location and the propagation of the cracks during the different repetition steps, strain plots computed from the DIC measurement system are correlated with the principal crack width plots of DIANA (Manie, 2016). Three different stages are showed: Repetition 1a (Figure 5.11), Repetition 4a (Figure 5.12) and Repetition 5a (Figure 5.13). The comparison during the first repetition (Figure 5.11) shows an agreement between the experimental tests and the model in terms of crack location and initiation. However, the crack on the bottom right corner results smaller in length than the one detected during the experiment.

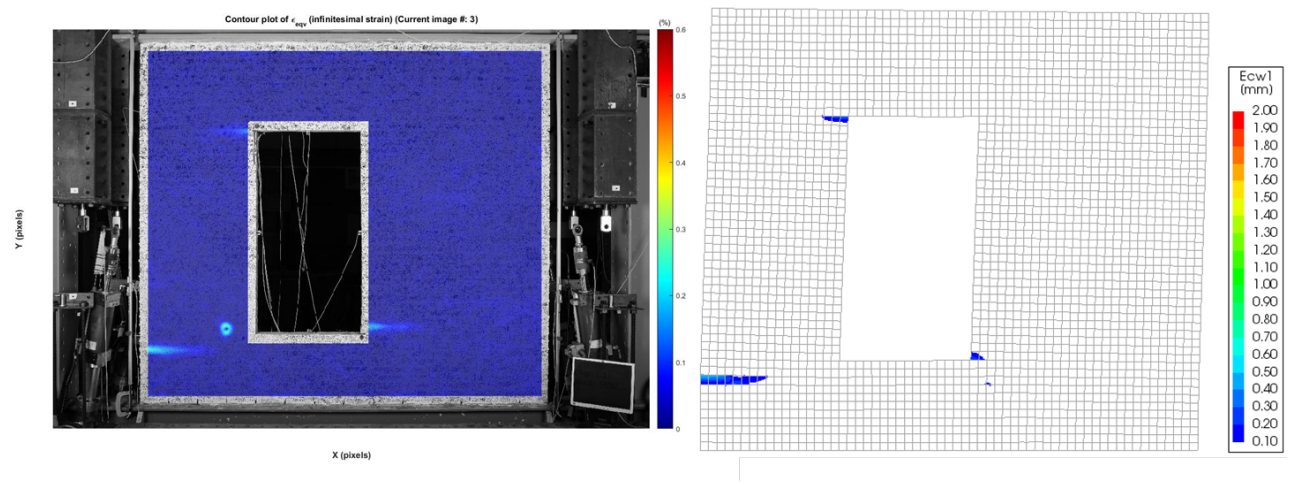

(a) (b)

Figure 5.11. TUD_COMP-41: R1a. Comparison between (a) strain plot of DIC related to experimental record number 5502 and (b) FEM post-test crack width plot. Model deformed shape magnified by 100.

During the higher amplitude repetitions no more cracks are detected in both test and FEM model (Figure 5.12). The three initial cracks increase length and width. In the test both the cracks on the left pier grow along the bed joint. The right window corner crack after R3a starts growing diagonally. In the model both principal directions of the cracks in the window corners develop following a stair case.

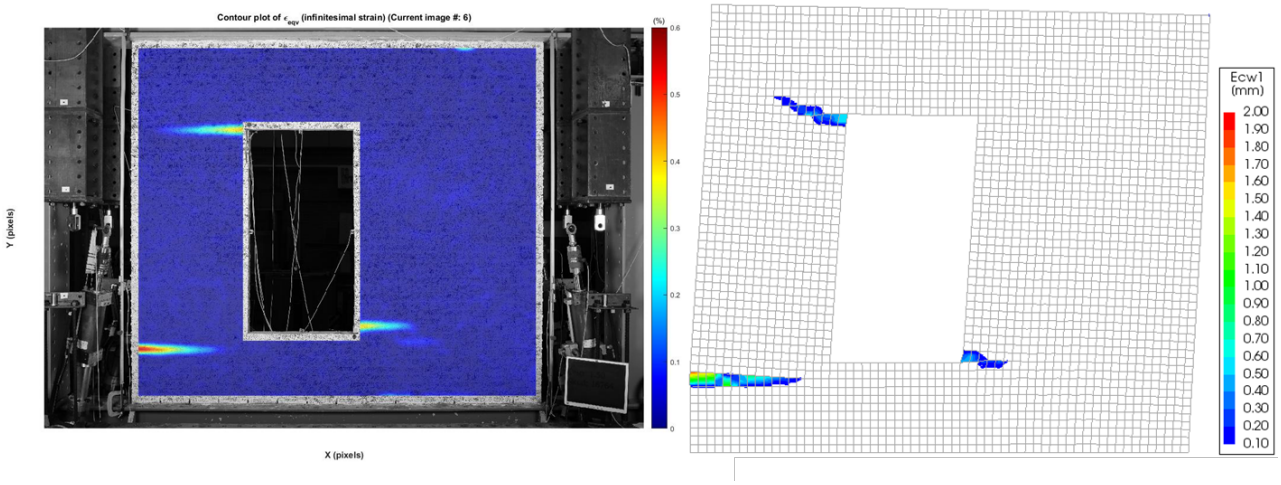

(a) (b)

Figure 5.12. TUD_COMP-41: R4a. Comparison between (a) strain plot of DIC related to experimental record number 16764 and (b) FEM post-test crack width plot. Model deformed shape magnified by 100.

In the last repetition (R5a) the length of the two cracks in the window corner is a bit underestimated (Figure 5.13).

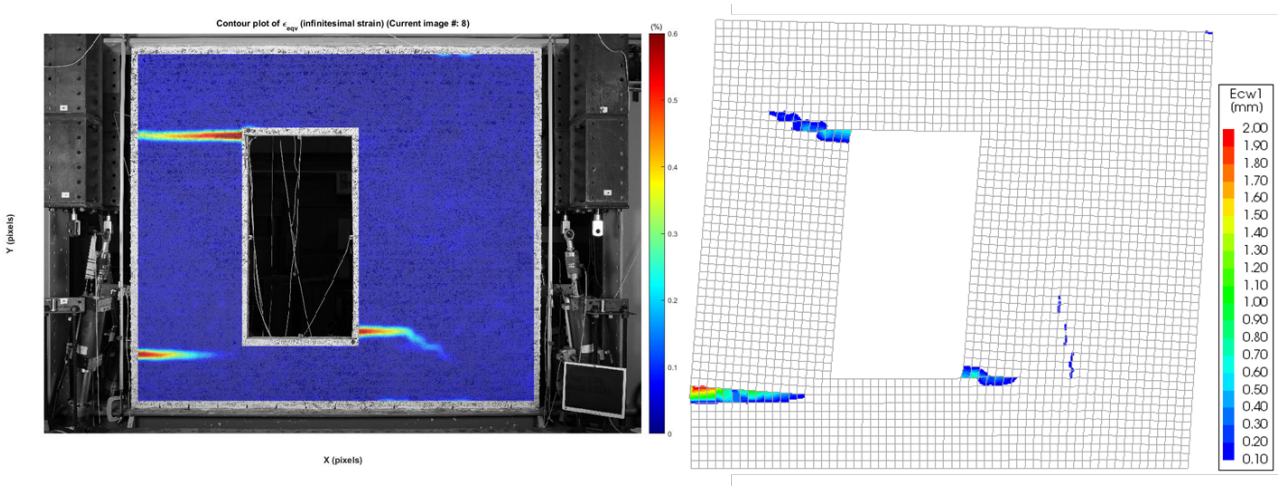

(a) (b)

Figure 5.13. TUD_COMP-41: R5a. Comparison between (a) strain plot of DIC related to experimental record number 22321 and (b) FEM post-test crack width plot. Model deformed shape magnified by 100.

Figure 5.14 shows the difference between the stress status in the model during the first repetition (R1a) and the last repetition (R5b). The plots are represented by using principal stress vectors. Throughout the initial stage (Figure 5.14a), high tensile stress is detected around the window corners and on the edge of the left pier which lead to crack growing in these three points. The compression state is quite relevant in the right pier and partially for the left pier. During the last stage (Figure 5.14b) higher compression in the bottom right corner of the wall is identified due to the large rotation of the right pier for a maximum principal compression stress of 2.78MPa still far from the compression strength of the masonry (14MPa). Moreover, the zones affected by tension are extending toward the wall corners, following the already existing cracks.

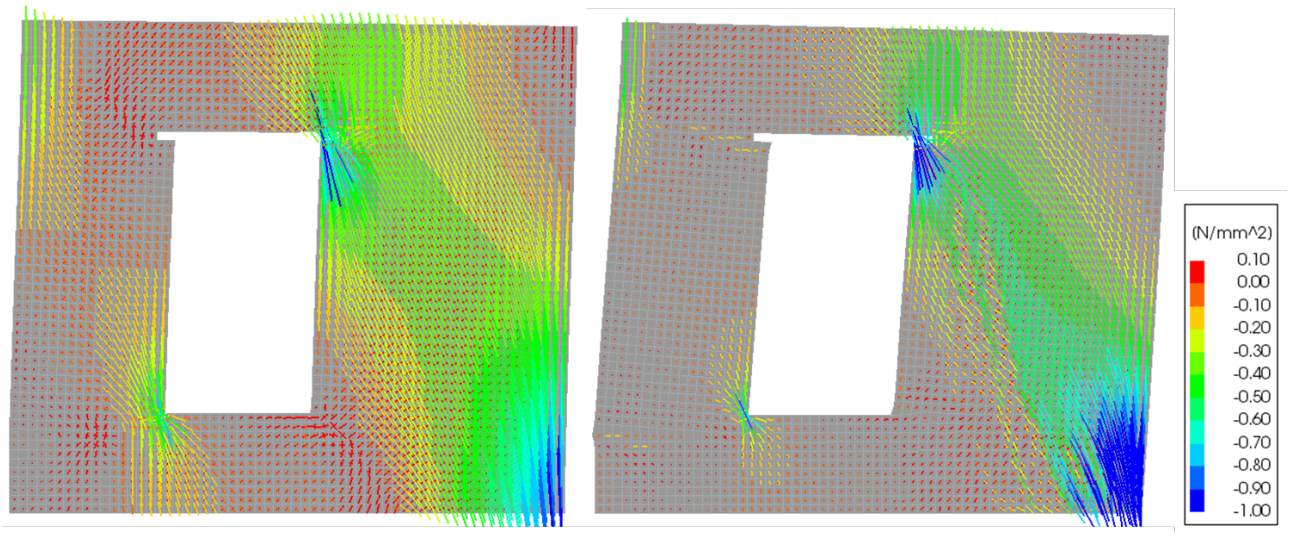

(a) (b)

Principal Stress, Min: -1.28MPa Max: 0.11MPa Principal Stress: Min: -2.78MPa Max: 0.16MPa

Figure 5.14. TUD_COMP-41: principal stress vector plot of the FEM post-test for (a) R1a and (b) R5b. Deformed shape magnified by 100. Concrete lintel is not shown.

TUD_COMP-42

In addition to the TUD_COMP-41, the experimental TUD_COMP-42 has been also analysed with the refined post-test model. The imposed deformation applied on the top edge of the wall is specified in Table 5.6. As for the previous in-plane wall, the TUD_COMP-42 was subjected to a repetitive pull as well. Its top displacement ranges from 0.59mm (R1) to 1.23mm (R5).

Figure 5.15 shows the difference between experimental and model force-displacement curve. The capacity of the TUD_COMP-42 wall is 22.63kN. The load is obtained during the repetition R5a. In the model a maximum force of 22.32kN (-1.3% to the original) reached throughout the repetition R5a as well.

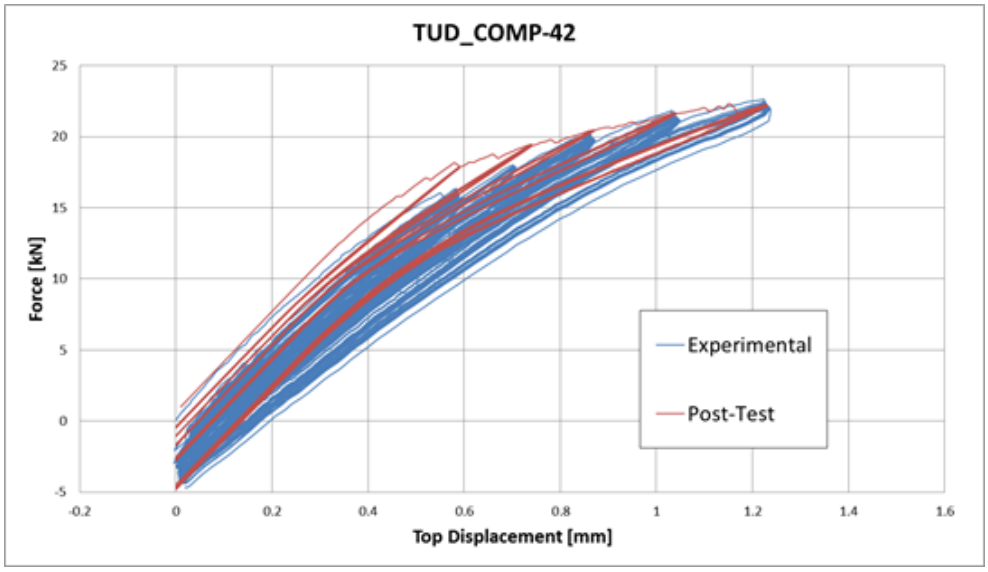

Figure 5.15. TUD_COMP-42: experimental and FEM post-test force-displacement curve.

Load values of the first two repetitions are slightly overestimated from the model. The reason could be associated to the presence of the transportation crack in the bottom part of the experimental wall (see Chapter 4). Load capacity and energy dissipation are quite well represented by the model.

A summary of maximum load and stiffness of experimental test and model is showed in Table 5.8. Initial and average stiffness during all the steps are well simulated from the model.

Table 5.8. TUD_COMP-42: load capacity and stiffness for experimental and FEM post-test.

Step	Load Capacity [kN]		Stiffness [kN/mm]	
	TUD_COMP_42	Post-Test	TUD_COMP_42	Post-Test
Initial		-	36.32	35.35
R1a	16.37	18.16	29.14	30.95
R1b	15.72	17.87	28.82	30.99
R2a	17.83	19.48	26.33	27.33
R2b	18.00	19.38	27.90	27.22
R3a	20.32	20.49	26.15	24.85
R3b	19.87	20.46	26.46	24.82
R4a	21.83	21.69	24.16	22.46
R4b	21.36	21.63	24.10	22.53

Step	Load Capacity [kN]		Stiffness [kN/mm]	
	TUD_COMP_42	Post-Test	TUD_COMP_42	Post-Test
R5a	22.63	22.32	21.59	20.85
R5b	22.14	22.20	21.64	20.99

The DIC strain plot associated with the repetition R5a is compared with the crack width plot of the FEM model (Figure 5.16). Both cracks in the window corners are well represented in the model, including their diagonal orientation. From the experimental test, no crack was detected starting from the left edge. In this case the different stress state produced from the horizontal transportation crack lead to a reduction of the vertical displacement (and rocking behaviour) of the wall left pier. Since the transportation crack has not been modelled in the FEM wall, the rocking mechanism of the left pier remain the principal failure mechanism in the wall associated to the left edge crack (Figure 5.16b).

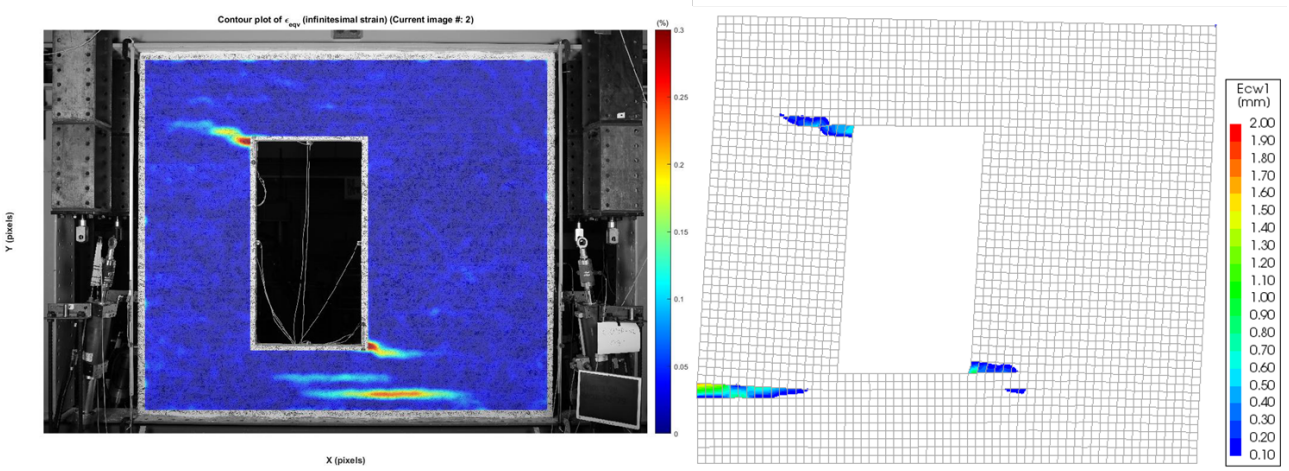

(a) (b)

Figure 5.16. TUD_COMP-42: R5a. Comparison between (a) strain plot of DIC and (b) FEM post-test crack width. Deformed shape magnified by 100.

5.2.4. Mesh Objectivity

The TUD_COMP-41 wall has been modelled with a finer mesh to attempt to catch possible improvements in the model due to mesh-size effect. In fact, according to the Finite Element Analysis (FEA) theory, the model with finer mesh (smaller element size) yields higher accuracy results but may require a longer computing time. To study this effect on the in-plane wall, the area of the single element is reduced by a factor 4. Thus the new elements' dimension is 25x25mm. The model is shown in Figure 5.17.

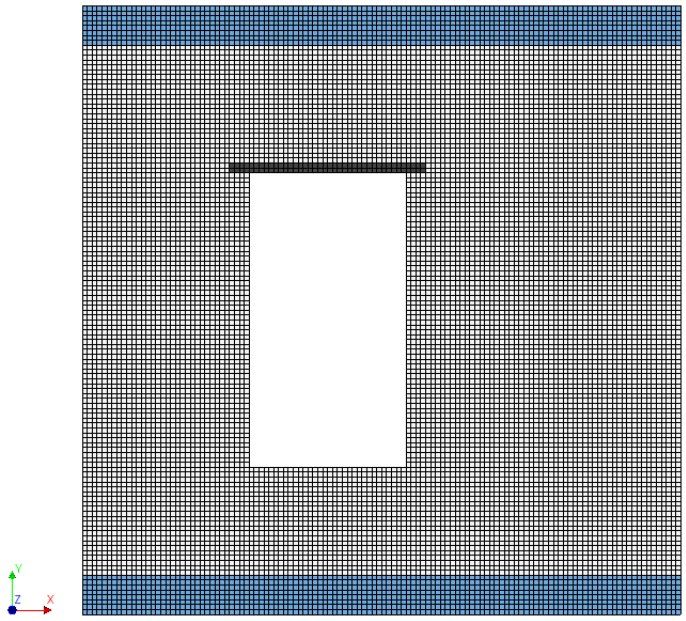

Figure 5.17. TUD_COMP-41: Diana FEM model of the in-plane wall. Mesh size 25x25mm.

Force-displacement curves are depicted in Figure 5.18. No big differences have been detected between the different mesh size models. The maximum load of the finer mesh model is slightly smaller than the coarse one during the last 3 repetitions. This means that the capacity of the wall with a smaller mesh size is about the same value of the coarse mesh (22.79kN against 22.81kN) but is now obtained during R4a as the experimental one. The mesh size does not affect the hysteresis curve which remains slightly overestimated as the model with a coarse mesh.

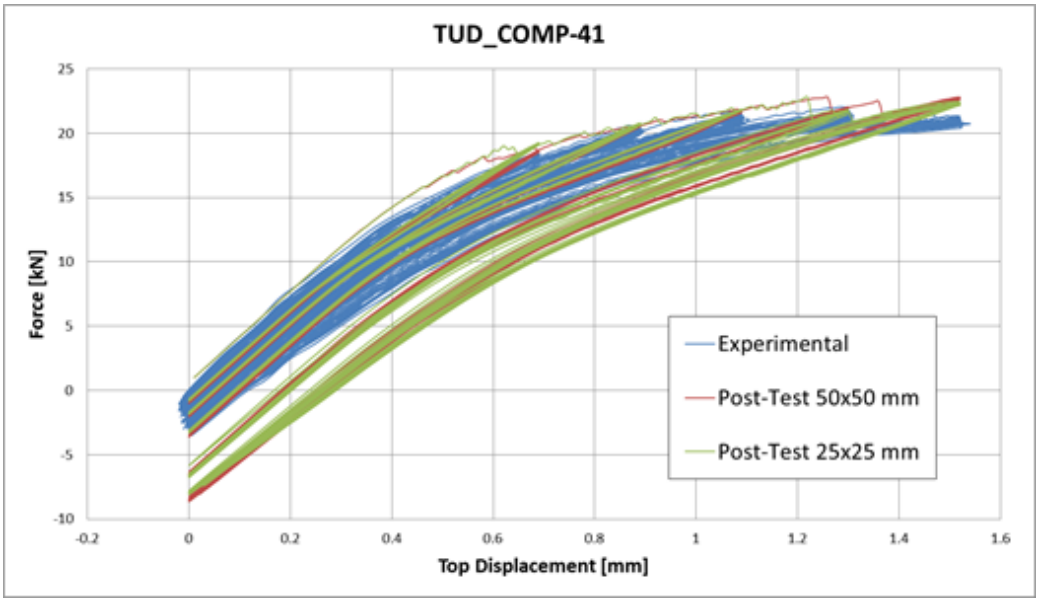

Figure 5.18. TUD_COMP-41: experimental and FEM post-test force-displacement curve varying mesh size.

The overall results of the 50x50mm model and 25x25mm model in terms of maximum force and stiffness, is presented in Table 5.9.

Table 5.9. TUD_COMP-41: load capacity and stiffness for experimental and FEM post-tests varying mesh size.

Step	Load Capacity [kN]			Stiffness [kN/mm]		
	TUD_COMP_41	Post-Test, mesh 50x50	Post-Test, mesh 25x25	TUD_COMP_41	Post-Test, mesh 50x50	Post-Test, mesh 25x25
Initial	-	-	-	38.14	35.35	35.32
R1a	20.35	18.84	19.28	25.59	28.22	28.54
R1b	18.46	18.70	19.17	26.88	28.29	28.53
R2a	20.63	20.61	20.81	23.44	24.75	24.63
R2b	20.50	20.60	20.68	23.60	24.81	24.64
R3a	21.78	21.89	21.98	19.88	22.34	22.09
R3b	21.33	21.78	21.84	20.07	22.42	22.18
R4a	22.05	22.78	22.79	16.99	21.04	20.96
R4b	21.45	22.02	21.78	17.20	21.21	21.21
R5a	21.43	22.81	22.46	14.81	19.93	19.57
R5b	20.93	22.70	22.30	11.52	20.01	19.68

Considerable differences have not been found concerning the crack pattern. Moreover, a deviation between crack width and length of the two models has not been detected.
Additional analyses have been run with two coarser meshes with a size of 100x100mm and 200x200mm. The two models are shown in Figure 5.19.

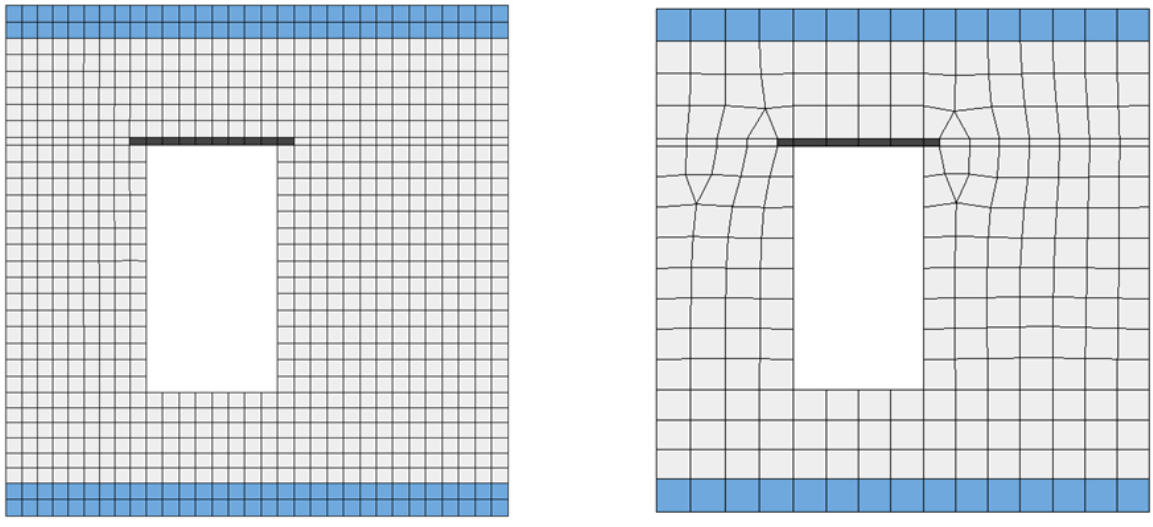

(a) Mesh size 100x100mm (b) Mesh size 200x200mm

Figure 5.19. TUD_COMP-41: Diana FEM model of the in-plane wall, coarser meshes. (a) Mesh size 100x100mm; (b) Mesh size 200x200mm.

The comparison between the backbone force-displacement curves of different mesh size models is plotted in Figure 5.20. In the first part of the protocol the three curves remain mostly overlapped. The finer mesh model predicts the drop in force better due to small cracks in the elements. Remarkable differences are

detected in the capacity during the last part of the protocol. Quite a large gap is observed at the last displacement peak.

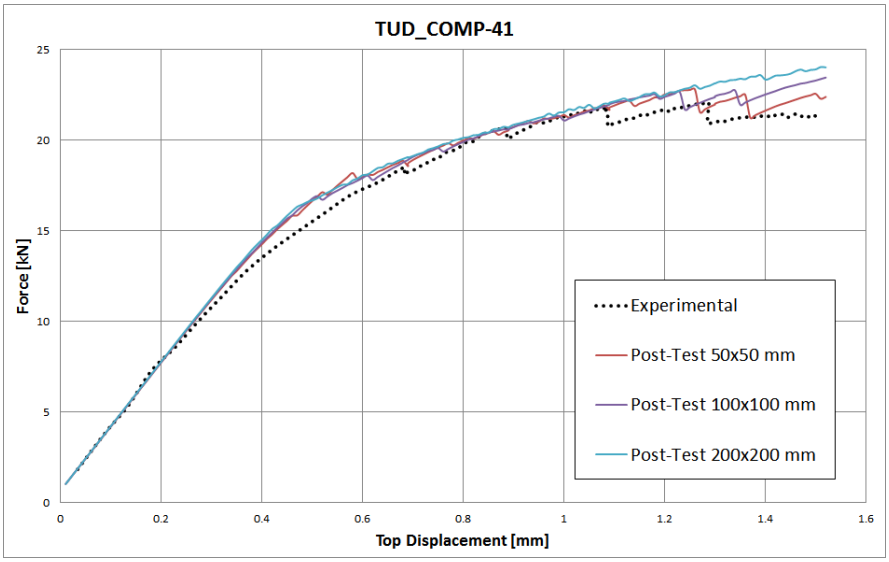

Figure 5.20. TUD_COMP-41: experimental and FEM post-test force-displacement backbone curve varying mesh size.

The deviations in the load capacity between different mesh size models and experiment are listed in Table 5.10. As already mentioned, only a small difference in the capacity is found between the finest mesh (25x25mm) and the reference mesh (50x50mm). In contrast, larger discrepancy is identified in the maximum force for the coarser meshes as 100x100mm and 200x200mm.

In order to avoid convergence issues and increase the reliability of the analysis, a relatively small step size has been selected for the analyses: 0.01mm/step. To compare the computational time of the analyses, Table 5.10 reports the approximate duration to compute the entire loading protocol (Table 5.6) for each mesh size model.

Table 5.10. TUD_COMP-41: Approximate duration, load capacity and its relative difference with the experiment for FEM post-tests varying mesh size.

Mesh size	Approximate analysis duration [min]	Normalised to Reference Case	Load Capacity [kN]	Capacity Relative Difference to Experiment [%]
25x25 mm	1500	4.29	22.79	+3.36%
50x50[1] mm	350	1.00	22.81	+3.45%
100x100 mm	80	0.23	23.43	+6.26%
200x200 mm	30	0.09	24.01	+8.89%

[1] Reference case

Despite the time saving, the damage pattern of the two coarsest meshes appear less accurate and more noisy. Moreover, with bigger elements it becomes more difficult to estimate the location and more importantly, the difference in length of the cracks. The damage patterns of the different models are depicted in Figure 5.21.

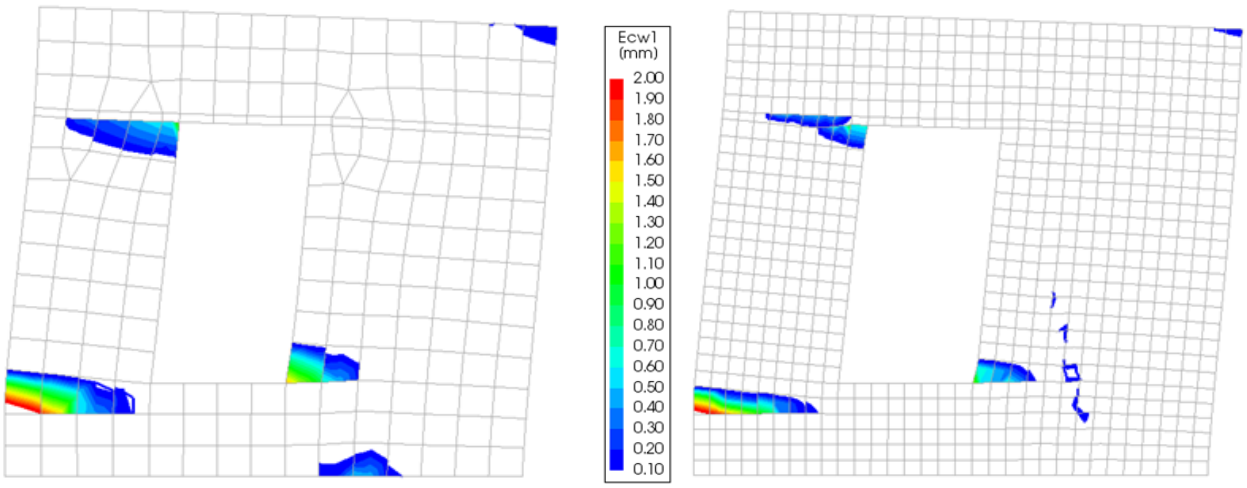

(a) Mesh size 200x200mm (b) Mesh size 100x100mm

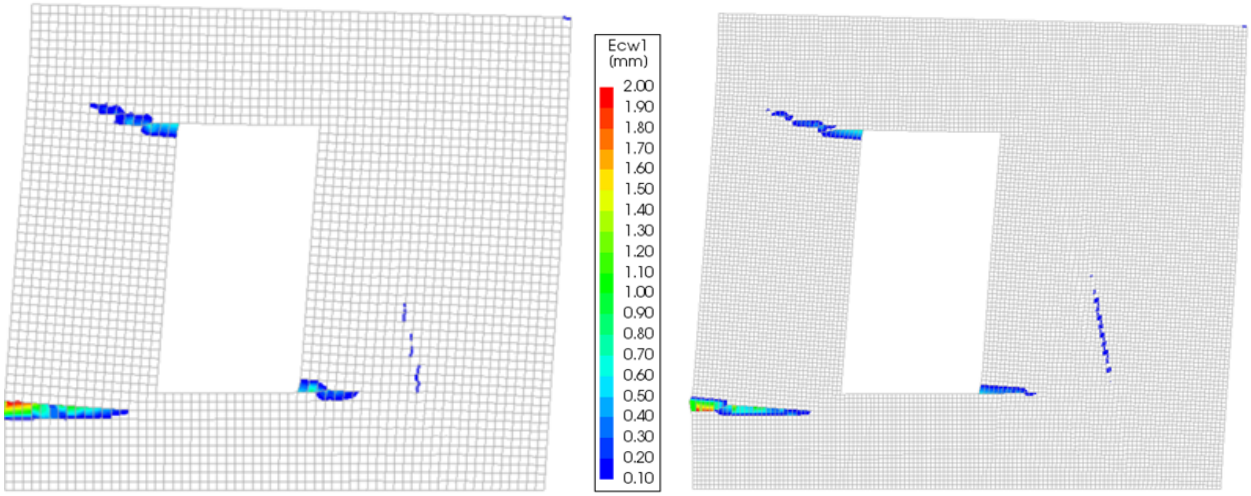

(a) Mesh size 50x50mm (b) Mesh size 25x25mm

Figure 5.21. TUD_COMP-41: R5a. FEM principal crack width plot for different mesh size model: (a) 200x200mm; (b) 100x100mm; (c) 50x50mm; (d) 25x25mm. Model deformed shape magnified by 100.

In conclusion, only a small improvement has been discovered in the in-plane wall by using a finer mesh size mostly based on capacity and average stiffness. On the other hand, the computational time from this model is extremely high, the increase is four-fold respect to the 50x50mm mesh. With a mesh size so small, the ratio between accuracy and efficiency is not maximised anymore. Moreover, a model that requires high computational time is not useful for NL-TH-A, necessary for the resistivity curves modelling.
The coarser meshes speed up the analyses, but they affect the precision achievable in the crack width/ length as well as the load capacity of the model. Nonetheless, these meshes are anyway able to give a rough estimation of the expected damage pattern in the wall and to calibrate some parameters e.g. initial stiffnesses. Consequently, for larger walls, the use of a coarser mesh (as 100x100mm) is certainly possible.
Note that varying the mesh also affects the analysis of damage performed by the program (see Section 2.6). Here, a finer mesh is welcome, but the results obtained with the damage program were sufficiently good.

Consequently, the results are based on the in-plane wall with a mesh size of 50x50mm which is later also used for the assessment of the model for the resistivity curves.

5.3. Conclusions of Chapter Five

In accordance to the experimental tests on the clay brick masonry walls, post-diction models for the samples TUD_COMP-41 and TUD_COMP-42 have been elaborated and analysed. The aim of the study was to produce a smeared, continuum-approach model capable of reproducing the overall behaviour of the experiments in terms of capacity, stiffness, and cracking patters.

First, the prediction model and the experiment results were compared. A Total-Strain based model was used for the prediction and it represented the energy dissipated in the experiments poorly, although crack initiation and crack growing were present.

The model was then updated with an orthotropic model for masonry, the Engineering Masonry model. The constitutive model is capable of distinguishing cracks in the joint directions as well as stair-case cracks. Moreover, it shows a better behaviour during the unloading phase, including more reasonable hysteretic loops. Furthermore, the model is a good choice for non-linear, time history analyses.
In addition to the constitutive model, the masonry parameters were calibrated and set based on the results of the actual experiments as well as on companion tests.
The results of the model were compared with the experimental ones. Large improvements in respect to the prediction and good agreement for load capacity and hysteretic behaviour were found. Crack patterns and crack propagation were quite well represented too.
Nonetheless, additional investigation regarding the growing of the crack width during each single run of a repetition (the pure material degradation) is still required. In fact, the Engineering Masonry model loses some accuracy regarding the degradation due to pure tensile stresses which are better represented by the principal strain based Total-Strain Crack model.

For additional comparison with the experimental test, the results of the model were compared with the DIC plots. The measurement system, used to track the wall state during the test, was extremely useful for this. Displacements and strain contour plots were produced and analysed along with computational results. Satisfactory consistency in the results were found.

A sensitivity study by reducing the mesh size of the model was conducted in order to evaluate potential improvements by reducing the element size. When decreasing the area of the elements by a factor of four, no considerable differences were found in terms of capacity/hysteresis/crack pattern. Contrarily, the computational time was increased four-fold, making the finer mesh model inefficient.

Chapter 6

Computational Models for Resistivity Curves

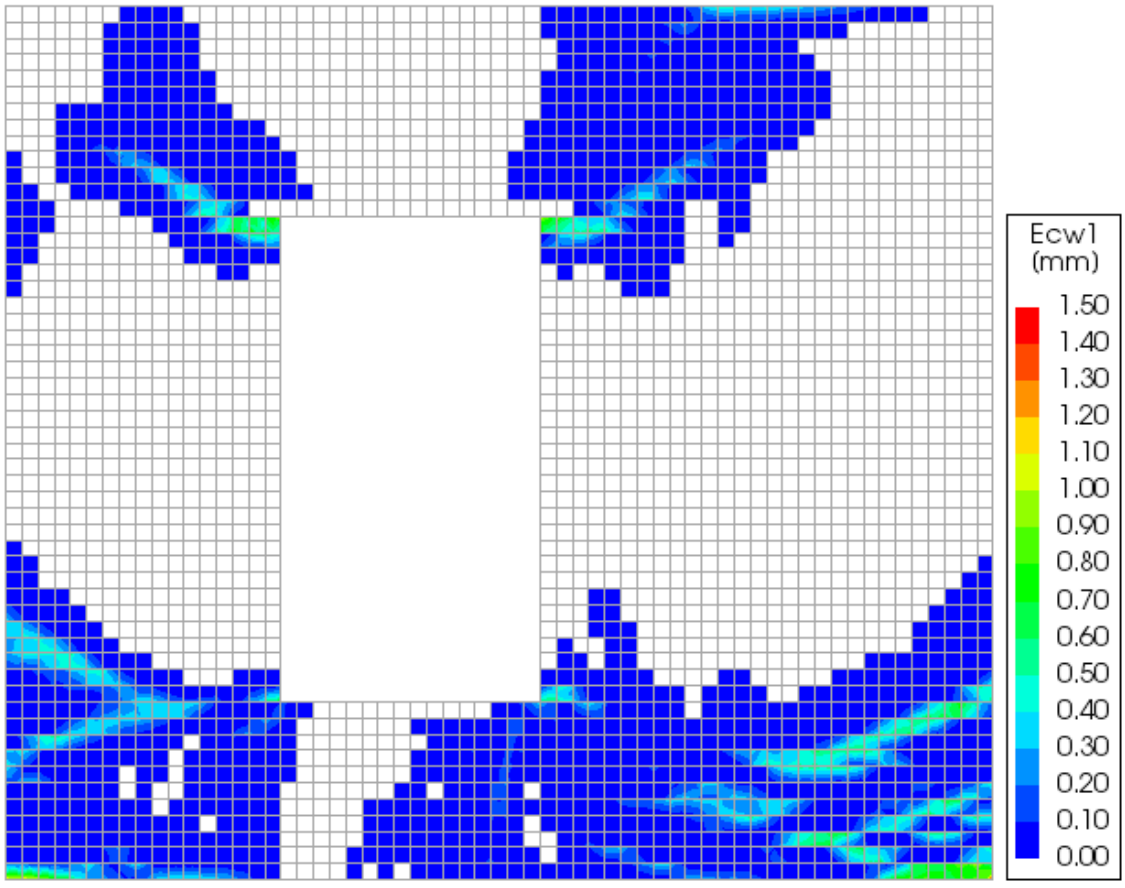

TU Delft

6. Computational Models for Resistivity Curves

6.1. Introduction

As detailed in Chapter 2, one prominent failure mechanism for the lowest damage states in (structural) masonry components corresponds to the initiation of cracking. The bond between mortar and brick elements can be extremely weak, especially if other actions, such as the crystallisation of salts or frost (Larby, 2004), have already acted to damage the structure. Recent laboratory tests at the TU Delft (Esposito et al., 2016.b), set the tensile strength of reproduced, undamaged, weak-mortar masonry bond around 150kPa for typical clay brick masonry in the Netherlands. Moreover, since weaker mortar joints typically occur in the structure, specially among the vertical joints, the real tensile strength can easily drop to 25kPa. With such a low value defining the tensile strength and also because large masonry parts in existing structures are likely to be pre-cracked due to various loadings during the life time of the structure, it follows that some design codes, particularly the EuroCode, assume that un-reinforced masonry has no tensile strength.
Nevertheless, some actions such as thermo-hygro expansion and contraction, differential settlements, or ground vibrations may cause tensile stresses in the structure which will lead to cracks. Under some circumstances these cracks may widen and becoming visible, thus affecting the perception of damage about the structure.

Precisely, it is a combination of actions that may accumulate sufficient minor damage in the masonry elements such that this becomes visible. However, laboratory experiments are not well suited to measure and analyse the interaction of various actions influencing a specimen simultaneously: variables and effects become mixed and difficult to interpret, and testing multiple specimens carries an elevated cost. Hence, it is necessary to assess the cumulation of minor damage with numerical tools, capable of identifying the influence of each parameter accurately, and being able to simulate as many cases as are needed to understand the physical behaviour of the structure. Then again, it is difficult to assess whether the computational models resemble the real situations satisfactorily.
Consequently, an analysis into the initiation and cumulation of minor damage requires a combination of laboratory experiments to validate the computational models to be used.

The smeared continuum model, used to study the experimental in-plane walls after the tests, has been adopted to analyse and compute the data for additional scenarios used for the resistivity curves as described later in Chapter 7.
The model has been adapted to apply a dynamic excitation instead of a static load. In addition to the dynamic load, different initial stress and pre-damage conditions have been introduced into the in-plane wall. Initial damage due to earthquake, settlement, and shrinkage has been taken into account in the models.
Moreover, different PGAs for the dynamic load, different material values for the masonry wall, and different levels of settlement or shrinkage have been applied. Considering the permutation of possible scenarios, the total amount of models analysed is 114.
The result in terms of displacements and crack width have been analysed with a specially developed algorithm in order to get the Ψ damage parameter values. The parameter Ψ summarises in one value the degree of damage of a masonry element (Chapter 2). The damage states of all models are then interpreted and used to compute the resistivity curves for the in-plane wall (Chapter 7).

6.2. Model Description

6.2.1. Geometry

The model is based on the one calibrated and validated in the previous chapter. Some small adjustments have been applied to the model: Firstly, tyings on the wall top edge have been removed since the input motion is not applied to the top part of the wall anymore (no horizontal displacement of the top edge is required). Cantilever boundary conditions are kept for the wall. Vertical and horizontal motion has been applied on the base nodes of the bottom beam. The same level of vertical pre-compression has been used: 0.12MPa. The line load to apply the overburden to the wall has been replaced by applying a material density to the top steel beam. The outcome of the these two methods is identical. The choice to replace the line load with the beam density is for practical reasons: to simplify the analysis steps. In this way the overburden has been taken into account already during the application of the gravity load. Moreover, linear mass elements have been added to the top beam, such that the total mass that acts on top of the wall during the dynamic phase is equal to 8 tons. The hypothesis is to represent the additional mass which acts in the horizontal direction throughout the dynamic phase induced by a fictitious slab and roof. This more realistic assumption affects the natural frequency of the wall driving the period of the modes to higher values. The base model is shown in Figure 6.1.

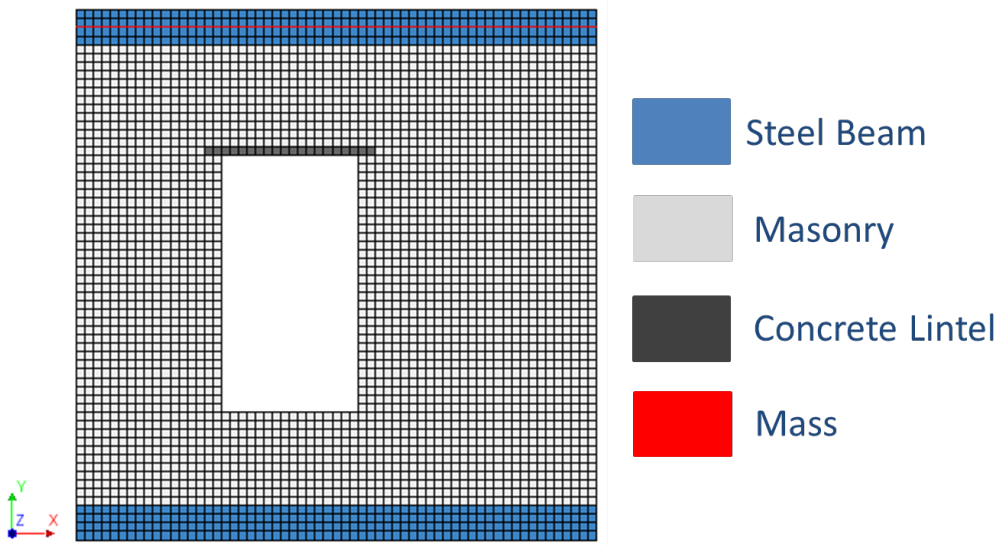

Figure 6.1. Diana FEM in-plane wall model for resistivity curves.

The properties used for masonry and lintel are the same as the post-test simulations (Table 5.5).

Rayleigh damping of 2% has been included in the model. It has been based on the first two modes in terms of participating mass. An eigenvalue analysis has been performed to extract the Rayleigh coefficients. The first two modes of the model are depicted in Figure 6.2.

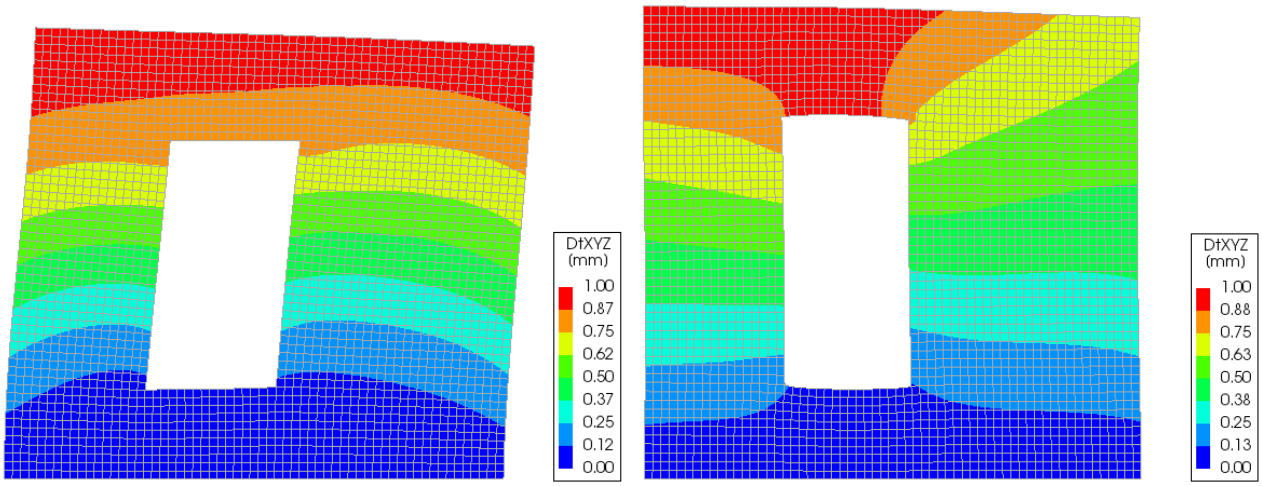

(a) MODE 1, T=0.100s, 9.96Hz (b) MODE 2, T=0.034s, 29.41Hz

Figure 6.2. Global displacements of MODE 1 and MODE 2 for the model for resistivity curves. Deformed shape magnified by 200.

For mode 1 a period of 0.10s has been detected; the second mode has a natural period of 0.034s. The Rayleigh coefficients computed from 2% damping and applied to the model then result as: 1.8699Hz for the mass factor (a) and 0.00016172s for the stiffness factor (b).

6.2.2. Input Ground Motions

The base motion applied to the wall is divided into two components: horizontal and vertical. Both of them are expressed by representative ground motions for the Groningen region. For the acceleration time history of the horizontal component, the earthquake of 16th of August of 2012 with epicentre near Huizinge has been used (Dost et al., 2013).

The plot of the ground acceleration motion is shown in Figure 6.3.

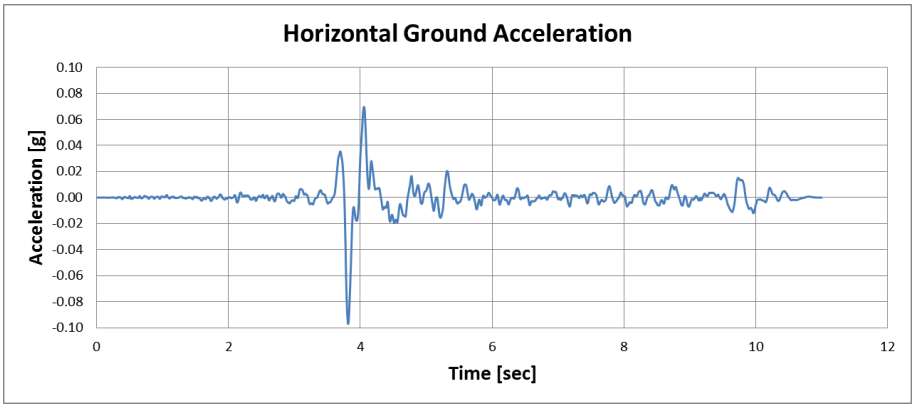

Figure 6.3. Time vs acceleration graph of the horizontal component of the Huizinge earthquake (2012).

Along with the acceleration ground motion, the ground velocity and a Fast Fourier Transform (FFT) have been computed. They are presented in Figures 6.4 and 6.5 respectively. The FFT plot shows the contents in frequency of the earthquake, which exhibits high values in frequencies between 1.5 and 4Hz.

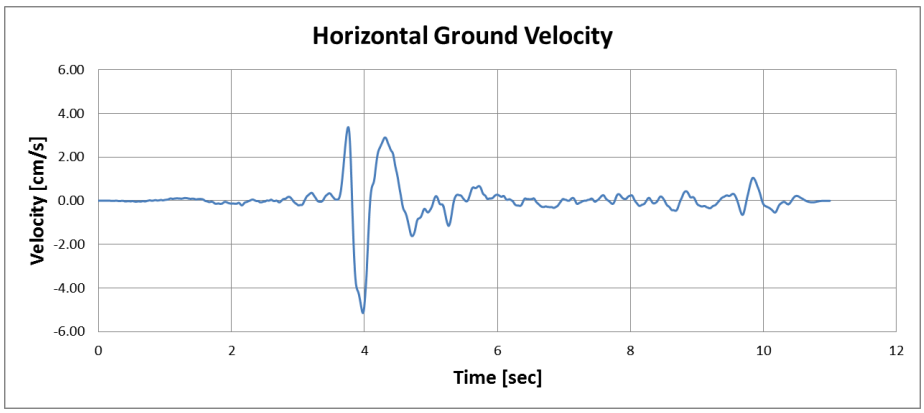

Figure 6.4. Time vs velocity graph of the horizontal component of the Huizinge earthquake (2012).

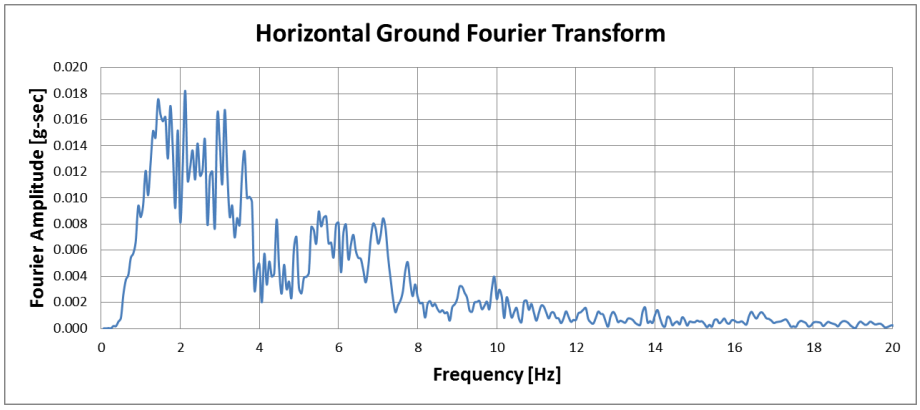

Figure 6.5. Fourier transform graph of the horizontal component of the Huizinge earthquake (2012).

For the vertical component, a vertical ground motion recorded in the Groningen field has been applied (Tomassetti et al., 2017) simultaneously with the horizontal component. Several ground-motions recorded in the Groningen field show high ratios of the vertical to horizontal motion. The recommendations (Bommer et al., 2016) to produce a vertical spectrum are to amplify by 2 the lower period motions (below 0.2s). The plot of the input accelerogram is shown in Figure 6.6.

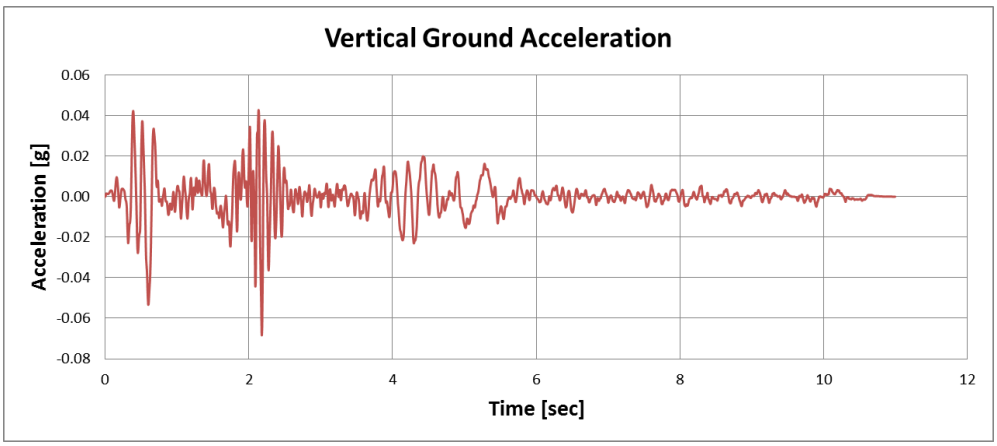

Figure 6.6. Time vs acceleration graph of the vertical component of the motion.

Peak Ground Velocity (PGV) plot and Fast Fourier Transform have been evaluated as well for the vertical motion and are depicted in Figure 6.7, Figure 6.8.

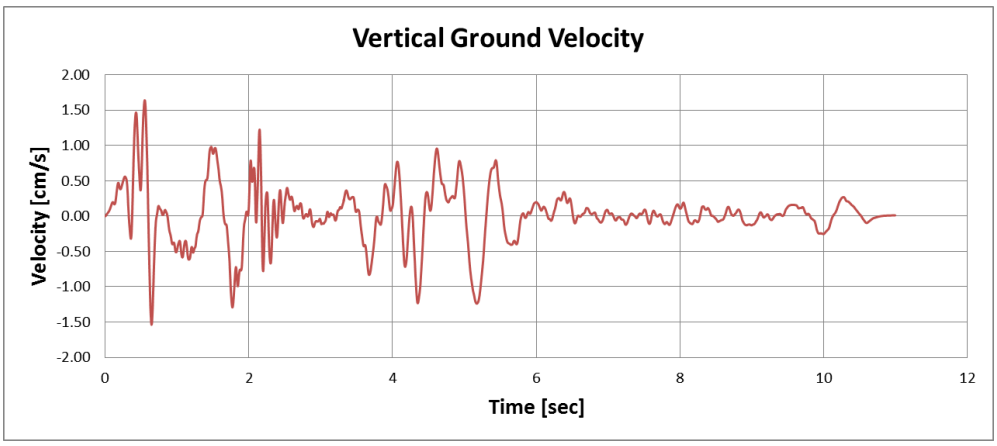

Figure 6.7. Time vs velocity graph of the vertical component of the motion.

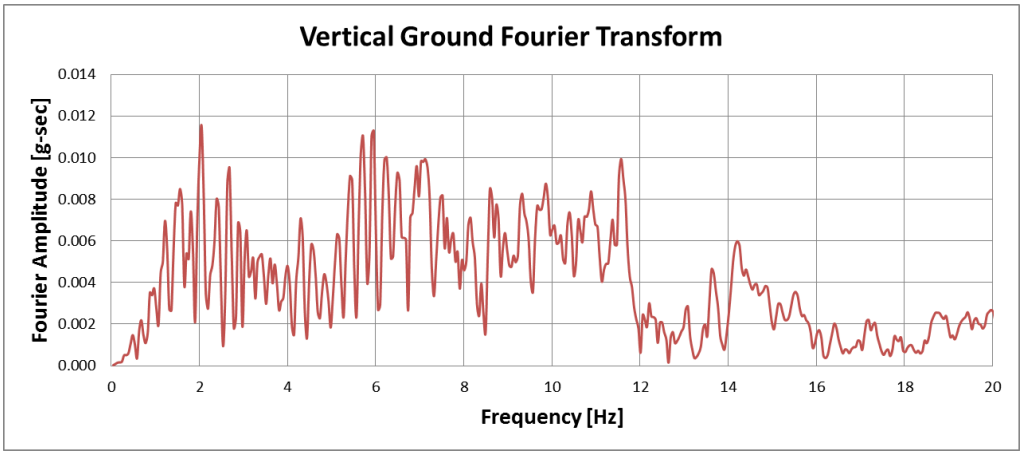

Figure 6.8. Fourier transform graph of the vertical component of the motion.

A plot of the two ground motions applied is shown in Figure 6.9:

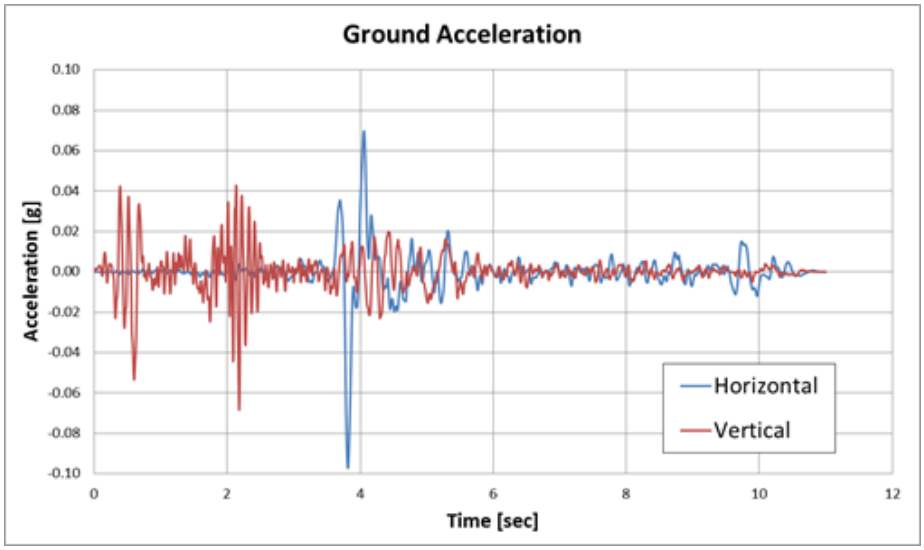

Figure 6.9. Time vs acceleration graph of the two components of the ground motion applied to the model.

The acceleration amplitude of these two records have been scaled to produce different levels of damage in the in-plane wall. For the horizontal PGAs a range between 0.05g and 0.30g has been chosen. The vertical amplitude of the motion has been scaled with the same ratio of the original motion.
Table 6.1 lists the original motions and the different amplitude records applied in the model.

Table 6.1. Horizontal and vertical PGAs of the different motions applied in the models.

Motion number	Horizontal PGA [g]	Vertical PGA [g]
Original	0.097	0.068
Motion 1	0.050	0.035
Motion 2	0.100	0.070
Motion 3	0.150	0.105
Motion 4	0.200	0.140
Motion 5	0.250	0.176
Motion 6	0.300	0.211

The earthquake motion in the two orthogonal directions is applied at the base of the bottom beam as a base excitation.

6.2.3. Static Versus Dynamic Condition

A crack width comparison between the repetitive static analysis and the dynamic analysis (no pre-damage) is presented in Figure 6.10. The results from the two models are confronted for a similar top horizontal displacement. Hence, for the static repetitive test the largest amplitude (1.52mm of top horizontal displacement) is chosen. The same horizontal displacement for the dynamic case is detected in the first part of the 0.30g motion. Figure 6.10 illustrates that very similar crack patterns are predicted. The diagonal cracks in the two window corners are slightly longer than in the static case. Nevertheless the maximum crack width is higher in the static repetitive model. The wider crack occurs at the lateral edge, showing a more localized rocking behaviour of the pier. The slight difference in the two results can be explained from the dynamic component of the motion which leads to a different stress distribution in the wall. Especially during the first part of the earthquake, cycles with small amplitudes induce distributed micro-cracks that affect the subsequent crack propagation phase.

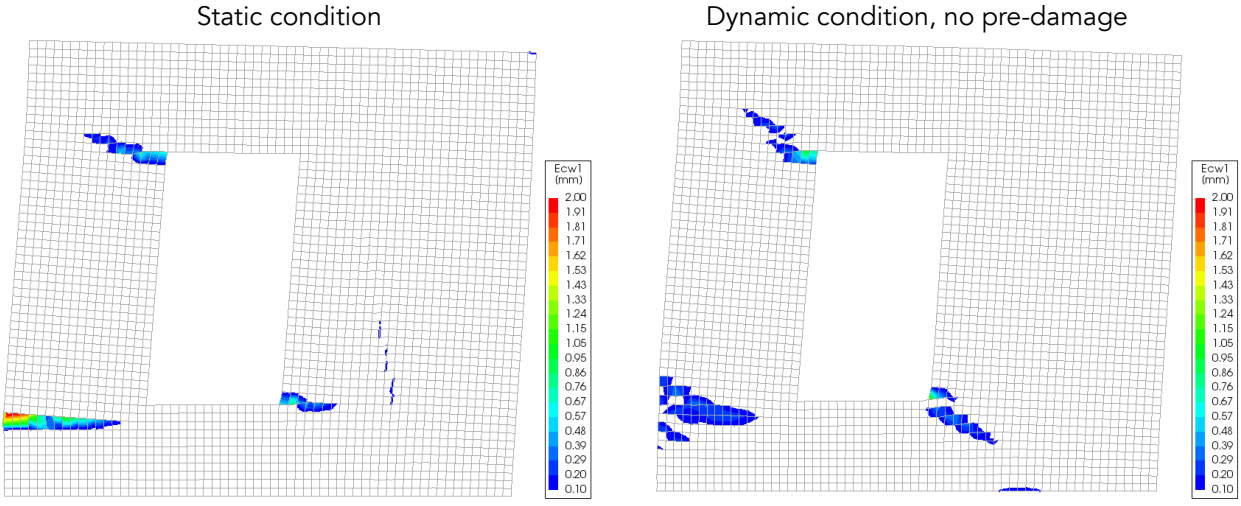

(a) Max crack width: 2.19mm (b) Max crack width: 1.50mm

Figure 6.10. Crack width plots comparison between: (a) repetitive test model TUD_COMP-41 during repetition R5a (1.52mm), (b) dynamic test, no pre-damage, at the moment of top horizontal displacement equal to 1.52mm. Deformed shape magnified by 100.

6.2.4. The Effect of the Vertical Component of the Motion

A set of Non Linear Time History Analyses (NL-TH-A) have been performed to estimate the importance of the vertical motion in the model. The model, described in Section 6.2.1, has been subjected to two different input conditions. In the first, both horizontal and vertical ground motion have been considered. In the second, only the horizontal acceleration has been applied. The time-acceleration plots of the horizontal and vertical ground motions are shown in the previous section in Figure 6.3 and Figure 6.6 respectively. As already explained above (Section 6.2.2) the PGAs of the two components have been scaled to generate six different input combinations. PGA values for the different scaled motions are reported in Table 6.1.
Before the application of the earthquake motions, gravity load and overburden of 0.12MPa have been applied to the model.
The results of the analyses are compared in terms of maximum crack width. These values are presented in Table 6.2.

Table 6.2. Comparison of the max crack width and its relative difference for the situation with horizontal and vertical motion and the situation with only horizontal motion.

Motion number	Horizontal + Vertical Motion Max Crack Width [mm]	Horizontal Motion Max Crack Width [mm]	Max Crack Width Relative Difference [%]
Motion 1	0.00	0.00	0%
Motion 2	0.06	0.06	0%
Motion 3	0.24	0.24	0%
Motion 4	0.80	0.84	5%
Motion 5	2.25	2.37	5.3%
Motion 6	2.41	2.31	-4.2%

The same crack openings are found for the first three models. The lower intensity motions (up to 0.15g for the horizontal PGA) don't provide any deviation in the results. Small differences in crack width start to appear from the motion number 4 (0.20g for horizontal PGA). The maximum deviation is obtained for the motion 5 with a relative difference of +5.3% in the crack width. The crack patterns of the models with and without vertical motion are depicted in Figure 6.11.a and Figure 6.11.b, respectively.

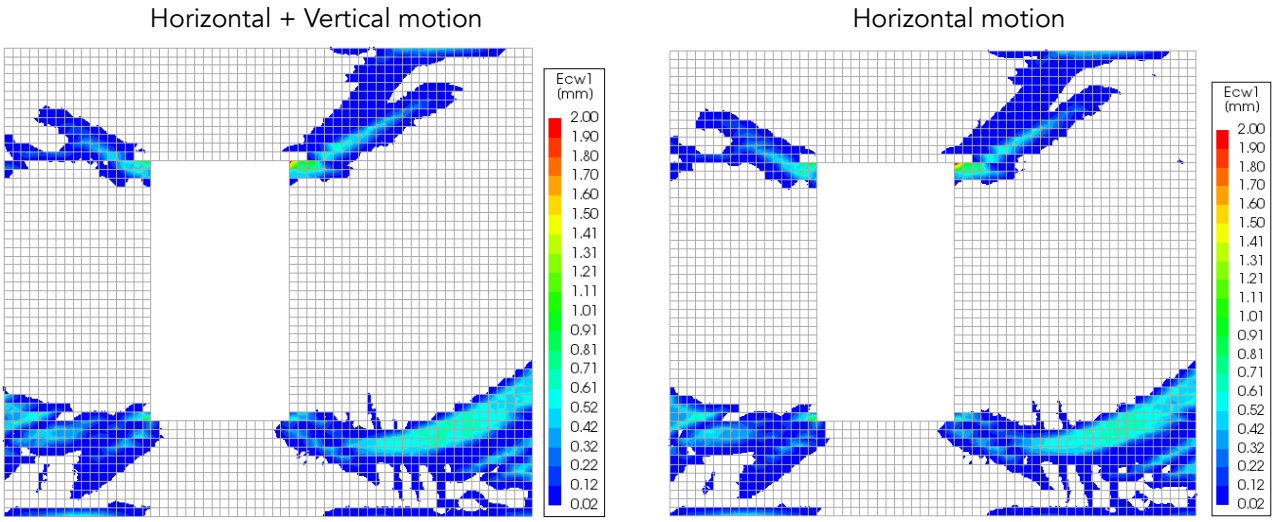

(a) Max crack width: 2.25mm (b) Max crack width: 2.37mm

Figure 6.11. Cumulative crack width plots for 0.25g motion for: (a) horizontal and vertical motion, (b) only horizontal motion. Undeformed mesh.

From the contour plot, no significant deviation in the crack pattern is detected. The number and the location of the major cracks are well comparable between the two walls.

In conclusion, the difference between the width of the major crack for two models is negligible for the lower PGAs motion and around 5% for the higher PGAs. The overall damage pictures of the walls are very similar in all six scenarios. In sum, the vertical motion can be neglected in this model.

6.3. Pre-Damage Scenarios

In order to study the effect of different initial damage states in the wall and understand how its presence affects the overall structural behaviour in combination with the earthquake, four different pre-damage scenarios have been applied to the model: no pre-damage, pre-earthquake, settlement and, restrained shrinkage. For each case, two levels of pre-damage have been set in order to later establish a relationship between the intensity of the pre-damage and the final damage (see Chapter 7).

These three types of pre-damage cases have been selected to represent potential prior damage of the structures. Earthquakes represent previous earthquakes and vibrations; restrained shrinkage stands for hygro-thermal variations during construction or during daily or seasonal changes; and, middle-sagging settlement has been selected as one of the myriad of different settlement alternatives. This is based on the analysis of a few damage cases but whether it corresponds to the most observed type of settlement has not been investigated. The purpose of the scenarios is to evidence a relationship between pre-damage and final damage. Additional reasoning for the selection of these cases can be found in Section 7.3.2.

In addition to different pre-damage cases, different parameters for the masonry material have been taken into account. Material strength and elastic modulus have been modified ±30% and ±50% in order to represent weak, standard, and strong materials, respectively; the mean and variations follow values from results from the material companion test campaigns; see Table 9.1. In this way, the variability of the masonry material can be included in the resistivity curves. The different scenarios for the masonry properties are extrapolated from the material tests and from the current knowledge of the clay masonry. The properties of the three materials are listed in Table 6.4.

Table 6.3. Horizontal and vertical PGAs applied for the pre-earthquake damage condition for the three different materials.

Pre-Earthquake number	Material 1 - Weak		Material 2 - Standard		Material 3 - Strong	
	Horizontal PGA [g]	Vertical PGA [g]	Horizontal PGA [g]	Vertical PGA [g]	Horizontal PGA [g]	Vertical PGA [g]
Pre-Earthquake 1	0.050	0.035	0.130	0.091	0.200	0.141
Pre-Earthquake 2	0.075	0.053	0.170	0.119	0.220	0.155

A brief description of the different pre-damage cases is given below, along with the resulting small adjustments to the wall model:

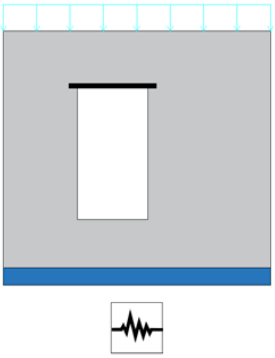

NO PRE-DAMAGE:
The analyses for this initial condition have been performed with the model described in the previous Section (6.2). Hence, the dynamic excitation has been applied to the lower part of the bottom beam as base motion. The wall has been pre-stressed with gravity load and an overburden of 0.12MPa before shaking. Different PGAs have been used for both horizontal and vertical component for a total of 6 motions (Table 6.1).

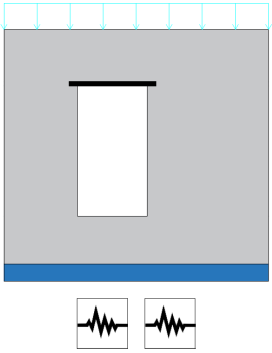

PRE-EARTHQUAKE DAMAGE:
The FEM model was kept the same as for the no pre-damage condition. The earthquake pre-damage has been generated with the same earthquake accelerogram scaled in order to have two damage levels in the wall. To have comparable initial damage (in terms of Ψ) due to the pre-shaking, different PGAs have been calibrated for the three different material properties. Gravity load and top vertical compression have been applied before the pre-earthquake. The pre-earthquakes applied are listed in Table 6.3.

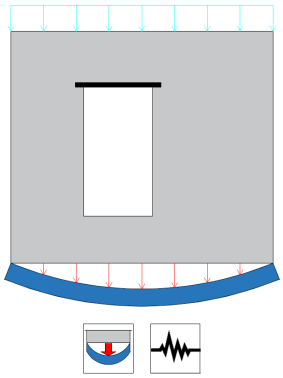

SETTLEMENT PRE-DAMAGE:
Parabolic sagging has been set on the bottom part of the wall. Two different amplitudes in settlement have been used: 2mm and 5mm at the middle-span. For the example, these values and the sagging profile were considered to be realistic cases as compared to other settlement studies like Giardina et al. (2015). Since in the base model the nodes of the top edge of the bottom beam were merged with the lower edge of the wall, interface elements have been added between wall and beam. Six nodes, 2D line interface elements were applied. Discrete cracking material, with tensile strength equal to 0.075MPa and brittle softening has been used. For this interface between wall and beam, normal and shear interface stiffnesses have been set based on the formulation 100·E/L, meaning that the stiffness is 100 times larger than the stiffness of a piece of adjacent masonry element with length of 50mm. The settlement pre-damage case is divided in two loading phases by using the phased analysis option in DIANA. Firstly, the sagging settlement has been applied as prescribed deformation to the top edge nodes of the bottom beam elements. Then, the supports have been moved to the base of the bottom beam and the motions in the two different directions have been added.

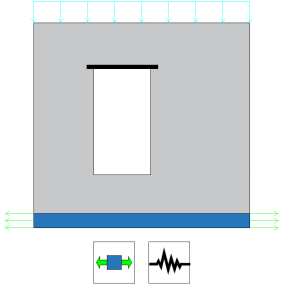

SHRINKAGE PRE-DAMAGE:
Masonry and concrete material are usually characterised by a relative high measure of shrinkage or expansion and low values in tensile strength. Restraint of shrinkage by adjacent structural components can produce cracks. For instance, attached concrete floors will restrain the shrinkage of masonry walls. To simulate this condition, a strain has been imposed to the bottom beam. Two different levels of shrinkage have been applied in the model: 0.2‰ and 0.4‰ (Rots et al., 1997). The pre-shrinkage condition requires different boundary conditions in order to be applied properly. To this end, the phased analysis option in DIANA has been used. In the first phase, the shrinkage has been imposed via strain loading in the bottom beam elements, while the lower part of the bottom beam has been constrained in the vertical direction only with horizontal rollers. In the second phase, the bottom edge of the beam has been supported in the horizontal direction, too. Then the earthquake motion has been applied.

Table 6.4. Three different scenarios for the clay masonry material properties.

Clay Masonry Properties – Engineering Masonry model				
Properties		**Material 1- Weak**	**Material 2 - Standard**	**Material 3 - Strong**
Density	ρ	1680Kg/m^3	1680Kg/m^3	1680Kg/m^3
Young's modulus perpendicular to bed-joints	E_y	1700MPa	3400MPa	5100MPa
Young's modulus parallel to bed-joints	E_x	1100MPa	2200MPa	3300MPa
Shear modulus	G_{xy}	650MPa	1300MPa	1950MPa
Tensile strength perpendicular to bed-joints	f_t	0.07MPa	0.10MPa	0.13MPa
Tensile fracture energy	G_f^I	5N/m	5N/m	5N/m
Compressive Strength	f_c	9.8MPa	14.0MPa	18.2MPa
Compressive Fracture Energy	G_c	20000N/m	20000N/m	20000N/m
Friction angle	φ	0.6rad	0.6rad	0.6rad
Cohesion	c	0.105MPa	0.150MPa	0.195MPa
Predefined angle for diagonal cracking	α	0.5rad	0.5rad	0.5rad

Since the material properties differ in the three cases, eigenvalue analyses have been performed before the NL-TH-A to adjust the Rayleigh damping coefficients. A summary of the eigenvalue analyses, including natural periods and Rayleigh damping coefficients is given in Table 6.5.

Table 6.5. Eigenvalue analyses results and Rayleigh damping coefficient for models with three different materials.

Eigenvalue analyses and Rayleigh damping coefficients							
Description		**Material 1 - Weak**		**Material 2 - Standard**		**Material 3 - Strong**	
Mode 1	T1	0.141s	7.08Hz	0.100s	9.96Hz	0.082s	12.14Hz
Mode 2	T2	0.048s	20.85Hz	0.034s	29.41Hz	0.028s	35.94Hz
Mass Factor	a	1.3295Hz		1.8699Hz		2.2805Hz	
Stiffness Factor	b	0.00022788s		0.00016172s		0.00013242s	

In summary, six incremental dynamic motions have been analysed for:

- one virgin case without pre-damage;
- two scenarios of initial pre-earthquake damage;
- two scenarios of initial restrained shrinkage damage;
- two scenarios of initial settlement damage;

All of them are combined with three different scenarios of masonry materials (weak, standard, strong)

Once all the different models were set, more than one-hundred analyses have been run. In Section 7.4.1 an overview of all the possible cases is summarised.

6.4. Model Results

Displacements and crack width have been extrapolated from all the models. With automatic software as developed and explained in Section 2.6.3, the damage parameter Ψ which for each case has been post-processed and used for the computation of the resistivity curves (see Section 7.4.1). In this way the overall damage of the wall is summarised into one parameter.

Apart from Ψ-values, results in terms of different crack patterns and crack width have been extracted and interpreted from the analyses of different initial combinations of pre-damage/material/dynamic load. The major findings are elucidated in this section, while the Ψ-values and its interpretation towards resistivity curves are projected in Chapter 7.
Figure 6.12 compares the damage patterns induced by the different pre-damage scenarios. The three plots correspond to the standard material model. Micro-cracks (crack widths below 0.02mm) are shown as well. The pre-earthquake damage plot for a motion of 0.17g at the moment when maximum damage is shown is presented in Figure 6.12.a. Most of the cracks are spread around the window corners and the bottom right part of the wall.
For the settlement pre-damage in Figure 6.12.b, a crack of 0.12mm in width is detected at the bottom left window corner. In addition, some vertical cracks appear in the bottom part of the wall due to the increase of the bending moment in that area. This corresponds to a stress field and crack patterns obtained by Giardina et al. (2015), for similar sagging cases.
Differential shrinkage deformation of 0.4‰ (Figure 6.12.c) leads to a vertical crack in the middle beneath the window and horizontal openings (or delamination cracks) in the wall bottom corners. This complies well with the tensile stress field for restrained shrinkage cases studied by Rots et al. (1997).

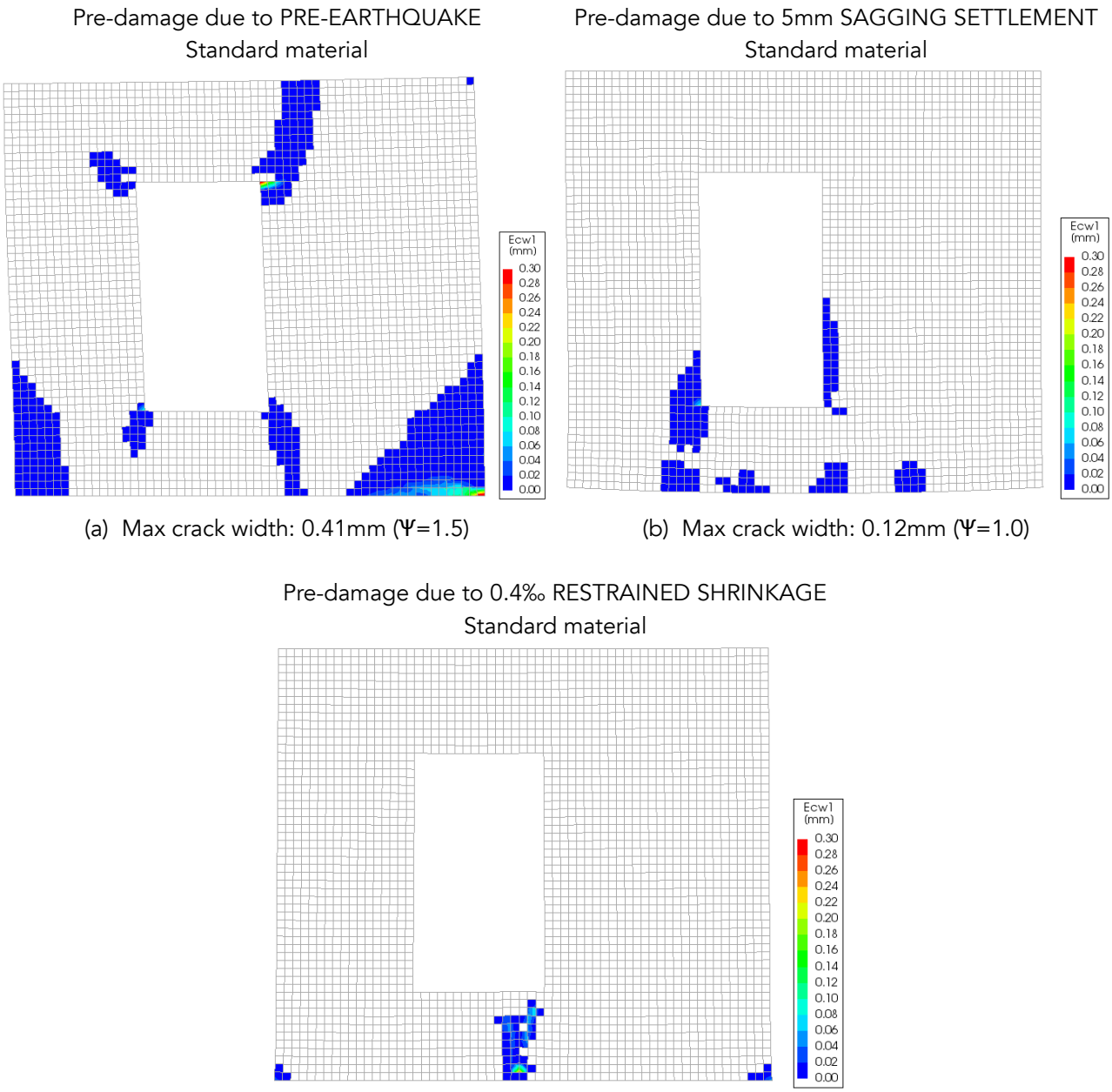

(a) Max crack width: 0.41mm (Ψ=1.5)

(b) Max crack width: 0.12mm (Ψ=1.0)

(c) Max crack width: 0.29mm (Ψ=1.4)

Figure 6.12. Crack width plots related to the moment of maximum pre-damage for the standard material scenario due to: (a) pre-earthquake (0.17g), (b) 5mm sagging settlement, (c) 0.4‰ restrained shrinkage. Deformed shape magnified by 100. More information about the Ψ values can be found in Section 7.4.

Based on the damage pictures, the chosen scenarios seem to lead to meaningful, realistic initial damage patterns.

The evolution of the damage due to an earthquake of 0.10g PGA for the scenarios already shown in Figure 6.12, is depicted in Figure 6.13.

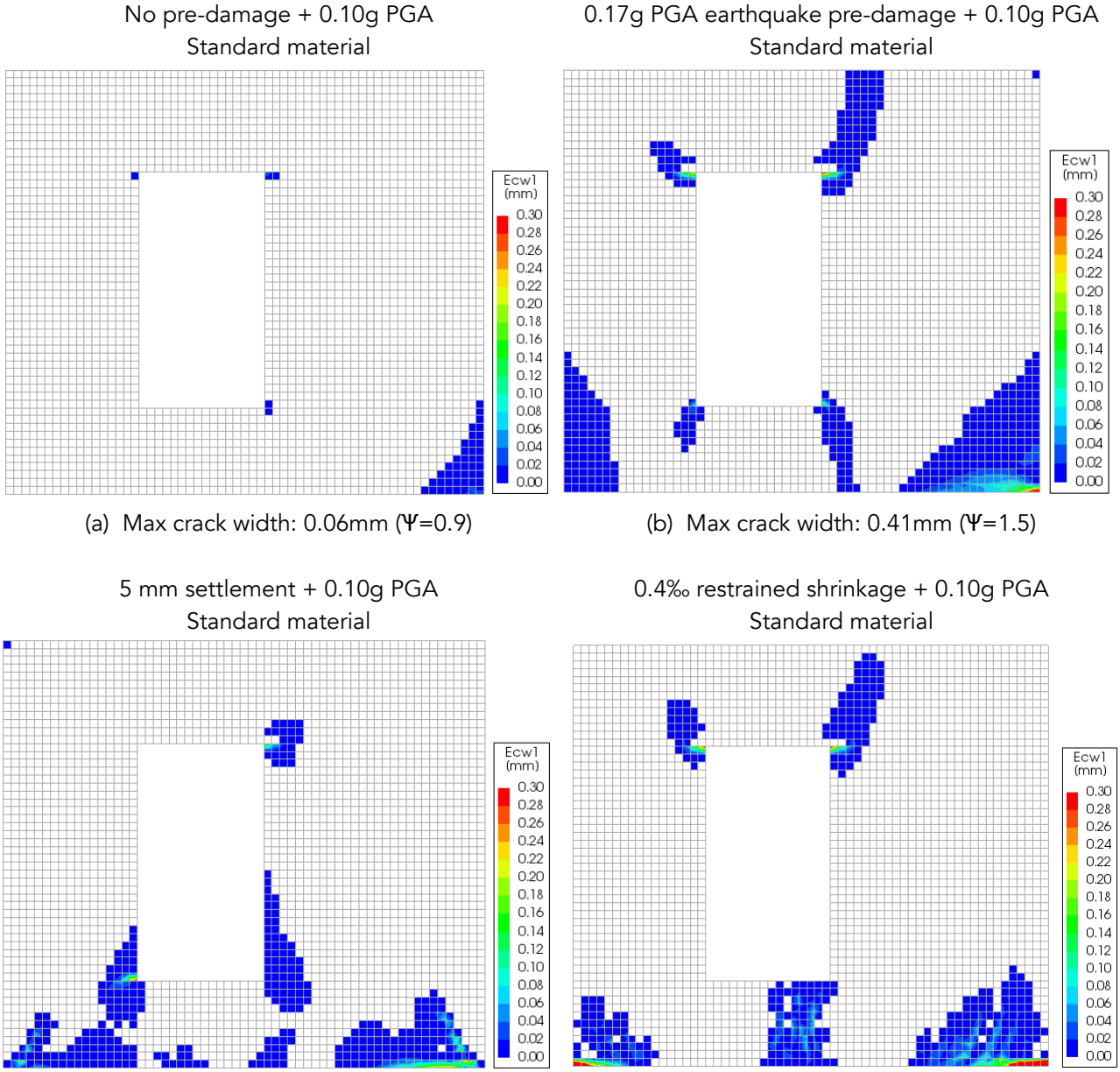

Figure 6.13. Cumulative crack width plots for standard material at the end of 0.10g motion for different initial conditions: (a) no pre-damage, (b) pre-earthquake (0.17g), (c) 5mm sagging settlement, (d) 0.4‰ restrained shrinkage. Undeformed mesh. More information about the Ψ values can be found in Section 7.4.

The damage pattern generated to a 0.10g earthquake is shown in Figure 6.13.a. No pre-damage was applied for this analysis. Figure 6.13.b describes the cumulative damage due to a 0.10g PGA motion applied after the initial earthquake of 0.17g. Neither additional cracks nor considerable crack width increase are detected. Hence the damage value Ψ remains constant.

The same earthquake results are more severe for the initial settlement condition (Figure 6.13.c). A new crack appears at the top right window corner and existing cracks grow at the base of the wall. Maximum crack width increases about 0.22mm. The damage parameter Ψ grows to 1.7 (+70%). Cracks develop in the top window corners in the shrinkage pre-damage scenario (Figure 6.13.d) as well as delamination cracks in the wall corners. An increase of 36% is detected in the Ψ value.

Figure 6.14 shows a comparison for the three different materials. As an example, the scenario corresponding to 0.4‰ shrinkage pre-damage was taken in combination with a 0.20g PGA earthquake motion. As expected, the most damaged model is the one with the weaker masonry parameters (Figure 6.14.a) which suffers a clear rocking of the right pier. Large cracks are detected in two window corners and at the bottom of the right pier. Moreover the damage underneath the window already induced from the

shrinkage pre-damage (Figure 6.12.c) extends due to the shaking. The damage pattern results in all the three cases quite similar except for the width of the cracks, which is larger for the weaker material.

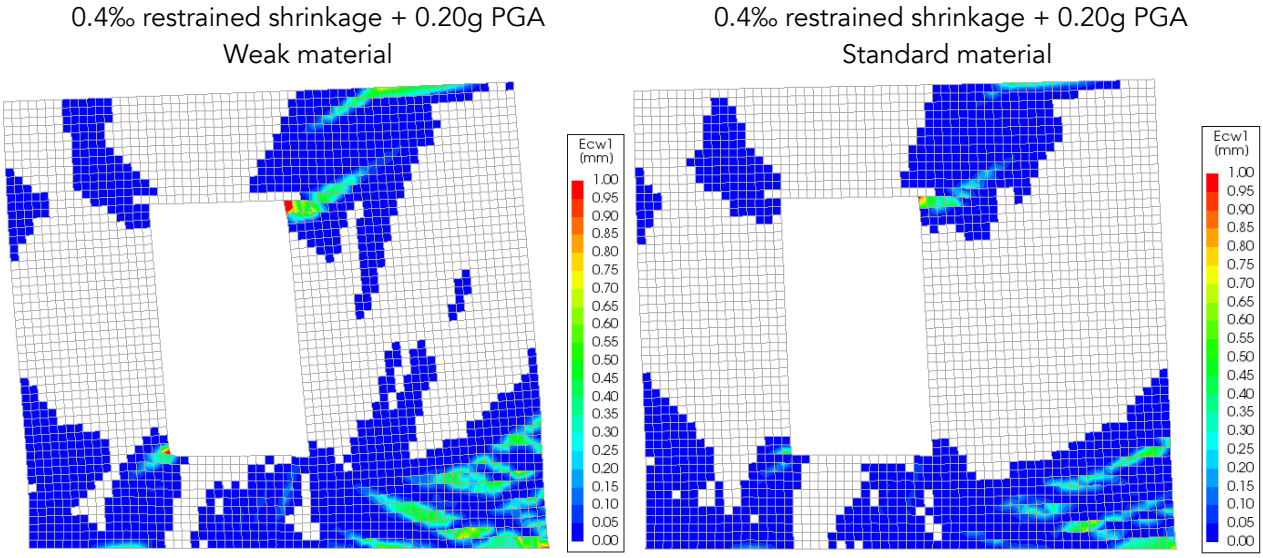

(a) Max crack width: 2.06mm (Ψ=2.9) (b) Max crack width: 1.11mm (Ψ=2.5)

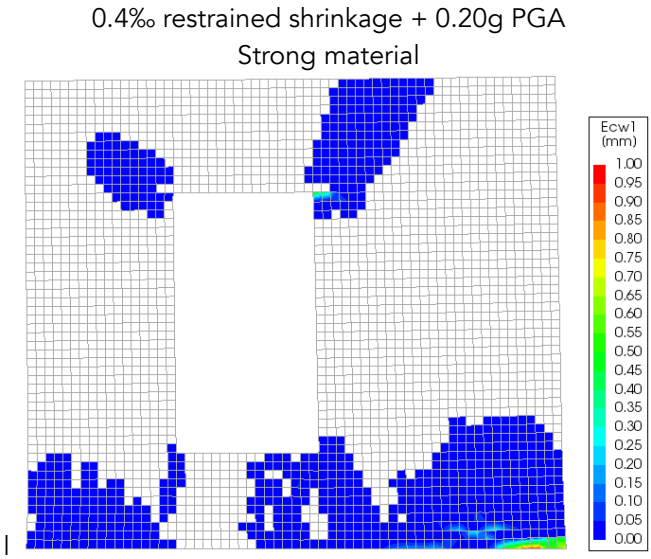

(c) Max crack width: 1.00mm (Ψ=2.2)

Figure 6.14. Crack width plots related to the moment of maximum damage during 0.20g motion for the 0.4‰ shrinkage pre-damaged condition: (a) weak, (b) standard, (c) strong material. Deformed shape magnified by 50. More information about the Ψ values can be found in Section 7.4.

Next, two additional motions (PGA=0.20g and 0.30g) are investigated for different pre-damage scenarios and the standard material. Figure 6.15 and Figure 6.16 present the cumulative maximum crack width generated during the entire analysis for the models with the standard material and motion PGA equal to 0.20g and 0.30g respectively.

No pre-damage + 0.20g PGA
Standard material

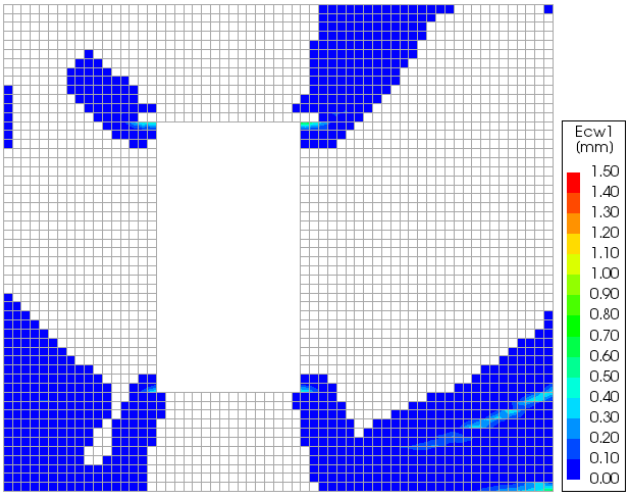

(a) Max crack width: 0.80mm (Ψ=1.9)

0.17g PGA earthquake pre-damage + 0.20g PGA
Standard material

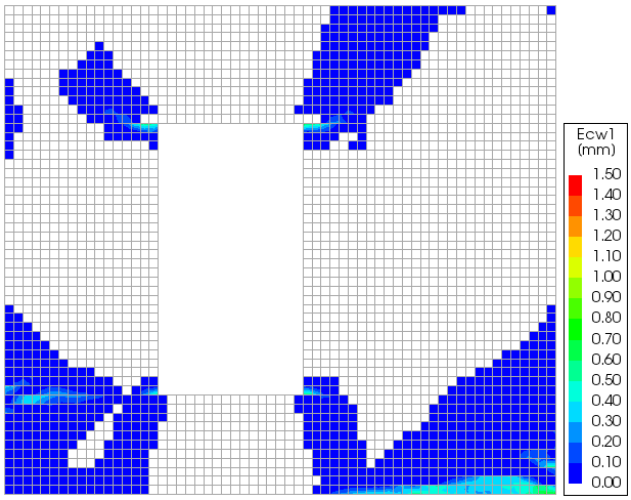

(b) Max crack width: 0.90mm (Ψ=2.2)

5mm settlement + 0.20g PGA
Standard material

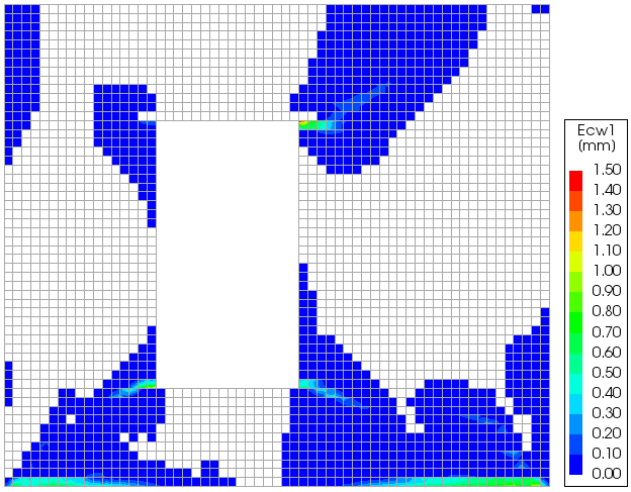

(c) Max crack width: 1.82mm (Ψ=2.7)

0.4‰ restrained shrinkage + 0.20g PGA
Standard material

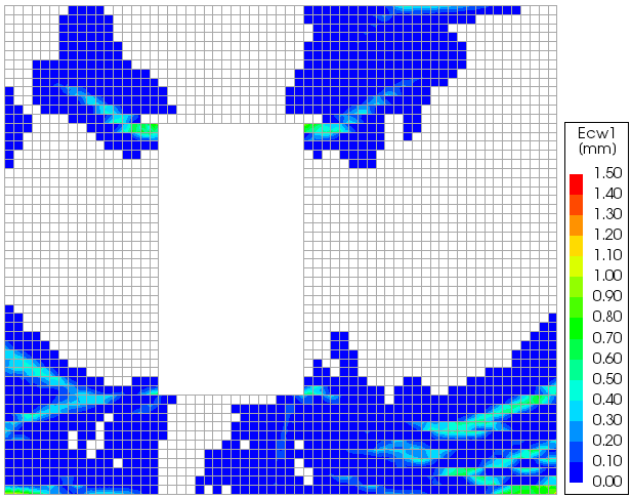

(d) Max crack width: 1.67mm (Ψ=2.5)

Figure 6.15. Cumulative crack width plots for standard material at the end of 0.20g motion for different initial conditions: (a) no pre-damage, (b) pre-earthquake of 0.17g, (c) 5mm settlement, (d) 0.4‰ restrained shrinkage. Undeformed mesh. More information about the Ψ values can be found in Section 7.4.

All the plots show cracking of both the wall piers, near top and bottom of the window. The scenarios where the model are pre-damaged with settlement (Figure 6.15.c and Figure 6.16.c) reveals slightly less damage on top of the wall. In all cases, major cracks extend from the window corners to the wall corners. Slight vertical cracking in the middle bottom part of the wall is detected, especially for the pre-damage due to shrinkage, where this zone was already integrally cracked (Figure 6.12.c). The crack widths there, however, remain small (Figure 6.15.d and Figure 6.16.d). Major cracks are located in the window corners for all the cases.

No pre-damage + 0.30g PGA
Standard material

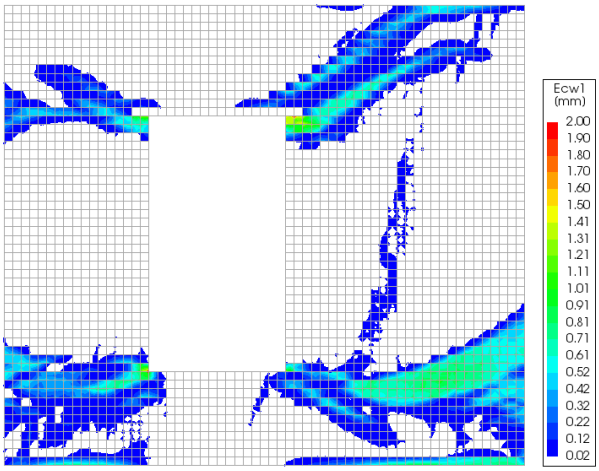

(a) Max crack width: 2.41mm (Ψ=3.2)

0.17g PGA earthquake pre-damage + 0.30g PGA
Standard material

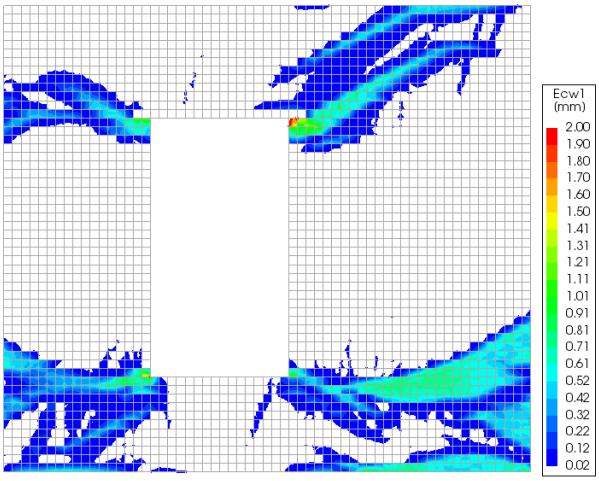

(b) Max crack width: 2.71mm (Ψ=3.4)

5mm settlement + 0.30g PGA
Standard material

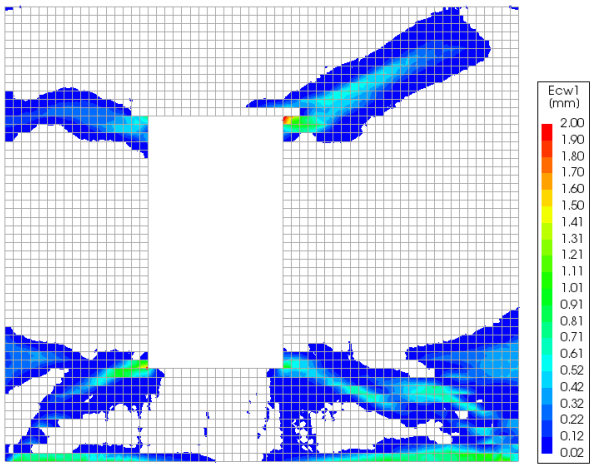

(c) Max crack width: 2.70mm (Ψ=3.2)

0.4‰ restrained shrinkage + 0.30g PGA
Standard material

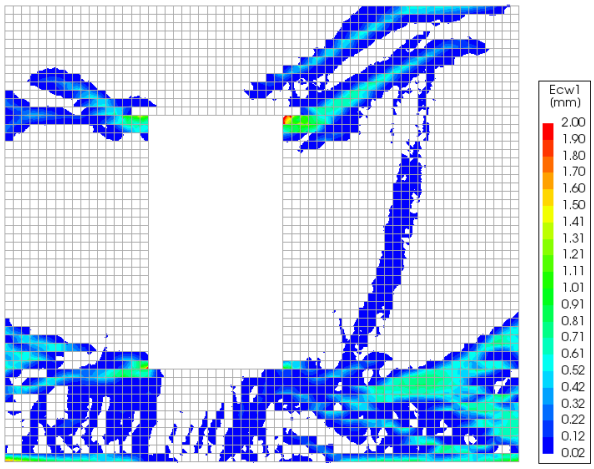

(d) Max crack width: 2.65mm (Ψ=3.0)

Figure 6.16. Cumulative crack width plots for standard material at the end of 0.30g motion for different initial conditions: (a) no pre-damage, (b) pre-earthquake of 0.17g, (c) 5mm settlement, (d) 0.4‰ restrained shrinkage. Undeformed mesh. More information about the Ψ values can be found in Chapter 7.4.

Two interesting scenarios in which the same PGA motion is applied in a repetitive way have been analysed. The purpose is to check whether an increment of damage occurs.
The maximum crack width and the damage parameter Ψ of the two cases are summarised in Table 6.6.

Table 6.6. Comparison of the maximum crack width and its relative difference before and after the repetitive earthquake.

Scenario	Pre-damage Max Crack Width [mm]	Final damage Max Crack Width [mm]	Max Crack Width Relative Difference [%]
0.05g PGA earthquake pre-damage + 0.05g PGA earthquake. Weak material	0.101 (Ψ=1.0)	0.111 (Ψ=1.1)	+9.90% (+10.0%)
0.20g PGA earthquake pre-damage + 0.20g PGA earthquake. Strong material	0.144 (Ψ=1.1)	0.264 (Ψ=1.3)	+83.33% (+18.2%)

For the model with the weak material in which a 0.05g earthquake is applied twice, an increase of about 10% in the maximum crack width is identified. Similar behaviour is found in the scenario with the 0.20g earthquake for the strong material: growth in the crack width is observed as well, though significantly larger.

When a smaller motion in PGA is employed after a certain motion, no increase of crack width and damage pattern is noticed.

The final table filled in with the results of the damage parameter Ψ for all the scenarios is shown in Section 7.4.1, Table 7.2. It gives an overview of the overall damage (by using the parameter Ψ) generated by the pre-damage case and its evolution after the dynamic motion.

6.5. Conclusions of Chapter Six

The in-plane wall model, calibrated on the experiments in Chapter 5, was employed for the assessment of the resistivity curves. Instead of a static repeated loading, a dynamic base excitation was used to apply the earthquake in the two horizontal and vertical directions. A representative earthquake motion of the Groningen region was applied. Overburden and material properties have been kept as in the validated model of Chapter 5. For a more realistic hypothesis, mass elements have been implemented on top of the wall in order to consider the additional inertia generated by a fictitious slab and roof. Results of the dynamic analyses are in line with the repetitive static model. The damage configuration in the model wall reproduce fairly well the ones found in the experimental test and in the validated model.
Future investigations are required to fully validate the model from an experimental dynamic test. Sensitivity analyses to determine the effect of the vertical motion on the model were performed. Two models, with and without the vertical earthquake, were implemented. Negligible differences in crack pattern and maximum crack width are observed between the two different models.

To take into account the variability likely found in real cases, different pre-damage scenarios were considered: one virgin case without pre-damage, two initial pre-damage earthquakes, two scenarios of shrinkage, and two cases of middle-sagging settlement. Moreover, different PGA amplitudes and three different material properties were considered as well in the computational framework.
More than one-hundred NL-TH-A were run and analysed. For each analysis, the overall damage state of the wall was estimated by using the damage parameter Ψ. Comparing the damage induced by the initial condition with literature cases as Giardina et al. (2015) and Rots et al. (1997), reasonable damage patterns were obtained. Small cracks underneath the window and at the bottom corners of the window are detected for the initial settlement scenario. A vertical crack grows in the window bank along with delamination damage in the bottom wall corners for the restrained shrinkage scenario.

Comparing the influence of the material properties, models with weaker material properties seem to suffer more damage than the stronger ones.
From the all damage pictures, the settlement pre-damage scenario seems the one affected the most from the dynamic load especially for standard and strong material. Earthquake and shrinkage pre-damage cases experienced a lower increase in damage than the settlement pre-damage.

From the analyses of repetitive dynamic tests of few scenarios, in which two identical motions were applied sequentially, an increase of the overall damage was observed (by 10%). The influence of additional earthquakes in the increment of damage needs thus to be further investigated.

Chapter 7

Probabilistic Framework Towards Resistivity Curves

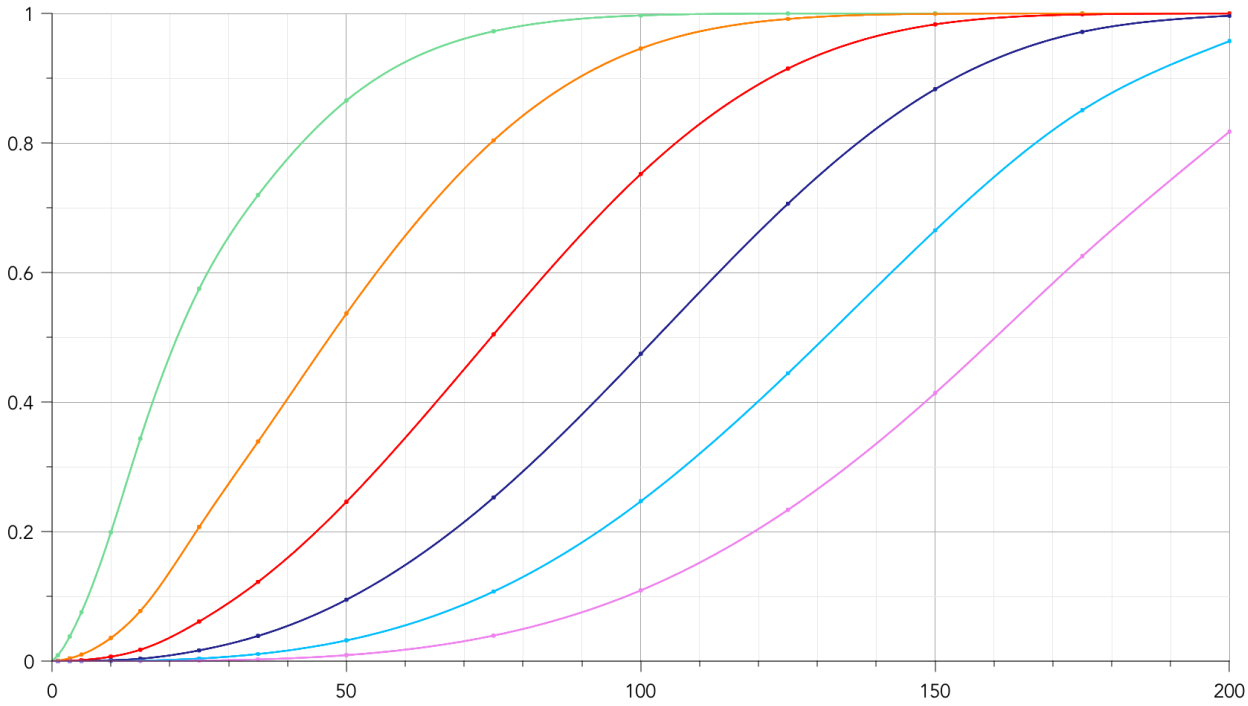

TU Delft

7. Probabilistic Framework Towards Resistivity Curves

7.1. Introduction

This chapter attempts to collect and extrapolate the findings of previous chapters into a comprehensive set of 'resistivity curves'. To accomplish this, relationships and uncertainties are studied.

First, a brief discussion of the nature of the curves is required: Resistivity curves, vulnerability curves, damage curves, or fragility curves are S-like, cumulative probability curves that present the probability of exceedance of a certain condition for a given return period or a given intensity of a hazard or multi-hazard. While similar, some subtle differences exist by convention. The curves presented here have been denoted 'resistivity curves' because they mainly focus on the resistance side (R), less so on the solicitations (S) and are specific to one structure and so lack the comparison of different structure types more typical of vulnerability curves, or the structural representativeness of loading and resistance as done by fragility curves. Similarly, they are fabricated upon a relevant yet limited representation of the hazard, thus are more specific than fragility curves. Finally, because they show the resistance to damage, they have been denoted resistivity curves. To express the preliminary nature of the curves, they are also denoted as indicative resistivity curves.

To fabricate these curves, however, it is necessary to elaborate a framework to determine all the elements that partake and are relevant in causing light damage. The framework includes a look into the nature of the earthquakes that damage the structures, other damage causes for the structures, and the structures themselves. It also shows the areas into which the work was divided and how these interact with each other.

In this context, the framework of Waarts (1997) is first analysed as an important reference as guide for light damage from vibration sources. It serves as a comparison point for the framework of this report and results derived with it.

The resistivity curves are derived for both computational and experimental cases. The material, the uncertainty in the observed relationships, the stiffness, and the level of pre-damage are some of the variables incorporated into these curves. Nonetheless, the curves presented in this report are a first glance into light damage and have thus important limitations, the reader is here referred to Section 7.6.2.
Rough resistivity curves are derived from the experimental laboratory tests to provide another comparison for the results of the more-encompassing computational models.

Key questions answered in this chapter are thus:

- What is the framework of Waarts (1997), which hazards and effects does it contemplate and what kind of probability is computed?
- What actions and effects have been deemed relevant to contribute to the development of damage in masonry as part of the framework of this study?
- How are resistivity curves produced from the computational and experimental results and what are the key observations from these?
- How do these resistivity curves based on the damage level parameter compare to more simple definitions of damage state one (DS1) and to guidelines for vibration-induced damage, for instance, the SBR?

7.2. Background: Reproduced Framework of Waarts (1997)

In the late nineties, it was necessary to understand what was the probability of damage when masonry buildings were subjected to vibrations produced by traffic and construction activities such as piling. A limit for the peak particle velocity (PPV or PGV) measured near the building was set at 5 mm/s, but this wasn't related to a probability of damage. Risk management required that the levels of vibrations be related to failure probabilities.
In this context, Waarts (1997) produced a framework to compute the probability of damage (initiation) in masonry given PPVs, essentially, a fragility curve for peak particle velocities.

Due to the lack of fragility curves relating earthquake vibrations and the initiation of damage (or the lower damage states), the outcome of Waarts' framework was used to evaluate masonry structures affected by earthquakes.
For this reason, Waart's framework has been analysed and reproduced as part of this study, also updating the input values to match recent laboratory investigations into site material parameters, further expanding the comparison. This chapter details the reproduction and application of the aforementioned framework.

7.2.1. Description of the Framework of Waarts

The framework is based upon a simple limit state function to assess whether the tensile strength has been exceeded somewhere in the structure. An overview of the framework is shown in Figure 7.1.

$$\mathbf{Z=f_t-\sigma_{ini}-E\cdot\varepsilon}$$

Where:

f_t	is the tensile strength of masonry
σ_{ini}	is a random initial stress
E	is the stiffness of masonry (Young Modulus)
ε	is the strain caused by the vibrations

The strain caused by vibrations is determined in combination with a dynamic analysis from Raaijmakers (1994) and with a linear elastic model of a wall with a window. The procedure is as follows:
The study from Raaijmakers (1994) is used to relate the PPV to a maximum strain in a solid wall. Raaijmakers computed the dynamic amplification caused by ground vibrations acting on a solid wall. The vibrations take the form of surface waves that cause a deformation at the bottom of the wall in the shape of an oscillating sine valley or a full sine cycle (see Figure 7.1). The vibration frequency is modified to observe its influence in the relation of PPV and maximum strain:

$$\mathbf{\varepsilon_s=PPV\cdot H(f)}$$

Where:

εs	is the maximum tensile strain in the solid wall
H(f)	is the transfer function between strain and PPV depending on the frequency of the vibration.

Waarts continues by modelling different wall configurations with varying window positions. For the case of one static sine valley, the strain obtained is compared to that of the solid wall for the same ground deformation. In this way, a relationship is found between the PPV and the maximum strain in a wall with a window. From all the modelled cases, the maximum strain amplification factor is used:

$$\mathbf{\varepsilon=k\cdot\varepsilon_s}$$

Where:

k	is the amplification factor due to stress concentrations by window

Finally, all parameters are assigned a probabilistic distribution with corresponding parameters, and the limit state function is evaluated with a FORM (First Order Reliability Method) for discrete PPV values to compute the probability of exceedance of the tensile strength.

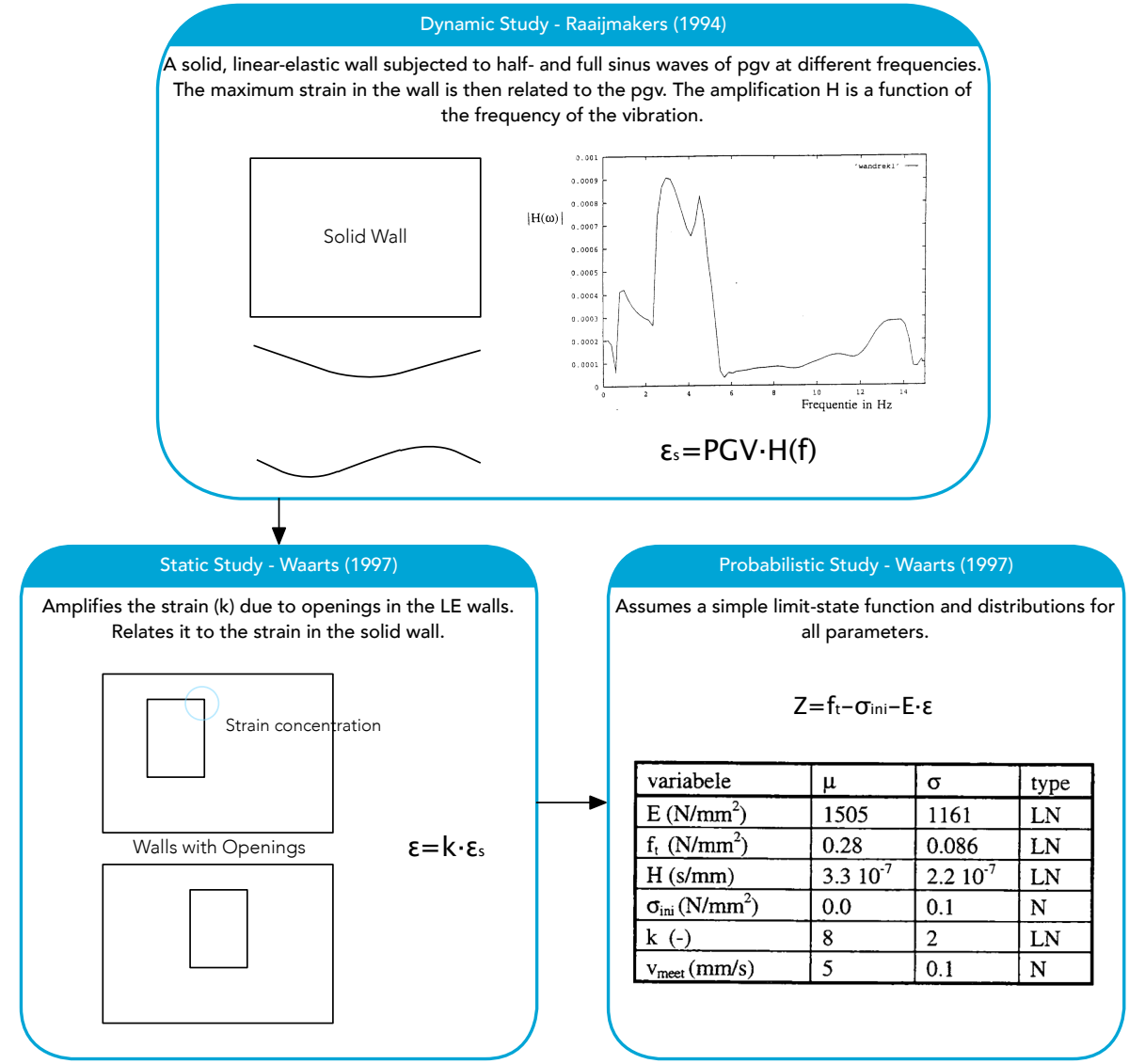

Figure 7.1. Overview of the framework from Waarts (1997).

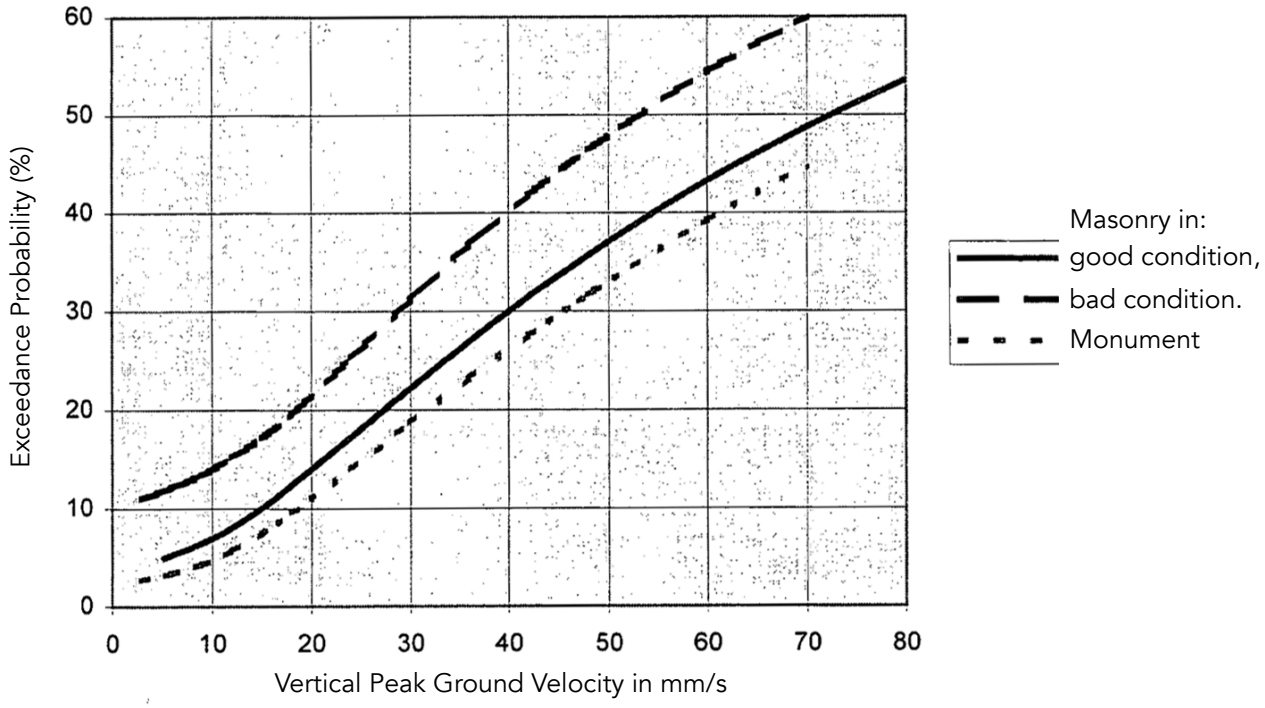

Figure 7.2. Fragility curves by Waarts (1997). Adapted descriptions.

7.2.2. Limitations of the Framework of Waarts

Foremost it must be said that the limitations of Waart's framework are reasonable given the tools available twenty years ago and the context in which it was formulated. It is important to observe that the purpose of the framework was to provide probabilistic values from which the initiation of damage could be estimated when a masonry structure was subjected to nearby vibration sources.
Nevertheless, it is vital to understand its limitations to realise why its use is disputable for vibrations coming from earthquakes and for damage categorised into states.

Firstly, the computed probabilities mark the exceedance of the tensile strength at one point in the structure. This corresponds to the very initiation of damage (Ψ_D>0), but whether this damage is influential for the behaviour of the structure or corresponds to the formation of cracks that can be observed (c_w>0.1mm, Ψ_D>1), is not and can not be described by the framework.

Secondly, the framework was developed to assess the influence of vertical vibrations coming from nearby-sources. While the underlying study of Raaijmakers (1994) does work with coupled horizontal and vertical excitations, Waarts (1997) only performs static analyses in the vertical direction.
Earthquake vibrations travelling from further away do not commonly deform the soil with sine-shape wavelengths short enough to produce vertical deformations that would cause bending in the foundations of walls. However, in cases of very bad soil conditions (unusual in the area of Groningen affected by earthquakes, such as revealed in the studies by ARUP, 2013) and longer walls (such as farm houses), these surface deformations may be able to produce non-negligible deformations, but then, stronger foundations are also more likely on bad soils.
Lateral excitations, instead of vertical base excitations common to the actions of earthquakes are not contemplated by the framework.

Thirdly, the framework does not relate the frequency of the vibrations to the expected wavelength of the soil deformation. This is a conservative simplification of the framework which is included in the uncertainty assigned to the transfer function parameter, but, the wavelength is dependent on a relation between the stiffness of the soil and the frequency of the vibration, meaning that only specific frequencies will produce the sine valley (worse case deformation) assumed by the framework. Moreover, for vibrations travelling from farther away, the natural frequencies of the soil also becomes important, further modifying the wavelength and (reducing) the strain amplification employed by the framework.
In sum, the framework is conservative in selecting the soil deformation at the foundation, and this is reflected in higher uncertainty in the final function.

Fourthly, the change in dynamic behaviour of the solid reference wall used in the study by the inclusion of openings or by the varying mass of other connected structural components (such as the one of attached floors) is not observed by the framework. This is in line with the other dynamic simplifications of the framework.

Fifthly, because the framework does not accept input regarding the configuration of the wall or its initial stress condition (beyond an assumed random value of stress), it can only (and is meant to) be applied in a general way to a pool of structures and will not be as reliable when used for individual cases.

Finally, since the framework is based on an elastic analysis it cannot be used to observe the change in dynamic behaviour of the structure because of the new damage nor the propagation of damage beyond its initiation.

In conclusion, the limitations of the framework, originally intended to provide understanding of a safe boundary up from which damage can be expected when unreinforced masonry walls are subjected to (vertical) vibrations from nearby sources, make it less suited for the analysis of quantifiable damage caused by earthquake vibrations.

7.2.3. Reproduction of the Framework of Waarts

In spite of the aforementioned limitations, the framework from Waarts (1997) provides a basis upon which to build a framework tailored towards the analysis of lower damage levels resulting from earthquake actions. Moreover, it is insightful to observe how the results offered by the original framework are modified when the input parameters are updated to match recent material studies.

For these purposes, the framework from Waarts (1997) has been reproduced using the original input values and distributions, and the same limit state function, but with a fully probabilistic analysis (MonteCarlo) as opposed to the semi-probabilistic analysis (FORM) originally employed. This is because with current computational resources, a fully probabilistic approach is more straight-forward to implement and will produce more accurate results, and because the precise type of FORM approach applied in Waarts' report is not known, making the use of a different FORM approach questionable.

The result of this fully probabilistic exercise if shown in Figure 7.3.

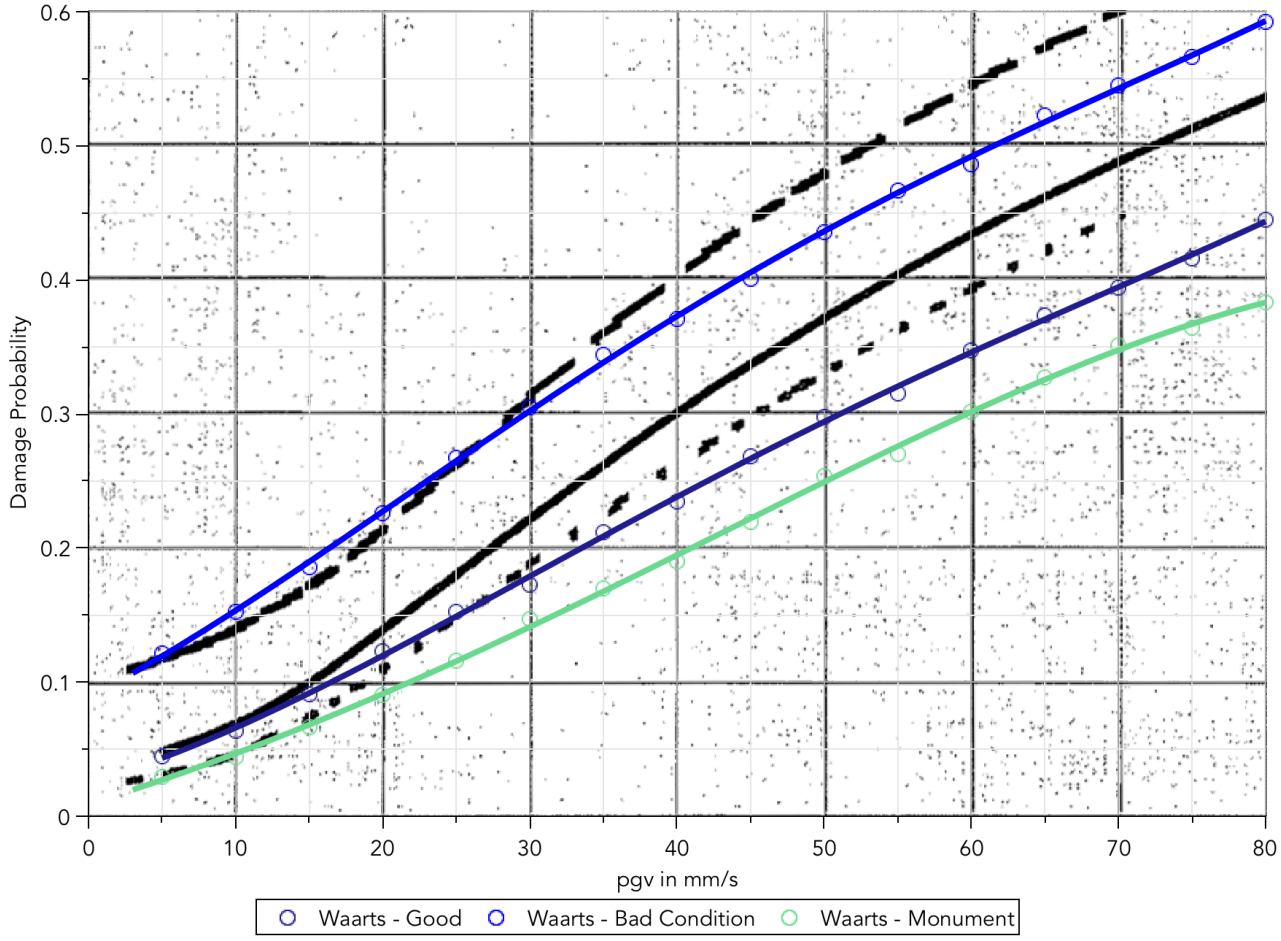

Figure 7.3. Reproduced curves of Waarts (1997) in colour, overlaid on original black graph.

7.2.4. Comparison and Discussion

In Figure 7.3 it can be observed that the curves match the order and overall gradient of the original curves. Also, the points for a PGV value of 5mm/s are exactly the same. However, as the PGV increases, the reproduced curves diverge from the original ones. There are two possible explanations for this:
First, the fully probabilistic method of a MonteCarlo simulation run with a sufficient (exaggerated) number of samples will be more accurate in evaluating the reality of the limit state function than a FORM approximation. Because of this, some divergence between the methods is expected, especially when the probabilities are not small, as the linearisation around a design point employed by the FORM method becomes less accurate. However, the observed differences of up to 20% in respect to the original curves seems excessive to be attributable alone to the differences in method.
Hence, barring any undetected computational errors on any of the two methods, the only other difference must lie with the input values. While the input values used in the original framework are reported, they are not consistent throughout the report. For instance, the values reported in a table are modified in a paragraph later on, so that no summary table with all the definitive input values exists. Similarly, it is possible that the values and parameters input to the FORM software were not exactly the same as those reported; in fact, in conversation with colleagues familiar with the matter, this seems to have been the case.

Nevertheless, the input values can be modified from the ones reported to match updated knowledge regarding the strength and stiffness of masonry material in the area prone to earthquakes.
Table 7.1 summarises the modified input values adapted from recent companion material tests to ensure comparability with the curves presented later in this chapter. For clay, the values are taken from averages of NAM2 and NAM3 projects where available (see Appendix, Table 9.1), and for calcium-silicate, from NPR.

Table 7.1. Modified input values for use in the reproduced Waarts framework.

Property	Waarts (1997)		Current Knowledge				Comments
	Good Condition		Calcium Silicate		Clay		
	Mean	St dev	Mean	St dev	Mean	St dev	
E (MPa)	1505	1161	4000	1400	3630	828	Recent masonry tests have revealed stiffer values
f_t (MPa)	0.28	0.086	0.20	0.050	0.12	0.058	From fw - bond strength
H dynamic A.F H=strain/PGV	3.3E-07	2.2E-07	5.0E-07	3.0E-07	5.0E-07	3.0E-07	Considering soil in frequencies lower than 10Hz, more representative.
σ initial tensile stress (MPa)	0	0.13	0	0.20	0	0.20	Increased by settlements, thermo-hygro effects, and other pre-damage actions - estimation
k window amplification	8	2	8	2	8	2	Kept equal pending further research

As can be observed in Figure 7.4, the curves with updated values have a higher probability of damage for all values of PGV. This is respectively due to the weaker but stiffer masonry properties.
However, the curves seem to be more realistic than the original curves because:
It would seem that the updated curves intersect the horizontal axis indicating that there is a PGV boundary below which no damage is expected.
Also, a high probability of damage for higher PGVs is a reasonable outcome as only the initiation of damage, not the propagation or quantification, is being contemplated. It is logical that at vibration levels of 50mm/s, most structures have exceeded their tensile strength somewhere in the structure; whether this represents detectable damage is not shown by Waarts' framework.

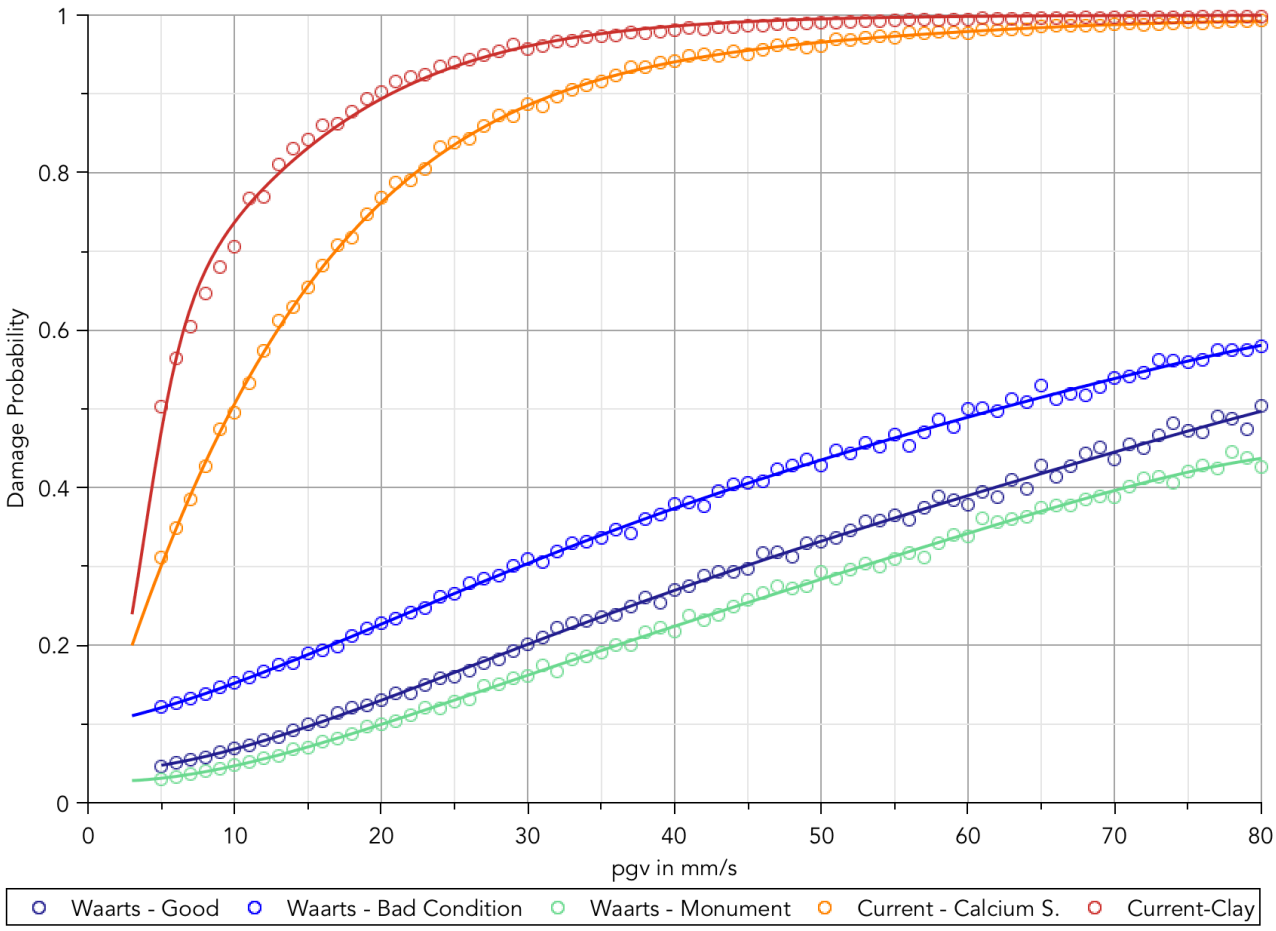

Figure 7.4. Reproduced curves from Waarts (1997) and updated values with the same methodology.

The difference in the curves also demonstrate that the linear methodology is very sensitive to the selected input values. Since the updated curves utilise lower values for the tensile strength, they lead to a higher probability. The type of damage shown by the curves will then depend on the input tensile strength. If the direct tensile strength is used, then the curves will show the probability for the very initiation of damage; but, when a higher value is used, as for instance the flexural tensile strength, then the curves will relate to some degree of (un-quantifiable) damage. Since the linear calculations can only indicate the initiation of damage, curves which correspond to some damage, cannot be accurate.

In conclusion, the framework of Waarts (1997) has been successfully reproduced using a MonteCarlo simulation and the observed results show that unreinforced masonry structures seem to be more vulnerable towards high-PPV surface-wave vibrations originating from nearby sources than the original results showed. However, the framework has limited applicability in the ambit of earthquakes, precisely due to its focus on vertical ground deformations and the fact that it only serves to predict the initiation of damage.

Nevertheless, its understanding provides a good base to build a framework that incorporates the effects relevant to earthquake actions such as lateral base excitations, quantifiable damage, and initial pre-damage.

7.3. General Overview of the *Light Damage Framework*

To be able to give the laboratory experiments and computational models a realistic background, base them on representative cases, and put their results into perspective, a framework, identifying and relating the various elements that participate in helping to explain and assess cracking, was required.
Additionally, the analyses needed to include the results of the study into an illustrative set of resistivity curves, are also given a place in the framework.

This subchapter describes and reasons the inclusion of each element in the framework and details what the approach is or has been to bring them to resolution.

7.3.1. Overview and Description of the Framework and its Elements

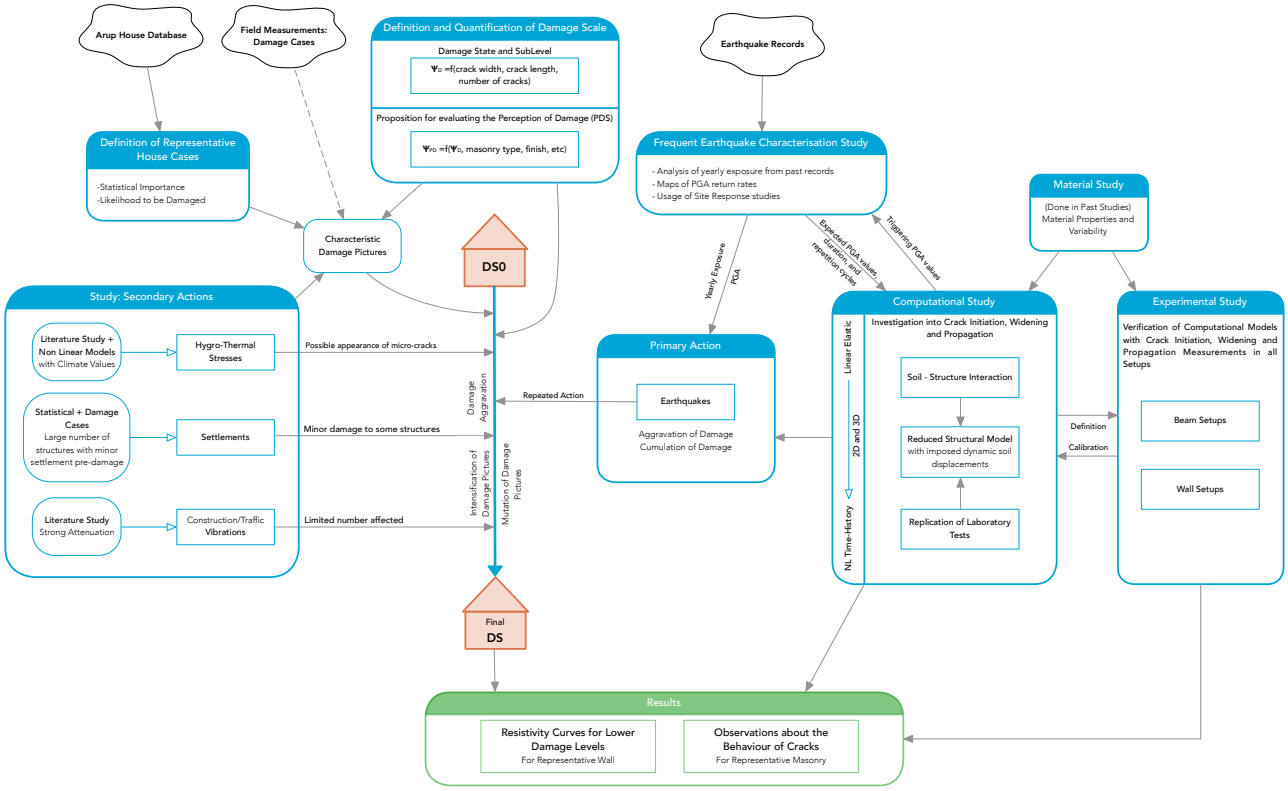

Figure 7.5. Complete overview of all the elements observed during the study and how they relate to each other in the framework (see next page for larger size).

Figure 7.5 gives a total overview of all the elements in the framework. These are all the points that need to be considered when contemplating this study of crack initiation and propagation in masonry.

Firstly, it is important to realise that the state of damage is a cumulation of the effects of many actions over time. Consequently, the framework has to observe the typical actions on masonry structures and evaluate their contribution to damage. It is thus also necessary to look at the pool of typical structures and relate the effects of these actions to characteristic crack patterns on these typical structures. Additionally, the intensity or degree of damage of these crack patterns needs to be assessed on a damage scale.

Secondly, from all the actions, earthquakes need to be given special attention. First, a characterisation of the earthquakes in the area, looking at their intensity and return period, is helpful in giving computational and experimental tests a realistic boundary. Then, a computational study based on non-linear models and tuned by a material and an experimental study, is used to evaluate the actions of earthquakes.

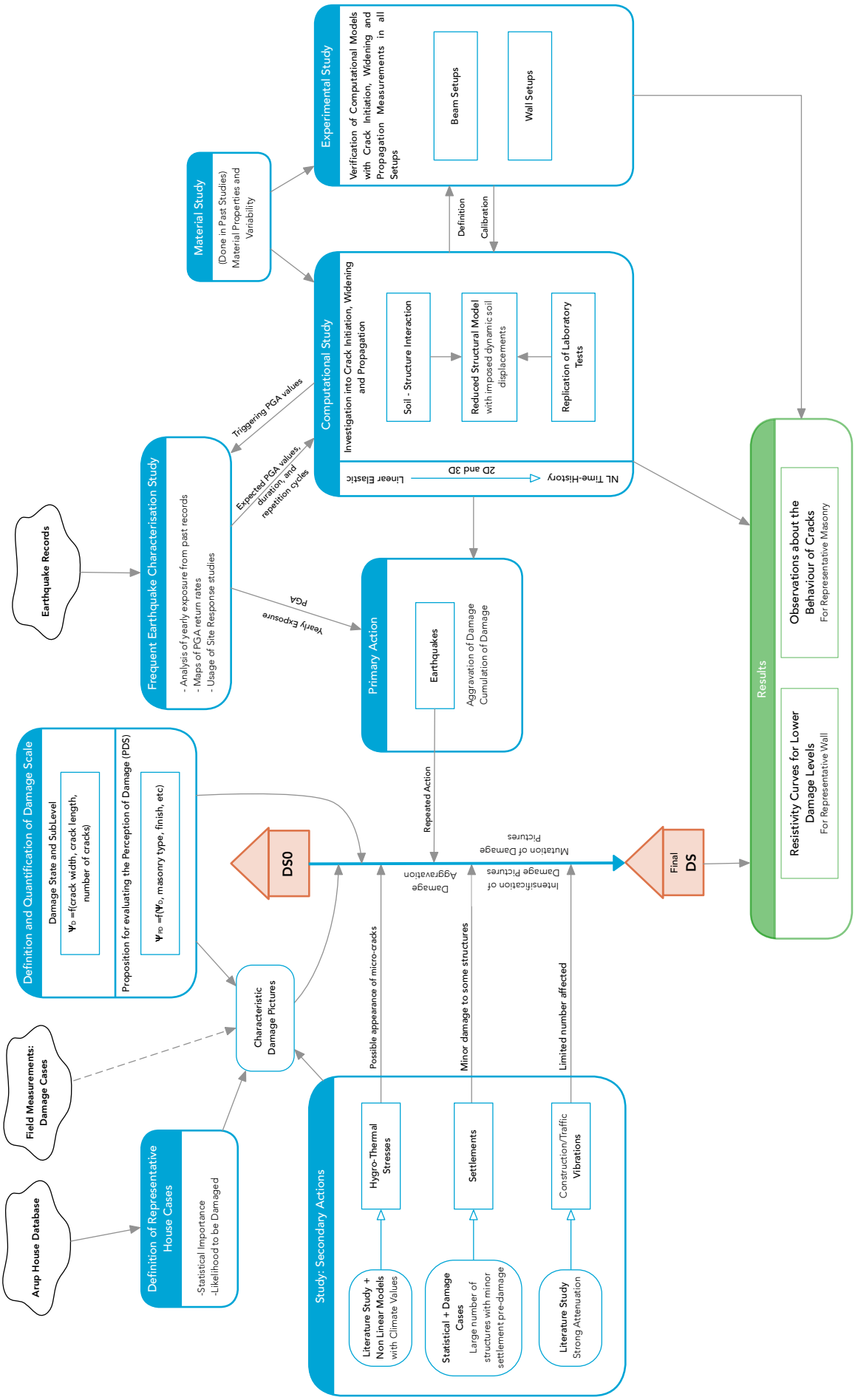
Experimental Study
Verification of Computational Models with Crack Initiation, Widening and Propagation Measurements in all Setups
Beam Setups
Wall Setups
Material Study
(Done in Past Studies)
Material Properties and Variability
Definition
Calibration
Computational Study
Investigation into Crack Initiation, Widening and Propagation
Soil - Structure Interaction
Reduced Structural Model with imposed dynamic soil displacements
Replication of Laboratory Tests
Linear Elastic
2D and 3D
NL Time-History
Triggering PGA values
Expected PGA values, duration, and repetition cycles
Earthquake Records
Frequent Earthquake Characterisation Study
- Analysis of yearly exposure from past records
- Maps of PGA return rates
- Usage of Site Response studies
Yearly Exposure
PGA
Primary Action
Earthquakes
Aggravation of Damage
Cumulation of Damage
Results
Observations about the Behaviour of Cracks
For Representative Masonry
Resistivity Curves for Lower Damage Levels
For Representative Wall
Definition and Quantification of Damage Scale
Damage State and SubLevel
Ψ_D =f(crack width, crack length, number of cracks)
Proposition for evaluating the Perception of Damage (PDS)
Ψ_{PD} =f(Ψ_D, masonry type, finish, etc)
Repeated Action
DS0
Mutation of Damage Pictures
Final DS
Damage Aggravation
Intensification of Damage Pictures
Characteristic Damage Pictures
Field Measurements: Damage Cases
Arup House Database
Definition of Representative House Cases
-Statistical Importance
-Likelihood to be Damaged
Study: Secondary Actions
Possible appearance of micro-cracks
Minor damage to some structures
Limited number affected
Hygro-Thermal Stresses
Settlements
Construction/Traffic Vibrations
Literature Study + Non Linear Models with Climate Values
Statistical + Damage Cases
Large number of structures with minor settlement pre-damage
Literature Study
Strong Attenuation

Description of the Elements of the Framework

Next, a description of the elements of the framework is presented.

Definition and Quantification of Damage

In this part of the project, the ways in which damage is displayed in unreinforced masonry structures is observed. A representative damage scale was devised to account for damage typically attributed to earthquakes. Light damage expressions are given emphasis and a methodology is sought, which allows comparison of real, experimental, and computational damage cases.
This was treated separately in Chapter 2.

Definition of Representative House Cases

A literature study complemented with the input from ARUP is used to define representative cases for the analyses. Initially, for this report, the cases have been limited to one wall panel. The boundary conditions (and window size) for these walls are selected based on the observed cases.

Study into Secondary Actions

Actions which trigger damage that is comparable or can be aggravated by earthquakes are revised. In particular, hygro-thermal effects, vibrations, and settlements are investigated. Typical crack patterns left by these actions are evaluated and compared to the results of computational models; typical intensities for these actions are defined.

Characterisation of Earthquakes

Earthquakes which may cause minor damage need to be characterised, that is, their intensity and the return period of this intensity, and their typical frequency content need to be assessed. Based on previous records and updated yearly rate, the intensity of frequent earthquakes can be defined.

Computational Study

This part of the project is based on a material characterisation study that has been previously performed at the Technical University of Delft. Its aim is to produce models that can accurately evaluate damage from earthquake actions. The models are used to expand the results from laboratory tests to more encompassing cases such as earthquake actions on slightly cracked walls from thermal and hygro stresses. The interaction with the soil is also analysed. The reader is referred to Chapters 3, 5 and 6.

Experimental Study

The experimental part of the project is aimed at researching the mechanics of fracture in masonry specimens subjected to various stress conditions and repetition cases. The laboratory tests have been treated in Chapter 4. These results can also be extrapolated to produce resistivity curves that can be compared to the computational results and provide a direct link from the experimental results.

7.3.2. Actions: Frequent Earthquakes and Secondary Actions

Actions on structures are any phenomena that lead to loads, deformations or changes in the structure. In all these cases, the actions impart stresses on the structure. High and/or sustained internal stresses can lead to plastic deformations, cracks and damage.

When evaluating the contribution of earthquakes to damage, it is necessary to analyse what other phenomena are acting on the structure and what their effect on the structure is before the earthquakes arrive.

- What are relevant actions that may (pre-)damage structures before earthquakes? How can these actions be characterised?
- What are typical damage pictures from the various relevant actions?
- What is the yearly rate of earthquake and their expected intensity?

For this study, only a limited number of actions are contemplated; these are:

- Environmental changes
  - Changes in temperature and humidity shortly after construction and on a daily or seasonal basis will lead to stresses on structures.
- Vibrations (other than earthquakes)
  - Vibrations from traffic or rail, from construction activities such as piling or the use of heavy machinery, may travel through the ground and induce deformations on the foundations of structures or vibrations in the structures themselves.
- Settlements
  - The consolidation of the ground due to changes in the humidity of the soil, additional loads, or strong vibrations may lead to settlements of the foundation of the structure, differential settlements will produce high stresses in structures. Mining and gas extraction also lead to general ground subsidence, but these have a smaller impact on localised differential settlements.
- Earthquakes
  - Earthquakes induce vibrations in structures which lead to stresses.

Internal actions, that is, normal use or change of use or configuration of the structure, are accompanied by a design evaluation and their effect is thus observed directly. Therefore, this type of action have not been considered.

An overview of the observed actions is provided in Figure 7.6.

*Figure 7.6. Overview of **external** actions that may lead or contribute to damage.*

Different actions will stress structures in distinct ways. Three general categories can be established:

- Restrained hygro-thermal expansion or contraction
- Induced vibrations in the structure
- Induced deformations or vibrations in the ground below the structure
  - These are either static due to the compaction of the soil for example, or dynamic due to traveling vibrations. An overview of the possible deformations of the soil is depicted in Figure 7.7.

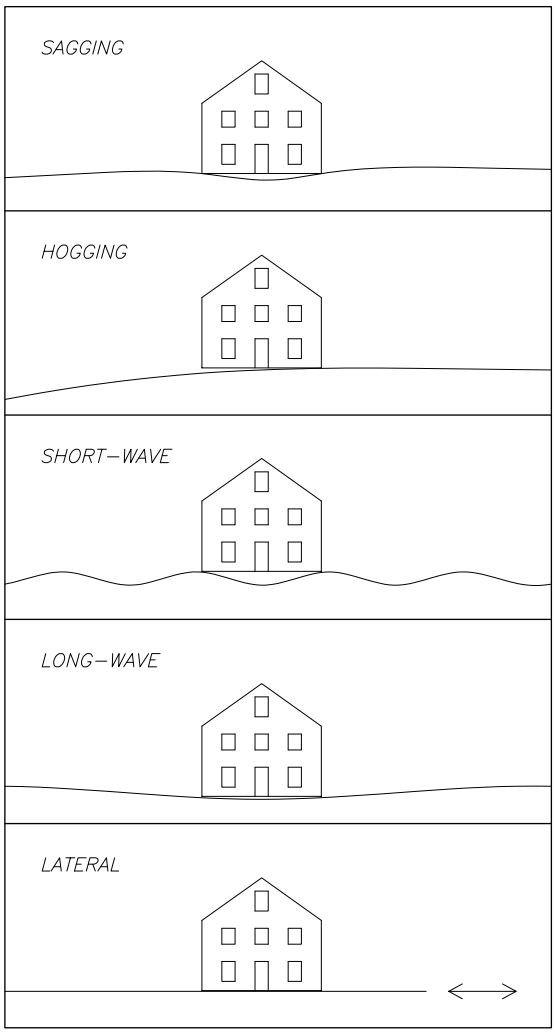

Figure 7.7. Overview of ground deformations. Exaggerated scaling.

Hygro-Thermal Changes

Changes in the humidity and temperature of the environment and the interior of the structure will lead to differential expansion and contraction between the masonry and the other elements of the structure; this is denoted hygro-thermal changes. Because different parts of the structure expand or contract at different rates (e.g. a wall built from humid, wet calcium silicate material that subsequently shrinks but is restrained by other elements like floors or beams), or because they are subjected to different temperatures (for instance a wall exposed to the sun restrained by a foundation in the cold ground), they will have differences in strain. This will lead to stresses in the elements.

Rots et al. (1997) analyses this phenomenon and gives an example of representative strain differences between values of 0.2‰ and 0.4‰.

Vibrations

Vibrations will damage masonry structures by inducing vibrations on the structure and by deforming the ground below the foundation of the structure. These vibrations come from piling operations, traffic, rail, and other construction activities like vibratory soil compaction or the use of heavy machinery.
The source of these vibrations is at or very near the surface, for which they differ significantly from earthquakes originating much deeper below the surface.

The SBR guidelines (2006)[1] give criteria to minimise damage to existing structures. Their values, based on other codes and empirical estimations, give contractors maximum peak particle velocities of the ground vibrations that they should guarantee at neighbouring structures to avoid damaging them. There are many empirical (Svinkin, 1999) and theoretical (Deckner, 2013) formulas to estimate vibrations based on the source energy, the soil, and the distance between the source and the point of interest. However, extensive research is available that proves that surface vibrations are attenuated quickly.
For example, Forbes et al. (2013) measured peak particle velocity (PPV) near piling operations for the installation of electricity transmission lines and also close to houses in a range from 1m to 35m. They observed that, while vibrations (of 25Hz) very close to the equipment exceeded limits (75mm/s), at a distance of 35m, they were down to 5mm/s.
Dungca et al. (2016) also performed a similar study measuring vibration levels not only at the surface but also at different soil layers up to 20m below the ground and confirmed that PGV of 100mm/s at 3m distance, drop down to 8mm/s at 30m. Moreover, they observed that silty soils attenuated the vibrations even quicker.
Jurevicius et al. (2015) conducted a similar study but instead of hammering piles, they used a vibratory soil compaction roller. They also monitored the development of damage in the nearby masonry house. They observed that at a close distance of 1m from the roller, vibrations of 50mm/s resulted in additional damage to the house by growth of existing cracks and development of new cracks. At a distance of 14m, however, they measured a PPV of 5.5mm/s and noted no damage.
Finally, Stagg et al. (1984) monitored the vibrations and damage on a wood-frame house over a two year period, built next to the path of an advancing open mine that used blasting. They equipped the house with strain gauges in numerous locations and measured the vibration levels. While the vibrations due to blasting were significantly more intense (up to 180mm/s) at the house, he also measured strains in the house produced by other actions and compared them to the level of vibration required to achieve similar strains. These results are observed in Figure 7.8.

While the tests on a wood-frame house are not directly applicable, it gives a good impression of how vibration-induced stresses compare to those of other actions. It is sensible to think that masonry structures, being more rigid, will be less susceptible to these types of vibrations.
Deckner (2013) states vibration values on masonry structures for actions similar to Stagg et al. (1984) around 30% lower than those in wood-frame houses.

1. The referenced report has been updated as of November of 2017.

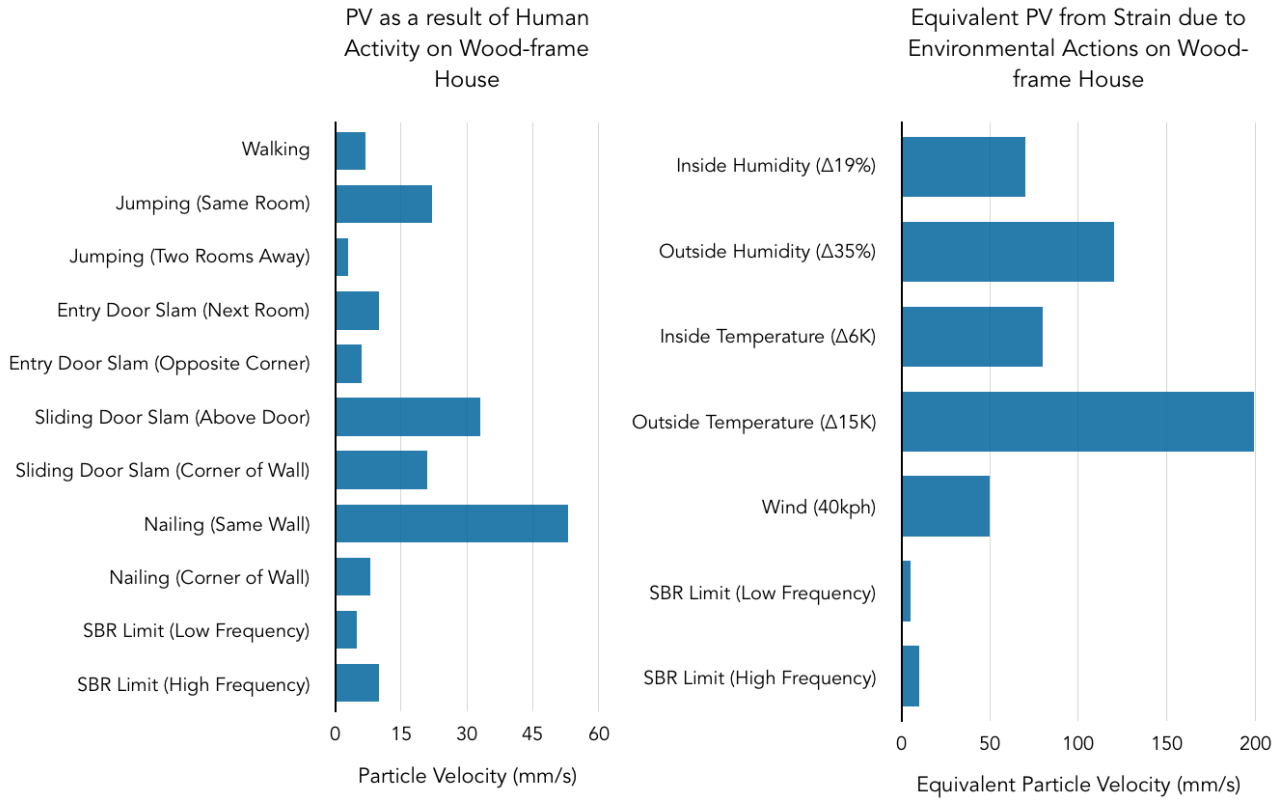

Figure 7.8. Equivalent PPV for different actions on a wood-frame house.

The SBR guidelines (2006) suggest a maximum value of 5mm/s (3mm/s for historic buildings or buildings in bad state, or 10mm/s for high frequency sources) for the PGV, and it has now been shown that for common vibration sources, attenuation assures this value at distances beyond 50m.

Moreover, soft soil layers like the ones in the area of Groningen, as was surveyed by Arup (2015), not only attenuate vibrations quicker, but also shift vibrations originating from impacts (as is the case with many forms of piling techniques) to lower frequencies. Arup (2015) observed that the frequencies of the surface soil in the area vary from 2 to 5Hz, and they also measured wave speeds in the ground of the order of 100 to 200m/s. This corresponds to wavelengths of 40 to 50m, which produce soil deformations similar to the long-wave depiction in Figure 7.7 for most structures.

Additional studies of masonry structures on a piece of soil subjected to traffic, piling, etc. were analysed by Raaijmakers, 1994. 2D plane strain models were implemented to understand the propagation of different surface waves through the soil. The models were later reproduced and cross-validated with DIANA by Korswagen et al., 2017. Both 2D and 3D analyses were performed.

Amplification of vibrations can occur if the frequency of one of the vibration modes of the structure matches the frequency of the vibrations or of the soil. Since vibrations are attenuated quickly and shifted according to the frequency of the soil, only structures matching the frequency of the soil will be able to amplify the vibrations. Moreover, the direction of the vibration is also relevant; vertical vibrations are seldom amplified by structures as structures tend to be rigid in the vertical direction, with the exception of some flexible floors.

In sum, in the context of this framework, it can be stated that houses located farther than 50m from heavy construction sites are unlikely to have experienced vibrations that can lead to damage. Damage is specially improbable when compared to other actions which are more likely to be responsible for any minor damage. Therefore, for simplification, pre-damage from vibrations is not explicitly included in this framework.

Vibration-Induced Settlements

Vibrations may also induce settlements by compacting the ground below the foundation of structures. As with vibrations affecting the structures directly, a minimum level of vibration is required to compact the soil. Moreover, different types of soil will require different amounts of energy, and some types are not prone to vibratory-compactions. Massarsch (2002) explores the deep-compactability of soils and states that only granular soils with less than 10% of fines are compactable; moreover, even for granular soils, the distance from the source at which compaction through vibration occurs is limited.

Therefore, in this framework, vibration-induced settlements are not considered explicitly either. Damage patterns are likely to be similar to settlement pre-damage scenarios.

Earthquakes

Earthquakes in the area of Groningen have been monitored for the past few decades. The magnitude of the tremors and the contour curves of PGA are registered via a network of seismographs. Figure 7.9 depicts the area and the earthquakes registered up to 2013.

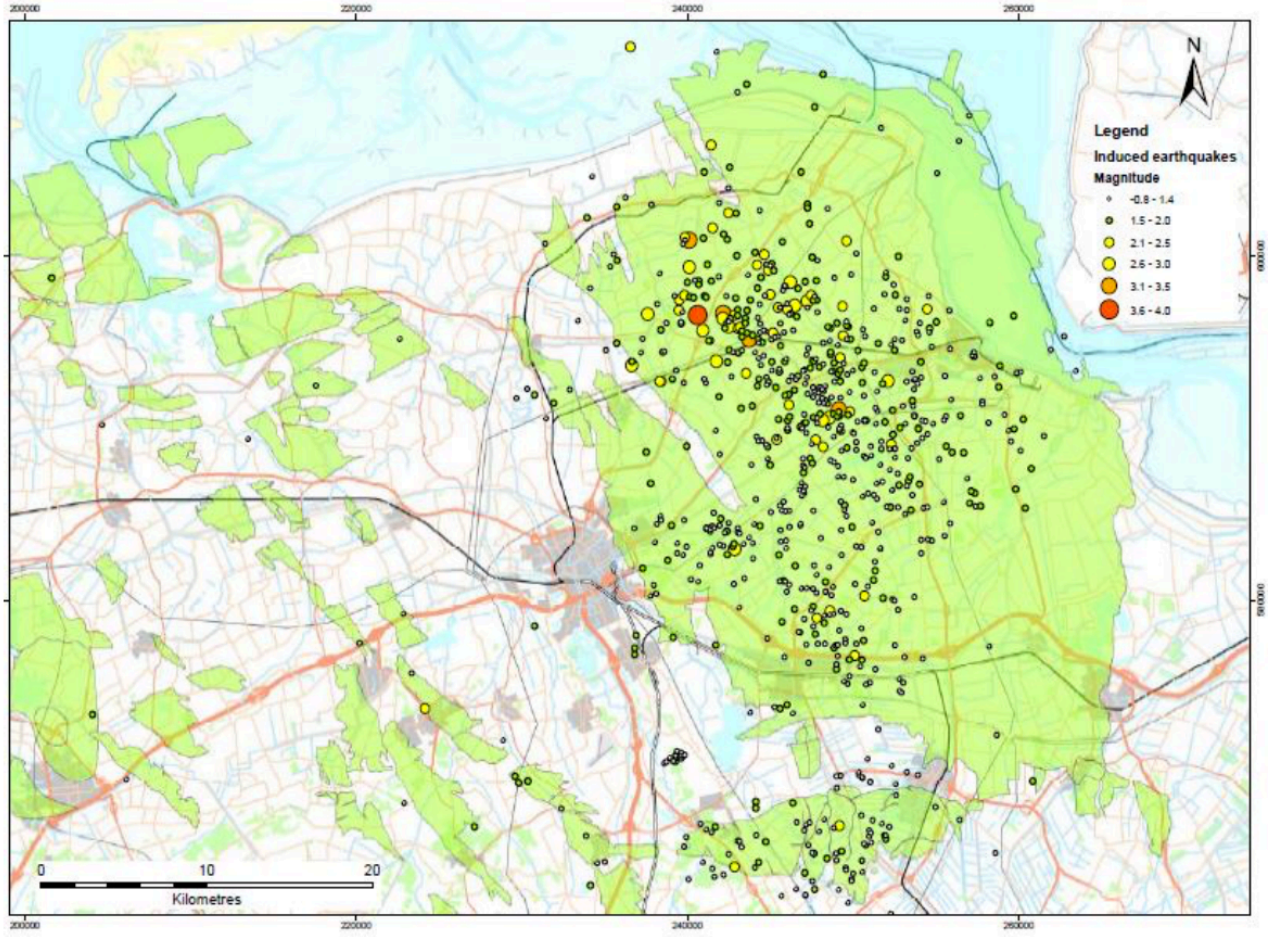

Figure 7.9. From NAM (2013). Earthquakes and their magnitude in the Groningen area in the period from the late 1980's to 2013.

The largest earthquake occurred in Zeerijp in 2018 with a magnitude of 3.4 and registered a maximum (horizontal) PGA of 0.11g; the second largest earthquake, had its epicentre in Huizinge in 2012 with a magnitude of 3.6 and registered a maximum (vertical) PGA of 0.08g. Figure 7.10 shows the registered contour maps for the surface vibration triggered by the Zeerijp earthquake; these given an impression of the area affected by an earthquake.

In this light, a limited area seems to be affected by a PGA of approximately 0.08g every ten years (around 25 mm/s).

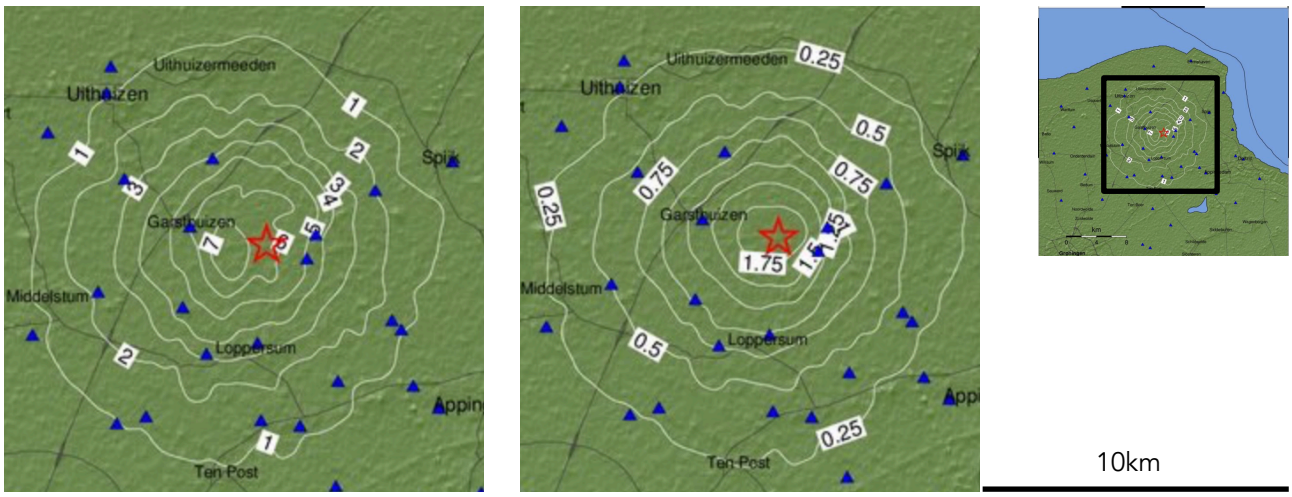

Figure 7.10. Historical map by the dutch institute of meteorology (KNMI) - updated for the Zeerijp earthquake on January 8th, 2018. Left, PGA values in percentage of g, and right, PGV values in cm/s. Blue triangles mark the measurement devices.

Settlements

Small settlements of structures are a normal phenomenon since the added weight of the new structure will deform the soil. This results in small cracks in the structure, which are usually not visible; it is excessive differential settlement which causes visible damage to structures.

Settlements may occur due to:

- Ground compaction or expansion
  - Changes in the water table
  - Biological influence such as trees
  - Flow of ground water
  - Changes in the chemical balance of the soil
  - Added load from other buildings
  - Poorly accounted long-term plastic deformations
  - Strong vibrations
  - Liquefaction
  - Regional subsidence with local concentrations due to soil layer changes
  - Mining
  - Tunneling
  - Nearby Excavations

Serious cases of settlement damage are usually investigated directly, but minor cases are possibly only reported when they aggravate. The reasons for which minor settlement pre-damage can occur is vast, so it is not possible to assess settlement quantitatively in this study. Instead, different degrees of settlement pre-damage will be assumed based on a statistical distribution; from this, the process in which earthquakes further degrade the structure and the change in probability of damage can be investigated.

7.4. Indicative Resistivity Curves From Computational Models

To assemble resistivity curves from computational models, first, these models need to be calibrated based on the results from the laboratory tests. Then, several additional models need to be run and their results be analysed to compute their corresponding damage value in order to provide the insight required for the curves. Next, a relationship needs to be established regarding the involved parameters and the damage value. From this, a probabilistic analysis can be performed and the resistivity curves drawn. This process is illustrated in Figure 7.11 and will be detailed in this subchapter.

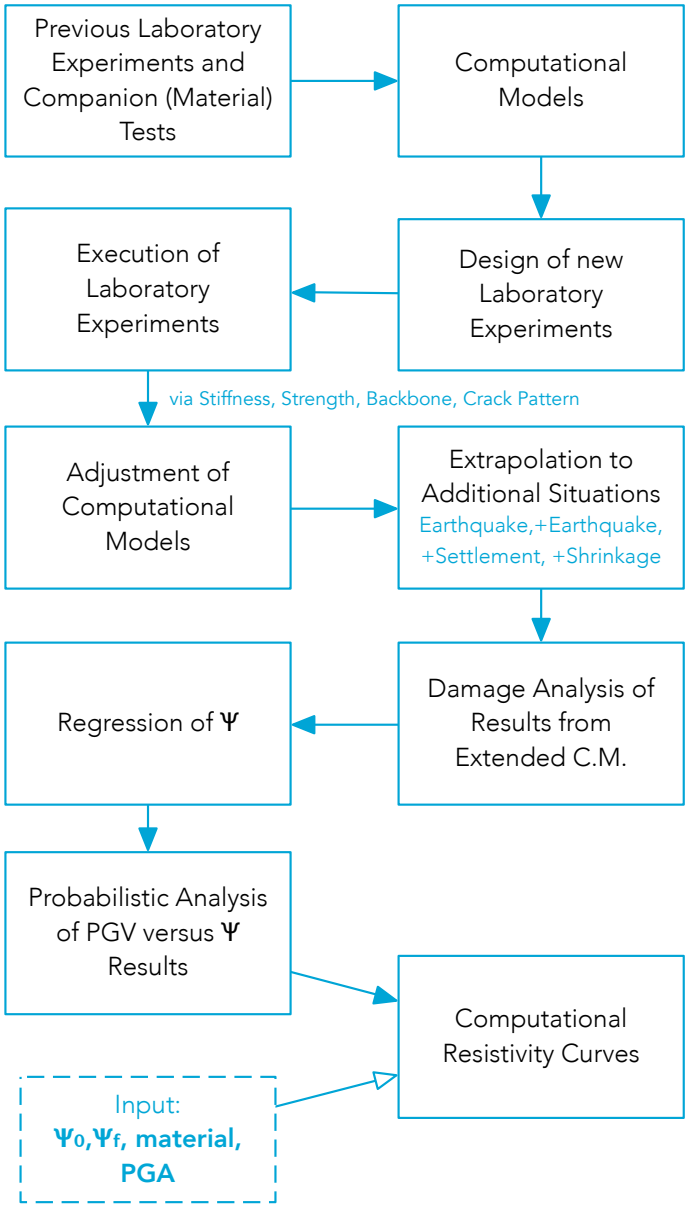

Figure 7.11. Work flow for producing resistivity curves from computational models.

7.4.1. Expanded Computational Models and Their Results

After the model of the laboratory walls has been tuned to the laboratory results (see Chapters 3 and 5), approximately one hundred additional computational models have been run and evaluated to provide sufficient information to infer relationships between the parameters of interest and which have been deemed the most influential towards damage. These are denoted 'extended computational models'.

Firstly, the models vary in PGA intensity as stronger earthquakes will logically produce more damage. Secondly, models differ in material strength to provide input as to how the structure's strength affects damage and allow for the inclusion of the variability inherent in masonry strength and stiffness in the resistivity curves. Thirdly, the models differ in the type and level of pre-damage. Here four cases can be distinguished: no pre-damage, earthquake, shrinkage and settlement pre-damage. For the pre-damaged cases, two levels of pre-damage are set. See Chapter 6 for additional details about the computational models. A summary of the number of models is shown in Figure 7.12.

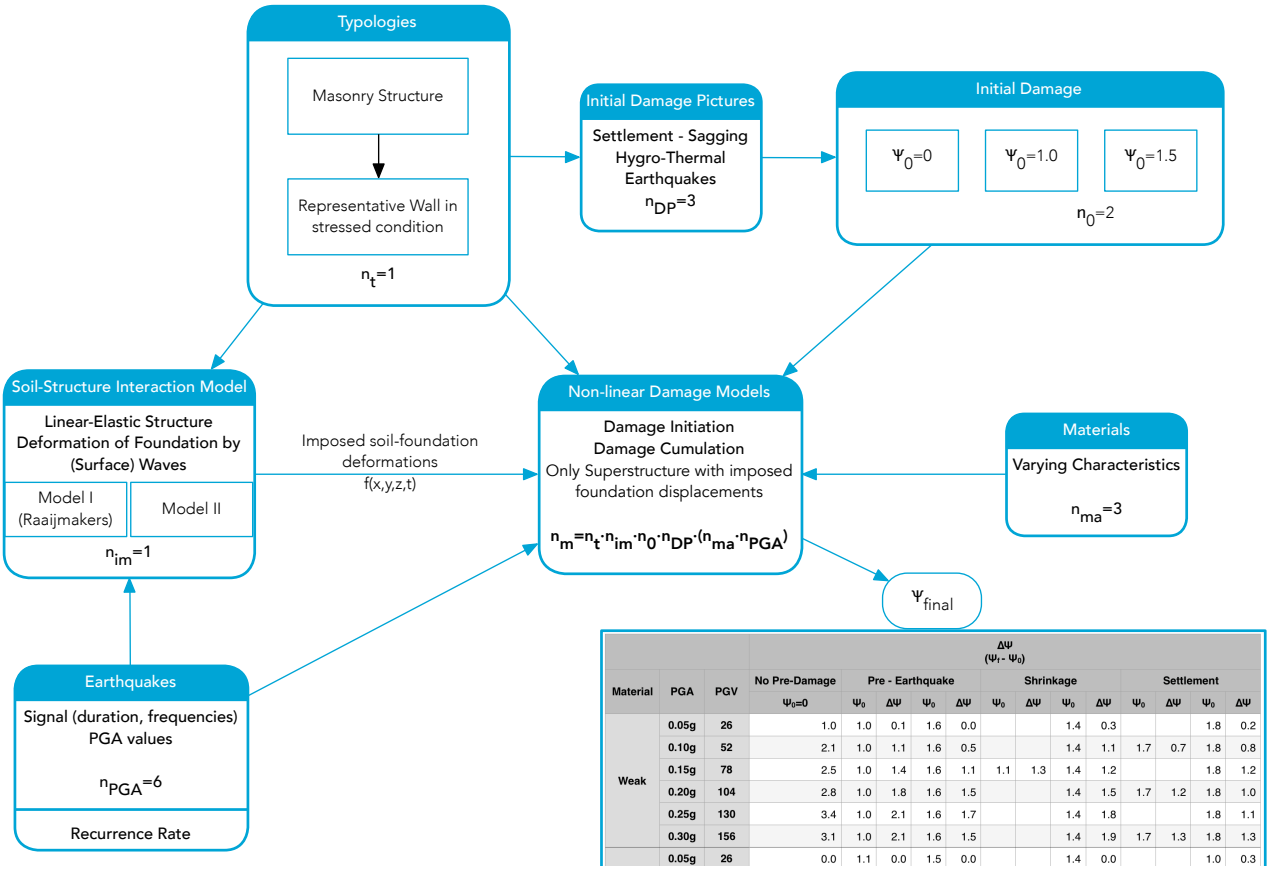

Material	PGA	PGV	ΔΨ (Ψ_i - Ψ_0) No Pre-Damage Ψ_0=0	Pre - Earthquake Ψ_0	Pre - Earthquake ΔΨ	Pre - Earthquake Ψ_0	Pre - Earthquake ΔΨ	Shrinkage Ψ_0	Shrinkage ΔΨ	Shrinkage Ψ_0	Shrinkage ΔΨ	Settlement Ψ_0	Settlement ΔΨ	Settlement Ψ_0	Settlement ΔΨ
Weak	0.05g	26	1.0	1.0	0.1	1.6	0.0			1.4	0.3			1.8	0.2
	0.10g	52	2.1	1.0	1.1	1.6	0.5			1.4	1.1	1.7	0.7	1.8	0.8
	0.15g	78	2.5	1.0	1.4	1.6	1.1	1.1	1.3	1.4	1.2			1.8	1.2
	0.20g	104	2.8	1.0	1.8	1.6	1.5			1.4	1.5	1.7	1.2	1.8	1.0
	0.25g	130	3.4	1.0	2.1	1.6	1.7			1.4	1.8			1.8	1.1
	0.30g	156	3.1	1.0	2.1	1.6	1.5			1.4	1.9	1.7	1.3	1.8	1.3
	0.05g	26	0.0	1.1	0.0	1.5	0.0			1.4	0.0			1.0	0.3

Figure 7.12. Number of computational models to run.

The displacement and crack width results of the models were analysed directly with a self-written program to obtain the value of Ψ (see Chapter 2 for a definition of this damage parameter and Section 2.6.3 for its assessment). These results are presented in Table 7.2.

Table 7.2. Results from computational models showing the initial value for Ψ and its increase after the earthquake.

			ΔΨ ($\Psi_f - \Psi_0$)												
Material	PGA	PGV	No Pre-Damage	Pre - Earthquake				Shrinkage				Settlement			
			Ψ_0=0	Ψ_0	ΔΨ	Ψ_0	ΔΨ	Ψ_0	ΔΨ	Ψ_0	ΔΨ	Ψ_0	ΔΨ	Ψ_0	ΔΨ
Weak	**0.05g**	26	1.0	1.0	0.1	1.6	0.0			1.4	0.3			1.8	0.2
	0.10g	52	2.1	1.0	1.1	1.6	0.5			1.4	1.1	1.7	0.7	1.8	0.8
	0.15g	78	2.5	1.0	1.4	1.6	1.1	1.1	1.3	1.4	1.2			1.8	1.2
	0.20g	104	2.8	1.0	1.8	1.6	1.5			1.4	1.5	1.7	1.2	1.8	1.0
	0.25g	130	3.4	1.0	2.1	1.6	1.7			1.4	1.8			1.8	1.1
	0.30g	156	3.1	1.0	2.1	1.6	1.5			1.4	1.9	1.7	1.3	1.8	1.3
Normal	**0.05g**	26	0.0	1.1	0.0	1.5	0.0			1.4	0.0			1.0	0.3
	0.10g	52	0.9	1.1	0.0	1.5	0.0			1.4	0.5	0.9	0.5	1.0	0.7
	0.15g	78	1.3	1.1	0.4	1.5	0.0	1.2	0.7	1.4	0.8			1.0	1.0
	0.20g	104	1.9	1.1	1.1	1.5	0.7			1.4	1.1	0.9	1.6	1.0	1.7
	0.25g	130	3.0	1.1	1.9	1.5	1.3			1.4	1.6			1.0	1.7
	0.30g	156	3.2	1.1	2.5	1.5	1.9			1.4	1.6	0.9	1.9	1.0	2.2
Strong	**0.05g**	26	0.0	1.1	0.0	1.6	0.0			1.4	0.1			0.7	0.5
	0.10g	52	0.4	1.1	0.0	1.6	0.0			1.4	0.0	0.6	0.5	0.7	0.8
	0.15g	78	0.9	1.1	0.0	1.6	0.0	0.9	0.6	1.4	0.5			0.7	1.4
	0.20g	104	1.1	1.1	0.3	1.6	0.0			1.4	0.8	0.6	1.2	0.7	1.3
	0.25g	130	1.8	1.1	0.9	1.6	0.3			1.4	1.3			0.7	1.6
	0.30g	156	2.9	1.1	1.9	1.6	1.2			1.4	1.6	0.6	2.0	0.7	2.1

The earthquake accelerogram was scaled based on the signal from the earthquake of Huizinge in 2012.
To simulate weak, normal and strong material properties, the tensile strength was modified by 30% (reduced and increased, respectively) and the stiffness modulus was changed 50% based on the observed relationship between tensile strength and stiffness from the material tests.
Shrinkage pre-damaged was determined for 0.2‰ and 0.4‰, while settlement pre-damage was set at 2mm and 5mm for middle-span sagging. Earthquake pre-damage was generated with the same earthquake signal scaled such that two different damage levels were obtained.

7.4.2. Regression of the Results From EC Models

These results can be plotted such that a relationship between the parameters becomes clear (see Figure 7.13). Note that the results vary for initial values of Psi (Ψ_0) and this is identifiable by the changing colour of the spheres in the graph (from yellow to blue), but is not easily recognisable.

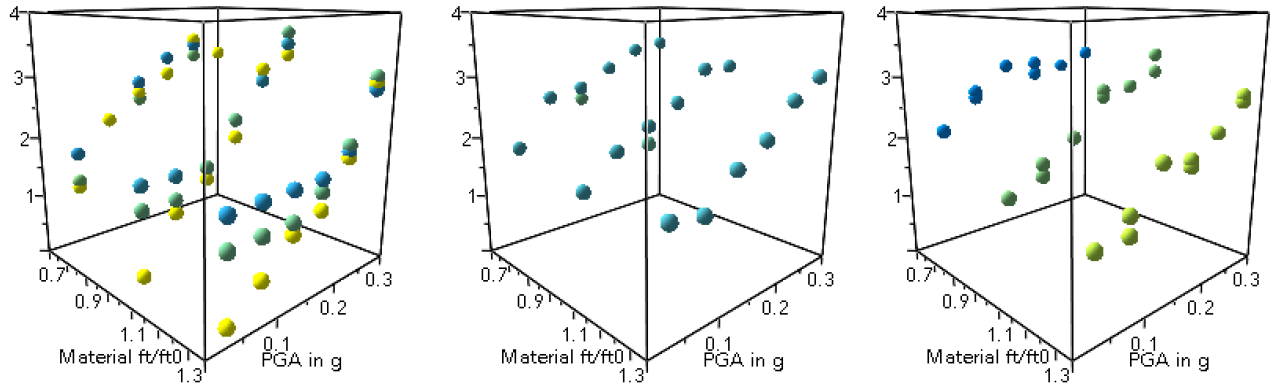

Figure 7.13. 3D graphs showing the final damage given various values of material, PGA, pre-damage type and initial damage value (from 0 to 1.8, respectively yellow-green-blue). Values directly from Table 7.2.

The following can be observed:

- A higher PGA leads to higher damage
- A weaker material (low value) also produces more damage
- Higher pre-damage results in most cases to higher final damage
- The type of pre-damage has a low influence in the final damage, however, settlement damage seems to result in higher final damage.

Based on these observations, a regression model was produced in the form:

$$\Psi_F=\Psi_0+\alpha_1\cdot PGA^{\left(\alpha_2+\alpha_3\cdot\Psi_0^{\alpha_5}+\alpha_4\cdot m\right)} \quad (7.1)$$

Where:

Ψ_F	is the final damage value
Ψ_0	is the initial damage value
PGA	is the Peak Ground Acceleration in g
m	is the normalised material ratio ft/ft0
α	1 to 5, are regression coefficients for each pre-damage type (three sets).

The number of coefficients was kept as low as possible while still reproducing the observed behaviour of the data. The computed parameters are summarised in Table 7.3.

Table 7.3. Summary of regression parameters for computational results.

Regression Parameters	Earthquake Pre-Damage	Shrinkage Pre-Damage	Settlement Pre-Damage
α_1	10.4451	8.9805	7.4902
α_2	0.2817	0.2626	0.1467
α_3	0.3338	0.2843	0.2134
α_4	0.7510	0.6634	0.6682
α_5	1.2821	0.9983	2.1300

The average standard deviation of the residuals is 0.29. This means that around 70% of the points are less than 0.3 damage points away from the regressed curves, the average distance is 0.21. This was deemed a good fit. Figure 7.14 shows the regressed curves for a few values of initial damage (Ψ_0=0, Ψ_0=1.0, Ψ_0=1.6). The behaviour of the various parameters and their influence towards the final damage can be observed.

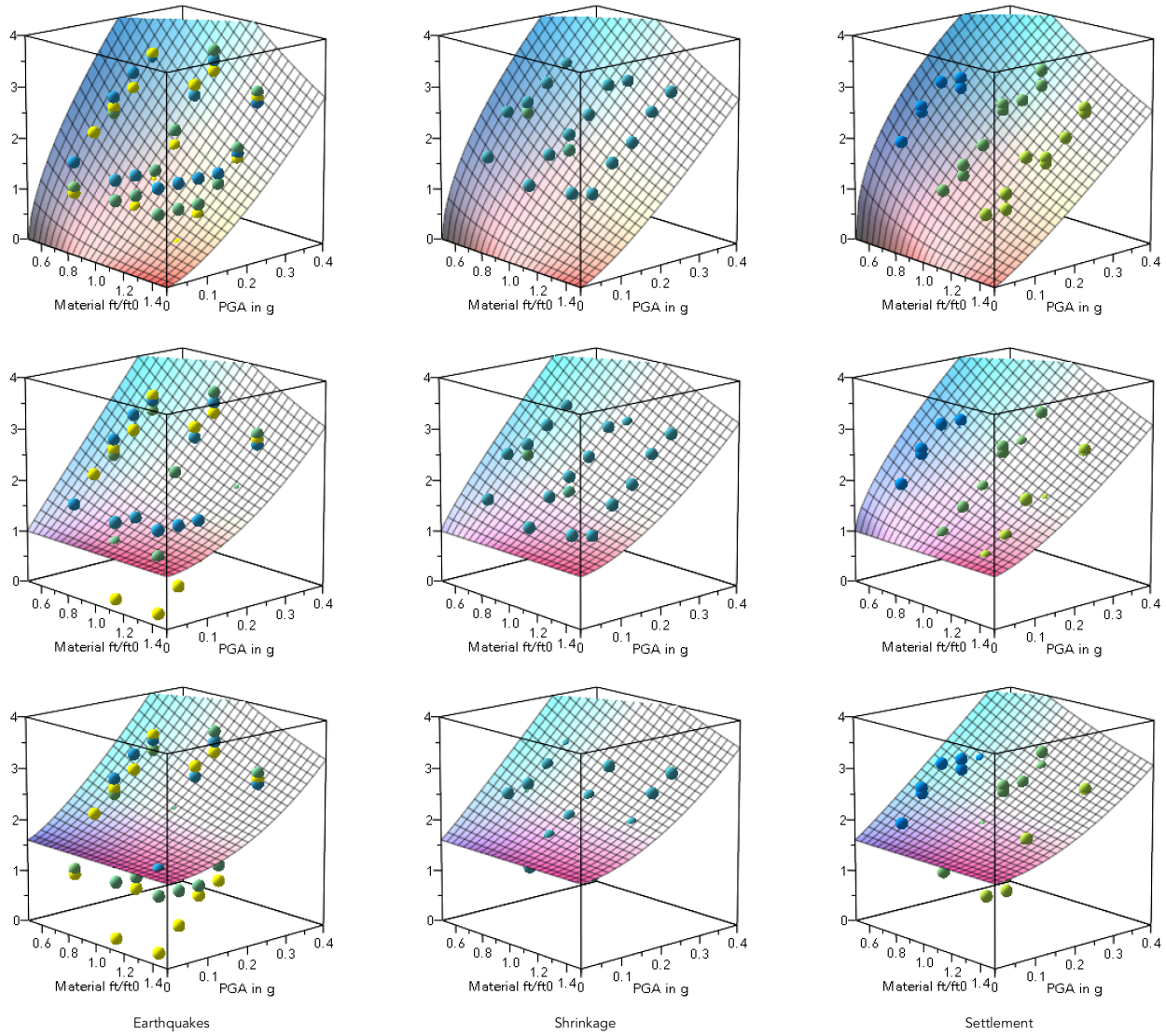

Figure 7.14. Results from computational models as points and regressed curves for initial damage values of 0, 1, and 1.6 on the first, second and third rows respectively.

From these curves, using the standard deviation of the regression as a normal distribution, a higher number of points can be sampled; this can be seen in Figure 7.15. The sampled points (smaller size) surround and represent well the original points.

It can be observed that the coefficients independent of the pre-damage value (Psi) are not the same for the three sets (Table 7.3). This means that they are also influenced by the pre-damage. However, not enough data was available to establish such a relationship; instead, the good fit was achieved with a particular, unavoidable variability. Cases with a pre-damage of zero, were set to use the first set of coefficients.

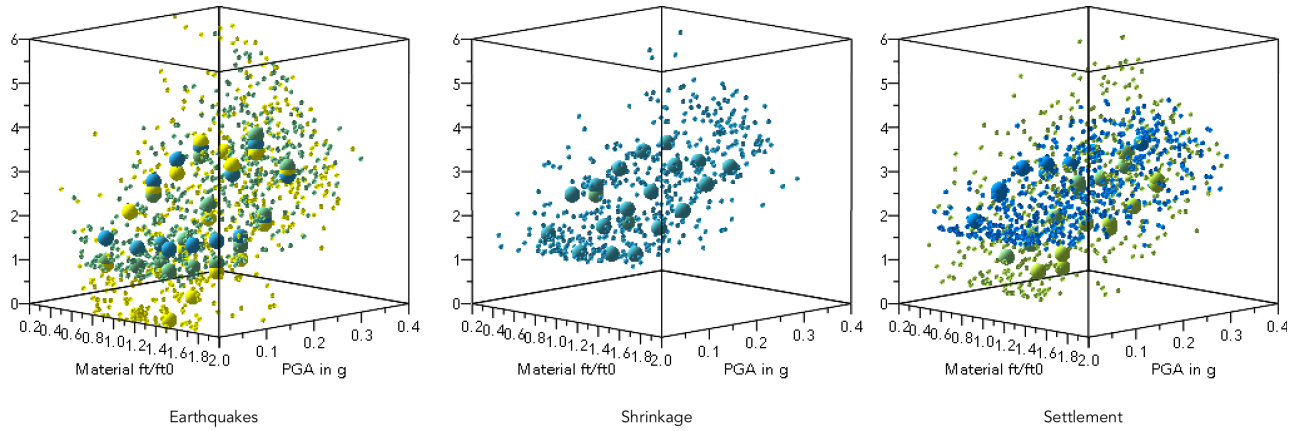

Figure 7.15. Sampled points from the regressed curves and their uncertainty. Only 500 points per colour and only up to two colours per graph.

Then, the relative material strength is assigned a beta distribution in the interval of 0 to 2 with an average of 1 and a standard deviation of 0.3. This is in line with the variability observed in the companion material tests (see Table 9.1). The pre-damage types are assumed to be uniformly distributed, this means that there is an equal number of pre-damaged cases from each type. The uncertainty of the regression is included as a normal distribution with a variation of 0.30, this also constitutes the uncertainty in the computational model and damage analysis. This is summarised in Table 7.4.

Table 7.4. Summary of Variables for the resistivity curves of computational models.

Variable	Distribution	Mean	St. Dev. or 2nd Parameter
Material Strength	Normal	1.0	0.3
Pre-Damage Type	Discrete Uniform	1.0	3.0
Model and Regression Uncertainty	Normal	0.0	0.3

Finally, for various values of initial damage and PGA, the probability of being or exceeding a certain final damage level is computed with a MonteCarlo simulation. With the relationship of PGA/PGV for the earthquake signal, additional cases are sampled for various PGV values. In total, one billion points were sampled; this allows for the elaboration of the resistivity curves shown in Figure 7.16 to Figure 7.24 in the next section.

Now, the material distribution requires some discussion. The computational results are based on models which have a constant material property. This means that, if a high material value is selected, the model will output a lower damage value. The variability and potential strength values for the material come from material companion tests which evaluate the strength of a few failure surfaces: the bond test is the result of one surface, while the flexural strength test comprises two or three common failure points. In contrast, an entire wall may fail in any of many failure points. High stresses will concentrate around the window corners for instance, but the crack may develop in any of the many (head an bed) joints surrounding the corner. Since 50% of the potential failure surfaces are weaker than the mean of the material tests and failure is likely to occur at the weakest point, the failure of the wall corresponds to a material value weaker than the average. When calibrating the computational models, this is clearly observed: the models use a tensile strength of around 100kPa, while the average of the bond tests is 150kPa. However, the variability used in the computational models is assumed to be the same of the material tests, because computing the variability of the weaker samples is based on the aforementioned hypothesis and is thus uncertain. Nevertheless, simulations of a system with five failure points, each of which follows a normal distribution with 30% variation, show that the average of the weaker point is 33% below the average of each point (so 100 of 150kPa), and that the variability of this weak joint distribution is lower than that of each point (at approximately 18%). If the material distribution had a variability of 18% instead of 30% as shown in Table 7.4, the curves would appear slightly steeper (see Figure 7.42 in the next subsection).

7.4.3. Figures of Indicative Resistivity Curves From Computational Models

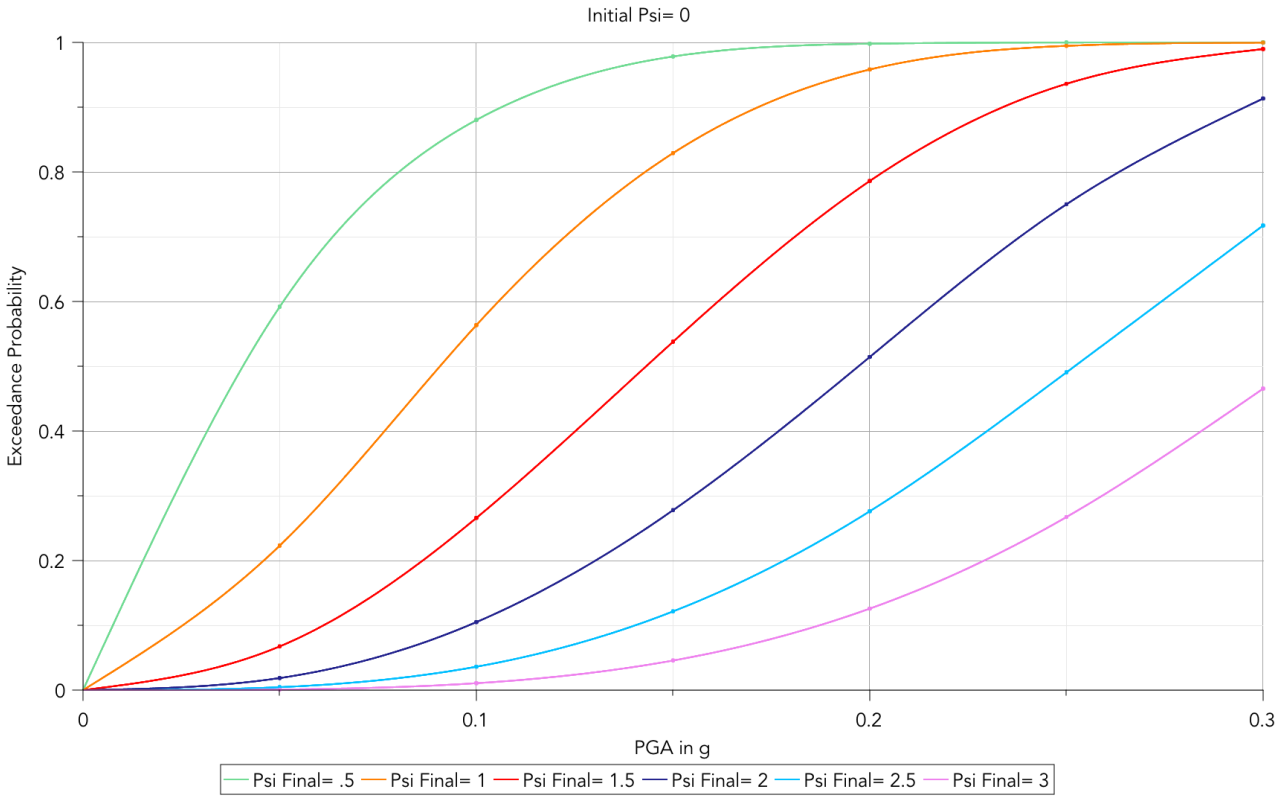

Figure 7.16. Indicative Resistivity curves for computational results for Ψ_0=0 against PGA.

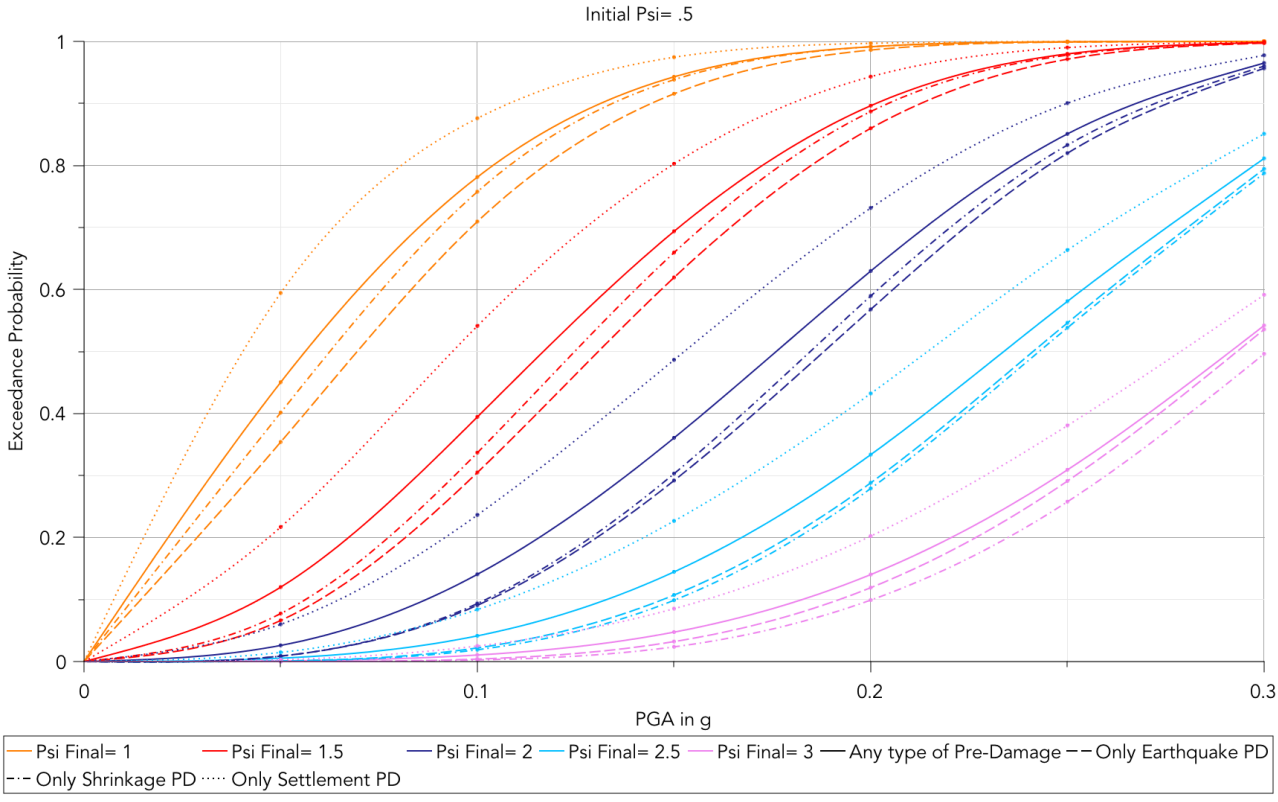

Figure 7.17. Indicative Resistivity curves for computational results for Ψ_0=0.5 against PGA. Showing also the difference between pre-damage types.

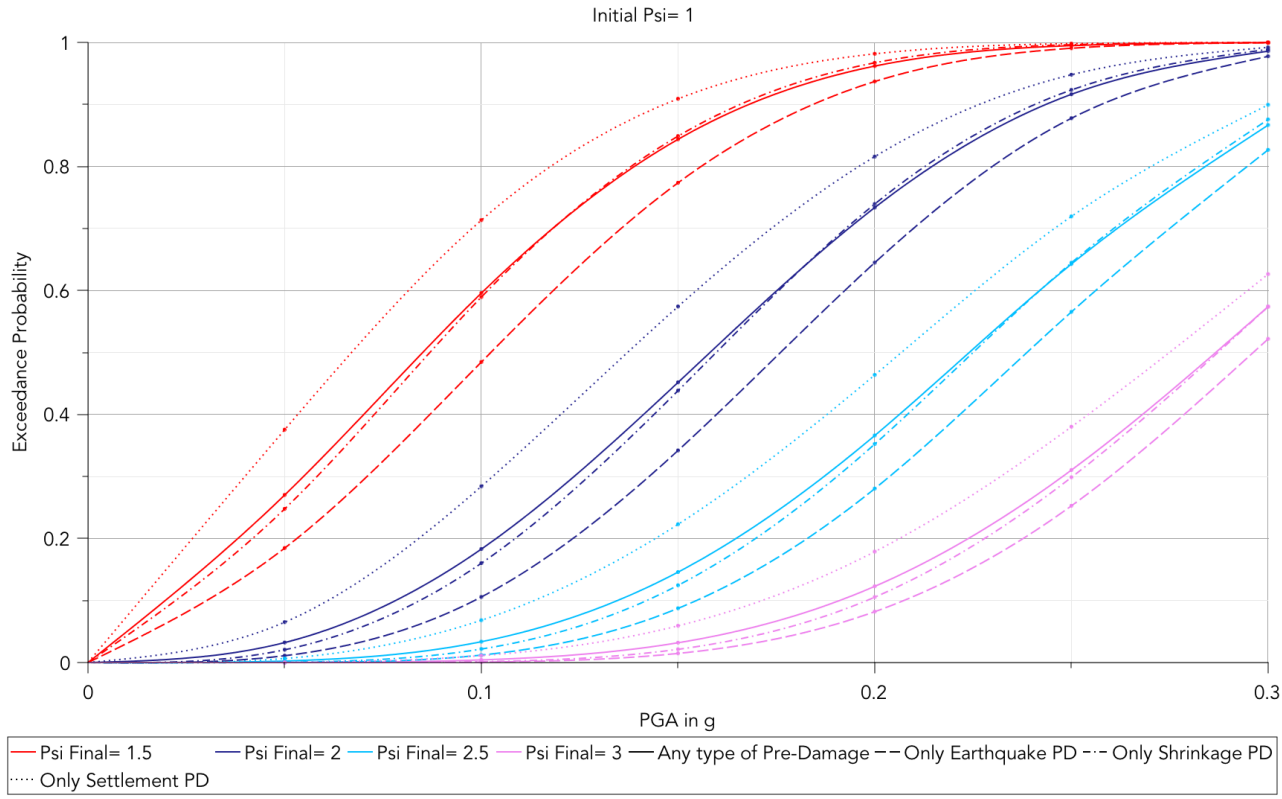

Figure 7.18. Indicative Resistivity curves for computational results for Ψ_0=1.0 against PGA. Showing also the difference between pre-damage types.

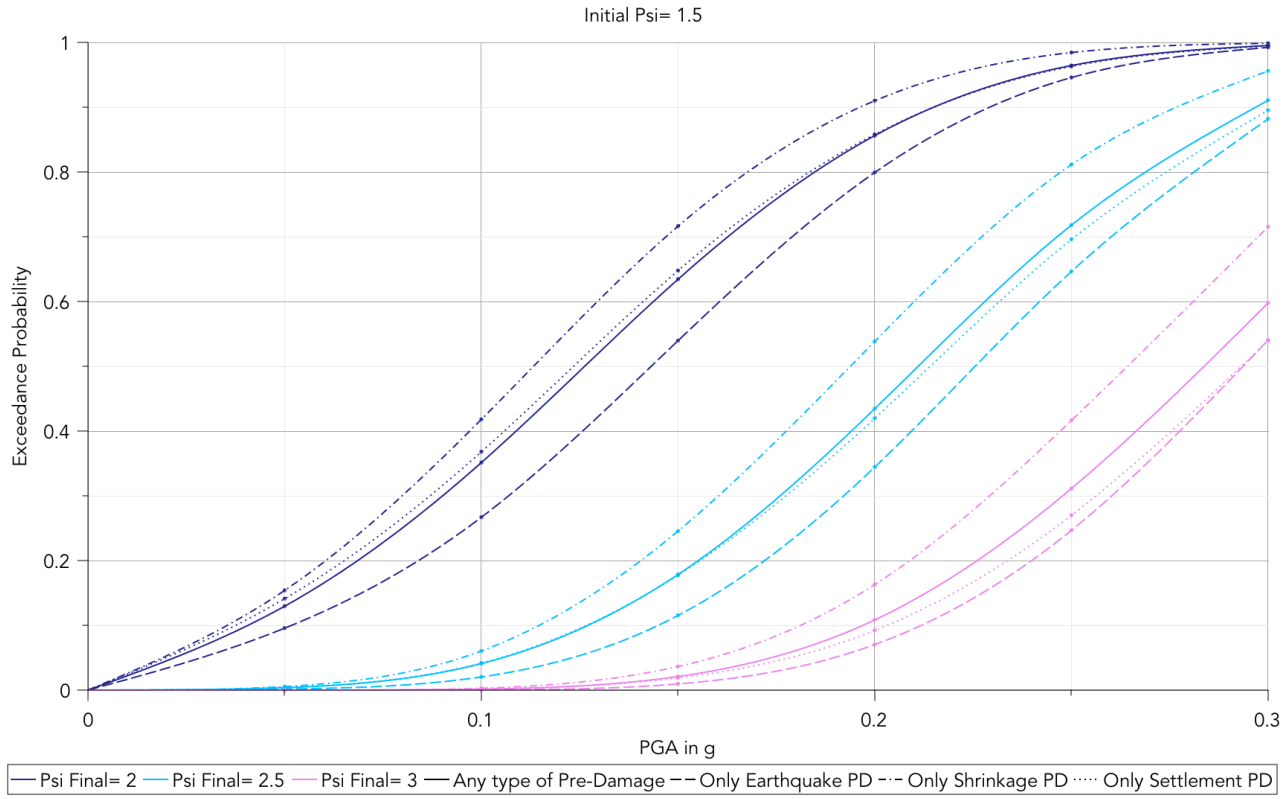

Figure 7.19. Indicative Resistivity curves for computational results for Ψ_0=1.5 against PGA. Showing also the difference between pre-damage types.

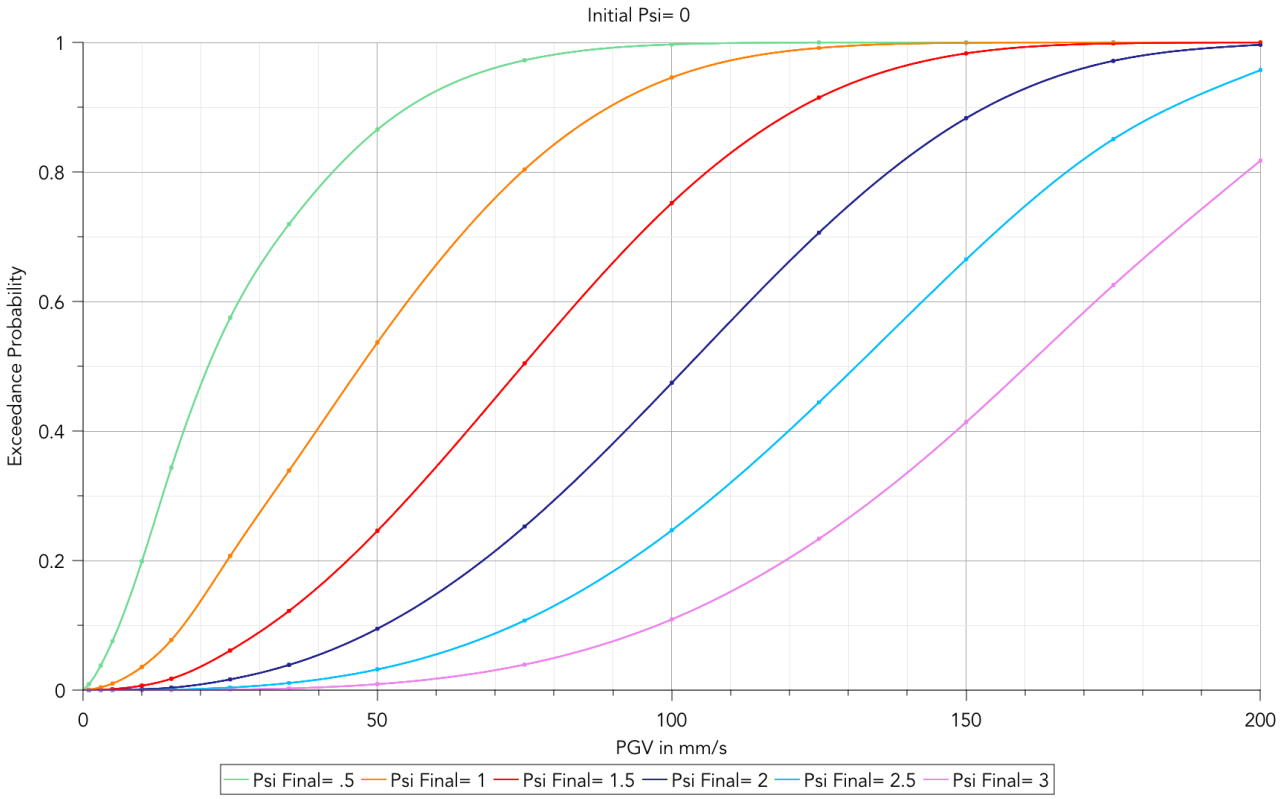

Figure 7.20. Indicative Resistivity curves for computational results for Ψ_0=0 against PGV.

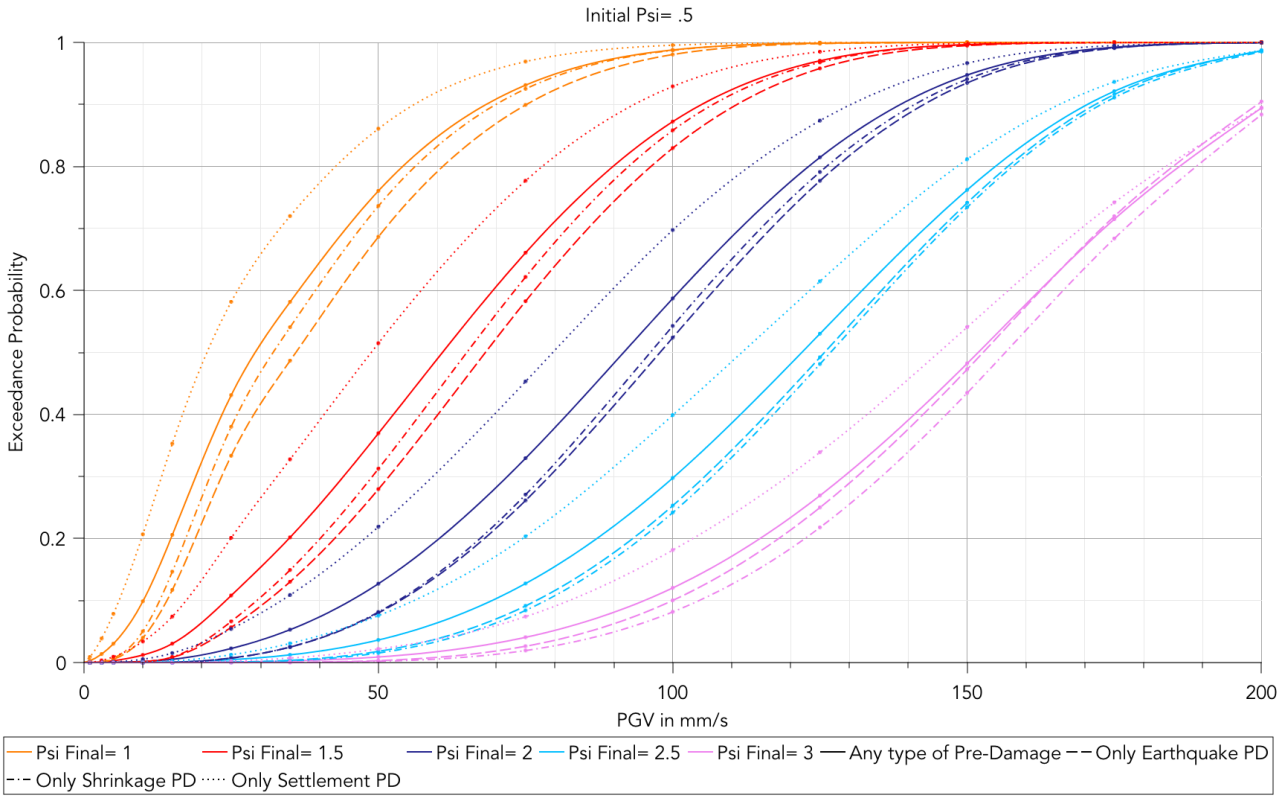

Figure 7.21. Indicative Resistivity curves for computational results for Ψ_0=0.5 against PGV. Showing also the difference between pre-damage types.

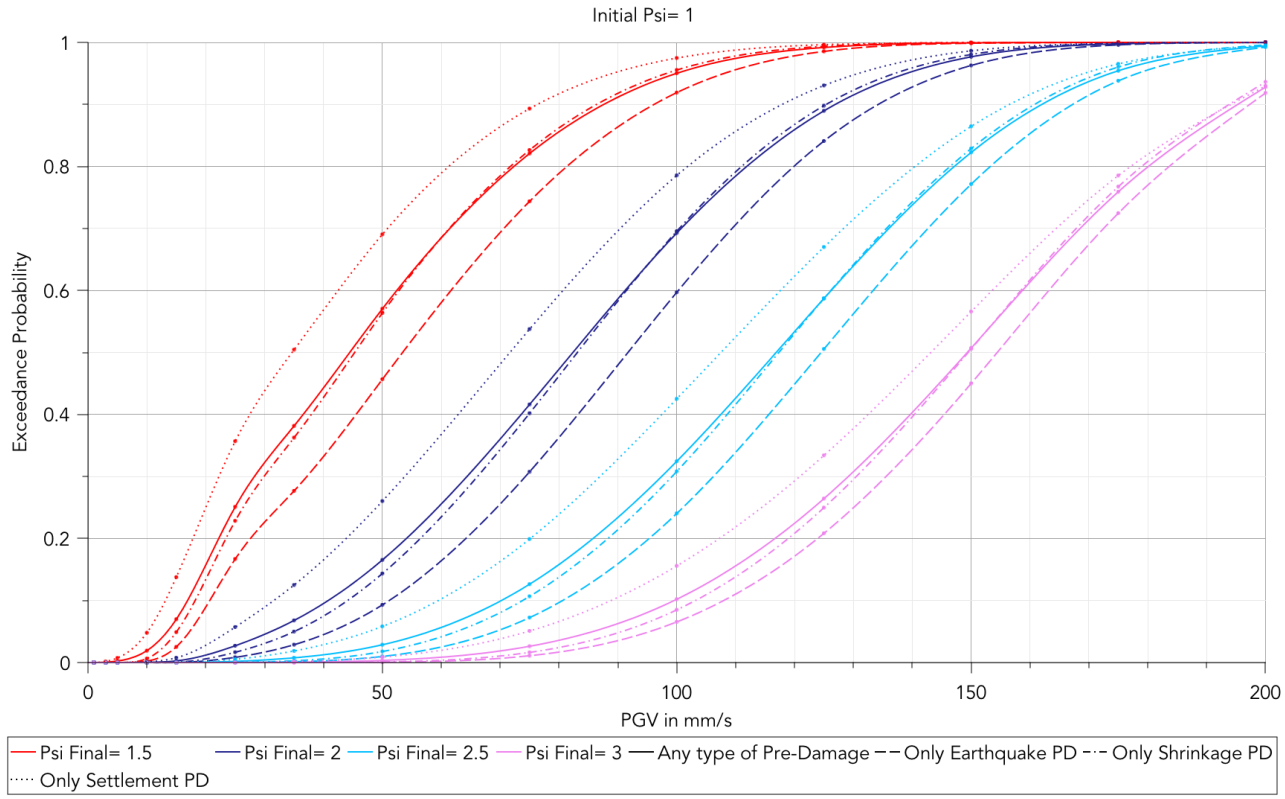

Figure 7.22. Indicative Resistivity curves for computational results for Ψ_0=1.0 against PGV. Showing also the difference between pre-damage types.

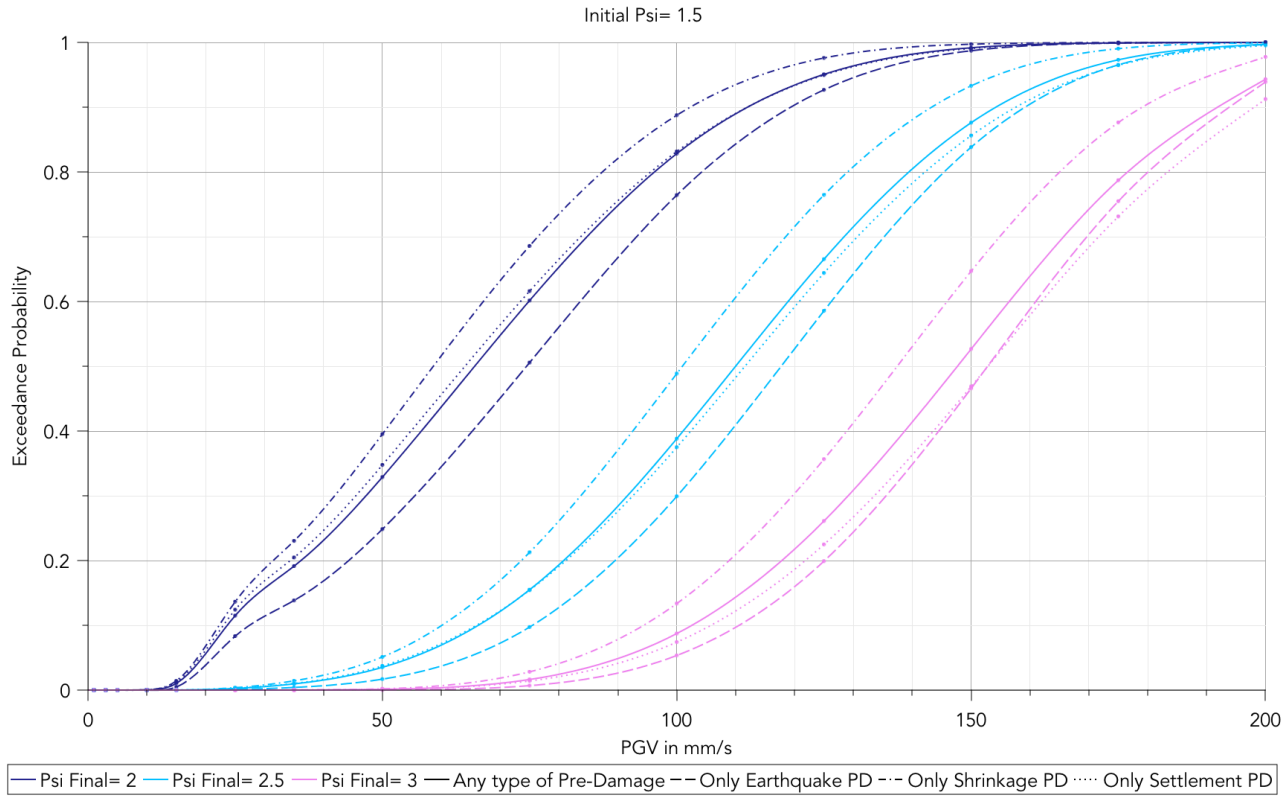

Figure 7.23. Indicative Resistivity curves for computational results for Ψ_0=1.5 against PGV. Showing also the difference between pre-damage types.

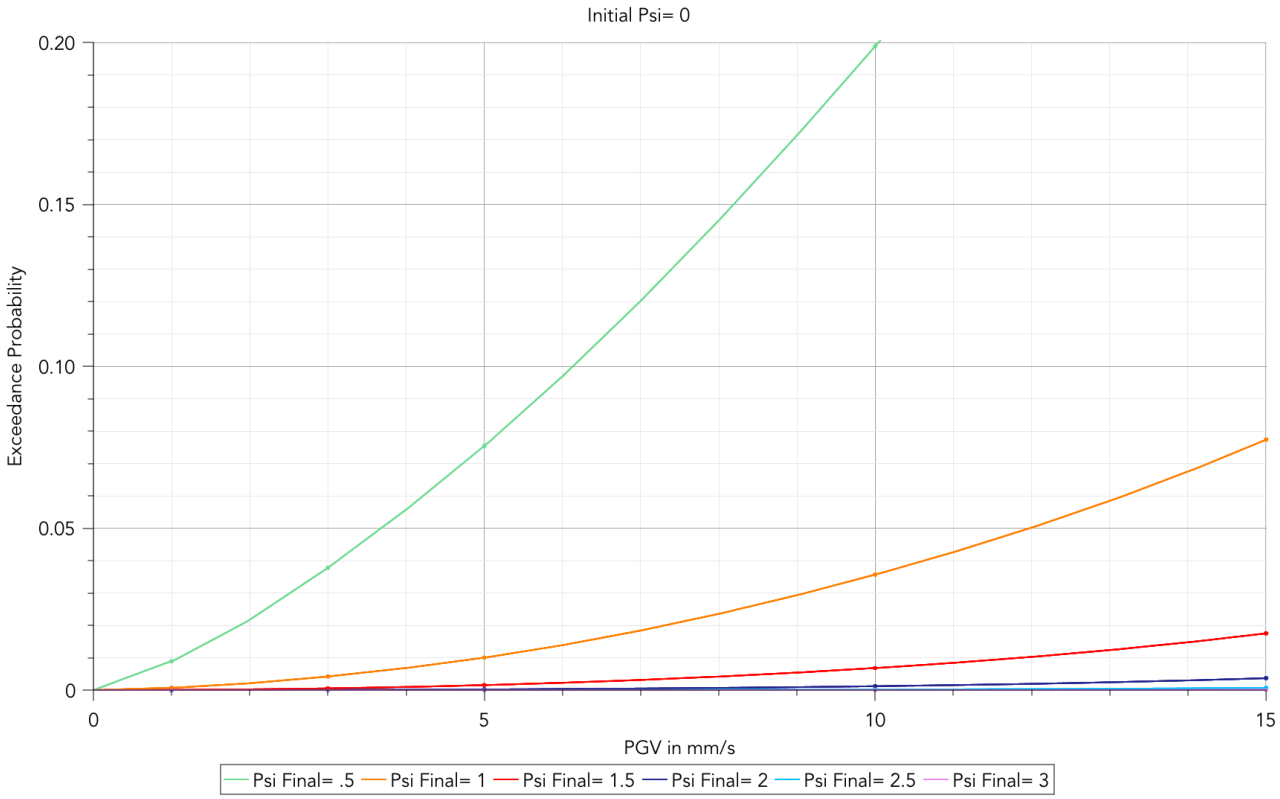

Figure 7.24. Indicative Resistivity curves for computational results for Ψ_0=0 against PGV in the range of 0 to 15mm/s.

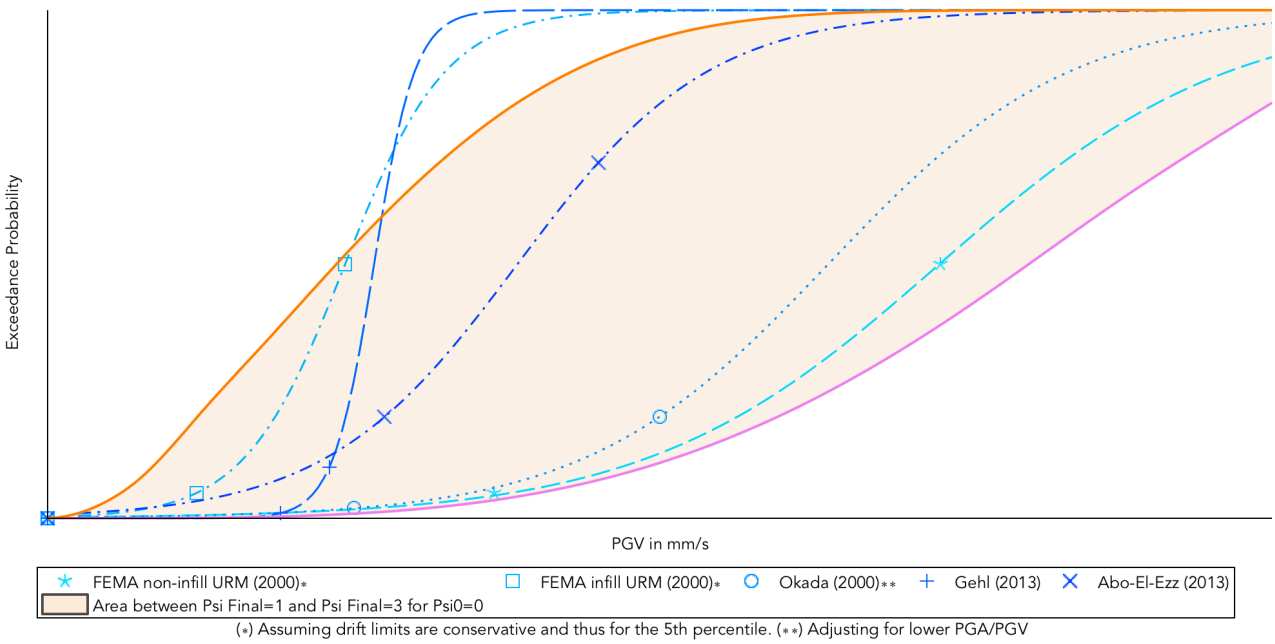

Figure 7.25. Comparison with curves and points for DS1 from various authors. According to the definition for the damage level, depending on the structure, DS1 starts between Ψ=1 and Ψ=3. Indicative Resistivity curves for computational results for Ψ_0=0 against PGV for these two values are shown.
Note that the comparison curves are log-normal S-curve fits to a few available points and that their behaviour away from the marked points may differ.

7.4.4. Discussion of the Computational Resistivity Curves

The curves show the characteristic behaviour of damage curves following an S-like path. The probability of damage starts with a mild slope, then becomes steeper and finally milder again until reaching an asymptote of 1. Here it can be observed, for instance in Figure 7.16, that for an earthquake that reaches a PGA value of approximately 0.09g, the probability of being or exceeding damage level one (Ψ=1) is 50%. If the approximate equivalency presented in Table 2.3 is used, for a PGA of 0.15g, the probability of having entered DS1 would be 50%, while the probability of having left and exceeded DS1 (roughly Ψ=3) is 1%.
However, if the example wall was already damaged, perhaps imperceptibly (Ψ_0=0.5), the probability of Ψ=1 would increase to 75%. Depending on the type of pre-damage, this may vary between 60% and 85%.

This variability depends on the type of pre-damage that the structure started with. From the graphs, it would seem that when the wall was subjected to settlement pre-damage, the probability for further damage is higher, followed by shrinkage pre-damage and lastly, damage by a previous earthquake. The intensity of the damage is irrelevant, as this is the same for each graph (e.g. Figure 7.26 is for an initial value of pre-damage of 0.5, Ψ_0=0.5). Because the ratio of pre-damage types in the field is unknown, the final curve has been drawn as the average of the three contemplated types.

In comparing the curves to guidelines and other studies (Figure 7.25), it can be observed that most limits and definitions for DS1 fit within the region defined by Ψ=1 (start of perceivable damage) and Ψ=3 (end of light damage). It must be noted that the damage level does not necessarily correspond to a measure of structural safety (see Chapter 2), which makes this comparison difficult.
Firstly, FEMA (2000) specifies drift limits for the DS1 grade; since the limits are suggestions to help the design of a structure prevent the incursion of said structure into the grade, it has been assumed that they correspond to the fifth percentile, that is, that at this value, there is a 5% probability of the pool of structures exceeding DS1. The drift limit for structural walls is higher than for infilled walls; it follows that walls without a vertical compression stress are more vulnerable than bearing walls. The former fit to the beginning of DS1 as defined by Ψ=1, while the later fit the curve for Ψ=3. It would seem that for the non-structural walls, light damage is considered more critical.
Next, the study by Okada et al. (2000) looks at the characterisation of damage states for masonry in earthquakes. This curve has been adjusted for a low PGA/PGV ratio. Gehl et al. (2013) shows that fragility curves are highly dependent on the ratio between PGA/PGV, with higher ratios corresponding to more damage. The earthquake signal of Huizinge has a ratio of 19, while the average ratio (for the earthquakes studied by Gehl et al., 2013) is closer to 10. It follows that the study by Okada et al. (2000), looking at a pool of earthquakes, needs to be adjusted to be comparable to the signal of this study. When doing so, the probability for damage increases and fits inside the range shown in Figure 7.25.
Thirdly, curves by Gehl et al. (2013) can also be compared and seen to fit partially inside the range. This is because these curves are steep: inside a 20 mm/s interval, the curves show a damage increase of more than 90%. For structures where the material strength is key in determining damage (a change of one standard deviation results in approximately 35% change in the results), and when the strength of multiple samples has been verified to have a high variability (30%) even in laboratory conditions, the presence of steep curves is strange. It is possible that the curves for DS1 are based on information sampled for higher damage states and are thus an imprecise extrapolation. Nonetheless, if the curves were less steep, stretching from their middle point, they would fit well inside the range. Another possibility is that curves do not follow a lognormal S-fit and their shape curves inward to stay in the range.
Fourthly, the study by Abo-El-Ezz (2013) obtains fragility curves for historic stone masonry in Canada; while this is not directly comparable, the material resembles the low tensile strength and cracking-oriented failure of the masonry studied in this report. It would seem that their definition of DS1 also fits nicely within the surface.
Finally, Tomassetti et al. (2017) conducted dynamic shake-table tests on an entire masonry house and also determined some drift-limits corresponding to the ingress to damage states of the house. The single value of 0.47‰ of drift represented DS1 for their test-house. A displacement of 1.25mm roughly corresponds to a damage value of Ψ=1.3 (see next section) which would place this drift-value inside the surface. This can be extrapolated from Figure 7.35 and Figure 7.36.

In sum, the intention of discretising DS1 into several damage levels is allowing for a better representation of light damage, as such, DS1 constitutes a range between damage levels 1 and 3. Inside this range, traditional definitions of DS1 appear to fit well.

7.5. Resistivity Curves From Experimental Tests

Similarly to the computational models, the experiments can provide a relationship between an intensity and a level of damage. Since the walls were not shaken at their base, and most tests were conducted quasi-statically, the top lateral displacement of the walls becomes the ideal parameter to relate to a degree of damage.
To be able to compare these curves against computational ones and extract additional information from them, they can also be converted to have PGV as the main axis, this is done using a simplified single degree of freedom model.

The procedure to compute these curves is then as follows: First, clear and relevant points from the laboratory experiments are analysed with the DIC method and their damage level is assessed (see Chapter 2). The value pairs are then regressed linearly to obtain a relationship between the top displacement and a level of damage. Similarly, with the SDoF model, the relationship between PGV and top lateral displacement is established. From this, the curves can be produced. This procedure is shown in Figure 7.26 and it and its results will be detailed in this subchapter.

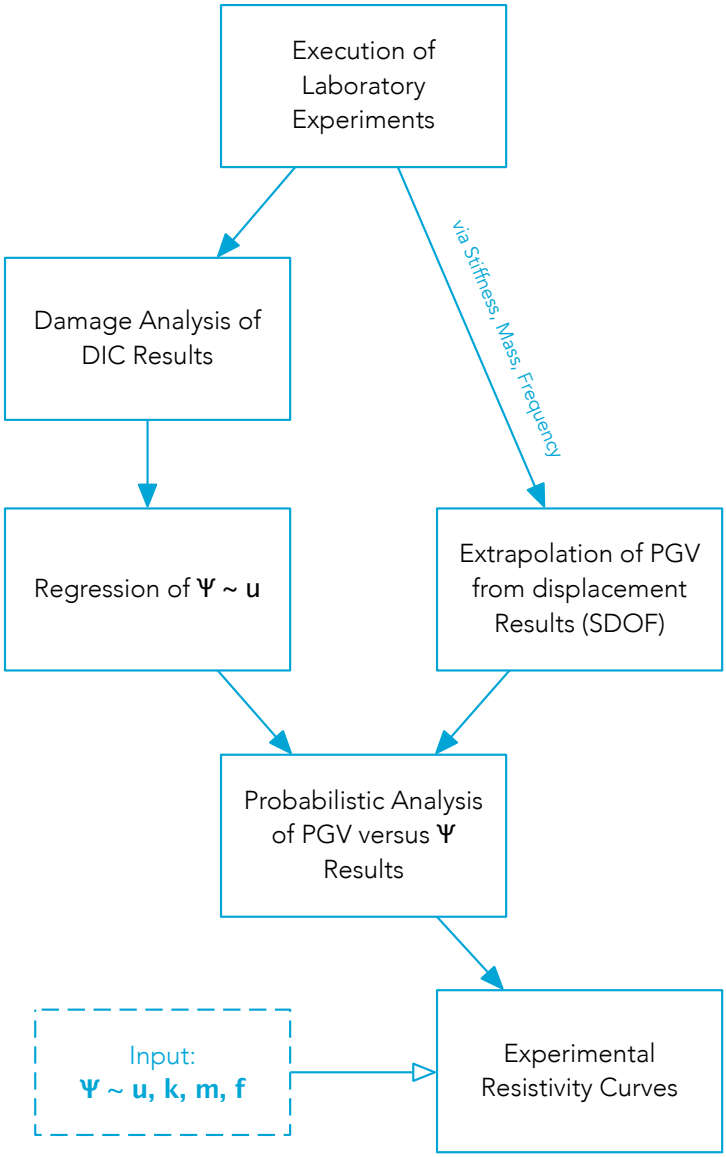

Figure 7.26. Workflow for producing resistivity curves based on the laboratory experiments.

7.5.1. Results and Regression From the Experimental Tests

The first step is obtaining a relation between the displacement and the damage value. These value pairs for cases selected from the five walls have been located in Figure 7.27 next.

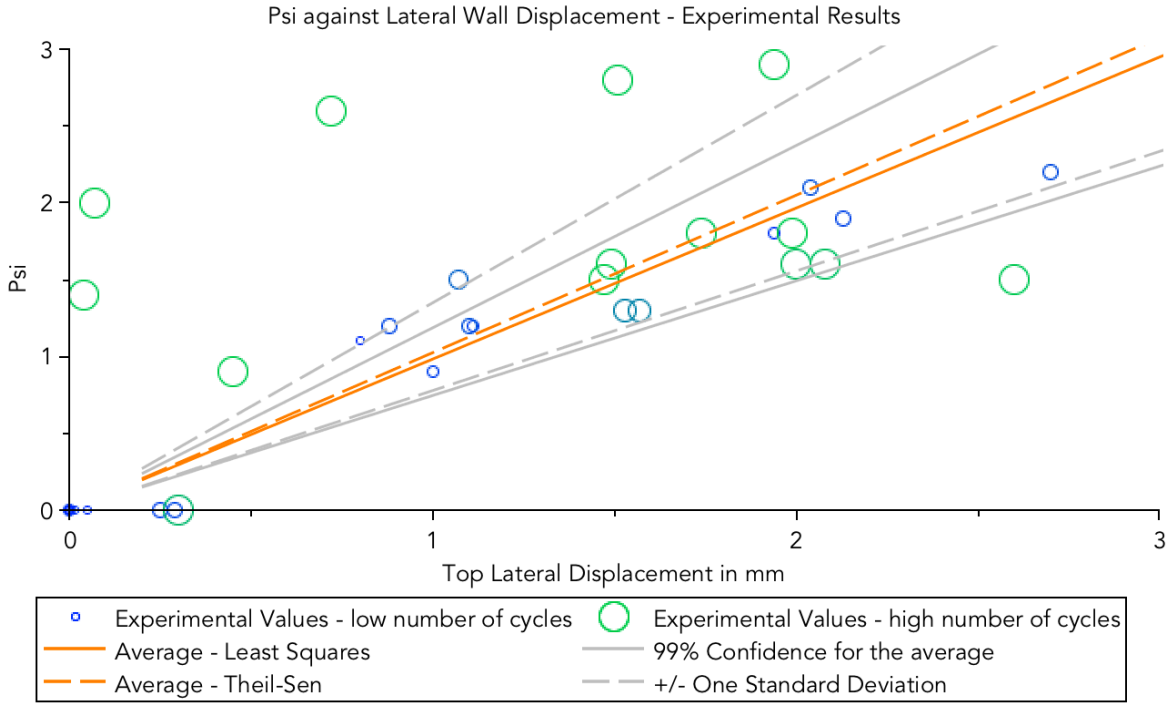

Figure 7.27. Top lateral displacement of the experimental walls against the damage measured from DIC results.

As can be observed, it would seem that a linear relationship between the lateral displacement and damage exists. Two simple linear regression methods have been used to produce a relation between the two variables. The least squares method minimises the squares of the distance of the points to the line, but is thus more sensitive to outliers. The Theil-Sen method takes the median of the slopes to each point and is so better equipped to handle points that are far away from the general tendency.

However, by looking closely at the outliers, it will be seen that these correspond to measurements taken towards the end of the tests. It is reasonable that a small displacement can still correlate to a high damage value because the walls have already been damaged extensively throughout the test. As such, it would be sensible to disregard these extreme points when computing the tendency of the pool. Figure 7.28 marks the points considered and the regression line traced.

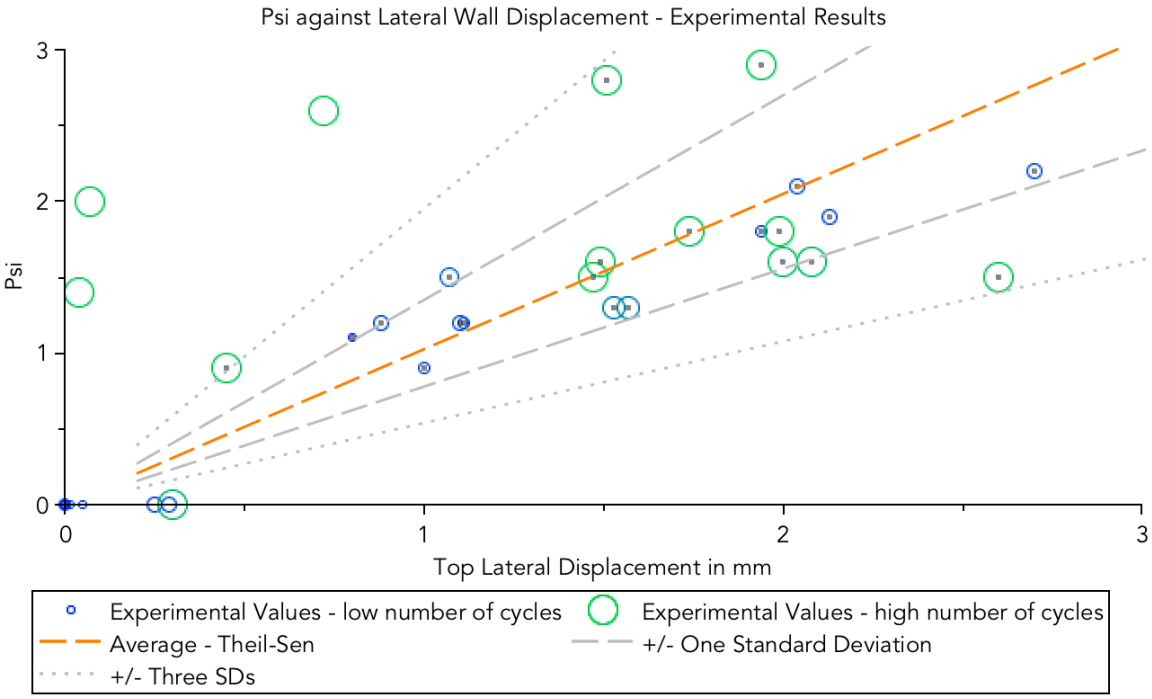

Figure 7.28. Regression line for the relationship between displacement and Ψ, marking the points considered.

The model then follows the form:

$$\Psi = \bar{\alpha} \cdot u_{Lat} \quad (7.2)$$

Where:

Ψ	is the final damage value
u_{Lat}	is the top lateral displacement, and
$\bar{\alpha}$	is the slope of the regression with a value of 1.025.

Since the slope ($\bar{\alpha}$) cannot be negative, but may still require very high values, it has been assigned a lognormal probabilistic distribution, which, with a long tail, is capable of reproducing this behaviour. The parameters of the distribution were obtained by setting the first and third quartiles equal. This distribution is shown in Figure 7.29. The fitted lognormal distribution receives the parameters 0.0246 and 0.278 as mean and scale, respectively.

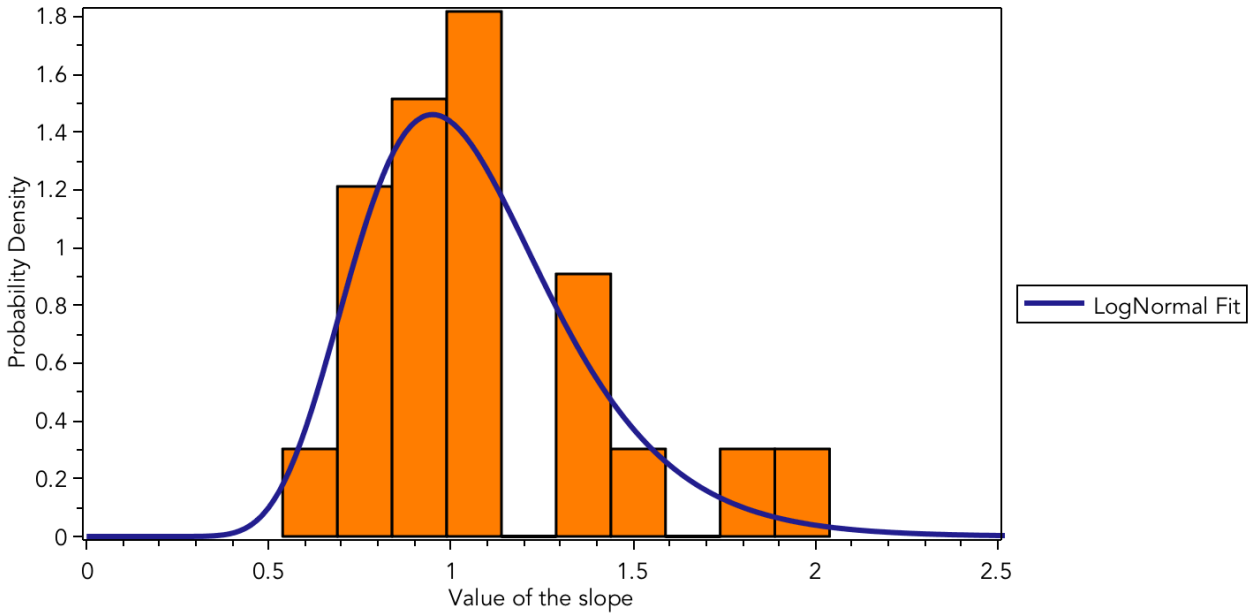

Figure 7.29. Histogram of the slope between Ψ and u_{Lat} and the fitted lognormal distribution.

Now, it is possible to attempt to include some measure of the degree in which the walls were pre-damaged by the time the value pairs were registered. By taking roughly the number of cycles that the wall endured, this can be plotted as shown in Figure 7.30.

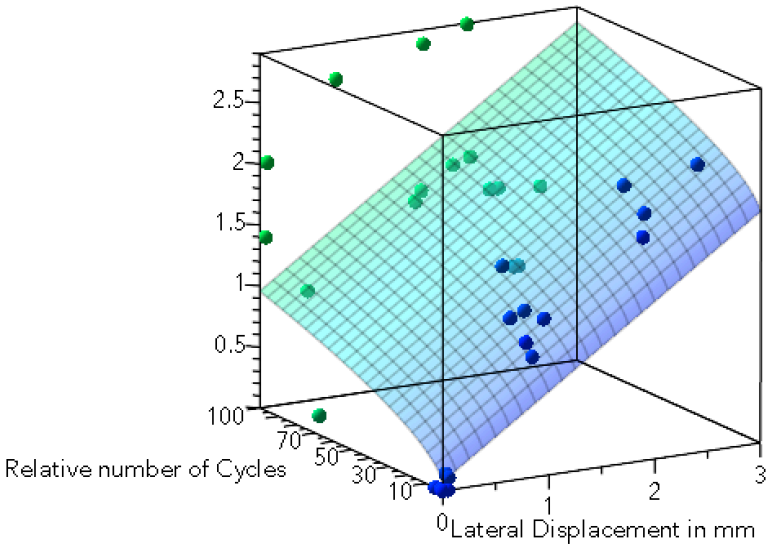

Figure 7.30. Psi-displacement value pairs including their position along the test.

It is also possible to complement the linear regression with a power law for the relative number of cycles and draw a surface as shown in Figure 7.30. Here it can be observed that value pairs towards the end of the tests are clearly higher than at the beginning and that an initial value of average pre-damage appears to exist.

However, there is not enough data to validate these observations; therefore, the simple linear regression model as shown in Figure 7.28 will be adopted.

Having established a relationship between damage and displacement, and characterised it with an uncertainty distribution, many more value pairs can be sampled as shown in Figure 7.31.

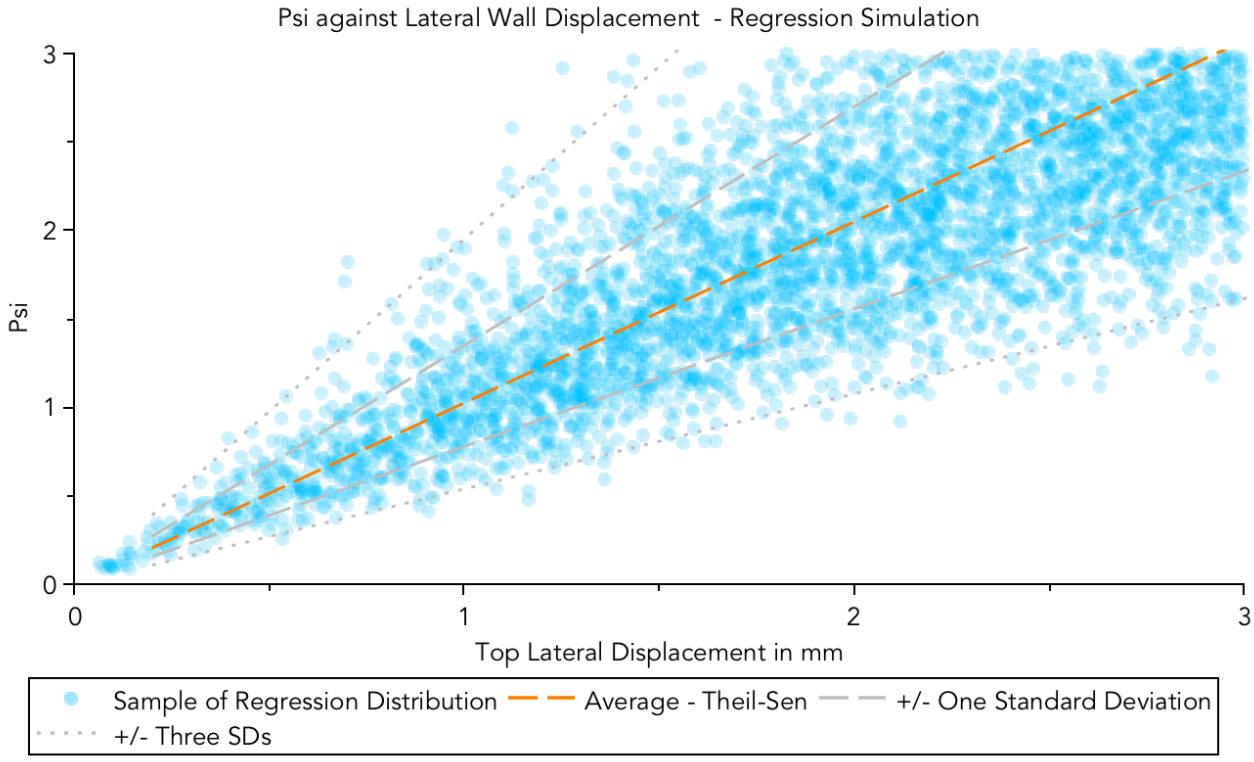

Figure 7.31. Sample value pairs.

7.5.2. Parameters and Single Degree of Freedom Model for Experimental RCs

To relate the lateral in-plane displacement at the top of the wall to a PGV value at the base of the wall, a single degree of freedom model will be used. This model computes the displacement that would result from a harmonic excitation at the base. To do so, the lateral stiffness of the wall and the equivalent mass on top are required. Further, the frequency of the harmonic excitation is key in determining the relation between displacement and PGV.

It would also be possible to integrate the response of the SDoF model to the PGV signal of an earthquake over time, but this defeats the purpose of using a simple SDoF model, in particular because the lateral stiffness would have to be modified over time and this behaviour is difficult to characterise accurately without introducing additional uncertainties. Moreover, the response to a single frequency, because it is not mixed with other frequencies, is more representative of potential future earthquakes that may carry that frequency predominantly. Additionally, if the probability of the exposure to a range of individual frequencies is observed, the behaviour will be able capture the most damaging frequencies.

The single degree of freedom model can be simplified to:

$$u=PGV\cdot Re\left(\frac{1}{\omega}\cdot\frac{K+i\cdot\omega\cdot c}{-\omega^2\cdot M+i\cdot\omega+K}\right) \qquad \begin{matrix} c=c_R\cdot 2\cdot\sqrt{K\cdot M} \\ \omega=2\cdot\pi\cdot f \end{matrix} \tag{7.3}$$

Where:

u	is the lateral displacement at the top of the wall
PGV	is the velocity at the base of the wall
K	is the lateral stiffness of the wall
M	is the equivalent mass at the top of the wall
c_R	is the ratio of critical damping
f	is the frequency of the harmonic excitation at the base of the wall

When taking the real part of this expression, the ratio between u and PGV can be computed. The lateral stiffness of the wall can be read from the five force displacement curves (see Chapter 4) and has a value of 34.1kN/m with a standard deviation of 3.9kN/m.

The mass on top of the wall corresponds to the weight of the steel beam and the equipment that is resting on the wall, which is around 3600kg (and produces the pre-compression value of 0.12MPa). Comparatively, the mass of the wall is in total 1200kg, but most of it is closer to the base such that its contribution to a SDoF system is lower. In fact, this warrants the use of a single degree of freedom instead of adding additional degrees of freedom throughout the height of the wall. Figure 7.32 shows the distribution of mass along the height and its moment in respect to the base. The mass of the piece of wall on top of the window is approximately 500kg. Based on this, the equivalent mass has been assigned a mean of 3800kg with a standard deviation of 200kg.

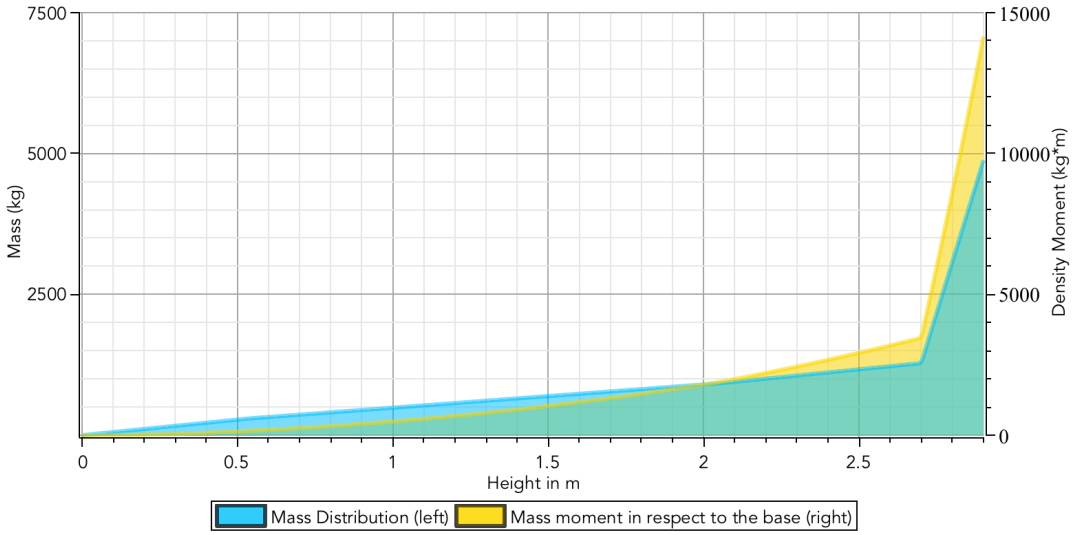

Figure 7.32. Mass distribution along the wall showing concentrated mass on top.

The damping ratio for masonry is around 5% of the critical damping. Additional information regarding this parameter is not available so it will be assumed that it follows a normal distribution with a mean of 5% and a standard deviation of 1%. The normal distribution is formed using a beta distribution to avoid negative values.

Finally, the frequency of the excitation needs to correspond to the frequency content of the earthquake's accelerogram. In Figure 7.33, the FFT of frequencies is displayed, together with the computed displacement of the SDoF system for a given frequency (with the mean values of the aforementioned parameters), and the normalised pseudo-velocity spectrum. It can be observed that the accelerogram is mostly empty above 20Hz and that the displacement for frequencies in this range is also negligible. Hence, only the range of 0 to 20Hz will be considered. To replicate the frequency content, an empirical probabilistic distribution has been generated with a probability density function that follows the FFT. This means that frequency values which have a higher presence in the Fourier transform, are also more likely in the distribution. A sample of this distribution is given in Figure 7.34.
The normalised pseudo-velocity spectrum gives a representation of the intensity of the PGV for each frequency. This means that, while a low frequency is more likely, and its amplification is higher, the earthquake signal didn't allow for the high amplification to occur. To reflect this, the amplification for very low frequencies (below 1Hz) was limited.

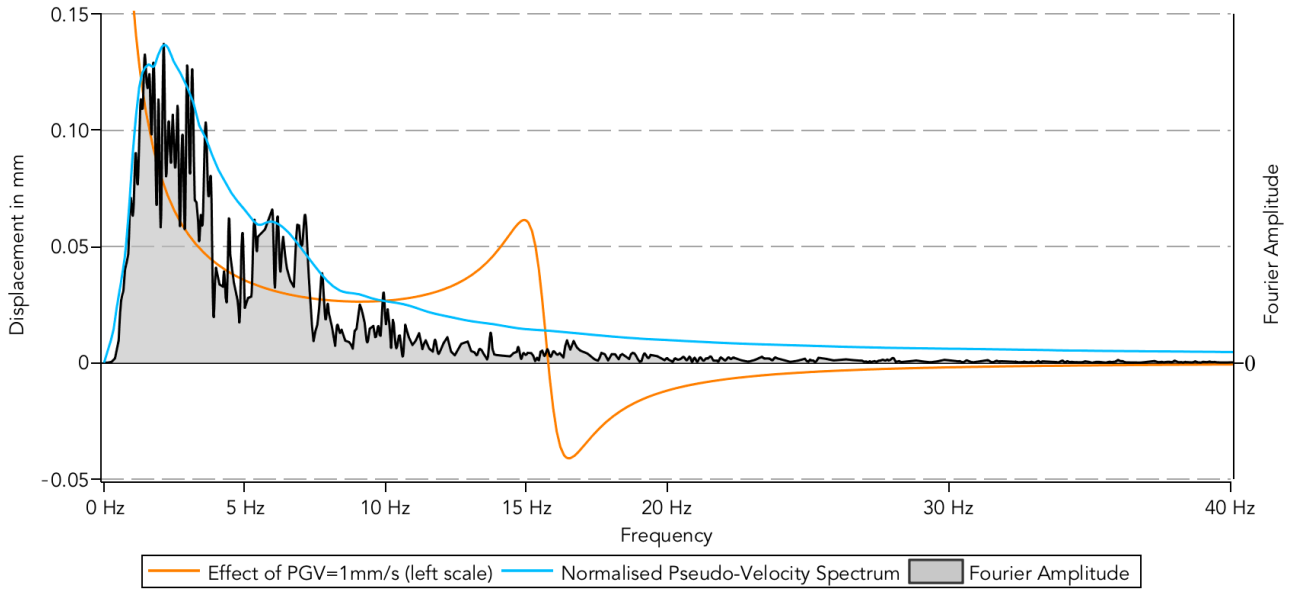

Figure 7.33. Frequency content of the spectrum for the chosen acceleration signal (see Chapter 6), and top lateral displacement for a PGV value of 1mm/s.

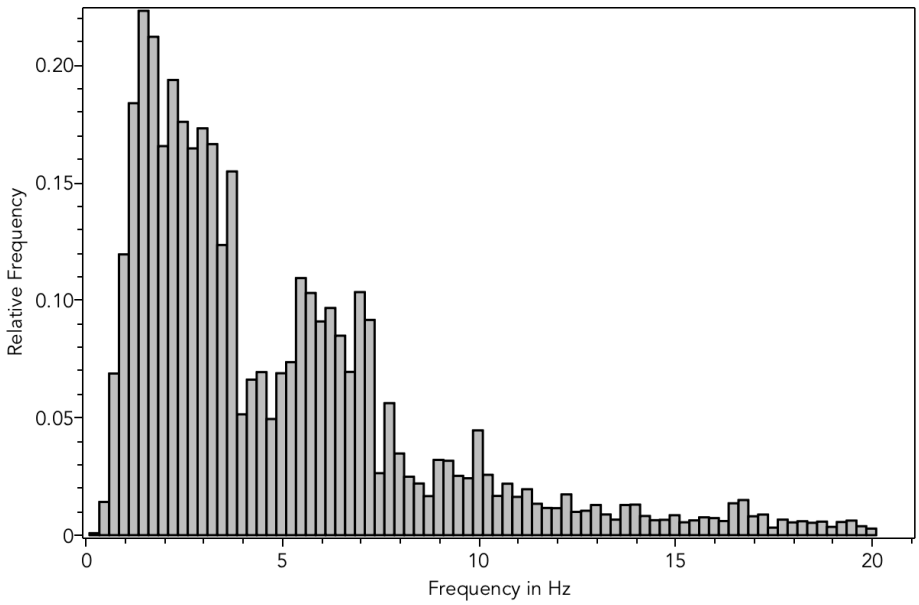

Figure 7.34. Sample of the empirical probabilistic distribution used to replicate the frequency content of the earthquake.

An overview of all the parameters involved in the computation of the experimental resistivity curves are summarised in Table 7.5 in the next section.

7.5.3. Figures of Experimental Resistivity Curves

Table 7.5. Summary of parameters for experimental curves.

Parameter	Symbol	Distribution	Mean	St. Deviation
Regression slope	$\tilde{\alpha}$	LogNormal	1.025	(scale) 0.278
Lateral wall stiffness	K	Normal	34.084	3.9121
Equivalent top mass	M	Normal	3800	200
Critical damping ratio	C_R	Pseudo-Normal	0.05	0.01
Frequency (harmonic)	f	Empirical	(5.9)	-

Based on these parameters, the probability of different damage levels for various displacement and PGV values can be computed; in total, 26 million cases were simulated. The first set of curves is given for a top displacement and hence only includes the uncertainty of the regression parameter between damage and top displacement (see Figure 7.35). For a lateral displacement of 1mm, or a drift of 0.37‰, the probability for the wall to be or exceed the first damage level (Ψ=1) is approximately 50%. Tomassetti et al. (2017) indicates that at a drift of 0.47‰ (or 1.25mm), the masonry structure of their study had reached DS1; for the experimental wall, this corresponds to a probability of 80% of Ψ=1 or 30% of Ψ=1.5, which fits well with the definition presented in Chapter 2.

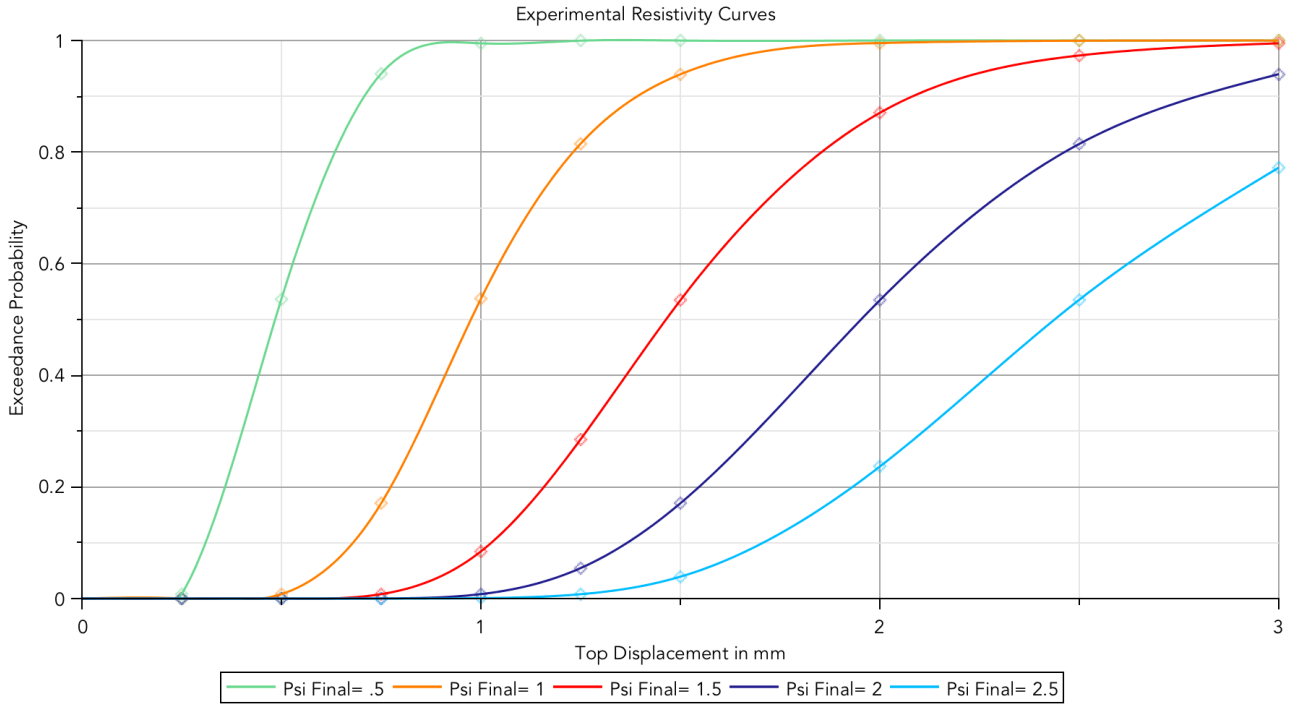

Figure 7.35. Experimental resistivity curve for given top lateral displacements.

During the experiment, the displacement of the wall was controlled such that the crack widths at the corners of the windows were 0.1mm. This was accomplished for a lateral displacement of 0.9mm on average. Moreover, at this displacement, for most cases, another crack had already open at the side of the wall with a slightly larger crack width. This would correspond to an estimated Ψ=1.2. For 0.9mm, the curves show a probability of exceeding Ψ=1.2 of 25%. This is a sensible value.

Including the rest of the parameters allows for the elaboration of PGV-based resistivity curves shown in Figure 7.36 and Figure 7.37 next.

Now, these curves are the extrapolation of all the experimental results, meaning that no difference is made if the walls were 'virgin' or already pre-damaged. As has been mentioned, there is not enough data to

assert a distinction or influence in the predicted final damage value. However, a rough estimation can be inferred from the value pairs that were registered closer to start of each test. For these points, the slope is around 0.65, 35% lower than the value of 1.025 for the entire pool. Using this slope, the curves for the initially 'undamaged' cases can be computed (Ψ_0=0). These are shown in Figure 7.37 and can be seen to have exceedance probabilities significantly lower than the more certain curves.

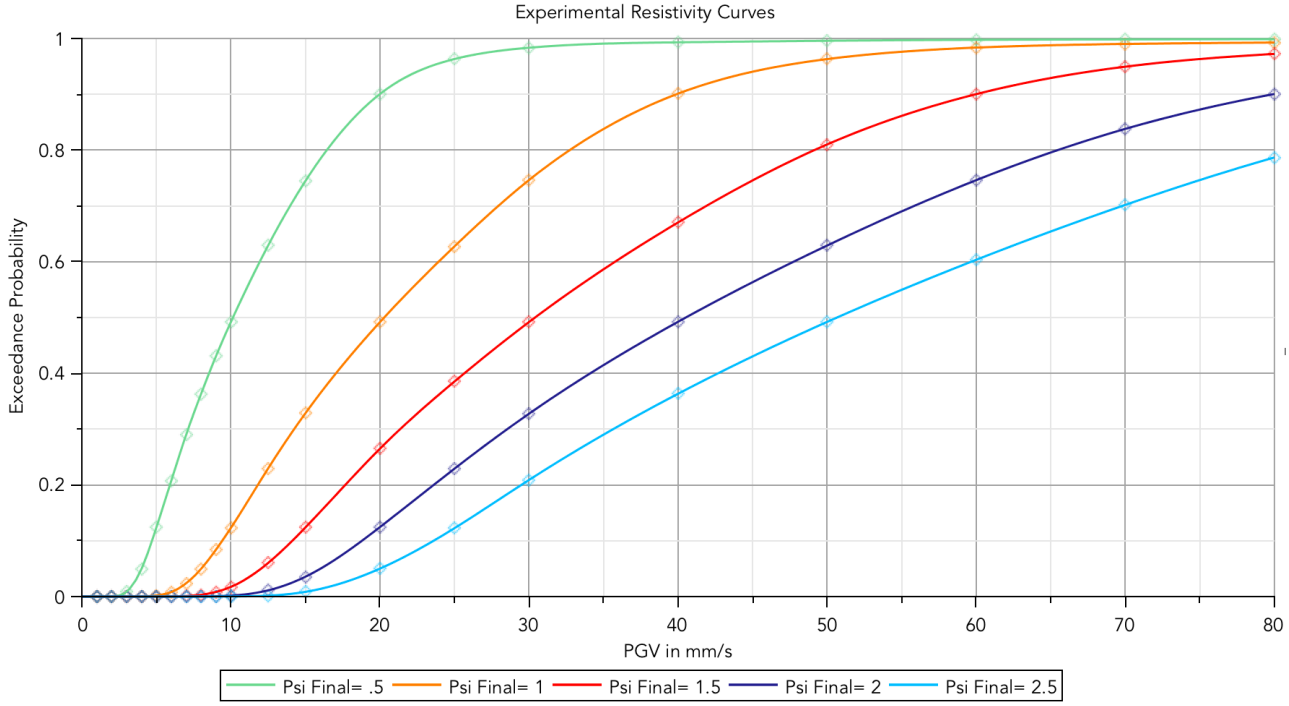

Figure 7.36. Experimental resistivity curves for given PGV values.

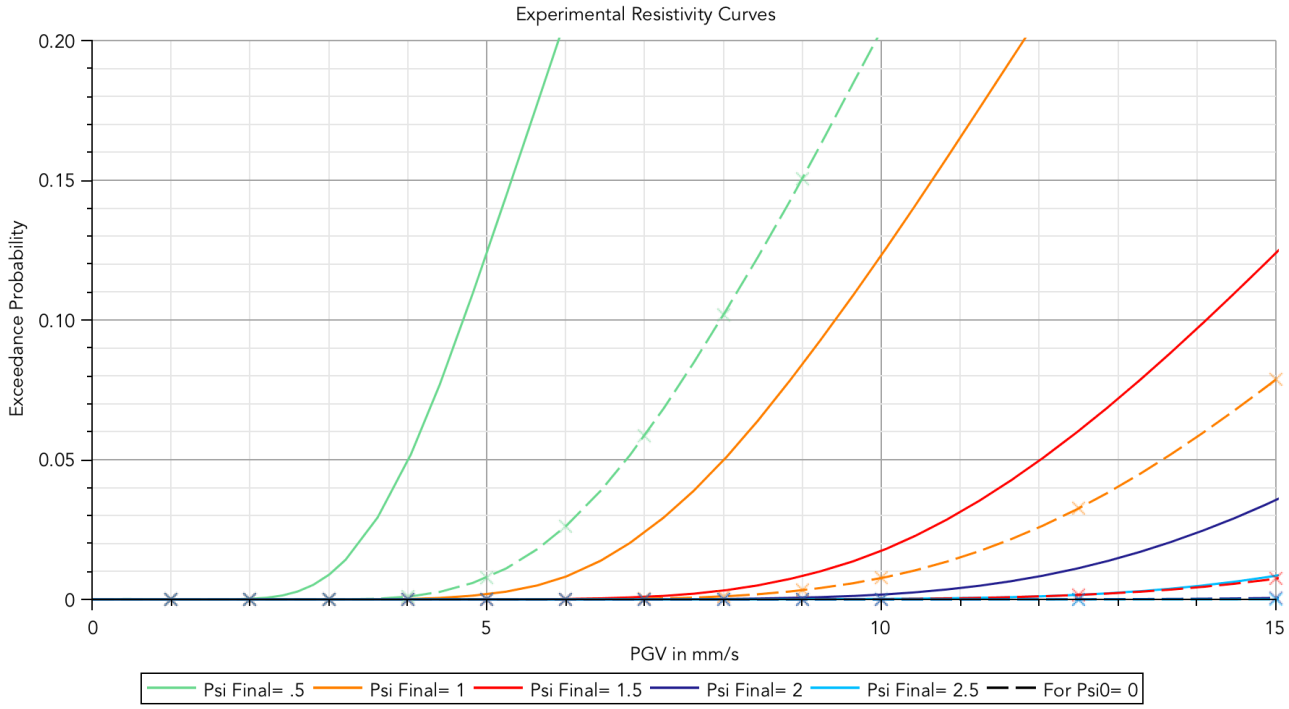

Figure 7.37. Experimental resistivity curves for given PGV values in the smaller range of 0 to 15mm/s. Additionally, rough estimation for the curves computed for undamaged cases.

7.5.4. Discussion of the Experimental Resistivity Curves

The difference between the solid lines (regression with the full results) and the dashed lines (rough estimation of the regression for undamaged cases) in Figure 7.37 is precisely because the influence of the regression slope is high. A change of one standard deviation in the mean of the regression parameter ($\bar{\alpha}$) modifies the expected displacement by 27%. A change of one standard deviation of the lateral wall stiffness, affects the results by 5.4%, a change of the equivalent mass, by 3%, and the critical damping by 0.7%. These sensitivity values are weighted averages over the frequency interval; their computation is explained next.

Modifying the stiffness, for instance, shifts the natural frequency of the wall. This means that where before the displacement was damped, now it may be amplified; this would be an important change. However, the frequency content of the earthquake signal may be low around this point, such that the influence of the important change becomes diminished. Similarly, while the change around the predominant frequencies of the earthquake is small, the greater likelihood of these frequencies, may make this change important.

It is thus necessary to multiply the change caused by a certain variable (as a function of the frequency $\Delta(f)$) with the available frequency content of the earthquake (S_F). This value is then divided by the area of the frequency content.

This weighted average can be computed with:

$$\dot{\Delta}_\sigma = \frac{\int_0^{20\,Hz} \Delta(f)\cdot S_F(f)\cdot df}{\int_0^{20\,Hz} S_F(f)\cdot df} \tag{7.4}$$

Where:

$\dot{\Delta}_\sigma$ is the weighted change (sensitivity) of the expected lateral displacement due to the change of one standard deviation of the parameter in question

Δ is the absolute percentage change of the parameter as a function of the frequency

S_F is the Fast Fourier transform of the earthquake signal

df is the integration variable (over the frequency interval)

This can be understood by observing Figure 7.38. Here, the solid lines show the absolute change as a function of the frequency ($\Delta(f)$). It can be seen that the change is greater around 15Hz; however, the frequency content (grey background) is lower in this range. Multiplying both, results in the dashed lines which are more constant through the entire interval. Finally, the average effect of the multiplication with the spectrum is removed and the horizontal lines are computed ($\dot{\Delta}_\sigma$).

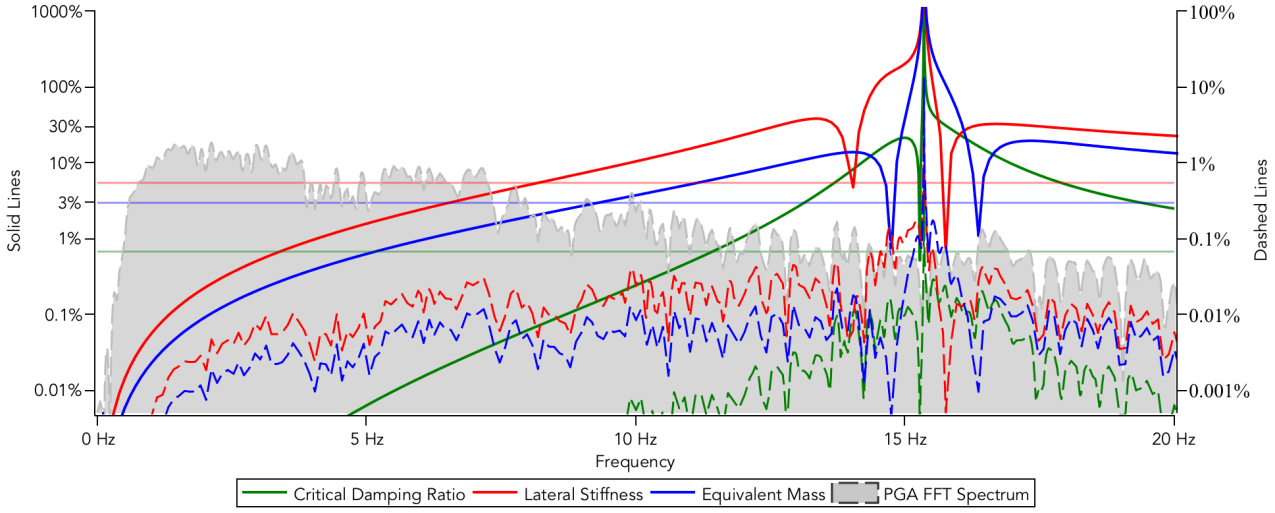

Figure 7.38. Overview of sensitivity for various parameters.

The last parameter to assess is the frequency. It should be clear that its influence is the most important: a high frequency will yield a displacement of zero for any PGV, while a very low frequency will generate a high displacement even with a low PGV. However, the frequency is defined for each earthquake; to observe a change, the signal of a different earthquake needs to be evaluated. The FFT of the synthetic signal from a possible future earthquake as defined by Tomassetti et al. (2017) is shown in Figure 7.39. It can be seen that the frequency content is different to that of the Huizinge signal used for the elaboration of the curves. The change on the average expected displacement is then of 7%. This is due to the high content of lower frequencies which are detrimental to the wall.

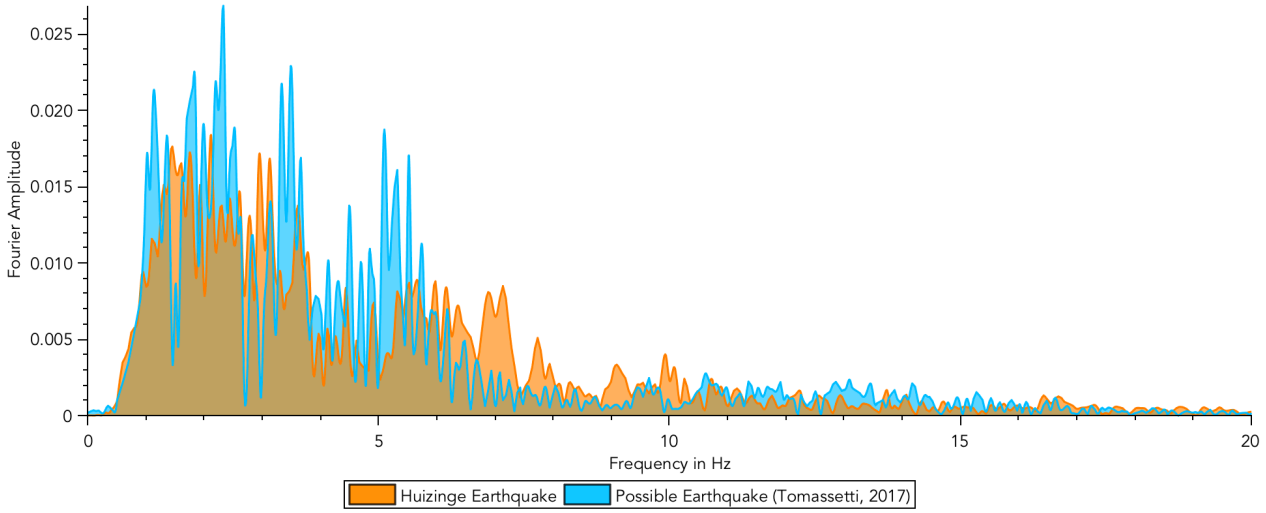

Figure 7.39. Comparison of two earthquake signals.

*Table 7.6. Summary of sensitivity for the probabilistic parameters. *Sensitivity defined as the weighted variation of the expected result for a change of one standard deviation.*

Parameter	Symbol	Sensitivity*
Regression slope	$\tilde{\alpha}$	27%
Lateral wall stiffness	K	5.4%
Equivalent top mass	M	3.0%
Critical damping ratio	C_R	0.7%
Frequency	f	7.0%

Note that the influence of the frequency is highly dependent on the earthquake signal analysed. The possible earthquake predicted by Tomassetti et al. (2017) was assumed to be representative but conservative, meaning that differences with real, measured earthquakes exist. These differences should also produce a greater change.

During the laboratory tests, one wall was excited dynamically to compare damage caused by quasi-static or dynamic loading. From these tests, a relationship between the peak velocity applied at the top of the wall and the top lateral displacement was obtained. The SDoF model also produces a relationship between the velocity at the base and the displacement at the top. This is compared in Figure 7.40 next.

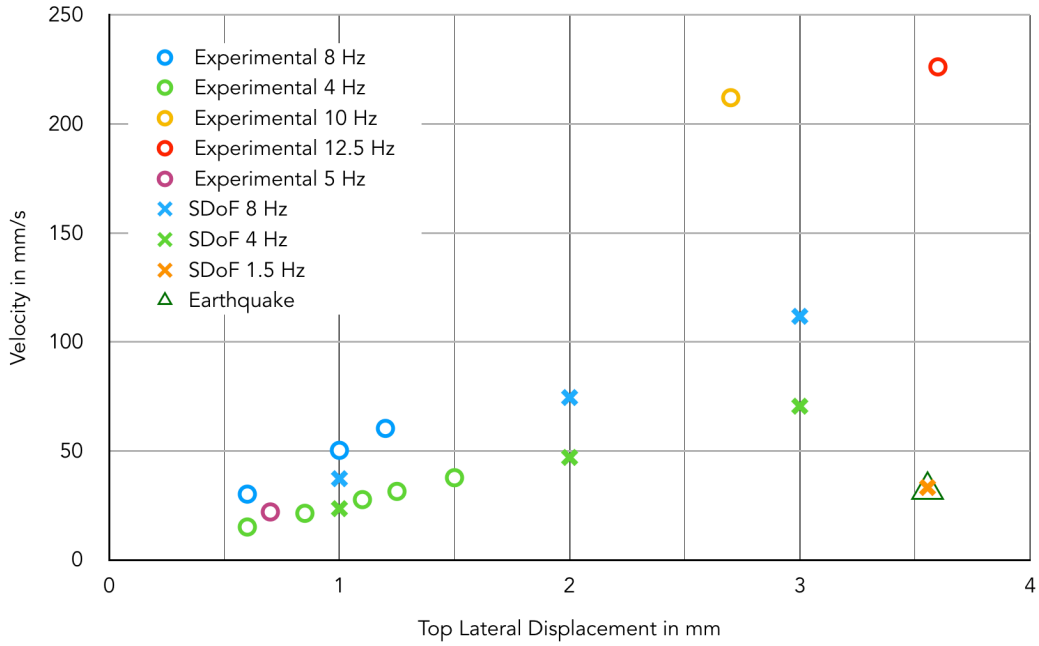

Figure 7.40. Velocities and displacements from dynamic excitations.

Figure 7.40 shows that the application of the velocity at the top during the laboratory test is comparable to an excitation at the base when the frequencies are low. This is coherent with the observation that vibrations at high frequencies are damped by the wall. Moreover, to obtain the ratio of PGV and displacement seen from the earthquake's signals, the SDoF model seems to require a frequency of 1.5Hz. This validates the observation that the lowest available frequency in the signal, together with the higher amplification of low signals by the wall (see Figure 7.33), are key in determining the behaviour of the wall.

Considering the sensitivity and variability of all the involved parameters, a rough estimation of the confidence interval for the resistivity curves can be produced; these are plotted next. Here, the 75% confidence interval is shown. It can be observed that the intervals are not small. This is mainly due to the high uncertainty in the regression between displacement and damage values. Additional value pairs would be required in order to reduce the uncertainty; this would comprise the analysis of an increased number of walls and the registry of more points along the tests, possibly with a relation towards the pre-damage.

Specific Limitations of the Experimental Resistivity Curves

The resistivity curves drawn directly from the experiments carry significant uncertainty and debatable assumptions. They have been elaborated to provide additional verification to the computational curves and gain further insight into the progression of damage, but have not been used to draw any conclusions on their own.

Firstly, their elaboration is based on the damage analysis of a few walls. This is not sufficient to reliably draw conclusion about the behaviour of masonry.

Secondly, multiple value pairs are taken from each wall, meaning that a certain level of pre-damage is present for all but the first points obtained from each wall. Because of this, assumptions have been made to exclude what seem to be pairs where pre-damage significantly affect the results. Moreover, inferring final damage values below $\Psi=1$ is difficult because no experimental results lie in this range.

Thirdly, the walls have been tested statically and a SDoF model is used to extrapolate their behaviour to a dynamic situation. Whether this simple model represents the walls sufficiently is uncertain.

In sum, care needs to be exercised when comparing and observing the experimental resistivity curves.

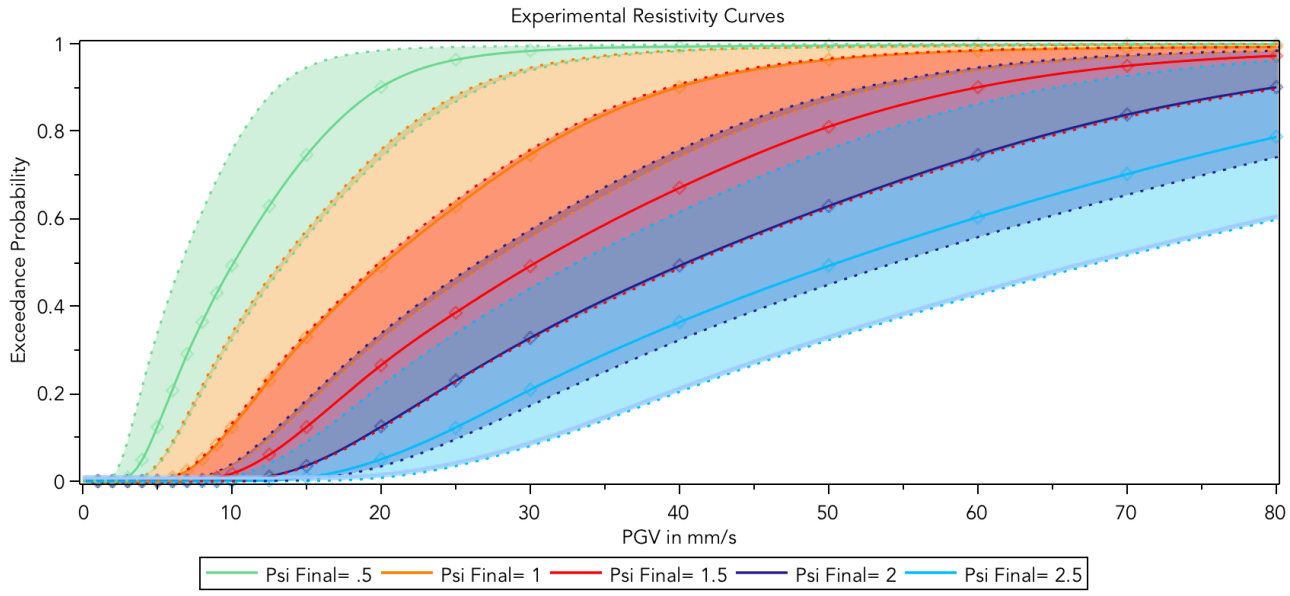

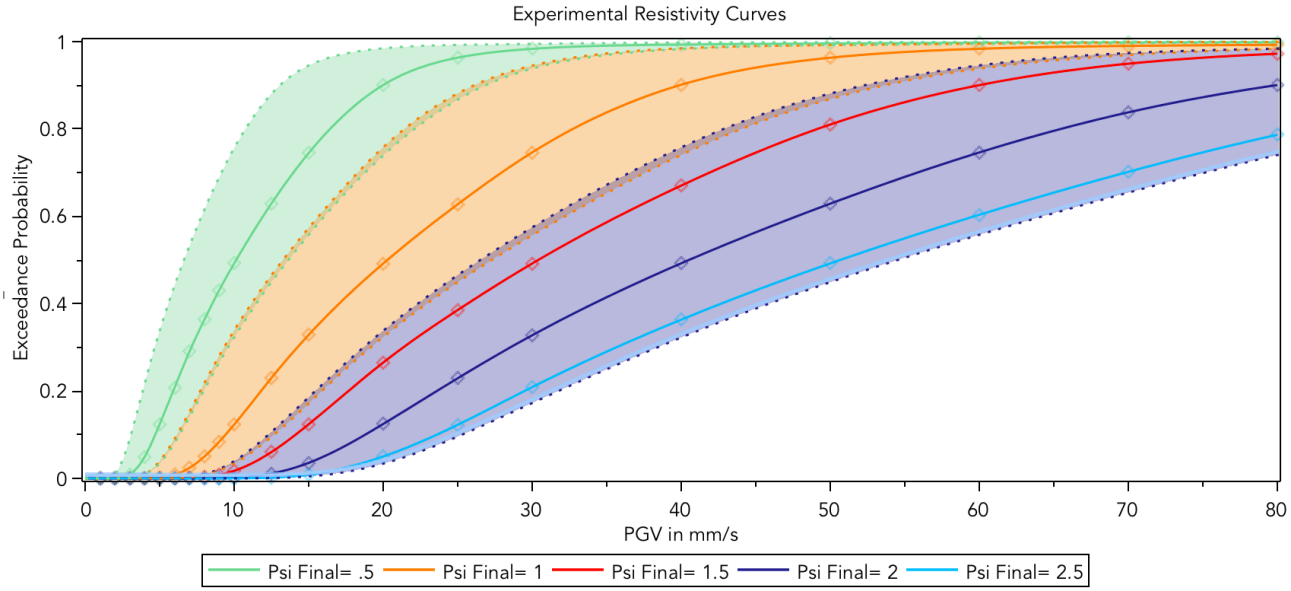

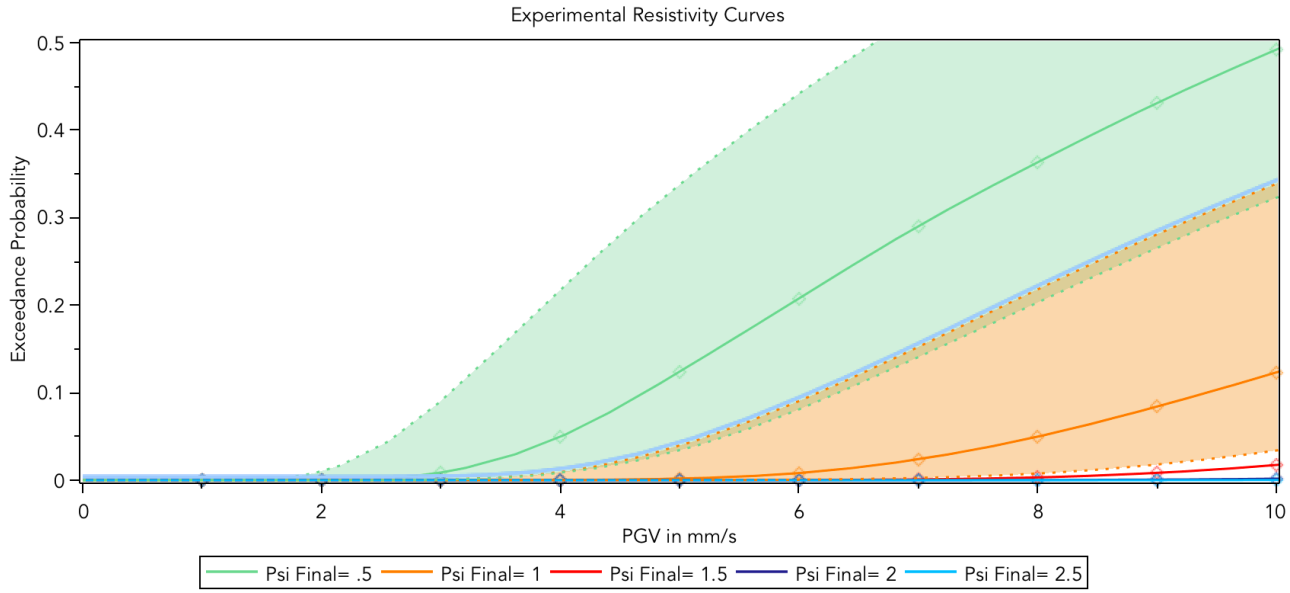

Figure 7.41. Experimental resistivity curves showing a rough estimation of the confidence interval (75% confidence). All graphs are the same but display a different number of curves and intervals for clarity.

7.6. Discussion of Computational and Experimental Curves

7.6.1. Comparison Between Computational and Experimental Curves

Since the computational models have been calibrated based on the laboratory tests, the curves fabricated from these models should be similar to the curves extrapolated directly from the tests. However, both procedures possess and introduce uncertainties that will make the results differ from each other. A few of the most relevant factors are: the aleatory uncertainty in the material, the uncertainty in the regression procedures, the simplification when using a SDoF model, and the variability of the damage assessment method. In particular, the largest difference is expected to lie in the SDoF which tries to give the experimental curves a PGV value for comparison: while the computational models are based on a time-history analysis, the experimental curves reproduce the frequency content of the earthquake with an empirical distribution and the amplification of the wall. Since the excitation for the SDoF is an isolated harmonic, it will produce higher damage values than the time-history analysis.

Additionally, the computational models include the corresponding earthquake signal in the vertical direction, in contrast to the experimental test which was only pushed laterally; but, the influence of the vertical vibrations was observed to be negligible.

Further, the material variability of the computational models may have been exaggerated. Due to the fact that failure of the wall occurs at the weakest point, and the distribution of the weakest points has a lower variability than that of the individual points, the variability of the computational models may be lower. If this is the case, the curves will be steeper, that is, with a lower probability at the lower PGV values and a higher probability at the higher PGV values.

This is precisely what is observed in Figure 7.42: overall, the experimental results seem to produce probabilities higher than the computational curves. However, many interesting observations can be made:

- The original curve from Waarts (A) seems closer to the computational curve for Ψ=1.5 (H),
- However, when the methodology from Waarts is updated with material values that better reflect the masonry properties of this study (see Section 6.1), the curve changes drastically (B), indicating a high sensitive to these values. This new curve is above all others, which is logical since it corresponds to the probability of damage initiation (Ψ>0).
- The curve for lowest perceivable damage Ψ=1.0 (E) is roughly a fifth of the updated Waart's curve (B). This would mean that while the probability for the initiation of damage is high, the probability for damage that can actually be observed is significantly lower.
- The experimental curve for Ψ=1.0 (C), however, is close to these two curves corresponding to unperceivable damage (G and J). This would mean that experimental results show that damage is more probable than what the numerical methods show, but this would be an incorrect conclusion because:
- The experimental results include cases for the wall where damage has already occurred. If only the cases with less pre-damage are considered, the curve moves down (D) and initially resembles the computational curve with no pre-damage (E) while later following the computational curve with some earthquake pre-damage (F).
- Additionally, when including the computational curves with diminished material variability (I, J, K), these seem to follow the experimental curves much closer. It would seem that the material of the experimental cases was very similar, and as such, these curves resemble them better; however, if the wall is to be representative of cases in the field, the material variability is expected to be higher.

When observing the curves in the interval of 5 to 20mm/s some additional observations can be made:

- Many of the curves intersect in this range. This means that the variability of the phenomenon in this interval is high and that each methodology shows a different PGV value below which the probability for damage is negligible. Nonetheless, both experimental and computational curves, especially if some degree of pre-damage is accounted for, show a clear PGV boundary for damage.
- The experimental curves (C and D) clearly show zero probability of damage below 5mm/s, but this increases rapidly above 5mm/s. Curve D, for the experimental, less pre-damaged cases, shows the start of damage at a higher value of PGV of approximately 8mm/s.

- The curves with less material variability (I, J, K) also show a smaller damage probability in this lower PGV range.

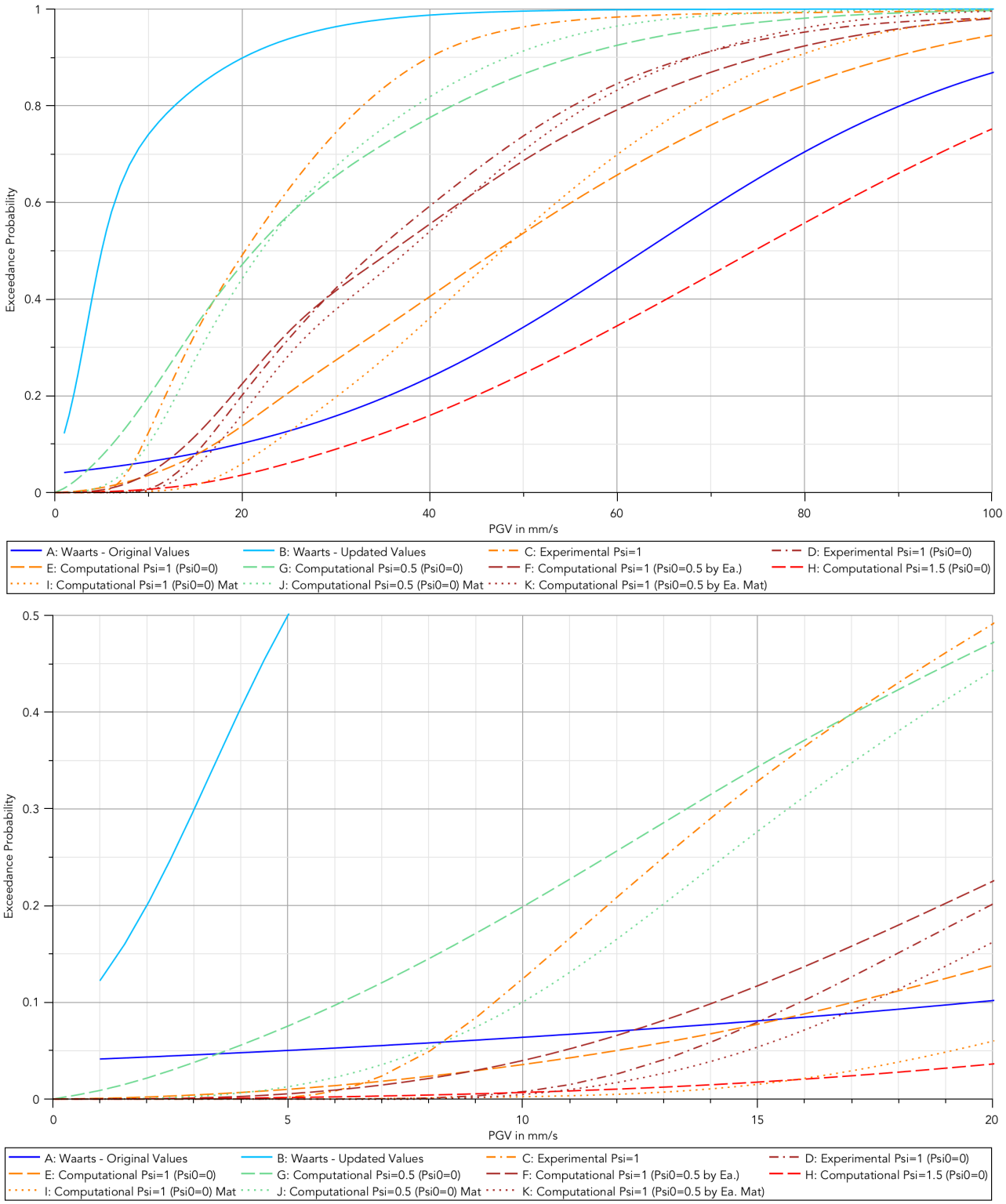

Figure 7.42. Comparison between computational and experimental resistivity curves and Waart's curves.

7.6.2. Limitations of the Resistivity Curves of This Report

It is paramount to note that the curves presented in this chapter have important limitations and are a first glance into the probability for light damage to masonry structures:

Firstly, they have been constructed based on the detached behaviour of a wall. This wall has only been analysed in-plane and its potentially complex interaction with the rest of a structure has not been observed. The inclusion and significance of out-of-plane effects and whole-structure behaviour needs to be included.

Secondly, the material modelled for the wall is intended to reproduce masonry of baked-clay bricks with traditional cement mortar joints. This is typical of pre 1950s construction techniques, but ageing effects and deviations with laboratory conditions are expected. An uncertainty has been included in the parameters of the material, but its correlation to real cases can only be asserted to a limited degree of representativeness. Moreover, the wall was modelled of a single leaf as opposed to the double-wythe traditional of the time with the purpose of making the analysis of damage in laboratory conditions more transparent, but this is also bound to affect the outcome of damage.

Thirdly, the curves have been produced on the basis of one earthquake accelerogram. The signal used corresponds to the earthquake of Huizinge of 2012. Damage from additional earthquakes has not been included as of yet, but is required to increase the reliability of the curves. This limitation is partly responsible for denoting the curves as "resistivity" instead of "fragility" curves (see Section 7.1).

Fourthly, the pre-damage scenarios have been selected based on the qualitative analysis of damage cases, but divergence between these fictitious scenarios and real cases is expected. In Figure 7.21 for instance, one can observe that the difference in probability of damage between one type of pre-damage case and another (both with the same value of initial pre-damage) can amount to 40%. The pre-damage scenarios are included to illustrate that structures with some level of pre-damage influence the probability of further damage, but the number and type of most representative configurations, and the sensitivity of including these scenarios has not yet been investigated.
Moreover, the behaviour of the computational models has not been validated experimentally for these pre-damaged scenarios. It has been argued that these scenarios have been modelled numerically with calibrated models precisely due the complexity of testing combination of actions in the laboratory. However, additional variations should be tested in the laboratory to provide a stronger foundation for the models.
Additionally, the computational models have not been validated against dynamic conditions, either. The experiments have been conducted statically, but the models have been extrapolated to dynamic loads. It is possible that fast loading (as it occurs under dynamic conditions) and inertia effects are not being well represented by the models.

Further, resistivity curves have been elaborated directly from experimental results. These curves are subjected to strong assumptions and simplifications and serve only as a point of comparison.

In sum, limitations such as a single wall geometry, one type of masonry material, one earthquake accelerogram, and limited statistical properties for the inputs, indicate that care needs to be exercised when using these curves.

Nonetheless, the resistivity curves presented in this report should be more reliable in describing the probability of light damage due to earthquakes than the framework of Waarts (1997) described at the beginning of the chapter. In particular, the framework of this report includes a quantification of detectable damage, the effect of existing pre-damage of varying intensity, the inclusion of changes in the dynamic behaviour of the wall as it becomes damaged, and the direct analysis of earthquake signals (instead of an average of frequency-responses). Table 7.7 provides a comparison between the two frameworks.

Table 7.7. Summary and Comparison of Frameworks.

Criteria	Waarts (1997)	Light Damage Framework (Chapter 7)	Light Damage Framework (Potential Future Improvements)
Loading	Surface Vibrations *Base Soil* *Sine-shaped Vertical Deformations*	Earthquake Accelerogram *Lateral and Vertical Base Displacements*	Earthquake Accelerograms *Lateral and Vertical Base Displacements*
Loading Modifications	None	None	Multiple Earthquakes
Type of Loading	Static	Dynamic	Dynamic
Type of Analysis	Elastic	Non-Linear	Non-Linear
Pre-compression Stress(es)	One: 0.5 MPa	One: 0.12 MPa	Two. Values TBD
Frequency Dependent	No	Included in Accelerogram	Included in Accelerograms
Damage Criteria	Exceedance of Horizontal Tensile Stress	Crack Development	Crack Development
Damage Output	Only Initiation	Discretised Damage Levels	Discretised Damage Levels
Damage Progression	No	Yes, During Earthquake	Yes, During Earthquake
Damage Aggravation	No	Yes, With Pre-Damage Levels	Yes, With Pre-Damage Levels
Initial Condition Variations	Yes, one or two states: *Good (2) & Bad (1)*	Yes, four states: *Virgin, Earthquake, Settlement, Shrinkage*	Yes, four states: *Virgin, Earthquake, Settlement, Shrinkage*
Structure Type	Single Wall	Single Wall	Single Wall
Structure Modifications	Window Position	None	Wall Size, Configuration, and Boundaries
Out-of-plane Effects	No	No	Yes
Number of Masonry Types	Two	One	Two or more
Masonry Type	• Baked-clay Bricks (?) with Cement Mortar (pre 1950) • Brick and Mortar (pre 1900)	• Baked-clay Bricks with Cement Mortar (pre 1950)	• Baked-clay Bricks with Cement Mortar (pre 1950) • Calcium Silicate Bricks (post 1960)
Masonry Wythe	N.A.	Single-wythe	Single-wythe & Double-wythe
Soil Dependent	Yes	No	No
Soil Type Variations	No	No	No

7.7. Conclusions of Chapter Seven

The Light Damage Framework developed for this research project includes non-linear models that output cracking directly and thus allow for a quantitative interpretation of damage. As such, the framework builds upon and extends a previous framework by Waarts (1997) that was based on linear analyses and focused on the onset of cracking rather than quantifiable crack propagation and crack width.

Based on over 100 scenario analyses for the limited case of a single masonry wall, indicative resistivity curves have been elaborated.
From these, the probability for visible damage (cracks of at least 0.1mm in width corresponding to a damage level of $\Psi>1$) when exposed to a scaled version of the Huizinge (2012) earthquake with a PGV of 20mm/s (in the horizontal direction) is approximately 15%; for the unscaled accelerogram of the Huizinge earthquake (48mm/s), this probability is around 50%.

However, the framework is capable of including some degree of pre-damage before the evaluation of the earthquake. In the framework, pre-damage can be due to previous earthquakes, settlements, or hygro-thermal effects. Minor and imperceptible pre-damage ($\Psi_0=0.5$) seems to be capable of doubling the probability for visible damage ($\Psi>1$) from 15% to 30% for a PGV of 20mm/s, and for a PGV of 48mm/s from 50% to 75% (when the average of the pre-damage types is considered).
Nonetheless, preliminary analyses indicate that the probability for damage to become more severe than aesthetic damage ($\Psi>3$) is negligible at 20mm/s and approximately 5% at 48mm/s. Considering pre-damaged structures does not alter these values noticeable, in fact, some minor pre-damage reduces the probability for further damage. Apparently, a lightly damaged structure seems capable of releasing energy from the earthquake through the existing cracks.

Resistivity curves were also extrapolated from the limited experimental results. These curves seem to indicate a higher probability for damage; however, a certain degree of pre-damage is inherently included in most of the experimental results (after the first test on each specimen). Additionally, the experimental curves are fabricated upon discrete harmonic excitations which are more damaging than a single earthquake accelerogram already including many important frequencies.
In this light, the curves seem to be comparable to those derived with computational models.

When comparing the indicative resistivity curves elaborated for light damage against existing definitions of damage state one (DS1), most comparison curves fit within the range described by the light damage curves (see Figure 7.25). This seems to indicate that both the curves and the representativeness of the study case wall are in line and are compatible with other studies.

Chapter 8

Conclusions and Recommendations

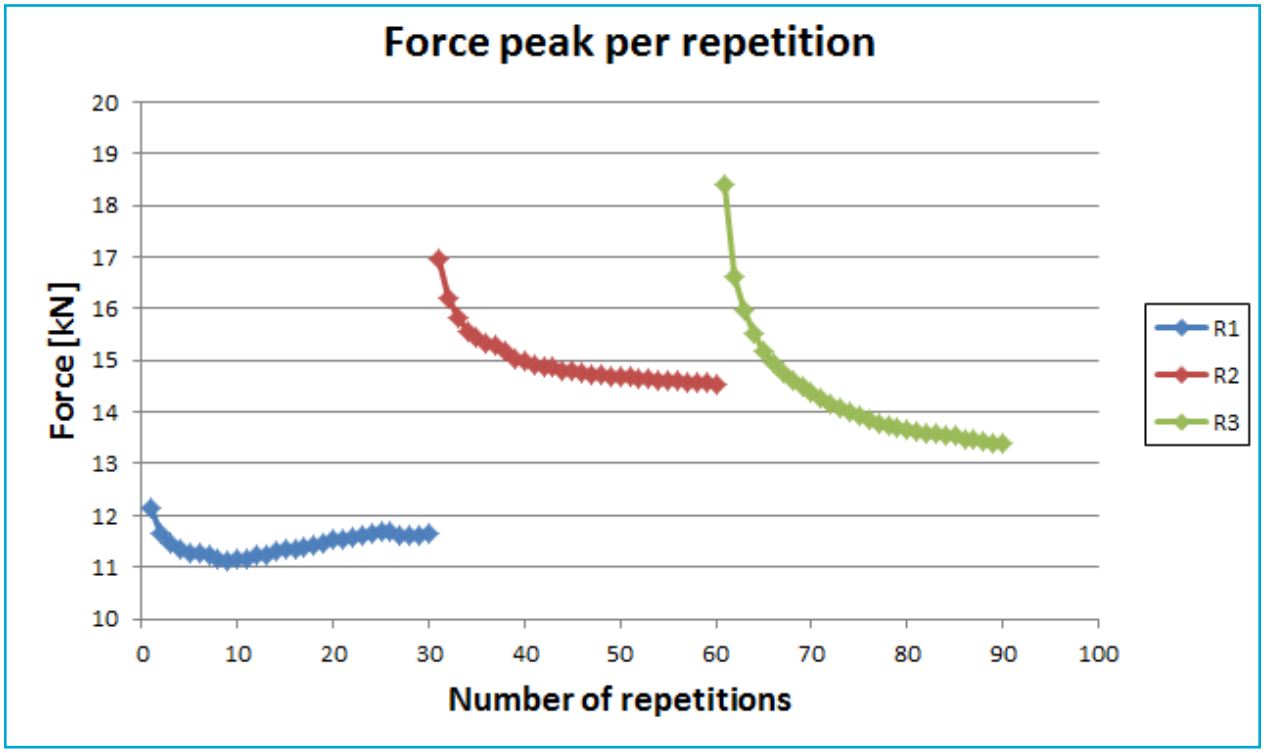

TU Delft

8. Conclusions and Recommendations

8.1. Conclusions

This study is conducted to investigate how cracks, characteristic of the lower damage states, initiate and propagate through unreinforced masonry typical of the Groningen area.

In Chapter 2 a method is proposed to quantitatively and objectively determine damage based on the intensity of cracks in masonry (damage level, Ψ). This method can be useful for future damage assessment in the field but is currently focused on helping categorise and correlate damage observed in laboratory tests and numerical models.
With this damage scale, masonry exhibiting cracks of at least 0.1mm in width is assigned a damage level of Ψ=1; values lower than 1 correspond to undetectable damage.

It is first important to emphasise that the conclusions provided here are derived from the representative, albeit limited cases treated in this study. They are applicable insofar the geometry, excitations, and material do not deviate significantly from the studied cases. The results are presented for the case of old, baked-clay single-wythe masonry walls without important interaction with the rest of a structure and subjected mainly to in-plane loads. A limited number of walls have been tested experimentally and models have been calibrated on these tests.

Accordingly, properly validated models are key in gaining a better understanding of damage in masonry caused by multiple sources. Many variations have to be modelled for this purpose, which then requires an accurate yet still affordable model. In this sense, experimental tests (of an in-plane wall and separately, its window bank) performed for this project and described in Chapter 4 have a twofold purpose: Firstly, to be able to physically test interesting masonry configurations to gain better insight into the behaviour of crack initiation and propagation in masonry for the lower damage state when loaded with multiple repetitions; Secondly, the experimental tests are used to validate and calibrate the numerical models.

The prediction models in Chapter 3 give a good indication of where the crack initiation was to be expected in the experimental tests and how the cracks propagate. The predictions were concluded towards a detailed design of the laboratory tests and their incremental, repetitive loading schemes.
In the post-test calibrations (Chapter 5), different material models were tried out to find the most suitable one for matching the experimental tests. The constitutive Engineering Masonry Model is capable to distinguish cracks in the joint directions as well as stair-case cracks. With this material model, crack pattern and crack propagation are quite well presented. The contrast between the inferior results of the prediction models and the accurate results from the post-diction models argues for the use of the Engineering Masonry Model, a refined, regular mesh, and better material parameters.

The Digital Image Correlation measurement system has proven to be an excellent tool to capture the crack initiation and propagation in the experimental tests described in Chapter 4, as well as to analyse damage directly. The results of the DIC are also used to validate and calibrate the computational models. Sensors are used to measure the samples' displacements and forces required to achieve a certain damage state. Since in both the in-plane wall (IP) test and the window bank test the displacement of the sample is controlled, the observed reduction of force for a certain repetition displacement step can be considered as degradation of resistance or, in other words, progression of damage in the sample. In both types of tests there was a clear trend in which the resistance reduces significantly in the first couple of repetitions of a certain displacement compared to the latter repetitions in that set. The effect of reducing resistance is largest when the displacement of the sample is close to the displacement at maximum load capacity (about 3% for the IP test and 21% for the window bank test). However, in the first part of the force displacement curve the reduction of resistance within a repetition displacement step is significantly lower (about 1% for the IP test and 10% for the window bank test).

Based on the reduction of resistance of both the full-scale wall test and window bank test, it can be concluded that the material degradation mainly takes place in the first repetitions of a certain applied displacement. It appears that after 10 repetitions the reduction of resistance and likely crack progression will not proceed significantly and might stabilise also for the higher repetition displacement steps when many more repetitions are applied. It is important to note that a repeating load fostering crack propagation is similar to the phenomenon of fatigue, but unlike fatigue where the behaviour is completely elastic and thousands of cycles are required, the loads observed in this study are beyond the fully-elastic behaviour of the material and only tens of repetitions have been tested.

The experimental tests can be considered as undamaged and unstressed samples (except for TUD_COMP-42 as was described in Section 4.1.4) that have no significant loading history by any type of source. In reality, structures are subjected to many more loading sources that introduce stresses and incipient (Ψ_0=0.5) or light damage to the structures. The calibrated computational models in Chapter 6 are used to apply multiple pre-damages or stress states to investigate cumulation of minor damage and how this pre-damage affects the probability of damage due to a following earthquake. This involves more than 100 scenarios of pre-damage followed by time-history analyses for the earthquake.

The results from the expanded computational models were processed to fabricate resistivity curves in Chapter 7. The conclusions drawn from this extrapolation are limited by the single earthquake signal employed and the uncalibrated damage-combination scenarios used in the models. Additionally, it must be emphasised that these curves were derived from tests attempting to replicate masonry corresponding to the use of baked-clay bricks before the 1950s; see a comprehensive discussion of the limitations in Section 7.6.2. Note also, that both laboratory experiments and computational models employed in this study utilise the measure of the maximum crack width. This measure is more easily obtainable from experiments and is directly comparable with models. Moreover, the maximum crack width is a better indication of the level of damage of a structure when further damaging actions need to evaluated. Yet, it is expected that the residual damage (or crack width) will be lower than the maximum crack width occurred during an earthquake. See section 2.5.2 for a more in-depth discussion.

Nevertheless, it can be observed that structures that had some degree of settlement pre-damage are more likely to experience higher damage when subjected to earthquake vibrations than structures with a similar level of pre-damage due to other causes. Additionally, structures with some pre-damage were also more likely to be further damaged. For instance, for an intensity of 20mm/s corresponding to that of frequent earthquakes, the probability for structures to develop visible damage (Ψ=1) was seen to be between 20% and 45%, however, for the same intensity, no matter the level of pre-damage, the probability for structures to exceeded DS1 (that is Ψ>3) was negligible.
In comparison to curves for DS1 found in literature, most fit nicely into the range given for DS1 by the damage level parameter. The curves of Waarts (1997) seem to underestimate damage when the original material values are employed, but match a fictitious curve for the initiation of damage (Ψ>0) when updated with current knowledge about the material. In the range below 15mm/s, the Waarts' curves significantly overestimate damage.
In the analysis of Waarts' curves, it is evidenced that the methodology used is directed towards vertical vibrations and deformations in the soil generated by nearby-sources. This is not directly applicable to earthquake vibrations since these are mostly uniform lateral vibrations originated from sources farther away.

Resistivity curves were also derived from the experimental results. Since laboratory walls were controlled via displacement at the top instead of shaken at the bottom, significant extrapolations are necessary to be able to compare these to the computational curves, however, the behaviour seems to be adequate.

8.2. Recommendations

For the continuation of the research project, it is proposed to:

- ◉ Reuse tested in-plane walls by applying a larger number of repetitions for higher displacement steps to investigate whether the progression of material degradation stabilises.
- ◉ Finish the re-tested in-plane walls at the ultimate limit state to investigate drift limits for a pre-damaged wall. The ultimate limit state is not in the scope of this project but the test data can be of large value for other Groningen earthquake projects.
- ◉ Formulate, develop and improve models for continuum smeared macro-, meso- and micro-models subjected to monotonic, repetitive as well as cyclic loading. This includes improving the constitutive Engineering Masonry model with masonry degradation behaviour as was observed in the experimental tests.
- • Study and elaborate computational models including spatial variability of the material to observe potential changes in failure mechanisms and crack propagation.
- ◉ Test and model different in-plane wall geometries, material types, earthquake motions and loading situations based on Groningen damage case studies to improve the damage framework and resistivity curves, as well as to further validate the computational models.
- • Investigate cumulation of minor damage in the case of in-plane and out-of-plane dynamic loading of a wall by using a shaking table and also to validate and calibrate the dynamic numerical models.
- ◉ Develop different models including foundation and soil-structure interaction to investigate the effect of the vibration transfer from the soil to the structure.
- ◉ Perform more extensive analyses of the collected data for DIC (such as the photos taken from the back of the wall) and develop improvements for the DIC measurement system and analysis for future experimental tests.
- ◉ Obtain greater insight into (pre-) damage cases in the field by means of analysis of actual damage cases to incorporate a schematic representation of this information in the development of improved resistivity curves.

** Bullet points marked with concentric circles have been explored in a second stream of this project.*

References

Abo-El-Ezz. 2013 | Probabilistic seismic vulnerability and risk assessment of stone masonry structures. Thèse de Doctorat, École de Technologie Supérieure, Université du Québec, Montréal, Québec, Canada

AeDES. 2007 | Field Manual for post-earthquake damage and safety assessment and short term countermeasures. - European Commission - Joint Research Centre - Institute for the Protection and Security of the Citizen

Alberto. 2011. & Antonaci, Valente ∑Damage analysis of brick-to-mortar interfaces. – Procedia Engineering 10 (2011) 1151–1156

Almeida. 2012. & Lourenço, Barros | Characterisation of brick and brick–mortar interface under uniaxial tension. – International Seminar of Structural Masonry for Developing Countries

Arup. 2013 | Groningen 2013 - Implementation Study. - Arup

Arup. 2015 | Groningen Earthquakes Structural Upgrading - Site Response Analysis. - ARUP

Arup. 2016 | Groningen Earthquakes Structural Upgrading - Martini Type K As-Built Assessment Report. - ARUP

Arup. 2016. & Merrifield, Elser, van Wijk | Martini Type K – As-Built - Assessment Report. – Arup

Arup. 2016* | Groningen Earthquakes - Structural Upgrading - Expert System Modelling Methods and Assumptions. - Arup

Bird. 2005. & Bommer, Crowley, Pinho | Modelling liquefaction-induced building damage in earthquake loss estimation. – Soil Dynamics and Earthquake Engineering 26 (2006) 15–30

Boffi. 1988. & Castellani | Effects of Surface Waves on the Rotational components of earthquake motion. – Proceedings of Ninth World Conference on Earthquake Engineering, 1988 Tokyo-Kyoto, Japan

Bommer. 2015.a. & Stafford, Edwards, Dost, Ntinalexis | Development of GMPEs for Response Spectral Accelerations and for Strong-Motion Durations . – NAM

Bommer. 2015.b. & Dost, Edwards, Rodriguez-Marek, Kruiver, Meijers, Ntinalexis, Stafford, van Elk, Doornhof | Development of Version 2 GMPEs for Response Spectral Accelerations and Significant Durations from Induced Earthquakes in the Groningen Field. – NAM

Bommer. 2016. & Dost, Edwards, Kruiver, Meijers, Ntinalexis, Rodriguez-Marek, Stafford | Development of V3 GMPEs for Response of Spectral Accelerations and Significant Durations from Induced Earthquakes in the Groningen Field, Version 0, 8 July, 476 pp

Boulanger. 2014. & Idriss | CPT and SPT based Liquefaction Triggering Procedures. – Center for Geotechnical Modeling - Department of Civil and Environmental Engineering - University of California

Castellani. 1986. & Boffi | Rotational components of the surface ground motion during an earthquake. – Earthquake engineering and structural dynamics vol 14, 751-767

Červenka. 1998. & Chandra, Saouma | Mixed Mode Fracture of Cementitious Bimaterial Interfaces. – Engineering Fracture Mechanics Vol. 60, No. 1, pp. 95±107

CUR. 1990. | CUR-report-90-6. Pre-advice Computational Masonry Mechanics, final report CUR committee PA33 'Masonry Mechanics', Jansenn, Rots, Walraven, CUR, Gouda, 1990

Curtin. 2008. & Shaw, Beck, Bray, Easterbrook. | Structural masonry designers' manual.. – John Wiley & Sons

de Boer. 2016. & van den Bos, van Es, Kostense, Krijgsman, Manie, Meijers, Ringers, Roijakkers, Verweij, van der Vliet, Vonk, Vásconez Gutiérrez | Guideline for NLTH Earthquake Analyses of Existing Buildings in Groningen Performed with DIANA FEM Software. – ABT-Wassenaar, ARCADIS, ROYAL HASKONINGDHV, TNO

de Vent. 2011. & Rots, van Hees | Structural Damage in Masonry - Developing diagnostic decision support. – TU Delft

Deckner. 2013 | Ground vibrations due to pile and sheet pile driving – influencing factors, predictions and measurements . - KTH Royal Institute of Technology

Didier. 2017. & Abbiati, Broccardo, Beyer, Danciu, Petrović, Mojsilović, Stojadinović | Quantification of Non-Structural Damage in Unreinforced Masonry Walls Induced by Geothermal Reservoir Exploration using Quasi-Static Cyclic Tests. – Proceedings of the 13th Canadian Masonry Symposium, Halifax, Canada, June 2017

Dost . 2013. & Kraaijpoel | The August 16, 2012 earthquake near Huizinge (Groningen). – KNMI report. January 2013

Dungca. 2016. & Acosta, Juego, Sanches H., Sanches I. | The Propagation Behavior Of Pile-Driving-Induced Vibration Done On Soil At Varying Distances And Its Effects On Existing Structures. – International Journal of GEOMATE, May, 2016, Vol. 10, Issue 21, pp. 1877-1883

Ellsworth. 2016. & McGarr | Review of "Hazard and Risk Assessment for Induced Seismicity in Groningen – Update 7th November 2015". – USGS

Esposito. 2016.a. & Terwel, Ravenshorst, Schipper, Messali, Rots | Cyclic pushover test on an unreinforced masonry structure reseambling a typical Dutch terraced house. – TU Delft

Esposito. 2016.b. & Meulman, Jafari, Ravenshorst | Quasi-static cyclic tests on masonry components. – Delft University of Technology. Report number C31B67WP3-3, version 2, 13 December 2016

Eurocode 6. 2013 | Design of masonry structures - Part 1-1: General rules for reinforced and unreinforced masonry structures. - NEN-EN 1996-1-1+A1, January 2013

Ewing. 2004. & Kowalsky | Compressive Behavior of Unconfined and Confined Clay Brick Masonry. – Journal Struct. Eng., 2004, 130(4): 650-661

Fathy. 2008. & Planas, Sancho | A numerical study of masonry Cracks II. – Anales de Mecánica de la Fractura 25, Vol. 1 (2008)

FEMA. 2000 | Pre-Standard and Commentary for the Seismic Rehabilitation of Buildings. - FEMA

FEMA. 2012 | Hazus MH 2.1. - FEMA

FEMA. 2013 | Hazus MH MR5. - FEMA

Forbes. 2013. & Camp | Settlement & Vibration Monitoring for Transmission Line Foundation Installation. – S&ME, NCDOT Conference

Forrest. 1999 | Modelling of Ground Vibration from Underground Railways. - University of Cambridge

Gehl. 2013. & Seyedi, Douglas | Vector-valued fragility functions for seismic risk evaluation. – Bull Earthquake Eng (2013) 11:365–384 -DOI 10.1007/s10518-012-9402-7

Gehwolf. 2015 | Numerical Modelling of the Small Scale Rock Cutting Test. - BHM, 160. Jg. (2015), Heft 12

Giardina. 2008. & Hendriks, Rots | Numerical analyses of tunnel-induced settlement damage to a masonry wall. – 7th fib PhD Symposium in Stuttgart, Germany

Giardina. 2012. & Marini, Hendriks, Rots, Rizzardini | Experimental analysis of a masonry façade subject to tunnelling-induced settlement. – Engineering Structures 45 (2012) 421–434

Giardina. 2013.a. | Modelling of Settlement Induced Building Damage. – TU Delft

Giardina. 2013.b. & vd Graaf, Hendriks, Rots, Marini | Numerical analysis of a masonry façade subject to tunnelling-induced settlements. – Engineering Structures 54 (2013) 234–247

Giardina. 2015. & Hendriks, Rots | Sensitivity study on tunnelling induced damage to a masonry façade. – Engineering Structures 89 (2015) 111–129

Giardina. 2015. & DeJong, Mair | Interaction between surface structures and tunnelling in sand: Centrifuge and computational modelling. – Tunnelling and Underground Space Technology 50 (2015) 465–478

Gondrie. 2015 | Renovation - Leasing a Prefab Renovation in the Netherlands. - TU Delft

Grünberg. 2005. & Meincke, Radtke | Experimentelle und numerische Untersuchungen des Materialverhaltens von Mauerwerk unter Erdbebenlasten. – Ernst & Sohn Verlag für Architektur und technische Wissenschaften GmbH & Co. KG, Berlin · Mauerwerk 9, Heft 6

Hillerborg. 1976. & Modéer, Petersson | Analysis of crack formation and crack growth in concrete by means of fracture mechanics and finite elements. - Division of Building Materials, Lund Institute of Technology, Lund, Sweden - Cement and Concrete Research. Vol. 6, pp. 773-782, 1976

Hillerborg. 1985 | The theoretical basis of a method to determine the fracture energy of concrete - Rilem Technical Committees, Vol. 18- N ~ 106 - Materiaux et Constructions

Hordijk. 1991 | Local approach to fatigue of concrete - Delft University of Technology

Ingham. 2015. & Dizhur | Seismic Improvement of Loadbearing Unreinforced Masonry Cavity Walls. – University of Auckland funded by the Building Research Levy

Jafari. 2016. & Esposito | Material tests for the characterisation of replicated clay brick masonry – Delft University of Technology. Report number C31B67WP1-12, version 01, 14 November 2016

Jeary. 2015. & Winant, Bunyan | Some Aspects Of The Measurement Of Vibration Intensity For The Assessment Of Building Structures. – Forensic Engineering 7th Congress Performance of the Built Environment November 15 – 18, 2015

Jones. 2015 | Documentation for Matlab-based DIC code Version 4. - University of Illinois at Urbana-Champaign

Jurevicius. 2015. & Stead, Barry | A Case Study Of Damage Effects To Residential Buildings Caused By Vibratory Compaction Equipment. – Acoustics Hunter Valley

Kim. 1999. & Lee | Propagation and attenuation characteristics of various ground vibrations – Soil Dynamics and Earthquake Engineering

KNMI. 2013. & Dost, Caccavale, van Eck, Kraaijpoel | Report on the expected PGV and PGA values for induced earthquakes in the Groningen area. – KNMI

Korswagen. 2017. & Longo, Meulman, van Hoogdalem, Gena | NAM - Damage sensitivity of Groningen masonry structures. WP0-Progress Overview – Delft University of Technology. Report number C31B69WP0-3, version 1.0, 2 June 2017

Kowalewski. 2015. & Gajewski | Determination of failure modes in brick walls using cohesive elements approach. – Procedia Engineering 111 (2015) 454 – 461

Kralj. 1990. & Pande, Middleton | On the mechanics of frost damage to masonry. – Computers and Structures, Vol 41, no 1, pp 53-66, 1991

Larby. 2004 | Microscopy applied to the diagnosis of the deterioration of brick masonry. - Construction and Building Materials 18 (2004) 299–307

Lourenço. 1995. & Rots, Blaauwendraad | Two approaches for the analysis of masonry structures: micro and macro-modeling. – HERON. Vol. 40. No.4 ISSN 0046-7316

Lourenço. 1996 | Computational strategies for masonry structures. - TU Delft

Manie. 2016 | DIANA FEA user's manual - Release 10.1. - DIANA FEA

Massarsch. 2002 | Effects of Vibratory Compaction. - Geo Engineering AB, Stockholm, Sweden

Meillyta. 2012 | Finite Element Modelling of Unreinforced Masonry (URM) Wall with Openings: Studies in Australia. - The Proceedings of 2nd Annual International Conference Syiah Kuala University 2012 & 8th IMT-GT Uninet Biosciences Conference Banda Aceh, 22-24 November 2012

Messali. 2017. & Mariani | Blind prediction modelling and analysis of in-plane test TUD_COMP-23. – Delft University of Technology. Draft, 26 April 2017

Meulman. 2017. & Van Hoogdalem, Gena, Korswagen | Experimental tests on masonry components. – Delft University of Technology. Report number C31B69WP3-1, version 2, 8 September 2017

Michel. 2010. & Zapico, Lestuzzi, Molina, Weber | Quantification of fundamental frequency drop for unreinforced masonry buildings from dynamic tests. – Earthquake Eng Struct. Dyn. 2011; 40:1283–1296

Mosalam. 2009. & Glascoe, Bernier | Mechanical Properties of Unreinforced Brick Masonry, Section 1. – Lawrence Livermore National Laboratory LLNL-TR-417646

NAM. 2013 | Technical Addendum to the Winningsplan Groningen 2013 - Subsidence, Induced Earthquakes and Seismic Hazard Analysis in the Groningen Field. - NAM

NAM. 2015. & Pickering, van Elk, Doornhof | An estimate of the earthquake hypocenter locations in the Groningen Gas Field. – NAM

NAM. 2016 | Production, Subsidence, Induced Earthquakes and Seismic Hazard and Risk Assessment in the Groningen Field. - NAM, Technical Addendum to the Winningsplan Groningen 2016

NEN. 2015 | NPR 9998. - NEN

Nrgulescu. 2014. & Ulrich, Baills, Seyedi | Fragility curves for masonry structures submitted to permanent ground displacements and earthquakes. – Nat Hazards (2014) 74:1461–1474 -DOI 10.1007/s11069-014-1253-x

Okada. 2000. & Takai | Classifications of Structural Types and Damage Patterns of Buildings for Earthquake field Investigation. – Structural and Construction Engineering (Transactions of AIJ) · DOI: 10.3130/aijs.64.65_5

Olivito. 2001. & Stumpo | Fracture mechanics in the characterisation of brick masonry structures. – Materials and Structures/Matériaux et Constructions, Vol. 34, May 2001, pp 217-223

Österberg. 1935. | Topography of the layer of rods and cones in the human retina. – Acta Ophthalmol [Suppl] 13:6,1–102

Page. 1995 | Unreinforced Masonry Structures - an australian overview. - Pacific conference on earthquake engineering (PCEE 95), Melbourne

Palmisano. 2016. & Vitone, Cotecchia | Methodology for Landslide Damage Assessment. – ScienceDirect

Raaijmakers. 1994 | Modellering van Constructies bij een Dynamische Excitatie via de fundering. - TNO

Reyes. 2008. & Casati, Gálvez | Cohesive crack model for mixed mode fracture of brick masonry. – Int J Fract (2008) 151:29–55

Robertson. 1998. & Wride | Evaluating cyclic liquefaction potential using the cone penetration test. – Can. Geotech. J. 35: 442–459

Rodriguez. 2013. & Martinez, Martí | Concrete Constitutive Model, Calibration and Applications . – 2013 SIMULIA Community Conference

Rots. 1985. & Nauta, Kuster, Blaauwendraad | Smeared Crack Approach and Fracture Localization in Concrete. HERON, 30 (1), 1-48, 1985

Rots. 1997. & vd Pluijm, Vermeltfoort | Structural Masonry - An Experimental/Numerical Basis for Practical Design Rules. – Balkema - ISBN 90 5410 680 8

Rots. 2016. & Messali, Esposito, Jafari, Mariani | Computational Modelling of Masonry with a view to Groningen induced Seismicity. – 10th SAHC Structural Analysis of Historical Construction, Leuven

Rots. 2016. & van Staalduinen | Plan of approach NAM/TU Delft Program "Damage Sensitivity of Groningen Masonry Structures - Computational and Experimental Studies" . – TU Delft

Sarhosis. 2014. & Garrity, Sheng | Influence of brick–mortar interface on the mechanical behaviour of low bond strength masonry brickwork lintels. – Engineering Structures 88 (2015) 1–11

SBR. 2006 | Schade aan gebouwen. - SBR

SBR. 2010 | Schade aan gebouwen. - SBR

Schneemayer. 2014. & Schranz, Kolbitsch, Tschegg | Fracture Mechanical Properties of Mortar to Brick Interfaces. – J. Mater. Civ. Eng., 2014, 26(9): -1–1, ASCE

Schreppers. 2016. & Garofano, Messali, Rots | DIANA Validation report for Masonry modelling. – DIANA FEA BV and TU Delft, DIANA FEA report 2016-DIANA-R1601, 19 November 2016

Simulia. 2014 | Abaqus 6.14 Online Documentation. - Dassault Systèmes

Sousa. 2014. & Thomaz, Roman, Morton, Silva, Corrêa, Pfeffermann, Lourenço, Vicente, Sousa | Defects in masonry walls. Guidance on cracking: identification, prevention and repair. International council for research and innovation in building and construction

Spetzler. 2016. & Dost | Probabilistic Seismic Hazard Analysis for Induced Earthquakes in Groningen. – KNMI

Stagg. 1984. & Siskind, Stevens, Dowding | Effects of Repeated Blasting on a Wood-Frame House. – US Department of Interior - Office of Surface Mining

Steenbergen. 2016. & Geurts | Relatie tussen PGA waarden en kans op schade voor geïnduceerde aardbevingen in Groningen. – TNO

Suhairy. 2000 | Prediction of Ground Vibration from Railways. - SP Swedish National Testing and Research Institute

Sümer. 2015. & Aktas | Defining parameters for concrete damage plasticity model. – Challenge journal of structural mechanics 1 (3) (2015) 149–155

Svinkin. 1999 | Prediction and Calculation of Construction Vibrations. - Deep Foundations Institute

Svinkin. 2013 | Forensic engineering of construction vibrations. - Forensic Engineering

Tomassetti. 2017. & Kallioras, Graziotti, Correia | Preliminary report on the construction of the building prototype at the LNEC laboratory. – Lisbon, March 2017

van der Salm. 2012. & Hölscher, Snechlage | SBR-A richtlijn niet eenduidig voor trillinggevoelige funderingen. – Geotechniek

van Hees. 2004. & Binda, Papayianni, Toumbakari | Characterisation and damage analysis of old mortars. – Materials and Structures, Vol 37, pp664-648

van Staalduinen. 1993. & Smits | Trillingscriteria voor schade aan gebouwen. – TNO

van Zijl. 2001. & Borst, Rots | The Physical Role of Crack Rate Dependence in the Long-Term Behaviour of Cementitious Materials. – International Journal Solids & Structures 38, pp 5063-5079

Vandoren. 2012. & de Proft, Simone, Sluys | Modelling of Crack Initiation and Propagation using the Partition of Unity Method. – VIII International Conference on Fracture Mechanics of Concrete and Concrete Structures FraMCoS-8

van der Pluijm. 1997 | Non-Linear Behaviour of Masonry under Tension. - Heron, Vol 42 No 1 ISSN 0046-7316

Verghese. 1984 | Excessive Settlement in Buildings. - International Conference on Case Histories in Geotechnical - Engineering. Paper 17

Vermeltfoort. 2005 | Brick-mortar interaction in masonry under compression. Technische Universiteit Eindhoven, Eindhoven. DOI: 10.6100/IR589402

Waarts. 1997 | Kans op schade aan bouwwerken door trillingen. - TNO

Wald. 1999. & Quitoriano, Heaton, Kanamori | Relationships between Peak Ground Acceleration, Peak Ground Velocity and Modified Mercalli Intensity in California. – Earthquake Spectra, Volume 15, No 3, August 1999

Wang. 2012. & Sloan, Abbo, Masia, Tang | Numerical simulation of the failure process of unreinforced masonry walls due to concentrated static and dynamic loading. – International Journal of Solids and Structures 49 (2012) 377–394

Wassing. 2012. & Dost | Seismisch hazard van geïnduceerde aardbevingen - Integratie van deelstudies. – TNO/KNMI

Zucchini. 2006. & Lourenço | Homogenization of Masonry Using a Micro-mechanical Model Compressive Behaviour. – III European Conference on Computational Mechanics Solids, Structures and Coupled Problems in Engineering C.A

Zuccaro. 2010. & Cacace, Rauci | A Multimedia and didactic handbook for seismic Damage evaluation. – Urban Habitat Constructions under Catastrophic Events

Appendix

Damage sensitivity of Groningen Masonry Structures

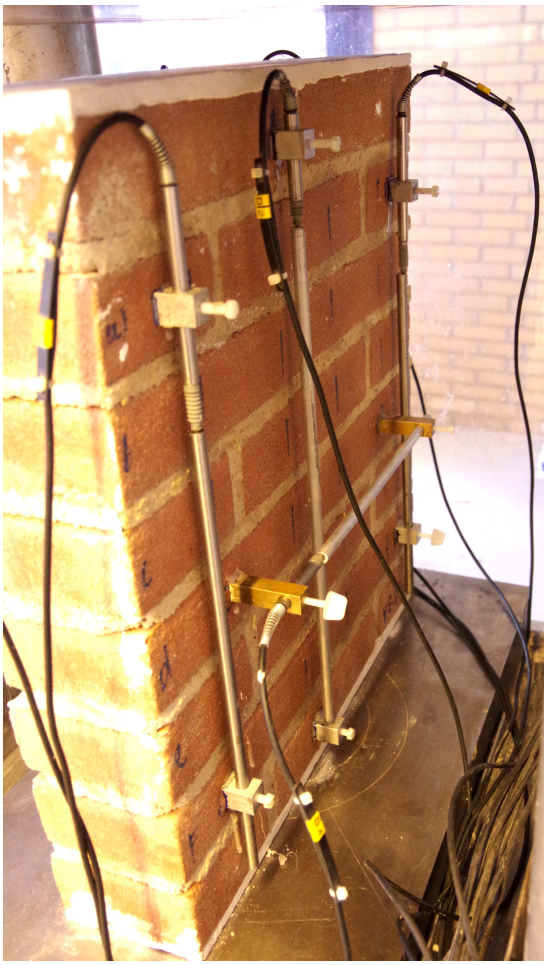

TU Delft

9. Appendix

9.1. List of Figures and Tables....iii
9.2. Companion Tests....xii
9.3. Nomenclature....xiii
9.3.1. Symbols....xiii
9.3.2. Abbreviations....xvi
9.4. Abaqus Modelling....xviii
9.4.1. Discussion: Modelling with Abaqus/Explicit....xviii
9.4.2. Constitutive Models....xxii
9.4.3. Calibration & Examples....xxv
9.4.4. Prediction Models....xxxi
9.4.5. Post-diction Models - Window Bank....xxxiii
9.4.6. Conclusions of Explicit Modelling with Abaqus....xxxvi
9.5. Experimental Pre-compression Test Results....xxxvii
9.6. Program to Analyse Damage....xxxviii

9.1. List of Figures and Tables

I. Summary I

Figure I.1. (1.1) Dimensions of the in-plane solid clay wall with asymmetric window opening. I

Figure I.2. (2.13) Examples of analyses with the damage assessment program for numerical output (top) and DIC output (bottom). The former corresponds to shrinkage damage followed by earthquake damage and results in a value of Ψ=2.5, while the latter computes to Ψ=1.7 due to a lateral top displacement of the wall of 2mm (Wall TUD-COMP-40, Test 79, Record 1075). I

Figure I.3. (3.8) Final damage pattern of the in-plane wall in terms of principal crack width with the prediction computational model..... 2

Figure I.4. (4.54) Strain plots of repetition R5 of TUD_COMP-40, TUD_COMP-41 and TUD_COMP-42..... 2

Figure I.5. (4.8) Left: Average crack opening displacement at bottom-right and top-left corner of window. (4.12) Right: Force peak per repetition. 2

Figure I.6. (4.71) Left: DIC strain plot of sample TUD_MAT-50J. (4.84) Right: Force vs number of repetitions of sample TUD_MAT-50M..... III

Figure I.7. (5.9) TUD_COMP-41: R4a. Horizontal displacement comparison between (left) DIC related to experimental record number 16764 and (right) FEM post-test. Model deformed shape magnified by 100..... III

Figure I.8. (5.15) TUD_COMP-42: experimental and FEM post-test force-displacement curve. III

Figure I.9. (6.12) Crack width plots related to the moment of maximum pre-damage for: (a) pre-earthquake (0.17g), (b) 5mm settlement, (c) 0.4‰ shrinkage. Deformed shape magnified by 100. 4

Figure I.10. (part of 6.13) Cumulative crack width plots for standard material at the end of 0.10g motion for different initial conditions: (a) pre-earthquake (0.17g), (b) 5mm settlement, (c) 0.4‰ restrained shrinkage. Undeformed mesh..... 4

Figure I.11. (7.20) Indicative resistivity curves for computational wall results for zero initial damage, Ψ0=0 against PGV... V

Figure I.12. (7.22) Indicative resistivity curves for computational wall results for some initial pre-damage Ψ0=1.0 against PGV. Showing also the difference between pre-damage types. V

Table I.1. Interest values read from the indicative resistivity curves. VII

II. Table of Contents 8

1. Introduction 2

Figure 1.1 Dimensions of the in-plane, solid-clay wall with asymmetric window opening..... 4

2. Damage in Masonry and its Assessment..... 6

Figure 2.1. Tension stress-strain diagram illustrating the behaviour difference between ductile (plastic, hardening) and brittle (with softening, i.e. quasi-brittle) materials. 7

Figure 2.2. Photography of a bond-wrench test showing a clean debonding occurring at the interface between brick and mortar..... 8

Figure 2.3. Behaviour possibilities for illustrative crack propagation when subjected to a load repetition of equal intensity. 8

Table 2.1. Common qualitative descriptions of Damage States..... 11

Figure 2.4. Typical lateral capacity curve related to crack characteristics..... 12

Figure 2.5. Left, Small crack, around 1mm running through the mortar between bricks, DS1, part of this study. Right, major crack running through bricks, around 25mm, DS3-DS4, not part of this study..... 12

Table 2.2. Expressions of damage commonly associated with various processes with mostly mechanically-based processes at the top and chemically-based processes at the bottom..... 13

Table 2.3. Damage scale with damage levels based on ease or repair. From Giardina (2013.a)..... 15

Table 2.4. Categorisation of DL by the result of a damage parameter..... 16

Figure 2.6. Ruler to measure observed crack width. Scale on A4 paper is 1:1. Right: usage of such a ruler in the field; the ruler is positioned next to a crack so that the inspector can note its width by comparing the crack to the thickness of the lines on the ruler. 16

Figure 2.7. Graph showing the relationship of Psi (ΨD) for a given crack width. Cracks below 0.1mm require special attention to be detected. 17

Figure 2.8. Examples of a wall with various crack patterns (cw;cL) and its corresponding computed crack parameter. 18

Table 2.5.a. Influence value scale. 21

Table 2.5.b. Influence values for various non-structural aspects influential in damage perception. Empiric exemplary values. 21

Figure 2.9. Patterns being applied to the wall. 23

Figure 2.10. Examples of filled contour plots of vertical displacements (left) and computed infinitesimal strain (right) obtained from a DIC analysis of wall TUD-COMP-40 towards the end of the test (Test 65, Record point 2742). The maximum crack width is 0.6mm. 24

Figure 2.11. Global displacement and crack-width output of a DIANA numerical model for the case of a wall damaged by a combination of sagging settlement and earthquake excitation. Deformed shape magnified by 50. 24

Figure 2.12. Flowchart for the process of computing the damage parameter from DIC or computational results. 25

Figure 2.13. Examples of analyses with the damage assessment program for numerical output (top) and DIC output (bottom). The former corresponds to shrinkage damage followed by earthquake damage and results in a value of Ψ=2.5, while the latter computes to Ψ=1.7 due to a lateral top displacement of the wall of 2mm (Wall TUD-COMP-40, Test 79, Record 1075). 26

Figure 2.14. The main parameters categorising damage. 27

3. Preliminary Computational Models to Define Tests 30

Figure 3.1. Dimensions of the in-plane solid clay wall with asymmetric window opening. (Meulman et al., 2017). 31

Figure 3.2. Diana FEM model of the in-plane wall. 32

Figure 3.3. Notches in the opening corners: (a) top left window corner and (b) bottom right window corner. 32

Figure 3.4 Total Strain Crack Model, defined softening for (a) tensile behaviour and (b) compressive behaviour. (Manie, 2016). 33

Table 3.1. Clay masonry material properties for the in-plane FEM wall. 33

Table 3.2. Concrete material properties for the lintel above the window. 33

Table 3.3 Steel material properties for the beam above the wall. 34

Table 3.4. Loading protocol for in-plane test. (Meulman et al., 2017). 34

Figure 3.5 Loading protocol for the first 20 steps for the in-plane wall. 35

Figure 3.6. Full loading protocol for the in-plane wall. 35

Table 3.5. Loading protocol for the FEM in-plane wall. 36

Figure 3.7. Evolution of the crack pattern in terms of principal crack width at different stage: (a) after applying the monotonic loading, (b) at the first peak of 1.25 times the first displacement, (c) at the first peak of 1.75 times the first displacement and (d) at the first peak of 2 times the first displacement. 37

Figure 3.8. Final damage pattern of the in-plane wall in terms of principal crack width. 37

Figure 3.9. Failure mechanism of the FEM in-plane wall. 38

Figure 3.10. Crack width evolution for the three cracks during the entire loading process. 38

Table 3.6. Crack width evolution during the loading protocol. 38

Figure 3.11. Force-displacement curve for the FEM model. 39

4. Experimental Tests 42

Table 4.1. Samples and loading protocol. 43

Figure 4.1. Set-up and wall sample at the initial stage of the test. 43

Figure 4.2. IP wall test sample. 44

Table 4.2. Repetitive pull loading protocol of TUD_COMP-40 (Meulman et al., 2017). 45

Figure 4.3. Notches sensors at the window corners. 45

Table 4.3. Jack and average wall top displacement. (* measured value, ** calculated with use of multiple sensors). 46

Figure 4.4. Beam horizontal displacement. 46
Figure 4.5. Average wall top horizontal displacement. 46
Figure 4.6. Hysteresis graph for the repetitive pull test. 47
Figure 4.7. Hysteresis plots for each repetition displacement step. 48
Table 4.4. Wall drift during the repetitive pull test of TUD_COMP-40. 48
Figure 4.8. Average opening displacement of notch 1 and 2. 49
Figure 4.9. Average opening displacement of notch 1 and 2 per number of repetitions. 49
Table 4.5. Notch opening increase within repetition displacement step of N1. 50
Figure 4.10. Notch displacement increase between first and last repetition within a repetition displacement step. 50
Figure 4.11. Reduction in measured horizontal force within a repetition displacement step expressed in percentage. 51
Figure 4.12. Force peak per repetition. 51
Figure 4.13. A crack plot of R1 of the repetition displacement steps. 52
Figure 4.14. A crack plot of R2 of the repetition displacement steps. 53
Figure 4.15. A crack plot of R3 of the repetition displacement steps. 53
Figure 4.16. A crack plot of R4 of the repetition displacement steps. 54
Figure 4.17. A crack plot of R5 of the repetition displacement steps. 54
Figure 4.18. Top: back side of the wall at bottom right corner of window (when in front view). Bottom: zoomed in section on crack, location marked by red rectangle. 55
Table 4.6. Repetitive pull loading protocol of TUD_COMP-41. (Meulman et al., 2017) 56
Figure 4.19. N3 opening displacement in R1a to determine top beam displacement for R1 56
Figure 4.20. Top beam horizontal displacement of R1a. 57
Figure 4.21. Jack horizontal displacement of R1a. 57
Table 4.7. Beam and AVG wall top displacement. (* measured value, ** calculated with use of multiple sensors). 58
Figure 4.22. Top beam horizontal displacement. 58
Figure 4.23. Wall horizontal displacement. 58
Figure 4.24. Hysteresis graph for the repetitive pull test TUD-COMP-41. 59
Figure 4.25. Hysteresis plots for each repetition displacement step. 60
Table 4.8. Wall drift during the repetitive pull test TUD_COMP-41. 61
Figure 4.26. Average opening displacement of Notch 3 and 4. 61
Figure 4.27. Average opening displacement of Notch 3 and 4 per number of repetitions. 62
Table 4.9. Notch opening increase within each displacement step with respect to the N3 displacement. 62
Figure 4.28. Notch displacement increase between first and last repetition within a repetition displacement step. 63
Figure 4.29. Reduction in measured horizontal force within a repetition displacement step expressed in percentage. 63
Figure 4.30. Force peak per repetition. 64
Figure 4.31. A crack plot of R1 of the repetition displacement steps. 64
Figure 4.32. A crack plot of R2 of the repetition displacement steps. 65
Figure 4.33. A crack plot of R3 of the repetition displacement steps. 65
Figure 4.34. A crack plot of R4 of the repetition displacement steps. 66
Figure 4.35. A crack plot of R5 of the repetition displacement steps. 66
Table 4.10. Repetitive pull loading protocol of TUD_COMP-42. (Meulman et al., 2017) 67
Figure 4.36. N1 opening displacement in R1a to determine top beam displacement for R1 67
Table 4.11. Top beam and wall displacement. (* measured value, ** calculated with use of multiple sensors). 68
Figure 4.37. Top beam horizontal displacement. 68

Figure 4.38. Horizontal wall displacement. 69
Figure 4.39. Hysteresis graph for the repetitive pull test TUD-COMP-42. 69
Figure 4.40. Hysteresis plots for each repetition displacement step. 71
Table 4.12. Wall drift during the repetitive pull test TUD_COMP-42. 71
Figure 4.41. Average opening displacement of notch 1 and 2. 71
Figure 4.42. Average opening displacement of notch 1 and 2 per number of repetitions. 72
Table 4.13. Crack increase within repetition displacement step of N1 72
Figure 4.43. Notch displacement increase between first and last repetition within a repetition displacement step. 73
Figure 4.44. Reduction in measured horizontal force within a repetition displacement step expressed in percentage. 73
Figure 4.45. Force peak per repetition. 74
Figure 4.46. A crack plot of R1 of the repetition displacement steps. 74
Figure 4.47. Horizontal crack in the bottom middle part of the wall. 75
Figure 4.48. A crack plot of R2 of the repetition displacement steps. 75
Figure 4.49. A crack plot of R3 of the repetition displacement steps. 76
Figure 4.50. A crack plot of R4 of the repetition displacement steps. 76
Figure 4.51. A crack plot of R5 of the repetition displacement steps. 77
Table 4.14. Top beam displacement at 0.1mm notch opening displacement (R1) 78
Figure 4.52. Comparison of the notch displacement increase per repetition displacement step of the slow repetitions (Rxa). 78
Figure 4.53. Comparison Force reduction per repetition displacement step 79
Figure 4.54. Crack plots of repetition R5 of TUD_COMP-40, TUD_COMP-41 and TUD_COMP-42. 79
Figure 4.55. Comparison Force reduction per repetition displacement step 80
Figure 4.56. Comparison force peak per repetition of TUD_COMP-41 and TUD_COM-42 for R3-R5. 81
Figure 4.58. Example of COMP-41 of which the sequence of cracks is identified by the program for repetitions R1 to R4. 82
Figure 4.59a. Crack length comparison of COMP-40 and COMP-41 (preliminary results). 82
Figure 4.59b. Crack length increase comparison of COMP-40 and COMP-41 (preliminary results). 83
Figure 4.60. Window bank test sample (front side). 85
Figure 4.61. Window bank test sample (back side). 85
Figure 4.62. Bending moment diagram of the window bank samples. 86
Table 4.15. Overview of the monotonically tested window bank samples. 87
Figure 4.63. Force-displacement graph of the monotonic samples with loading rate of 0.0005mm/s (slow). 88
Figure 4.64. Notch opening displacement graph of the monotonic samples with loading rate of 0.0005mm/s (slow). 88
Figure 4.65. Moment curvature graph of the monotonic samples with loading rate of 0.0005mm/s (slow). 89
Figure 4.66. Stress-strain graph of the monotonic samples with loading rate of 0.0005mm/s (slow). 89
Figure 4.67. DIC crack plot of sample TUD_MAT-50E. 90
Figure 4.68. DIC crack plot of sample TUD_MAT-50G. 90
Figure 4.69. Force-displacement graph of the monotonic samples with loading rate of 0.005mm/s (fast). 91
Figure 4.70. Notch opening displacement graph of the monotonic samples with loading rate of 0.005mm/s (fast). 91
Figure 4.71. Moment-curvature graph of the monotonic samples with loading rate of 0.005mm/s (fast). 92
Figure 4.72. Stress-strain graph of the monotonic samples with loading rate of 0.005mm/s (fast). 92
Figure 4.73. DIC crack plot of sample TUD_MAT-50J. 92
Table 4.16. Comparing average values of the samples tested slow and fast loading rate. 93

Figure 4.74. Force-displacement graph of all monotonic samples....93
Figure 4.75. Notch opening displacement graph of all monotonic samples. 94
Figure 4.76. Moment-curvature graph of all monotonic samples....94
Figure 4.77. Stress-strain graph of all monotonic samples. 94
Table 4.17. Overview of the repetitive tested window bank samples. 95
Figure 4.78. Backbone curve repetitive samples with 10 repetitions per repetition displacement step. 96
Figure 4.79. Backbone curve repetitive samples with 30 repetitions per repetition displacement step. 96
Figure 4.80. Backbone curve all repetitive samples. 97
Figure 4.81. Force displacement graph of TUD_MAT-50U. 97
Figure 4.82. DIC crack plot of sample TUD_MAT-50U. 98
Figure 4.83. Force vs number of repetitions of sample TUD_MAT-50U. 98
Figure 4.84. Force-displacement graph of TUD_MAT-50M. 99
Figure 4.85. DIC crack plot of sample TUD_MAT-50M. 99
Figure 4.86. Force versus number of repetitions of sample TUD_MAT-50M. 100
Figure 4.87. Force-displacement graph of TUD_MAT-50P. 100
Figure 4.88. DIC crack plot of sample TUD_MAT-50P. 101
Figure 4.89. Force vs number of repetitions of sample TUD_MAT-50P. 101
Table 4.18. Force reduction per repetition displacement step expressed in percentage of the force measured in the first repetition in that particular step. 102
Figure 4.90. Force reduction per repetition displacement step plot of Table 4.18. 102
Figure 4.91. Protuberances at the micro-level dislodge or break between repetitions making the crack interface weaker every time. 104

5. Validation and Calibration of Computational Models....108

Table 5.1. Comparison between the loading protocol of FEM prediction model and experimental tests of the in-plane walls TUD_COMP-41/42. 108
Figure 5.1. TUD_COMP-41: experimental and FEM prediction force-displacement curve. 109
Figure 5.2. TUD_COMP-42: experimental and FEM prediction force-displacement curve. 109
Table 5.2. Load capacity and stiffness for experimental and FEM in-plane walls 110
Figure 5.3. TUD_COMP-41 DIC Equivalent strain plot at top displacement about 0.69mm (during R1b). 111
Figure 5.4. Crack width plot at wall top displacement of 0.70mm (R5b). 111
Figure 5.5. Diana FEM model of the refined post-test of the in-plane wall. 113
Table 5.3. Steel material properties for the beams above and below the wall. 113
Table 5.4. Concrete material properties for the lintel above the window. 113
Table 5.5. Clay masonry material properties for the refined post-test of the in-plane wall. 114
Table 5.6. Loading protocol for the FEM models based on the experimental tests of the in-plane walls TUD_COMP-41/42. 115
Figure 5.6. TUD_COMP-41: experimental and FEM post-test force-displacement curve. 116
Table 5.7. TUD_COMP-41: load capacity and stiffness for experimental and FEM post-test. 117
Figure 5.7. TUD_COMP-41: R4a. Horizontal displacement comparison between (a) DIC related to experimental record number 16764 and (b) FEM post-test. Model deformed shape magnified by 100. 117
Figure 5.8. TUD_COMP-41: R5a. Horizontal displacement comparison between (a) DIC related to experimental record number 22321 and (b) FEM post-test. Model deformed shape magnified by 100. 118
Figure 5.9. TUD_COMP-41: R4a. Horizontal displacement comparison between (a) DIC related to experimental record number 16764 and (b) FEM post-test. Model deformed shape magnified by 100. 118

Figure 5.10. TUD_COMP-41: R5a. Horizontal displacement comparison between (a) DIC related to experimental record number 22321 and (b) FEM post-test. Model deformed shape magnified by 100. 119

Figure 5.11. TUD_COMP-41: R1a. Comparison between (a) strain plot of DIC related to experimental record number 5502 and (b) FEM post-test crack width plot. Model deformed shape magnified by 100. 119

Figure 5.12. TUD_COMP-41: R4a. Comparison between (a) strain plot of DIC related to experimental record number 16764 and (b) FEM post-test crack width plot. Model deformed shape magnified by 100. 120

Figure 5.13. TUD_COMP-41: R5a. Comparison between (a) strain plot of DIC related to experimental record number 22321 and (b) FEM post-test crack width plot. Model deformed shape magnified by 100. 120

Figure 5.14. TUD_COMP-41: principal stress vector plot of the FEM post-test for (a) R1a and (b) R5b. Deformed shape magnified by 100. Concrete lintel is not shown. 121

Figure 5.15. TUD_COMP-42: experimental and FEM post-test force-displacement curve. 122

Table 5.8. TUD_COMP-42: load capacity and stiffness for experimental and FEM post-test. 122

Figure 5.16. TUD_COMP-42: R5a. Comparison between (a) strain plot of DIC and (b) FEM post-test crack width. Deformed shape magnified by 100. 123

Figure 5.17. TUD_COMP-41: Diana FEM model of the in-plane wall. Mesh size 25x25mm. 124

Figure 5.18. TUD_COMP-41: experimental and FEM post-test force-displacement curve varying mesh size....124

Table 5.9. TUD_COMP-41: load capacity and stiffness for experimental and FEM post-tests varying mesh size. 125

Figure 5.19. TUD_COMP-41: Diana FEM model of the in-plane wall, coarser meshes. (a) Mesh size 100x100mm; (b) Mesh size 200x200mm. 125

Figure 5.20. TUD_COMP-41: experimental and FEM post-test force-displacement backbone curve varying mesh size. 126

Table 5.10. TUD_COMP-41: Approximate duration, load capacity and its relative difference with the experiment for FEM post-tests varying mesh size. 126

Figure 5.21. TUD_COMP-41: R5a. FEM principal crack width plot for different mesh size model: (a) 200x200mm; (b) 100x100mm; (c) 50x50mm; (d) 25x25mm. Model deformed shape magnified by 100. 127

6. Computational Models for Resistivity Curves 130

Figure 6.1. Diana FEM in-plane wall model for resistivity curves. 131

Figure 6.2. Global displacements of MODE 1 and MODE 2 for the model for resistivity curves. Deformed shape magnified by 200. 132

Figure 6.3. Time vs acceleration graph of the horizontal component of the Huizinge earthquake (2012). 132

Figure 6.4. Time vs velocity graph of the horizontal component of the Huizinge earthquake (2012). 133

Figure 6.5. Fourier transform graph of the horizontal component of the Huizinge earthquake (2012). 133

Figure 6.6. Time vs acceleration graph of the vertical component of the motion. 133

Figure 6.7. Time vs velocity graph of the vertical component of the motion. 134

Figure 6.8. Fourier transform graph of the vertical component of the motion. 134

Figure 6.9. Time vs acceleration graph of the two components of the ground motion applied to the model. 134

Table 6.1. Horizontal and vertical PGAs of the different motions applied in the models. 135

Figure 6.10. Crack width plots comparison between: (a) repetitive test model TUD_COMP-41 during repetition R5a (1.52mm), (b) dynamic test, no pre-damage, at the moment of top horizontal displacement equal to 1.52mm. Deformed shape magnified by 100. 135

Table 6.2. Comparison of the max crack width and its relative difference for the situation with horizontal and vertical motion and the situation with only horizontal motion. 136

Figure 6.11. Cumulative crack width plots for 0.25g motion for: (a) horizontal and vertical motion, (b) only horizontal motion. Undeformed mesh. 137

Table 6.3. Horizontal and vertical PGAs applied for the pre-earthquake damage condition for the three different materials. 138

Table 6.4. Three different scenarios for the clay masonry material properties. 140

Table 6.5. Eigenvalue analyses results and Rayleigh damping coefficient for models with three different materials. 140

Figure 6.12. Crack width plots related to the moment of maximum pre-damage for the standard material scenario due to: (a) pre-earthquake (0.17g), (b) 5mm sagging settlement, (c) 0.4‰ restrained shrinkage. Deformed shape magnified by 100. More information about the Ψ values can be found in Section 7.4. 142

Figure 6.13. Cumulative crack width plots for standard material at the end of 0.10g motion for different initial conditions: (a) no pre-damage, (b) pre-earthquake (0.17g), (c) 5mm sagging settlement, (d) 0.4‰ restrained shrinkage. Undeformed mesh. More information about the Ψ values can be found in Section 7.4. 143

Figure 6.14. Crack width plots related to the moment of maximum damage during 0.20g motion for the 0.4‰ shrinkage pre-damaged condition: (a) weak, (b) standard, (c) strong material. Deformed shape magnified by 50. More information about the Ψ values can be found in Section 7.4. 144

Figure 6.15. Cumulative crack width plots for standard material at the end of 0.20g motion for different initial conditions: (a) no pre-damage, (b) pre-earthquake of 0.17g, (c) 5mm settlement, (d) 0.4‰ restrained shrinkage. Undeformed mesh. More information about the Ψ values can be found in Section 7.4. 145

Figure 6.16. Cumulative crack width plots for standard material at the end of 0.30g motion for different initial conditions: (a) no pre-damage, (b) pre-earthquake of 0.17g, (c) 5mm settlement, (d) 0.4‰ restrained shrinkage. Undeformed mesh. More information about the Ψ values can be found in Chapter 7.4. 146

Table 6.6. Comparison of the maximum crack width and its relative difference before and after the repetitive earthquake. 147

7. Probabilistic Framework Towards Resistivity Curves 150

Figure 7.1. Overview of the framework from Waarts (1997). 152

Figure 7.2. Fragility curves by Waarts (1997). Adapted descriptions. 152

Figure 7.3. Reproduced curves of Waarts (1997) in colour, overlaid on original black graph. 154

Table 7.1. Modified input values for use in the reproduced Waarts framework. 155

Figure 7.4. Reproduced curves from Waarts (1997) and updated values with the same methodology. 156

Figure 7.5. Complete overview of all the elements observed during the study and how they relate to each other in the framework (see next page for larger size). 157

Figure 7.6. Overview of external actions that may lead or contribute to damage. 161

Figure 7.7. Overview of ground deformations. Exaggerated scaling. 162

Figure 7.8. Equivalent PPV for different actions on a wood-frame house. 164

Figure 7.9. From NAM (2013). Earthquakes and their magnitude in the Groningen area in the period from the late 1980's to 2013. 165

Figure 7.10. Historical map by the dutch institute of meteorology (KNMI) - updated for the Zeerijp earthquake on January 8th, 2018. Left, PGA values in percentage of g, and right, PGV values in cm/s. Blue triangles mark the measurement devices. 166

Figure 7.11. Work flow for producing resistivity curves from computational models. 167

Figure 7.12. Number of computational models to run. 168

Table 7.2. Results from computational models showing the initial value for Ψ and its increase after the earthquake. 169

Figure 7.13. 3D graphs showing the final damage given various values of material, PGA, pre-damage type and initial damage value (from 0 to 1.8, respectively yellow-green-blue). Values directly from Table 7.2. 170

Table 7.3. Summary of regression parameters for computational results. 170

Figure 7.14. Results from computational models as points and regressed curves for initial damage values of 0, 1, and 1.6 on the first, second and third rows respectively. 171

Figure 7.15. Sampled points from the regressed curves and their uncertainty. Only 500 points per colour and only up to two colours per graph. 172

Table 7.4. Summary of Variables for the resistivity curves of computational models. 172

Figure 7.16. Indicative Resistivity curves for computational results for Ψ0=0 against PGA. 173

Figure 7.17. Indicative Resistivity curves for computational results for Ψ0=0.5 against PGA. Showing also the difference between pre-damage types. 173

Figure 7.18. Indicative Resistivity curves for computational results for Ψ0=1.0 against PGA. Showing also the difference between pre-damage types. 174

Figure 7.19. Indicative Resistivity curves for computational results for Ψ0=1.5 against PGA. Showing also the difference between pre-damage types. 174

Figure 7.20. Indicative Resistivity curves for computational results for Ψ0=0 against PGV. 175

Figure 7.21. Indicative Resistivity curves for computational results for Ψ0=0.5 against PGV. Showing also the difference between pre-damage types. 175

Figure 7.22. Indicative Resistivity curves for computational results for Ψ0=1.0 against PGV. Showing also the difference between pre-damage types. 176

Figure 7.23. Indicative Resistivity curves for computational results for Ψ0=1.5 against PGV. Showing also the difference between pre-damage types. 176

Figure 7.24. Indicative Resistivity curves for computational results for Ψ0=0 against PGV in the range of 0 to 15mm/s. 177

Figure 7.25. Comparison with curves and points for DS1 from various authors. According to the definition for the damage level, depending on the structure, DS1 starts between Ψ=1 and Ψ=3. Indicative Resistivity curves for computational results for Ψ0=0 against PGV for these two values are shown. Note that the comparison curves are log-normal S-curve fits to a few available points and that their behaviour away from the marked points may differ. 177

Figure 7.26. Workflow for producing resistivity curves based on the laboratory experiments. 179

Figure 7.27. Top lateral displacement of the experimental walls against the damage measured from DIC results. 180

Figure 7.28. Regression line for the relationship between displacement and Ψ, marking the points considered. 181

Figure 7.29. Histogram of the slope between Ψ and uLat and the fitted lognormal distribution. 181

Figure 7.30. Psi-displacement value pairs including their position along the test. 182

Figure 7.31. Sample value pairs. 182

Figure 7.32. Mass distribution along the wall showing concentrated mass on top. 184

Figure 7.33. Frequency content of the spectrum for the chosen acceleration signal (see Chapter 6), and top lateral displacement for a PGV value of 1mm/s. 184

Figure 7.34. Sample of the empirical probabilistic distribution used to replicate the frequency content of the earthquake. 185

Table 7.5. Summary of parameters for experimental curves. 186

Figure 7.35. Experimental resistivity curve for given top lateral displacements. 186

Figure 7.36. Experimental resistivity curves for given PGV values. 187

Figure 7.37. Experimental resistivity curves for given PGV values in the smaller range of 0 to 15mm/s. Additionally, rough estimation for the curves computed for undamaged cases. 187

Figure 7.38. Overview of sensitivity for various parameters. 188

Figure 7.39. Comparison of two earthquake signals. 189

Table 7.6. Summary of sensitivity for the probabilistic parameters. *Sensitivity defined as the weighted variation of the expected result for a change of one standard deviation. 189

Figure 7.40. Velocities and displacements from dynamic excitations. 190

Figure 7.41. Experimental resistivity curves showing a rough estimation of the confidence interval (75% confidence). All graphs are the same but display a different number of curves and intervals for clarity. 191

Figure 7.42. Comparison between computational and experimental resistivity curves and Waart's curves. 193

Table 7.7. Summary and Comparison of Frameworks. 195

8. Conclusions and Recommendations. 198

References 201

9. Appendix ii

Table 9.1. Overview of average material properties from NAM-2 (2016) and NAM-3 (2017) companion test results. xii

Table 1. Properties for mortar elements. xxii

Figure A.1. Left, strain-stress tensile behaviour of mortar (bed joints), and right, shear retention factor of mortar. xxiii

Table 2. Properties for brick elements. xxiii

Figure A.2. Stress-strain tensile behaviour for brick elements, showing potential damage paths. xxiii

Figure A.3. Four-point in-plane bending test. Top graph and photographs: laboratory tests; bottom: computational model. xxv

Figure A.4. Out of plane bending tests. Experimental graph at the top and computational models at the bottom. The modelled crack patters are identical to some of the laboratory specimens. xxvii

Figure A.5. Comparison of wall with a window. xxviii

Figure A.6. Shear wall in cyclic laboratory test versus the same wall in a monotonic numerical model. xxix

Figure A.7. A wall with a window employing a soldier lintel. Cyclic lateral displacement (increased scale) in numerical model. xxix

Figure A.8. Left, top to right, bottom: a) Experimental model of façade subjected to hogging settlement with overview of main cracks; b) Depiction of model with scheme of main cracks compared to the result of the modelling approach of this study; and c) smeared crack model from Giardina et al. (2012), compared to d) mortar-brick discrete crack damage model tailored for this study. xxx

Figure A.9. Left: top lateral displacement applied in the model; right: base shear force registered; bottom: crack mouth opening displacements for cracks on the window corners, crack 2: bottom right; crack 3: top left. xxxi

Figure A.10. FEM showing crack initiation (cw>0.1mm) for a top lateral displacement of 2mm. High compressive stresses are shown in yellow, while high tension stresses are shown in green. The arrows indicate the displacement of the model elements revealing quasi-rigid body rotations. xxxii

Figure A.11. Model for post-diction of window bank. In blue: supports, and the point of application of jacks and counterweights is shown. xxxiii

Figure A.12. Sequence of strain plots from the post-diction window bank model in Abaqus showing the progression of the vertical crack in the middle. xxxiii

Figure A.13. Force-displacement curves comparing five models with seven laboratory curves (see Section 4.2). Top: linear displacement scale; bottom: logarithmic displacement scale. xxxiv

Table 3. Micro-model property comparison for post-diction of window bank. xxxv

Figure A.14. Explanation for the importance of shear stiffness and capacity during crack opening for zig-zagging cracks. . xxxv

Figure A.15. Comparison of in-plane four-point bending laboratory test and numerical model. xxxvi

Table 4. Summary of runnable micro-models. xxxvi

Figure A.16. Pre-test results of TUD_COMP-40, TUD_COMP-41 and TUD_COMP-42. xxxvii

9.2. Companion Tests

Table 9.1. Overview of average material properties from NAM-2 (2016) and NAM-3 (2017) companion test results.

			NAM-2 2016			NAM-3 2017		
			Average	St. dev.	C.o.V.	Average	St. dev.	C.o.V.
Compressive strength of mortar	f_m	MPa	3.81	0.34	0.09	3.84	0.43	0.11
Flexural strength of mortar	f_{mt}	MPa	1.40	0.17	0.12	1.57	0.11	0.07
Normalized compressive strength of element prescribed by producer	f_b	MPa	28.31	2.92	0.10			
Flexural strength of brick	f_{bt}	MPa	6.31	0.72	0.11			
Elastic modulus of brick from bending test	E_b	MPa	8049	423	0.05			
Compressive strength of masonry in the direction perpendicular to bed joints	f'_m	MPa	14.02	0.56	0.04	11.35	0.83	0.07
Elastic modulus of masonry in the direction perpendicular to bed joints	E_1	MPa	4380	605	0.14	2919	442.00	0.15
	E_2	MPa	4068	783	0.19	2731	732.00	0.27
	E_3	MPa	4590	603	0.13	3087	315.00	0.10
Poisson ratio of masonry in the direction perpendicular to bed joints	ν	-	0.14	0.02	0.11	0.14	0.004	0.03
Fracture energy in compression for loading perpendicular to bed joints	$G_{f\text{-}c}$	N/mm	28.52	3.4	0.12	26.05	3.15	0.12
Compressive strength of masonry in the direction parallel to bed joints	$f_{m,h}$	MPa	13.11	2.41	0.18			
Elastic modulus of masonry in the direction parallel to bed joints	$E_{1,h}$	MPa	3332	565.00	0.17			
	$E_{2,h}$	MPa	3664	689.00	0.19			
	$E_{3,h}$	MPa	3207	592.00	0.18			
Fracture energy in compression for loading parallel to bed joints	$G_{f\text{-}c,h}$	N/mm	35.1	6.63	0.19			
Masonry bending strength with the moment vector parallel to the bed joints and in the plane of the wall	f_{x1}	MPa	0.16	0.03	0.18			
Youngs modulus from OOP1	E_{fx1}	MPa	3756	1789	0.21			
Masonry bending strength with the moment vector orthogonal to the bed joint and in the plane of the wall	f_{x2}	MPa	0.65	0.17	0.25			
Youngs modulus from OOP2	Efx2	MPa	7080	593	0.08			
Masonry bending strength with the moment vector orthogonal to the plane of the wall	f_{x3}	MPa	0.46	0.09	0.20	0.35	0.14	0.40
Youngs modulus from IP bending	E_{fx3}	MPa	2924	480	0.16	2084	526	0.25
Flexural bond strength	f_w	MPa	0.15	0.05	0.32	0.09	0.03	0.35
Masonry (bed joint) initial shear strength	f_{v0}	MPa	0.20			0.14		
Masonry (bed joint) shear friction coefficient	μ		0.69			0.79		
Residual masonry (bed joint) initial shear strength	$f_{v0,res}$	MPa	0.05			0.03		
Residual masonry (bed joint) shear friction coefficient	$\mu_{\rho\varepsilon\sigma}$		0.60			0.71		

9.3. Nomenclature

9.3.1. Symbols

This report adopts mainly the nomenclature used in Eurocode 6. In addition, symbols used in the codes for testing are adopted.

α	Masonry (bed joint) angle of internal friction
α^*	Angle of internal friction of the dry connection (mortar bed joint) between concrete floor and masonry wall
α_{res}	Masonry (bed joint) residual angle of internal friction
α^*_{res}	Residual angle of internal friction of the dry connection (mortar bed joint) between concrete floor and masonry wall
ν	Poisson ratio of masonry
μ	Masonry (bed joint) shear strength coefficient
μ^*	Shear strength coefficient of bed joint between concrete and masonry
μ_{res}	Masonry (bed joint) residual shear strength coefficient
μ^*_{res}	Residual shear strength coefficient of bed joint between concrete and masonry
d_1	Distance between bearing supports
d_2	Distance between loading supports
d_3	Distance between the loading and bearing supports (four-point bending test)
f_b	Compressive strength of masonry unit
f_{bt}	Flexural strength of masonry unit
f_{cc}	28-day cubic compressive strength of concrete
f_{ik}	Characteristic value of the i-th property
$f_{ik,EC6}$	Characteristic value of the i-th property as prescribed by Eurocode 6
$f_{ik,NPR}$	Characteristic value of the i-th property as prescribed by NPR 9096-1-1:2012
f_m	Compressive strength of masonry mortar
f_{mt}	Flexural strength of masonry mortar

$f_m^{'}$	Compressive strength of masonry in the direction perpendicular to the bed joints
$f_{m,h}^{'}$	Compressive strength of masonry in the direction parallel to the bed joints
f_p	Applied lateral pre-compression stress
f_{x1}	Masonry flexural strength with the moment vector parallel to the bed joints and in the plane of the wall, which generates a plane of failure parallel to the bed joints
f_{x2}	Masonry flexural strength with the moment vector orthogonal to the bed joints and in the plane of the wall, which generates a plane of failure perpendicular to the bed joints
f_{x3}	Masonry flexural strength with the moment vector orthogonal to the plane of the wall
f_{v0}	Masonry (bed joint) initial shear strength
f_{v0}^{*}	Initial shear strength of the dry connection (mortar bed joint) between concrete floor and masonry wall
$f_{v0,res}$	Masonry (bed joint) residual initial shear strength
$f_{v0,res}^{*}$	Residual initial shear strength of the dry connection (mortar bed joint) between concrete floor and masonry wall
f_w	Masonry uniaxial bond strength between the masonry unit and the mortar
l_j	Length of the mortar bed joint in a masonry specimens
l_m	Length of the mortar specimen
l_s	Length of the masonry specimen as built
l_p	Length of the loading plate for compression tests on mortar specimens
l_u	Length of the masonry unit as used in the construction of masonry
h_m	Height of the mortar specimen
h_s	Height of the masonry specimen as built
h_u	Height of the masonry unit as used in the construction
t_s	Thickness of the masonry specimen as built
t_m	Thickness of the mortar specimen
t_u	Thickness of the masonry unit as used in the construction of masonry

$s_{F_{c,0}}$	Slip of the tie corresponding to the maximum compressive force $F_{c,0}$
$s_{F_{c,2}}$	Slip of the tie corresponding to the maximum compressive force $F_{c,2}$
$s_{F_{po,0}}$	Slip of the tie corresponding to the maximum tensile force $F_{po,0}$
$s_{F_{po,1}}$	Slip of the tie corresponding to the maximum tensile force $F_{po,1}$
$s_{F_{po,2}}$	Slip of the tie corresponding to the maximum tensile force $F_{po,2}$
v_{el}	Vertical displacement corresponding to the load F_{el}
w_j	Width of the mortar bed joint in a masonry specimen
A_s	Cross sectional area of the specimen parallel to the bed joints (shear test)
E_{bt}	Elastic modulus of masonry unit
E_1	Secant elastic modulus of masonry subject to a compressive loading perpendicular to the bed joints, evaluated at 1/3 of the maximum stress
E_2	Secant elastic modulus of masonry subject to a compressive loading perpendicular to the bed joints, evaluated at 1/10 of the maximum stress
E_3	Chord elastic modulus of masonry subject to a compressive loading perpendicular to the bed joints, evaluated at between 1/10 and 1/3 of the maximum stress
$E_{1,h}$	Secant elastic modulus of masonry subject to a compressive loading parallel to the bed joints, evaluated at 1/3 of the maximum stress
$E_{2,h}$	Secant elastic modulus of masonry subject to a compressive loading parallel to the bed joints, evaluated at 1/10 of the maximum stress
$E_{3,h}$	Chord elastic modulus of masonry subject to a compressive loading parallel to the bed joints, evaluated at between 1/10 and 1/3 of the maximum stress
F_1	Applied vertical load (bond-wrench test)
F_2	Vertical load due to the weight of the top clamping system (bond-wrench test)
F_3	Vertical load due to the top masonry unit (bond-wrench test)
$F_{c,0}$	Maximum compressive load capacity of tie subject monotonic compressive load
$F_{c,2}$	Maximum compressive load capacity of tie subject fully cyclic load
F_{el}	Selected vertical load value in the linear elastic stage (flexural test of masonry unit)
$F_{\max}$	Maximum vertical load

F_p	Applied lateral pre-compression force (shear test)
$F_{po,0}$	Maximum tensile load capacity of tie subject monotonic tension load
$F_{po,1}$	Maximum tensile load capacity of tie subject cyclic tension load
$F_{po,2}$	Maximum tensile load capacity of tie subject fully cyclic load
G_{f-c}	Fracture energy in compression for loading perpendicular to the bed joints
$G_{f-c,h}$	Fracture energy in compression for loading parallel to the bed joints
P_i	i-th property (used for comparison)
$M_{\max}$	Maximum bending moment
W	Section modulus

9.3.2. Abbreviations

Avg.	Average
C.o.V.	Coefficient Of Variation
CMOD	Crack Mouth Opening Displacement
CS	Calcium Silicate
DIC	Digital Image Correlation
DS	Damage State
FEM	Finite Element Method
FFT	Fast Fourier Transform
FORM	First Order Reliability Method
IP	In-Plane
LDF	Light Damage Framework
LVDT	Linear Variable Differential Transformer
NAM	Nederlandse Aardolie Maatschappij
NL-TH-A	Non Linear Time History Analysis
NPR	Nederlandse Praktijk Richtlijn
OOP	Out-Of-Plane
PGA	Peak Ground Acceleration
PGV	Peak Ground Velocity

PPV	Peak Particle Velocity
SBR	Stichting Bouwresearch
SDoF	Single Degree Of Freedom
SPH	Smooth Particle Hydrodynamics
St. dev.	Standard Deviation
URM	Unreinforced Masonry

9.4. Abaqus Modelling

To complement the models discussed in Chapters 2 and 4, an alternative modelling technique was pursued. In contrast to the implicit solving method employed by the DIANA models, explicit Abaqus models were made. However, the explicit meso and micro models were too computationally expensive to be employed for the analysis of multiple cases and were only used to verify the predictions of the DIANA models. Because of this, they have not been included as part of the main report, but are presented here.

9.4.1. Discussion: Modelling With Abaqus/Explicit

This subchapter aims at providing a description, discussion and reasoning for the techniques adopted to fulfil the requirements of the different kinds of models. These requirements are also reasoned here.
Since this discussion is essentially a timeline of the decisions taken during the modelling exploration, the reader might want to refer to the following chapters for a more concise description and overview of the choices made and a presentation of the working models.

First Models: Input and Modelling for Monotonic Displacements

- Mortar and bricks can be continuum elements.
- Mortar is better characterised with the brittle cracking model. The concrete plasticity damage model does not support element deletion and, because cracks have very large strains, they are outside the relevant part of the damage model thus disabling any benefits the plasticity damage model may have. Additionally, the heavily distorted elements unrealistically modify the behaviour of the complete model, and the 1% bottom limit stress for all elements unrealistically add post-failure forces which modify crack patterns.
  - Comparisons of reproduced laboratory tests show the brittle cracking model with element deletion for the mortar elements to be the best model for reproducing observed crack patterns.
- The tension strength of the mortar continuum elements should correspond to that of the bond between bricks and mortar: f_w.
- Comparisons have also consistently shown that the vertical mortar joints are weaker than the horizontal mortar joints.
- For weak masonry with an average of f_w=150kPa, modelled mortar joints need to be weaker to reflect:
  - As-built mortar joints being weaker than brick-mortar-brick bond tests.
  - Statistically, 50% of mortar joints being weaker than the average and cracks starting at these positions; hence the model should use values weaker than the average.
- Extrapolating from the reproduced laboratory tests:
  - horizontal mortar joints seem to have a bond strength of 50-100kPa, half the average from dedicated bond tests.
  - Vertical mortar joints are much weaker at 20-40kPa.
- Models have also shown that horizontal joints should consider bi-directional failure criteria while vertical joints are sufficiently well reproduced with one-directional criteria. This allows for horizontal joints to develop realistic shear strength values. In larger models, where mode I fracture is more relevant, a one directional criterion is better.
- Shear retention values for the continuum elements of the mortar joints can be set to drop linearly from the strain corresponding to the bond strength, down to the point where the crack is considered fully open.
  - Alternatively, a decaying exponential law can be used, describing loss of shear resistance all the way to element deletion. A power of 3 has produced reasonable results.
- When specifying the mode I fracture energy, the failure criterion is the displacement corresponding to the lower bound crack width.
- Fracture energy corresponding to the first mode seems to be around 5-10N·m/m^2, inline with Rots et al. (1997) and Almeida et al. (2012), Schneemayer et al. (2014), among others.
- Bricks can be modelled to be linear-elastic when any of the following take place:
  - the ratio between mortar strength and brick strength is low (less than 1/5 appears reasonable).

  - In situations where flexural damage is to be expected and the cracks are concentrated in the mortar.
  - Only minor damage is expected.
- Bricks should be non-linear when:
  - The ratio of bond/brick-tension-strength is higher than 1/5.
  - Heavy shear deformation is expected requiring cracks to go through bricks.
  - Failure is also expected to involve compression damage of bricks (crushing).
- Non-linear bricks can follow the concrete plasticity damage model or the brittle cracking model.
  - The first is convenient when minor damage or serious brick compression damage is expected.
  - When the damage is intense and the model has a great number of elements, significantly distorted elements need to be deleted; then, the brittle cracking model that disregards compression damage needs to be used; however, brittle failure mechanisms (such as shear) will not be well described with the brittle model, because of its "explosive" nature.
- To speed up calculations, a regular mesh should be used. This can be accomplished by modelling bricks of 210x50x100mm and mortar joints of 10mm.
- In small specimens, the mesh can be refined around the expected crack areas. However, failure displacement criteria need to be adapted.
- Final crack width can be measured by looking at the displacement Δ between two brick edges
- Clay bricks have typical values of (Esposito et al., 2016.b):
  - E=11.4GPa, f_t=6.3MPa, $G_{f,I}$=2000N/m, f_c=27MPa.
- Mortar joints vary around:
  - E=1.0-1.5GPa, f_w=20-100kPa, $G_{f,I}$=5-10N/m.
- The E of mortar can be deduced from the measured E of masonry and E of brick.
- Blocks with a rotational point serve well as reproduced roller supports spreading the load on a bricks.
- All models are very sensitive to boundary conditions. These need to be observed and restrict only the DOFs required, while also implementing the interactions imposed during the laboratory tests.
- Settlements are sensitive to the interface between the foundation and the applied displacement. For settlement models, an interface that doesn't resist tension needs to be implemented.
- Compressive stress values in walls vary around 0.4MPa and these are influential in the damage outcomes.
- Strains due to hygro-thermal action vary around 0.34‰ for clay and 0.44‰ for calcium silicate.
- Models with regular meshes, linear-elastic bricks, mortar with element deletion, and no highly-non-linear soil interfaces run the fastest.

Preliminary Comments About Actions Evaluated on First Models

- **Settlement** damage is dependent on the gravity forces acting on the wall and the ratio of length/width of the wall. If the gravity forces are not high enough to make the wall follow the settlement deformation of the soil, no damage will occur.
- **Shrinkage** of the wall due to hygro and/or thermal changes when foundations or slabs restrict free movement, does lead to the initiation of damage. This is concentrated in areas without existing compression stresses such as at window banks.
- Regular vertical vibrations which seem to be the only expression of potential earthquake **surface waves** do not lead to the initiation of damage for values of pgv below 100mm/s, unless there are prominent structural irregularities such as balconies and shallow beams above windows.
  - Surface waves from earthquakes do not have wavelengths shorter than common wall lengths, which makes the vertical deformations virtually parallel for walls shorter than 10m.
  - Rocking due to these surface waves is consequently also negligible.
  - However, long structures such as terraced house may be affected by these surface waves.
- **Earthquakes** with lateral accelerations of 0.10g always lead to the initiation of damage when no damage is present.
  - Lower accelerations with and without existing pre damage still need to be explored.

Second Models: Specific Limitations of Abaqus/Explicit and Micro-Modelling of Masonry for Cyclic Displacements

- Contact formulations do not allow for a negative clearance (required to mimic mortar) when using anything else besides general contact with contact being specified automatically for all surfaces/edges.
- Contact pairs (an alternative to general contact) cannot be used with shell edges. This can be used if the elements are solids and 2D surfaces become the interaction boundaries.
- Not using mortar elements, but interface elements from the start, requires each brick to be drawn into position in Abaqus. Importing the whole wall from AutoCad doesn't create the required surfaces.
  Bricks can be replicated as instances using a linear pattern and this works for small specimens, but is cumbersome for big walls with windows and complex shapes.
  Moreover, this contact definition (interphase elements) needs to be assigned a cohesion and damage properties which Abaqus/Explicit does not support when using edge-to-edge shell, plane stress elements or 3D elements with automatically defined surfaces. Essentially: cohesive interactions are not supported by Abaqus/Explicit.
  Additionally, interphases do not show crack propagation as elegantly as the use of continuum elements.
  - Using interphase elements (cohesive interactions) with Abaqus/Standard does work, but modelling entire walls is slow and when observing complex and cyclic failure mechanisms, is also prone to non-convergence.
- When using 3D elements for large models, the computations may take too long. Attempting to reduce the time with mass scaling may introduce noise at the boundaries (due to significant element mass differences and kinematic contact constraints).
  - Using different size meshes with tie constraints doesn't work well either.
- In cyclic tests, after the mortar elements have been deleted from the analysis, contact is specified between the bricks, simulating friction. Additionally, in these type of tests, crushing due to compression can also occur. In both these cases, brick elements can become severely damaged and deformed. The concrete plasticity damage model does not support element deletion thus leading to termination of the analysis when severe distortion occurs.
  - It is possible to improve the concrete damage model that Abaqus uses by writing a user subroutine that implements element deletion into this model (Rodriguez et al., 2013; Gehwolf, 2015); however, this requires the installation of a Fortran compiler that needs to be linked to the Abaqus code. This is difficult to implement if several systems are being used. Moreover, the use of the subroutine requires additional tests and validations. Literature on the success of this approach is scarce and contradicting.
  - Abaqus supports conversion of 3D elements to particles (SPH) which allow for extreme distortions (and also mimic quite well the behaviour under crushing); however, the limitations incurred by the use of SPH make models unattractive for brick-mortar interactions because:
    - SPH only support general contact, meaning that the contact pairs required for mimicking the presence of a mortar layer cannot be used.
    - SPH conversion by strain criteria do not support domain decomposition, meaning that models can only run in one processor, effectively multiplying the computation time by a factor of at least 10.
    - Gehwolf (2015) also reached similar conclusions.
  - Adaptive re-meshing is a powerful tool that allows for the control of the distortion of elements generated by intense plasticity. However, it is not effective at controlling instabilities of the model or rapid detachment of material. It has proven to be unsuccessful in controlling early analysis termination due to crushing of the bricks.
- Modelling the mortar joints as cohesive elements themselves allows for a good estimation of damage evolution without needing to implement element deletion as cohesive elements can acquire zero stiffness, this is explored, for example, by Kowalewski et al. (2015). Ranges of crack width can be assigned different colours. However, the reduction of stiffness due to damage affects also the shear behaviour of the elements, meaning that they offer unrealistically small shear resistance during advanced cycles, making the use of these elements inaccurate.
  - In various tests, cohesive elements were not successful at mimicking complex cracking patterns.

Summary of Modelling Techniques for Cyclic Loads

Based on the aforementioned modelling choices and on the limitations for modelling discussed above, the following approach is taken for observing damage due to cyclic actions:

- Bricks and mortar are individual parts.
- The model is done in 3D with a thickness of 1 mesh element and restraints in the out-of-plane direction, or with the real thickness if out-of-plane effects are being observed. This allows the automatic selection of surfaces and the definition of complex brick-to-brick interactions.
- Mortar elements follow the brittle cracking model and are deleted once they have failed. This allows for the initial cohesion of the joints, both for normal and tangential behaviour.
- The deletion of mortar elements presents an indication of the crack patterns, the crack width that triggers element deletion can be specified. A value of 0.1mm seems to work adequately.
- Interactions between bricks mimic the presence of a 10mm mortar gap and comes into effect after the mortar elements have been deleted. The interaction includes static and kinetic shear.
- Bricks follow a linear elastic model in the cases where damage is expected only at the interface. When bricks are expected to be damaged, they can selectively be chosen to follow the concrete plasticity damage model with stiffness damage parameters for both tension and compression.
- The model is quasi-static and uses a time increment factor and, if possible, mass scaling. The linear and quadratic bulk viscosity factors are increased. To prevent collapsing of neighbouring elements when some elements are deleted, the quadratic factor needs to be adjusted around values of 10.

Discussion About the Limitations of the Chosen Model

The brittle cracking model of Abaqus is intended for materials with a low fracture energy where softening and damage during the short softening region are not very relevant. The power of this model lays in its simplicity and support for element deletion. Nevertheless, because in its simplicity, the material does not support damage, elements that have entered into the softening region but have not reached the specified deletion displacement, will regain their full stiffness when load reversal takes place. Even if the deletion (strain) is set to match the end of the softening curve precisely, a small range remains in which the element takes damage which is not accounted by the model if the element doesn't reach the removal criterion in the same cycle. Setting the removal criterion too close to the stress peak may lead to instabilities in the model, so this is also not desirable.

Consequently, it is important to define the crack width that triggers element deletion at the point where the crack is reasonably established, while also limiting the amount of damage that will be neglected by the model during cyclic events in the cases where a crack isn't formally detected.

Nonetheless, since the softening region of the brittle model is small, the influence of this effect is also expected to be small, but calibration is yet to be performed.

Main Difficulties

- The strength of the bond between brick and mortar is key in determining the initiation and propagation of damage. The results are extremely sensitive to this.
- The varying strength of this bond throughout one single masonry specimen makes the replication of complex damage patterns difficult. This is inherent to the heterogeneity of masonry.
- Reproducing the stress and strain configuration of (parts of) structural elements is, hence, uncertain and highly dependent on the actions.
- Determining the intensity and representative configuration of relevant actions is complex and also depends on the typology.
- Choosing one or two configurations of stresses and actions to fabricate laboratory specimens and run tests is not straightforward.

9.4.2. Constitutive Models

A vital part of any model is its representation of the material and/or elements that constitute the material. In the case of masonry, several approaches can be followed to attempt to reproduce masonry structural elements. Adapted from Lorenço (1996) and Rots et al. (1997), and in order of numerical complexity and computational expense, masonry can be successfully modelled using:

- Continuous elements of only one material (with anisotropic properties),
- Discrete elements of only one material and an interface between these elements,
- Discrete elements of two materials (brick and mortar),
- Discrete elements of two materials (brick and mortar) and an interface between these elements.

The selection of a certain alternative will depend on the application and accuracy required on the model.

The approach chosen here is a mixture of the last two alternatives. Before damage has occurred, the model consists of brick and mortar elements, the latter acting as the interface between bricks. This allows for a good replication of the elastic deformation of bricks and mortar joints. After damage has occurred, that is, cracks have appeared between the bricks at the mortar interface, the continuum mortar elements are removed, and an interface mimicking the presence of a damaged mortar layer is introduced; this interface reproduces the shear behaviour of an open mortar joint and is defined as contact between the bricks.
It must be noted that cracks can also run through the bricks, but this is part of the material model of the bricks.
In sum, mortar, brick and the post-crack interface need to be assigned adequate constitutive models.

Mortar

The mortar is modelled with shell or solid continuum elements that follow the brittle cracking model. This model is based on the work of Hillerborg (1985) and has been extensively explored by Alberto et al. (2011), Almeida et al. (2012) and Červenka et al. (1998), among others. The material develops perfectly elastic stress in tension up to a point of failure, after which it follows a rapid softening curve down to zero resistance; this corresponds to the brittle crack growth and the lack of tensile strength once the crack has been fully established. The latter part of this behaviour can be enforced by removing the element from the model.
The softening curve can easily be defined by using the fracture energy as a material property. In this case, the curve follows a linear decline. Figure A.1 illustrates the behaviour in tension.
In the case of load-reversal when the element is in the softening region, the stiffness is not damaged. The behaviour in compression is perfectly elastic.
The strength in shear reduces after tensile failure. However, before the crack is fully open, it can still resist shear forces. The drop in shear capacity is modelled with an exponential decay.
The values used to characterise the mortar are listed in Table 1.

Table 1. Properties for mortar elements.

Property			Mortar Joints	
			Horizontal	Vertical
Density	ρ	kg	2000	
Young's Modulus	E	MPa	1300	900
Poisson	ν	-	0.14	
Tensile Failure Stress	f_w	kPa	60	20
Fracture Energy	$G_{f,I}$	N/m	10	5
Crack failure displacement	c_w	mm	0.1	
Tensile strain for zero shear	$\varepsilon_{t,u,s}$	-	0.01	

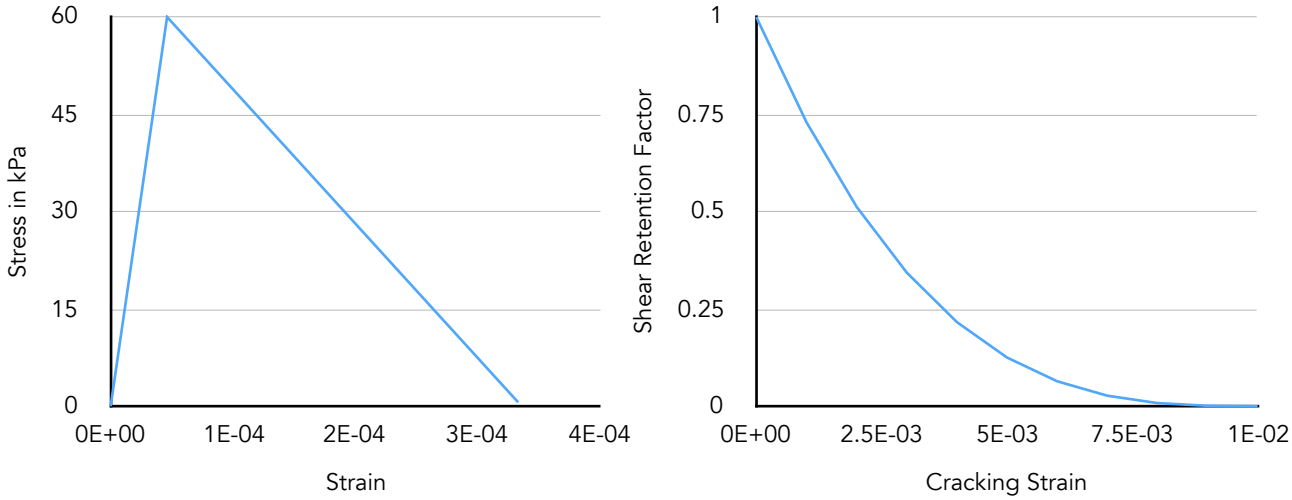

Property			Mortar Joints	
			Horizontal	Vertical
Shear exponential decay	α	-	3	

Figure A.1. Left, strain-stress tensile behaviour of mortar (bed joints), and right, shear retention factor of mortar.

Brick

Brick elements can be modelled non-linearly following a concrete plasticity model with stiffness damage (such as described for concrete by Sümer et al., 2015) or simply linear-elastically. In the case that bricks are able to acquire damage, this can occur for both tension and compression.

Table 2. Properties for brick elements.

Property			Brick
Density	ρ	kg	1700
Young's Modulus	E	MPa	11,400
Poisson	ν	-	0.14
Tensile Failure Stress	f_w	kPa	6,300
Fracture Energy	$G_{f,I}$	N/m	3,000
Ultimate Compression Strain	ε_{cu}	-	0
Dilation Angle	γ	°	12.0

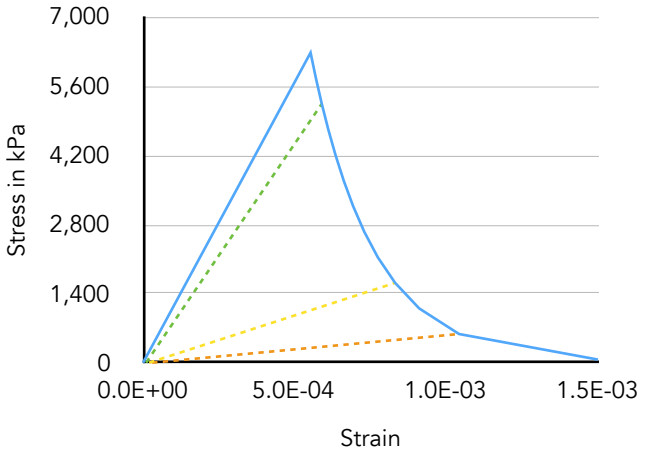

Figure A.2. Stress-strain tensile behaviour for brick elements, showing potential damage paths.

The softening region is characterised with an exponential decay according to the following law:

$$\sigma=\sigma_{peak}\cdot\exp\left(\alpha_1\cdot\left(\frac{\varepsilon-\varepsilon_{el,peak}}{\varepsilon_{0.01\sigma}}\right)^{\alpha_2}\right) \quad (A.1)$$

Where:

σ_{peak} is the maximum elastic stress
$\varepsilon_{el,peak}$ is the maximum elastic strain
$\varepsilon_{0.01\sigma}$ is the strain corresponding to 1% of σ_{peak}
α are curve shape parameters. In this case α_1=-4.6 and α_2=0.999

Brick-Brick Contact

After mortar elements have failed, a contact law is used to model the interaction between bricks. Since the mortar elements have been chosen to fail when a crack width of 0.1mm or more has been formed, this gap first needs to close before contact is established.

When the distance between bricks is 10mm, the contact pressure between these bricks starts following a linear elastic definition with the same young modulus as the deleted mortar elements.

Friction is enforced with a static friction coefficient of 1 and a dynamic (sliding) one of 0.5. The post-damage static and dynamic frictional (shear) behaviour of these mortar interfaces needs to be observed further based on upcoming companion laboratory tests.

9.4.3. Calibration & Examples

The material properties that will be used for this project have been investigated and reported in previous campaigns. Hence, several laboratory tests already exist and these can be used to calibrate and validate the computational models.

The models seek to replicate stiffness and strength values, curve shape and ductility values for force-displacement tests, and reasonable crack patterns.

In-Plane Flexural Test

Five four-point bending tests as shown in Figure A.3 have been conducted. The tests consist of a masonry sample that is gradually pushed on two points at the top with the use of a hydraulic jack. The horizontal displacement at the bottom row of bricks is monitored and used to control the applied force.

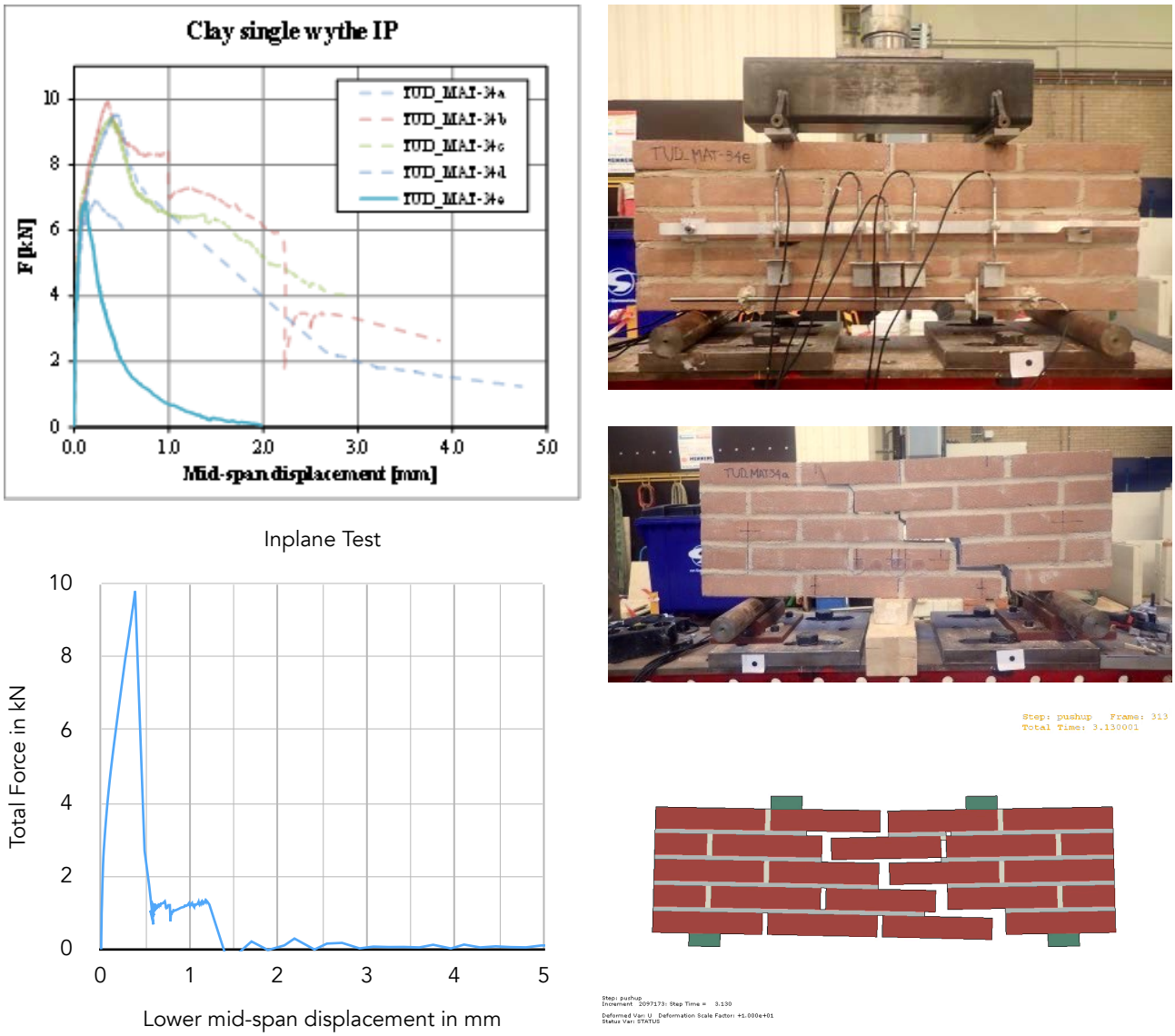

Figure A.3. Four-point in-plane bending test. Top graph and photographs: laboratory tests; bottom: computational model.

Overall, the computational model corresponding to the blue lines, mimics the laboratory test reasonably well. However, several aspects had to be observed when modelling:

First, for three of the bending tests performed, the roller supports at the bottom were generating excessive horizontal friction which is reflected on the curves as additional elastic and post-peak capacity. For the final test (34e), this issue was fixed thus bringing the post-peak capacity to zero. This was easily reproduced in the computational model (not shown). Additionally, the obtention of the observed crack pattern was partly conditioned by the type of top restraints chosen. As can be seen in the picture, the steel

plates are allowed to rotate around two cylinders which are welded to a beam. However, when the plates rotate, the also need to displace horizontally. This had to be implemented in the model to obtain an accurate crack pattern. It follows, that the boundary conditions need to be replicated and observed carefully.
Second, the maximum bending moment in a four-point being test is constant between the two load-application points and the shear force is theoretically zero between them. If this is the case, the greatest tensile stress would occur at the middle vertical joint, but, as can be observed in Figure A.3, the crack starts diagonally from one of the side vertical mortar joints. The aforementioned boundary conditions were partly responsible for this behaviour, but it was determined that additional factors were key in producing the diagonal crack pattern observed in all five of the laboratory experiments. It would seem that some or all of the vertical mortar joints on the first row are significantly weaker than the ones in the rest of the specimen; when this is the case, the crack follows a diagonal pattern. In the computational models, reducing the failure stress for all three bottom vertical joints leads to the observed pattern.
The reason behind the pre-weakening of these joints is suspected to lie in the construction and handling of the specimens. The bottom joints are more likely to have a lower quality due to placing of the bricks above during construction, while also experiencing the greatest shrinkage stresses due to the constraint of the bottom beam.

Out-of-Plane Flexural Tests

Similarly to the in-plane flexural test, two types of out-of-plane bending tests were conducted. These were also reproduced numerically.
The lessons from the in-plane test were applied to these models so that they were easier to reproduce. As can be observed in Figure A.4, the strength and ductility of both models matches those observed in some of the laboratory tests.

It is important to emphasise that the material properties used for all three models are the same. In this light it could be confirmed that the vertical mortar joints are significantly weaker that the horizontal mortar joints. This is due to the construction techniques used and the hardening process of masonry.

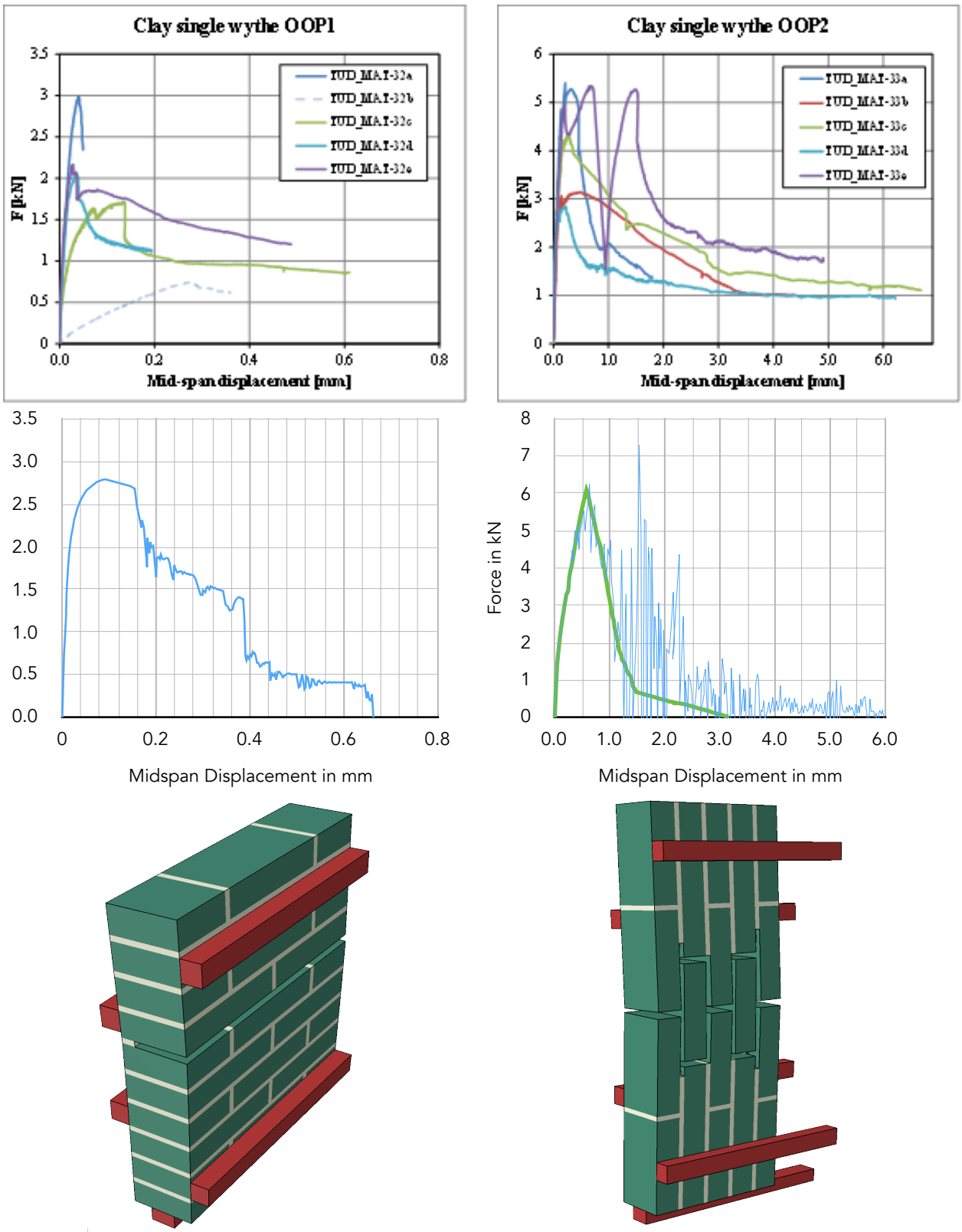

Figure A.4. Out of plane bending tests. Experimental graph at the top and computational models at the bottom. The modelled crack patters are identical to some of the laboratory specimens.

Pushover of Wall With a Window

A double-wythe wall with a jack-lintel was tested cyclically in-plane at the laboratory. Modelling of a double-wythe wall in a cyclic test introduced too many variables and was computationally too expensive for the damage micro-model run here, so this model was made single-wythe and pushed laterally in-plane in the hopes of observing its behaviour and comparing it qualitatively to the real wall.

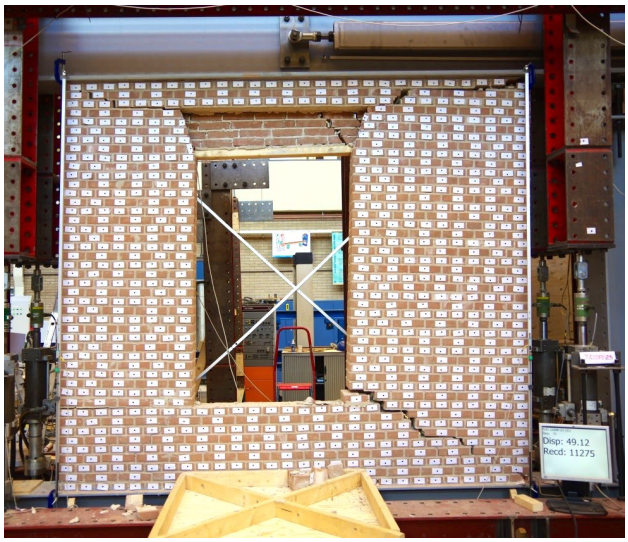

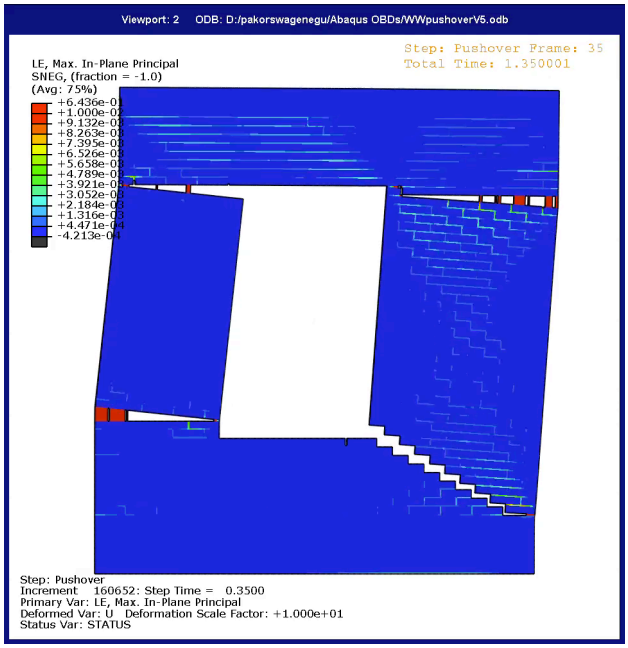

Figure A.5. Comparison of wall with a window.

Two important conclusions where drawn from this test: First, that cracks appear to be limited to the mortar interface, meaning that no damage occurs in the bricks when the wall's elements are subjected mostly to flexural stresses; and second, the vertical loads are influential in determining the lateral capacity of the wall, for high vertical stresses, the contribution provided by the bond between bricks and mortar becomes negligible.

Pushover of Shear Wall

Similarly, a squat shearwall tested cyclically in the laboratory, was reproduced monotonically with the numerical model (see Figure A.6); because of this, the results are not directly comparable but some conclusions can be drawn.

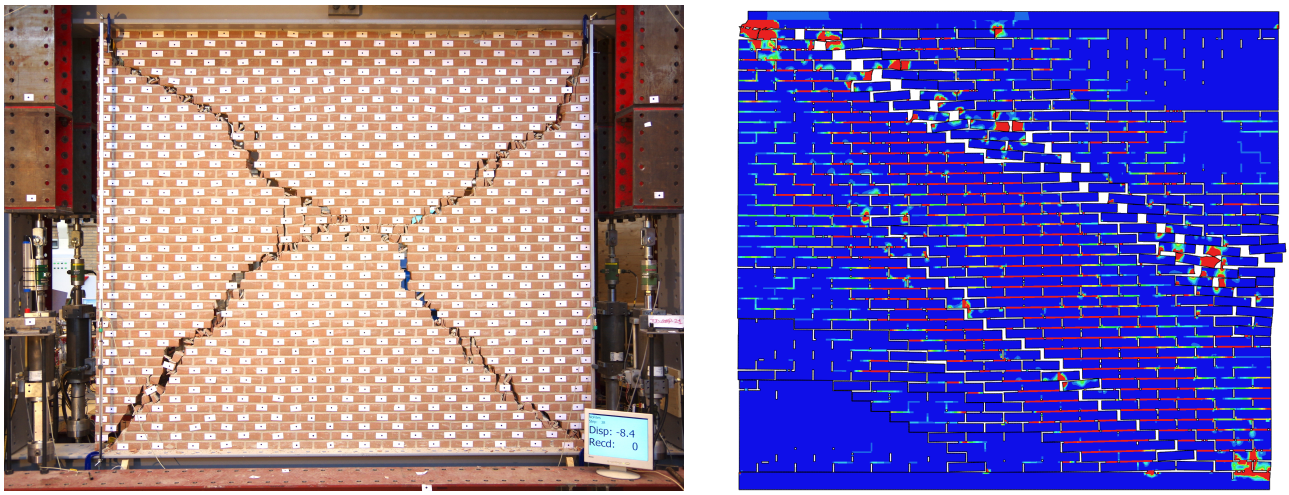

Figure A.6. Shear wall in cyclic laboratory test versus the same wall in a monotonic numerical model.

To complete a failure mechanism, the cracks have to go through the bricks, this occurs often in the middle of the brick, directly above or below a vertical mortar joint. Once this has occurred, the wall slides laterally.

Pushover of Wall With Soldier Lintel

As an example of how the numerical model can be applied, a variation of the wall with a window was modelled, here, employing a solder lintel. Sarhosis et al. (2014) and Meillyta (2012), for instance, argue that lintels and vertical stresses can influence or alter the behaviour of masonry walls.
The model was run cyclically to observe the influence of the lintel. As can be compared with Figure 4.3, the cracks at the top of the wall run in opposite directions (Figure A.7).

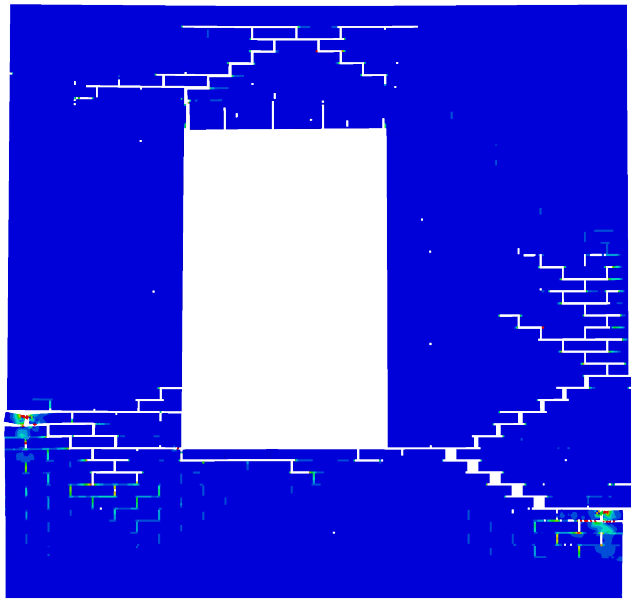

Figure A.7. A wall with a window employing a soldier lintel. Cyclic lateral displacement (increased scale) in numerical model.

Settlement of Façade

Finally, the model was applied to a settlement case. As part of the research of Giardina et al. (2013), a scale model of a façade was tested in the laboratory and attempted to be reproduced numerically (Figure A.8). The model employed contrasts with the one of this report by the use of a smeared crack single material model with continuum elements (see Section 3 for a distinction of masonry modelling techniques).

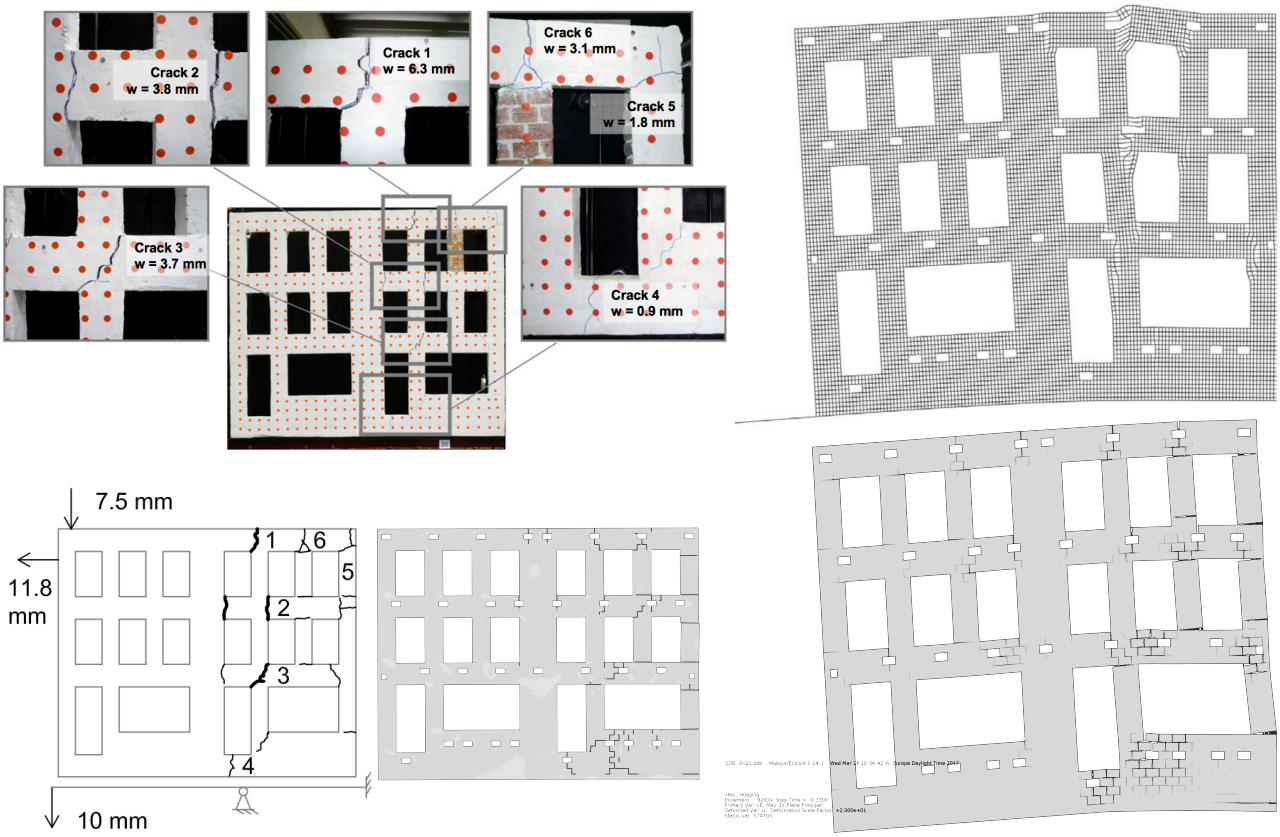

Figure A.8. Left, top to right, bottom:
a) Experimental model of façade subjected to hogging settlement with overview of main cracks;
b) Depiction of model with scheme of main cracks compared to the result of the modelling approach of this study; and
c) smeared crack model from Giardina et al. (2012), compared to
d) mortar-brick discrete crack damage model tailored for this study.

The model is able to reproduce all the crack regions and most discrete cracks.

9.4.4. Prediction Models

The refined model including post-crack interfaces was then used to predict the behaviour of the laboratory wall as described in Chapter 3. This prediction was compared to the continuum model detailed in Chapter 2, and was used to set the initial boundaries of the experimental wall.

However, since the model required 15 hours of computation and 5 hours of post-processing to evaluate 1 second of dynamic excitation, only a qualitative verification regarding the peak load, peak displacement, and crack opening and location was done. This is illustrated in the following figures.

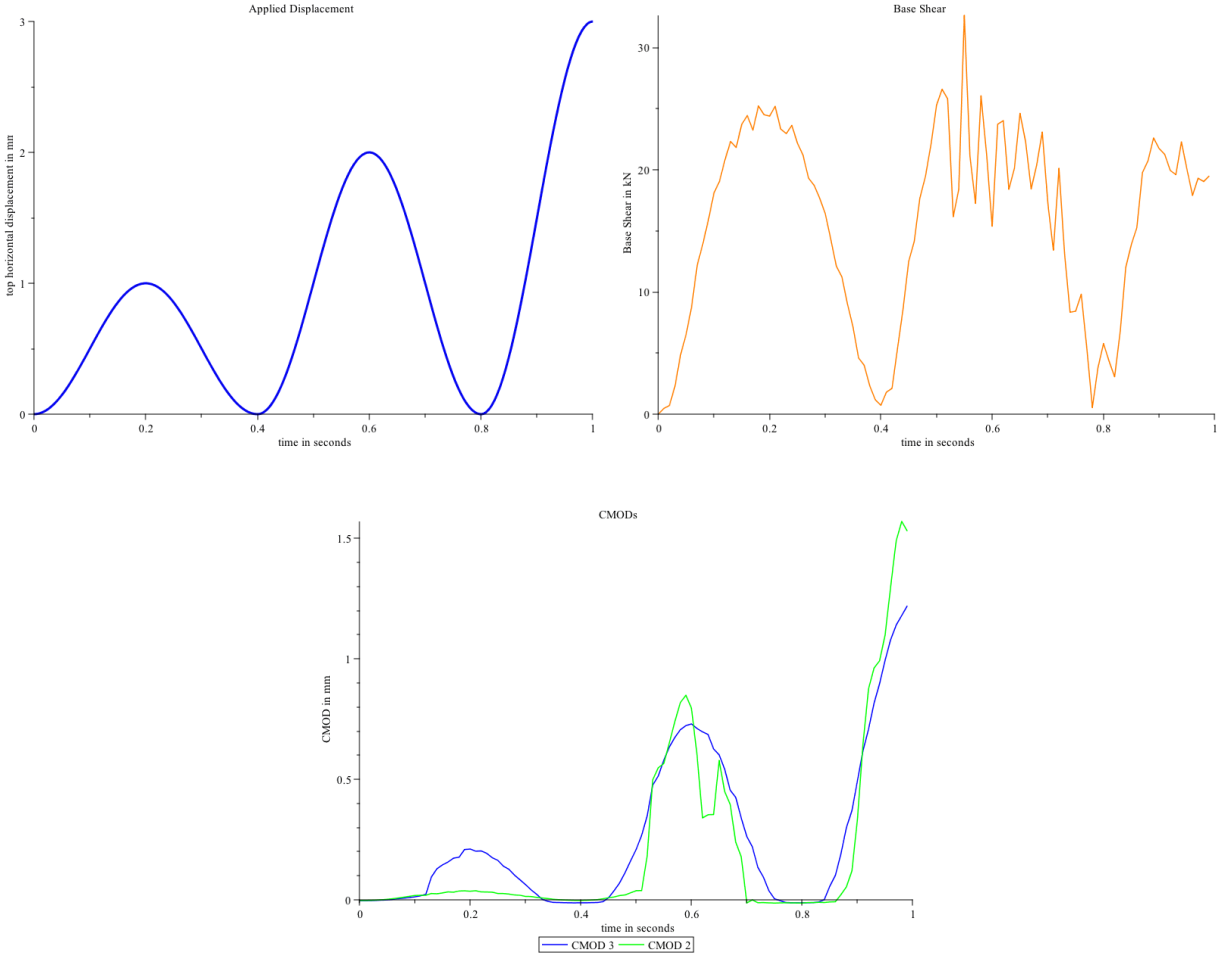

Figure A.9. Left: top lateral displacement applied in the model; right: base shear force registered; bottom: crack mouth opening displacements for cracks on the window corners, crack 2: bottom right; crack 3: top left.

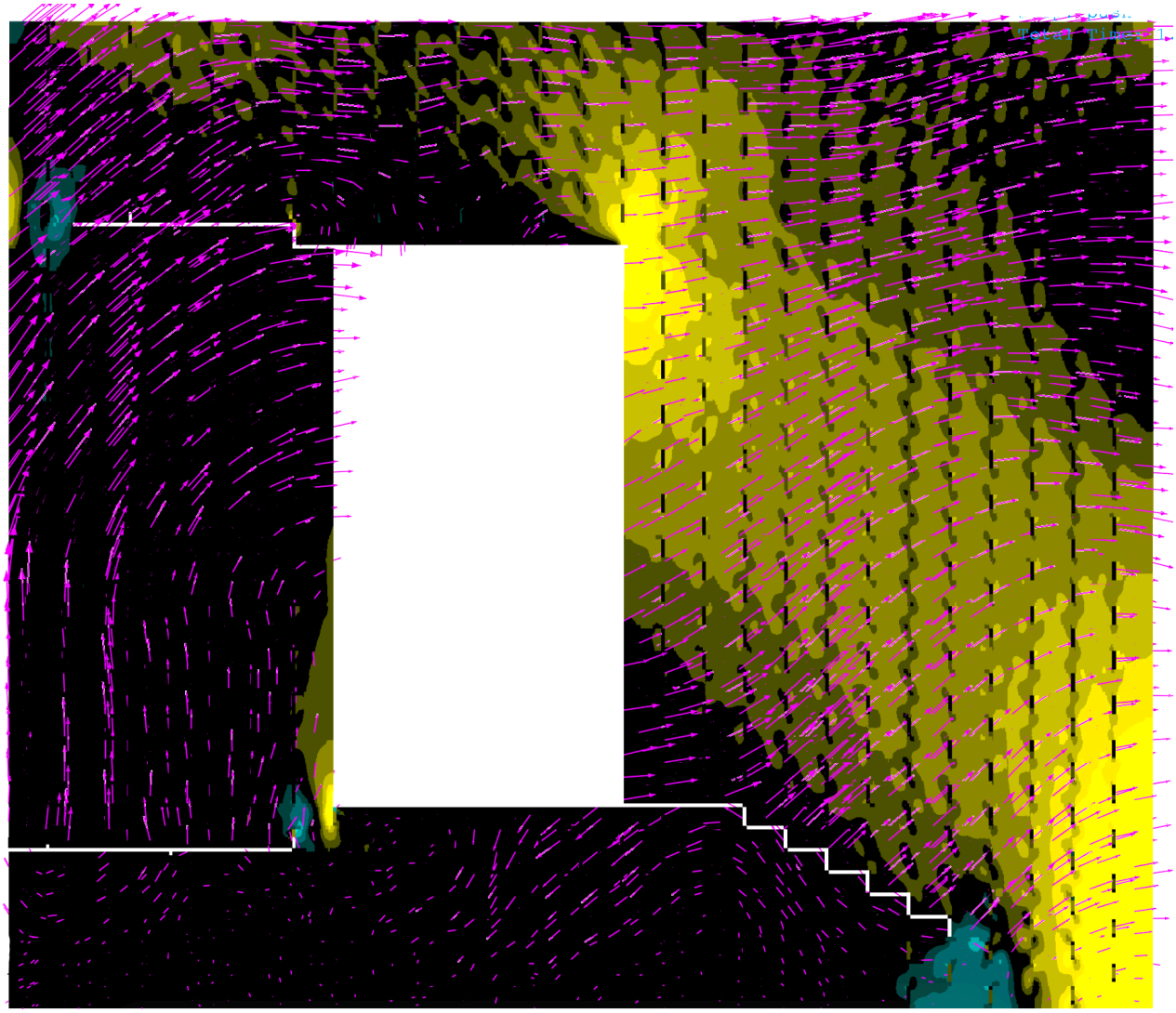

Figure A.10. FEM showing crack initiation (c_w>0.1mm) for a top lateral displacement of 2mm. High compressive stresses are shown in yellow, while high tension stresses are shown in green. The arrows indicate the displacement of the model elements revealing quasi-rigid body rotations.

In comparison to the experiments, the model proved to be quite accurate. The maximum shear load was predicted to be 25kN (filtering dynamic noise), in comparison to the experimental 23kN. Similarly, a crack width of 0.1mm was predicted at 0.70mm of top lateral displacement when in the experiments this was obtained at 0.69mm. Moreover, the location of the three cracks was almost identical. These values helped locate the sensors on the first wall and establish the first pre-test force values.

However, due to their computational expense, these models were not pursued further.

9.4.5. Post-Diction Models - Window Bank

Since the full model of the in-plane walls cannot be run for more than a few seconds of simulation due to its computational expense, only post-diction models for the window-bank tests will be elaborated. Both monotonic and repetitive tests will be replicated. However, in the appendix of this report, only the monotonic test is discussed because the repetitive tests still require validation. Figure A.11 shows an impression of the model which should be compared with Figure 4.60.

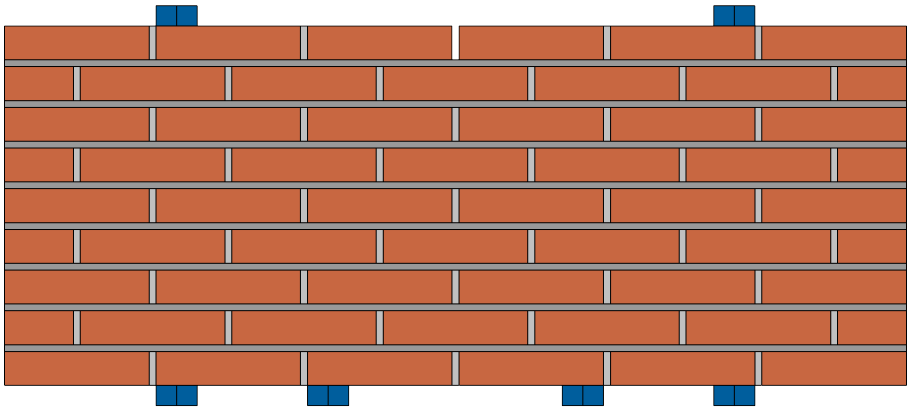

Figure A.11. Model for post-diction of window bank. In blue: supports, and the point of application of jacks and counterweights is shown.

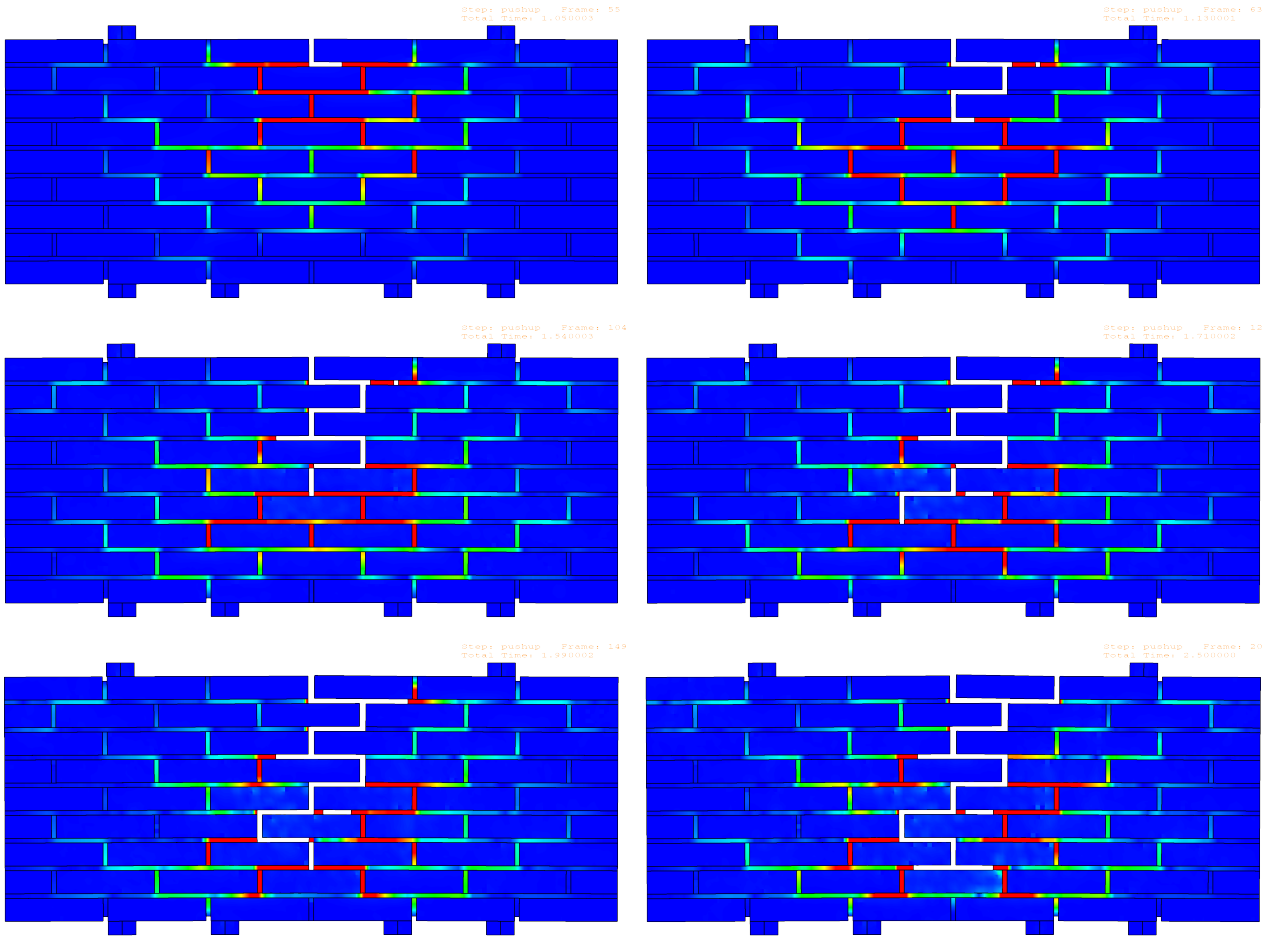

Figure A.12. Sequence of strain plots from the post-diction window bank model in Abaqus showing the progression of the vertical crack in the middle.

The model includes the continuum elements as mortar joints and the post-crack interface between bricks. It was run quasi-statically for 2 seconds to a maximum applied displacement at the jacks of 1mm. Gravity and the counterweight forces were included.

The main parameters to calibrate are: the tensile strength of the mortar (head and bed joints differing), the fracture energy of the joints to define softening, and the shear stiffness of the joints during softening. The first two parameters had already been calibrated with previous models and did not require much tweaking, nor did they influence the results considerably; while, the softening of the shear stiffness proved to be important for the type of de-interlocking crack observed and has been calibrated further. Figure A.12 shows the progression of the crack, and Figure A.13 presents a force-displacement (CMOD) graph comparing the results of the same model but with various parameter values, and multiple experimental curves.

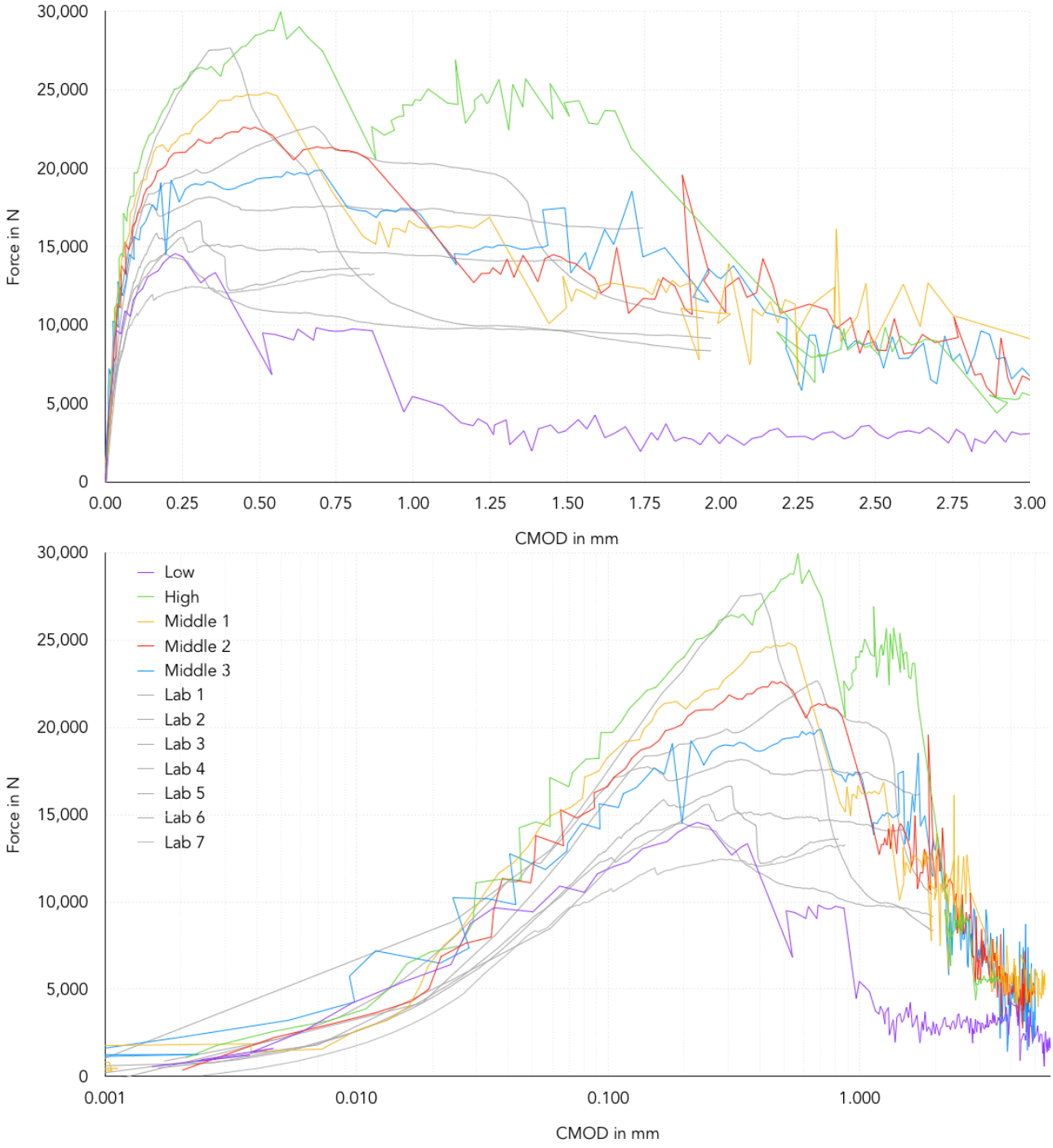

Figure A.13. Force-displacement curves comparing five models with seven laboratory curves (see Section 4.2). Top: linear displacement scale; bottom: logarithmic displacement scale.

Table 3. Micro-model property comparison for post-diction of window bank.

Model ID	End of shear softening (cracking strain)
High	2.0‰
Middle 1	1.0‰
Middle 2	0.8‰
Middle 3	0.5‰
Low	0.1‰

From Figure A.13 the following observations can be made:

- the models are able to replicate the maximum force reached by the various laboratory samples;
- the displacement at the peak is also shown quite accurately;
- in particular, the non-linear behaviour of the sample in the pre-peak zone is remarkably replicated;
- the post-peak model curves are also representative of the laboratory curves;
- the model curves are affected by dynamic noise in the late post-peak zone (quasi-static explicit analysis);
- varying only the limit shear softening strain modified heavily the maximum capacity of the model;
- the Young's modulus of the samples is significantly higher in the pre-peak region, approaching values of 9GPa in contrast with 4GPa for values computed with the peak force (see Equations 4.2 to 4.7);
- the non-linearity of the samples starts below equivalent values of stress of 0.1MPa (5kN in Figure A.13). This corresponds to the bond strength of 30kPa to 100kPa used in the models. This means that, as in the model, the non-linearity in the experiments seems to start when micro-cracks begin to form;
- if the inflexion point for the curves on the logarithmic scale (around 0.05mm) is representative of the bond strength, the equivalent flexural strength computed from the experiments (f_{x3}) seems to be 2 to 3 times higher than the bond strength (f_w) or tensile strength (f_t).

As the cracks begin to open, their shear stiffness and shear capacity drops to zero. Exactly how it drops and what is the corresponding value of cracking strain when the cracks can no longer support shear stresses can be obtained from a combined tension and shear test. These types of tests are difficult to perform, and as such, there is little information for the very weak bond of the type of masonry replicated in this study; however, performing tests like this will be necessary to further validate the behaviour of vertical cracks zig-zagging around the bricks. Figure A.14 gives an explanation of why the shear stiffness seems to play such an important role in this failure mechanism.

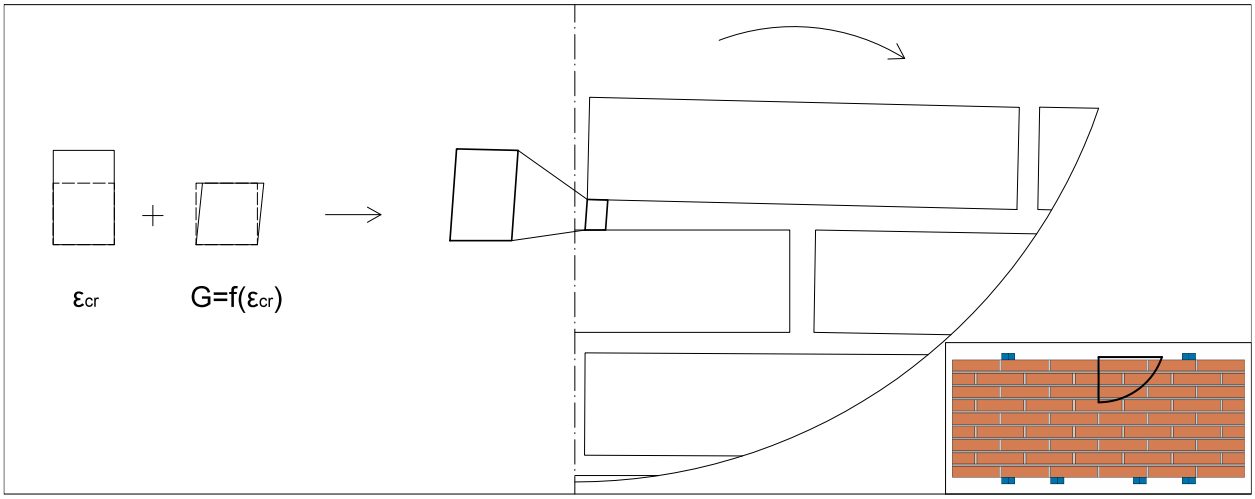

Figure A.14. Explanation for the importance of shear stiffness and capacity during crack opening for zig-zagging cracks.

9.4.6. Conclusions of Explicit Modelling With Abaqus

With the purpose of aiding the experimental investigation of brittle crack initiation and propagation in masonry walls, a discrete brick-mortar computational model was preliminary validated with Abaqus/ Explicit.
In these comparisons, the models seem to reproduce stiffness, strength, ductility and crack patterns adequately. However, cyclic actions and cyclic damage still needs to be investigated further.

The models are based on discrete mortar and brick elements, the former following a brittle cracking model based on mode I fracture energy, while the latter a concrete plasticity model that supports stiffness damage. The mortar elements are removed from participating in the model once a crack width of 0.1mm has been established. These parameters seem most successful at reproducing complex cracking patterns as seen for instance in the in-plane four-point bending test displayed in Figure A.15.

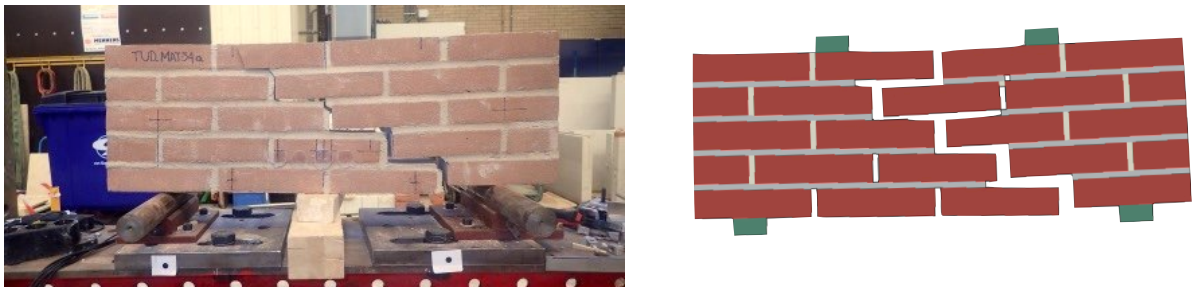

Figure A.15. Comparison of in-plane four-point bending laboratory test and numerical model.

To also reproduce reversal of loads during cyclic actions or stress releases, a brick-to-brick contact interaction is defined, which mimics the presence of a damaged mortar layer with friction and compressive load transfer.
Due to computational constraints, the micro-models can include up to 100 bricks when analysed with cyclic actions and up to 700 when the loading is limited to monotonic actions. This is summarised in Table 4.

Table 4. Summary of runnable micro-models.

Model Type and Size		Quasi-static		Dynamic	
		Monotonic	Cyclic	Up to 2s	Up to 5s
Small Specimen 4x5 Bricks	**In-Plane Out-of-Plane**	Yes	Yes	Yes	Yes
Laboratory Specimen 9x9 Bricks	**In-Plane Out-of-Plane**	Yes	Yes	Yes	Yes
Laboratory Wall 15x45 Bricks	**In-Plane**	Yes	**Limited**	Yes	**No**

9.5. Experimental Pre-Compression Test Results

Before the in-plane wall tests are conducted, a pre-test is performed. The pre-test is done by vertically loading the in-plane wall with a rate of 0.5kN/s. The pre-test has two purposes: to check the measuring system and to determine the stiffness of the wall which serves as a check that everything is in order and can also be used as an input for numerical models.
Figure A.16 shows the pre-test results of TUD_COMP-40, TUD_COMP-41 and TUD_COMP-42. It is known that TUD_COMP-42 was already damaged before the pre-test due to transportation of the wall as is described in more detail in Chapter 4. If the trendline is taken of all three samples the E-modulus is about 2700MPa. Since the transportation damage of TUD_COMP-42 could very likely influence the measured vertical stiffness of the wall, it was decided to also compute a trendline for TUD_COMP-40 and TUD_COMP-41 only. In this case the stiffness is about 3400MPa.

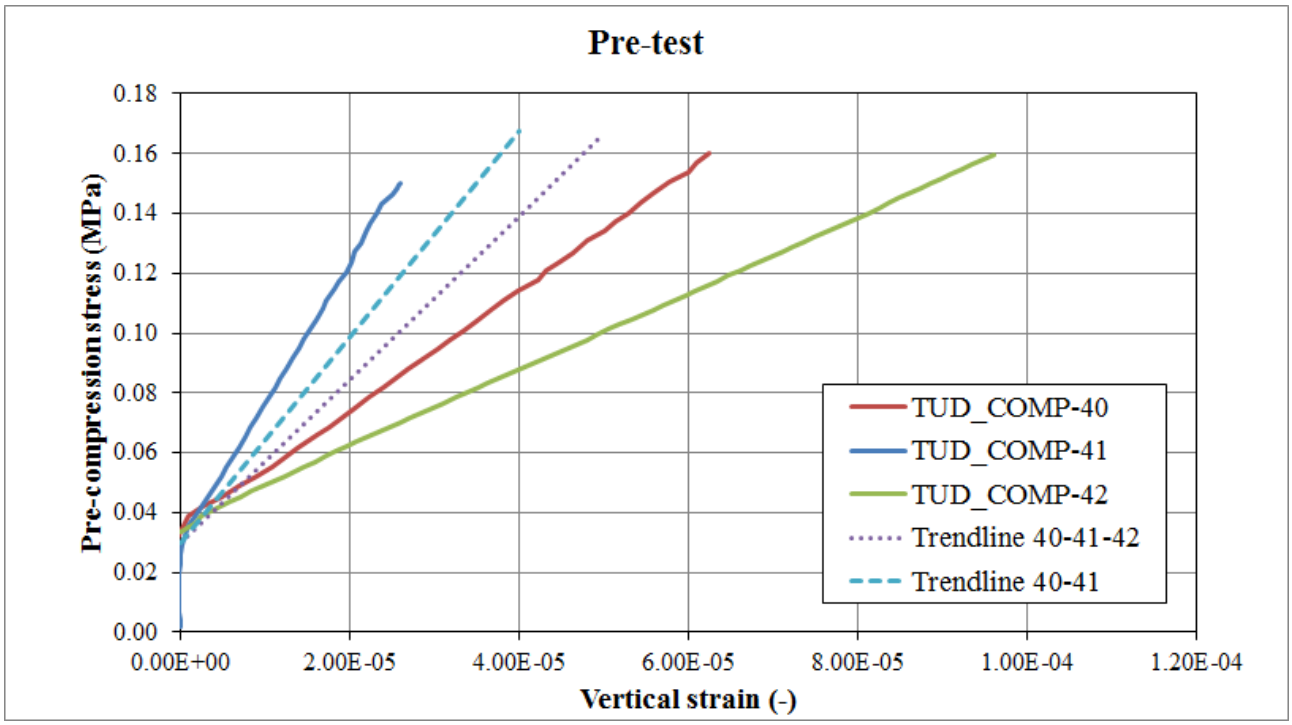

Figure A.16. Pre-test results of TUD_COMP-40, TUD_COMP-41 and TUD_COMP-42.

9.6. Program to Analyse Damage

In Section 2.6.3 the program used to analyse damage has been introduced. The workings of this first version of the program are further detailed here.
The program has proved to work reliably with computational results. Analysis of experimental results require verification and manual calibration of some program parameters to output coherent values. Future improvements of the program will focus on further automatising these steps.

The program can be subdivided into the following modules:
1. Detection of discontinuities and assignment of discontinuity value per cell
2. Grouping of nearby cells exceeding a certain discontinuity value
3. Removal of groups that fit noise criteria
4. Computation of crack width and crack length per group
5. Calculation of damage value
6. Export of summary table and verification plots

The program has been written to minimise the number of computations executed by the computer. As such, it is capable of analysing 80 cases from computational results per minute, or 10 cases of experimental results per minute; DIC results contain a significantly larger number of cells and noise.

Start Module - Configuration

Before performing any heavy calculations, the program verifies that the files provided contain consistent, numerical data. Customisation parameters are input and an estimation of the time necessary to complete the analyses is then provided by the program.
The following parameters are required by the program (defaults in brackets):
- Units (mm)
- Cell size (50 for computational data and 5.2 for experimental data)
- Minimum crack width to detect (0.1mm)
- Minimum crack length to consider (100mm)
- Distance for discontinuity check (1)
- Maximum number of merge operations (as needed)
- Export of graphs (yes, with color identification)

Module 1 - Detection of Discontinuities

Input	Output
Matrix of horizontal displacement values	Matrix of maximum discontinuity (horizontal)
Matrix of vertical displacement values	Matrix of maximum discontinuity (vertical)

The detection algorithm performs line scans to compute the difference between the current cell and the next one. If the difference is greater than a set value (say 0.1mm) it registered in a matrix. This is done in the two directions. Differences to cells with zero displacement (window, perimeter) are ignored.
To account for smoothing or de-noising of the DIC results, the detection algorithm also checks the difference in displacement with cells further away. This distance is estimated based on the size of the matrix and can be tweaked manually. In this case, the cell lying in the middle of the two check cells is assigned the discontinuity value in the matrix.

If the results are imported directly from computational exports, a third input matrix is expected already containing the discontinuities (crack width) per cell. From here on, both experimental and computational cases are treated equally by the program.

Module 2 - Grouping of Discontinuities

Input	Output
Matrix of maximum discontinuity (horizontal)	Matrix of crack group number
Matrix of maximum discontinuity (vertical)	Matrices of crack member's coordinates
	List of valid crack numbers

Neighbouring cells with discontinuities are assigned a crack number. The grouping algorithm executes a line scan in two directions and checks whether a cell with a discontinuity value neighbours other "cracked" cells. If it does, then it receives the crack number of neighbouring cells, if the neighbouring cells do not have a crack number yet, a new crack number is created. The coordinates of every cell with the same crack number is registered in a matrix for this crack number.
Because the line scan moves forward, it may fail to group cracks in a certain pattern. It is thus necessary to iteratively look for and merge neighbouring groups.
The algorithm compares a random coordinate of crack 1 with a random coordinate of crack 2. If they are found to be relatively close, all coordinates of crack 1 are compared to every coordinate of crack 2; if any are found to be neighbouring, the matrices of coordinates are merged, crack 2 is removed from the list of valid crack numbers, and the matrix with crack numbers per cell is overwritten for all coordinates of crack 2. This is done for all valid crack numbers without repeating any crack number combinations. After all cracks have been compared, the process is run again to further merge nearby groups of discontinuities. The merge iterations continue until no more groups can be merged, or up to a customisable limit number of runs.
The final output of this module are: a few matrices containing the coordinates of all the cells that belong to each group, the main matrix with the crack number of each cell, and a list with all valid crack numbers.

Module 3 - Removal of Noise

Input	Output
Matrix of crack group number	List of valid crack numbers
Matrices of crack member's coordinates	
List of valid crack numbers	

The following groups of cells (cracks) are considered noise and eliminated from the list with valid crack numbers:

- Groups with a few cells (customisable, the minimum is 1).
- Groups forming a crack with a length* shorter than specified (default 100mm).
- Groups forming a shape resembling a circle or spot.

* see next module.

Module 4 - Crack Width and Length

Input	Output
List of valid crack numbers	Matrix with width and length per crack
Matrices of crack member's coordinates	
Matrix of maximum discontinuity (horizontal)	
Matrix of maximum discontinuity (vertical)	

Next, an algorithm selects the crack width for each valid crack group by looking at the discontinuities found for each of the crack cell's coordinates and taking the maximum (or the value belonging to the 99th quantile if heavy noise has been found).
To compute the length, the algorithm looks at the extreme coordinate pairs of the group: either top-left and bottom-right or the other way around. Based on these coordinate pairs, a distance and an angle with the horizontal can be determined. Because cracks travel either horizontally or vertically along the joints, the real length of the crack can be computed based on the distance between the two extreme points and the angle of the distance vector. The length can attain a maximum value equal to the distance multiplied by $\sqrt{2}$.

Module 5 - Damage Value Ψ

Input	Output
List of valid crack numbers	Psi value
Matrix with width and length per crack	

Finally, based on the number of valid cracks, their width, and their length, the program computes the Psi value.

Module 6 - Export of Results

All the operations detailed above can be batch executed. This means that a large number of pairs of input matrices can be analysed by the program. All batch cases must have input matrices of equal size and be compatible with the same custom parameters (minimum crack width, length, etc.). This is the case for all computational results, and the experimental results separated into the batches of DIC.

The final psi values for each damage case are summarised into a table and exported as a spreadsheet. To verify that the program found correct cracks, a plot with the cracks overlaid on a scheme of the wall is exported as an image file for each of the damage cases. If desired, the cracks are identified with differing colors and their main properties.

Future Improvements

This is a first version of the program. Analysis of experimental results is not yet as reliable as that of computational results. Some points of improvement are noted:

- Adaptive distance for discontinuity check.
- Smarter noise removal looking at the distribution of discontinuity values per crack group.
- Comparable length of cracks between cases.